ТЕПЛО- И МАССООБМЕН В НАЗЕМНЫХ И КОСМИЧЕСКИХ ЭНЕРГЕТИЧЕСКИХ ДВУХФАЗНЫХ СИСТЕМАХ С ВЫСОКИМ ТЕПЛОВЫДЕЛЕНИЕМ

Подборка избранных опубликованных работ
в отечественных рецензируемых журналах (12),
в журналах Q1 (21) и патентов (14)

КАБОВ Олег Александрович

д.ф.-м.н., профессор, заведующий лабораторией
интенсификации процессов теплообмена

Институт теплофизики им. С.С. Кутателадзе
Сибирское отделение Российской академии наук
г. Новосибирск

2017 - 2022 г.

Краткая биография



Кабов Олег Александрович родился 10 января 1956 г., в с. Базанча Таштогольского района Кемеровской области.

В 1978 году окончил Томский государственный политехнический институт по специальности «теплофизика и атомные станции» и был зачислен в лабораторию теплообмена при фазовых переходах Института теплофизики СО АН СССР г. Новосибирск, возглавляемую академиком С.С. Кутателадзе.

С 1988 г. - организатор и заведующий лабораторией интенсификации процессов теплообмена Института теплофизики им. С.С. Кутателадзе СО РАН; с 1999 г. - доктор физико – математических наук; с 2007 г. - профессор; с 2015 - заведующий лабораторией энергонапряженных тепловых процессов физического факультета Новосибирского государственного университета (по совместительству); с 2019 г. - профессор кафедры «Тепловые электрические станции», Новосибирского государственного технического университета (по совместительству).

Подготовка кадров и научно - организационная работа

- h- индекс по базе данных «Web of Science» - 29, по «Scopus» - 32, по РИНЦ - 34.
- За последние пять лет опубликовано 12 статей в отечественных рецензируемых журналах, 21 статья в журналах Q1 (WoS и Скопус), получено 14 патентов.
- За последние 12 лет пяти студентам Лаборатории присуждены медали РАН в области физико-технических проблем энергетики (присуждается 1-2 медали в год).
- Научный руководитель девяти кандидатских диссертаций.
- Подготовлено два доктора наук, один из которых избран Профессором РАН и является деканом механико-математического факультета Новосибирского Госуниверситета.
- Один из учеников в 2018 году возглавил вновь созданную в ИТ СО РАН молодежную лабораторию энергоэффективных технологий для наземных и космических применений.
- Член двух диссоветов: Д 24.1.129.01 в ИТ СО РАН и Д 212.173.03 в НГТУ.
- Принимал участие в девяти кампаниях параболических полетов с использованием технической базы Европейского космического агентства (ЕКА) и лично руководил экспериментами. Награжден медалью ЕКА.
- Участник подготовки и проведения международного космического эксперимента «Многомасштабное кипение» на Международной космической станции (начало подготовки – 2005г., эксперимент – 2019 - 2021г.).
- С 2007 - член Национального комитета по тепломассообмену РАН.
- С 2013 организатор и главный редактор международного журнала «*Interfacial Phenomena and Heat Transfer*», Q3.
- С 2009 член редакционной коллегии международного журнала *Microgravity Science and Technology*, Q1.
- Организатор и сопредседатель двух международных конференций «Two-phase systems for Ground and Space applications» (с 2006) и «Interfacial Phenomena and Heat Transfer» (с 2016).

Кандидат в члены-корреспонденты РАН
по Отделению энергетики, машиностроения, механики и процессов управления РАН
на вакансию для Сибирского отделения РАН
по специальности "Энергетика, теплофизика"

КАБОВ Олег Александрович

Заведующий лабораторией ФБГУН Института теплофизики им. С.С. Кутателадзе СО РАН, г. Новосибирск, р. 10.01.1956, доктор физико-математических наук, профессор

Кабов О.А. – специалист в области интенсификации процессов теплообмена, теплообмена при фазовых переходах, двухфазных потоков и пленочных течений, автор и соавтор 216 статей в журналах Web of Sciences, 2 глав в монографиях, 24 российских и международных патентов, за последние пять лет 21 статьи в журналах Q1 (WoS. и Скопус). Индекс Хирша по WoS равен 29.

Основные научные результаты Кабова О.А.:

обнаружено и исследовано формирование самоорганизующихся пространственных течений в движущихся пленках жидкости при их локальном и однородном нагреве со стороны подложки;

решены задачи интенсификации процесса конденсации пара на поверхностях сложной формы в условиях определяющего влияния капиллярных сил, разработаны методы расчета;

создана новая система охлаждения электронного оборудования, основанная на испарении тонкого слоя жидкости увлекаемого потоком газа, с плотностью теплового потока до 1.3 кВт/см^2;

исследовано испарение в области линии контакта газ- жидкость – твердое тело, а также явление Лейденфроста для микрокапель 10 - 50 мкм, разработаны методы расчета;

выполнен цикл исследований по кипению жидкости на одиночном центре парообразования на МКС, а также по теплообмену в двухфазных системах при микро- и повышенной гравитации в условиях параболических полетов.

Кабовым О.А. подготовлены два доктора наук и 9 кандидатов наук, среди его учеников - профессор РАН и заведующий лабораторией. Пять студентов лаборатории получили медали РАН.

Кабов О.А. - организатор и главный редактор международного журнала «Interfacial Phenomena and Heat Transfer», организатор и сопредседатель двух международных конференций, член Национального комитета РАН по тепломассообмену, член двух диссертационных советов: Д 24.1.129.01 в ИТ СО РАН и Д 212.173.03 в НГТУ.

Кабов О.А. выдвинут кандидатом в члены-корреспонденты РАН по Отделению энергетики, машиностроения, механики и процессов управления РАН на вакансию для Сибирского отделения РАН по специальности "Энергетика, теплофизика" Ученым советом ФБГУН Института теплофизики им. С.С. Кутателадзе СО РАН, академиками РАН Алексеенко С.В., Марковичем Д.М. и Петровым О.Ф.

Публикации в рецензируемых отечественных журналах 2017-2022 (12) *

1. *Роньшин Ф.В., Чиннов Е.А., Дементьев Ю.А., Кабов О.А. Мостиковый режим течения в микроканалах // Доклады Российской академии наук. Физика, технические науки. – 2021. - Т. 499. – №1. – С. 43-47.
2. *Люлин Ю.В., Крета А.С., Кабов О.А. Влияние скорости потока газа на конвекцию в горизонтальном испаряющемся слое жидкости // Теплофизика и аэромеханика. – 2019. - Т. 26. – №1. – С. 141-146.
3. Чеверда В.В., Кабов О.А. Кризис теплообмена на микрооребрённом нагревателе при течении плёнки жидкости FC-72 под действием потока газа в миниканале // Теплофизика и аэромеханика. – 2019. - Т. 26. – №3. – С. 497-501.
4. *Кабова Ю.О., Кузнецов В.В., Кабов О.А. Движение ручейка жидкости в микроканале при спутном потоке газа // Теплофизика и аэромеханика. – 2018. - Т. 25. - № 6. - С. 899– 908.
5. *Роньшин Ф.В., Чеверда В.В., Чиннов Е.А., Кабов О.А. Влияние свойств жидкости на режимы двухфазного течения в широком прямоугольном микроканале // Письма в Журнал технической физики. – 2018. - Т. 44. - № 7. – С. 69-77.
6. Шатский Е.Н., Чиннов Е.А., Зайцев Д.В., Семенов А., Кабов О.А. Влияния вязкости жидкости на формирование термокапиллярных структур // Письма в журнал технической физики. – 2017. - Т.43. - №23. - С. 69-76.
7. *Чеверда В.В., Карчевский А.Л., Марчук И.В., Кабов О.А. Плотность теплового потока в области контактной линии капли, лежащей на горизонтальной поверхности тонкой нагреваемой фольги // Теплофизика и аэромеханика. – 2017. - Т. 24. - № 5. - С. 825-828.
8. *Гончарова О.Н., Резанова Е.В., Люлин Ю.В., Кабов О.А. Изучение конвективных течений жидкости и спутного потока газа с учетом испарения // Теплофизика высоких температур. – 2017. - Т. 55. - № 6. – С.1–13.
9. Люлин Ю.В., Спесивцев С.Е., Марчук И.В., Кабов О.А. Исследование динамики разрыва тонких слоев жидкости в условиях точечного нагрева и образования капельного кластера // Теплофизика и Аэромеханика. – 2017. – Т. 24. - № 6. – С. 977-980.
10. *Мальцев Л.И., Поджаров Ю.С., Кабов О.А. Критерий роста сухих пятен в изотермических пленках жидкости на горизонтальной подложке // Теплофизика и аэромеханика. – 2017. - Т. 24. - № 3. - С. 395-399.
11. Марчук И.В., Барский А.А., Кабов О.А. Моделирование пленочной конденсации пара на криволинейных ребрах с отсосом конденсата из межреберных канавок // Сибирский журнал индустриальной математики. – 2017. - Т. 20. - №3. - С. 63-69.
12. Чеверда В.В., Кабов О.А. Экспериментальное исследование ручейкового течения легкокипящей жидкости в мини-канале под действием потока газа // Письма в журнал технической физики. – 2017. - Т. 43. - № 6. - С. 31-38.

* - звездочкой отмечены статьи, включенные в подборку избранных трудов (7)

ДОКЛАДЫ РОССИЙСКОЙ АКАДЕМИИ НАУК. ФИЗИКА, ТЕХНИЧЕСКИЕ НАУКИ, 2021, том 499, с. 43–47

МЕХАНИКА

УДК 532.6

МОСТИКОВЫЙ РЕЖИМ ТЕЧЕНИЯ В МИКРОКАНАЛАХ

© 2021 г. Ф. В. Роньшин[1,*], Е. А. Чиннов[1], Ю. А. Дементьев[1], О. А. Кабов[1]

Представлено академиком РАН С.В. Алексеенко 28.05.2021 г.
Поступило 28.05.2021 г.
После доработки 28.05.2021 г.
Принято к публикации 03.06.2021 г.

В результате исследований двухфазных потоков в щелевых микроканалах обнаружен и изучен новый режим течения – мостиковый. Мостики представляют собой вертикальные перемычки между пленками жидкости, расположенными на нижней и верхней сторонах канала. Установлено, что с увеличением расходов газа и жидкости мостики начинают деформироваться, а затем разрушаться. Определены критические числа Вебера, характерные для деформации и разрушения жидкостных мостиков. Предложена новая классификация режимов двухфазного течения в микроканалах на основе полученных экспериментальных данных.

Ключевые слова: мостиковый режим течения, плоский микроканал, двухфазный поток

DOI: 10.31857/S2686740021040118

В настоящее время разрабатывается значительное количество микрофлюидных устройств: датчики расхода, клапаны, системы обработки жидкостей для химического анализа, насосы, разделительные и смешивающие каналы, детекторы химических веществ. Устройства микрофлюидики создаются для генерации и контроля монодисперсных капель и пузырьков. Данная область является одной из наиболее быстроразвивающихся благодаря широкому применению в биологии [1, 2], химии [3] и нанотехнологиях [4, 5]. Кроме того, в настоящее время происходит миниатюризация теплообменных устройств, вследствие чего микроканальные системы охлаждения получают широкое применение благодаря высокой эффективности [6].

Обзор работ по исследованию двухфазного течения в микроканальных системах представлен в [7, 8]. Показано, что в микроканальных системах капиллярные силы оказывают существенное влияние на двухфазное течение, появляются новые режимы и неустойчивости. В работе [9] показано, что с уменьшением размеров канала наблюдается тенденция образования капель в каналах. Детальный обзор работ по динамике капель в различных условиях в двухфазных системах недавно опубликован в [10]. В трубах диаметром более 1 мм при высоких скоростях газа (более 10 м/с) капли формируются при переходе от кольцевого режима к дисперсно-кольцевому. С уменьшением размеров каналов капли начинают формироваться и при меньших скоростях вследствие преобладания капиллярных сил. В плоских микроканалах обнаружен режим, в котором наблюдаются вертикальные мостики жидкости между верхней и нижней стенками микроканала. Данный режим наблюдается только в условиях хорошей смачиваемости, когда контактный угол близок к нулю. Целью данной работы является детальное изучение мостиков, представляющих вертикальные жидкостные перемычки, и режимов течения, в которых они формируются.

Рабочий участок, используемый в эксперименте, состоит из двух пластин (стекла и нержавеющей стали), между которыми зажимаются прокладки, регулирующие высоту микроканала. В нижней пластине из нержавеющей стали создано плоское сопло для ввода жидкости. При исследовании газожидкостного течения по каналу движется газ, а снизу под небольшим углом (11°, плавный смеситель) подводится жидкость. Таким образом, создается плоский микроканал с соотношением сторон более 100. В работе использовались микроканалы следующего поперечного сечения: 0.13 × 20 мм, 0.1 × 30 мм и 0.16 × 20 мм. В качестве газа использовался азот высокой чистоты. В качестве рабочих жидкостей использовались вода, изопропиловый спирт и FC-72. Перед экспериментом через микроканал длительное время прокачивалась жидкость для обеспечения условий хорошей смачиваемости. Газ поступает в микроканал из баллона, расход контролируется при по-

[1] *Институт теплофизики им. С.С. Кутателадзе Сибирского отделения Российской академии наук, Новосибирск, Россия*

*****E-mail: f.ronshin@gmail.com*

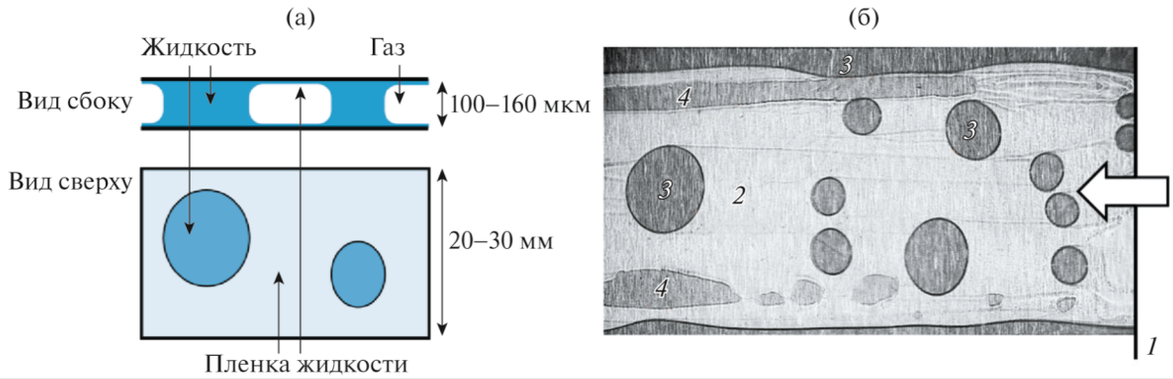

Рис. 1. Мостиковый режим течения: (а) схематическое изображение (б) шлирен-фотография в микроканале сечением 0.13 × 20 мм, жидкость – изопропиловый спирт, газ – азот. Обозначения: *1* – жидкостное сопло, *2* – пленки жидкости на верхней и нижней стенках микроканала, *3* – области, заполненные жидкостью, *4* – осушенные области.

мощи высокоточных регуляторов расхода Bronkhorst в диапазоне от 20 до 10 000 мл/мин. Жидкость подается в микроканал при помощи высокоточного шприцевого насоса Cole-Parmer EW-74905-54. Визуализация двухфазного течения происходит при помощи модификации шлирен-метода, описанной в работе [11]. Для визуализации быстропротекающих процессов в микроканале шлирен-система была модернизирована при помощи скоростной камеры Vision Research Phantom v.7.0 со скоростью съемки 1000 кадров в секунду с пространственным разрешением 50 мкм/пиксель. Далее полученные изображения обрабатываются и вычисляются параметры двухфазного течения.

Выполнено экспериментальное исследование газожидкостного течения. Обнаружена широкая область режимов течения, когда по микроканалу движутся жидкостные мостики (плоские “капли”). Верхняя и нижняя стенка микроканала при этом смочены, жидкостные перемычки движутся по пленкам жидкости. Характерный диаметр таких жидкостных мостиков может быть порядка ширины микроканала (несколько миллиметров), при этом их высота соответствует высоте микроканала (100, 130 и 160 мкм). Таким образом, в данном исследовании мостики предполагаются плоскими и исследуется плоское течение. На рис. 1 показан мостиковый режим течения (а) схематически и (б) шлирен-фотография в канале 0.13 × 20 мм, где в качестве жидкости используется изопропиловый спирт, а в качестве газа – азот. Формирование мостиков жидкости, как правило, происходит непосредственно возле жидкостного сопла вследствие фронтальной неустойчивости [12]. Далее мостики скользят по пленкам жидкости, оставляя за собой характерные следы (утолщение пленки жидкости). Также мостики могут отделяться от жидкости, движущейся вдоль боковых стенок канала вследствие развития волновой неустойчивости (Кельвина–Гельмгольца) [12]. Скорость жидкости, движущейся вдоль боковых стенок канала, меньше скорости газового потока в центральной части канала, за счет этого наблюдаются характерные волны. Когда амплитуда волн возрастает, наблюдаются выбросы жидкости в газовый поток, которые затем приобретают характерную эллипсоидальную форму. При этом форма мостиков, образованных вследствие этих двух различных механизмов (боковая и фронтальная неустойчивости) не отличается.

При небольших расходах газа и жидкости мостики имеют форму, близкую к кругу. С увеличением расходов мостики начинают деформироваться, приобретая эллипсоидальную форму. При дальнейшем увеличении расходов газа и жидкости мостики большого размера начинают разрушаться, формируя два мостика меньшего размера. Таким образом, можно выделить третий механизм формирования мостиков – вследствие разрушения крупных мостиков при достижении критического значения деформации. Исследована деформация мостиков жидкости, когда они имеют эллипсоидальную форму, в зависимости от числа Вебера смеси. Деформация определялась следующим образом:

$$\mathrm{Def} = \frac{a}{b}, \tag{1}$$

где a соответствует большой полуоси эллипсоидального мостика, а b – малой полуоси. Число Вебера определялось следующим образом:

$$\mathrm{We} = \frac{\rho D U_M^2}{\sigma}, \tag{2}$$

где ρ – плотность газа, $D = \sqrt{ab}$ – эквивалентный диаметр, $U_M = U_{SL} + U_{SG}$ – приведенная скорость смеси, σ – поверхностное натяжение. Приведенные скорости газа U_{SG} и жидкости U_{SL} определялись как объемный расход газа и жидкости соответственно, деленный на площадь поперечного

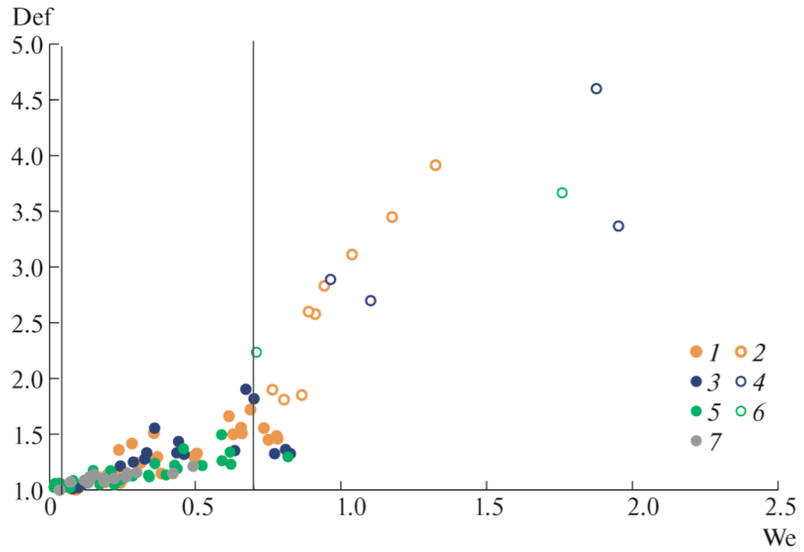

Рис. 2. Зависимость деформации мостиков от числа Вебера смеси. (*1*, *2*) – микроканал сечением 0.16 × 20 мм, жидкость FC-72, газ – азот, *1* – деформация мостиков; *2* – разрушение мостиков; (*3*, *4*) – микроканал сечением 0.13 × 20 мм, жидкость – изопропиловый спирт, газ – азот, *3* – деформация мостиков; *4* – разрушение мостиков; (*5*, *6*) – микроканал сечением 0.13 × 20 мм, жидкость FC-72, газ – азот; *5* – деформация мостиков; *6* – разрушение мостиков; *7* – микроканал сечением 0.1 × 30 мм, жидкость – вода, газ – азот, деформация мостиков.

сечения канала. На рис. 2 показаны значения деформации мостиков жидкости в зависимости от числа Вебера смеси для всех используемых рабочих жидкостей (вода, изопропиловый спирт, FC-72) и всех исследуемых в работе микроканалов (сечения 0.1 × 30 мм, 0.13 × 20 мм и 0.16 × 20 мм). Можно выделить три характерные области на графике. Первая, при небольших числах Вебера (We < 0.1), когда мостики имеют форму близкую к кругу. Деформация в этом случае не превышает 1%. С увеличением числа Вебера мостики начинают деформироваться. В диапазоне чисел Вебера 0.1 < We < 0.7 наблюдаются эллипсоидальные мостики жидкости, с ростом числа Вебера деформация возрастает. При этом, когда мостики формируются непосредственно возле жидкостного сопла, значение их деформации незначительное и возрастает по мере движения по каналу, пока не достигнет постоянного значения. Измерения проводились в тот момент, когда форма мостика переставала меняться. При больших значениях деформации разброс значений на графике выше за счет того, что форма мостика может незначительно изменяться со временем. При числах Вебера We > 0.7 деформация мостиков становится настолько большой, что возрастает со временем, а затем мостики разрушаются на два мостика меньшего размера. В этом случае деформация мостиков измерялась в момент перед распадом, когда они имеют форму, близкую к эллипсу. На графике мостики, которые после деформации распадались, указаны незакрашенными маркерами. Большой разброс на графике объясняется тем, что перед разрушением деформация мостика существенно изменяется.

Поперечные размеры таких мостиков существенно зависят от скоростей газа и жидкости. На рис. 3 представлены распределения размеров мостиков в микроканале сечением 0.16 × 20 мм, газ – азот, жидкость – FC-72 в зависимости от приведенных скоростей газа и жидкости. С увеличением приведенной скорости газа интенсивность формирования мостиков возрастает, а их характерный размер уменьшается. Связано это с тем, что при высоких расходах газа мостики большего размера, как правило, разрушаются, формируя мостики меньшего размера. При фиксированной приведенной скорости газа с увеличением приведенной скорости жидкости наблюдается обратная тенденция. С увеличением приведенной скорости жидкости наблюдается тенденция формирования мостиков большего размера. Связано это с тем, что газосодержание в потоке уменьшается и мостики начинают сливаться, формируя мостики большего размера. Механизмы этого процесса близки к механизмам коалесценции пузырей при пузырьковом режиме течения, когда с увеличением газосодержания пузыри начинают сливаться.

На рис. 4 представлена режимная карта двухфазных течений в микроканале сечением 0.13 × 20 мм, газ – азот, жидкость – FC-72. Маркерами на графике показаны классические режимы, характерные для плоских микроканалов: струйный, пузырьковый, вспененный, раздельный и кольцевой. Подробно методика определения границ режимов двухфазных течений описана в работе [10]. Результаты измерений показывают, что в плоских микроканалах в условиях хорошей смачиваемости необходима новая классификация

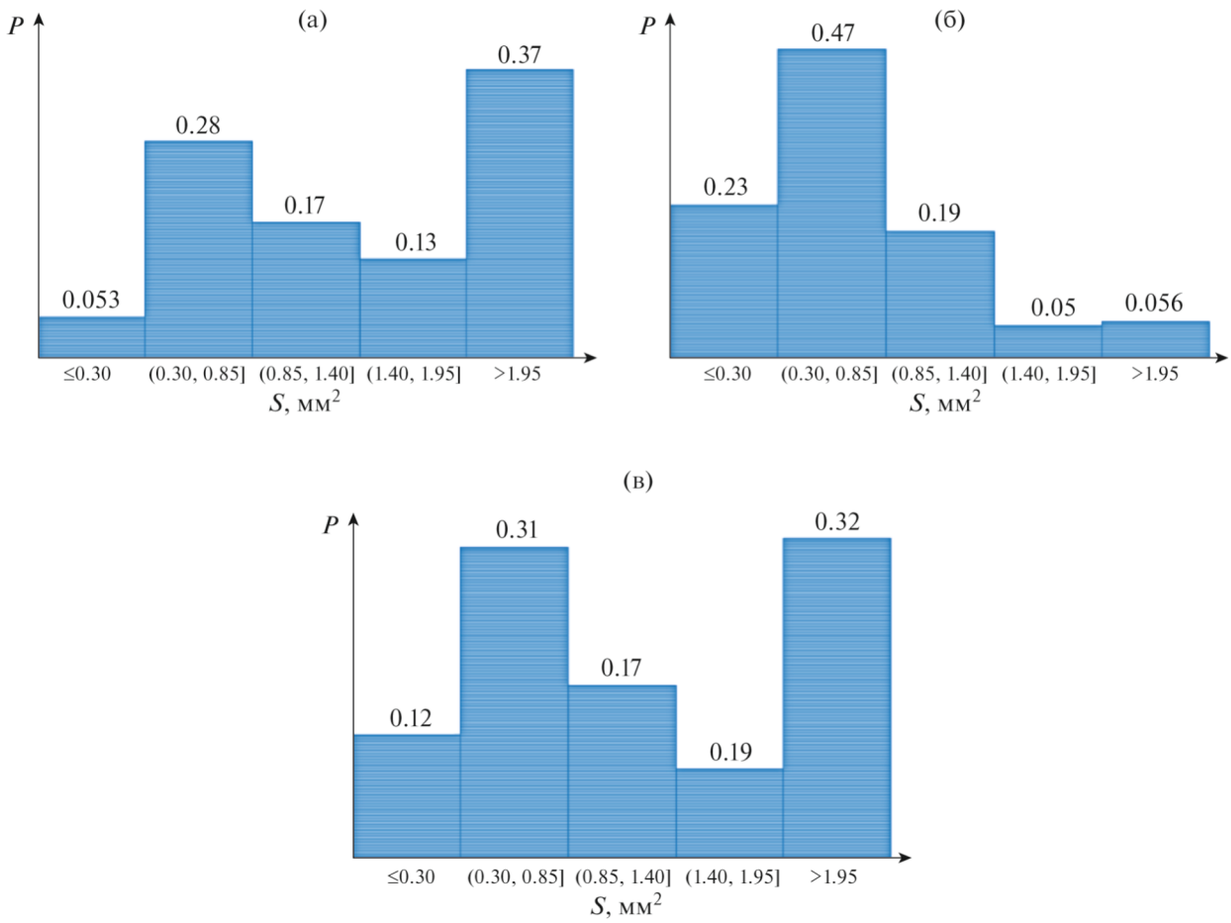

Рис. 3. Распределение площади мостиков в микроканале сечением 0.16 × 20 мм, газ – азот, жидкость – FC-72. (а) U_{SL} = = 0.0056 м/с; U_{SG} = 0.28 м/с; (б) U_{SL} = 0.0056 м/с; U_{SG} = 1.11 м/с; (в) U_{SL} = 0.028 м/с; U_{SG} = 1.11 м/с. S – интервал размеров мостиков; P – вероятность нахождения размера мостика в заданном интервале.

режимов двухфазных течений. Пузырьковый режим течения наблюдается, когда по микроканалу движутся пузыри газа, характерный размер которых меньше ширины микроканала. Мостиковый режим течения, или инверсионный, наблюдается, когда вертикальные перемычки жидкости между верхней и нижней стенками канала движутся по пленкам жидкости. Если рассматривать течение плоским, мостиковый режим течения напоминает инвертированный пузырьковый режим течения, когда вместо газовых пузырей наблюдаются вертикальные жидкостные перемычки (мостики). Область мостикового режима течения существенно зависит от высоты микроканала и смачиваемости поверхности, так как данный режим формируется только, когда обе стенки микроканала смочены. На рис. 4 зона мостикового режима течения закрашена. При использовании воды в качестве рабочей жидкости мостики впервые появляются в микроканале высотой 440 мкм [9] только при высоких расходах газа и жидкости. При уменьшении высоты канала интенсивность образования мостиков возрастает. В канале высотой 56 мкм такие мостики формируются практически во всем диапазоне расходов газа и жидкости [11]. В плоских микроканалах мостиковый режим течения можно разделить на три подрежима: струйный, вспененный и кольцевой. При высоких приведенных скоростях газа и небольших приведенных скоростях жидкости наблюдается раздельный режим, когда по нижней стенке канала движется пленка жидкости, увлекаемая потоком газа. Мостиков жидкости в таком режиме не наблюдается, так как верхняя стенка микроканала остается осушенной.

Таким образом, в настоящей работе проведено комплексное экспериментальное исследование нового режима двухфазных течений – мостикового, характерного для плоских микроканалов. Обнаружено три механизма формирования мостиков жидкости: отделение мостиков от жидкости, движущейся по боковым сторонам канала вследствие развития неустойчивости Кельвина–Гельмгольца; формирование непосредственно возле сопла жидкости (фронтальная неустойчивость); и вследствие разрушения вертикальных жидкостных перемычек

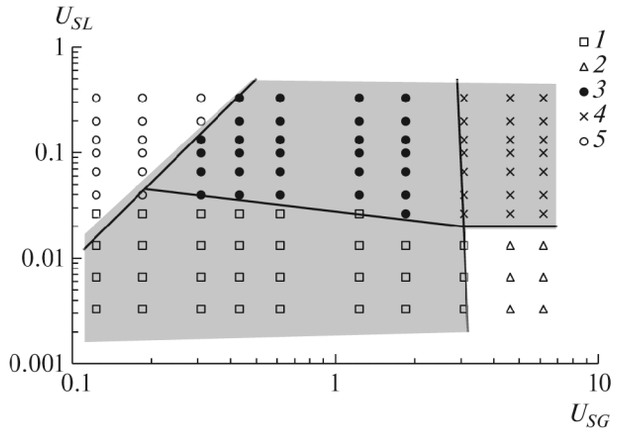

Рис. 4. Карта режимов двухфазных течений в микроканале сечением 0.13 × 20 мм^2, газ – азот, жидкость – FC-72. Режимы течения: *1* – струйный, *2* – раздельный, *3* – вспененный, *4* – кольцевой, *5* – пузырьковый. Закрашенная область соответствует области мостикового режима течения.

при деформации. Определены критические числа Вебера, при которых мостики начинают деформироваться и разрушаться. Предложена новая классификация режимов: пузырьковый (по каналу движутся пузырьки газа), инверсионный, или мостиковый (когда в классических режимах наблюдается движение мостиков жидкости, представляющих из себя вертикальные жидкостные перемычки) и раздельный режим, не содержащий мостики.

ИСТОЧНИК ФИНАНСИРОВАНИЯ

Исследование выполнено за счет гранта Российского научного фонда (соглашение 19-79-00256). Шлирен-система предоставлена в рамках государственного задания ИТ СО РАН (Номер гос. регистрации 121031800213-0).

СПИСОК ЛИТЕРАТУРЫ

1. *Sackmann E.K., Fulton A.L., Beebe D.J.* The present and future role of microfluidics in biomedical research // Nature. 2014. V. 507. № 7491. P. 181.
2. *Deng Y. et al.* An integrated microfluidic chip system for single-cell secretion profiling of rare circulating tumor cells // Scientific reports. 2014. V. 4. P. 7499.
3. *Zhu Y., Fang Q.* Analytical detection techniques for droplet microfluidics – A review // Analytica chimica acta. 2013. V. 787. P. 24–35.
4. *Kim J.H. et al.* Droplet microfluidics for producing functional microparticles // Langmuir. 2013. V. 30. № 6. P. 1473–1488.
5. *Zhang M. et al.* Controllable microfluidic strategies for fabricating microparticles using emulsions as templates // Particuology. 2016. V. 24. P. 18–31.
6. *Jaeseon L., Mudawar I.* Low-temperature two-phase microchannel cooling for high-heat-flux thermal management of defense electronics // Components Packaging Technol. IEEE Trans. 2009. V. 32. № 2. P. 453.
7. *Чиннов Е.А., Роньшин Ф.В., Кабов О.А.* Режимы двухфазного течения в микро-и миниканалах (обзор) // Теплофизика и аэромеханика. 2015. Т. 22. №. 3. С. 275–297.
8. *Ghiaasiaan S.M., Abdel-Khalik S.I.* Two-phase flow in microchannels // Advances in heat transfer. 2001. V. 34. P. 145–254.
9. *Чиннов Е.А., Кабов О.А.* Образование капель в микроканалах // Письма в ЖТФ. 2011. Т. 37. № 14. С. 47–53.
10. *Ajaev V.S., Kabov O.A.* Levitation and Self-Organization of Droplets // Annual Review of Fluid Mechanics. 2021. V. 53. P. 203–225.
11. *Ronshin F., Chinnov E.* Experimental characterization of two-phase flow patterns in a slit microchannel // Experimental Thermal and Fluid Science. 2019. V. 103. P. 262–273.
12. *Chinnov E.A., Ron'shin F.V., Kabov O.A.* Two-phase flow patterns in short horizontal rectangular microchannels // Int. J. Multiphase Flow. 2016. V. 80. P. 57–68.

BRIDGE FLOW REGIME IN MICROCHANNELS

F. V. Ronshin[a], E. A. Chinnov[a], Yu. A. Dementyev[a], and O. A. Kabov[a]

[a] *Kutateladze Institute of Thermophysics Siberian Branch of the Russian Academy of Sciences, Novosibirsk, Russian Federation*

Presented by Academician of the RAS S.V. Alekseenko

As a result of studies of the two-phase flow in slit microchannels, a new flow regime – bridge flow has been discovered and studied. The bridges are vertical bridges between liquid films located on the lower and upper walls of the channel. It was found that with an increase in the flow rate of gas and liquid, the bridges begin to deform and then collapse. The critical Weber numbers characteristic of the deformation and destruction of bridges are determined. A new classification of two-phase flow regimes in microchannels is proposed on the basis of the obtained experimental data.

Keywords: bridge flow regime, slit microchannel, two-phase flow

УДК 532.529.2

Влияние скорости потока газа на конвекцию в горизонтальном испаряющемся слое жидкости*

Ю.В. Люлин[1,2], А.С. Крета[2], О.А. Кабов[2,3]

[1]*Центр энергетических технологий*, *Сколковский институт науки и технологий*, *Москва*

[2]*Институт теплофизики им. С.С. Кутателадзе СО РАН*, *Новосибирск*

[3]*Новосибирский государственный университет*

E-mail: Y.Lyulin@skoltech.ru

Проведено экспериментальное исследование структуры конвективных течений в горизонтальном испаряющемся слое жидкости — этаноле — в зависимости от скорости обдувающего межфазную поверхность потока газа — воздуха. Измерение распределения двухмерного поля скоростей и визуализация конвективных течений в слое жидкости осуществлялись с помощью PIV-метода. Доказано существование вихревой структуры течения в испаряющемся слое жидкости, при которой межфазная поверхность движется навстречу потоку газа.

Ключевые слова: конвекция, термокапиллярная граница раздела, двухфазные течения, испарение, PIV-метод.

Исследование конвективных течений в жидкости при интенсивном испарении с межфазной поверхности в поток движущегося газа является одной из сложнейших задач теплофизики. От расхода испарения существенным образом зависит эффективность различных теплообменных аппаратов, где используются двухфазные потоки. Перспективной является двухфазная система охлаждения, в которой слой жидкости движется в плоском мини- или микроканале, увлекаемый потоком газа [1]. Конвективные течения жидкостей, сопровождающиеся испарением на границе раздела, активно изучаются экспериментально и теоретически [2–6]. Численное исследование развития конвективных течений в горизонтальных слоях жидкости разной толщины, испаряющихся под действием потока газа, было проведено в работе [4]. Было показано, что со временем увеличиваются как поперечные, так и продольные размеры вихревых структур, и отмечено, что увеличение толщины слоя жидкости также способствует росту размеров вихревых структур. Разработке математических моделей конвективных движений с учетом процессов тепломассопереноса на границе раздела и формулировке условий на границе раздела на основе точных решений уравнений Навье–Стокса в приближении Обербека–Буссинеска посвящены работы [5, 7]. В статье [7] было проведено сравнение

* Работа выполнена при поддержке РНФ (грант № 14-19-01755).

© **Люлин Ю.В., Крета А.С., Кабов О.А., 2019**

аналитических и экспериментальных результатов [2] по испарению жидкости с термокапиллярной границы раздела и выявлено их качественное совпадение.

Целью настоящей работы является экспериментальное исследование структуры конвективных течений в горизонтальном испаряющемся слое жидкости в зависимости от скорости обдувающего межфазную поверхность потока газа с помощью PIV (Particle Image Velocimetry) метода.

Экспериментальные исследования проводились на установке, схема которой представлена на рис. 1. Установка состоит из следующих основных компонентов: рабочий участок, газовый и жидкостной контуры, контрольно-измерительная система, система термостабилизации, PIV- и шлирен-аппаратура. Чистый газ из компрессора *1* движется в рабочий участок *2*. Массовый расход газа на входе в канал рабочего участка задается с помощью массового регулятора расхода *3*. Жидкость в рабочий участок подается с помощью высокоточного шприцевого насоса *4*, затем она испаряется под действием потока газа и парогазовая смесь поступает на выход газового канала рабочего участка. Поток парогазовой смеси на выходе измеряется с помощью массового расходомера *5*. Температура жидкости и газа в рабочем участке устанавливается с помощью двух термостатов — *6*, *7*. Температура жидкости в рабочем участке определяется температурой основания подложки *8*, которая регулируется термоэлектрическим модулем *9* и теплообменником *10*. Контроль положения уровня межфазной границы осуществляется с точностью 10 микрометров с помощью шлирен-метода через прозрачное окно *11* и шприцевого насоса *4*. Оптическая система шлирен-метода располагается над рабочим участком [2].

Рабочий участок состоит из нескольких блоков, которые формируют прямоугольный газовый канал длиной 150 мм, высотой 3 мм и шириной 40 мм, а также прямоугольную жидкостную камеру размером 40×40 мм^2. Между газовым каналом и камерой с жидкостью установлена металлическая пластина из нержавеющей стали толщиной 150 мкм с квадратным вырезом по центру, в котором происходит контакт жидкости и газа

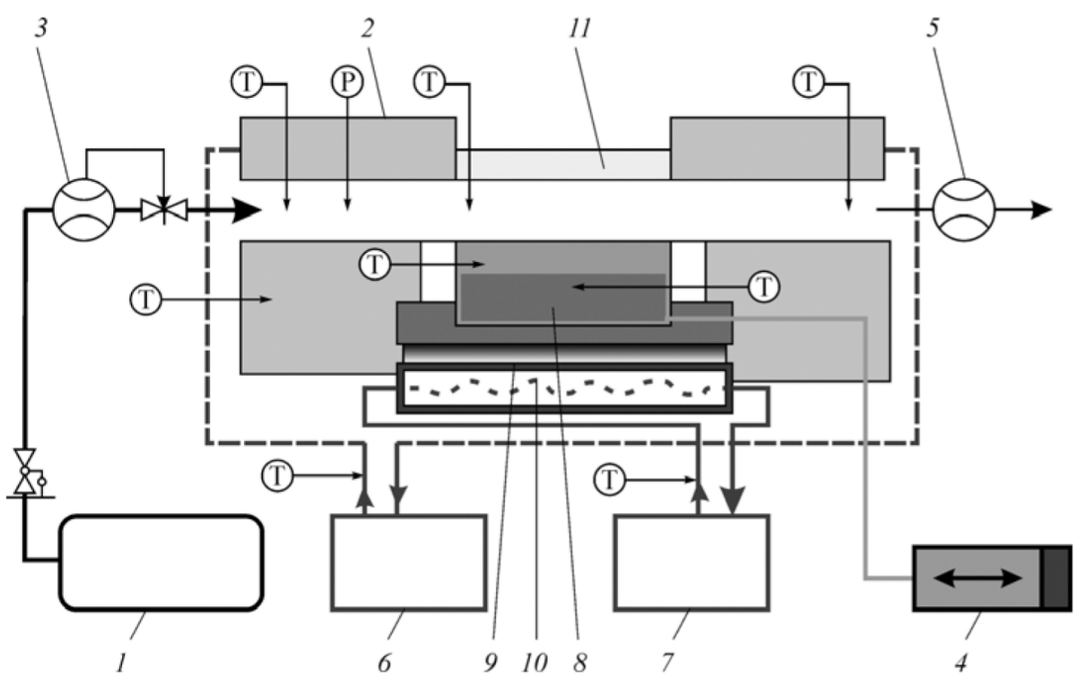

Рис. 1. Схема экспериментальной установки.

1 — компрессор, *2* — рабочий участок, *3* — регулятор расхода газа, *4* — шприцевой насос, *5* — расходомер газа, *6*, *7* — водяные термостаты, *8* — медная подложка, *9* — термоэлектрический модуль, *10* — теплообменник, *11* — прозрачное окно.

и формируется локальная область испарения. Размеры выреза в пластине могут варьироваться от 10×10 мм^2 до 30×30 мм^2. Стенки жидкостной камеры выполнены из прозрачного оргстекла, что дает возможность применения PIV-метода. Высота жидкости в камере изменяется от 1 до 10 мм с помощью медного основания и специальных регулирующих высоту пластин. В крышке рабочего участка над камерой с жидкостью установлено оптическое окно для использования шлирен-метода.

Регистрация структуры течения в слое жидкости, обдуваемом потоком газа, осуществляется с использованием метода PIV, схема которого показана на рис. 2. Метод позволяет определять форму, скорость вихревых структур, а также характер их распространения в слое жидкости в зависимости от различных режимных параметров эксперимента, таких как скорость потока газа, температура жидкости, высота слоя жидкости и др. Подробно описание PIV-метода приведено в монографии [8]. Измерение двухкомпонентного поля скоростей проводится в центральном сечении слоя жидкости. В начале эксперимента в жидкость добавляются частицы (трассеры) размером 5 мкм. Размер и плотность трассеров подбираются таким образом, чтобы частицы не оказывали влияние на структуру потока. Импульсный лазер создает тонкий (300 мкм) световой нож и освещает мелкие частицы. Положения частиц в момент двух последовательных вспышек лазера регистрируются двумя кадрами цифровой камеры. Цифровая камера расположена строго перпендикулярно световому ножу. Скорость потока определяется расчетом перемещения, которое совершают частицы за время между вспышками лазера. Определение перемещения основано на применении корреляционных методов к трассерным картинам с использованием регулярного разбиения на элементарные области. Обработка данных осуществляется с помощью программы ActualFlow. Двухкомпонентное поле скоростей в центральном сечении слоя жидкости строится с использованием итерационного кросс-корреляционного метода расчета двухкомпонентного поля скоростей. Основная идея метода состоит в обработке одной элементарной области несколько раз, при этом результат обработки предыдущей итерации используется для оценки параметров обработки на следующей итерации. Применение данного метода может способствовать значительному увеличению точности полученных данных. Область измерения составляет 14,2×3 мм или 1290×272 пикселей с разбиением на элементарные расчетные области размером 32×32 пикселей по горизонтали и вертикали. Межкадровая задержка камеры равна 100 мкс. Для анализа динамики и интенсивности конвективных течений в слое жидкости используется средняя скорость жидкости вблизи межфазной поверхности. В программе ActualFlow визуально определяется область поля скоростей, где существуют вихревые структуры

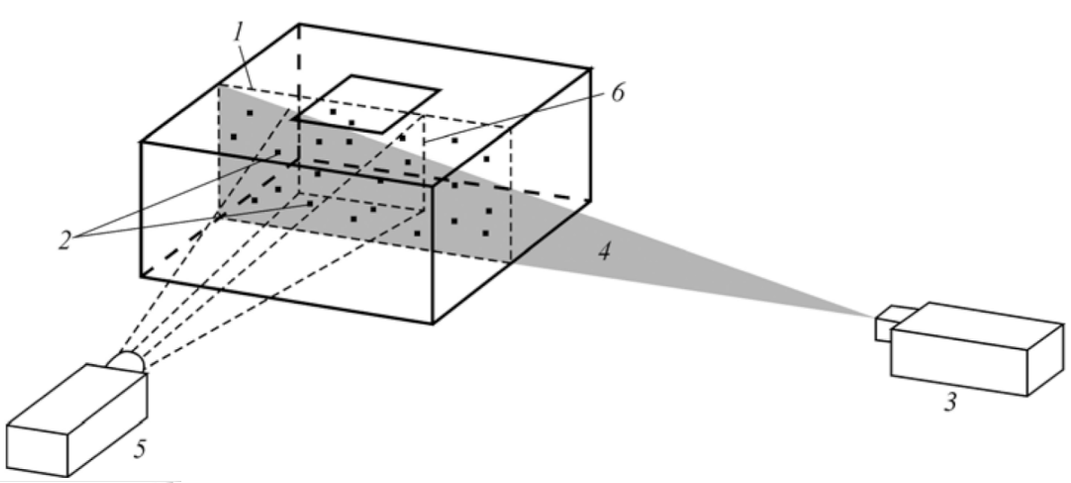

Рис. 2. Схема PIV-системы.

1 — продольный разрез слоя жидкости, *2* — трассеры, *3* — лазер, *4* — лазерный нож, *5* — цифровая видеокамера, *6* — область измерений.

течения. Над структурами выбирается прямоугольная область глубиной 0,5 мм от межфазной поверхности. Для каждой элементарной расчетной области определяется скорость по формуле $V_i = \sqrt{\left(V_{xi}^2 + V_{yi}^2\right)}$, где V_x, и V_{yi} — проекции скорости на оси x и y. Средняя скорость жидкости вблизи межфазной поверхности вычисляется как среднее значение всех скоростей в выбранной области по формуле: $V_{\text{av}} = (V_1 + V_2 + \ldots V_n)/n$. Для достоверности результатов осреднение проводилось по 20 кадрам.

Структура конвективных течений в слое жидкости существенно зависит от взаимодействия термокапиллярных сил и сил касательных напряжений, вызванных трением потока газа о межфазную поверхность. Термокапиллярные напряжения на поверхности слоя жидкости, вызванные действием термокапиллярного эффекта, рассчитываются по формуле $\tau_\sigma = \sigma_T\, \partial T/\partial X$, где $\sigma_T = \partial\sigma/\partial T$ — температурный градиент поверхностного натяжения, который для этанола равен $8\cdot10^{-5}$ Н/м·К. Градиент температуры на поверхности слоя жидкости определяется как $\partial T/\partial X = (T_{\text{in}} - T_{\text{fin}})/\Delta X$, где T_{in} и T_{fin} — температура поверхности жидкости на начальном и конечном участках соприкосновения жидкости и газа, ΔX — характерная длина области испарения. Для измерения распределения температур на межфазной поверхности использовалась инфракрасная камера Titanium 570M [9]. При расчете сил касательных напряжений предполагалось, что в газовом канале реализуется течение Пуазейля [9]. Граница раздела «жидкость–газ» рассматривалась как твердая поверхность. Касательные напряжения, вызванные трением потока газа о межфазную поверхность, рассчитывались по формуле $\tau_{\text{g}} = \mu\partial V/\partial y = -(H/2)\,(\partial P/\partial X)$, где H = 3 мм — высота газового канала, μ — динамическая вязкость воздуха. Градиент давления рассчитывается как $\partial P/\partial X = -12\mu V_{\text{g}}/\text{H}$, где V_{g} — средняя скорость потока газа в канале, рассчитываемая по формуле $V_{\text{g}} = G_{\text{g}}/S_{\text{g}}$, и G_{g} (м^3/с) — расход газа, S_{g} (м^2) — площадь поперечного сечения газового канала. Подробно методы расчета термокапиллярных напряжений и сил касательных напряжений, вызванных трением потока газа о межфазную поверхность, представлены в статье [10].

Эксперименты проводились при атмосферном давлении в рабочем участке и слое жидкости толщиной 3 мм. В качестве рабочей жидкости использовался этанол. Площадь поверхности испарения составляла 100 мм^2 с соответствующим размером выреза в пластине 10×10 мм^2. Расход газа варьировался от 100 до 1000 мл/мин с шагом 100 мл/мин, что соответствует его средней скорости от 0,0138 (Re = 5, 6) до 0,138 м/с (Re = 56). Температура системы «жидкость–газ» поддерживалась постоянной и составляла 20 °С с отклонением не более 0,1 °С.

На рисунке 3 представлено двухкомпонентное поле скоростей в центральном сечении слоя жидкости для различных скоростей газа: 0,0138, 0,0277, 0,0416, 0,0694 и 0,138 м/с. Значения скорости движения жидкости U изменяются от 0,05 до 0,4 м/с. На рис. 3*a* (скорость газа составляет 0,0138 м/с) видно, что на начальном участке соприкосновения жидкости и газа возникает вихревая структура течения жидкости, направление движения которой противоположно движению потока газа. Средняя скорость движения слоя жидкости вблизи межфазной поверхности составляет 0,178 м/с. Это обусловлено влиянием термокапиллярных напряжений, вызванных интенсивным испарением на межфазной границе раздела (τ_σ = 0,0023 Н/м^2). Поток газа охлаждает поверхность жидкости неравномерно. В результате на поверхности слоя жидкости возникает градиент температуры, что приводит к движению жидкости на поверхности слоя в обратном направлении потоку газа. Это обратное движение происходит за счет термокапиллярного эффекта (эффекта Марангони). Стоит отметить, что при малых скоростях потока газа термокапиллярные силы становятся на порядок больше сил касательных напряжений, которые равны 0,00048 Н/м^2. На рис. 3*b* (скорость газа составляет 0,0277 м/с) наблюдается формирование

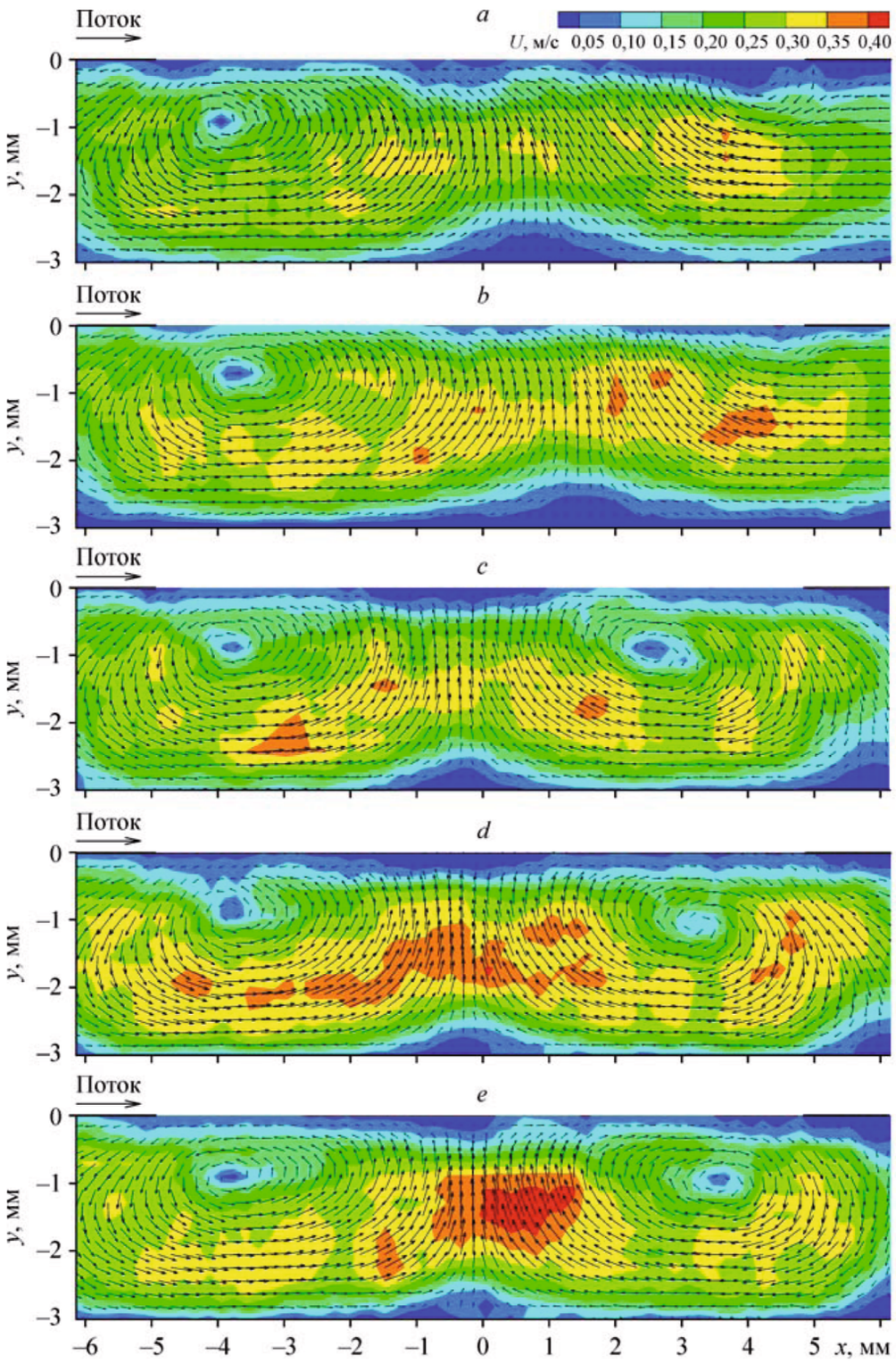

Рис. 3. Двухкомпонентное поле скоростей.
Скорость газа: 0,0138 (*a*), 0,0277 (*b*), 0,0416 (*c*), 0,0694 (*d*), 0,138 (*e*) м/с.

второй вихревой структуры на конечном участке соприкосновения жидкости и газа, при этом скорость жидкости вблизи межфазной поверхности возрастает до 0,193 м/с. Далее при увеличении скорости газа до 0,0416 м/с (рис. 3*c*) наблюдается образование двух вихревых структур течения жидкости. На начальном участке соприкосновения жидкости и газа вихрь движется против потока газа. Такое движение жидкости так же, как и в предыдущих случаях при скоростях газа 0,0138 и 0,0277 м/с, объясняется влиянием термокапиллярного эффекта. Второй вихрь движется в направлении, совпадающем с направлением

потока газа. Подобное движение жидкости возникает за счет действия касательных напряжений, вызванных потоком газа, и воздействия первой вихревой структуры. Касательные напряжения со стороны потока газа равны 0,0015 Н/м^2. Причем геометрический размер первого вихря больше, нежели второго, а скорости близки по значению и равны 0,178 и 0,183 м/с соответственно. При скорости газа, равной 0,0694 м/с (см. рис. 3*d*), размеры обоих вихрей начинают выравниваться, а скорости движения жидкости вблизи межфазной границы соразмерно увеличиваются и становятся равными 0,189 и 0,197 м/с соответственно. При максимальной скорости газа в эксперименте, равной 0,1388 м/с (рис. 3*e*), наблюдаются две достаточно симметричные вихревые структуры. Скорости жидкости вблизи межфазной поверхности близки здесь по значению и равны 0,215 и 0,217 м/с соответственно. Выравнивание скоростей происходит вследствие того, что термокапиллярные силы и силы касательных напряжений, которые вызваны трением потока газа о межфазную поверхность, при максимальной скорости потока газа в эксперименте становятся близкими по значениям: τ_σ = 0,0059 Н/м^2 и τ_g = 0,0049 Н/м^2 соответственно.

Таким образом, выполнено исследование динамики распространения конвективных течений в горизонтальном испаряющемся слое жидкости. Экспериментально выявлены конвективные структуры течения в слое жидкости, испаряющемся под действием потока газа. С использованием PIV-метода показано, что при увеличении скорости потока газа возрастает количество конвективных структур в горизонтально испаряющемся слое жидкости и увеличивается их скорость. Для минимальной скорости газа наблюдается одна конвективная вихревая структура течения, которая движется против потока газа. При дальнейшем увеличении скорости газа в слое жидкости происходит зарождение и образование второй вихревой структуры. По достижении максимальной скорости газа две вихревые конвективные структуры течения становятся почти симметричными и взаимообратными. Направление движения второй вихревой структуры обусловлено действием касательных напряжений, вызванных потоком газа, и влиянием первой вихревой структуры, которая закручивает вторую структуру в обратном направлении.

Список литературы

1. **Kabov O.A.** Interfacial thermal fluid phenomena in thin liquid films // Int. J. Emerging Multidisciplinary Fluid Sci. 2010. Vol. 2, No. 2–3. P. 87–121.
2. **Lyulin Yu.V., Kabov O.A.** Evaporative convection in a horizontal liquid layer under shear-stress // Int. J. Heat and Mass Transfer. 2014. Vol. 70. P. 599–609.
3. **Scheid B., Margerit J., Iorio C.S., Joannes L., Heraud M., Queeckers P., Dauby P.C., Colinet P.** Onset of thermal ripples at the interface of an evaporating liquid under a flow of inert gas // Experiments in Fluids. 2012. Vol. 52. P. 1107–1119.
4. **Machrafi H., Iorio C.S., Dauby P.C.** Relation between convective thermal patterns and heat flux through an evaporating surface via two-dimensional and three-dimensional numerica simulation // Int. Phenomena and Heat Transfer. 2014. Vol. 2, No. 3. P. 199–209.
5. **Goncharova O.N., Kabov O.A.** Mathematical and numerical modeling of convection in a horizontal layer under co-current gas flow // Int. J. of Heat and Mass Transfer. 2010. Vol. 53. P. 2795–2807.
6. **Goncharova O.N., Hennenberg M., Rezanova E.V., Kabov O.A.** Modeling of the convective fluid flows with evaporation in the two-layer systems // Interfacial Phenomena and Heat Transfer. 2013. Vol. 1, No. 3. P. 317–338.
7. **Гончарова О.Н., Резанова Е.В., Люлин Ю.В., Кабов О.А.** Моделирование двухслойных течений жидкости и газа с учетом испарения // Теплофизика и аэромеханика. 2015. Т. 22, № 5. С. 655–661.
8. **Raffel M., Willert C.** Particle image velocimetry. 2nd ed. Springer-Verlag, 2007. 448 p.
9. **Ландау Л.Д., Лифшиц Е.М.** Теоретическая физика. Гидродинамика // 3-е изд., испр. М.: Наука, 1986. 73 с.
10. **Kreta A., Lyulin Y.** Thermographic investigation of surface temperature of the evaporating liquid layer under the action of gas flow // MATEC Web of Conference. 2017. Vol. 92. P. 01048-1–01048-5.

Статья поступила в редакцию 21 марта 2017 г.,
после доработки — 20 ноября 2017 г.,
принята к публикации 11 декабря 2018 г.

УДК 532.54,532.64

Движение ручейка жидкости в микроканале при спутном потоке газа*

Ю.О. Кабова[1], В.В. Кузнецов[2,3], О.А. Кабов[1,3]

[1]*Институт теплофизики им. С.С. Кутателадзе СО РАН*, *Новосибирск*

[2]*Институт гидродинамики им. М.А. Лаврентьева СО РАН*, *Новосибирск*

[3]*Новосибирский государственный университет*

E-mail: kabov@itp.nsc.ru

Исследовано совместное установившееся движение ручейка несжимаемой жидкости и потока газа в микроканале с учетом действия сил гравитации, касательного напряжения на границе раздела газ–жидкость и сил Ван-дер-Ваальса. Для различных значений расходов жидкости и газа вычислены значения краевого угла. Показано, что для постоянного расхода жидкости увеличение скорости газа приводит к уменьшению высоты ручейка, поверхность ручейка при этом уплощается. Обнаружено существенное деформирующее влияние ручейкового течения на распределение скорости в газе.

Ключевые слова: двухфазные течения, ручейковые течения, микроканалы, численные исследования.

Введение

Ручейковые течения несжимаемой жидкости широко распространены в природе и технике. Быстрое развитие полупроводниковых технологий, уменьшение размеров деталей, увеличение плотности компоновки тепловыделяющих элементов и скорости коммутации привели к существенному усилению неоднородности нагрева микроэлектронного оборудования. Неоднородность нагрева выражается в появлении точек значительного локального нагрева поверхностей. В этих точках значения теплового потока достигают 1 кВт/см^2. Исследования показывают, что ручейки жидкости, увлекаемые движущимся потоком пара или газа в узких каналах (100–300 мкм), позволяют обеспечивать существенную интенсивность теплоотдачи особенно в областях линий контакта жидкости и нагретой поверхности [1–4]. Тем самым использование ручейковых течений для управления тепловыми режимами при работе с современным полупроводниковым оборудованием с большой мощностью рассеивания является перспективным методом, в частности для космических приложений, где предусмотрено производство энергии, охлаждение оборудования, поддержание работы систем жизнеобеспечения и т.д. [5]. Исследование и понимание закономерностей движения ручейка жидкости в узком канале даст ключ к использованию такого вида течений. В последние годы достаточно большое количество работ было посвящено решению этого вопроса. В работе [6] предлагалась

* Исследование выполнено за счет гранта РНФ (проект 14-19-01755).

© **Кабова Ю.О., Кузнецов В.В., Кабов О.А., 2018**

модель стекающего по наклонной плоскости ручейка с поверхностью постоянной кривизны. В публикации [7] рассматривалось стекание ручья по наклонному цилиндру. Движение ручейка жидкости, увлекаемого потоком газа в миниканале при различных значениях уровня гравитации, изучалось в работе [8]. Здесь рассматривалось стационарное движение изотермического ручейка жидкости с изначально заданным значением контактного угла. Было показано, что при пониженном уровне гравитации характер движения ручейка жидкости существенно изменяется. Кроме того, было обнаружено, что вид профиля ручейка зависит от расходов жидкости и газа, а также от уровня гравитации.

В настоящей работе решается задача определения полей скорости и положения межфазной границы ручейка несжимаемой жидкости при его установившемся движении по нижней стенке наклонного микроканала (с высотой 100–300 мкм) под действием гравитации и спутного потока газа, создающего касательное напряжение на границе раздела, а также сил Ван-дер-Ваальса. Считается, что температуры газа и жидкости равны одной и той же постоянной. Полагается, что толщина слоя жидкости мала по сравнению с поперечным размером микроканала, а ручеек является симметричным относительно продольной оси канала и его поверхность пологая. Подложка считается идеально гладкой, поэтому прекурсионная пленка покрывает ее полностью.

1. Постановка задачи

Рассматривается канал прямоугольного сечения неограниченной протяженности высотой d и шириной l, по нижней стенке которого движется ограниченная по ширине пленка несжимаемой жидкости (ручеек) (рис. 1). Движение жидкости и газа считается ламинарным и установившимся. Угол наклона канала к горизонту β может быть произвольным. Пусть декартова система координат (x, y, z) выбрана таким образом, что ось x ориентирована по длине канала, а плоскость Oxy совпадает с его дном. Тогда жидкость будет занимать область $G = \{-\infty < x < \infty,\ -l/2 < y < l/2,\ 0 < z < H(y)\}$, а газ располагаться в области $\Omega = \{-\infty < x < \infty,\ -l/2 < y < l/2,\ H(y) < z < d\}$. Будем считать, что движение в жидкой и газовой фазах описывается системой уравнений Навье–Стокса, содержащей уравнение импульсов и уравнение неразрывности для несжимаемой среды. Таким образом, в области G

$$\rho(\boldsymbol{v}\cdot\nabla)\boldsymbol{v} = -\nabla p + \rho\boldsymbol{g} + \mu\Delta\boldsymbol{v}, \quad \nabla\cdot\boldsymbol{v} = 0, \tag{1}$$

и в области Ω

$$\rho_{\mathrm{g}}(\boldsymbol{v}_{\mathrm{g}}\cdot\nabla)\boldsymbol{v}_{\mathrm{g}} = -\nabla p_{\mathrm{g}} + \rho_{\mathrm{g}}\boldsymbol{g} + \mu_{\mathrm{g}}\Delta\boldsymbol{v}_{\mathrm{g}}, \quad \nabla\cdot\boldsymbol{v}_{\mathrm{g}} = 0, \tag{2}$$

здесь v, v_{g} — векторы скорости в жидкости и газе, p, p_{g} — распределения давлений в жидкости и газе, $\boldsymbol{g} = \left(|\boldsymbol{g}|\sin\beta, 0, -|\boldsymbol{g}|\cos\beta\right)$ — ускорение свободного падения, ρ, ρ_{g} — плотности жидкости и газа, μ, μ_{g} — коэффициенты динамической вязкости жидкости

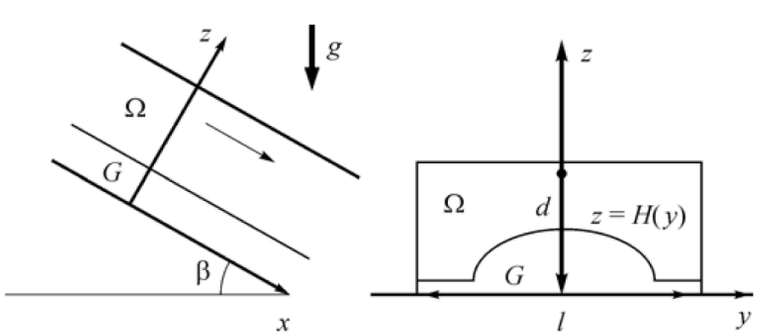

Рис. 1. Схема движения жидкости и газа в канале в сечениях вдоль и поперек потока.

и газа. Граничные условия для системы (1), (2) задаются следующим образом:
при $z = 0$ и $y = \pm l/2$, $z < H(\pm l/2)$

$$\boldsymbol{v} = 0\,, \tag{3}$$

при $z = d$ и $y = \pm l/2$, $z > H(\pm l/2)$

$$\boldsymbol{v}_{\mathrm{g}} = 0, \tag{4}$$

при $z = H(y)$

$$\boldsymbol{v} = \boldsymbol{v}_{\mathrm{g}}, \tag{5}$$

$$\left(P - P_{\mathrm{g}}\right)\boldsymbol{n} = 2\sigma K\boldsymbol{n} - \frac{A}{6\pi H^3}\boldsymbol{n}, \tag{6}$$

где σ — коэффициент поверхностного натяжения, K — средняя кривизна поверхности пленки $z = H(y)$, A — константа Гамакера, $\boldsymbol{n} = \left(0,\ -H'/\sqrt{1+H'^2}\,,\ 1/\sqrt{1+H'^2}\right)$ и $P_{ij} = -p\delta_{ij} + \mu\left(\partial v_i/\partial x_j + \partial v_j/\partial x_i\right)$, $P_{\mathrm{g}ij} = -p_{\mathrm{g}}\delta_{ij} + \mu_{\mathrm{g}}\left(\partial v_{\mathrm{g}i}/\partial x_j + \partial v_{\mathrm{g}j}/\partial x_i\right)$, здесь δ_{ij} — символы Кронекера. Тем самым на твердых границах канала для обеих сред справедливо условие прилипания, а на границе раздела имеет место непрерывность скорости и выполняется динамическое условие. В соотношении (6) учтено расклинивающее давление, возникающее вследствие действия сил Ван-дер-Ваальса [9]. Следует отметить, что образующийся вследствие действия сил Ван-дер-Ваальса тонкий слой пленки жидкости (прекурсионная пленка) на дне канала вблизи ручейка по теоретическим представлениям может быть ограничен только дефектами поверхности. Если считать дно канала идеально гладким, то можно заключить, что пленка покрывает всю поверхность дна. На самом деле это не имеет существенного значения, так как постоянная Гамакера очень мала, а в прекурсионной пленке имеем $H^3 \sim A$, следовательно, очень мала и толщина прекурсионной пленки. Соответственно суммарное количество жидкости в прекурсионной пленке составляет пренебрежимо малую часть всей жидкости независимо от того, насколько далеко от ручейка эта пленка простирается, поэтому ее наличие или отсутствие в удалении от ручейка не влияет на полученные результаты.

Решение задачи (1)–(6) будем искать в виде $\boldsymbol{v} = (v, 0, 0)$, $\boldsymbol{v}_{\mathrm{g}} = (v_{\mathrm{g}}, 0, 0)$, причем v, v_{g} являются функциями только координат y и z. Кроме того, полагаем, что $\rho_{\mathrm{g}} << \rho$ и гравитация не оказывает существенного влияния на движение в газовой фазе, которое происходит за счет созданного внешними устройствами продольного градиента давления. Этот градиент будем считать постоянным. Уравнения неразрывности в системах (1) и (2) при заданном виде полей скорости превращаются в тождества, а уравнения импульсов принимают следующий вид:
— в области, занятой жидкостью:

$$\frac{\partial^2 v}{\partial y^2} + \frac{\partial^2 v}{\partial z^2} = \frac{p_x - \rho g\sin\beta}{\mu}, \tag{7}$$

$$\partial p/\partial y = 0, \tag{8}$$

$$-\partial p/\partial z - \rho g\cos\beta = 0, \tag{9}$$

— в области, занятой газом:

$$\frac{\partial^2 v_{\mathrm{g}}}{\partial y^2} + \frac{\partial^2 v_{\mathrm{g}}}{\partial z^2} = -\frac{\lambda}{\mu_{\mathrm{g}}}, \tag{10}$$

$$p_g = p_0 - \lambda x, \quad p_0 = \mathrm{const}, \tag{11}$$

здесь λ — постоянный продольный градиент давления в газовой фазе, p_0 — давление в газе при $x = 0$. Проекция динамического условия (6) на орт оси Оx дает соотношение

$$\mu\left(-H'\frac{\partial v}{\partial y}+\frac{\partial v}{\partial z}\right)=\mu_{\mathrm{g}}\left(-H'\frac{\partial v_{\mathrm{g}}}{\partial y}+\frac{\partial v_{\mathrm{g}}}{\partial z}\right), \tag{12}$$

а проекция этого условия на нормаль $\boldsymbol{n}$ с учетом (11) дает

$$p-p_0+\lambda x=2\sigma K+A/6\pi H^3. \tag{13}$$

Так как для жидкости ищется решение с прямолинейными линиями тока и перемешивание отсутствует, то давление в жидкости становится гидростатическим:

$$p=p_1-\lambda x-\rho g z\cos\beta,\quad p_1=\mathrm{const}. \tag{14}$$

Тогда из условия (13) и определения средней кривизны следует уравнение для функции $z=H(y)$ вида

$$\frac{H''}{(1+H'^2)^{3/2}}-\frac{\rho g\cos\beta}{\sigma}H+C_1=\frac{A}{6\pi H^3\sigma} \tag{15}$$

с условием

$$H(0)=b, \tag{16}$$

где постоянная $C_1=(p_1-p_0)/\sigma$ подлежит определению, а b — искомая наибольшая высота ручейка. Здесь штрих означает дифференцирование по координате y. Следовательно, задача сводится к нахождению функции $z=H(y)$, задающей положение свободной границы, и распределений скорости в жидкой и газовой фазах $v(y,z)$, $v_g(y,z)$, а также постоянной C_1. Определить требуемые величины можно из решения системы уравнений (7), (10), (15) с условиями (3)–(5), (12) и (16). Каждое из условий (3)–(5) в силу одномерности векторов $\vec{v},\vec{v}_g$ эквивалентно одному скалярному равенству, а распределение давления в жидкости и в газе задается явными формулами (11) и (14).

2. Численный алгоритм

Для решения сформулированной выше задачи необходимо знать наибольшую высоту ручейка b и значение продольного градиента давления λ. Если они известны, то после решения задачи и вычисления полей скорости можно определить расходы жидкости и газа Q, Q_{g} по формулам

$$Q=\iint\limits_{G_0}v\,dydz,\quad Q_{\mathrm{g}}=\iint\limits_{\Omega_0}v_{\mathrm{g}}\,dydz, \tag{17}$$

где G_0, Ω_0 — сечения областей G, Ω плоскостью $x = \mathrm{const}$.

Рассматриваемую задачу можно назвать «прямой». В более простой постановке такая задача решалась в работе [10]. В ней поле скоростей в газе не рассчитывалось, а воздействие газового потока на жидкость заменялось наличием на границе раздела заданного постоянного касательного напряжения, направленного по оси x. При интерпретации результатов опытов и разработке технологических устройств гораздо большее применение имеет «обратная» задача, в которой расходы жидкости и газа заданы, а постоянные b и λ нужно рассчитать такими, чтобы после решения прямой задачи величины расходов, вычисленные по формулам (17), совпали с изначально заданными. В настоящей работе проводятся расчеты по заданным расходам жидкости и газа,

т.е. решается обратная задача. Будем считать, что при фиксированных b, λ (из некоторой области значений этих параметров) можно получить решение прямой задачи, и тогда становятся определенными функции $Q_0(b, \lambda)$, $Q_{0g}(b, \lambda)$, задающие значения расходов. Затем значения b, λ находятся из решения системы уравнений

$$Q_0(b, \lambda) = Q, \quad Q_{0g}(b, \lambda) = Q_g. \tag{18}$$

Системы (18) решались методом Ньютона, предназначенным для решения системы функциональных уравнений, а именно: выбиралось начальное приближение искомых величин b_0, λ_0 и затем решались прямые задачи со значениями параметров b_0, λ_0; $b_0 + \delta b, \lambda_0$; $b_0, \lambda + \delta\lambda$. Здесь δb, $\delta\lambda$ — малые приращения соответствующих величин. Вычисленные затем по формулам (17) величины $Q_0(b_0, \lambda_0)$, $Q_{0g}(b_0, \lambda_0)$, $Q_0(b_0 + \delta b, \lambda_0)$, $Q_{0g}(b_0 + \delta b, \lambda_0)$, $Q_0(b_0, \lambda_0 + \delta\lambda)$ и $Q_{0g}(b_0, \lambda_0 + \delta\lambda)$ позволяют получить значения частных производных функций Q_0, Q_{0g} и построить приближение искомых величин b_1, λ_1.

На каждом шаге итераций при решении прямой задачи сначала решалась задача определения поверхности раздела (15), (16), а затем система уравнений (7) и (10) для полей скорости v, v_g с граничными условиями (3)–(5) и (12). Последняя задача решалась методом конечных разностей с использованием метода дробных шагов по введенному для вычислений фиктивному времени [11]. При этом уравнения (7) и (10) заменялись параболическими уравнениями следующего вида:

$$\frac{\partial v}{\partial t} = \frac{\partial^2 v}{\partial y^2} + \frac{\partial^2 v}{\partial z^2} - \frac{p_x - \rho g \sin\beta}{\mu}, \tag{19}$$

$$\frac{\partial v_g}{\partial t} = \frac{\partial^2 v_g}{\partial y^2} + \frac{\partial^2 v_g}{\partial z^2} + \frac{\lambda}{\mu_g}. \tag{20}$$

В качестве начального задавалось нулевое распределение скоростей. После нахождения положения границы раздела газ–жидкость, функция $H(y)$, задающая это положение, заменялась ступенчатой функцией. При этом точки с рассчитанным значением $H(y)$ лежат точно на узлах расчетной сетки для поля скоростей. Уравнения (19) и (20) заменялись разностными аналогами с дробными по времени шагами:

— по направлению y:

$$\frac{v_{i,j}^{k+1/2} - v_{i,j}^{k}}{\tau/2} = \Lambda_{11}^{k+1/2} v_{i,j} + \Lambda_{22}^{k} v_{i,j} - \frac{p_x - \rho g \sin\beta}{\mu}, \tag{21}$$

$$\frac{v_{gi,j}^{k+1/2} - v_{gi,j}^{k}}{\tau/2} = \Lambda_{11}^{k+1/2} v_{gi,j} + \Lambda_{22}^{k} v_{gi,j} + \frac{\lambda}{\mu_g}, \tag{22}$$

— по направлению z:

$$\frac{v_{i,j}^{k+1} - v_{i,j}^{k+1/2}}{\tau/2} = \Lambda_{11}^{k+1/2} v_{i,j} + \Lambda_{22}^{k+1} v_{i,j} - \frac{p_x - \rho g \sin\beta}{\mu}, \tag{23}$$

$$\frac{v_{gi,j}^{k+1} - v_{gi,j}^{k+1/2}}{\tau/2} = \Lambda_{11}^{k+1/2} v_{gi,j} + \Lambda_{22}^{k+1} v_{gi,j} + \frac{\lambda}{\mu_g}, \tag{24}$$

здесь $\Lambda_{11}, \Lambda_{22}$ — операторы центральной разности, аппроксимирующие вторые производные вычисляемых функций, при этом $i = 2, 3, \ldots, n-1$; $j = 2, 3, \ldots, n_1 - 1$; $k = 1, 2, \ldots,$

где n и n_1 — число разбиений по направлениям y и z соответственно. Разностные уравнения (21)–(24) для расчета сеточных функций $v_{i,j}$ и $v_{gi,j}$ определены во всех узлах сетки (каждое в своей области), кроме граничных узлов. В силу граничного условия (5) скорость непрерывна на границе раздела газ–жидкость. Следовательно, скорости в жидкости и в газе можно искать методом сквозного счета, рассчитывая сеточную функцию $v_{i,j}$, которая в газовой фазе понимается как $v_{gi,j}$. При таком расчете каждой узловой точке (i, j), лежащей на границе раздела, должно соответствовать уравнение. Такими уравнениями являются разностные аналоги условия (12). Для точек, лежащих в левой половине области расчетов, это условие дает соотношение

$$\mu\left(-H_l'\frac{v_{i+1,j}-v_{i,j}}{h_y}+\frac{v_{i,j}-v_{i,j-1}}{h_z}\right)=\mu_g\left(-H_l'\frac{v_{i,j}-v_{i-1,j}}{h_y}+\frac{v_{i,j+1}-v_{i,j}}{h_z}\right), \tag{25}$$

здесь h_y, h_z — шаги сетки по осям y и z. Если граничная точка лежит в правой половине расчетной области, то это соотношение записывается аналогично.

Нетрудно видеть, что соотношение (25) имеет такой же трехточечный формат аппроксимации, что и соотношения (21) – (24). Таким образом, рассчитываемое поле скоростей будет удовлетворять всем граничным условиям. Вычисления ведутся при возрастании фиктивного времени до тех пор, пока решение не становится установившимся, т.е. когда суммарное относительное изменение скорости во всех точках оказывается меньше 10^{-8}. Стоит отметить, что фактически при численном решении задачи постоянная C_1 не рассчитывалась. Численно решалось уравнение, полученное после дифференцирования уравнения (15):

$$\left(\frac{H''}{(1+H'^2)^{3/2}}\right)'-\frac{\rho g\cos\beta}{\sigma}H'=-\frac{AH'}{2\pi H^4\sigma}. \tag{26}$$

Уравнение (26) является нелинейным обыкновенным дифференциальным уравнением 3-го порядка. Решение этого уравнения проводилось конечно-разностным методом, при котором производные заменяются их разностными аналогами. Разностная задача решалась методом итераций, и значения искомых функций для нелинейных членов задавались с предыдущего шага итераций. Начальное значение аппроксимировалось так, чтобы при заданных высоте ручейка и средней скорости движения жидкости его ширина (вне слоя тонкой пленки) обеспечивала заданный расход. Разностный аналог уравнения (26) на каждом шаге итераций имеет вид

$$a_ih_{i-2}+b_ih_{i-1}+c_ih_i+d_ih_{i+1}+e_ih_{i+2}=f_i,\qquad i=3,4,\ldots,n-2, \tag{27}$$

граничные условия определялись как

$$h_1=b,\quad h_2-h_1=0,\quad h_n-h_{n-1}=0,\quad h_{n-2}-2h_{n-1}+h_n=0. \tag{28}$$

Первое из условий (28) задает высоту ручейка жидкости, второе представляет собой условие симметрии относительно продольной оси канала, третье и четвертое условия означают, что на контактной линии, лежащей на боковой стенке канала, контактный угол равен 90°. Фактически этот угол неизвестен, но если задавать другие углы, не равные 90°, то это приведет к незначительным отличиям, локализованным вблизи боковых стенок канала, и не повлияет на полученные результаты. Поскольку в уравнение (26) входят разнопорядковые члены, то численный расчет выполнялся с повышенной точностью. А именно: каждое вещественное число с плавающей запятой занимало 16 байт,

что гарантировало достаточную точность расчетов при операциях с величинами разных порядков. Это позволило провести сквозной расчет толщины ручейка. При расчетах ширина канала делилась на $n-1$ равных частей. После проведения расчетов число разбиений удваивалось. Если результат не изменялся, то число разбиений считалось достаточным. Приведенные результаты численного исследования соответствуют значению $n = 1601$. Задача нахождения функции $H(y)$ на каждом шаге итераций решалась в интервале $(0, l/2)$, а затем положение поверхности ручейка достраивалось симметрично в интервале $(-l/2, 0)$.

3. Результаты исследования

При проведении расчетов свойства жидкостей в газовой фазе соответствовали азоту, а в жидкой фазе — фторуглеродной жидкости FC-72. Значения параметров были следующими: $\mu = 0{,}735\cdot10^{-3}$ кг/мс, $\mu_g = 17{,}75\cdot10^{-6}$ кг/мс, $\rho = 1687{,}8$ кг/м^3, $\rho_g = 1{,}2505$ кг/м^3, $\sigma = 12{,}57\cdot10^{-3}$ Н/м; угол наклона канала к горизонту $\beta = 0$, то есть движение жидкости обуславливалось только действием потока газа; высота канала $d = 250$ мкм, ширина канала $l = 4$ см, свойства жидкостей соответствовали температуре $T = 20$ °C, константа Гамакера $A = 10^{-20}$ м^{2}кг/с^2, числа Рейнольдса определялись как $\mathrm{Re} = Q\rho/l\mu_0$, $\mathrm{Re}_g = Q_g\rho_g/l\mu_{0g}$, где Q, Q_g — расходы потоков жидкости и газа. Результаты расчетов представлены на рис. 2–6 в размерной форме, значение производной $H'(y)$ на рис. 4 безразмерно. В работе также численно было исследовано влияние скорости газа на вид профиля ручейка жидкости в микроканале. Показано, что для постоянного значения Re = 8 величина расхода жидкости $Q = 0{,}3\cdot10^{-7}$ м^3/с, увеличение расхода газа приводит к уменьшению высоты ручейка жидкости, при этом верхняя граница ручейка уплощается, так как касательное напряжение на свободной поверхности существенно возрастает (рис. 2). Изменение значений расхода газа Q_g, средней скорости жидкости u и газа u_g, а также высоты ручейка жидкости b с ростом числа Рейнольдса газа Re_g представлено в таблице.

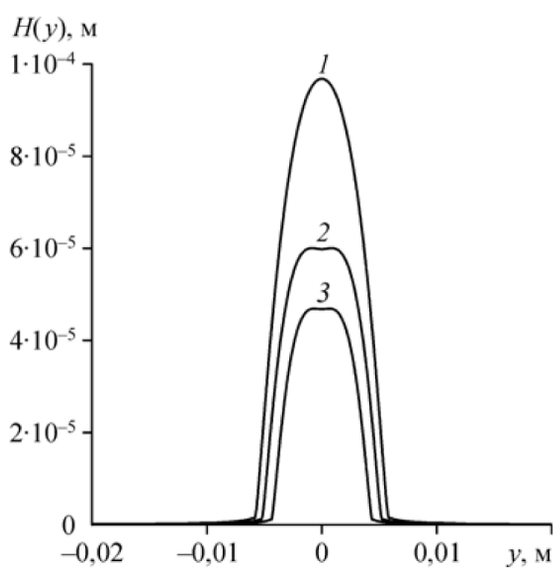

Рис. 2. Профили ручейка жидкости в сечении, перпендикулярном потоку, при различных скоростях газа.
Re = 8; *1* — $\mathrm{Re}_g = 5$ ($Q = 0{,}3\cdot10^{-7}$ м^3/с, $Q_g = 0{,}283\cdot10^{-5}$ м^3/с, $u = 3{,}59$ см/с, $u_g = 0{,}284$ м/с, $b = 96{,}751$ мкм); *2* — $\mathrm{Re}_g = 25$ ($Q = 0{,}3\cdot10^{-7}$ м^3/с, $Q_g = 0{,}14\cdot10^{-4}$ м^3/с, $u = 5{,}82$ см/с, $u_g = 1{,}419$ м/с, $b = 59{,}797$ мкм); *3* — $\mathrm{Re}_g = 50$ ($Q = 0{,}3\cdot10^{-7}$ м^3/с, $Q_g = 0{,}283\cdot10^{-4}$ м^3/с, $u = 7{,}438$ см/с, $u_g = 2{,}839$ м/с, $b = 46{,}818$ мкм).

Изменение значений расхода газа Q_g, средней скорости жидкости u и газа u_g, а также высоты ручейка жидкости b с ростом числа Рейнольдса газа Re_g

Re_g	Q_g, м^3/с	u, см/с	u_g, м/с	b, мкм
5	$0{,}283\cdot10^{-5}$	3,59	0,284	96,751
25	$0{,}14\cdot10^{-4}$	5,82	1,419	59,797
50	$0{,}283\cdot10^{-4}$	7,438	2,839	46,818

На рис. 2 на кривых *2* и *3* на вершине ручейка заметно формирование участка плоской поверхности, а на кривой *3* это выражено совершенно отчетливо. Формирование таких участков происходит при росте числа Re_g, который приводит к уменьшению высоты ручейка. Наличие подобных участков плоской поверхности отмечалось в работе [8]. На рис. 3 видно, что хотя по условию задачи ручеек вместе с тонкой пленкой жидкости покрывает все дно микроканала, фактически существует его ярко выраженная граница: виден кажущийся излом свободной поверхности (кажущийся, так как функция $H(y)$ имеет непрерывные производные до третьего порядка). Будем считать угол наклона поверхности жидкости в области излома краевым углом. Однако, поскольку шаг разбиения мал, то не очевидно в какой точке поверхности значение производной функции $H(y)$ по y задает значение краевого угла. Похожим образом значение контактного угла рассчитывалось в работе [12], где пленка стекала по наклонной подложке, образуя движущуюся переднюю кромку. Здесь также учитывалось наличие перкуссионного слоя и полагалось, что при удалении от движущейся кромки поверхность жидкости становится плоской. На рис. 3 видно, что угол сглаживается, и выбор расчетной точки при подсчете угла наклона не может быть произвольным. Следует также отметить, что $H = H_0 = \mathrm{const}$ при исчезающе малых числах Re_g являются асимптотическим решением уравнения (15). Установлено (см. рис. 4), что в области кажущегося излома существует участок практически постоянного значения производной функции $H(y)$ по y. Очевидно, что это значение и должно быть использовано для расчета контактного угла. На рис. 4 изображены значения $H'(y)$ вблизи кажущихся изломов для профилей ручейков, представленных на рис. 2. Участок с практически постоянным значением производной функции $H(y)$ по y существует при всех трех значениях расхода. Для этих случаев значения рассчитанных контактных углов φ при $\mathrm{Re}_g = 5, 25, 50$ составят соответственно 1,81°, 1,48°, 1,46°. Обнаружено существенное деформирующее влияние ручейка на распределение скорости в микроканале. На рис. 5 представлено поле скоростей в поперечном сечении микроканала, а также профиль ручейка жидкости. Видно, что скорость жидкости много меньше скорости газа. Из результатов расчетов можно заключить, что наличие даже микромасштабного ручейкового течения на нижней стенке канала существенно изменяет поле скоростей в газе, разделяя область течения газа на три части. На рис. 6 показаны профили скорости жидкости и газа в сечениях при $y = -1{,}25$ см, что соответствует области вне ручейка жидкости,

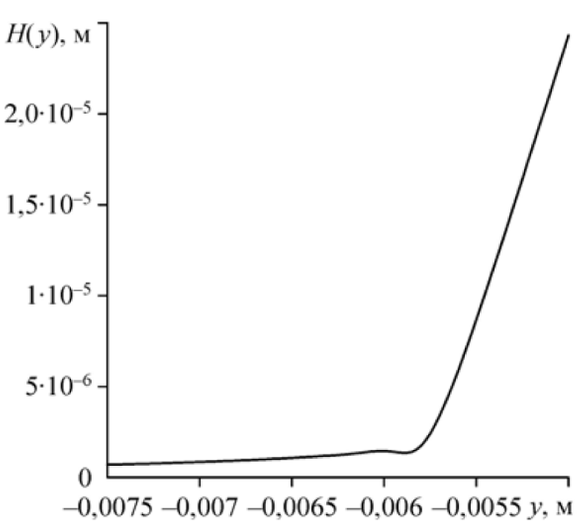

Рис. 3. Положение границы раздела газ–жидкость в области линии контакта. $\mathrm{Re} = 8$, $\mathrm{Re}_g = 5$.

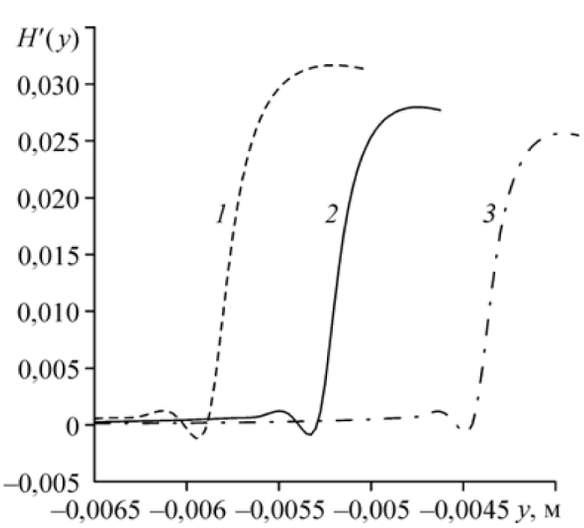

Рис. 4. Значения производной $H'(y)$ вблизи края ручейка при $\mathrm{Re} = 8$. $\mathrm{Re}_g = 5$ (*1*), 25 (*2*) и 50 (*3*).

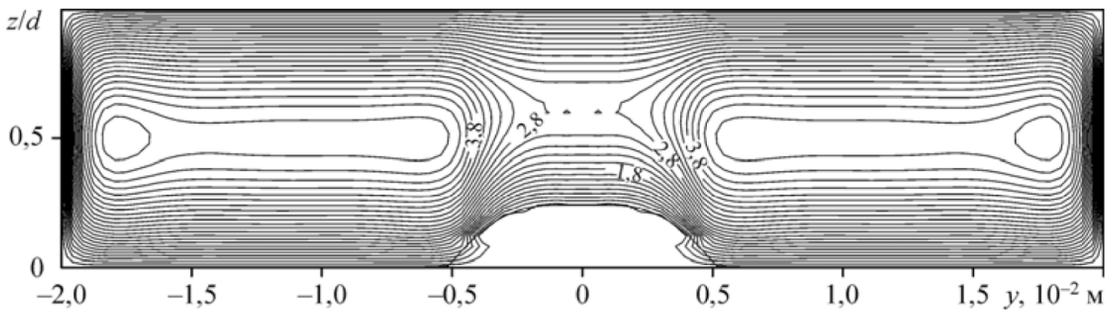

Рис. 5. Изолинии поля скорости (м/с) и профиль поверхности ручейка в поперечном сечении микроканала при Re = 8 и Re_g = 25.
Координата *z* отнесена к высоте канала *d*.

Рис. 6. Профили скорости *v*(*z*) для жидкости и для газа в сечениях при *y* = 0 (*1*) (осевое сечение ручейка) и *y* = $-1{,}25\cdot10^{-2}$ м (*2*) (соответствует области вне ручейка жидкости).
Re = 8, Re_g = 25.

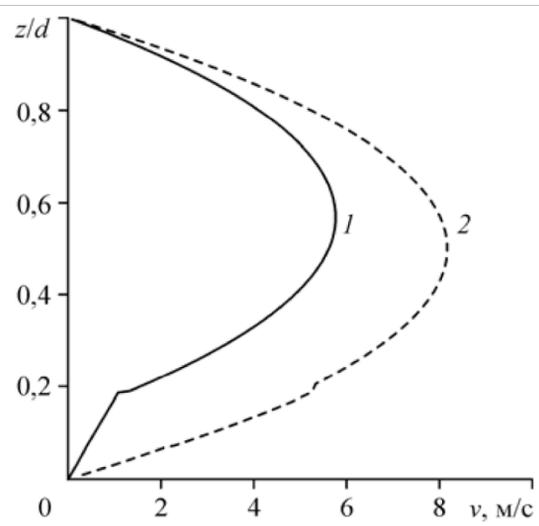

и *y* = 0, что соответствует осевому сечению ручейка. Видно, что вне ручейка профиль скорости имеет параболический вид. Небольшие возмущения (или отличия от случая одномерного течения) обусловлены наличием боковых стенок и влиянием ручейка. В плоскости сечения *y* = 0 профиль скорости состоит из двух участков парабол. Причем участок, соответствующий скорости в жидкости, является практически прямолинейным, что хорошо согласуется с результатами, представленными в работе [13].

Выводы

Построена математическая модель установившегося совместного движения ручейка несжимаемой жидкости и потока газа в микроканале с учетом действия сил гравитации, касательного напряжения на границе раздела газ–жидкость, а также сил Ван-дер-Ваальса. Рассчитаны скорость в жидкости и газе, а также положение границы раздела газ–жидкость. Для различных значений расходов жидкости и газа вычислены значения контактного угла. Показано, что при постоянном расходе жидкости увеличение скорости газа приводит к уменьшению высоты ручейка жидкости, при этом его верхняя граница уплощается. Обнаружено существенное деформирующее влияние ручейкового течения на распределение скорости в газовой фазе.

Список литературы

1. **Stephan P., Brandt C.** Advanced capillary structures for high performance heat pipes / ed. S.G. Kandlikar // Proc. I Int. Conf. on Microchannels and Minichannels, Rochester, NY, 24–25 April. 2003. P. 69–75.
2. **Rednikov A.Ye., Colinet P**. Truncated versus extended microfilms at a vapor-liquid contact line on a heated substrate // Langmuir. 2011. Vol. 27, No. 5. P. 1758–1769.
3. **Ajaev V.S., Gatapova E.Ya., Kabov O.A**. Stability and break-up of thin liquid films on patterned and structured surfaces // Advances in Colloid and Interface Sci. 2016. Vol. 228. P. 92–104.

4. Karchevsky A.L., Marchuk I.V., Kabov O.A. Calculation of the heat flux near the liquid-gas-solid contact line // Applied Mathematical Modeling. 2016. Vol. 40. P. 1029–1037.
5. Cheverda V.V., Glushchuk A., Queeckers P., Chikov S.B., Kabov O.A. Liquid rivulets moved by shear stress of gas flow at altered levels of gravity // Microgravity Sci. and Technol. 2013. Vol. 25, No. 1. P. 73–81.
6. Towell G.D., Rothfeld L.B. Hydrodynamics of rivulet flow // AIChE J. 1966. Vol. 12, No. 5. P. 972–980.
7. Алексеенко С.В., Гешев П.И., Куйбин П.А. Течение жидкости со свободной границей по наклонному цилиндру // Докл. РАН. 1997. Т. 354, № 1. С. 47–50.
8. Барташевич М.В., Кузнецов В.В., Кабов О.А. Динамика ограниченной по ширине пленки жидкости при спутном потоке газа в микроканале // Изв. РАН. Механика жидкости и газа. 2010. № 6. С. 110–116.
9. Дерягин Б.В., Чураев Н.В., Муллер В.М. Поверхностные силы. М: Наука, 1985. 398 с.
10. Myers T.G., Liang H.X., Wetton B. The stability and flow of a rivulet driven by interfacial shear and gravity // Int. J. Non-Linear Mech. 2004. Vol. 39. P. 1239–1249.
11. Самарский А.А. Введение в теорию разностных схем. М.: Наука, 1971. 553 с.
12. Ajaev V.S., Gambaryan-Roisman T., Stephan P. Static and dynamic contact angles of evaporating liquids on heated surfaces // J. of Colloid and Interface Sci. 2010. Vol. 342. P. 550–558.
13. Kabova Yu., Kuznetsov V.V., Kabov O., Gambaryan-Roisman T., Stephan P. Evaporation of a thin viscous liquid film sheared by gas in a microchannel // Int. J. Heat and Mass Transfer. 2014. Vol. 68. P. 527–541.

Статья поступила в редакцию 15 мая 2017 г.,
после доработки — 2 июля 2018 г.

03

Влияние свойств жидкости на режимы двухфазного течения в широком прямоугольном микроканале

© *Ф.В. Роньшин*[1,2], *В.В. Чеверда*[1,2], *Е.А. Чиннов*[1,2], *О.А. Кабов*[1,3]

[1] Институт теплофизики им. С.С. Кутателадзе СО РАН, Новосибирск, Россия
[2] Национальный исследовательский Новосибирский государственный университет, Новосибирск, Россия
[3] Национальный исследовательский Томский политехнический университет, Томск, Россия
E-mail: f.ronshin@gmail.com

Поступило в Редакцию 19 мая 2017 г.

В микроканале высотой 150 μm и шириной 20 mm выполнено экспериментальное исследование двухфазного течения с использованием различных жидкостей: очищенной воды фирмы Milli-Q, 50% водно-спиртового раствора и FC-72. До и после эксперимента контролировались высота микроканала, смачиваемость его стенок, поверхностное натяжение жидкостей. С использованием шлирен-метода выявлены основные характеристики двухфазного течения в широких диапазонах значений расхода газа и жидкости. Обнаружено, что механизм формирования режима зависит от свойств используемой жидкости. Зарегистрирован режим течения, когда по микроканалу движутся капли, являющиеся вертикальными жидкостными перемычками. Показано, что при использовании FC-72 пленка жидкости на верхней стенке канала формируется во всем диапазоне значений расхода газа и жидкости.

DOI: 10.21883/PJTF.2018.07.45887.16881

Одной из актуальных задач теплофизики в наши дни является проблема охлаждения микроэлектронного оборудования. Разрабатываются компоненты микроэлектроники, микроэлектромеханические системы (МЭМС, микросистемы, микромашины), представляющие собой трехмерные мини- и микрообъекты, в которых характерные размеры элементов составляют миллиметры или микрометры, где наблюдаются высокие тепловые потоки (до 1 kW/cm^2). Эффективным решением пред-

ставляется уменьшение размеров жидкостного теплообменника, так как отношение площади поверхности теплообмена к объему увеличивается обратно пропорционально поперечному размеру. Использование микроканалов позволяет существенно уменьшить среднюю толщину пленки при двухфазных течениях, что ведет к глобальной интенсификации теплообмена при испарении. В связи с этим для широкого круга технических приложений важнос значснис имсст понимание гидродинамики в микроканалах, которые обеспечивают наиболее эффективные процессы тепло- и массопередачи. Обзор публикаций по двухфазному течению в микроканалах содержится в [1–4]. Анализ исследований показывает, что на структуру двухфазного потока в основном влияют следующие параметры: геометрия и размеры канала, параметры входного участка [5] и свойства жидкости, такие как вязкость и поверхностное натяжение. В работах [6,7] проведено исследование механизмов, оказывающих влияние на формирование двухфазного течения. Выделено два новых вида неустойчивости (фронтальная и боковая), которые отвечают за формирование режимов в микроканале. В работе [8] исследовано влияние контактного угла смачивания на структуру двухфазного потока в круглом канале диаметром 1.6 mm. Показано, что при изменении смачиваемости существенно меняются границы между режимами. В работе [9] проведено исследование влияния обработки поверхности на структуру двухфазного потока. Более регулярные стурктуры появились в гладком канале. В снарядном рсжимс в канале с тщатсльно обработанной поверхностью вместо капель наблюдалась пленка жидкости.

На основе анализа опубликованной литературы можно заключить, что смачиваемость микроканалов оказывает существенное влияние на режимы двухфазного течения. Целью настоящей работы является экспериментальное исследование двухфазного потока в прямоугольном микроканале высотой 150 μm, шириной 20 mm со следующими жидкостями: очищенная вода (Milli-Q), 50% водно-спиртовой раствор и FC-72.

Описание установки и конструкции микроканала представлено в работе [10]. Для регистрации пленок жидкости на нижней и верхней стенках канала и соответственно определения режима двухфазного течения используется модификация шлирен-метода, представленная в [10]. Высота микроканала измерена при помощи конфокального метода на установке confocalDT IFC2451 и составляет $151.4 \pm 6.2\,\mu$m. При помощи установки KRUSS DSA 100 проведены измерения поверхностного натяжения жидкостей, а также углов смачивания верхней и

Результаты измерения краевых углов смачивания

Жидкость	Краевой угол	Нержавеющая сталь	Кварц
Вода	Натекающий	$106 \pm 1^\circ$	$108 \pm 2^\circ$
	Оттекающий	$25 \pm 3^\circ$	$68 \pm 3^\circ$
50% водно-спиртовой раствор	Натекающий	$58 \pm 2^\circ$	$71 \pm 2^\circ$
	Оттекающий	$15 \pm 4^\circ$	$35 \pm 4^\circ$
FC-72	Натекающий	$12 \pm 2^\circ$	
	Оттекающий	$4 \pm 2^\circ$	

нижней стенок микроканала. Поверхностное натяжение воды и водно-спиртового раствора измерялось методом висящей капли, краевые углы смачивания измерялись методом лежащей капли. Для используемой воды поверхностное натяжение составляет 72 mN/m, для водно-спиртового раствора — 26 mN/m, а для FC-72 — 10 mN/m (указано производителем жидкости 3M^{TM}). Результаты измерения контактных углов приведены в таблице.

Исследованы основные режимы течения двухфазного потока и определены границы между ними. Зарегистрированы следующие режимы двухфазных течений: струйный, пузырьковый, раздельный, кольцевой и вспененный. Построены режимные карты двухфазного течения для каждой из исследуемых жидкостей. В качестве координат использованы приведенные скорости газа U_{SG} и жидкости U_{SL}, определяемые как отношение объемного расхода к площади поперечного сечения канала:

$$U_{SL} = \frac{Q_L}{bh}, \quad U_{SG} = \frac{Q_C}{bh}, \tag{1}$$

где Q_L — массовый расход жидкости, который задается шприцевым насосом Cole-Parmer EW-74905-54, Q_G — массовый расход газа, который задается регулятором расхода El-Flow фирмы Bronkhorst, b — ширина микроканала, h — высота микроканала.

Также построены режимные карты двухфазного течения для каждой из исследуемых жидкостей, где в качестве координат использованы безразмерные числа Вебера

$$\mathrm{We}_{SL} = \frac{\rho_L d_h U_{SL}^2}{\sigma}, \quad \mathrm{We}_{SG} = \frac{\rho_G d_h U_{SG}^2}{\sigma}, \tag{2}$$

где ρ_L — плотность жидкости, ρ_G — плотность газа, d_h — гидравлический диаметр микроканала, σ — поверхностное натяжение жидкости, измеренное на установке KRUSS.

При малых приведенных скоростях жидкости наблюдается струйный режим, когда газ движется в центральной части микроканала, а основная часть жидкости перемещается по его периферии вдоль боковых стенок. С увеличением приведенной скорости жидкости она начинает занимать значительно бóльшую часть микроканала, а по центру движется газовая струя. При использовании водно-спиртового раствора и воды пленка на верхней стенке микроканала на образуется. В случае жидкости FC-72 на верхней стенке микроканала всегда формируется пленка жидкости, а также наблюдается движение вертикальных жидкостных перемычек (между верхней и нижней стенками микроканала), оставляющих за собой характерные следы на пленке жидкости (рис. 1, *a*). Струйный режим является специфическим для плоских мини- и микроканалов.

При увеличении приведенной скорости жидкости начинают формироваться стабильные горизонтальные перемычки жидкости, происходит переход от струйного режима к пузырьковому. В этом режиме по каналу движется жидкость, содержащая много небольших пузырьков газа. Размер и количество пузырьков изменяются в зависимости от расхода жидкости и газа, но размеры пузырьков всегда остаются гораздо меньшими ширины канала. Как правило, такие пузырьки движутся вдоль одной из стенок микроканала, что может быть обусловлено неоднородностью входного участка. С увеличением приведенных скоростей жидкости и газа частота пузырьков увеличивается.

При малых приведенных скоростях жидкости и больших приведенных скоростях газа наблюдается раздельный режим, в котором основная часть жидкости движется по нижней стенке микроканала в виде пленки, увлекаемой потоком газа. Верхняя стенка микроканала остается осушенной. Газ занимает больше половины сечения микроканала. Раздельный режим характерен только для некруглых микроканалов, так как в круглых микроканалах пленка замыкается, образуя кольцевой режим. При раздельном режиме можно наблюдать характерные волны на пленке жидкости (рис. 1, *b*). При использовании жидкости FC-72 раздельный режим не наблюдается, поскольку пленка на верхней стенке канала формируется во всем диапазоне значений расхода жидкости и газа.

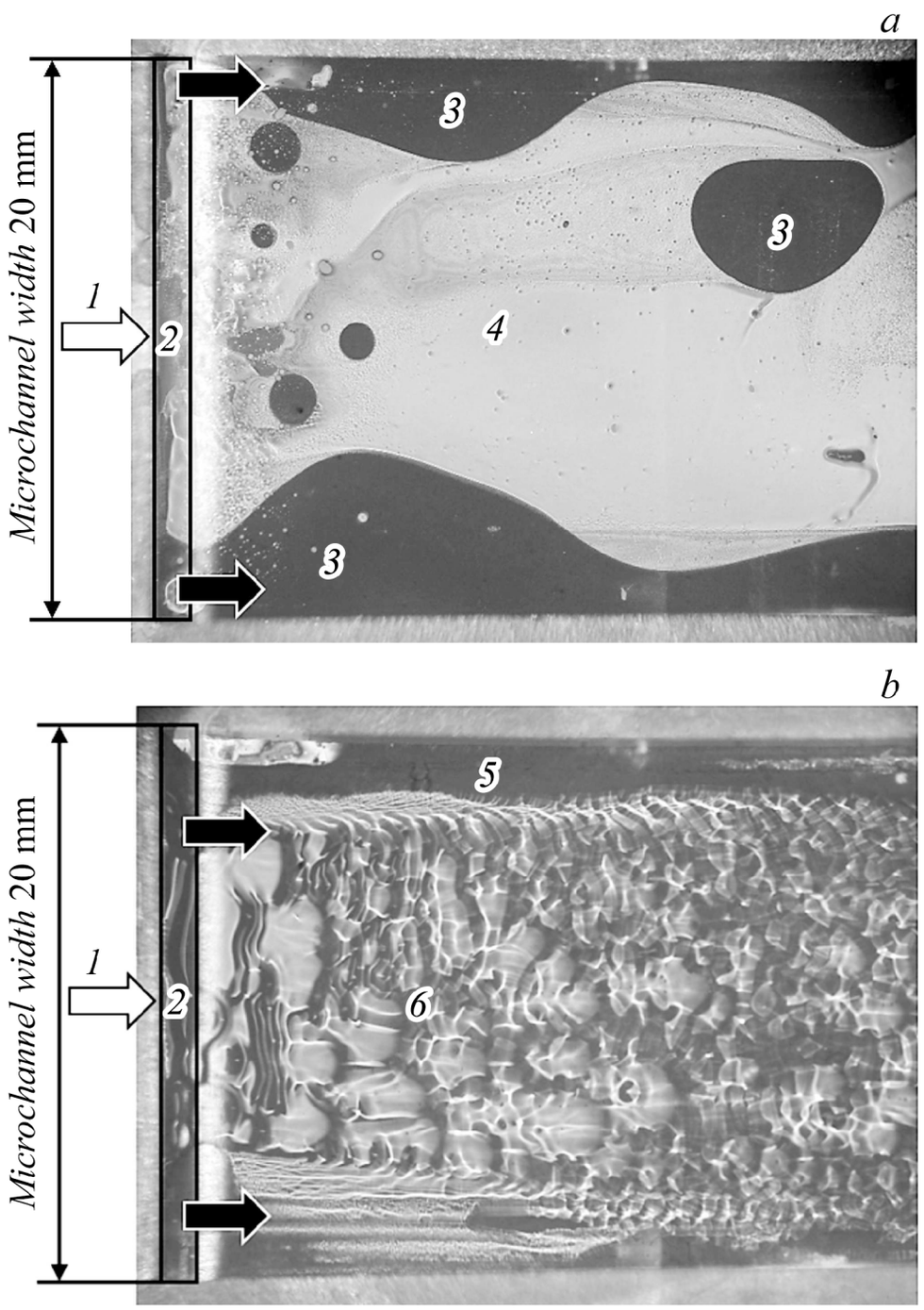

Рис. 1. Режимы двухфазного течения в микроканале сечением 0.15×20 mm. *a* — струйный режим при $U_{SG} = 0.556$ m/s, $U_{SL} = 0.011$ m/s с использованием FC-72; *b* — раздельный режим при $U_{SG} = 27.778$ m/s, $U_{SL} = 0.027$ m/s с использованием водно-спиртового раствора. *1* — вход газа в микроканал, *2* — вход жидкости в микроканал, *3* — жидкость, *4* — пленка на верхней стенке микроканала, *5* — осушенная область в микроканале, *6* — пленка жидкости на нижней стенке микроканала. Светлая стрелка — направление движения газа, темные стрелки — направления движения жидкости.

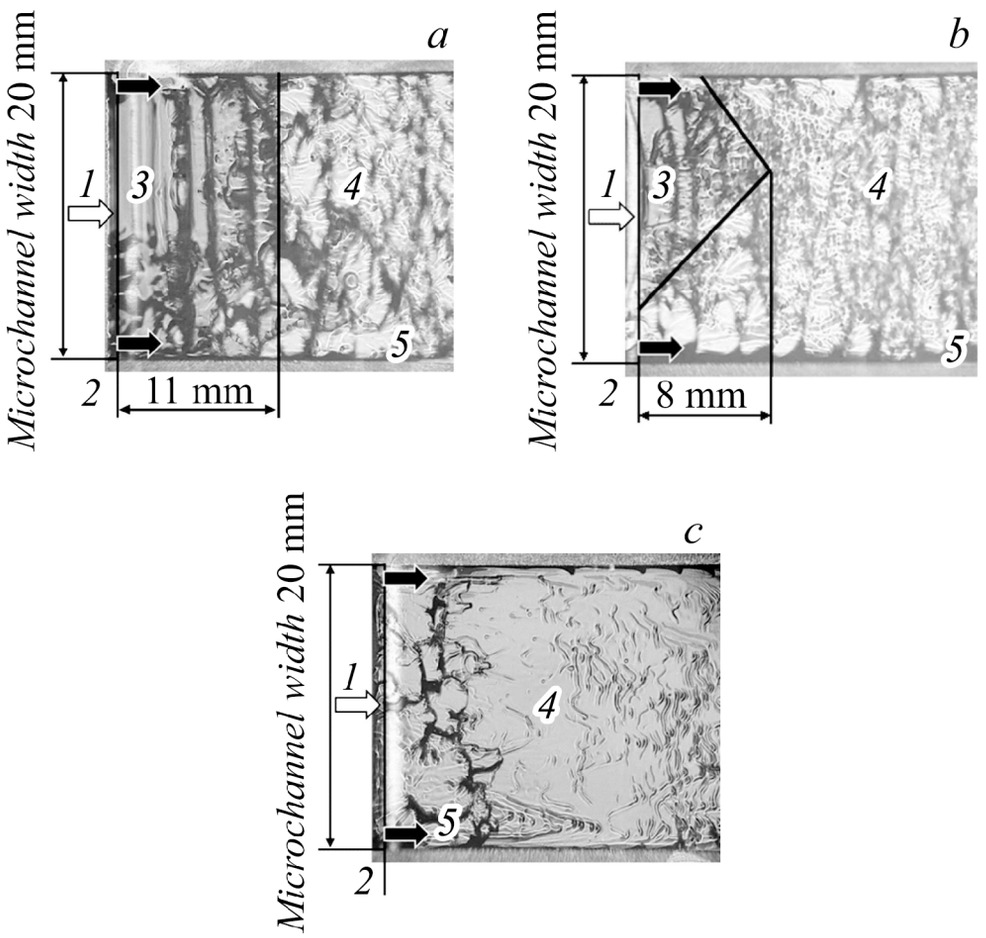

Рис. 2. Шлирен-фотографии кольцевого режима, где в качестве жидкости используются вода (a), водно-спиртовой раствор (b) и FC-72 (c). *1* — вход газа в микроканал, *2* — вход жидкости в микроканал, *3* — пленка на нижней стенке микроканала, *4* — пленка на верхней стенке микроканала, *5* — жидкость. Светлая стрелка — направление движения газа, темные стрелки — направления движения жидкости.

При увеличении приведенной скорости жидкости пленка образуется на верхней стенке микроканала, происходит переход к кольцевому режиму. При использовании в качестве жидкости воды пленка на верхней стенке микроканала формируется равноудаленно на расстоянии 11 mm от сопла жидкости (рис. 2, a). В случае водно-спиртового раствора формирование пленки жидкости на верхней стенке микроканала происходит сначала у боковых стенок микроканала, а затем в его центральной части, причем на расстоянии, меньшем, чем в случае использования в качестве рабочей жидкости воды (рис. 2, b). При использовании в качестве жидкости FC-72 пленка на верхней стенке

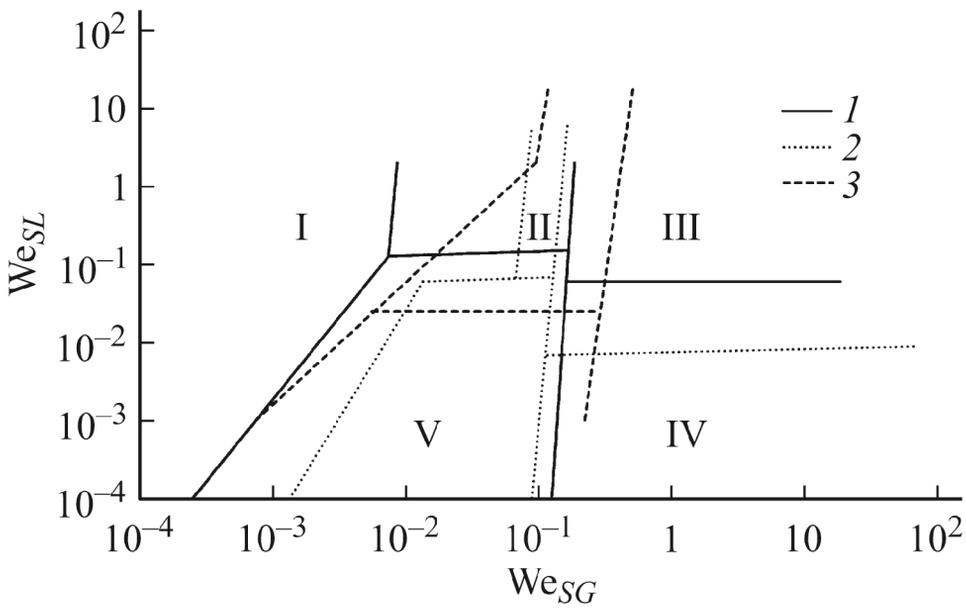

Рис. 3. Сравнительная режимная карта для микроканала сечением 0.15×20 mm при использовании воды (*1*), 50% водно-спиртового раствора (*2*) и FC-72 (*3*). Режимы течений: I — пузырьковый, II — вспененный, III — кольцевой, IV — раздельный, V — струйный.

микроканала формируется непосредственно возле сопла жидкости за счет набросов жидкости на верхнюю стенку микроканала (рис. 2, *c*). В этом случае пленка на верхней стенке микроканала формируется вследствие фронтальной неустойчивости. Таким образом, в зависимости от свойств жидкости за формирование пленки жидкости на верхней стенке микроканала отвечают различные механизмы.

При приведенных скоростях жидкости от 0.1 до 1 m/s и приведенных скоростях газа от 1 до 10 m/s наблюдается вспененный режим. Для данного режима характерны особенности как струйного, так и пузырькового режима. Характерной его особенностью является наличие сплошных и разорванных горизонтальных жидкостных перемычек между боковыми частями канала. Со временем такие перемычки могут как разрушаться, так и формироваться. Этот режим характерен для вертикальных каналов, а также наблюдается в широких горизонтальных микроканалах. Данный режим подробно рассмотрен в работе [7].

На рис. 3 представлено сравнение режимных карт, где в качестве координат используются числа Вебера. Видно, что при использовании FC-72 вспененный режим образуется при наименьших значениях We_{SL}.

При использовании водно-спиртового раствора и FC-72 переход от струйного к раздельному режиму (или к кольцевому для FC-72) наблюдается при меньших значениях We_{SG}, чем в случае использования воды. Происходит это потому, что водно-спиртовой раствор и FC-72 лучше смачивают поверхность, а значит, пленка жидкости образуется при меньших значениях расхода газа. Этим же можно объяснить сдвиг границы между раздельным и кольцевым режимами в сторону меньших значений We_{SL} при переходе от воды к водно-спиртовому раствору. При использовании FC-72 раздельный режим не зарегистрирован, пленка на верхней стенке канала образовывалась во всем диапазоне значений расхода газа и жидкости.

В заключение следует отметить, что для каналов с прямоугольным сечением и высотой $150\,\mu\mathrm{m}$ были обнаружены особенности режимов двухфазного течения, которые не наблюдались в предыдущих исследованиях. Установлены основные различия двухфазных течений в зависимости от свойств жидкости. Обнаружено, что в зависимости от используемой жидкости меняется механизм формирования режима двухфазного течения. Показано, как меняются границы между режимами в зависимости от используемой жидкости. В частности, обнаружено, что при использовании FC-72 пленка на верхней стенке канала образуется во всем диапазоне значений расхода газа и жидкости, из-за чего раздельный режим не формируется.

Исследование выполнено при финансовой поддержке РФФИ (№ 16-38-00713 мол_а).

Список литературы

[1] *Чиннов Е.А., Кабов О.А.* // Теплофизика высоких температур. 2006. Т. 44. № 5. С. 777–795.
[2] *Shao N., Gavriilidis A., Angeli P.* // Chem. Eng. Sci. 2009. V. 64. P. 2749–2761.
[3] *Ребров Е.В.* // Теорет. основы хим. технологии. 2010. Т. 44. № 4. С. 371–383.
[4] *Чиннов Е.А., Роньшин Ф.В., Кабов О.А.* // Теплофизика и аэромеханика. 2015. Т. 22. № 3. С. 265–284.
[5] *Минаков А.В., Шебелева А.А., Ягодницына А.А., Ковалев А.В., Бильский А.В.* // Письма в ЖТФ. 2017. Т. 43. В. 18. С 82–89.
[6] *Chinnov E.A., Ron'shin F.V., Kabov O.A.* // Interfacial Phenomena Heat Transfer. 2015. V. 3. N 3. P. 243–257.

[7] *Chinnov E.A., Ron'shin F.V., Kabov O.A.* // Int. J. Multiphase Flow. 2016. V. 80. P. 57–68.
[8] *Barajas A.M., Panton R.L.* // Int. J. Multiphase Flow. 1993. V. 19. N 2. P. 337–346.
[9] *Serizawa A., Feng Z., Kawara Z.* // Exp. Thermal Fluid Sci. 2002. V. 26. P. 703–714.
[10] *Ronshin F.V., Cheverda V.V., Chinnov E.A., Kabov O.A.* // Interfacial Phenomena Heat Transfer. 2016. V. 4. N 2-3. P. 191–205.

УДК 532.22

Плотность теплового потока в области контактной линии капли, лежащей на горизонтальной поверхности тонкой нагреваемой фольги*

В.В. Чеверда[1, 2], А.Л. Карчевский[2,3], И.В. Марчук[1,2], О.А. Кабов[1,4]

[1]*Институт теплофизики им. С.С. Кутателадзе СО РАН, Новосибирск*

[2]*Новосибирский государственный университет*

[3]*Институт математики им. С.Л. Соболева СО РАН, Новосибирск*

[4]*Томский политехнический университет*

E-mail: slava.cheverda@gmail.com

Экспериментально исследовались испаряющиеся капли воды, сидящие на горизонтальной нагреваемой подложке, в качестве которой использовалась константановая фольга толщиной 25 мкм, с размерами 42×35 мм^2. Эксперименты проводились с одной каплей или с ансамблем из двух или трёх капель на фольге. Температура нижней поверхности фольги измерялась ИК-сканером. Для определения плотности теплового потока при испарении жидкости вблизи контактной линии, решалась задача Коши для уравнения теплопроводности с использованием термографических данных. Результаты расчетов показали, что максимальная плотность теплового потока имеет место в области контактной линии и превосходит среднюю плотность теплового потока со всей поверхности фольги. Это объясняется притоком тепла с периферии фольги к капле за счет относительно высокого значения коэффициента теплопроводности материала фольги, а также высокой интенсивностью испарения в области контактной линии.

Ключевые слова: капля жидкости, локальный нагрев, контактная линия смачивания.

Изучение процессов переноса тепла в области динамической трехфазной контактной линии стенка–жидкость–пар является одной из важнейших задач физики. Недостаточно полное понимание процессов переноса в области линии контакта трех фаз сдерживает развитие исследований целого ряда явлений, таких как кипение, кавитация, ручейковые течения, разрушение пленок жидкости, растекание и испарение капель, капельная конденсация и др. [1, 2]. Толщина жидкости в этой области шириной порядка нескольких микрон, которую часто называют микрорегион, снижается от 1–3 мкм до 10–20 нм, т.е. до толщины адсорбированной пленки. Существенная кривизна границы раздела газ–жидкость в области микрорегиона, изменение толщины на 2–3 порядка, неравновесные эффекты (например, скачок температуры на границе раздела), влияние сил Ван-дер-Ваальса и структуры подложки вызывают трудности как для экспериментального, так и для теоретического исследования рассматриваемой проблемы.

* Работа выполнена за счет гранта РНФ (соглашение № 14-39- 00003).

© **Чеверда В.В., Карчевский А.Л., Марчук И.В., Кабов О.А., 2017**

Задача об определении интенсивности испарения и плотности теплового потока в нагреваемой жидкости в области трехфазной контактной линии активно исследуется в связи с важными практическими приложениями в энергетике, медицине, в химической, фармацевтической и пищевой промышленностях [3, 4]. Теоретические и экспериментальные исследования подтверждают, что интенсивность теплообмена в области контактной линии может быть более чем на порядок выше средней и вызывает локальный минимум температуры на твердой стенке. Однако прямых измерений плотности теплового потока в области микрорегиона, ширина которого по разным оценкам составляет от 0,5 до 10–20 мкм, провести пока не представляется возможным, поэтому используются различные косвенные методы и численные процедуры. В работе [5] исследовался мениск жидкости HFE7100, испаряющийся между двумя вертикальными нагреваемыми пластинами из металлической фольги. Было установлено, что локальная плотность теплового потока в области контактной линии в 5,4–6,5 раз больше, чем средняя плотность теплового потока на поверхности.

В работе экспериментально исследовались испаряющиеся капли воды, сидящие на горизонтальной нагреваемой подложке (см. рис 1). В качестве подложки использовалась константановая фольга (CuNi) толщиной 25 мкм, размером 88×35 мм^2, с коэффициентом теплопроводности 23 Вт/мК. Применялся джоулев нагрев фольги. Мощность тепловыделения в экспериментах составляла от 0,25 до 2,5 Вт. Фотографирование профиля капли проводилось с помощью оптической теневой системы с разрешением 8 мкм/пиксель. По фотографиям, сделанным методом Юнга–Лапласа [6], определялись геометрические параметры капель, которые в экспериментах были следующими: объем — 1,1÷39,3 мкл, диаметр основания (смоченного пятна) — 3÷7,19 мм, высота — 0,88÷1,81 мм, контактный угол смачивания — 50÷75° (средний угол 63°). Температура нижней поверхности фольги измерялась ИК-сканером Titanium 570M. Термографическая съемка проводилась с частотой записи 25 Гц, разрешением 640×512 пикселей и временем интегрирования 3050 мкс. Для увеличения минимальной разрешимой разности температур при использовании IR-камеры обратная сторона фольги покрывалась слоем сажи. Измеренная в экспериментах температура поверхности фольги лежала в диапазоне 29–86 °C. Средний коэффициент теплоотдачи от поверхности фольги к окружающему воздуху находился в пределах 16–20 Вт/м^{2}K (рис. 2).

Для более точной оценки интенсивности теплообмена при испарении жидкости вблизи контактной линии была сформулирована постановка задачи Коши для эллиптического уравнения (стационарной теплопроводности). На нижней стороне фольги задавались температура и плотность теплового потока, боковые стенки полагались адиабатическими. Задача Коши для уравнения Лапласа или эллиптического уравнения общего вида является одной из старейших некорректных задач. Ее решение является неустойчивым, т.е. малым вариациям в данных Коши могут соответствовать значительные изменения решения. Если предположить существование ограниченного решения, то возможно показать условную устойчивость. Неустойчивость решения задачи Коши проявляет себя при реализации любого численного метода ее решения. В настоящей работе использовался метод, который сводит решение задачи Коши к решению проблемы моментов [8]. В соответствии с ним в сопряженной задаче специальным образом выбирается краевое условие, и вычисление значения теплового потока на недоступной для измерений части границы сводится к суммированию соответствующего ряда. Рассматриваемый метод был применен к обработке экспериментальных данных в работах [8, 9]. Было показано наличие двух пиков в области контактной линии смачивания.

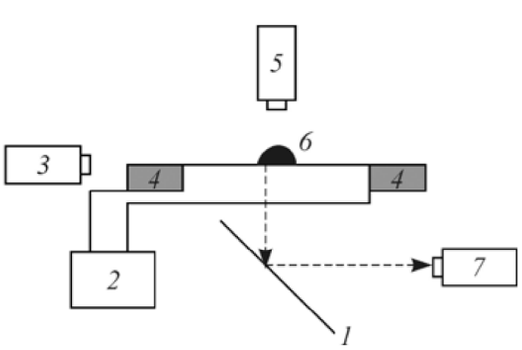

Рис. 1. Схема эксперимента.
1 — зеркало с золотым напылением, *2* — источник питания, *3* — теневая методика, *4* — латунные электроды, *5* — видеокамера, *6* — капля, *7* — ИК-сканер.

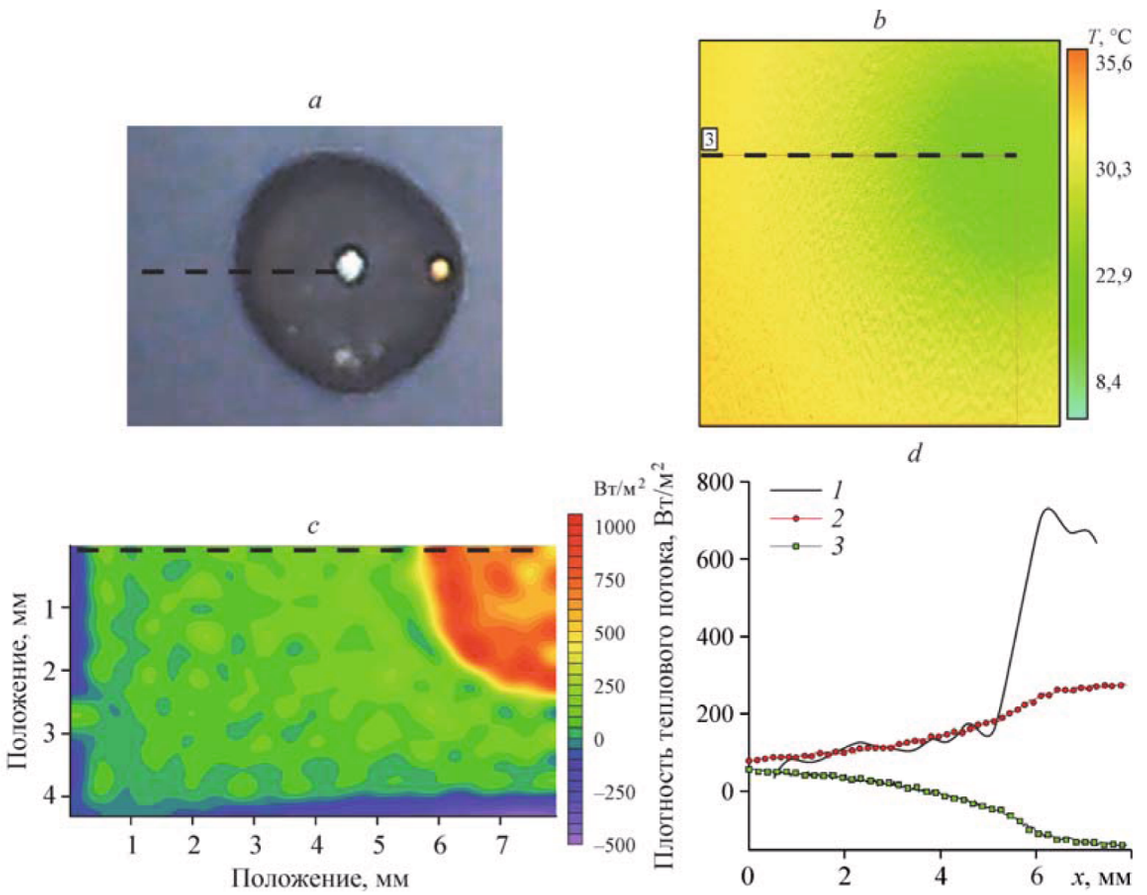

Рис. 2. Фото капли (*a*), распределения температуры фольги (*b*), плотности теплового потока для четверти капли (*c*) и плотности теплового потока вдоль штриховой линии на фрагментах *a*–*c* (*d*). Решение задачи Коши (*1*), расчет без учета перераспределения теплового потока в фольге (*2*), плотность теплового потока на нижней стороне фольги (*3*); неподвижная капля воды диаметром 3,4 мм, средняя плотность теплового потока q_{av} = 67,9 Вт/м^2.

С использованием предлагаемого метода решения задачи Коши по термографическим измерениям были рассчитаны распределения плотности теплового потока на поверхности фольги со стороны капли. На рис. 2 приведены первоначально измеренное с помощью ИК-макробъектива поле температур, рассчитанное распределение плотности теплового потока на подложке для четверти капли, а также распределение локальной плотности теплового потока вдоль штриховой линии, проходящей через центральное сечение капли. Результаты расчетов показали, что максимальная плотность теплового потока имеет место в области контактной линии и превосходит среднюю плотность теплового потока на всей поверхности фольги в 5 раз. Средняя плотность теплового потока в области смоченной каплей превосходит среднюю плотность теплового потока на всей поверхности фольги. Это объясняется притоком тепла с периферии фольги, обусловленного относительно высоким значением коэффициента теплопроводности материала фольги, а также высокой интенсивностью испарения в области контактной линии. На рис. 2*d* показан также расчет распределения локальной плотности теплового потока без учета перераспределения тепла, выделенного в фольге (линия *2*). Видно, что отсутствие учета теплопроводности подложки дает существенно заниженную плотность теплового потока и отсутствие пиков в области контактной линии. На рис. 3 представлены результаты измерений и расчетов для трех капель, одновременно в ряд сидящих на подложке, расстояние между которыми в среднем составляет 2 мм. Для каждой из капель нарушаются условия симметрии. В области контактной линии, расположенной между каплями, выраженных максимумов плотности теплового потока уже не наблюдается, так как в этом случае для каждой из капель уменьшается приток тепла с периферии, за который капли конкурируют.

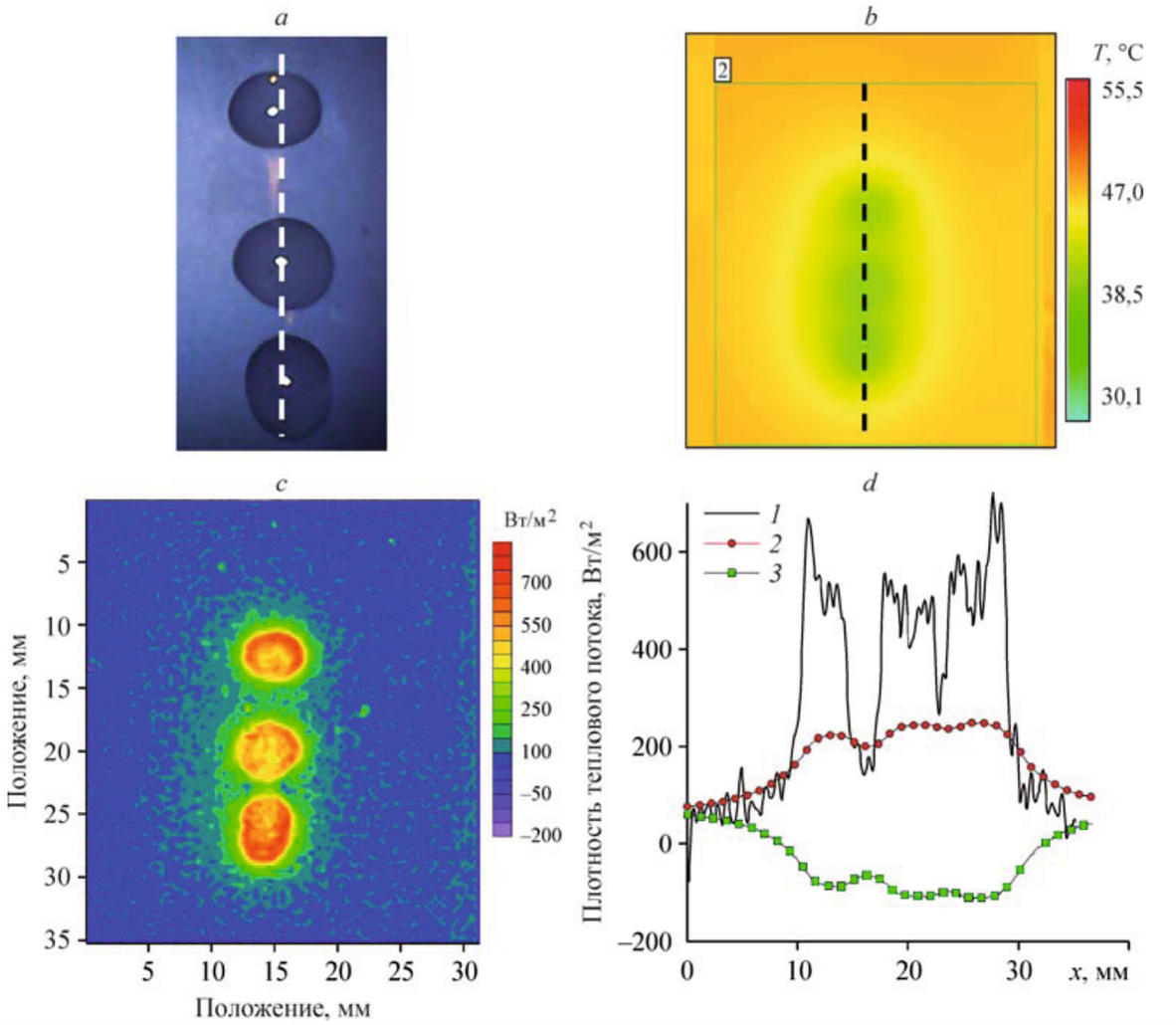

Рис. 3. Фото трех капель (*a*), распределения температуры фольги (*b*), плотности теплового потока (*c*) и плотности теплового потока вдоль штриховой линии на фрагментах *a* и *b* (*d*).

Решение задачи Коши (*1*), расчет без учета перераспределения теплового потока в фольге (*2*), плотность теплового потока на нижней стороне фольги (*3*); три неподвижных капли воды средним диаметром 3,3 мм, средняя плотность теплового потока $q_{av} = 67{,}9$ Вт/м^2.

Список литературы

1. **Sobac B., Brutin D.** Triple-line behavior and wettability controlled by nanocoated substrates: influence on sessile drop evaporation // Langmuir. 2011. Vol. 27. P. 14999–15007.
2. **Moraila-Martínez C.L., Cabrerizo-Vílchez M.A., Rodríguez-Valverde M.A.** Controlling the morphology of ring-like deposits by varying the pinning time of driven receding contact lines // Interfacial Phenomena and Heat Transfer. 2013. Vol. 1. P. 195–205.
3. **Kundan A., Plawsky J.L., Wayner P.C.** Thermophysical characteristics of a wickless heat pipe in microgravity — constrained vapor bubble experiment // Int. J. of Heat and Mass Transfer. 2014. Vol. 78. P. 1105–1113.
4. **Ajaev V.S., Gatapova E.Y., Kabov O.A.** Rupture of thin liquid films on structured surfaces // Physical Review E. 2011. Vol. 84. P. 041606-1–041606-7.
5. **Ibrahem K., Rabbo M.F.A., Roisman T.G., Stephan P.** Experimental investigation of evaporative heat transfer characteristics at the 3-phase contact line // Experimental Thermal and Fluid Sci. 2010. Vol. 34. P. 1036–1041.
6. **Марчук И.В., Чеверда В.В., Стрижак П.А., Кабов О.А.** Определение поверхностного натяжения и контактного угла смачивания по форме поверхности осесимметричных пузырей и капель // Теплофизика и аэромеханика. 2015. Т. 22, № 3. С. 311–317.
7. **Karchevsky A.L.** Reformulation of an inverse problem statement that reduces computational costs // Eurasian J. of Mathematical and Computer Applications. 2013. Vol. 1, No. 2. P. 4–19.
8. **Karchevsky A.L., Marchuk I.V., Kabov O.A.** Calculation of the heat flux near the liquid-gas-solid contact line // Applied Mathematical Modelling. 2016. Vol. 40, Iss. 2. P. 1029–1037.
9. **Чеверда В.В., Марчук И.В., Карчевский А.Л., Орлик Е.В., Кабов О.А.** Экспериментальное исследование теплообмена в стекающем по наклонной фольге ручейке // Теплофизика и аэромеханика. 2016. Т. 23, № 3. С. 431–436.

Статья поступила в редакцию
после доработки — 10 февраля 2017 г.

ТЕПЛОФИЗИКА ВЫСОКИХ ТЕМПЕРАТУР, 2017, том 55, № 6, с. 720–732

УДК 536.25

ИЗУЧЕНИЕ КОНВЕКТИВНЫХ ТЕЧЕНИЙ ЖИДКОСТИ И СПУТНОГО ПОТОКА ГАЗА С УЧЕТОМ ИСПАРЕНИЯ

© 2017 г. О. Н. Гончарова[1,2], Е. В. Резанова[1,2], Ю. В. Люлин[2,3,*], О. А. Кабов[2,3]

[1]Алтайский государственный университет, г. Барнаул, Россия

[2]Институт теплофизики им. С.С. Кутателадзе СО РАН, г. Новосибирск, Россия

[3]Национальный исследовательский Томский политехнический университет, г. Томск, Россия

*E-mail: lyulin@itp.nsc.ru

Поступила в редакцию 29.07.2015 г.

Изучаются конвективные течения жидкости и сопутствующего потока газа, сопровождающиеся испарением на границе раздела. Теоретическое исследование двухслойных течений проведено на основе математической модели, учитывающей испарение на термокапиллярной границе, а также эффекты термодиффузии и диффузионной теплопроводности в газопаровом слое. Представлены новые точные решения, описывающие стационарные двухслойные течения в канале с границей раздела, остающейся недеформированной, и примеры профилей скорости и температуры для системы HFE-7100 (жидкость)–азот (газ). Исследовано влияние продольных градиентов температуры, действующих вдоль границ канала, расхода газа и высоты слоя жидкости на характер течения и интенсивность испарения. Выполнено сравнение полученных расчетных данных и результатов экспериментальных исследований.

DOI: 10.7868/S0040364417060072

ВВЕДЕНИЕ

Конвективные течения жидкостей, сопровождающиеся испарением или конденсацией на границе раздела, часто возникают под действием сопутствующих потоков газа и активно изучаются экспериментально и теоретически [1–6]. С созданием новой экспериментальной установки [7] испарительная конвекция может изучаться в неподвижном и движущемся слое под действием сухого и влажного потоков газа, что является важнейшей мотивацией для развития теории конвекции в областях с границами раздела, поскольку дает возможность проводить апробацию математических моделей и сравнение с экспериментальными данными.

Разработке математических моделей конвективных движений с учетом процессов тепломассопереноса и формулировке условий на границе раздела посвящены работы [3, 4, 8–11]. Особый интерес всегда вызывала задача изучения решений специального вида для описания двухслойных или многослойных течений жидкостей, заполняющих бесконечные каналы и имеющих границы раздела [12–17]. Построение точных решений приобретает особую актуальность при изучении задач с учетом тепло- и массопереноса на границе раздела в связи с возможностью проводить с их помощью апробацию математических моделей, исследовать степень влияния различных физических факторов на характер течений и интенсивность испарения, а также делать прогнозы относительно экспериментов, в том числе готовящихся на Международной космической станции [3, 6, 18].

Один из первых примеров точных решений, описывающих двухслойные течения с учетом массопереноса, получен в [19] в случае границы раздела жидкость–жидкость. В работах [14, 15] точные решения построены для задачи о двухслойном течении жидкости и изотермического газа в полной постановке. При этом испарение в [14, 15] явно не учитывается, а моделируется с помощью условия для температуры на границе раздела. Точные решения, описывающие двухслойные течения с испарением с учетом эффекта Дюфура в газовой фазе [20], построены в [21] в случае заданного расхода газа и в [18] в условиях замкнутости потоков в обеих фазах. Построенные в работах [13–15, 18, 19, 21] решения могут быть названы обобщением известного решения [22] о конвекции в бесконечном слое с недеформируемой свободной границей, находящемся под действием поперечного поля силы тяжести и продольного градиента температуры.

Целью данной работы является аналитическое исследование стационарных течений жидкости под действием спутного потока газа с учетом испарения на термокапиллярной границе раздела, а кроме того, сравнение полученных результатов с экспериментальными данными. Математическое

моделирование двухслойных течений проводится с помощью точных решений уравнений Навье–Стокса в приближении Обербека–Буссинеска [23, 24]. В верхнем слое, представляющем собой смесь газа и паров жидкости, изучается процесс диффузии пара и учитываются эффекты термодиффузии и диффузионной теплопроводности (эффекты Соре и Дюфура) [20, 23, 25] (см. также [26–29]). Данные решения характеризуются тем, что продольные компоненты вектора скорости жидкости и газа отличны от нуля и зависят только от поперечной координаты. Функции температуры в верхнем и нижнем слоях, концентрации пара в газе и давление зависят от обеих координат, причем от продольной координаты – линейно.

В работе удалось получить точные решения исходной системы дифференциальных уравнений и предложить не только физическую интерпретацию этих решений, но и провести сравнение результатов моделирования конвективных течений с испарением, проводимого на основе точных решений, с экспериментальными данными. Проведено исследование особенностей двухслойных течений жидкости (HFE-7100) и газа (азот) и интенсивности испарения жидкости на границе раздела. Показано влияние изменения расхода газа, продольных градиентов температуры и эффекта Соре на профили скорости и температуры, а также массу испаряющейся с границы раздела жидкости. Представлены сопоставления теоретических и экспериментальных данных, отражающих зависимость интенсивности испарения со свободной границы от расхода газа и толщины жидкого слоя.

1. ПОСТАНОВКА ЗАДАЧИ О ДВУХСЛОЙНОМ ТЕЧЕНИИ С УЧЕТОМ ИСПАРЕНИЯ. ПОСТРОЕНИЕ ТОЧНОГО РЕШЕНИЯ

Пусть две несмешивающиеся, вязкие, несжимаемые жидкости (жидкость и смесь газа и пара) заполняют бесконечные слои толщиной l и h соответственно. Система координат выбрана таким образом, чтобы вектор силы тяжести $\mathbf{g}$ был направлен противоположно оси Oy ($\mathbf{g} = (0,-g)$) (см. рис. 1). Верхняя и нижняя стенки канала $y = h$ и $y = -l$ являются твердыми непроницаемыми границами, а общая граница раздела, здесь $y = 0$, останется недеформированной. Система уравнений Навье–Стокса в приближении Обербека–Буссинеска используется для моделирования течений жидкостей в нижнем и верхнем слоях в стационарном случае. Концентрация пара, считающегося пассивной примесью в газе, т.е. не влияющей на свойства газа, определяется с помощью уравнения диффузии. С учетом эффектов Соре и Дюфура в слое газа математическая модель представляет собой систему дифференциальных уравнений

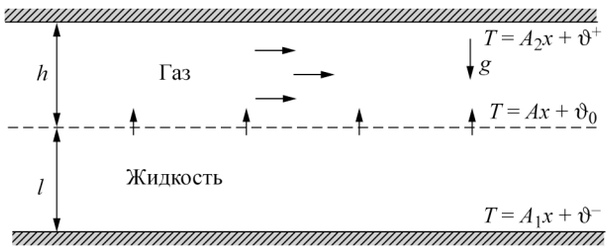

Рис. 1. Геометрия области течения.

$$u\frac{\partial u}{\partial x} + v\frac{\partial u}{\partial y} = -\frac{1}{\rho}\frac{\partial p'}{\partial x} + \nu\left(\frac{\partial^2 u}{\partial x^2} + \frac{\partial^2 u}{\partial y^2}\right), \qquad (1)$$

$$u\frac{\partial v}{\partial x} + v\frac{\partial v}{\partial y} = -\frac{1}{\rho}\frac{\partial p'}{\partial y} + \pi\left(\frac{\partial^2 v}{\partial x^2} + \frac{\partial^2 v}{\partial y^2}\right) + g(\beta T + \gamma C), \qquad (2)$$

$$\frac{\partial u}{\partial x} + \frac{\partial v}{\partial y} = 0, \qquad (3)$$

$$u\frac{\partial T}{\partial x} + v\frac{\partial T}{\partial y} = \chi\left(\frac{\partial^2 T}{\partial x^2} + \frac{\partial^2 T}{\partial y^2} + \delta\left(\frac{\partial^2 C}{\partial x^2} + \frac{\partial^2 C}{\partial y^2}\right)\right), \qquad (4)$$

$$u\frac{\partial C}{\partial x} + v\frac{\partial C}{\partial y} = D\left(\frac{\partial^2 C}{\partial x^2} + \frac{\partial^2 C}{\partial y^2} + \alpha\left(\frac{\partial^2 T}{\partial x^2} + \frac{\partial^2 T}{\partial y^2}\right)\right) \qquad (5)$$

и граничных условий, сформулированных ниже. Слагаемые γC и $\delta\Delta C$ в уравнениях (2) и (4) и уравнение (5) используются при моделировании течения в верхнем слое. Здесь u, v – проекции вектора скорости на оси декартовой системы координат, p' – модифицированное давление или отклонение от гидростатического давления ($p' = p - \rho\mathbf{g}\cdot\mathbf{x}$, $\mathbf{x} = (x, y)$, p – давление), T – температура, C – концентрация пара, ρ – плотность (относительное значение плотности), ν – коэффициент кинематической вязкости, χ – коэффициент температуропроводности, D – коэффициент диффузии пара в газе, β – коэффициент теплового расширения, γ – концентрационный коэффициент плотности, коэффициент δ характеризует эффект Дюфура, коэффициент α определяет эффект Соре в газопаровом слое.

Пусть решение u_i, v_i, p_i', T_i, C уравнений (1)–(5) имеет специальный вид [19, 22]:

$$u_i = u_i(y), \quad v_i = 0, \quad p_i' = p_i'(x, y),$$
$$T_i = (a_1^i + a_2^i y)x + \vartheta_i(y), \qquad (6)$$
$$C = (b_1 + b_2 y)x + \varphi(y).$$

Если функции или коэффициенты отмечены нижним либо верхним индексом i ($\underline{i} = 1, 2$), то при $i = 1$ они характеризуют жидкость, заполняющую нижний слой, а при $i = 2$ – жидкость (смесь газа и пара), заполняющую верхний слой. Отметим, что система уравнений (1)–(5), описывающая конвективные движения жидкостей, является достаточно сложной не только в силу своей нелинейности и высокого порядка, но и потому, что не относится к какому-либо классическому типу (см., например, [30]). Построение точных решений вида (6) позволяет перейти к решению уравнений меньшей размерности и исследовать течения, вызываемые совместным действием продольного градиента температуры и поперечно направленной силы тяжести. Систематический анализ точных решений уравнений конвекции, в том числе и определение вида решения, относится к задачам, решаемым с применением методов группового анализа дифференциальных уравнений [31, 32]. Групповая природа решения Бириха [22] и возможные обобщения данного решения в трехмерном случае представлены в [33], а решения уравнений Обербека–Буссинеска, в которых функция температуры линейно зависит от продольной координаты, впервые получены в [34].

Решение системы уравнений (1)–(5) вида (6) может быть представлено в следующей форме:

$$u_i = \frac{y^4}{24}L_4^i + \frac{y^3}{6}L_3^i + \frac{y^2}{2}c_1^i + yc_2^i + c_3^i, \qquad (7)$$

$$T_i = (a_1^i + a_2^i y)x + \frac{y^7}{1008}N_7^i + \frac{y^6}{720}N_6^i + \frac{y^5}{120}N_5^i + \\ + \frac{y^4}{24}N_4^i + \frac{y^3}{6}N_3^i + \frac{y^2}{2}N_2^i + yc_4^i + c_5^i, \qquad (8)$$

$$C = (b_1 + b_2 y)x + \frac{y^7}{1008}S_7 + \frac{y^6}{720}S_6 + \frac{y^5}{120}S_5 + \\ + \frac{y^4}{24}S_4 + \frac{y^3}{6}S_3 + \frac{y^2}{2}S_2 + yc_6^2 + c_7^2, \qquad (9)$$

$$p_i' = \left[d_3^i\frac{y^2}{2} + d_2^i y + d_1^i\right]x + \\ + \frac{y^8}{8}K_8^i + \frac{y^7}{7}K_7^i + \frac{y^6}{6}K_6^i + \frac{y^5}{5}K_5^i + \\ + \frac{y^4}{4}K_4^i + \frac{y^3}{3}K_3^i + \frac{y^2}{2}K_2^i + yK_1^i + c_8^i. \qquad (10)$$

Коэффициенты $L_4^i, L_3^i, N_j^i, S_j, K_m^i$ ($i = 1, 2$, $j = 2, 7$; $m = 1, 8$) выражаются через физические параметры задачи $g, \beta_i, \nu_i, \chi_i, \rho_i, D, \gamma$ и коэффициенты в продольных градиентах температуры и концентрации a_j^i, b_i ($i, j = 1, 2$) следующим образом:

$$L_4^i = \frac{g\beta_i a_2^i}{\nu_i} + \delta_{2i}\frac{g\gamma b_2}{\nu_2}, \quad L_3^i = \frac{g\beta_i A}{\nu_i} + \delta_{2i}\frac{g\gamma b_1}{\nu_2},$$

$$N_7^1 = \frac{g\beta_1\left(a_2^1\right)^2}{\nu_1\chi_1}, \quad N_6^1 = 5\frac{g\beta_1 A a_2^1}{\nu_1\chi_1},$$

$$N_5^1 = \frac{1}{\chi_1}\left(\frac{g\beta_1(A)^2}{\nu_1} + 3a_2^1c_1^1\right), \quad N_4^1 = \frac{1}{\chi_1}\left(Ac_1^1 + 2a_2^1c_2^1\right),$$

$$N_3^1 = \frac{1}{\chi_1}\left(Ac_2^1 + a_2^1c_3^1\right), \quad N_2^1 = \frac{A}{\chi_1}c_3^1,$$

$$N_7^2 = B_2\frac{g}{\nu_2}\left(\beta_2 a_2^2 + \gamma b_2\right),$$

$$N_6^2 = B_1\frac{g}{\nu_2}\left(\beta_2 a_2^2 + \gamma b_2\right) + 4B_2\frac{g}{\nu_2}(\beta_2 A + \gamma b_1),$$

$$N_5^2 = B_1\frac{g}{\nu_2}(\beta_2 A + \gamma b_1) + 3B_2c_1^2,$$

$$N_4^2 = B_1c_1^2 + 2B_2c_2^2, \quad N_3^2 = B_1c_2^2 + B_2c_3^2, \quad N_2^2 = B_1c_3^2,$$

$$d_3^i = \rho_i g\beta_i a_2^i + \delta_{2i}\rho_2 g\gamma b_2,$$
$$d_2^i = \rho_i g\beta_i A + \delta_{2i}\rho_2 g\gamma b_1, \quad d_1^i = \rho_i\nu_i c_1^i,$$

$$S_7 = \frac{g}{\nu_2}\left(\beta_2 a_2^2 + \gamma b_2\right)E_2,$$

$$S_6 = \frac{g}{\nu_2}\left\{E_1\left(\beta_2 a_2^2 + \gamma b_2\right) + 4E_2(\beta_2 A + \gamma b_1)\right\},$$

$$S_5 = \frac{g}{\nu_2}(\beta_2 A + \gamma b_1)E_1 + 3E_2c_1^2, \quad S_4 = E_1c_1^2 + 2E_2c_2^2,$$

$$S_3 = E_1c_2^2 + E_2c_3^2, \quad S_2 = E_1c_3^2.$$

$$K_8^1 = \frac{1}{1008}\frac{\left(g\beta_1 a_2^1\right)^2\rho_1}{\nu_1\chi_1}, \quad K_7^1 = \frac{1}{144}\frac{(g\beta_1)^2\rho_1}{\nu_1\chi_1}Aa_2^1,$$

$$K_6^1 = \frac{1}{120}\frac{g\beta_1\rho_1}{\chi_1}\left(\frac{g\beta_1(A)^2}{\nu_1} + 3a_2^1c_1^1\right),$$

$$K_5^1 = \frac{1}{24}\frac{g\beta_1\rho_1}{\chi_1}\left(Ac_1^1 + 2a_2^1c_2^1\right),$$

$$K_4^1 = \frac{1}{6}\frac{g\beta_1\rho_1}{\chi_1}\left(Ac_2^1 + a_2^1c_3^1\right), \quad K_3^1 = \frac{1}{2}\frac{g\beta_1\rho_1}{\chi_1}Ac_3^1,$$

$$K_2^1 = g\beta_1\rho_1 c_4^1, \quad K_1^1 = g\beta_1\rho_1 c_5^1,$$

$$K_8^2 = \frac{1}{1008}\frac{\rho_2 g^2}{\nu_2}\left(\beta_2 a_2^2 + \gamma b_2\right)\left[B_2(\beta_2 - \alpha\gamma) + \frac{\gamma b_2}{D}\right],$$

$$K_7^2 = \frac{1}{720}\frac{\rho_2 g^2}{\nu_2}\left\{\left(\beta_2 a_2^2 + \gamma b_2\right)\left[B_1(\beta_2 - \alpha\gamma) + \frac{\gamma b_1}{D}\right] + \right.$$
$$\left. + 4(\beta_2 A + \gamma b_1)\left[B_2(\beta_2 - \alpha\gamma) + \frac{\gamma b_2}{D}\right]\right\},$$

$$K_6^2 = \frac{1}{120}\rho_2 g\left\{\frac{g}{\nu_2}(\beta_2 A + \gamma b_1)\left[B_1(\beta_2 - \alpha\gamma) + \frac{\gamma b_1}{D}\right] + \right.$$
$$\left. + 3\left[B_2(\beta_2 - \alpha\gamma) + \frac{\gamma b_2}{D}\right]c_1^2\right\},$$

$$K_5^2 = \frac{1}{24}\rho_2 g\left\{\left[B_1(\beta_2 - \alpha\gamma) + \frac{\gamma b_1}{D}\right]c_1^2 + \right.$$
$$\left. + 2\left[B_2(\beta_2 - \alpha\gamma) + \frac{\gamma b_2}{D}\right]c_2^2\right\},$$

$$K_4^2 = \frac{1}{6}\rho_2 g\left\{\left[B_1(\beta_2 - \alpha\gamma) + \frac{\gamma b_1}{D}\right]c_2^2 + \right.$$
$$\left. + \left[B_2(\beta_2 - \alpha\gamma) + \frac{\gamma b_2}{D}\right]c_3^2\right\},$$

$$K_3^2 = \frac{1}{2}\rho_2 g\left[B_1(\beta_2 - \alpha\gamma) + \frac{\gamma b_1}{D}\right]c_3^2,$$

$$K_2^2 = \rho_2 g\beta_2 c_4^2 + \rho_2 g\gamma c_6^2, \quad K_1^2 = \rho_2 g\beta_2 c_5^2 + \rho_2 g\gamma c_7^2. \tag{11}$$

Здесь δ_{2i} – символ Кронекера, B_1 и B_2 определяются из следующих соотношений:

$$B_1 = \frac{DA - \chi_2\delta b_1}{D\chi_2(1 - \alpha\delta)}, \quad B_2 = \frac{Da_2^2 - \chi_2\delta b_2}{D\chi_2(1 - \alpha\delta)},$$
$$E_1 = \frac{b_1}{D} - \alpha B_1, \quad E_2 = \frac{b_2}{D} - \alpha B_2. \tag{12}$$

В формулах (11), (12) при вычислении коэффициентов уже учтено, что $a_1^1 = a_1^2 = A$ (см. (5)), как следствие условия непрерывности температуры на границе раздела $y = 0$. Коэффициенты c_j^i ($i = 1, 2$; $j = 1, ..., 8$) являются константами интегрирования и будут найдены с помощью граничных условий (см. разделы 1.1, 1.2).

1.1. Граничные условия в задаче о двухслойном течении с учетом испарения. Пусть на нижней $y = -l$ и верхней $y = h$ твердых непроницаемых стенках канала (см. рис. 1) выполнены условия прилипания для скорости (см. также (6)):

$$u_1\,|_{y=-l} = 0, \quad u_2\,|_{y=h} = 0, \tag{13}$$

а температура распределена линейно относительно продольной координаты:

$$T_1\,|_{y=-l} = A_1 x + \vartheta^-, \quad T_2\,|_{y=h} = A_2 x + \vartheta^+. \tag{14}$$

Рассмотрим два вида граничных условий для концентрации пара на верхней твердой границе $y = h$. В первом случае будем предполагать так называемую полную абсорбцию пара

$$C\big|_{y=h} = 0. \tag{15}$$

Во втором случае полагаем отсутствие потока пара

$$\left.\frac{\partial C}{\partial y}\right|_{y=h} = 0. \tag{16}$$

Пусть расход газа в верхнем слое задан и определяется соотношением

$$Q = \int_0^h \rho_2 u_2(y)\,dy. \tag{17}$$

Потребуем, чтобы на термокапиллярной границе раздела $y = 0$ были выполнены условия непрерывности скорости и температуры:

$$u_1\,|_{y=0} = u_2\,|_{y=0}, \quad T_1\,|_{y=0} = T_2\,|_{y=0}\,. \tag{18}$$

На термокапиллярной границе раздела также должны быть выполнены кинематическое и динамические условия [23]. Первое из них выполняется автоматически ($\upsilon_1\,|_{y=0} = 0$, $\upsilon_2\,|_{y=0} = 0$, см. вид точного решения (6)), а динамические условия на границе y=0 можно записать следующим образом:

$$\rho_1\nu_1 u_{1y} = \rho_2\nu_2 u_{2y} + \sigma_T\left.\frac{\partial T_1}{\partial x}\right|_{y=0}, \quad p_1 = p_2. \tag{19}$$

Здесь σ_T – температурный коэффициент поверхностного натяжения σ. Предполагается линейная зависимость поверхностного натяжения от температуры: $\sigma = \sigma_0 + \sigma_T(T - T_0)$, $\sigma_T = \text{const}$, $\sigma_T < 0$. Баланс теплового потока записывается с учетом диффузионного потока массы испаряющейся жидкости на границе раздела (см. [21, 23]):

$$\kappa_1\frac{\partial T_1}{\partial y} - \kappa_2\frac{\partial T_2}{\partial y} - \delta\kappa_2\left.\frac{\partial C}{\partial y}\right|_{y=0} = -\lambda M. \tag{20}$$

Здесь λ – теплота испарения, M – массовая скорость ($M = \text{const}$) испаряющейся с единицы площади поверхности в единицу времени жидкости, κ_1 и κ_2 – коэффициенты теплопроводности. Уравнение баланса масс с учетом эффекта термодиффузии на границе раздела имеет следующий вид [19, 21, 23]):

$$M = -D\rho_2\left(\left.\frac{\partial C}{\partial y}\right|_{y=0} + \alpha\left.\frac{\partial T_2}{\partial y}\right|_{y=0}\right). \qquad (21)$$

Концентрация насыщенного пара на границе раздела будет определяться с помощью соотношения

$$C\,|_{y=0} = C_*\left[1 + \varepsilon\left(T_2\,|_{y=0} - T_0\right)\right], \qquad (22)$$

являющегося следствием уравнения Клапейрона–Клаузиуса $P = P_0\exp[(\lambda\mu / R)(1/T_0 - 1/T)]$ и уравнения Менделеева–Клапейрона для идеального газа $\rho_v RT = \mu P$ ((P_0, T_0) – некоторое исходное состояние, $\rho_v = C\rho_2$) [35]. Уравнение (22) получено в условиях малости параметра εT_* для умеренных перепадов температуры [18, 21, 36]. Здесь T_0 – некоторая начальная температура, C_* – концентрация насыщенного пара при $T_2 = T_0$ (T_0 полагается равным 20°C в [19, 21]), $\varepsilon T_* = \lambda\mu / (RT_0^2)$, μ – молярная масса испаряющейся жидкости, R – универсальная газовая постоянная, T_* – характерное значение перепада температуры. Следует заметить, что уравнения (1)–(5) и граничные условия (13)–(22) допускают замену искомых функций T_i вида $(T_i - T_0)$, тогда можно принять выполненным условие

$$C\,|_{y=0} = C_*\left[1 + \varepsilon T_2\,|_{y=0}\right], \qquad (23)$$

аналогично принятому в [19] (см. также [21]). Если при реализации алгоритма расчета констант интегрирования будет использоваться условие (23), то речь пойдет о нахождении функции температуры вида $(T - T_0)$.

Заметим, что точное уравнение баланса массы пара [10] требует, чтобы коэффициент D в уравнении (21) был поделен на $(1 - C)$ (см. также [37, 38]). Условия малости параметра $(C_*\varepsilon T_*)$ позволяют вычислять величину массовой скорости испарения M согласно (21), где под D следует понимать приведенный коэффициент диффузии, равный коэффициенту диффузии, деленному на $(1 - C_*)$.

1.2. Определение неизвестных коэффициентов в случае граничного условия (15) для концентрации пара на верхней границе. Рассмотрим случай, когда на верхней границе канала выбирается условие (15) для концентрации C. Условие равенства нулю концентрации пара (15) может быть объяснено свойством границы впитывать пар мгновенно (т.е. свойство полной абсорбции пара [19]). Для реальных физических ситуаций, в случае конденсации или вымораживания пара, граничное значение C на верхней твердой стенке может меняться и быть функцией температуры.

С учетом эффекта термодиффузии в газопаровом слое из условия (15) имеем

$$b_2 = -b_1/h, \quad \varphi(h) = 0\,. \qquad (24)$$

Принимая во внимание вид решения (6) и условие непрерывности температуры на границе раздела (18), получим, что коэффициенты a_1^1, a_1^2 равны между собой: $a_1^1 = a_1^2 = A$ (учтено в (11); $A = \text{const}$). Условия непрерывности скорости и температуры (18) на границе $y = 0$ влекут за собой равенства

$$c_3^1 = c_3^2, \quad c_5^1 = c_5^2\,. \qquad (25)$$

Из уравнения (22) (или (23)) для концентрации насыщенного пара следует

$$b_1 = C_*\varepsilon A, \quad c_7^2 = C_* + C_*\varepsilon\left(c_5^2 - T_0\right). \qquad (26)$$

Тогда коэффициент b_2, входящий в продольный градиент концентрации, определяется с помощью следующего выражения: $b_2 = -C_*\varepsilon A/h$ (см. (24) и (26)). Вследствие линейного распределения температуры на твердых границах системы относительно продольной координаты (14) выполняются равенства

$$a_2^1 = (A - A_1)/l, \quad a_2^2 = (A_2 - A)/h, \qquad (27)$$

а также

$$\vartheta_1(-l) = \vartheta^-, \quad \vartheta_2(h) = \vartheta^+. \qquad (28)$$

Уравнение баланса массы (21) диктует выполнение соотношений

$$b_2 = -\alpha a_2^2, \quad M = -D\rho_2\left(c_6^2 + \alpha c_4^2\right). \qquad (29)$$

Отсюда следует, что продольные градиенты температуры на верхней границе и границе раздела связаны следующим образом: $A_2 = A + C_*\varepsilon A/\alpha$. Условие теплопереноса на границе раздела (20) требует, чтобы выполнялись соотношения

$$\kappa_1 a_2^1 - \kappa_2 a_2^2 - \delta\kappa_2 b_2 = 0,$$

$$\kappa_1 c_4^1 - \kappa_2 c_4^2 - \delta\kappa_2 c_6^2 = -\lambda M. \qquad (30)$$

Тогда вследствие (27) и первых уравнений в (29) и (30) определяется взаимозависимость градиентов A и A_1. Тем самым установлена связь между продольными градиентами температуры A, A_1 и A_2, которые требуется поддерживать на границах канала:

$$A_2 = A + C_*\varepsilon A/\alpha\,,$$

$$A_1 = A + A(l/h)(\kappa_2/\kappa_1)(C_*\varepsilon/\alpha)(\alpha\delta - 1). \qquad (31)$$

Из динамических условий (19) следуют выражения

$$c_1^1 = c_1^2 \rho_2 \nu_2/(\rho_1 \nu_1),$$
$$c_2^1 = c_2^2 \rho_2 \nu_2/(\rho_1 \nu_1) + \sigma_T A / (\rho_1 \nu_1). \qquad (32)$$

Вторые соотношения, представленные в (29) и (30), устанавливают следующую связь между константами интегрирования c_6^2, c_4^1 и c_4^2:

$$c_6^2 = c_4^1 \kappa_1/(\lambda D \rho_2 + \delta\kappa_2) - c_4^2(\kappa_2 + \lambda D \rho_2 \alpha)/(\lambda D \rho_2 + \delta\kappa_2). \qquad (33)$$

Константы интегрирования c_1^2, c_2^2, c_3^2 определяются как решения системы линейных алгебраических уравнений, продиктованной условиями прилипания (13) на границах $y = -l$, $y = h$ и заданным расходом газа (17) в верхнем слое:

$$\frac{l^2}{2}\frac{\rho_2 \nu_2}{\rho_1 \nu_1} c_1^2 - l\frac{\rho_2 \nu_2}{\rho_1 \nu_1} c_2^2 + c_3^2 = \frac{\sigma_T A l}{\rho_1 \nu_1} - \frac{g\beta_1}{\nu_1}\left(a_2^1 \frac{l^4}{24} - A\frac{l^3}{6}\right),$$

$$\frac{h^2}{2} c_1^2 + h c_2^2 + c_3^2 = -\frac{g}{\nu_2}\left[\frac{h^4}{24}\left(\beta_2 a_2^2 + \gamma b_2\right) + \frac{h^3}{6}\left(\beta_2 A + \gamma b_1\right)\right],$$

$$\frac{h^3}{6} c_1^2 + \frac{h^2}{2} c_2^2 + h c_3^2 = \frac{Q}{\rho_2} - \frac{g}{\nu_2}\left[\frac{h^5}{120}\left(\beta_2 a_2^2 + \gamma b_2\right) + \frac{h^4}{24}\left(\beta_2 A + \gamma b_1\right)\right]. \qquad (34)$$

С учетом вторых условий в (25), (26) и связи между константами (33) можно определить неизвестные c_4^1, c_4^2, c_5^1 из следующей системы уравнений, продиктованной условиями для температуры и концентрации (см. второе условие в (24) и соотношения (28)):

$$-l c_4^1 + c_5^1 = \vartheta^- + \frac{l^7}{1008}\frac{g\beta_1 (a_2^1)^2}{\nu_1 \chi_1} - \frac{l^6}{144}\frac{gA\beta_1 a_2^1}{\nu_1 \chi_1} + \frac{l^5}{120}\left(\frac{g\beta_1 (A)^2}{\nu_1 \chi_1} + \frac{3a_2^1}{\chi_1} c_1^1\right) - \frac{l^4}{24}\left(\frac{A}{\chi_1} c_1^1 + \frac{2a_2^1}{\chi_1} c_2^1\right) + \frac{l^3}{6}\left(\frac{A}{\chi_1} c_2^1 + \frac{a_2^1}{\chi_1} c_3^1\right) - \frac{l^2}{2}\frac{A}{\chi_1} c_3^1,$$

$$h c_4^2 + c_5^1 = \vartheta^+ - \frac{h^7}{1008}\frac{g}{\nu_2} B_2\left(\beta_2 a_2^2 + \gamma b_2\right) - \frac{h^6}{720}\frac{g}{\nu_2}\left[B_1\left(\beta_2 a_2^2 + \gamma b_2\right) + 4B_2\left(\beta_2 A + \gamma b_1\right)\right] - \frac{h^5}{120}\left[\frac{g}{\nu_2} B_1 (\beta_2 A + \gamma b_1) + 3B_2 c_1^2\right] - \frac{h^4}{24}\left[B_1 c_1^2 + 2B_2 c_2^2\right] - \frac{h^3}{6}\left[B_1 c_2^2 + B_2 c_3^2\right] - \frac{h^2}{2} B_1 c_3^2,$$

$$h\frac{\kappa_1}{D\rho_2\lambda + \delta\kappa_2} c_4^1 - h\frac{\lambda D \rho_2 \alpha + \kappa_2}{D\rho_2\lambda + \delta\kappa_2} c_4^2 + C_* \varepsilon c_5^1 = -\frac{h^7}{1008}\frac{g}{\nu_2} E_2\left(\beta_2 a_2^2 + \gamma b_2\right) - \frac{h^6}{720}\frac{g}{\nu_2}\left[E_1\left(\beta_2 a_2^2 + \gamma b_2\right) + 4E_2\left(\beta_2 A + \gamma b_1\right)\right] - \frac{h^5}{120}\left[\frac{g}{\nu_2} E_1 (\beta_2 A + \gamma b_1) + 3E_2 c_1^2\right] - \frac{h^4}{24}\left[E_1 c_1^2 + 2E_2 c_2^2\right] - \frac{h^3}{6}\left[E_1 c_2^2 + E_2 c_3^2\right] - \frac{h^2}{2} E_1 c_3^2 - C_* + C_* \varepsilon T_0. \qquad (35)$$

При известных значениях c_1^2, c_2^2, c_3^2 и c_4^1, c_4^2, c_5^1 значения констант интегрирования c_1^1, c_2^1, c_3^1, c_5^2 определяются согласно (25), (32). Для определения c_6^2 имеет место соотношение (33), а константа интегрирования c_7^2 может быть найдена с помощью условия (26), если известна c_5^1.

В случае, когда все константы интегрирования известны, массовая скорость M испаряющейся с границы раздела жидкости определяется с помощью, например, второго из соотношений (29).

Если действие эффекта Соре в верхнем слое системы не принимается во внимание, то условие баланса масс (21) и граничное условие (15) для концентрации пара приведут к необходимости положить равным нулю коэффициент, определяющий градиент температуры вдоль границы раздела $A = 0$. Тем самым моделирование двухслойных стационарных течений сведется к течениям жидкостей с границей раздела $y = 0$ типа жидкость–жидкость. При этом концентрация пара в слое газа не будет зависеть от продольной координаты, поскольку $b_1 = 0$, $b_2 = 0$ (см. первые соотношения в (24) и (26)). Из условия теплопереноса на границе раздела (см. первое равенство в (30)) следует, что необходимо обеспечить задание таких продольных градиентов температуры на верхней и нижней

твердых стенках канала, которые удовлетворяют соотношению

$$A_2 = -A_1(h/l)(\kappa_1/\kappa_2). \qquad (36)$$

При этом имеем $a_2^1 = -A_1 / l$, $a_2^2 = A_2 / h$ (см. (27) при $A = 0$). В итоге неизвестные константы интегрирования c_1^2, c_2^2, c_3^2 и c_4^1, c_4^2, c_5^1 будут определяться из систем линейных алгебраических уравнений (34) и (35), в которых должны быть учтены вышеуказанные значения градиентов температуры и концентрации (A, a_2^1, a_2^2, b_1, b_2), зависимость A_2 вида (36) и значение $\alpha = 0$.

1.3. Определение неизвестных коэффициентов в случае граничного условия (16) для концентрации пара на верхней границе. Пусть эффект Соре учитывается при постановке задачи (1)–(22). В случае, когда в качестве условия для концентрации пара на верхней стенке канала принимается условие нулевого потока пара (16) (см., например, [17, 37, 38], а также [21]), имеют место равенства

$$b_2 = 0,\ \varphi'(h) = 0, \qquad (37)$$

являющиеся следствием этого условия (здесь штрих означает производную по y). Условия непрерывности скорости и температуры (18) на термокапиллярной границе $y = 0$ требуют выполнения равенств (25). Исходя из условий линейного распределения температуры на твердых границах $y = -l$ и $y = h$ (14), имеем равенства вида (27), (28). Условие баланса масс (21) приводит к соотношениям (29), первое из которых с учетом (37) влечет равенство нулю коэффициента

$$a_2^2 = 0. \qquad (38)$$

Следствиями условия теплопереноса (20) на границе раздела $y = 0$ являются уравнения (30). Из первого уравнения в (30) следует равенство нулю коэффициента

$$a_2^1 = 0, \qquad (39)$$

поскольку выполняется (38) и первое из условий (37). Из (27), (38) и (39) следует равенство продольных градиентов температуры на твердых и свободной границах:

$$A = A_1 = A_2. \qquad (40)$$

Выполнение уравнения для концентрации насыщенного пара в форме (22) влечет за собой соотношения (26). Динамические условия (19) приводят к выполнению равенств (32), связывающих константы интегрирования c_1^1 и c_1^2, а также c_2^1 и c_2^2.

С учетом приведенных выше рассуждений получаем систему уравнений для определения неизвестных констант c_1^2, c_2^2, c_3^2 из условий прилипания (13) и выражения, определяющего расход газа в верхнем слое канала (17), а также с учетом формул (25) и (32):

$$\frac{l^2}{2}\frac{\rho_2\nu_2}{\rho_1\nu_1}c_1^2 - l\frac{\rho_2\nu_2}{\rho_1\nu_1}c_2^2 + c_3^2 = \frac{l^3}{6}\frac{g\beta_1 A}{\nu_1} + \frac{\sigma_T A l}{\rho_1\nu_1},$$

$$\frac{h^2}{2}c_1^2 + hc_2^2 + c_3^2 = -\frac{h^3}{6}\frac{g}{\nu_2}(\beta_2 A + \gamma b_1),$$

$$\frac{h^3}{6}c_1^2 + \frac{h^2}{2}c_2^2 + hc_3^2 = \frac{Q}{\rho_2} - \frac{h^4}{24}\frac{g}{\nu_2}(\beta_2 A + \gamma b_1).$$

При найденных c_1^2, c_2^2, c_3^2 определяются c_1^1, c_2^1, c_3^1 из (25), (32). С учетом (37)–(39) второе из соотношений (37) определяет константу интегрирования

$$c_6^2 = -\frac{h^4}{24}\frac{g}{\nu_2}(\beta_2 A + \gamma b_1)E_1 - \frac{h^3}{6}E_1 c_1^2 - \frac{h^2}{2}E_1 c_2^2 - hE_1 c_3^2.$$

Константы c_4^1, c_5^1 находятся из системы уравнений (28)

$$-lc_4^1 + c_5^1 = \vartheta^- + \frac{l^5}{120}\frac{g\beta_1(A)^2}{\nu_1\chi_1} - \frac{l^4}{24}\frac{A}{\chi_1}c_1^1 + \frac{l^3}{6}\frac{A}{\chi_1}c_2^1 - \frac{l^2}{2}\frac{A}{\chi_1}c_3^1,$$

$$h\frac{\kappa_1}{\kappa_2 + \lambda D\rho_2\alpha}c_4^1 + c_5^1 = \vartheta^+ - \frac{h^5}{120}\frac{g}{\nu_2}B_1(\beta_2 A + \gamma b_1) - \frac{h^4}{24}B_1 c_1^2 - \frac{h^3}{6}B_1 c_2^2 - \frac{h^2}{2}B_1 c_3^2 + h\frac{\delta\kappa_2 + \lambda D\rho_2}{\kappa_2 + \lambda D\rho_2\alpha}c_6^2.$$

Для вычисления E_1, B_1 см. (12). Заметим, что уравнение, определяющее константу интегрирования c_4^2, получено с использованием вторых соотношений в (30) и (29):

$$c_4^2 = c_4^1\frac{\kappa_1}{\kappa_2 + \lambda D\rho_2\alpha} - c_6^2\frac{\delta\kappa_2 + \lambda D\rho_2}{\kappa_2 + \lambda D\rho_2\alpha},$$

а c_7^2 находится с помощью второй формулы в (26). Массовая скорость M испаряющейся с границы раздела жидкости может быть найдена, например, с помощью второго из уравнений (29).

В случае, когда эффект Соре не учитывается при моделировании, условие нулевого потока пара

(16) приводит к равенствам (37), а из условий, обеспечивающих тепловой режим на границах канала (см. (27) и первое соотношение в (30)), следует зависимость продольного градиента A_2 от A и A_1:

$$A_2 = A + (A - A_1)(h / l)(\kappa_1 / \kappa_2). \qquad (41)$$

Заметим, что два из трех продольных градиентов температуры на границах канала можно считать заданными (a_2^1 и a_2^2 вычисляются согласно (27)). Уравнение (22) диктует выполнение соотношений (26) и определяет коэффициент b_1, динамические условия (19) и условия непрерывности (18) потребуют выполнения равенств (32) и (25) и определят связи между c_1^2, c_2^2, c_3^2 и c_1^1, c_2^1, c_3^1, c_5^1 и c_5^2. С учетом приведенных рассуждений система уравнений для определения неизвестных c_1^2, c_2^2, c_3^2 следует из условий (13) и (17). При известных c_1^2, c_2^2, c_3^2 константа интегрирования c_6^2 определяется исходя из второго из условий (37). Тогда сразу может быть найдена массовая скорость M испаряющейся с границы раздела жидкости из второго соотношения (29), записанного при $\alpha = 0$. Для нахождения c_4^1, c_5^1 служит система линейных алгебраических уравнений, являющаяся следствием условий для температуры на твердых границах канала (28).

Таким образом, могут быть определены все неизвестные константы интегрирования c_j^i ($i = 1, 2; j = 1,...,7$), построены точные решения (u_i, p_i', T_i, C), удовлетворяющие уравнениям (1)–(5) и граничным условиям (13)–(22), а также найдена массовая скорость M испарения.

2. РЕЗУЛЬТАТЫ АНАЛИТИЧЕСКИХ РАСЧЕТОВ И СРАВНЕНИЕ С ЭКСПЕРИМЕНТАМИ

Рассмотрим систему жидкости и газа вида HFE-7100–азот. В качестве изучаемой жидкости выбрана HFE-7100 в силу ее физико-химических свойств. Жидкость HFE-7100 относится к классу гидроэфиров и имеет следующие свойства: легкоиспаряющаяся (температура кипения – 61°C); низкое поверхностное натяжение (13.6 мН/м); диэлектрическая; низкий потенциал глобального потепления; нулевой потенциал озоноразрушения; совместима с большинством металлов, пластмасс и эластомеров и др. Данная жидкость используется в различных отраслях промышленности, в том числе в качестве теплоносителя и охлаждающей жидкости в системах термостабилизации и охлаждения. Жидкость HFE-7100 принята как рабочая жидкость для проведения ряда космических экспериментов [39, 40] в условиях невесомости на борту Международной космической станции, поскольку удовлетворяет необходимым свойствам и является негорючей, нетоксичной и безопасной. Свойства и подробное описание жидкости представлены на сайте производителя [41] и в работах [6, 42]. Верхний слой канала заполнен азотом. Основные физические параметры системы имеют следующие значения (см. [6, 20, 25, 42, 43]): $\rho_1 = 1.4 \times 10^3$ кг/м^3, $\rho_2 = 1.2$ кг/м^3 – плотности жидкости и газа; $\nu_1 = 0.38 \times 10^{-6}$ м^2/с, $\nu_2 = 0.15 \times 10^{-4}$ м^2/с – коэффициенты кинематической вязкости; $\chi_1 = 0.3 \times 10^{-4}$ м^2/с, $\chi_2 = 0.4 \times 10^7$ м^2/с – коэффициенты температуропроводности; $\kappa_1 = 0.07$ Вт/(м K), $\kappa_2 = 0.0251$ Вт/(м K) – коэффициенты теплопроводности; $\beta_1 = 1.8 \times 10^{-3}$ K^{-1}, $\beta_2 = 3.37 \times 10^{-3}$ K^{-1} – коэффициенты теплового расширения жидкости и газа; $\gamma = -0.62$ – концентрационный коэффициент плотности (см. [19], но для пары “бензин–воздух”), $\varepsilon = 0.04$ (K^{-1}), $C_* = 0.7$ (см. (22)), если $T_0 = 20^\circ$C, $\sigma_T = -1.5 \times 10^{-5}$ Н/(м K) – температурный коэффициент поверхностного натяжения; $D = 2 \times 10^{-5}$ м^2/с – коэффициент диффузии пара в верхнем слое. Коэффициенты Дюфура и Соре полагаются равными $\delta = 10^{-3}$, $\alpha = -5 \times 10^{-3}$, -5×10^{-4} (в предположении о нормальной термодиффузии возможные значения данных коэффициентов могут быть найдены в [23], см. также цитируемую там литературу).

Экспериментальные исследования проведены на стенде по изучению конвекции, обусловленной интенсивным испарением жидкости в горизонтальной кювете ограниченного размера под действием потока газа [5, 6]. Между жидкостной кюветой (длина – 40 мм, ширина – 40 мм) и газовым каналом (ширина – 100 мм, высота – 5 мм) установлена разделительная пластина толщиной 200 мкм. Эта пластина имеет квадратный вырез (10×10 мм) по центру, где происходит соприкосновение жидкости и газа. Расход подаваемой жидкости (HFE-7100) изменялся от 40 до 350 мкл/мин, что соответствует массовой скорости испарения от 0.014 до 0.11 кг/м^{2}с. Расход газа (азот – 99.8%) варьировался от 0.1 до 5 л/мин. Значение числа Рейнольдса меняется в диапазоне 40–200, что соответствует средней скорости газа от 0.014 до 0.24 м/с. Температура жидкости и газа изменялась от 20 до 40°C и выше, толщина слоя жидкости – от 1.5 до 8 мм.

2.1. Влияние эффекта Соре на структуру течения, распределение температуры и концентрации пара в системе. На рис. 2 и 3 представлены профили скорости (рис. 2а, 3а), температуры (рис. 2б, 3б) и концентрации (рис. 3в) без учета и с учетом влияния эффекта термодиффузии в газопаровом слое для различных значений расхода газа в верхнем слое системы, полученные с помощью аналитических формул. Расчеты проведены для случая, когда на верхней твердой стенке канала полагается выполненным условие абсорбции пара (15), на нижней стенке задан продольный градиент температуры $A_1 = -30$ K/м, а высота слоев газа h и жидкости l равна 0.5×10^{-2} м. В обоих случаях, как с учетом

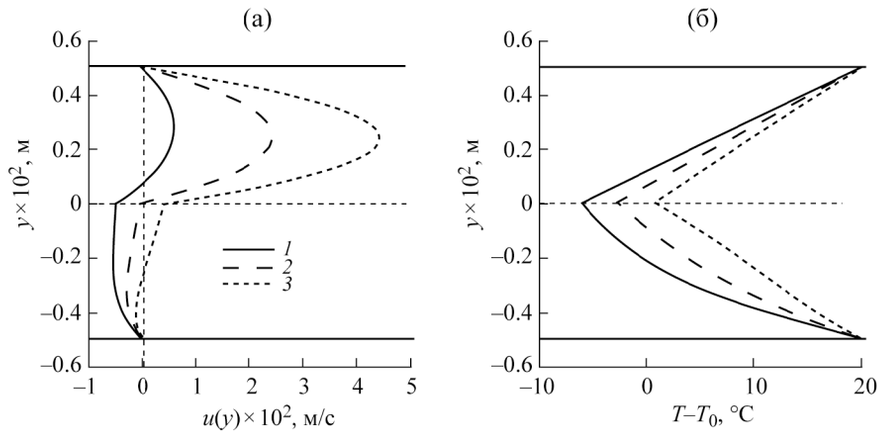

Рис. 2. Профили скорости (а) и температуры (б) в системе HFE-7100–азот при $h = 0.5 \times 10^{-2}$ м, $l = 0.5 \times 10^{-2}$ м, $A_1 = -30$ К/м и различных значениях расхода газа в верхнем слое без учета эффекта Соре: $1 - Q = 1.8\times10^{-5}$ кг/(м с), 2–9.6×10^{-5}, 3 – 1.8×10^{-4}; $A = 0$ К/м, $A_2 = 82.5$ К/м.

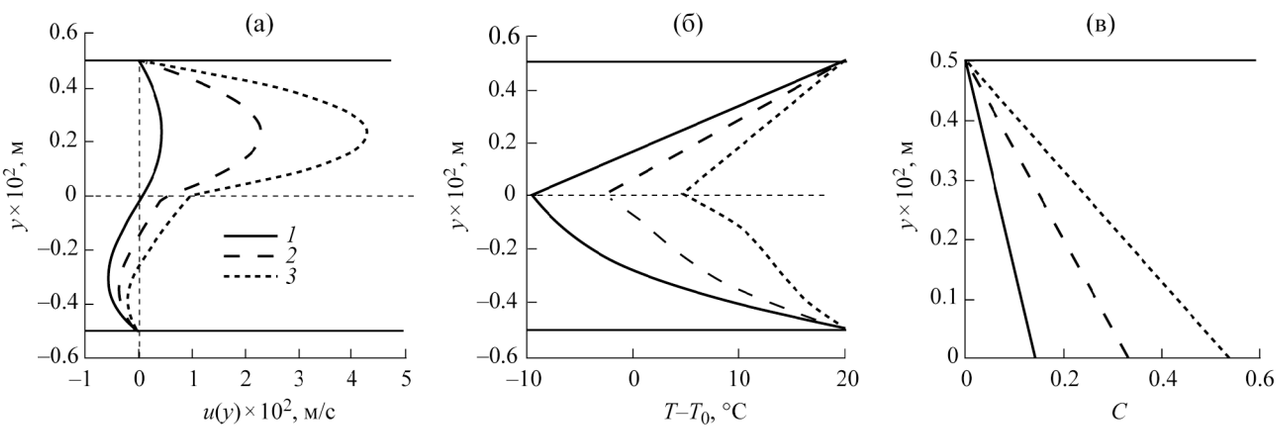

Рис. 3. Профили скорости (а), температуры (б) и концентрации (в) в системе HFE-7100–азот с учетом эффекта Соре: параметры те же, что на рис. 2; $A = -9.88$ К/м, $A_2 = 45.5$ К/м, $\alpha = -5 \times 10^{-3}$.

эффекта Соре, так и без него, увеличение расхода газа влечет возрастание интенсивности течения жидкости (рис. 2а, 3а). Профили скорости при этом имеют схожий характер (см. рис. 2а, 3а), но имеются некоторые качественные и количественные различия. Так, в случае, когда эффект термодиффузии не принимается во внимание (рис. 2а), скорость U на границе раздела сред $y = 0$ принимает значение -0.48×10^{-2} м/с при расходе газа Q, равном 1.8×10^{-5} кг/(м с). При $Q = 9.6 \times 10^{-5}$ кг/(м с) данный показатель достигает значения -5.5×10^{-4} м/с. Таким образом, при указанных расходах газа в слое жидкости наблюдается течение в противоположном в сравнении с потоком газа направлении. С увеличением расхода газа, при $Q = 1.8 \times 10^{-4}$ кг/(м с), скорость U на границе раздела равна 4.04×10^{-2} м/с. В случае, когда эффект Соре учитывается, а коэффициент термодиффузии $\alpha = -5 \times 10^{-3}$, значения U при тех же величинах расхода газа (1.8×10^{-5} кг/(м с), 9.6×10^{-5} кг/(м с), 1.8×10^{-4} кг/(м с)) достигают 0.68×10^{-3}, 0.5×10^{-2} и 0.95×10^{-2} м/с соответственно. Тем самым в случае, когда эффект термодиффузии принимается во внимание, возвратного течения не возникает, имеет место расслоение течения (см. рис. 3а). Распределение температуры при изменении значения Q качественно меняется (рис. 2б, 3б). В верхнем слое нелинейность в распределении температуры довольно слабо проявляется как в случае учета, так и без учета эффекта Соре. В жидкости (нижний слой на рис. 2б, 3б) в случае, когда эффект термодиффузии принимается во внимание (рис. 3б), отмечается более сильная нелинейность, чем без учета этого эффекта. С увеличением расхода газа растет концентрация пара на границе $y = 0$ (рис. 3в). Данный эффект может быть вызван интенсификацией конвективного теплообмена более теплого газа и холодной границы раздела. Следует отметить, что при любом значении расхода газа температура на границе раздела существенно снижается относительно задаваемой на твердых границах канала. Подобный эффект

качественно находит отражение и в экспериментальных исследованиях [5, 6].

2.2. Влияние толщины жидкого слоя на структуру течения, распределение температуры и концентрации пара в системе.

Достаточно сильное влияние на профили скорости, распределение температуры и концентрацию пара оказывает толщина жидкого слоя l. Так, например, в случае учета эффекта Соре при $l = 0.5 \times 10^{-2}$ м наблюдаются возвратные течения в нижнем слое (рис. 3а), тогда как при $l = 0.15 \times 10^{-2}$ м движение жидкости однонаправленное, причем она движется только по направлению потока газа (рис. 4а). Отмечены существенные качественные и количественные отличия профилей температуры при различных значениях толщины слоя жидкости l. При малых значениях толщины l (см. рис. 4б) нелинейность в распределении температуры наблюдается достаточно слабая и можно говорить о близком к линейному распределении температуры в системе. С увеличением толщины l нижнего слоя в нем ярче проявляется нелинейность профиля температуры (рис. 3б), при этом изменение расхода газа влияет на профили температуры значительно сильнее, нагрев границы раздела $y = 0$ происходит более интенсивно, но она остается более холодной, чем в двухслойной системе с меньшей толщиной l (см. рис. 3б, 4б). При исследовании распределения концентрации пара в газовой среде установлено, что при $l = 0.15 \times 10^{-2}$ м на границе $y = 0$ достигаются бóльшие значения концентрации, чем при $l = 0.5 \times 10^{-2}$ м. Так, при $Q = 1.8 \times 10^{-5}$ в случае, когда толщина жидкого слоя $l = 0.5 \times 10^{-2}$ м, концентрация пара на границе $y = 0$ достигает значения, равного 0.14, а в случае, когда $l = 0.15 \times 10^{-2}$ м, это значение равно 0.59. При $Q = 9.6 \times 10^{-5}$ кг/(м с) $C|_{y=0} = 0.33$ для $l = 0.5 \times 10^{-2}$ м и $C|_{y=0} = 0.60$ для $l = 0.15 \times 10^{-2}$ м. При наибольшем значении расхода газа $Q = 1.8 \times 10^{-4}$ кг/(м с) в случае, когда толщина слоя жидкости равна $l = 0.5 \times 10^{-2}$ м, имеем $C|_{y=0} = 0.54$, а при $l = 0.15 \times 10^{-2}$ м концентрация пара на границе раздела равна $C|_{y=0} = 0.61$. Заметим также, что изменение расхода газа оказывает на профили концентрации меньшее влияние при меньшей толщине слоя $l = 0.15 \times 10^{-2}$ м, чем при толщине, равной 0.5×10^{-2} м.

2.3. Влияние расхода газа на интенсивность испарения. При сравнении экспериментальных и аналитических результатов по зависимости количества испарившейся на границе раздела жидкости (или массовой скорости испарения M) от величины расхода газа Q выявлено, что, хотя данные результаты и имеют качественно одинаковый характер (увеличение M с ростом Q), но количественно они отличаются. Для экспериментальных данных зависимость M от Q имеет нелинейную форму (см. *1* на рис. 5а), в то время как аналитические расчеты показывают линейную зависимость (*3–5* на рис. 5а). Разумеется, аналитические расчеты, проведенные для двухмерного случая, не учитывают все факторы, которые присутствуют в эксперименте. Для сравнения экспериментальных результатов с аналитическими расчетами используется линейная аппроксимация экспериментальных данных (*2* на рис. 5а). Из графиков, представленных на рис. 5а, а также значений, приведенных на рис. 5б и в таблице, видно, что существуют такие значения продольного градиента температуры, когда экспериментальные значения и результаты аналитических расчетов близки как количественно (таблица), так и качественно (рис. 5). Так, для продольного градиента температуры на нижней твердой границе $A_1 = -55$ К/м наблюдаются отличия в значениях расхода испарения не более чем в два раза, угол

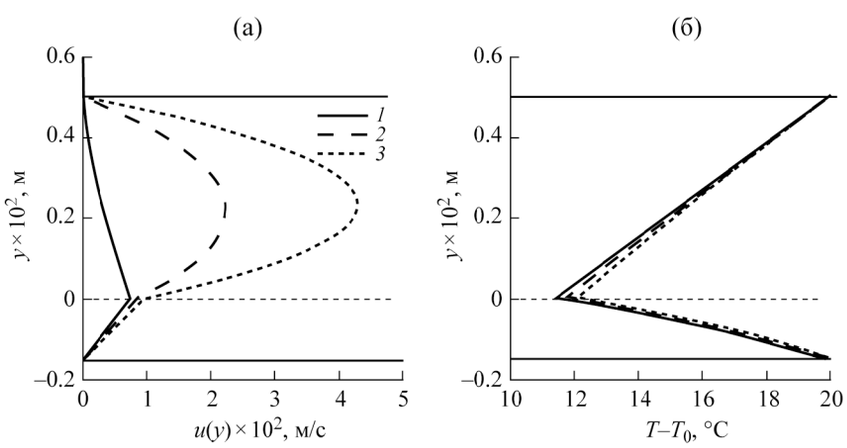

Рис. 4. Профили скорости (а) и температуры (б) в системе HFE-7100–азот при $h = 0.5 \times 10^{-2}$ м, $l = 0.15 \times 10^{-2}$ м, $A_1 = -30$ К/м и различных значениях расхода газа в верхнем слое с учетом эффекта Соре: *1* – $Q = 1.8 \times 10^{-5}$ кг/(м с), *2* – 9.6×10^{-5}, *3* – 1.8×10^{-4}; $A = -18.6$ К/м, $A_2 = 85.66$ К/м.

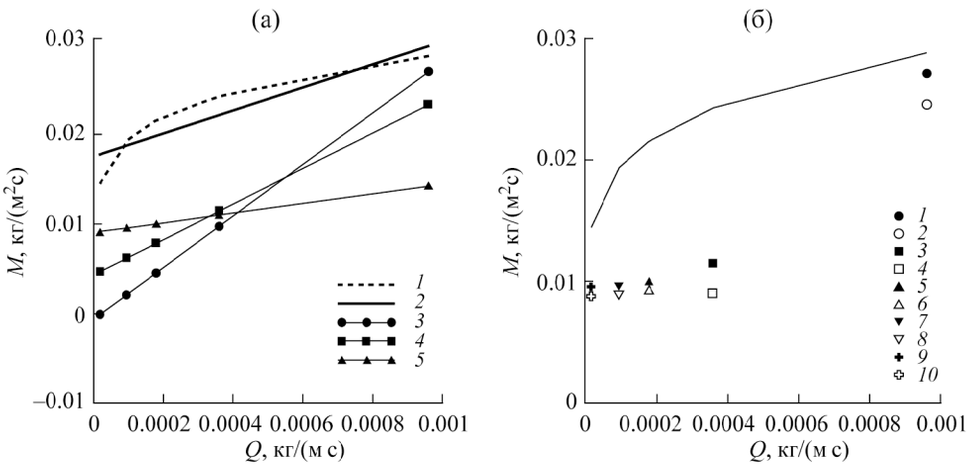

Рис. 5. Зависимость интенсивности испарения жидкости от расхода газа, $h = 0.5 \times 10^{-2}$ м, $l = 0.5 \times 10^{-2}$ м: (а) *1* – экспериментальные данные, *2* – линия тренда экспериментальных данных, *3–5* – расчеты при $A_1 = -80$, -55 и -15 К/м соответственно; (б) сплошная линия – аппроксимация экспериментальных данных (таблица), точки – теоретические результаты: *1* – $M = 2.7 \times 10^{-2}$ кг/(м^2 с), $A_1 = -80$ К/м; *2* – 2.45×10^{-2}, -80; *3* – 1.14×10^{-2}, -55; *4* – 0.9×10^{-2}, -55; *5* – 1.01×10^{-2}, -15; *6* – 0.94×10^{-2}, -15; *7* – 0.96×10^{-2}, -10; *8* – 0.89×10^{-2}, -10; *9* – 0.94×10^{-2}; -3; *10* – 0.87×10^{-2}, -3.

наклона прямой и близок по значению с углом наклона линии тренда (линейная аппроксимация) экспериментальных данных (см. рис. 5а, *1* и *4*). Для продольного градиента температуры на нижней твердой границе, равного $A_1 = -80$ К/м, для наибольшего из рассмотренных значений расхода газа Q в верхнем слое ($Q = 9.6 \times 10^{-4}$ кг/(м с)) аналитические расчеты дают наиболее близкое к экспериментальному значение массовой скорости испарения M ($M = 2.7 \times 10^{-2}$ кг/(м^2 с), здесь $A_1 = -80$ К/м, $A = -20.47$ К/м, $A_2 = 143.26$ К/м). В таблице отражены данные сравнения интенсивности испарения с границы раздела, полученные в результате физических экспериментов (второй столбец), а также вычисленные аналитически для различных значений продольных градиентов температуры и расхода газа в верхнем слое (третий столбец). При $Q = 3.6 \times 10^{-4}$ кг/(м с) значение $M = 1.14 \times 10^{-2}$ кг/(м^2 с) достигается при $A_1 = -55$ К/м (здесь $A = -14.07$ К/м, $A_2 = 98.49$ К/м). При $Q = 1.8 \times 10^{-4}$ кг/(м с) значение $M = 1.01 \times 10^{-2}$ кг/(м^2 с) получено в случае, если $A_1 = -15$ К/м ($A = -3.84$ К/м, $A_2 = 26.86$ К/м). При значении расхода газа, равном $Q = 9.6 \times 10^{-5}$ кг/(м с), значение массовой скорости испарения $M = 9.62 \times 10^{-3}$ кг/(м^2 с) достигается при $A_1 = -10$ К/м ($A = -2.56$ К/м, $A_2 = 17.91$ К/м), а при $Q = 1.8 \times 10^{-5}$ кг/(м с) значение $M = 9.43 \times 10^{-3}$ кг/(м^2 с) получено при $A_1 = -3$ К/м ($A = -0.77$ К/м, $A_2 = 5.37$ К/м). Необходимо отметить, что в силу неоднородного испарения значения продольных градиентов температуры порядка 3–80 К/м, используемых в аналитических расчетах, вполне реальны для эксперимента [6]. Однако лучшего совпадения

Таблица

Q, кг/(м с)	M, кг/(м^2 с), эксперимент	M, кг/(м^2 с), теория
9.6×10^{-4}	2.873×10^{-2}	2.7×10^{-2}
3.6×10^{-4}	2.425×10^{-2}	1.14×10^{-2}
1.8×10^{-4}	2.151×10^{-2}	1.01×10^{-2}
9.6×10^{-5}	1.929×10^{-2}	9.62×10^{-3}
1.8×10^{-5}	1.444×10^{-2}	9.43×10^{-3}

аналитических результатов с экспериментальными данными (таблица) удается добиться для более высоких значений T_0 (см. (22), $T_0 = 60^\circ$C) и, соответственно, более высоких значений ϑ^+, ϑ^- (см. (14); ϑ^+, ϑ^- изменяются в диапазоне 40–80 °C).

Увеличение поперечного перепада температуры (здесь $|\vartheta^+ - \vartheta^-|$) приводит к увеличению интенсивности испарения M на границе раздела при проведении вычислений на основе аналитических соотношений (рис. 5б). Все расчеты проведены для экспериментальных значений расхода газа Q (см. таблицу, первый столбец).

ЗАКЛЮЧЕНИЕ

Представлены результаты математического моделирования стационарных двухслойных течений, проведенного на основе точных решений уравнений Навье–Стокса в приближении Буссинеска. При построении решений учитывается испарение на границе раздела, а также

термодиффузия и диффузионная теплопроводность в верхнем слое системы. Отметим, что именно точные решения дают возможность проанализировать формулировку математической модели с точки зрения адекватности описания двухслойных течений жидкостей, имеющих границу раздела, и выявления значимых факторов, влияющих на характеристики течения. Оказалось, что учет эффекта Соре позволяет рассматривать границу раздела в качестве термокапиллярной поверхности в случае, когда верхняя стенка канала обладает свойством абсорбции пара. Если на верхней твердой границе области течения поставить условие, характерное для абсорбции пара, а эффект Соре не учитывать, то при моделировании двухслойных течений вида (6) необходимо положить равным нулю продольный градиент температуры A на границе раздела. При учете эффекта термодиффузии задание на границе одного из продольных градиентов температуры определяет значение двух других через своеобразные условия связи (см. (31)). При условии нулевого потока пара на верхней твердой стенке канала осуществляется моделирование двухслойных течений при заданном, одинаковом для всех границ канала, продольном градиенте температуры, если эффект Соре учитывается (см. условие (40)). Если эффект Соре не учитывать при проведении моделирования с условием отсутствия потока пара на верхней границе, то два из трех продольных градиентов температуры на границах канала можно считать заданными (см. (41)). Таким образом, учет эффекта Соре ведет к изменению количественной и качественной картины течения, а также представляет возможность изменять механизм управления картиной течения с помощью задания продольных градиентов температуры на границах канала и согласования их значений.

Приведены примеры профилей скорости, температуры и концентрации для системы жидкость–газ вида HFE-7100 – азот для различных значений расхода газа в верхнем слое с учетом и без учета эффекта Соре при различных значениях толщины слоя жидкости. Произведено сравнение аналитических и экспериментальных результатов по зависимости массовой скорости M испарения жидкости на термокапиллярной границе раздела от величины расхода газа, значений продольных градиентов температуры. Выявлено их качественное, а в некоторых случаях и приближенное количественное совпадение.

Работа выполнена при поддержке РФФИ (проект № 14-08-00163) и Российского научного фонда (грант № 14-19-01755).

СПИСОК ЛИТЕРАТУРЫ

1. *Scheid B., Margerit J., Iorio C.S., Joannes L., Heraud M., Queeckers P., Dauby P.C., Colinet P.* Onset of Thermal Ripples at the Interface of an Evaporating Liquid under a Flow of Inert Gas // Exp. Fluids. 2012. V. 52. P. 1107.
2. *Kabov O.A., Zaitsev D.V., Cheverda V.V., Bar-Cohen A.* Evaporation and Flow Dynamics of thin, Shear-Driven Liquid Films // Exp. Therm. Fluid Sci. 2011. V. 35. № 5. P. 825.
3. *Iorio C.S., Goncharova O.N., Kabov O.A.* Study of Evaporative Convection in an Open Cavity under Shear Stress Flow // Microgravity Sci. Technol. 2009. V. 21. № 1. P. 313.
4. *Iorio C.S., Goncharova O.N., Kabov O.A.* Heat and Mass Transfer Control by Evaporative Thermal Pattering of thin Liquid Layer // Computational Thermal Sci. 2011. V. 3. № 4. P. 333.
5. *Люлин Ю.В., Кабов О.А.* Измерение массовой скорости испарения в горизонтальном слое жидкости, частично открытом в движущийся газ // Письма в ЖТФ. 2013. Т. 39. № 17. С. 88.
6. *Lyulin Yu.V., Kabov O.A.* Evaporative Convection in a Horizontal Liquid Layer under Shear-Stress // Int. J. Heat Mass Transfer. 2014. V. 70. P. 599.
7. *Люлин Ю.В., Феоктистов Д.В., Афанасьев И.А., Чачило Е.С., Кабов О.А., Кузнецов Г.В.* Измерение скорости испарения с локальной поверхности слоя жидкости под действием потока газа // Письма в ЖТФ. 2015. Т. 41. Вып. 14. С. 1.
8. *Кузнецов В.В.* Тепломассообмен на поверхности раздела жидкость–пар // МЖГ. 2011. № 5. С. 97.
9. *Das K.S., Ward C.A.* Surface Thermal Capacity and its Effects on the Boundary Conditions at Fluid-Fluid Interfaces // Phys. Rev. E. 2007. V. 75. P. 065303.
10. *Гончарова О.Н.* Моделирование течений в условиях тепло- и массопереноса на границе раздела // Изв. АлтГУ. 2012. № 1/2(73). С. 12.
11. *Margerit J., Colinet P., Lebon G., Iorio C.S., Legros J.C.* Interfacial Nonequilibrium and Benard-Marangoni Instability of a Liquid-Vapor System // Phys. Rev. E. 2003. V. 68. P. 041601.
12. *Андреев В.К., Бекежанова В.Б.* Устойчивость неизотермических жидкостей. Красноярск: Сиб. фед. ун-т, 2010. 356 с.
13. *Goncharova O.N., Pukhnachov V.V., Kabov O.A.* Solutions of Special Type Describing the three Dimensional Thermocapillary Fows with an Interface // Int. J. Heat Mass Transfer. 2012. V. 54. № 5. P. 715.
14. *Гончарова О.Н., Кабов О.А.* Гравитационно-термокапиллярная конвекция жидкости в горизонтальном слое при спутном потоке газа // ДАН. 2009. Т. 426. № 2. С. 1.
15. *Goncharova O.N., Kabov O.A.* Mathematical and Numerical Modeling of Convection in a Horizontal Layer under co-Current Gas Flow // Int. J. Heat Mass Transfer. 2010. V. 53. P. 2795.

16. *Lyubimova T.P., Lyubimov D.V., Morozov V.A., Scurdin R.V., Ben Hadid H., Henry D.* Stability of Convection in a Horizontal Channel Subjected to a Longitudinal Temperature Gradient. Part 1. Effect of Aspect Ratio and Prandtl Number // J. Fluid Mech. 2009. V. 635. P. 275.
17. *Nepomnyashchy A.A., Simanovskii I.B.* Convective Flows in a Two-Layer System with a Temperature Gradient along the Interface // Phys. Fluids. 2006. V. 18. P. 032105.
18. *Goncharova O.N., Hennenberg M., Rezanova E.V., Kabov O.A.* Modeling of the Convective Fluid Flows with Evaporation in the Two-Layer Systems // Interfacial Phenomena and Heat Transfer. 2013. V. 1. № 4. P. 317.
19. *Шлиомис М.И., Якушин В.И.* Конвекция в двухслойной бинарной системе с испарением // Уч. зап. Пермск. гос. ун-та. Сер. Гидродинамика: Сб. науч. тр. 1972. № 4. С. 129.
20. *Гебхард Б., Джалурия Й., Махаджан Р., Самакия Б.* Свободноконвективные течения. Тепло- и массообмен. Кн. 1. М.: Мир, 1991. 678 с.
21. *Гончарова О.Н., Резанова Е.В.* Пример точного решения стационарной задачи о двухслойных течениях с испарением на границе раздела // ПМТФ. 2014. № 2. С. 68.
22. *Бирих Р.В.* О термокапиллярной конвекции в горизонтальном слое жидкости // ПМТФ. 1966. № 3. С. 69.
23. *Андреев В.К., Гапоненко Ю.А., Гончарова О.Н., Пухначев В.В.* Современные математические модели конвекции. М.: Наука, 2008. 368 с.
24. *Джозеф Д.* Устойчивость движений жидкости. М.: Мир, 1981. 639 с.
25. *Гроот С.Р.* Термодинамика необратимых процессов. М.: Гос. изд-во техн.-теор. лит., 1956. 281 с.
26. *Мациев Л.Ф., Стасенко А.Л.* Испарение капли в сильно перегретой бинарной смеси // Изв. АН СССР. Энергетика и транспорт. 1987. № 1. С. 112.
27. *Мациев Л.Ф., Рябинина Т.Н., Стасенко А.Л.* Испарение капли в "горячей" двухкомпонентной струе с учетом термодиффузии и перекрестного эффекта // Моделирование в механике. 1987. Т. 1(18). № 6. С. 106.
28. *Андреев В.К., Собачкина Н.Л.* Движение бинарной смеси в плоских и цилиндрических областях. Красноярск: Сиб. фед. ун-т, 2012. 188 с.
29. *Рыжков И.И.* Термодиффузия в смесях: уравнения, симметрии, решения и их устойчивость. Новосибирск: Изд-во СО РАН, 2013. 200 с.
30. *Пухначев В.В.* Нестационарные аналоги решения Бириха // Изв. АлтГУ. 2011. № 1/2(69). С. 62.
31. *Катков В.Л.* Точные решения некоторых задач конвекции // ПММ. 1968. Т. 32. № 3. С. 482.
32. *Гончарова О.Н.* Групповая классификация уравнений свободной конвекции // Динамика сплошной среды. 1987. Вып. 79. С. 22.
33. *Пухначев В.В.* Теоретико-групповая природа решения Бириха и его обобщения // Тр. Междунар. конф. "Симметрия и дифференциальные уравнения". Красноярск: Ин-т вычисл. моделирования СО РАН, 2000. С. 180.
34. *Остроумов Г.А.* Свободная конвекция в условиях внутренней задачи. М.-Л.: Гос. изд-во техн.-теор. лит., 1952. 256 с.
35. *Пригожин И.* Химическая термодинамика. Новосибирск: Наука, 1966.
36. *Ghezzehei T.A., Trautz R.C., Finsterle S. et al.* Modeling Coupled Evaporation and Seepage in Ventilated Cavities // Vadose Zone J. 2004. № 3. P. 806.
37. *Gatapova E. Ya., Kabov O.A.* Shear-Driven Flows of Locally Heated Liquid Films // Int. J. Heat Mass Transfer. 2008. V. 51. P. 4797.
38. *Накоряков В.Е., Буфетов Н.С., Григорьева Н.И., Дехтярь Р.А.* Тепломассоперенос при абсорбции пара неподвижным слоем раствора // ПМТФ. 2003. № 2. С. 101.
39. *Pacros A., Minster O.* The ESA Contribution to Space Research on Two-Phase Systems // Microgravity Sci. Technol. 2007. V. 19. № 3–4. P. 9.
40. *Toth B.* Future Experiments to Measure Liquid-Gas Phase Change and Heat Transfer Phenomena on the International Space Station // Microgravity Sci. Technol. 2012. V. 24. P. 189.
41. 3M, 3M™ Novec™ 7100 Engineered Fluid – Data Sheet. http://multimedia.3m.com/mws/mediawebserver?mwsId=SSSSSufSevTsZxtU4Y_G5x_eevUqevTSevTSevTSeSSSSSS—&fn=prodinfo_nvc7100.pdf
42. *Machrafi H., Sadoum N., Rednikov A., Dehaeck S., Dauby P.C., Colinet P.* Evaporation Rates and Benard-Marangoni Supercriticality Levels for Liquid Layers under an Inert Gas Flow // Microgravity Sci. Technol. 2013. V. 25. № 4. P. 251.
43. Краткий справочник физико-химических величин / Под ред. Равделя А.А., Пономаревой А.М. СПб.: Спец. лит., 1998. 232 с.

Теплофизика и аэромеханика, *2017*, *том 24*, *№ 3*

УДК 536.423

Критерий роста сухих пятен в изотермических пленках жидкости на горизонтальной подложке*

Л.И. Мальцев[1], Ю.С. Поджаров[1], О.А. Кабов[1,2]

[1]*Институт теплофизики им. С.С. Кутателадзе СО РАН, Новосибирск*

[2]*Новосибирский государственный университет*

E-mail: Maltzev@itp.nsc.ru

Предложен критерий развития сухих пятен в изотермических пленках жидкости на горизонтальной подложке. Выведены формулы для сил гравитации и сил поверхностного натяжения, действующих в плоскости подложки на валик, окружающий сухое пятно, баланс которых определяет, какое из малых начальных пятен закроется, а какое разовьется в большое пятно.

Ключевые слова: пленка жидкости, сухое пятно, критерий роста сухого пятна, гравитация, капиллярность, краевой угол смачивания.

Введение

Процессы, происходящие в пристенных пленках жидкости, широко используются в промышленности, в частности, для интенсификации тепломассообмена. При этом снижение толщины пленки позволяет существенно повысить их эффективность. Субмикронная пленка жидкости, образующаяся на границе сухих пятен, за счет интенсивного испарения может вносить большой вклад в суммарный тепломассообмен. Так, авторами работы [1] в режимах пленочного течения с мелкомасштабными смываемыми сухими пятнами был получен тепловой поток, на порядок превышающий тепловой поток, реализуемый при сплошном течении пленки под действием гравитации в рамках того же расхода жидкости. В то же время хорошо известно, что тонкие пленки подвержены разрывам, а это может резко уменьшить эффективность аппаратов, использующих тонкие пленки для испарительного охлаждения, и даже привести к выходу их из строя. Поэтому вопрос об организации охлаждения перегретых поверхностей с помощью пленок жидкости переменной толщины и возможного их разрыва приобретает большое значение. Важным аспектом проблемы разрыва пленки жидкости является влияние смачиваемости подложки [2–4]. В большинстве теоретических моделей разрыва изотермической пленки жидкости равновесный краевой угол смачивания выступает как основной параметр, определяющий критическую толщину пленки [5]. Эксперименты по разрыву пленки

* Работа выполнена при финансовой поддержке Минобрнауки РФ (соглашение № 14.613.21.0011, идентификатор проекта RFMEFI61314X0011).

© **Мальцев Л.И., Поджаров Ю.С., Кабов О.А., 2017**

жидкости при отсутствии нагрева качественно подтверждают зависимость критической толщины пленки от равновесного краевого угла смачивания [6]. Последний используется как основной параметр во многих моделях разрыва нагреваемой пленки жидкости [7]. Однако это не согласуется с некоторыми экспериментальными работами [8, 9].

Во второй половине XX столетия появилась серия работ по образованию сухих пятен в пленках жидкости, стекающих по твердой стенке. В работе [10] был предложен критерий появления разрыва в стекающей изотермической пленке жидкости, который получил название критерия Хартли–Мургатройда. Критерий основан на балансе сил поверхностного натяжения и величин потери импульса в стекающей пленке на верхней границе сухого пятна. При расчете сил поверхностного натяжения авторы [10] учитывали только кривизну поперечного сечения свободной границы валика, примыкающего к сухому пятну. То есть априори предполагалось, что сухое пятно является достаточно большим. Поэтому критерий Хартли–Мургатройда дает заниженные оценки для области параметров, определяющих появление сухих пятен. В дальнейшем критерий Хартли–Мургатройда был распространен на пленки, обдуваемые потоком газа, и пленки, находящиеся в условиях тепломассообмена [11, 12]. В работе [13] был предложен более строгий учет сил поверхностного натяжения и сформулирован новый критерий, который позволил оценивать поведение пятна: закроется начальное сухое пятно в пленке или будет развиваться. Показано, что при новом подходе диапазон изменения размеров закрывающихся сухих пятен в рассматриваемой пленке оказывается существенно большим, чем предсказывает критерий Хартли–Мургатройда.

В настоящей работе на основе подхода, примененного в работе [13], выполнен теоретический анализ влияния равновесного краевого угла смачивания, поверхностного натяжения и сил гравитации на критические размеры сухих пятен в изотермической пленке жидкости заданной толщины на горизонтальной плоской подложке.

Анализ сил, действующих на валик, окружающий сухое пятно

Пусть на горизонтальной плоскости в поле сил тяжести находится неподвижная пленка капиллярной жидкости. Допустим, что в некоторый момент в пленке возникло сухое пятно в форме круга. В экспериментальной практике пятно, как правило, окружено характерным жидким валиком. На рис. 1 показаны общий вид сухого пятна с окружающим его валиком и поперечное сечение валика в плоскости, проходящей через его ось симметрии.

На каждый элемент валика, вырезанный центральным углом $\delta\varphi$, действуют сила тяжести и сила, обусловленная наличием поверхностного натяжения на криволинейной поверхности валика. Выпишем выражения для этих сил, действующих в плоскости пластины. Введем следующие обозначения: ρ — плотность жидкости, r_0 — радиус сухого пятна, g — ускорение силы тяжести, h — толщина жидкой пленки. За счет действия сил гравитации в пленке возникает статическое давление $P = \rho g z$, где координата z цилиндрической системы координат (r, φ, z) направлена вдоль оси симметрии валика.

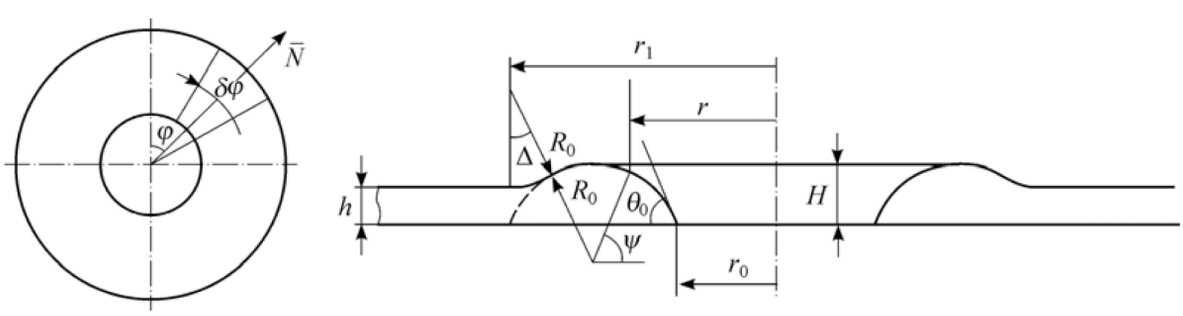

Рис. 1. Схематическое изображение сухого пятна в пленке жидкости.

Суммарное действие сил давления на элемент валика в плоскости подложки составляет $P = -\rho g h^2 r_1 \delta\phi/2$.

Капиллярную силу N, действующую на элемент валика также в плоскости подложки, можно представить в виде $N = \sigma\delta\varphi \int\limits_{(L)} (k_1 + k_2) r(\psi) \cos\psi dS$, здесь σ — коэффициент поверхностного натяжения жидкости, k_1 и k_2 — главные кривизны поверхности валика в точках контура L его поперечного сечения. Согласно теореме Менье [14], кривизна, связанная с осевой симметрией валика, записывается как $k_1 = \cos\psi/r$. Вторая кривизна, связанная с формой контура L, имеет вид $k_2 = d\vartheta/dS$, где $\vartheta = \pi/2 + \psi$ — угол между подложкой и касательной к контуру L. Следовательно,

$$N = \sigma\delta\varphi \left[-\int\limits_{(L)} \cos^2\psi R(\psi) d\psi + \int\limits_{(L)} r(\psi) \sin\vartheta d\vartheta \right], \tag{1}$$

здесь $R(\psi)$ — радиус локальной кривизны контура L.

Условие критического состояния сухого пятна в пленке

Под действием сил, действующих на элементы валика в плоскости подложки, валик начинает симметрично расширяться, вбирая в себя жидкость пленки, или сокращаться. Будем считать, что каждый элемент валика движется вдоль его соответствующего радиуса как единое целое. Тогда поведение малого сухого пятна в пленке определяется знаком при величине суммарной силы, действующей на элемент валика в направлении радиуса сухого пятна: пятно закрывается, если эта сила направлена к центру валика, и вырастает в размерах, если сила направлена от центра. Следовательно, равенство

$$P + N = 0 \tag{2}$$

является условием равновесного положения валика.

В преобладающем числе работ, посвященных моделированию сухих пятен и ривулетов, стекающих вдоль границ пятен, границы поперечного сечения валика или ривулета аппроксимируются дугами окружности [15–17]. В настоящем случае также будем считать, что криволинейная граница сечения валика составлена из дуг окружности радиуса R_0 (рис. 1). Наиболее наглядной характеристикой начального возмущения, очевидно, является высота валика H, которая связана с радиусом R_0 соотношением $H = R_0 (1 - \cos\theta_0)$.

Рассмотрим подробно частный, физически наиболее вероятный сценарий образования начального сухого пятна. В пленке жидкости непосредственно на стенке возникает газовый (паровой) пузырек, отделенный от атмосферы тонкой пленкой-мембраной. В некоторый момент времени мембрана разрушается, и в пленке образуется сухое пятно круглой формы без валика. В таком случае $H = h$ и поперечное сечение валика представляет собой половину сегмента окружности радиуса R_0, примыкающей к подложке под углом, равным θ_0. Тогда $R_0 = h/(1 - \cos\theta_0)$, $r_1 = r_0 + R_0 \sin\theta_0$, $r(\psi) = r_1 - R_0 \cos\psi$.

После того, как форма поперечного сечения валика описана, интегралы в выражении для N принимают вполне определенные значения:

$$N = \sigma\delta\varphi \left[-R_0 \int\limits_{\pi/2-\theta_0}^{\pi/2} \cos^2\psi d\psi + r_1 \int\limits_{\pi/2-\theta_0}^{\pi/2} \cos\psi d\psi - R_0 \int\limits_{\pi/2-\theta_0}^{\pi/2} \cos^2\psi d\psi \right].$$

Выполнив вычисления, получим: $N = \sigma\delta\varphi \left[-R_0 \left(\theta_0 - \sin 2\theta_0/2 \right) + r_1 (1 - \cos\theta_0) \right]$.

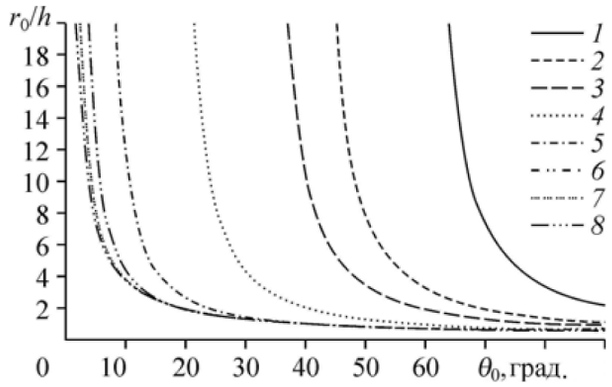

Рис. 2. Результаты расчетов критических значений радиуса сухого пятна в пленке жидкости в зависимости от краевого угла смачивания и числа Бонда.

Bo = 1 (*1*), 2 (*2*), 3 (*3*), 10 (*4*), 10^{-2} (*5*), 10^{-3} (*6*), 10^{-4} (*7*), 10^{-6} (*8*).

Подставив равенства для P и N в уравнение (2) и решив его относительно параметра r_0/h, можем записать выражение для определения критических значений размера сухого пятна в форме

$$\overline{r_0} = \frac{\theta_0 - (1 - \mathrm{Bo}/2)\sin\theta_0}{(1-\cos\theta_0)(1-\cos\theta_0 - \mathrm{Bo}/2)}, \text{ где } \mathrm{Bo} = \frac{\rho g h^2}{\sigma} \text{ — число Бонда.}$$

На рис. 2 показаны критические значения отношения r_0/h в зависимости от числа Бонда и краевого угла смачивания. При каждом значении числа Бонда по знаку равнодействующей силы $F = N + P$ видно, что в области, находящейся выше и правее соответствующего графика на рис. 2, сухое пятно имеет тенденцию к расширению, в области ниже и левее графика — к его сужению, вплоть до исчезновения. Как видим, при числах Бонда, меньших Bo = 0,001, критические значения r_0/h практически от него не зависят и определяются величиной краевого угла смачивания.

В литературе уделяется существенное внимание исследованию разнообразных аспектов растекания жидкости по подложке при различных значениях коэффициента гравитационной перегрузки $n = g/9{,}8$, где g есть ускорение свободного падения, выраженное в м/с^2 [18]. В экспериментальной практике для создания условий с пониженной гравитацией проводят параболические полеты на самолетах, используют космические аппараты и др. В условиях параболического полета коэффициент перегрузки принимает значение порядка n = 0,1 и менее [18]. В условиях международной космической станции (МКС) $n = 10^{-3}$, в условиях свободного падения на башнях сбрасывания $n = 10^{-5}$. В качестве примера, применительно к пленкам воды толщиной 0,25 мм, в таблице показаны числа Бонда, соответствующие различным значениям коэффициента перегрузки n.

Из данных, приведенных на рис. 2, следует, что для тонких пленок воды условий параболического полета практически достаточно для моделирования явлений, связанных с образованием сухих пятен в пленках, как в условиях МКС, так и в условиях полной невесомости.

Таблица

Число Бонда, соответствующее значениям коэффициента гравитационной перегрузки

n	10^{-5}	10^{-3}	10^{-1}	1	2	5
Bo	$8{,}33\cdot10^{-8}$	$8{,}33\cdot10^{-6}$	$8{,}33\cdot10^{-4}$	$8{,}4\cdot10^{-3}$	0,0168	0,042

Выводы

Критические значения отношения радиуса сухого пятна к толщине пленки жидкости определяются числом Бонда и величиной краевого угла смачивания. При углах смачивания, превышающих значение θ_0 = 70–80 градусов, влияние числа Бонда на величину отношения r_0/h невелико и сами значения r_0/h малы; однако при средних и малых значениях θ_0 роль числа Бонда исключительно велика, а отношение r_0/h принимает большие критические значения. То есть при малых значениях θ_0 и большие сухие пятна

имеют тенденцию к закрытию. В условиях полной невесомости, а также в условиях, приближенных к ним (параболический полет, МКС), критические значения отношения радиуса сухого пятна к толщине слоя жидкости практически не зависят от числа Бонда и определяются величиной краевого угла смачивания. Следовательно, условия параболического полета достаточны для моделирования явлений, связанных с образованием сухих пятен в пленках жидкости, как в условиях МКС, так и в условиях полной невесомости.

Список литературы

1. **Зайцев Д.В., Родионов Д.А., Кабов О.А.** Критический тепловой поток в локально нагреваемой пленке жидкости, движущейся под действием потока газа в мини-канале // Письма в ЖТФ. 2009. Т. 35, вып. 14. С. 88–94.
2. **Ajaev V.** Instability and rupture of thin liquid films on solid substrates // Interfacial Phenomena and Heat Transfer. 2013. Vol. 1, iss. 1. P. 81–92.
3. **Зайцев Д.В., Кириченко Д.П., Кабов О.А.** Влияние смачиваемости подложки на разрыв локально-нагреваемой пленки жидкости // Письма в ЖТФ. 2015. Т. 41, вып. 11. С. 79–85.
4. **Ajaev V.S., Gatapova E.Ya., Kabov O.A.** Stability and break-up of thin liquid films on patterned and structured surfaces // Advances in Colloid and Interface Sci. 2016. Vol. 228. P. 92–104.
5. **El-Genk M.S., Saber H.H.** Minimum thickness of a flowing down liquid film on a vertical surface // Int. J. Heat and Mass Transfer. 2001. Vol. 44. P. 2809–2825.
6. **Kadoura M., Chandra S.** Rupture of thin liquid films sprayed on solid surfaces // Experiments in Fluids. 2013. Vol. 54, No. 2. P. 1465-1–1465-11.
7. **El-Genk M.S., Saber H.H.** An investigation of the breakup of an evaporating liquid film, falling down a vertical, uniformly heated wall // J. Heat Transfer. 2002. Vol. 124. P. 39–50.
8. **Кабов О.А.** Разрыв пленки жидкости, стекающей по поверхности с локальным источником тепла // Теплофизика и аэромеханика. 2000. Т. 7, № 4. С. 537–545.
9. **Зайцев Д.В., Кабов О.А., Чеверда В.В., Буфетов Н.С.** Влияние волнообразования и краевого угла смачивания на термокапиллярный разрыв стекающей пленки жидкости // Теплофизика высоких температур. 2004. Т. 42, № 3. С. 449–455.
10. **Hartley D.E., Murgatroyd W.** Criteria for the break-up of thin liquid layers flowing isothermally over solid surfaces // Int. J. Heat and Mass Transfer. 1964. Vol. **7**. P. 1003–1015.
11. **Ponter A.B., Davies G.A., Ross T.K., Thornley P.G.** The influence of mass transfer on liquid film breakdown // Int. J. Heat and Mass Transfer. 1967. Vol. 10. P. 349–359.
12. **Zuber N., Staub F.W.** Stability of dry patches forming in liquid films flowing over heated surfaces// Int. J. Heat and Mass Transfer. 1966. Vol. 9. P. 897–905.
13. **Мальцев Л.И., Заварзин Д.С.** Критерий роста малых сухих пятен в стекающих пленках жидкости // Теплофизика и аэромеханика. 2007. Т. 14, № 2. С. 239–248.
14. **Корн Г., Корн Т.** Справочник по математике. М.: Наука, 1968. 720 с.
15. **Bankoff S.G.** Minimum thickness of a draining liquid film // Int. J. Heat and Mass Transfer. 1971. Vol. 14. P. 2143–2146.
16. **Wilson S.D.R.** The stability of a dry patch on a wetted wall // Int. J. Heat and Mass Transfer. 1974. Vol. 17. P. 1607–1615.
17. **Мальцев Л.И., Заварзин Д.С.** Математическое моделирование пленочных течений жидкости с «сухими» пятнами // Теплофизика и аэромеханика. 2012. Т. 19, № 6. С. 711–718.
18. **Кабов О.А., Зайцев Д.В.** Влияние гистерезиса смачивания на растекание капли под действием гравитации // Докл. РАН. 2013. Т. 451, № 1. С. 37–40.

Статья поступила в редакцию 25 июля 2016 г.,
после доработки — 21 сентября 2016 г.

Публикации в журналах Q1 2017-2022 (21) *

1. * Kochkin D., Mungalov A., Zaitsev D., Kabov O. Use of the reflective background oriented schlieren technique to measure free surface deformations in a thin liquid layer non-uniformly heated from below // **Experimental Thermal and Fluid Science**. – 2022. Volume 133, no. 110576. (**WoS: Q1, IF=3.77; Scopus: Q1**).
2. * Zaitsev D., Kochkin D., Kabov O. Dynamics of liquid film rupture under local heating // **International Journal of Heat and Mass Transfer**. – 2022. - Vol. 184, no. 122376. (**WoS: Q1, IF=5.24; Scopus: Q1**).
3. * Somwanshi Praveen M., Cheverda V. V., Muralidhar K., Khandekar S., Kabov O. A. Understanding vertical coalescence dynamics of liquid drops over a superhydrophobic surface using high-speed orthographic visualization // **Experiments in Fluids**. – 2022. - Vol. 63, no. 47. (**WoS: Q2, IF=2.87; Scopus: Q1**).
4. * Sielaff A.,Mangini D., Kabov O., Raza M.Q., Garivalis A.I., Zupančič M., Dehaeck S., Evgenidis S., Jacobsi C., Van Hoof D., Oikonomidou O., Zabulisj X., Karamaounasj P., Bender A., Ronshin F., Schinnerl M., Sebilleau J., Colin C., Marco P. Di, Karapantsios T., Golobič I., Rednikov A., Colinet P., Stephan P., Tadrist L. The Multiscale Boiling Investigation on-board the International Space Station: An overview // **Applied Thermal Engineering**. – 2022. - Volume 205, no. 117932. (**WoS: Q1, IF=5.17; Scopus: Q1**).
5. Mohseni-Gharyehsafa Behnam, Lyulin Yuriy V., Evlashin Stanislav A., Kabov Oleg A., Ouerdane Henni. Characterization and performance of a 3D-printed two-phase closed thermosiphon // **Thermal Science and Engineering Progress**. – 2022. - Vol. 28, no. 01001. (**Scopus: Q1**).
6. * Ajaev Vladimir S., Kabov Oleg A. Levitation and Self-Organization of Droplets // **Annual Review of Fluid Mechanics**. – 2021. - Vol. 53, pp. 203-225. (**WoS: Q1, IF=19.95; Scopus: Q1**).
7. * Khandekar S., Sahu G., Muralidhar K., Gatapova E.Y., Kabov O.A., Hu R., Luo X.B., Zhao L. Cooling of High-Power LEDs by Liquid Sprays: Challenges and Prospects // **Applied Thermal Engineering**. – 2021. - Vol. 184, no. 115640. (**WoS: Q1, IF=5.17; Scopus: Q1**).
8. * Ajaev Vladimir S., Zaitsev Dmitry V., Kabov Oleg A. Levitation of evaporating microscale droplets over solid surfaces // **Physical review fluids**. – 2021. - Vol. 6, is. 5, no. 053602. DOI: 10.1103/PhysRevFluids.6.053602. (**WoS: Q2, IF=2.66; Scopus: Q1**).
9. Zaitsev D.V., Batishcheva K.A., Kuznetsov G.V., Kabov O.A., Orlova E.G. Effect of mechanical polishing of aluminum alloy surfaces on wetting and droplet evaporation at constant and cyclically varying pressure in the chamber // **Journal of Materials Science**. – 2021. - Vol. 56, pp. 20154–20168. doi.org/10.1007/s10853-021-06565-y. (**WoS: Q2, IF=3.69; Scopus: Q1**).
10. * Karchevsky A.L., Cheverda V.V., Marchuk I.V., Ponomarenko T.G., Sulyaeva V.S., Kabov O.A. Heat flux density evaluation in the region of contact line of drop on a sapphire surface using infrared thermography measurements // **Microgravity Science and Technology.** – 2021. - Vol. 33, no. 53. doi.org/10.1007/s12217-021-09892-6. (**WoS: Q2, IF=1.69; Scopus: Q1**).

11. Zaitsev Dmitry V., Kirichenko Dmitry P., Kabov Oleg A. Levitation conditions for condensing droplets over heated liquid surfaces // **Soft Matter**. – 2021. - Is. 17, pp. 4623-4631. (**WoS: Q2, IF=3.7; Scopus: Q1**).

12.* Ajaev Vladimir S., Gatapova Elizaveta Ya., Kabov Oleg A. Interaction of advancing contact lines with defects on heated substrates // **Physical Review E**. – 2020. - Vol. 101, Is. 2 , no. 022801. (**WoS: Q1; IF=2.41; Scopus: Q1**).

13. Gatapova E.Y., Kabov O.A., Ajaev V.S. Evaporation and interface dynamics in microregion on heated substrate of non-uniform wettability International // **Journal of Heat and Mass Transfer.** - 2019. - Vol. 142, no.118355. (**WoS: Q1; IF= 5.24; Scopus: Q1**).

14. Polikarpov A.P., Graur I.A., Gatapova E.Y., Kabov O.A. Kinetic simulation of the non-equilibrium effects at the liquid-vapor interface // **International Journal of Heat and Mass Transfer**. – 2019. - Vol. 136, pp. 449-456. (**WoS: Q1, IF=5.24; Scopus: Q1**).

15. Gatapova Elizaveta Ya., Shonina Anna M., Safonov Alexey I., Sulyaeva V.S., Kabov O.A. Evaporation dynamics of a sessile droplet on glass surfaces with fluoropolymer coatings: focusing on the final stage of thin droplet evaporation // **Soft Matter**. – 2018. - Vol. 14, is. 10, pp. 1811-1821. (**WoS: Q2, IF=3.7; Scopus: Q1**).

16. Machrafia H., Lyulin Y., Iorio C.S., Kabov O., Dauby P.C. Numerical parametric study of the evaporation rate of a liquid under a shear gas flow: Experimental validation and the importance of confinement on the convection cells and the evaporation rate // **International Journal of Heat and Fluid Flow**. – 2018. - Vol. 72, pp. 8-19. (**WoS: Q2, IF=2.8; Scopus: Q1**).

17. Zaitsev Dmitry V., Kirichenko Dmitry P., Ajaev Vladimir S., Kabov O.A. Levitation and Self-Organization of Liquid Microdroplets over Dry Heated Substrates // **Physical Review Letters**. - 2017. - Vol. 119, Is. 9, no. 094503. (**WoS: Q1, IF=9.04; Scopus: Q1**).

18. Wen Boyao, Sun Chengzhen, Bai Bofeng, Gatapova E.Y., Kabov O.A. Ionic hydration-induced evolution of decane-water interfacial tension // **Physical Chemistry Chemical Physics**. – 2017. - Vol. 19, is. 22, pp. 14606-14614. (**WoS: Q1; IF=3.8; Scopus: Q1**).

19. Ajaev Vladimir S., Kabov Oleg. Heat and mass transfer near contact lines on heated surfaces // **International Journal of Heat and Mass Transfer**. – 2017. - Vol. 108, pp. 918-932. (**WoS: Q1, F=5.24; Scopus: Q1**).

20. Gatapova Elizaveta Ya., Graur Irina A., Kabov Oleg A., Aniskin V.M., Filipenko M.A., Sharipov F., Tadrist L. The temperature jump at water - air interface during evaporation // **International Journal of Heat and Mass Transfer**. – 2017. - Vol. 104, pp. 800-812. (**WoS: Q1, IF=5.24; Scopus: Q1**).

21. Kabov Oleg A., Zaitsev Dmitry V., Kirichenko Dmitry P., Ajaev V.S. Interaction of Levitating Microdroplets with Moist Air Flow in the Contact Line Region // **Nanoscale and Microscale Thermophysical Engineering.** – 2017. - Vol. 21, is. 2, pp. 60-69. (**WoS: Q2, IF=3.68; Scopus: Q1**).

* - звездочкой отмечены статьи, включенные в подборку избранных трудов (9)

Experimental Thermal and Fluid Science 133 (2022) 110576

Contents lists available at ScienceDirect

Experimental Thermal and Fluid Science

journal homepage: www.elsevier.com/locate/etfs

Use of the reflective background oriented schlieren technique to measure free surface deformations in a thin liquid layer non-uniformly heated from below

D. Kochkin [a,b,*], A. Mungalov [a,c], D. Zaitsev [a,c], O. Kabov [a,b]

[a] Kutateladze Institute of Thermophysics, Russian Academy of Sciences, Prosp. Lavrentyeva 1, Novosibirsk 630090, Russia
[b] Novosibirsk State Technical University, Prosp. K. Marksa 20, Novosibirsk 630073, Russia
[c] Novosibirsk State University, Pirogova Str. 2, Novosibirsk 630090, Russia

ARTICLE INFO

Keywords:
Synthetic Schlieren technique
Free-surface deformations
Thermocapillary convection
Thin liquid layer

ABSTRACT

To measure liquid film surface deformations, we use the Background Oriented Schlieren (BOS) technique with a reflective optical scheme, which includes a random dot pattern located above the liquid surface, and a camera that captures its reflection from the liquid interface. The substrate was covered with a special black coating to minimize stray light reflection, which allowed to provide clear visualization of the dot pattern reflected from the free surface even for very thin liquid films. Local slopes of the film surface cause the dot displacement on the pattern image relative to the pattern image captured in the absence of any free-surface deformations. Hence, the topography of the liquid film surface is encoded by the apparent displacement of the dot pattern. Using the cross correlation image processing, the displacement vector field was determined, which was then substituted in Poisson equation to reconstruct the free-surface profile of the liquid film. The main advantages of this technique are: applicability for liquids with surface temperature inhomogeneities, experimental simplicity, sensitivity and applicability for both transparent and opaque liquids. Using the reflective BOS technique and using substrate with black coating we measure the free-surface deformation field of a thin layer of silicone oil non-uniformly heated from below. Despite the fact that thermocapillary shear stresses tend to decrease the thickness of the liquid layer in hotter regions, in the experiment, a convex deformation of the liquid film surface was observed above the heater for a few seconds immediately after the start of heating. This phenomenon is explained by the expansion of the liquid induced by the heating, due to the dependence of the liquid density on temperature. The measurement results are compared with those obtained in a single point using the confocal sensor. A good agreement is achieved.

1. Introduction

Liquid films are encountered in various types of heat and mass transfer equipment in industry and in many types of technological applications. The thickness of the liquid film is one of the key factors to govern the film flow characteristics and heat and mass transfer rates. In the case of falling liquid films [1] and shear - driven liquid films moving in the channels under the influence of gas or steam flow [2] the intensity of heat transfer at evaporation is roughly inversely proportional to the thickness of the liquid layer. That is why it is of paramount importance to develop experimental techniques for precise measurement of the instantaneous local thickness of the liquid film as well as full-field film thickness distribution. A comprehensive review of the literature on methods for measuring the thickness of a liquid film deposited on a solid substrate is presented in [3].

To measure liquid free surface deformations, Kurata et al. [4] proposed an optical measurement technique that is relatively simple in terms of the necessary equipment, since it only requires a camera. In the proposed method, the water surface topography is measured using the transmitted image of a striped grating located at the bottom of the channel and used as a pattern. Later, Moisy et al. [5] presented a free-surface synthetic Schlieren technique (or equivalently BOS), which is based on the cross-correlation analysis of the refracted images of a random dot pattern visualized through the interface. Recently, Vinnichenko et al. [6] proposed a new modification of the BOS method for measurement of the free-surface topography over deep liquid layers,

* Corresponding author at: Kutateladze Institute of Thermophysics, Russian Academy of Sciences, Prosp. Lavrentyeva 1, Novosibirsk 630090, Russia.
E-mail address: kochkin1995@mail.ru (D. Kochkin).

https://doi.org/10.1016/j.expthermflusci.2021.110576
Received 27 May 2021; Received in revised form 1 November 2021; Accepted 7 December 2021
Available online 10 December 2021
0894-1777/© 2021 Elsevier Inc. All rights reserved.

based on cross-correlation image processing, as in the BOS technique, but using the reflective optical scheme. This method is called moon-glade BOS method, since surface deformation results in deflection of the reflected rays and distortion of the background pattern image – similarly to moon-glade due to water ripples at sea. The moon-glade BOS method was compared with traditional BOS method (using refractive optical scheme), and was found to be more sensitive, allowing to reliably measure free surface perturbations as small as 1 μm.

2. Experimental setup

As a test section we use a cylindrical cuvette (having inner diameter of 88 mm) with the locally heated bottom (Fig. 1). The heating element is a copper cylinder, the protruding part of which has a square section of size 10×10 mm^2 and is pressed into the cuvette bottom. Nichrome wire, connected to a power source, is used to heat the copper rod. The cuvette has a groove around its perimeter in which a copper tube is laid. By water pumping inside the tube, thermal stabilization of the cuvette perimeter is ensured. The water temperature is controlled by a thermostat and is kept to 23 °C. The test section and experimental equipment are installed on an optical table, which is a rigid platform set strictly parallel to the horizon. The optical table also performs the function of vibration damping. The test section is open to the atmosphere. The experiments are carried out at the ambient temperature of 23–25 °C and relative humidity of about 40%. As the working liquid PDMS-100 silicone oil (with kinematic viscosity of 100 cS, density of 963 kg/m3, surface tension of 20.9 mN/m, refractive index of 1.403) is used. The liquid film thickness in the experiments did not exceed 1.5 mm.

The moon-glade (reflective) BOS method is used for the free surface topography measurements. The optical scheme of the method consists of a remotely controlled Nikon CCD-camera and a LED panel (size of 147×147 mm^2, power of 18 W, light temperature of 4000 K) with a glued dot pattern, both installed above the liquid surface Fig. 1. To validate the measurement results obtained, the local film thickness is additionally measured using the Micro-Epsilon controller IFC2451 with confocal chromatic sensor IFS2405-3 (the accuracy of about 1.5 μm, the measuring range of about 3 mm and the measurement frequency of 0.3 kHz). The confocal sensor is installed on a positioning system with a linear stage for moving the sensor along the cuvette.

3. Methodology

Fig. 2 shows the optical scheme of the reflective BOS method. The background (dot pattern) and the camera are installed above the liquid layer at an angle to the horizon in such a way that the background reflection from the liquid surface is detected by the CCD-camera. Since the camera is aligned non-perpendicularly to the liquid surface the captured background pattern images have keystone distortion. Therefore, the images are digitally corrected using a calibration rectangular piece of paper attached to the background and depicted in the images as a trapezoid, the parallel sides of which determine the distortion factor. To minimize stray light reflection from the substrate, the substrate is covered with a special black coating. This allows to measure very thin liquid layers, unlike the case when no coating is applied [6].

As the background, a LED panel is used on which a transparent polyester film with a printed pattern of random dots is glued. Defor-

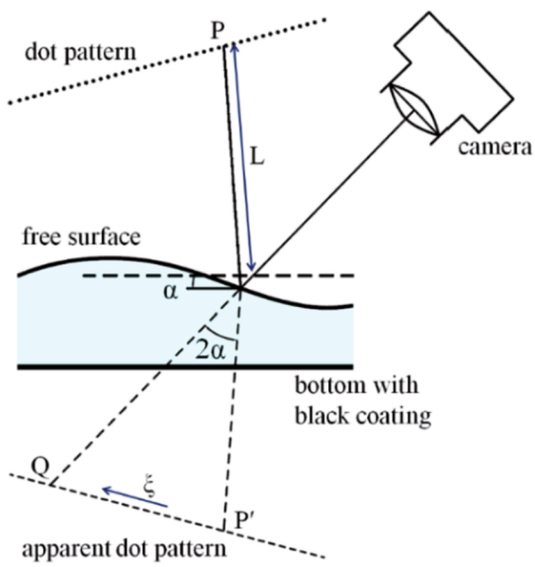

Fig. 2. Optical scheme of the BOS method with reflection from the free surface.

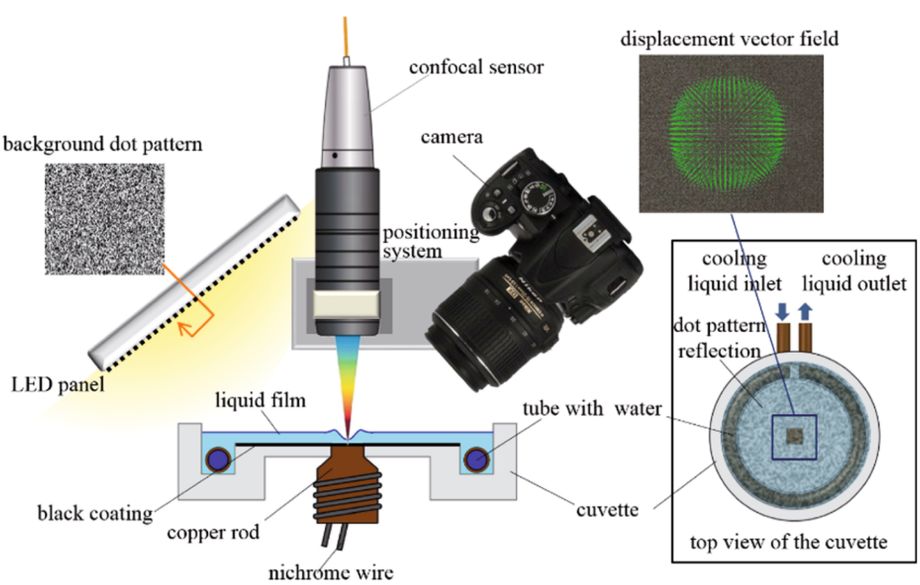

Fig. 1. Experimental setup.

mation of the liquid surface causes the displacement of dots in the background pattern image. The displacement angle of the beam reflected from a deformed surface relative to the beam reflected from a flat undisturbed surface is twice the inclination angle of the surface, Fig. 2. Thus, for small surface deformations in paraxial approximation the background pattern dot displacement in the x-direction and y-direction can be written as:

$$\xi_x = 2L\frac{\partial h}{\partial x}, \tag{1}$$

$$\xi_y = 2L\frac{\partial h}{\partial y}, \tag{2}$$

where L is the distance between the dot pattern and the liquid film surface.

To determine the apparent displacement of the dots a Digital-Image-Correlation algorithm (DIC) is used. The reference image captured when the film surface is flat (undisturbed surface at the beginning of the experiment) is digitally compared to the images obtained in presence of perturbations. DIC procedure is as follows: the reference image is split into regions of equal size (interrogation windows) with many background dots inside them. On the image with disturbed dots, for each interrogation window a search window is defined that includes the interrogation window. Then the cross-correlation function is calculated, its maximum corresponds to the most probable displacement of the group of dots within the interrogation window. Thus, each interrogation window contains one vector of displacement of a group of dots. To increase the resolution of the method, the reference image can be divided into interrogation windows with overlapping. As a result of cross correlation image processing, we obtain the displacement vector field that is substituted in Poisson equation

$$\frac{\partial^2 h}{\partial x^2} + \frac{\partial^2 h}{\partial y^2} = \frac{a_{pat}}{2La_{surf}}\left(\frac{\partial \xi_x}{\partial x} + \frac{\partial \xi_y}{\partial y}\right), \tag{3}$$

to reconstruct the liquid surface profile, where a_{pat} and a_{surf} are image resolution (mm/pix) relative to the dot pattern plane and the free surface plane, respectively [6]. Eq. (3) is obtained by adding Eqs. (1) and (2) differentiated with respect to x and y, respectively.

4. Experiments

Non-uniform heating of thin liquid layers leads to free surface deformations caused by the thermocapillary effect producing surface shear stresses [7]

$$\tau_{sur} = grad\sigma,$$

arising due to surface tension temperature dependence

$$grad\sigma = \frac{\partial \sigma}{\partial T} gradT.$$

For most liquids $\partial\sigma/\partial T$ is negative, i.e. the surface tension decreases with increasing T. Therefore, the surface force arising during heating acts in the opposite direction as compared to gradT. Surface force moves liquid from warmer areas to less heated ones. Paper by [8] was one of the pioneering in experimental and theoretical studying the thermocapillary convection in a locally heated thin horizontal layer of liquid with a deformable gas – liquid interphase. With an increase in the temperature gradient along the liquid layer, the deformations of the free surface increase so that the free liquid surface can reach the substrate with the formation of a dry spot. In the present work we study the primary perturbations of the film surface caused by non-uniform heating.

Experiments were performed with a horizontal layer of PDMS-100 silicone oil in the cuvette with a locally heated bottom. The initial layer thickness was about 1.25 mm. The electrical power supplied to the heating element was 5 W. The water temperature in the thermal stabilizing circuit was 23 °C. The background-to-surface and lens-to-surface distances are 13 and 17 cm, respectively, the incidence angle is about 18°. The pattern of random dots (with size of 0.1 mm) was printed with resolution 1400 dpi. The camera field of view was 55 × 67 mm. The resolution of the image was 5568 × 3712 pixels. Images of the background pattern were captured at 1 fps. The procedure for reconstructing the surface profile from the obtained images was carried out after the experiment. The processing time of one image was about ten seconds. In cross-correlation image processing, the interrogation window size was 128 × 128 or 64 × 64 pixels with 50% overlap, depending on the reconstructed surface profile (lower value for smaller deformations). Poisson equation (3) is solved numerically by a second order finite-difference scheme. The distance between two adjacent nodes is equal to the step of cross-correlation (half the size of the interrogation window). The assumption that liquid film has constant height at the edge of the studied area is used as boundary condition. The absence of dot displacement along the edge of the processed image as well as measurement of the layer thickness with the confocal sensor at the distance of 2 cm from the cuvette center during the experiment confirm the validity of this assumption. Several images captured with undisturbed film were cross-correlated to detect spurious noise. The detected deviations did not exceed 0.05 μm.

Figs. 3, 4 present reconstructed surface profile of the liquid film non-uniformly heated from below at different times. After heating is initiated, a liquid bump forms above the heater, followed by the formation of a hollow in the top of the bump. This was also observed in [9] dealing with the heating of a heavy oil layer using a laser beam. The authors made a theoretical analysis based on the stationary solution of the Navier-Stokes equation and concluded that the phenomenon observed was due to competition between the density- and surface-tension gradients. Another interesting phenomenon observed in our study is slight movement of the maximum of the deformation at the initial stage of the heating (Fig. 4a). This sort of a wave is predicted by the numerical model by [10] and is explained by displacement of the liquid from the center toward the periphery. This model also predicts the absence of this wave in stationary conditions.

The amplitude of the wave observed in our study is quite small and is less than one micrometer (Fig. 4a). It can be seen that the wave crest is formed at a distance of about 1 mm from the edge of the heater, then the wave moves at an average speed of about 0.7 mm/s, while its amplitude decreases with some oscillations. It is also worth noting that the process of deepening deformation (negative) develops very slowly over 30–40 s, compared to the development of positive deformations observed only during a few seconds after the start of the heating (Fig. 4).

5. Validation and limitations of the method

5.1. Influence of the interrogation window size on the reconstructed free-surface profile

In digital image processing for the surface height reconstruction, the interrogation window size varied from 200 × 200 to 32 × 32 pixels in order to choose a reasonable amount of smoothing. The computational grid varied from 32 × 32 to 194 × 196, respectively. When using a large interrogation window size, the dots displacement within a measurement area is averaged, as a result of which the measured deformation is underestimated. Accordingly, for more correct measurements, the interrogation window size should be reduced. The smoothing analysis was carried out for different values of deformations, since the dot displacement increases with increasing deformations, which requires an increase in the interrogation window size to determine the displacement vector field. An appropriate size of the interrogation window is selected provided that a decrease in the interrogation window by several times does not lead to a spread of values in the layer height by more than 1%.

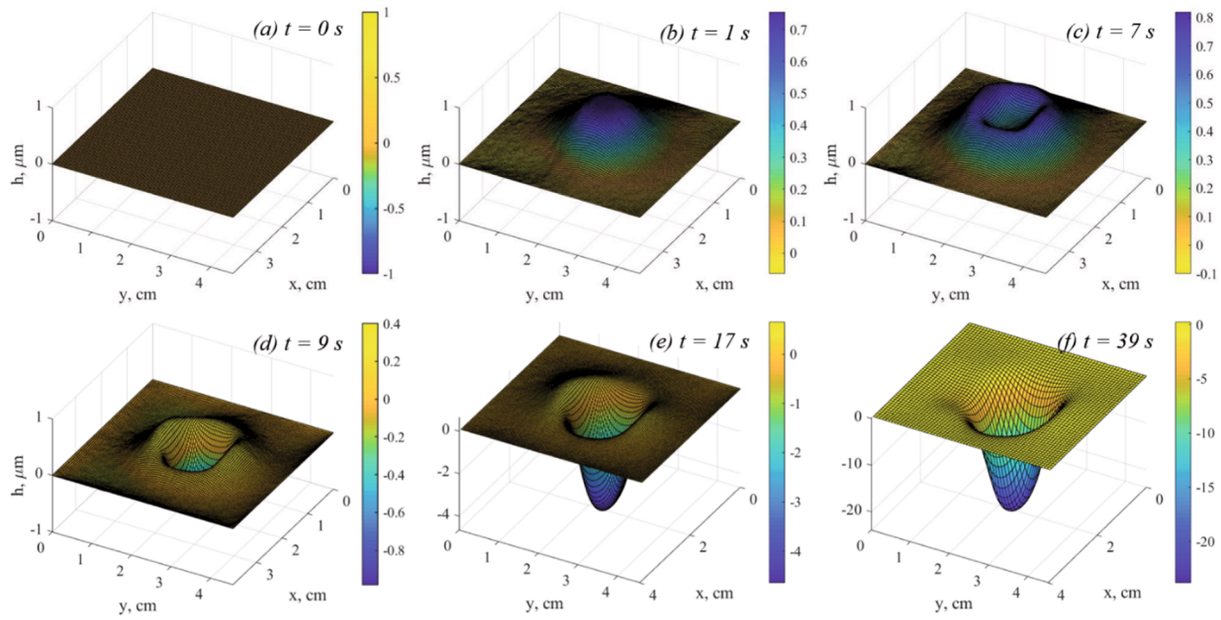

Fig. 3. Evolution of the reconstructed surface topography in time.

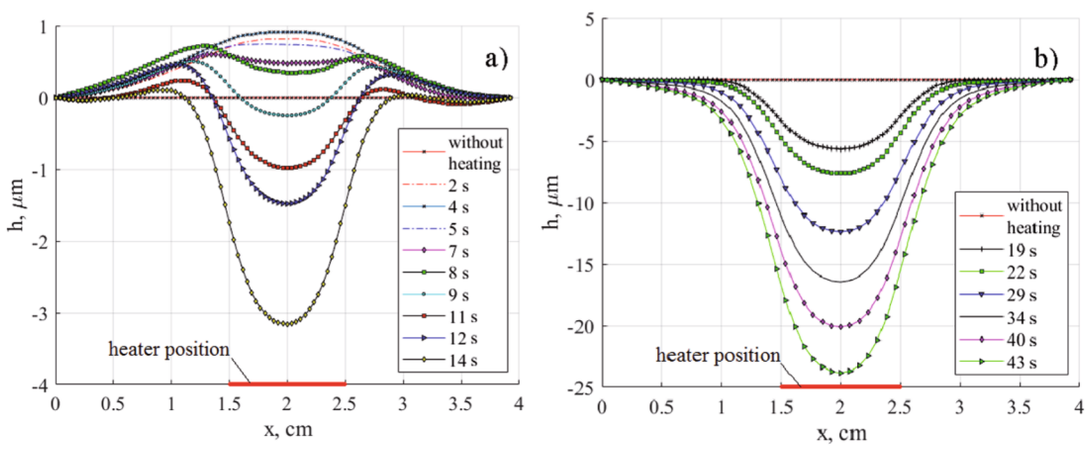

Fig. 4. Film surface profiles at different times after heating starts.

5.2. *Least count of measurement and effect of surface-to-dot pattern distance on measurements*

The least count of free-surface profile measurement is associated with the cross-correlation accuracy. We performed the cross-correlation analysis of the reference background image and the same image with an artificial dots displacement by several pixels. The deviation of the measured dots displacement value from the specified one did not exceed 0.2 px, which corresponds to the values presented in (Vinnichenko et al. 2020). From equation (1) we can estimate that for our experimental parameters (L = 13 cm, a_{pat} = 15 μm, a_{surf} = 13 μm) the value of the cross-correlation accuracy of 0.2 px results in the sensitivity of the presented method of about 10 μrad. To increase the sensitivity of the method, the distance from the surface of the liquid layer to the background should be increased. With the same experimental parameters, an increase in the distance L to 1 m will make it possible to measure surface slopes from about 2 μrad, which corresponds to the value presented in (Vinnichenko et al., 2020).

The maximum slope that can be measured by the proposed method is limited by the curvature of the measured surface. The strong curvature causes the ray crossing (caustics) as a result of which the captured background image is blurred and cannot be processed. It is possible to prevent the image blur and accordingly increase the limit of the measured surface slope by decreasing the distance between the background and the surface of the liquid layer. The strong curvature and/or large surface-pattern distance also limit the measurement range of another version of the background schlieren method, based on the analysis of the refracted image of a random dot pattern visualized through the interface [5].

5.3. *Comparison with the confocal method*

In order to verify the reconstructed relief of the liquid film surface, the results of measurements obtained by the reflective BOS method were compared with single point measurements by the confocal method. Fig. 5 shows the change in the local film thickness measured by these

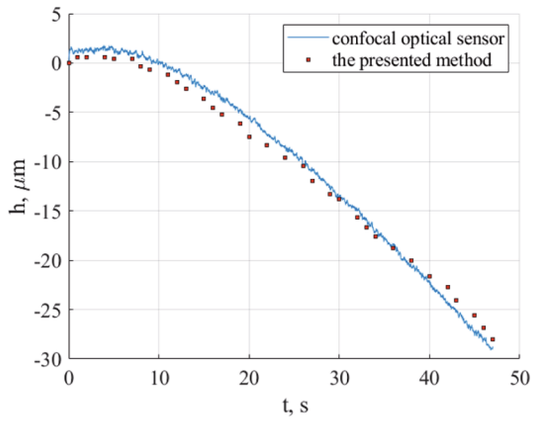

Fig. 5. Film thickness in the center of the cuvette after heating starts, measured by two methods.

two methods above the heater center during the experiment. Note that the reflective BOS and confocal measurements shown in Fig. 5 were obtained under the same conditions, but for different runs. The reflective BOS measurement results are in good agreement with data obtained by the confocal method.

6. Conclusions

In this paper, we use the synthetic schlieren method with a reflective optical scheme to measure liquid film free surface deformations. The substrate was covered with black covering which allowed to measure very thin liquid films. Measurements have been performed for film of silicone oil non-uniformly heated from below. The concave deformation of the surface caused by the thermocapillary effect is preceded by the expansion of the liquid in the hotter region. It has been found that a local heating of the horizontal liquid layer produces a liquid wave around the heater at the initial stage of heating. The wave is explained by movement of the liquid from the center of cuvette toward the periphery. A comparison of the reconstructed topography with confocal method measurements was performed. The measurement results obtained by two methods are in good agreement.

Funding

This work was supported by the Russian Foundation for Basic Research (Project No. 18-29-19197). The test section was designed under the support of the Russian Science Foundation (Project No. 19-19-00695).

CRediT authorship contribution statement

D. Kochkin: Conceptualization, Methodology, Validation, Investigation, Data curation, Writing – original draft, Writing – review & editing. **A. Mungalov:** Methodology, Software, Validation, Investigation, Writing – review & editing. **D. Zaitsev:** Methodology, Validation, Writing – review & editing. **O. Kabov:** Conceptualization, Writing – review & editing, Supervision.

Declaration of Competing Interest

The authors declare that they have no known competing financial interests or personal relationships that could have appeared to influence the work reported in this paper.

References

[1] D.V. Zaitsev, O.A. Kabov, Study of the thermocapillary effect on a wavy falling film using a fiber optical thickness probe, Exp. Fluids. 39 (4) (2005) 712–721, https://doi.org/10.1007/s00348-005-0003-y.
[2] O.A. Kabov, D.V. Zaitsev, V.V. Cheverda, A. Bar-Cohen, Evaporation and flow dynamics of thin, shear-driven liquid films in microgap channels, Exp. Therm. Fluid Sci. 35 (5) (2011) 825–831, https://doi.org/10.1016/j.expthermflusci.2010.08.001.
[3] C.B. Tibiriçá, F.J. do Nascimento, G. Ribatski, Film thickness measurement techniques applied to micro-scale two-phase flow systems, Exp. Therm. Fluid Sci. 34 (4) (2010) 463–473, https://doi.org/10.1016/j.expthermflusci.2009.03.009.
[4] J. Kurata, K.T.V. Grattan, H. Uchiyama, T. Tanaka, Water surface measurement in a shallow channel using the transmitted image of a grating, Rev. Sci. Instrum. 61 (2) (1990) 736–739.
[5] F. Moisy, M. Rabaud, K. Salsac, A synthetic Schlieren method for the measurement of the topography of a liquid interface, Exp. Fluids. 46 (6) (2009) 1021–1036, https://doi.org/10.1007/s00348-008-0608-z.
[6] N.A. Vinnichenko, A.V. Pushtaev, Y.Y. Plaksina, A.V. Uvarov, Measurements of liquid surface relief with moon-glade background oriented Schlieren technique, Exp. Therm. Fluid Sci. 114 (2020) 110051, https://doi.org/10.1016/j.expthermflusci.2020.11005.
[7] V.G. Levich, Fiziko-khimicheskaya gidrodinamika, 2nd ed., Gos.izd. fiz.-mat. literatury, Moscow, 1959.
[8] A.F. Pshenichnikov, G.A. Tokmenina, Deformation of the free surface of a liquid by thermocapillary motion, Fluid Dyn. 18 (3) (1983) 463–465.
[9] G. Da Costa, Competition between capillary and gravity forces in a viscous liquid film heated by a Gaussian laser beam, J. Phys. 43 (1982) 1503–1508, https://doi.org/10.1051/jphys.
[10] I.V. Marchuk, Thermocapillary deformation of a horizontal liquid layer under flash local surface heating, J. Eng. Thermophys. 24 (4) (2015) 381–385, https://doi.org/10.1134/S181023281504013X.

International Journal of Heat and Mass Transfer 184 (2022) 122376

Contents lists available at ScienceDirect

International Journal of Heat and Mass Transfer

journal homepage: www.elsevier.com/locate/hmt

Dynamics of liquid film rupture under local heating

D. Zaitsev [a], D. Kochkin [a,b,*], O. Kabov [a,b]

[a] Kutateladze Institute of Thermophysics, Russian Academy of Sciences, Prosp. Lavrentyeva 1, Novosibirsk 630090, Russia
[b] Novosibirsk State Technical University, Prosp. K. Marksa 20, Novosibirsk 630073, Russia

ARTICLE INFO

Article history:
Received 23 August 2021
Revised 16 November 2021
Accepted 2 December 2021
Available online 13 December 2021

Keywords:
Thermocapillary convection
Thin liquid layer
Residual film
Dry spot
Confocal method

ABSTRACT

Rupture dynamics of a horizontal liquid film non-uniformly heated from below was experimentally studied in a wide range of liquid viscosity. To visualize the liquid surface deformations and disruption of the film, an optical schlieren system was used. The instantaneous local film thickness was measured using a chromatic confocal sensor. In order to measure the thickness of thin liquid films, the substrate was covered with a black coating eliminating reflection of the incident light. Angular and frequency characteristics of the confocal sensor were studied in detail. The process of film rupture can be divided into three stages: 1) film thinning down to a residual film on the heater; 2) existence of a stable residual film for some time; 3) rupture and dry out of the residual film. The thickness of the residual film was found to strongly depend on the liquid viscosity: for water it is about 10 μm, whereas for silicone oil PMS-200 it is about 275 μm. The data obtained for various working liquids were generalized by a dimensionless correlation.

© 2021 Elsevier Ltd. All rights reserved.

1. Introduction

There are many practical applications associated with the process of heat transfer between a solid wall and a liquid film, as thin layers of liquid provide high intensity of heat transfer at relatively low liquid consumption. Liquid films on a heated plate are susceptible to thermocapillary instabilities driven by the shear stresses arising from the temperature dependence of the surface tension (the so-called Marangoni effect). This phenomenon can lead to the film rupture with the formation of a dry spot at the heated plate. Understanding of the mechanisms of film rupture is essential to ensure stable film flow without dry spots.

Thermocapillary rupture of liquid films has been extensively studied in the literature for various conditions: a still horizontal liquid layer non-uniformly heated from the substrate [1,2], a liquid film flowing along a horizontal plate with a local heat source [3], a liquid film flowing under the action of gravity down a vertical plate with a local heat source [4,5], a still horizontal liquid layer locally heated from above by a laser beam [6]. It is shown that with a decrease in the thickness of the liquid layer and the flow rate of the liquid, the film flows are less stable and prone to rupture with the formation of a dry spot. Thermocapillary rupture of a liquid layer is a complex physical phenomenon in which the film thickness changes by several orders of magnitude (from several millimeters to several micrometers or even nanometers), with different forces prevailing on different scales. Moreover, liquid film rupture is closely related to the **physics of the contact line** [7–9], which is responsible for the behavior of a dry spot after its nucleation.

It was first discovered in [10] that thermocapillary rupture of a liquid film (distilled water) occurs with the formation of a thin residual film covering the heater surface before the formation of a dry spot. The phenomenon of residual film was observed both on relatively large heaters (150 × 150 mm) [11] and on small ones (22 × 6.5 mm) [10], and both with vertical and horizontal arrangement of the substrate. Later in [12], using a schlieren optical technique, the residual film was clearly visualized in a thin (0.3–0.7 mm) ethanol layer placed on a horizontal substrate heated by a small circular (Ø 1.6 mm) heater. However, no work provides quantitative data on the thickness of the residual film.

For the study of processes in liquid films, in particular, the destruction of liquid films, accurate methods of measuring the thickness of layers are of paramount importance. A comprehensive review of the literature on methods for measuring the thickness of a liquid film deposited on a solid substrate is presented in [13–15]. Depending on the principle of operation, liquid film thickness measurement techniques can be divided into four main groups: **mechanical** [2,3], **electrical** [16,17], acoustic [18,19], **nucleonic** [20,21] and **optical**. Since optical measurement techniques have important advantages of being non-intrusive and relatively affordable, they are more commonly used. Different types of optical meth-

* Corresponding author at: Kutateladze Institute of Thermophysics SB RAS: FGBUN Institut teplofiziki imeni S Kutateladze Sibirskogo otdelenia Rossijskoj akademii nauk, Russia.
E-mail address: kochkin1995@mail.ru (D. Kochkin).

https://doi.org/10.1016/j.ijheatmasstransfer.2021.122376
0017-9310/© 2021 Elsevier Ltd. All rights reserved.

Table 1
Table 1 Literature review of the chromatic confocal method.

author	object of study	working liquid	heating	thickness range (mm)	measurement frequency	sensor
1) Helbig et al. (2005), Helbig et al. (2009) [49,50]	falling and shear-driven thin films on smooth and grooved surfaces in a ring shaped channel	water	+	0.2–0.5	n/a	n/a
2) Lel et al. (2005) [22]	liquid film flowing down the plate	silicone fluid	–	0.2–1.4	2 kHz	STIL CHR-450
3) Rulliere et al. (2007) [51]	meniscus curvature radius along the grooves	water, methanol, n-pentane	+	up to 0.35	n/a	n/a
4) Lel et al. (2008) [52]	liquid film flowing down the plate	silicone fluid	+	0.2–1.6	n/a	STIL CHR-450
5) Dietze et al. (2008) [53]	liquid film flowing down the plate	silicone fluid DMS-T05	–	0.4–1.7	800 Hz	n/a
6) Zhou et al. (2009) [23]	wavy water film falling down a flat plate	water	–	0.2–0.75	2 kHz	STIL CHR-150E
7) Dietze et al. (2009), G. Dietze and R. Kneer (2011) [54,55]	falling liquid film flowing down the inside of the glass body	dimethylsulfoxide (DMSO)–water solution	–	0.2–0.6	800 Hz	STIL CHR-540
8) Gong et al. (2010) [56]	isothermal liquid film flowing over a horizontal silicon wafer / evaporating film on a horizontal silicon wafer surface	water	-/+	up to 0.84	up to 30 kHz	controller optoNCDT2431 sensors IFS2431–3 and IFS2431–0.3
9) Gong et al. (2011) [57]	liquid films evaporating on horizontal surfaces	water, hexane, ethanol	+	up to 0.3	up to 30 kHz	Controller optoNCDT2431 sensors IFS2431–3 and IFS2431- 0.3
10) Rohlfs et al. (2012) [58]	liquid film flowing down the plate in electric field	silicone fluid DMS T12	–	0.5–2	n/a	Micro–Epsilon optoNCDT 2451 with a probe IFS 2401–3
11) Rohlfs et al. (2013) [59]	liquid film flowing down the plate in electric field	silicone fluid DMS T12	+	0.5–2.3	n/a	Micro–Epsilon optoNCDT 2451 with a probe IFS 2401–3
12) Gong et al. (2014) [60]	liquid film boiling/pool boiling	water	+	1.4–2.3	up to 30 kHz	controller optoNCDT2431, sensors IFS2431–3 and IFS2431–0.3
13) Rietz et al. (2015) [61]	liquid film flowing down the plate	silicone fluid DMS T12	+	0.3–1.6	n/a	IFS 2401–3
14) Wang et al. (2017), K. Wang et al. (2016) [62,63]	thin liquid film sheared by the co-flowing air from above and heated from below in a horizontal channel	water	+	0.1–1.7	1 kHz	optoNCDT2431 IFS2431–3
15) Swartz and Yao (2017) [64]	turbulent natural-convective condensation on a vertical wall with smooth and wavy film interface	water	–	0.1–0.5	4 kHz	Precitec Chrocodile M4
16) Leng et al. (2018) [65]	shear-driven film flow	water	–	0.02–1	n/a	ACR-HNDS100 (Schmitt Industries)

ods for measuring liquid film thickness are as follows: confocal [22,23], fiber-optical [11,24,25], laser focus displacement [26–28], schlieren and shadow [29–31], phase-shifting schlieren [32], interferometry [33–35], total internal reflection [36–38], fluorescence [39–43], emission reabsorption laser induced fluorescence [44], luminescence [45], laser light absorption [46], laser scattering [47], refractive index matching [48].

The chromatic confocal technique is a factory-made ready-to-use measuring system, which is one of the promising methods for measuring the instantaneous local thickness of a liquid film with high spatial and temporal resolution. Table 1 contains the list of available works from the literature where the chromatic confocal method was applied for measuring liquid film thickness, with indication of the object of the study and main experimental parameters.

From Table 1 one can see that the confocal sensor is used for measurement of the liquid film thickness under a variety of conditions: for still and flowing films with smooth and wavy film interfaces; with and without heating; for direct measurements and for measurements through an optically transparent wall. A wide range of liquids have been investigated, but the vast majority of research has been done for water and silicone oils. It should be noted that the measurements were carried out at a high frequency of the order of 1 kHz and higher. The confocal sensor is mainly used to measure liquid films with the thickness from 100 μm to 1–2 mm. Measurements of thin liquid films less than 100 μm are difficult due to the limitation of the sensor on the minimum measurable thickness, which, according to the manufacturer, is several tens of micrometers, depending on the sensor model. However, in [57], liquid films with the thickness of several micrometers were measured using a confocal sensor, but it is not described how this was done.

In the current work we study the horizontal liquid film rupture using an improved chromatic confocal technique with blackening of the substrate, which allowed to measure ultra-thin liquid films.

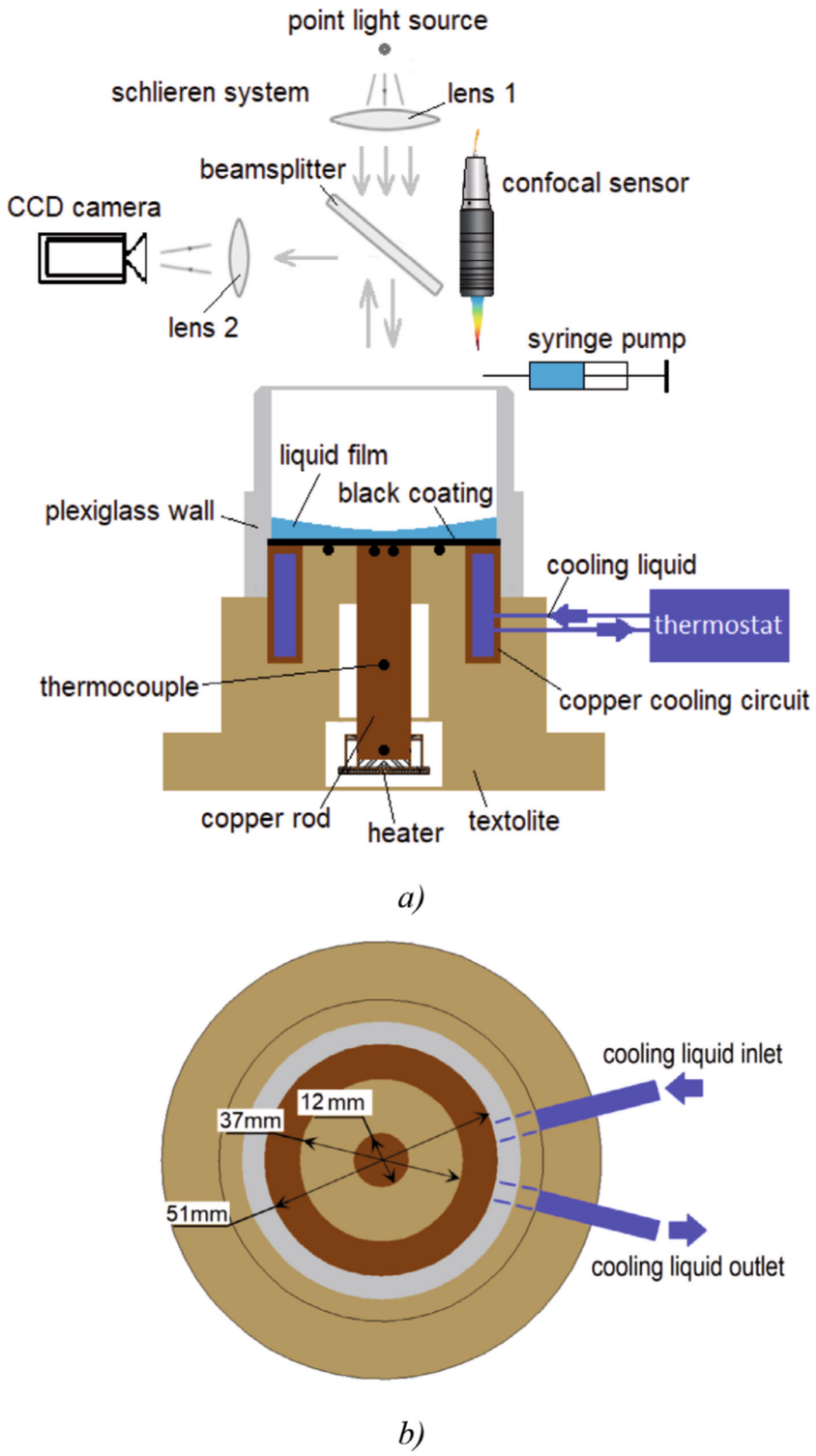

Fig. 1. Schematic of the test section. Side view (*a*), top view (black coating and liquid film are not shown) (*b*).

2. Experimental equipment and methods

2.1. Test section

The test section is a textolite plate with an embedded copper rod as a heater having the diameter of 12 mm and length of 47 mm (Fig. 1). Along the perimeter of the substrate, a copper cooling circuit is mounted, with the temperature of the cooler (water) kept at 5°C throughout the experiment. The copper rod is heated by an electrical heating element attached to its bottom edge. In the experiments, the maximum electrical power on the

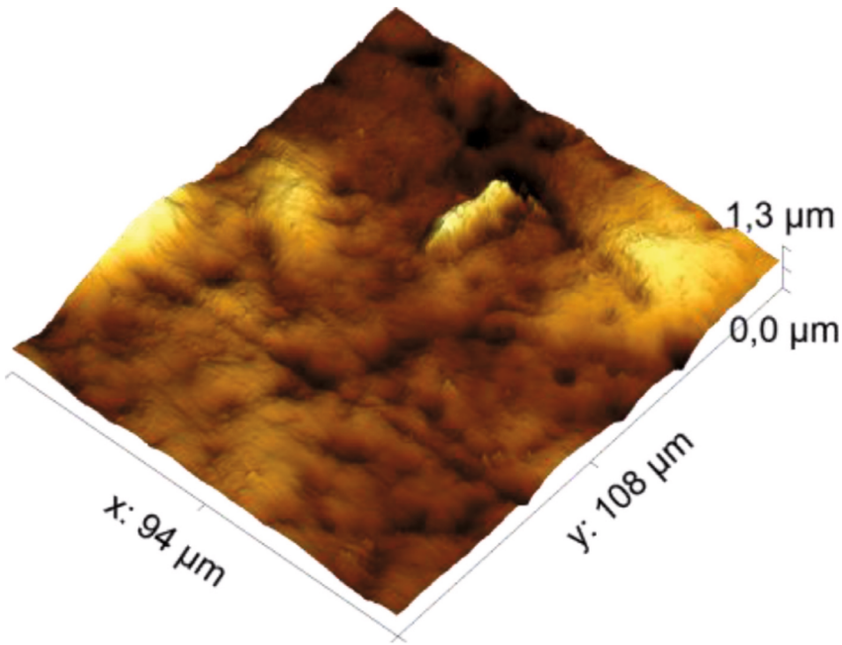

Fig. 2. Morphology of the surface of the coating.

heating element was 75 W, while the maximum temperature of the surface of the copper rod, measured with 2 thermocouples, was 87 °C. A plexiglass cylinder is mounted on the test section, as shown in Fig.1. The test section is open to the atmosphere. The experiments are carried out at the ambient temperature of 23–25 °C and relative humidity of about 60%. To form a liquid film, a predetermined volume of the working liquid with the initial temperature of 25°C is fed to the substrate via a syringe pump. The initial average film thickness in the experiment varies from about 400 to 700 μm, which corresponds to the initial volume of liquid from about 0.81 to 1.43 ml, respectively.

2.2. Substrate coating

To minimize light reflection from the substrate and also to achieve homogeneous wettability, the textolite plate along with the surface of the copper rod are covered with a thin layer of special black paste and are carefully polished (for more details on the role of the coating see Sect. 2.5.4). An estimated average thickness of the coating is 30 μm. Particular attention was paid to control and characterization of the coating surface. The morphology of the coating surface (Fig. 2) was analyzed using an atomic force microscope on a 94 μm x 108 μm area. The root mean square (Sq) surface roughness was found to be 150 nm, while the maximum peak height (Sp) and maximum pit height (Sv) were 0.66 and 0.63 μm, respectively. The wettability of the working surface was measured at different points using a drop shape analysis system (DSA100 by Krüss GmbH). At room temperature, the static advancing contact angle was 85±5°, whereas the static receding contact angle was 13±4°

2.3. Working liquids

Four different working liquids with the kinematic viscosity varying 200 times were used: ultrapure water (Milli-Q), silicon oils PMS-5, PMS-100 and PMS-200. PMS silicone oils are chosen as working liquids since they allow to vary the viscosity in a wide range while the rest of the thermophysical properties remain practically the same. Table 2 shows the main properties of the working liquids at the temperature of 25 °C.

Table 2
Properties of working liquids at 25 °C.

Liquid	water	PMS 5	PMS 100	PMS 200
ρ, kg/m^3	998.1	920	963	966
$\nu \times 10^6$, m^2/s	1.004	5	100	200
λ, W/mK	0.603	0.12	0.15	0.15
$\sigma \times 10^3$, N/m	72.8	19.2	20.9	21.0

2.4. Visualization system

To visualize the liquid surface deformations and disruption of the film, we used a Nikon D500 digital camera (shot at 60 fps) coupled with an optical schlieren system. The field of view of the system is 32×18 mm^2. Resolution of the image is 1920×1080 pixels. The main purpose of the schlieren system is to determine the curvature of the liquid surface. The scheme of the system is shown in Fig. 1a. A collimating lens placed in front of a light source (which is in the focal plane of the lens) generates collimated light that is directed into a beam splitter (set at 45 ° to the horizontal plane) that splits a beam of light in two. Half of the light is specularly reflected away from the beam splitter, while the other half passes through the beam splitter towards the liquid-coated substrate. Then part of the light is reflected from the free surface of the liquid layer, and part of it passes through the liquid layer and is almost completely absorbed by the substrate covered with the black coating. The reflected light is directed to the beam splitter again, where it is split into two beams. Part of the light beam is transmitted by the beam splitter, and part is directed by it into the camera lens, as a result of which an image of the surface of the liquid layer is captured. When surface deformation appears, the light beam deviates from the direction perpendicular to the substrate, which causes a decrease in the image intensity in the area of inclination of the free surface relative to the intensity of the image captured when the liquid film surface is flat (undisturbed surface at the beginning

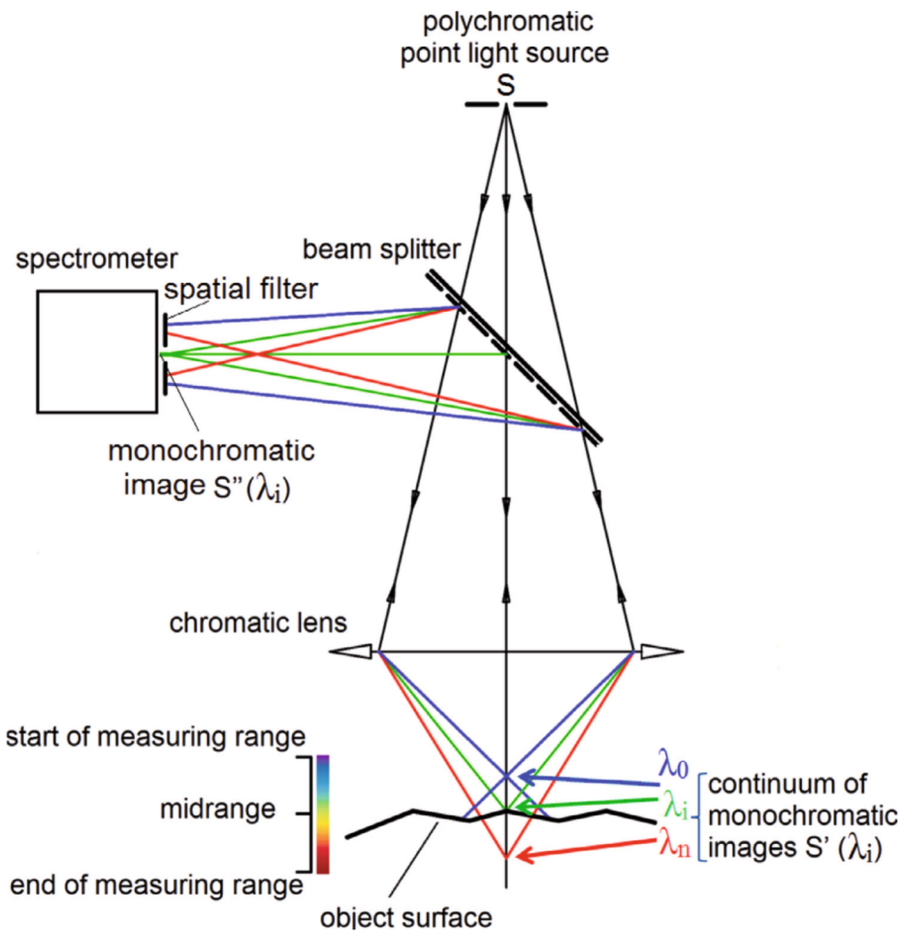

Fig. 3. Operational principle of the confocal sensor.

Table 3
The parameters of the confocal sensors.

Sensor model	IFS2405–0.3	IFS2405–3
Measuring range	0.3 mm	3 mm
Start of measuring range	6 mm	20 mm
Numerical aperture	0.60	0.45
Light spot diameter	6 µm	9 µm
Resolution	10 nm	36 nm
Max. tilt (in the midrange)	± 34°	± 24°

of the experiment). Finally, the intensity of the images obtained is related to the inclination angle of the film surface. The schlieren method is suitable for measuring film surface deformations with a tilt angle of no more than 3–5° and requires a reference point for measuring the absolute film thickness.

In our work, the schlieren method was used only for visualization without measuring surface deformation.

2.5. Film thickness measurement using chromatic confocal sensor

2.5.1. Measuring principle

To measure the instantaneous local film thickness, Micro-Epsilon controller IFC2451 with chromatic confocal sensors IFS2405–0.3 and IFS2405–3 was used. Table 3 presents the main parameters of the sensors from a data sheet of the producer. The measurement frequency of the controller IFC2451 can be adjusted from 0.1 to 10 kHz. The sensor is positioned on the free surface side of the film and oriented perpendicularly to the substrate surface. Film thickness measurements are performed at a fixed point located above the heater.

Fig. 3 shows the measuring principle of the chromatic confocal sensor. Polychromatic white light is focused onto the target surface by a multilens optical system. The lenses are arranged so that the light is dispersed into a monochromatic wavelengths by controlled chromatic aberration. A specific distance to the target is assigned to each wavelength by a factory calibration. Only the wavelength which is exactly focused on the target is used for the measurement. The light reflected from this point is imaged by an optical arrangement onto a light sensitive sensor element, on which the associated spectral color is detected and evaluated. The material thickness can be determined using two reflected light rays from the upper and lower surfaces of the object. In this case, one must know the refractive index of the object material.

The chromatic confocal sensor can operate in two regimes: distance measurement mode and thickness measurement mode (if the material of the sample is transparent). Measurements in the thickness mode, when the temperature of the measured object is not controllable, have lower accuracy since the refractive index depends on temperature. In this work all the film thickness measurements under heating were performed in distance measurement mode. The local film thickness is determined as the difference between the distance to the substrate (measured without liquid) and the distance to the film surface.

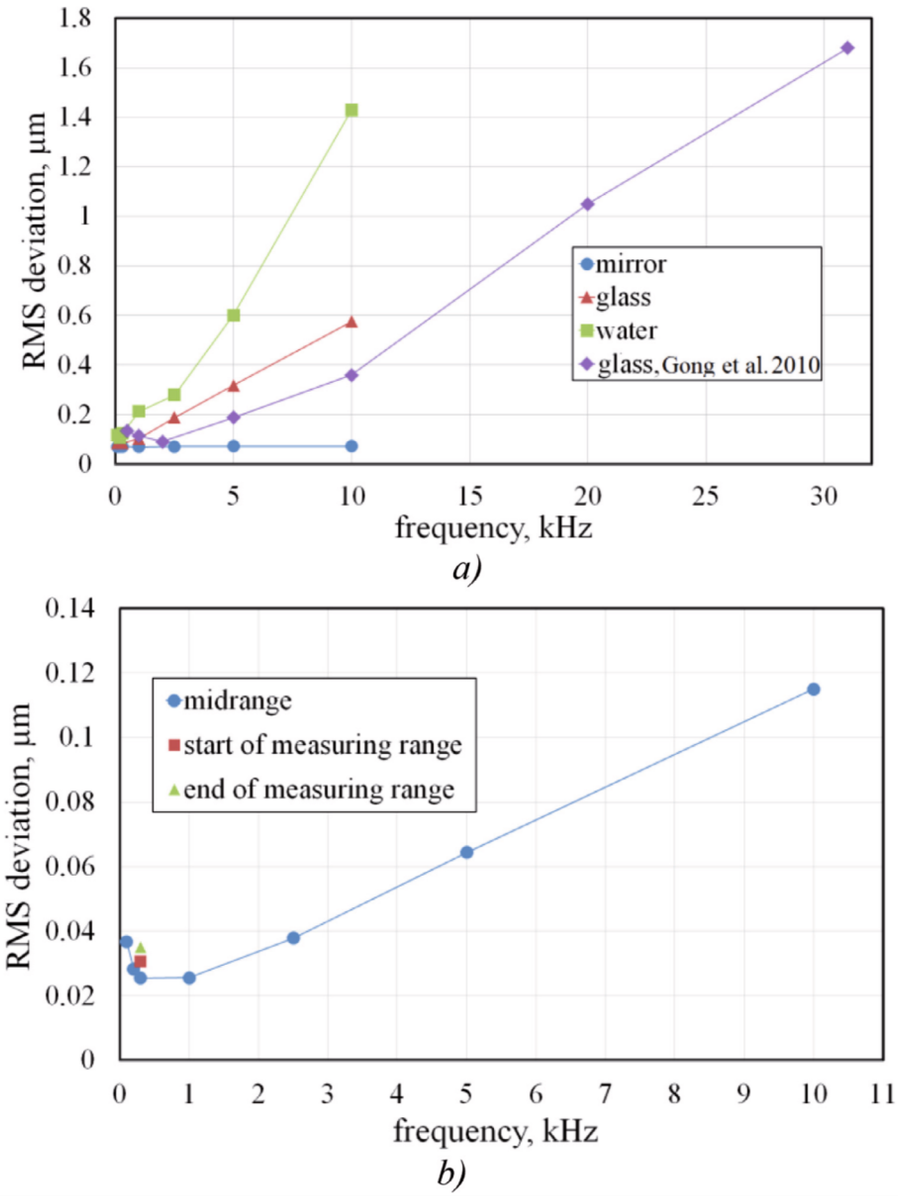

Fig. 4. Frequency characteristic. IFS2405–3 sensor (a), IFS2405–0.3 sensor, water surface (b).

2.5.2. Frequency characteristics

In [56] it was shown that the recording speed of the confocal sensor affects the measurement accuracy. This fact is explained by the decrease in signal intensity with increasing sampling rate, similar to a decrease in signal quality at small exposure times in high-speed photography. To determine the frequency characteristics of the sensor, the authors of [56] measured distance to the surface of a glass target. We carried out similar tests using IFS2405–3 sensor, but with measurements of the distance not only to the glass surface but also to the surface of the mirror and water. The reflection coefficient of the mirror, glass and water was 0.85, 0.04 and 0.02, respectively. Root mean square (RMS) deviation was calculated using 500 data points. Measurement frequency varied from 0.1 to 10 kHz. Measurements were carried out in the middle of the sensor measuring range. When measuring the distance to the surface with a high reflection coefficient (mirror), the RMS deviation is almost independent of the measurement frequency (Fig. 4a). However, when measuring distance to the surfaces with lower reflection coefficients, the RMS deviation increases with measurement frequency.

We also conducted tests with measuring the distance to the water film surface using the IFS2405–0.3 sensor, and as can be seen from Fig. 4b the RMS deviation in this case does not exceed 0.12 μm for the measurement frequency of up to10 kHz. When operating at the beginning and at the end of the sensor's measuring range (at the frequency of 1 kHz), the RMS deviation is slightly larger than in the middle of the range (Fig. 4b).

2.5.3. Angular characteristics

A relatively small beam spot diameter of the confocal sensor makes it possible to measure small scale surface deformations. However, a large measurement error may occur if the deformation scale is comparable to the beam spot diameter or if the inclination

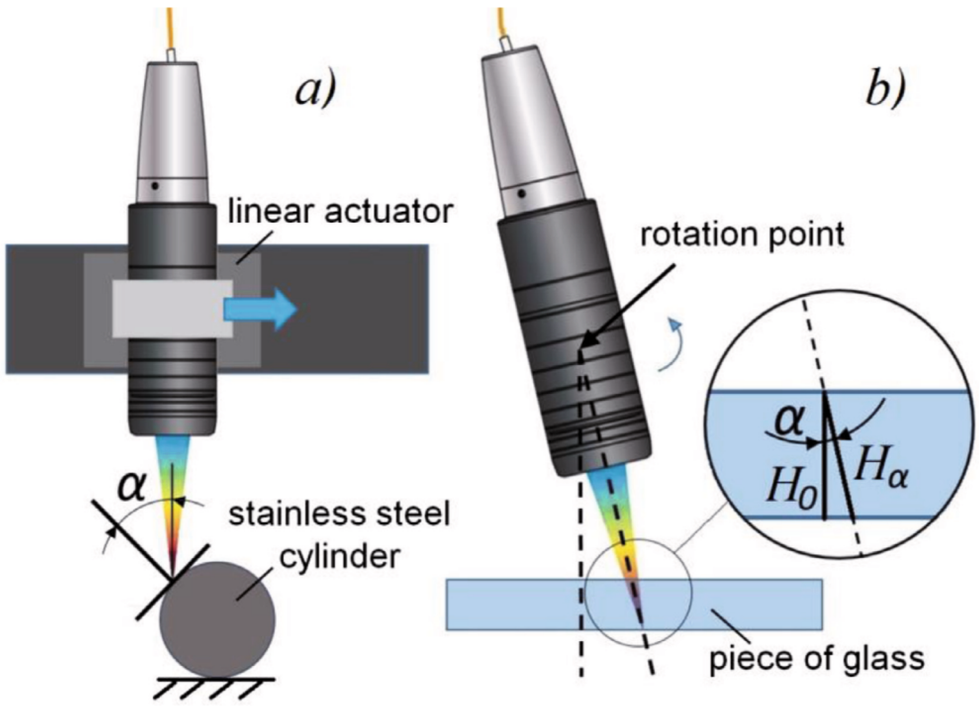

Fig. 5. Schematic of the experiment when determining angular characteristics of the sensors. Distance mode (a), thickness mode (b).

angle of the surface is so high as to exceed the maximum working tilt angle of the sensor.

The maximum working tilt angle of the sensor was determined by measuring the surface profile of a sample with circular cross section (Fig. 5a). A stainless steel cylinder with the diameter of 1.5 mm was used as a sample , which allowed the tilt angle to vary −90° to 90°. The sensor was mounted on the positioning system and moved using a linear actuator along the measurement axis at a speed of 5 mm/s and a step of 1 μm. Measurement frequency was 1 kHz.

Figs. 6a and 6b show the deviation of the distance, measured by a sensor, from the distance predicted basing on the sulcular profile of the sample, for sensors IFS2405–3 and IFS2405–0.3, respectively. It is seen that for both sensors, when the tilt angle exceeds a certain value, the deviation increases dramatically and further measurement becomes impossible. From Figs. 6a and 6b it is seen that when the measurement is carried out in the middle of the sensor measuring range, the maximum working tilt angle is about 57° for IFS2405–3 sensor and 43° for IFS2405–0.3 sensor. The obtained data exceed values specified in the data sheet for the sensors (Table 2). When measuring the surface profile at the start and at the end of the sensor measuring range for IFS2405–3 sensor, the maximum tilt angle is about 41° and 35°, respectively (Fig. 6a). As one can see From Fig. 6, the deviation of the measured surface profile (provided maximum tilt angle is not reached) does not exceed approx. 9 μm for the IFS2405–3 sensor and approx. 4 μm for the IFS2405–0.3 sensor (Fig. 6a,b). These deviations may be caused by the vibration of the sensor when moved by the actuator, as well as by the unevenness and roughness of the sample surface.

To determine the effect of the tilt angle on measurement error when sensor is operating in thickness measurement mode, tests were performed on a piece of glass with thickness of 2.94 mm (IFS2405–3 sensor). The tilt angle was varying via sensor rotation as shown in Fig. 5b. Fig. 7*a* represents comparison between the measured and theoretical thickness, depending on the tilt angle α. The theoretical thickness H_α calculated as the hypotenuse of a right triangle with the leg H_0 and the angle α (Fig. 5b). Fig. 7*b* shows the dependence of the measured value deviation (relative to the theoretical thickness) on the tilt angle. The deviation at the tilt angle $\alpha = 21º$ is about 1%.

2.5.4. Measurement of ultra-thin liquid films

When measuring liquid films on reflective substrates, confocal sensor has limitation in the minimum thickness that can be measured. As the film thickness decreases, the signals from the film and the substrate come close to each other (Fig. 8a), and ultimately only the signal from the substrate is recorded, making further measurements impossible. The smallest thickness of a water layer on a typical metal substrate, measured by the IFS2405–3 and IFS2405–0.3 sensors, is about 80 and 30 µm, respectively. To overcome this limitation, we applied a special black coating onto the substrate, which allowed to reduce by two orders of magnitude the signal from the metal substrate (Fig. 8b) and therefore provided a clear signal from the water surface, regardless of the thickness of the liquid layer. Such modification of the substrate allows to measure thickness of ultra-thin liquid films (less than 1 µm thick) operating in the distance measurement mode of the sensor: the instantaneous local film thickness is determined as the difference between the distance to the substrate (measured without liquid) and the distance to the film surface.

3. Experimental results

3.1. Film rupture for water at local heating

The appearance of a temperature gradient along the surface of a liquid film placed on a solid substrate leads to free surface deformations caused by the thermocapillary effect producing surface shear stresses [66]

$$\tau_{sur} = grad\sigma,$$

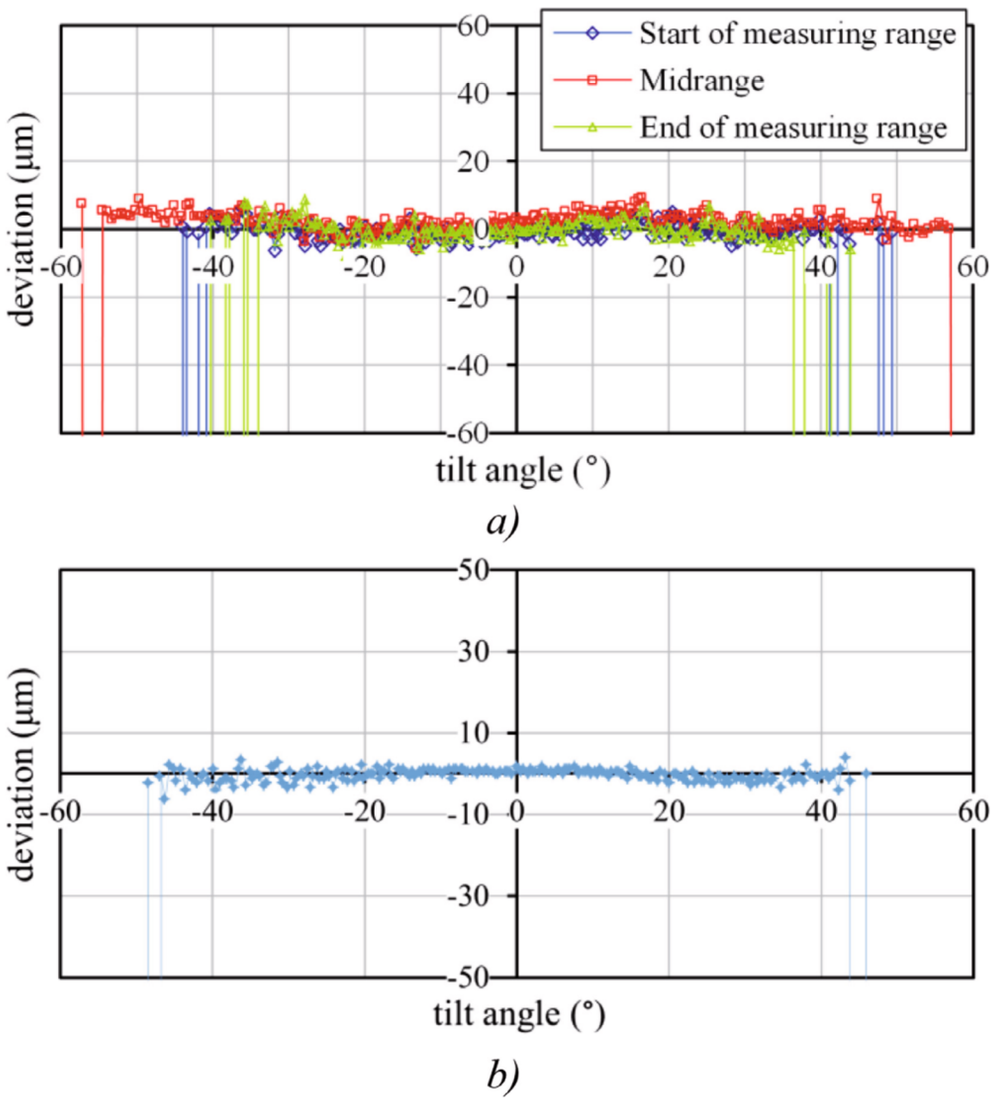

Fig. 6. Angular characteristic of the confocal sensors (distance mode). IFS2405–3 sensor (a), IFS2405–0.3 sensor, midrange (b).

arising due to surface tension temperature dependence

$$grad\sigma = \frac{\partial \sigma}{\partial T} gradT.$$

For most liquids $\partial\sigma / \partial T$ is negative, i.e. the surface tension decreases with increasing T. Therefore, the surface force arising during heating acts in the opposite direction as compared to gradT. Surface force moves liquid from warmer areas to colder ones.

Fig. 9 shows the sequence of top-view schlieren images of the water film deformations and rupture in the process of increasing substrate temperature. The flat horizontal free surface of the liquid film is white on the images captured by schlieren technique, while the surface inclined to the horizon is dark. Without heating, the liquid film in the investigated area is flat (Fig.9, Image 1). After the heating is initiated, the free surface is being deformed with the formation of a depression above the heater, which has a nearly flat bottom and becomes deeper with an increase in the temperature gradient as the film warms up. As soon as the deepest deformation is reached, the moving front of the liquid forms a residual film on the heater, which, as can be seen from the schlieren images, is practically flat (Fig.9, Image 5). Also, one can see that the boundary of the residual film is quite clear, which indicates a sharp transition from the residual film to the meniscus of the liquid. Finally, the continuous residual film breaks to form a dry spot (Fig.9, Image 6). The residual film rupture initiates at the edge of the heater, where the temperature gradient is maximum. Due to the fact that the liquid molecules are attracted to each other more strongly than to the coating molecules, the non-evaporated «residues» of the residual film are collected in a droplet (Fig.9, Image 7). The droplet almost always forms in the center of the heater and complicates the local measurement of the liquid film thickness in this area. Therefore, measurements were taken at a point near the center (shown with a blue cross in Fig. 9, Image 1), where the drop did not interfere with the measurements. A typical change of the local film thickness above the heater with time is shown in Fig. 10. It is seen that the film is sharply thinning down to a residual film with thickness of about 10 μm, which exists for several seconds. The measurement of the residual film is carried out with the IFS2405–0.3 sensor, since it is more accurate. The red line in Fig. 10 is the dependence of the heater surface temperature on

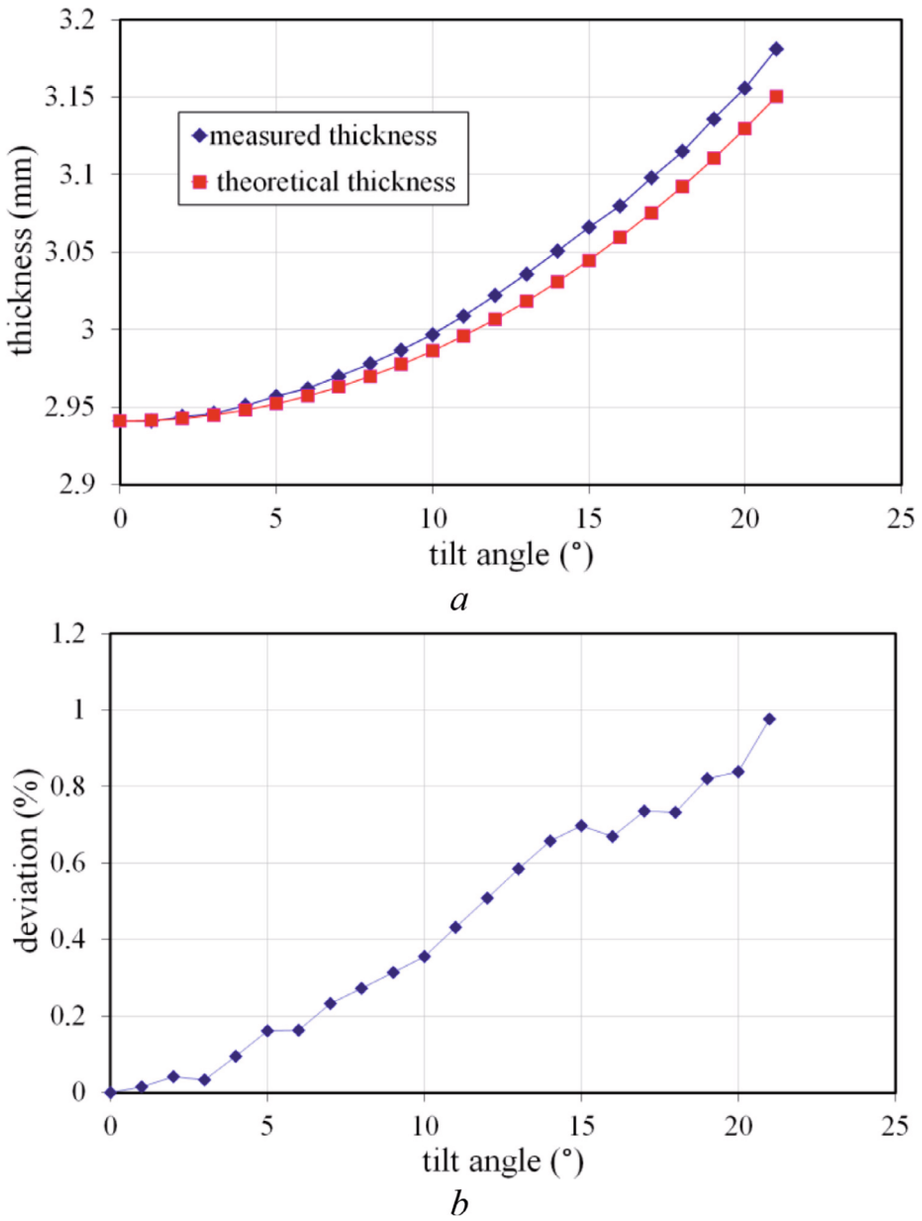

Fig. 7. Angular characteristic (IFS2405–3 sensor, thickness mode). The measured and theoretical thickness (a), relative deviation (b).

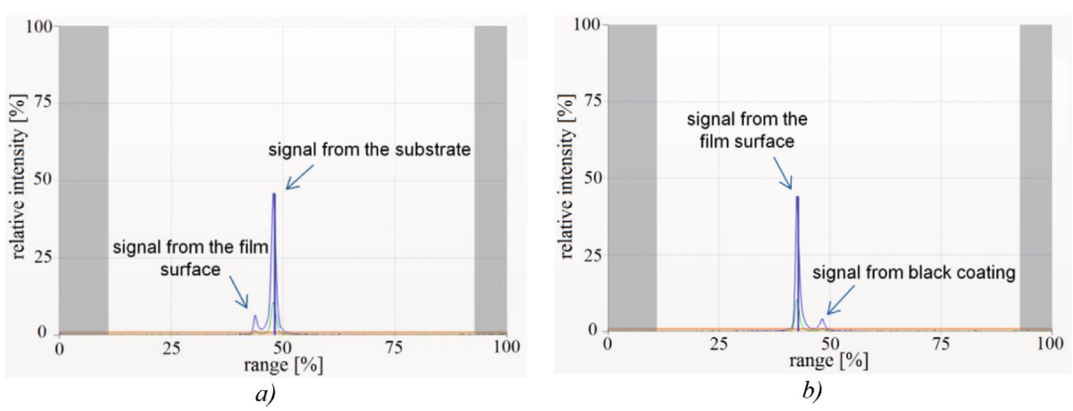

Fig. 8. Signals from film surface and substrate. Without black coating (a), with black coating (b).

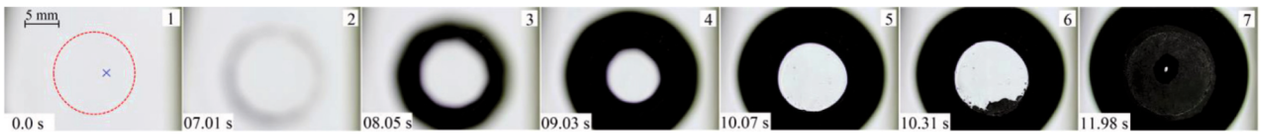

Fig. 9. Sequence of schlieren images showing dynamics of water film rupture (top view). White – horizontal surface, black - slope. Initial film thickness is 400 mm, heating power is 75 W. Red circle indicates position of the heated rod. (For interpretation of the references to colour in this figure legend, the reader is referred to the web version of this article.)

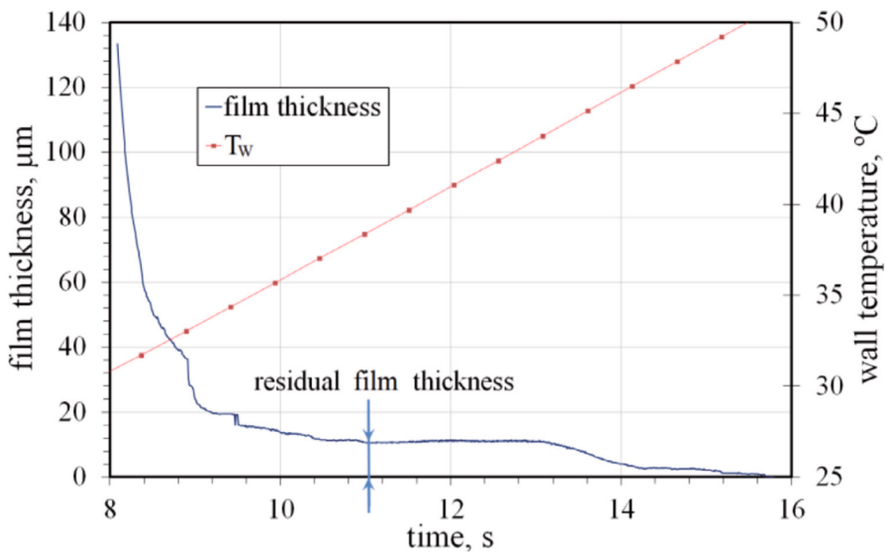

Fig. 10. Film thickness and wall temperature vs. time for water. Measurement was taken with the IFS2405–0.3 confocal sensor at the point indicated in Fig. 9, measuring rate is 0.3 kHz, initial film thickness is 400 μm, heating power is equal to 75 W.

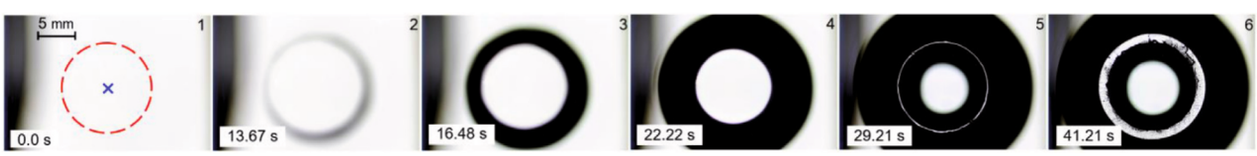

Fig. 11. Sequence of schlieren images showing dynamics of silicone oil (PMS-100) film rupture (top view). Initial film thickness is about 600 μm, heating power is 75 W. Red circle indicates position of the heater. (For interpretation of the references to colour in this figure legend, the reader is referred to the web version of this article.)

time after the heating is initiated. Please note that data presented in Figs. 9 and 10 were obtained under the same conditions (water, initial average film thickness of about 400 μm, heating power of 75 W) but for different runs.

It is assumed that the phenomenon of the residual film arises from friction, which prevents the movement of liquid from the heating area, thereby resisting to film rupture.

3.2. Film rupture for silicone oils at local heating

PMS silicone oils were used to test the effect of friction on residual film formation, since they allow to vary the viscosity in a wide range while the rest of the thermophysical properties remain practically the same. Fig. 11 shows schlieren images from top, illustrating the rupture dynamics of PMS 100 silicone oil. In contrast to the rupture of the water layer, as a result of which the surface of the heater is almost free of liquid, in the case of silicone oil, stable residual film covers the entire heater, contributing to the formation of the ring shape dry spot strictly along the heater edge. However, the dry spot is **conditionally** dry, since it is covered with a thin absorbed layer of oil. The formation of an adsorbed layer during thermocapillary rupture of the silicone oil layer is also reported in [2].

The change in the thickness of the PMS-100 silicone oil layer in the center of the cuvette during the experiment is illustrated in Fig. 12 for different initial layer thicknesses. It is seen that with an increase in the initial layer thickness from 414 to 656 μm the thickness of the residual film remains practically the same (about 250 μm).

The film rupture dynamics for PMS-5 and PMS-200 silicone oils is similar to the dynamics for PMS 100 film (Fig. 11). Fig. 13 shows data on film thickness dynamics and wall temperature for different silicon oils. Comparing Figs. 10, 12 and 13 one may conclude that the thickness of the residual film strongly depends on the liquid viscosity: for water it is about 10 μm, whereas for PMS-200 it is about 275 μm. It should be noted that with the heating power of 75 W, the dependence of the heater temperature on time is almost the same in all experiments and virtually does not depend on the working liquid.

3.3. Data analysis

Experimental data on the residual film thickness are generalized as follows. The residual film thickness h is scaled by the initial thickness h_0 and is represented as a power function of the capil-

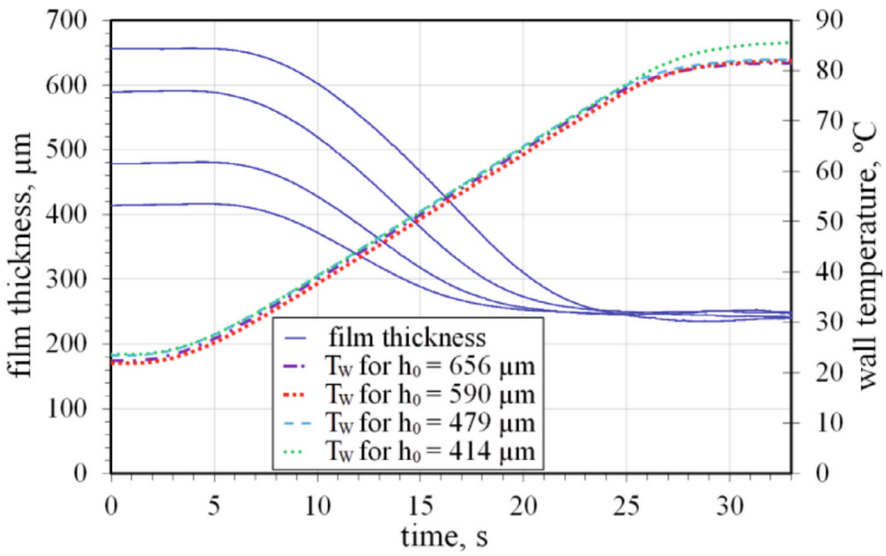

Fig. 12. Film thickness and wall temperature vs. time for silicone oil PMS-100 with different initial layer thicknesses. Measurement was taken with the IFS2405–3 confocal sensor at the point indicated in Fig. 11, measuring rate is 0.3 kHz, heating power is 75 W.

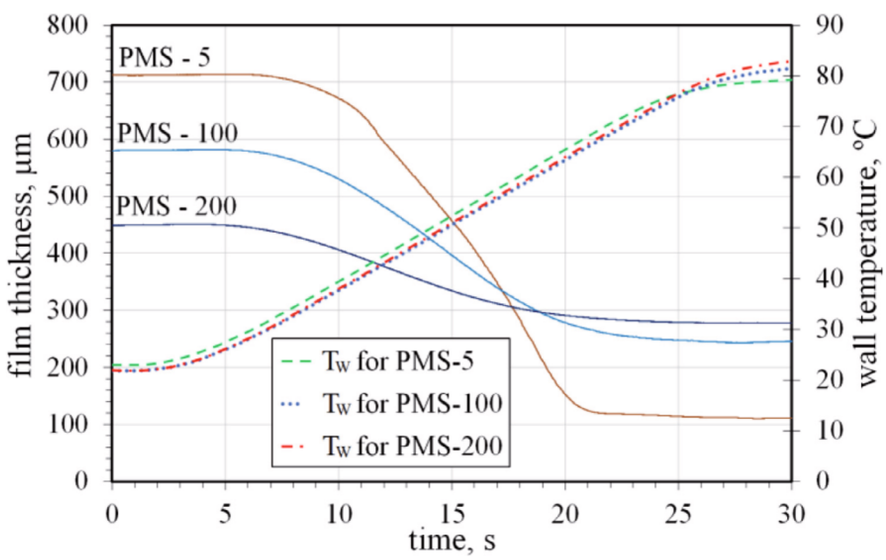

Fig. 13. Film thickness and wall temperature vs. time for different silicone oils. Measurement was taken with the IFS2405–3 confocal sensor at the point located in the heater center, measuring rate is 0.3 kHz, heating power is 75 W.

lary number. The capillary number

$Ca = \mu U/\sigma$

is a dimensionless quantity representing the relative effect of viscous drag forces versus surface tension forces acting across the gas-liquid interface, where μ is the dynamic viscosity of the liquid, U is a characteristic velocity and σ is the surface tension. The velocity of the liquid front during the formation of the residual film was used as the characteristic velocity. As we do not measure the liquid temperature during the experiment, we take properties of the liquid at the initial temperature $T_0 = 25$ °C. The liquid front velocity was measured from schlieren images (with an accuracy of about 10%). The following correlation was obtained from experimental data for various working liquids (Fig. 14)

$$h/h_0 = 27.9(Ca)^{0.64} \quad (1)$$

Let us now compare our results with some related problems of fluid dynamics. Landau–Levich flow or the Landau–Levich problem describes the flow created by a submerged plate that is pulled out at a certain velocity U from a liquid bulk (Fig.15,a). The problem assumes that the plate is dragged out of the liquid slowly, so that the three major forces which are in balance are viscous force, the force due to gravity, and the force due to surface tension. Basing on these assumptions, Landau and Levich [67] theoretically obtained the entrained film thickness h_∞, as

$$h_\infty = 0.9458 l_c Ca^{2/3} \quad (2)$$

where $l_c = (\sigma/\rho g)^{1/2}$ is the capillary length with ρ being the liquid density and g being gravitational acceleration.

The Landau - Levich flow is closely related to the Bretherton problem (Fig.15, b), where bubbles are transported in tubes containing a fluid [68]. The presence of a thin film of fluid along the

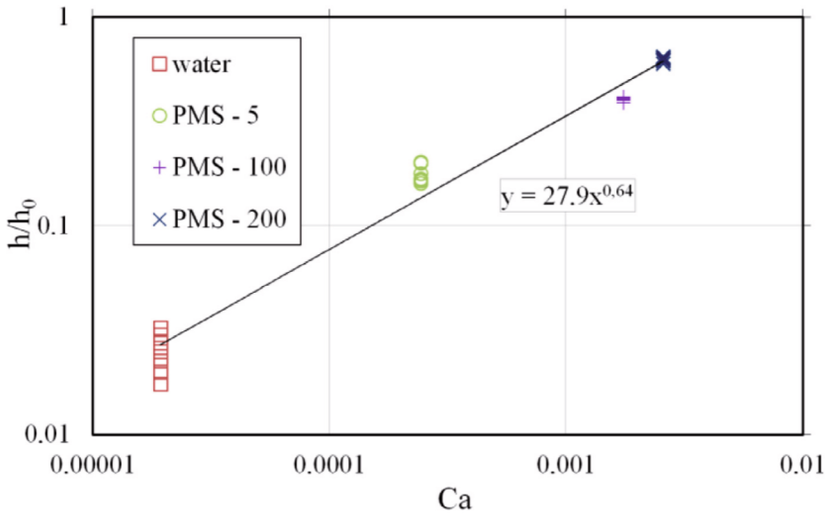

Fig. 14. Generalization of data on residual film thickness (data for several runs for each liquid are presented).

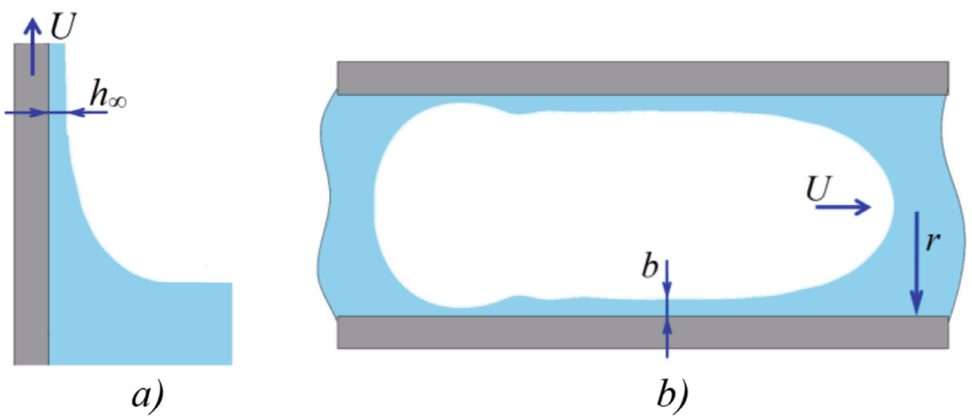

Fig. 15. Landau - Levich problem (a). Bretherton problem (b).

tube walls causes the velocity of the bubble to differ from the average fluid velocity. Bretherton [68] derived a model to describe this phenomenon for pressure driven flows based on a lubrication approach coupled with surface deformation of the bubble. Bretherton found that the parameter governing the physics involved is the capillary number (Ca) which expresses the relationship between speed of the bubble, surface tension, and viscosity of the liquid. The thickness of the film b formed by a gas bubble moving at a velocity U along a pipe of radius r is expressed as

$$b/r = 0.643(3Ca)^{2/3} \tag{3}$$

From Eqs. (2) and (3) one can see that, despite the different conditions for the formation of a thin film deposited on a solid wall, its thickness follows the same $Ca^{2/3}$ power law. The exponent 0.64 in our generalization (Eq. (1)) is very close to 2/3. Thus, we can conclude that the formation of the residual film in our experiment is similar, from the point of view of physics, to the formation of a thin film in the Landau - Levich and Bretherton problems and is caused by the movement of the liquid relative to the substrate.

4. Conclusion and discussion

As it was found in several previous works [10–12], the rupture of a non-uniformly heated liquid film sometimes occurs through the formation of a thin residual film on the heater. Stable flat residual film may exist for some time at the substrate before the formation of dry spots. In the current work, we have studied the dynamics of thermocapillary film rupture using a chromatic confocal sensor. To minimize reflection of the incident light from the substrate, the heater was covered with a thin layer of special black paste, which allowed to measure ultra-thin liquid films. Using the adapted chromatic confocal method the thickness of the residual film has been measured for the first time.

Four different working liquids with the viscosity changing 200 times were used: ultrapure water (Milli-Q), silicon oils PMS-5, PMS-100 and PMS-200. The thickness of the residual film was found to strongly depend on the liquid viscosity: for water it is about 10 μm, whereas for PMS-200 oil it is about 275 μm. The data obtained for various liquids were generalized by the $Ca^{0.64}$ power law with the exponent close to the exponent 2/3 in the related Landau - Levich and Bretherton problems.

A detailed study of the residual liquid film is important not only from fundamental point of view, but also from practical point of view. The presence of a dynamic ultrathin liquid film may significantly intensify heat transfer in liquid flows with dry spots formation. It can be assumed that if the process of evaporation is realized in a thin layer of liquid, where dynamic dry spots form and disappear, then this process can be more efficient than evapora-

tion of a continuous liquid layer. The intensification of heat transfer may take place both due to anomalously intense evaporation in the region of the contact line [7–9], as well as due to the evaporation of the ultrathin residual liquid film. Thus, a new potential mechanism is revealed for the intensification of heat transfer in evaporating liquid films. However, detailed measurements of the unsteady local heat transfer coefficients during the evaporation of the dynamic ultrathin residual liquid film are beyond the scope of this work.

Funding

This work was supported by the Russian Science Foundation (Project No. 19-19-00695).

Declaration of Competing Interest

The authors declare that they have no known competing financial interests or personal relationships that could have appeared to influence the work reported in this paper.

CRediT authorship contribution statement

D. Zaitsev: Conceptualization, Methodology, Investigation, Data curation, Validation, Writing – review & editing. **D. Kochkin:** Conceptualization, Methodology, Software, Investigation, Data curation, Validation, Writing – original draft, Writing – review & editing. **O. Kabov:** Conceptualization, Writing – review & editing, Supervision.

References

[1] A.F. Pshenichnikov, G.A. Tokmenina, Deformation of the free surface of a liquid by thermocapillary motion, Fluid Dyn 18 (1983) 463–465.
[2] J.P. Burelbach, S.G. Bankoff, S.H. Davis, Steady thermocapillary flows of thin liquid layers, II. Experiment, Phys. Fluids A Fluid Dyn 2 (1990) 322–333, doi:10.1063/1.857782.
[3] A. Orell, S.G. Bankoff, Formation of a Dry Spot in a Horizontal Liquid Film Heated from Below, Int. J. Heat Mass Transf. 14 (1971) 1835–1842.
[4] O.A. Kabov, Heat transfer from a small heater to a falling liquid film, Heat Transf. Res. 27 (1996) 221–226.
[5] O.A. Kabov, Breakdown of a liquid film flowing over the surface with a local heat source, Thermophys. Aeromechanics. 7 (2000) 513–520.
[6] B.A. Bezuglyi, N.A. Ivanova, A.Y. Zueva, Laser – induced thermocapillary deformation of a thin liquid layer, J. Appl. Mech. Tech. Phys. 42 (2001) 493–496, doi:10.1023/A:1019207023086.
[7] V.S. Ajaev, O.A. Kabov, Heat and mass transfer near contact lines on heated surfaces, Int. J. Heat Mass Transf. 108 (2017) 918–932, doi:10.1016/j.ijheatmasstransfer.2016.11.079.
[8] O.A. Kabov, D.V. Zaitsev, D.P. Kirichenko, V.S. Ajaev, Interaction of Levitating Microdroplets with Moist Air Flow in the Contact Line Region, Nanoscale Microscale Thermophys. Eng. 21 (2017) 60–69, doi:10.1080/15567265.2017.1279249.
[9] V.S. Ajaev, Instability and Rupture of Thin Liquid Films on Solid Substrates, Interfacial Phenom. Heat Transf. 1 (2013) 81–92.
[10] D.V. Zaitsev, O.A. Kabov, An Experimental Modeling of Gravity Effect on Rupture of a Locally Heated Liquid Film, Microgravity Sci. Technol. 19 (2007) 174–177.
[11] D.V. Zaitsev, D.A. Rodionov, O.A. Kabov, Study of Thermocapillary Film Rupture Using a Fiber Optical Thickness Probe, Microgravity Sci. Technol. 19 (2007) 100–103.
[12] Y.V. Lyulin, S.E. Spesivtsev, I.V. Marchuk, O.A. Kabov, Investigation of Disruption Dynamics of the Horizontal Liquid Layer with Spot Heating from the Substrate Side, Tech. Phys. Lett. 41 (2015) 1034–1037, doi:10.1134/S106378501511005X.
[13] S.V. Alekseenko, V.E. Nakoryakov, B.G. Pokusaev, Wave Flow of Liquid Films, Begell House, New York, 1994.
[14] W.W. Clark, Liquid film thickness measurement, Multiph. Sci. Technol. 14 (2002) 1–74.
[15] C.B. Tibiriçá, F.J. Nascimento, G. Ribatski, Film thickness measurement techniques applied to micro-scale two-phase flow systems, Exp. Therm. Fluid Sci. 34 (2010) 463–473, doi:10.1016/j.expthermflusci.2009.03.009.
[16] M.W.E. Coney, The theory and application of conductance probes for the measurement of liquid film thickness in two-phase flow, J. Phys. E. 6 (1973) 903–910.
[17] M.R. Özgü, J.C. Chen, N. Eberhardt, A capacitance method for measurement of film thickness in twophase flow, Rev. Sci. Instrum. 44 (1973) 1714–1716, doi:10.1063/1.1686039.
[18] Q. Lu, N.V. Suryanarayana, C. Christodoulu, Film thickness measurement with an ultrasonic transducer, Exp. Therm. Fluid Sci. 7 (1993) 354–361.
[19] P.C. Pedersen, Z. Cakareski, J.C. Hermanson, Ultrasonic monitoring of film condensation for applications in reduced gravity, Ultrasonics 38 (2000) 486–490.
[20] K. Mishima, T. Hibiki, Quantitative limits of thermal and fluid phenomena measurements using the neutron attenuation characteristics of materials, Exp. Therm. Fluid Sci. 12 (1996) 461–472.
[21] Y. Saito, K. Mishima, Y. Tobita, T. Suzuki, M. Matsubayashi, Measurements of liquid – metal two-phase flow by using neutron radiography and electrical conductivity probe, Exp. Therm. Fluid Sci. 29 (2005) 323–330, doi:10.1016/j.expthermflusci.2004.05.009.
[22] V.V. Lel, F. Al-sibai, A. Leefken, U. Renz, Local thickness and wave velocity measurement of wavy films with a chromatic confocal imaging method and a fluorescence intensity technique, Exp. Fluids. 39 (2005) 856–864, doi:10.1007/s00348-005-0020-x.
[23] D.W. Zhou, T. Gambaryan-Roisman, P. Stephan, Measurement of water falling film thickness to flat plate using confocal chromatic sensoring technique, Exp. Therm. Fluid Sci. 33 (2009) 273–283, doi:10.1016/j.expthermflusci.2008.09.003.
[24] D.V. Zaitsev, O.A. Kabov, A.R. Evseev, Measurement of locally heated liquid film thickness by a double-fiber optical probe, Exp. Fluids. 34 (2003) 748–754, doi:10.1007/s00348-003-0621-1.
[25] D.V. Zaitsev, O.A. Kabov, Study of the thermocapillary effect on a wavy falling film using a fiber optical thickness probe, Exp. Fluids. 39 (2005) 712–721, doi:10.1007/s00348-005-0003-y.
[26] T. Takamasa, T. Hazuku, Measuring interfacial waves on film flowing down a vertical plate wall in the entry region using laser focus displacement meters, Int. J. Heat Mass Transf. 43 (2000) 2807–2819.
[27] T. Hazuku, N. Fukamachi, T. Takamasa, T. Hibiki, M. Ishii, Measurement of liquid film in microchannels using a laser focus displacement meter, Exp. Fluids. 38 (2005) 780–788.
[28] Y. Han, N. Shikazono, Measurement of the liquid film thickness in micro tube slug flow, Int. J. Heat Fluid Flow. 30 (2009) 842–853, doi:10.1016/j.ijheatfluidflow.2009.02.019.
[29] B. Scheid, O.A. Kabov, C. Minetti, P. Colinet, J.C. Legros, Measurement of free surface deformation by reflectanceschlieren method, 3rd Eur. Therm. Sci. Conf. (2000) 651–657.
[30] B. Scheid, J. Margerit, C.S. Iorio, L. Joannes, M. Heraud, P. Queeckers, P.C. Dauby, P. Colinet, Onset of thermal ripples at the interface of an evaporating liquid under a flow of inert gas, Exp. Fluids. 52 (2012) 1107–1119.
[31] G.S. Settles, Schlieren and Shadowgraph Techniques: Visualizing Phenomena in Transparent Media, Springer-Verlag, Berlin, 2001.
[32] L. Joannes, F. Dubois, J. Legros, Phase-shifting schlieren : high-resolution quantitative schlieren that uses the phase-shifting technique principle, Appl. Opt. 42 (2003) 5046–5053.
[33] T. Ohyama, K. Endoh, A. Mikami, Y.H. Mori, Optical interferometry for measuring instantaneous thickness of transparent solid and liquid films, Rev. Sci. Instrum. 59 (1988) 2018–2022, doi:10.1063/1.1140018.
[34] P. Hariharan, Optical interferometry, Reports Prog. Phys. 54 (1991) 339–390.
[35] E.Y. Gatapova, A.M. Shonina, A.I. Safonov, V.S. Sulyaeva, O.A. Kabov, Evaporation dynamics of a sessile droplet on glass surfaces with fluoropolymer coatings: focusing on the final stage of thin droplet evaporation, Soft Matter 14 (2018) 1811–1821, doi:10.1039/C7SM02192E.
[36] M. Alonso, P.J. Kay, P.J. Bowen, R. Gilchrist, S. Sapsford, A laser induced fluorescence technique for quantifying transient liquid fuel films utilising total internal reflection, Exp. Fluids. 48 (2010) 133–142, doi:10.1007/s00348-009-0720-8.
[37] I.K. Kabardin, V.G. Meledin, I.A. Eliseev, V.V. Rakhmanov, Optical measurement of instantaneous liquid film thickness based on total internal reflection, J. Eng. Thermophys. 20 (2011) 407–415, doi:10.1134/S1810232811040072.
[38] F. Reuter, S.A. Kaiser, High-speed film-thickness measurements between a collapsing cavitation bubble and a solid surface with total internal reflection shadowmetry High-speed film-thickness measurements between a collapsing cavitation bubble and a solid surface with total inter, Phys. Fluids. 31 (2019) 1–15, doi:10.1063/1.5095148.
[39] A.E. Smart, R.A.J. Ford, Measurement of thin liquid films by a fluorescence technique, Wear 29 (1974) 41–47.
[40] A.C. Jones, M. Millington, J. Muhl, J.M. De Freitas, J.S. Barton, G. Gregory, Calibration of an optical fluorescence method for film thickness measurement, Meas. Sci. Technol. 12 (2001) 23–27.
[41] E.A. Chinnov, S.M. Kharlamov, A.D. Nazarov, E.E. Sokolov, D.M. Markovich, A.F. Serov, O.A. Kabov, Integrated Measurement of the Wave Characteristics of Heated Film of Liquid by the Capacitance and Fluorescence Methods, High Temp 46 (2008) 647–653, doi:10.1134/S0018151x0805009X.
[42] E.A. Chinnov, F.V. Ron'shin, V.V. Guzanov, D.M. Markovich, O.A. Kabov, Two Phase Flow in a Horizontal Rectangular Microchannel, High Temp 52 (2014) 681–687, doi:10.1134/S0018151x14040075.
[43] E.A. Chinnov, F.V. Ron'shin, O.A. Kabov, Study of gas-water flow in horizontal rectangular channels, Thermophys. Aeromechanics. 22 (2015) 621–629.
[44] C.H. Hidrovo, D.P. Hart, Emission reabsorption laser induced fluorescence (ERLIF) film thickness measurement, Meas. Sci. Technol. 12 (2001) 467–477.
[45] A. Schagen, M. Modigell, Local film thickness and temperature distribution measurement in wavy liquid films with a laser-induced luminescence technique, Exp. Fluids. 43 (2007) 209–221, doi:10.1007/s00348-007-0289-z.
[46] A.A. Mouza, N.A. Vlachos, S.V. Paras, A.J. Karabelas, Measurement of liquid film thickness using a laser light absorption method, Exp. Fluids. 28 (2000) 355–359, doi:10.1007/s003480050394.

[47] R.P. Salazar, E. Marschall, Thickness measurement in liquid film flow by laser scattering, Rev. Sci. Instrum. 46 (1975) 1539–1541, doi:10.1063/1.1134099.
[48] C.-.P. Ding, M. Sjöberg, D. Vuilleumier, D.L. Reuss, X. He, B. Böhm, Fuel film thickness measurements using refractive index matching in a stratified-charge SI engine operated on E30 and alkylate fuels, Exp. Fluids. 59 (2018) 59, doi:10.1007/s00348-018-2512-5.
[49] K. Helbig, A. Alexeev, T. Gambaryan-Roisman, P. Stephan, Evaporation of Falling and Shear-Driven Thin Films on Smooth and Grooved Surfaces, Flow, Turbul. Combust 75 (2005) 85–104.
[50] K. Helbig, R. Nasarek, T. Gambaryan-roisman, P. Stephan, Effect of Longitudinal Minigrooves on Flow Stability and Wave Characteristics of Falling Liquid Films, J. Heat Transfer. 131 (2009), doi:10.1115/1.2993539.
[51] R. Rulliere, F. Lefevre, M. Lallemand, Prediction of the maximum heat transfer capability of two-phase heat spreaders – Experimental validation, Int. J. Heat Mass Transf. 50 (2007) 1255–1262, doi:10.1016/j.ijheatmasstransfer.2006.09.015.
[52] V.V. Lel, A. Kellermann, G. Dietze, R. Kneer, A.N. Pavlenko, Investigations of the Marangoni effect on the regular structures in heated wavy liquid films, Exp. Fluids. 44 (2008) 341–354, doi:10.1007/s00348-007-0408-x.
[53] G.F. Dietze, A. Leefken, R. Kneer, Investigation of the backflow phenomenon in falling liquid films, J. Fluid Mech. 595 (2008) 435–459, doi:10.1017/S0022112007009378.
[54] G.F. Dietze, F. Al-Sibai, R. Kneer, Experimental study of flow separation in laminar falling liquid films, J. Fluid Mech. 637 (2009) 73–104, doi:10.1017/S0022112009008155.
[55] G.F. Dietze, R. Kneer, Flow separation in falling liquid films, Front, Heat Mass Transf 2 (2011), doi:10.5098/hmt.v2.3.3001.
[56] S. Gong, W. Ma, T.-.N. Dinh, Diagnostic techniques for the dynamics of a thin liquid film under forced flow and evaporating conditions, Microfluid, Nanofluid. 9 (2010) 1077–1089, doi:10.1007/s10404-010-0626-z.
[57] S. Gong, W. Ma, T.-.N. Dinh, An experimental study of rupture dynamics of evaporating liquid films on different heater surfaces, Int. J. Heat Mass Transf. 54 (2011) 1538–1547, doi:10.1016/j.ijheatmasstransfer.2010.11.036.
[58] W. Rohlfs, G.F. Dietze, H.D. Haustein, T.O. Yu, R. Kneer, Experimental investigation into three-dimensional wavy liquid films under the influence of electrostatic forces, Exp. Fluids. 53 (2012) 1045–1056, doi:10.1007/s00348-012-1342-0.
[59] W. Rohlfs, G.F. Dietze, H.D. Haustein, R. Kneer, Experimental investigation of 3-dimensional wavy liquid films under the coupled influence of thermo-capillary and electrostatic forces, Eur. Phys. J. Spec. Top. 219 (2013) 111–119, doi:10.1140/epjst/e2013-01786-2.
[60] S. Gong, W. Ma, H. Gu, An experimental investigation on bubble dynamics and boiling crisis in liquid films, Int. J. Heat Mass Transf. 79 (2014) 694–703, doi:10.1016/j.ijheatmasstransfer.2014.08.065.
[61] M. Rietz, W. Rohlfs, R. Kneer, B. Scheid, Experimental investigation of thermal structures in regular three-dimensional falling films, Eur. Phys. J. Spec. Top. 224 (2015) 355–368, doi:10.1140/epjst/e2015-02365-3.
[62] K. Wang, Y. Zhang, S. Gong, B. Bai, W. Ma, Dynamics of a thin liquid film under shearing force and thermal influences, Exp. Therm. Fluid Sci. 85 (2017) 279–286, doi:10.1016/j.expthermflusci.2017.03.014.
[63] K. Wang, R. Lin, N. Wu, W. Ma, B. Bai, Thin liquid film dynamics and bubble behavior in flow boiling, Interfacial Phenom, Heat Transf 4 (2016) 279–292.
[64] M.M. Swartz, S.-.C. Yao, Experimental study of turbulent natural-convective condensation on a vertical wall with smooth and wavy film interface, Int. J. Heat Mass Transf. 113 (2017) 943–960, doi:10.1016/j.ijheatmasstransfer.2017.04.076.
[65] M. Leng, S. Chang, H. Wu, Experimental investigation of shear-driven water fi lm fl ows on horizontal metal plate, Exp. Therm. Fluid Sci. 94 (2018) 134–147, doi:10.1016/j.expthermflusci.2018.02.004.
[66] V.G. Levich, Fiziko-khimicheskaya Gidrodinamika, 2nd ed., Gos.izd. fiz.-mat. literatury, Moscow, 1959.
[67] L. Landau, B. Levich, Dragging of a liquid by a moving plate, Acta Physicochim. URSS. 17 (1942) 42–54, doi:10.1016/B978-0-08-092523-3.50016-2.
[68] F.P. Bretherton, The motion of long bubbles in tubes, J. Fluid Mech. (1961) 166–188.

Experiments in Fluids (2022) 63:47
https://doi.org/10.1007/s00348-022-03394-w

RESEARCH ARTICLE

Understanding vertical coalescence dynamics of liquid drops over a superhydrophobic surface using high-speed orthographic visualization

Praveen M. Somwanshi[2] · V. V. Cheverda[2] · K. Muralidhar[1] · S. Khandekar[1] · O. A. Kabov[2]

Received: 10 November 2021 / Revised: 14 January 2022 / Accepted: 16 January 2022
© The Author(s), under exclusive licence to Springer-Verlag GmbH Germany, part of Springer Nature 2022

Abstract
Experiments on coalescence are carried out with two water drops over a chemically textured superhydrophobic surface (equilibrium contact angle ~ 150° and contact angle hysteresis ~ 10°), with one drop initially above the other, under atmospheric conditions. Drops are of equal volumes with a combined Bond number of 0.11. The coalescence events are imaged using two synchronized high-speed cameras in orthogonal directions. As the drops coalesce, a great variety of interface shapes appear as the merged drop approaches equilibrium. The velocity components of the combined drop, and hence the wall shear stress, are estimated by curve fitting the centroidal position data. Two distinct timescales are clearly revealed. These are related to the balance of inertia forces and surface tension on one hand and a balance of inertia and viscous forces on the other. The interface shapes in the two orthogonal views are seen to be similar, indicating the process to be practically axisymmetric during the entire time period. The drop shape gradually evolves over the shorter timescale with the appearance of a positive as well as negative curvature and leads to recoil. Wall shear stresses are estimated to be quite large during the early time period. At later times, it is characterized by small amplitude damped oscillations of a merged drop dominated by viscous dissipation. The scaling law for curvature seen during neck formation corroborates the one reported for drops coalescing in free space. Further, the bulge and neck curvatures as well as the drop shapes seen in experiments are in good agreement with numerical simulation carried out in an axisymmetric coordinate system.

✉ Praveen M. Somwanshi
praveen.somwanshi@gmail.com

[1] Department of Mechanical Engineering, Indian Institute of Technology Kanpur, Kanpur 208016, India

[2] Kutateladze Institute of Thermophysics SB RAS, Novosibirsk 630090, Russia

Published online: 19 February 2022

Graphical abstract

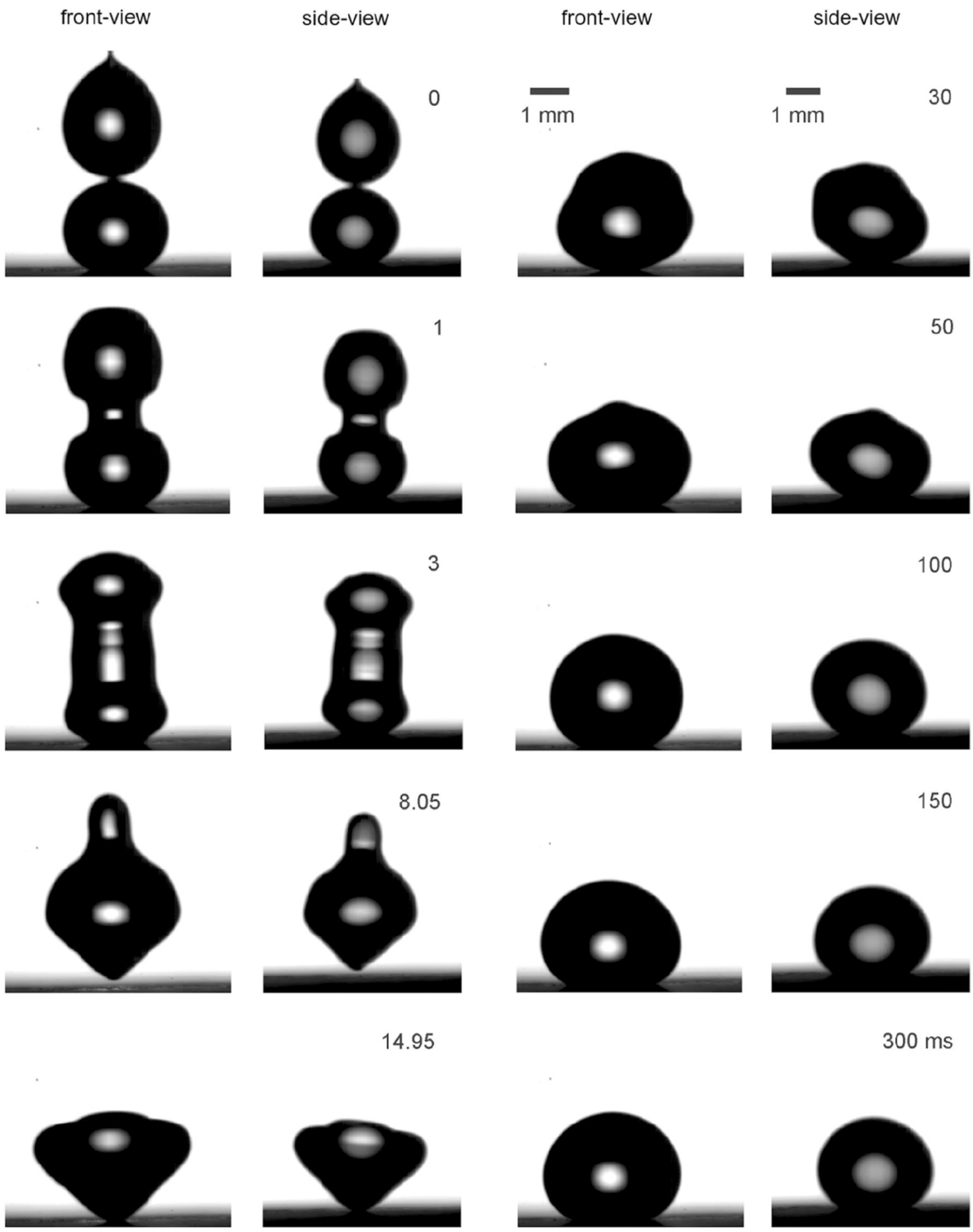

1 Introduction

Coalescence is an intense dynamic phenomenon seen when two drops contact each other to form a single drop. Various coalescence configurations arise in applications. These include merger in the vicinity of a wall as well as mixing in free space as in rain drops. In the former context, applications include spray cooling (Estes and Mudawar 1995), ink-jet printing (Kim et al. 2012), and dropwise condensation (Khandekar and Muralidhar 2014). Coalescence of two

isothermal water drops over a superhydrophobic surface at a combined Bond number of 0.11 is of interest to the present study.

Coalescence dynamics arises from the release of surface energy of the two-drop system as it evolves toward the shape of a single liquid drop, generating length, velocity and timescales at intermediate stages. Interface shapes acquired by the drops during coalescence over a textured surface are strongly influenced by the movement of the three-phase contact line. Heat and mass transfer rates have been reported to be large in the vicinity of the three-phase contact line (Ajaev and Kabov 2017, 2021; Kabov et al. 2017; Schweikert et al. 2019a, 2019b). Hence, the three-phase contact line is a boundary of interest.

Following Somwanshi et al. (2020a) and the discussion in references therein, initiation of coalescence can be connected to the formation of a neck when the two drops just touch each other. Differences in the local interface curvature result in pressure differences within the liquid mass and the appearance of large initial velocities. To begin with, the surface of the liquid drop has positive curvature, while the neck is a region of negative curvature, thus creating two adjacent sites of positive and negative pressures. For coalescence of drops of unequal diameters, the initial pressure difference also contributes to fluid velocities driving the merger process. The velocity and timescales generated are further modulated by the combined drop volume and wettability of the surface. For hydrophilic surfaces, drops spread over the surface and their motion are damped. For hydrophobic surfaces, wall dissipation is limited and clearly demarcated flow regimes are observed. In the long run, velocities are dissipated over the surface as well as the three-phase contact line and the combined drop approaches the final equilibrium shape. A study of coalescence where one of the drops has an initial velocity has been reported by Li et al. (2010), Castrejón-Pita et al. (2011), and Abouelsoud et al. (2018).

The motion of the three-phase contact line influences coalescence during short-term events such as bridge formation over a timescale of milliseconds. It is followed by the relatively long transient arising from internal dissipation as well as motion of the three-phase contact line (Andrieu et al. 2002; Plog et al. 2021). The initial interface oscillations are sensitive to external factors such as the mode of deposition of the drops, a syringe being distinct from vapor condensation (Narhe et al. 2004; Jaiswal and Khandekar 2021). Large velocities induced due to the formation and growth of the bridge in the early stages of coalescence results in recoil of the combined drop away from the surface (Yin et al. 2019; Chu et al. 2020). These velocities are also responsible for large wall shear stresses that have the ability to wear out surface coatings and reduce the extent of hydrophobicity (Somwanshi et al. 2018, 2020a). In low conductivity media such as water, fluid velocities substantially enhance convective mixing and the resulting wall heat fluxes (Somwanshi et al. 2020b). On hydrophobic surfaces, excess surface energy over and above viscous dissipation is available, resulting in the formation of a satellite drop (Zhang et al. 2009; Kumar et al. 2020).

Sankaran et al. (2021) studied the effect of an electric field on dynamics of a drop of water, n-butanol or motor oil impacting on dielectric non-wettable surfaces. Experiments were conducted on Teflon, parafilm and polypropylene surfaces. Experimental results were supplemented by simulations based on the Cahn–Hilliard and Navier–Stokes equations. The formation of a secondary drop was observed during recoil while coalescence of the primary and secondary drops was delayed. Since pressure in the air layer between two approaching droplets was higher, surface tension near the closest approaching location was lowered. In the absence of an electric field, impact of water drop on Teflon and parafilm showed recoil and was absent on polypropylene. Recoil was suppressed in the presence of an electric field during impact of a water drop on Teflon, parafilm and polypropylene.

In view of the large number of factors involved, the details of a coalescence process are configuration-specific. Drops merging in free space have been studied extensively in the literature from experiments as well as scale analysis. The focus has been the initial timescale in the micro- to millisecond regime during which the bridge develops at the interface of the two drops. The other extreme of two drops impacting each other has also been studied. Coalescence of two liquid drops in the presence of a superhydrophobic surface has received less attention and is addressed in the present study. Somwanshi et al. (2018) experimentally studied coalescence of drops placed side-by-side, while Somwanshi et al. (2020a, 2020b) studied coalescence and heat transfer between drops placed one above the other. The equilibrium contact angle of the surfaces studied was $150^{o} \pm 4^{\circ}$ with a contact angle hysteresis of 10 $(\pm 2)^{o}$. The experiments reported in these studies employed a camera speed in the range of 4000–6000 frames per second, and the imaging axis was restricted to one direction. The present work is an extension wherein a camera speed of 20,000 frames per second is employed, and the coalescence process is imaged simultaneously from two orthogonal directions. This approach yields substantially improved data, particularly in the initial stages of the process. Experimentally recorded drop shapes are additionally compared with numerical simulation.

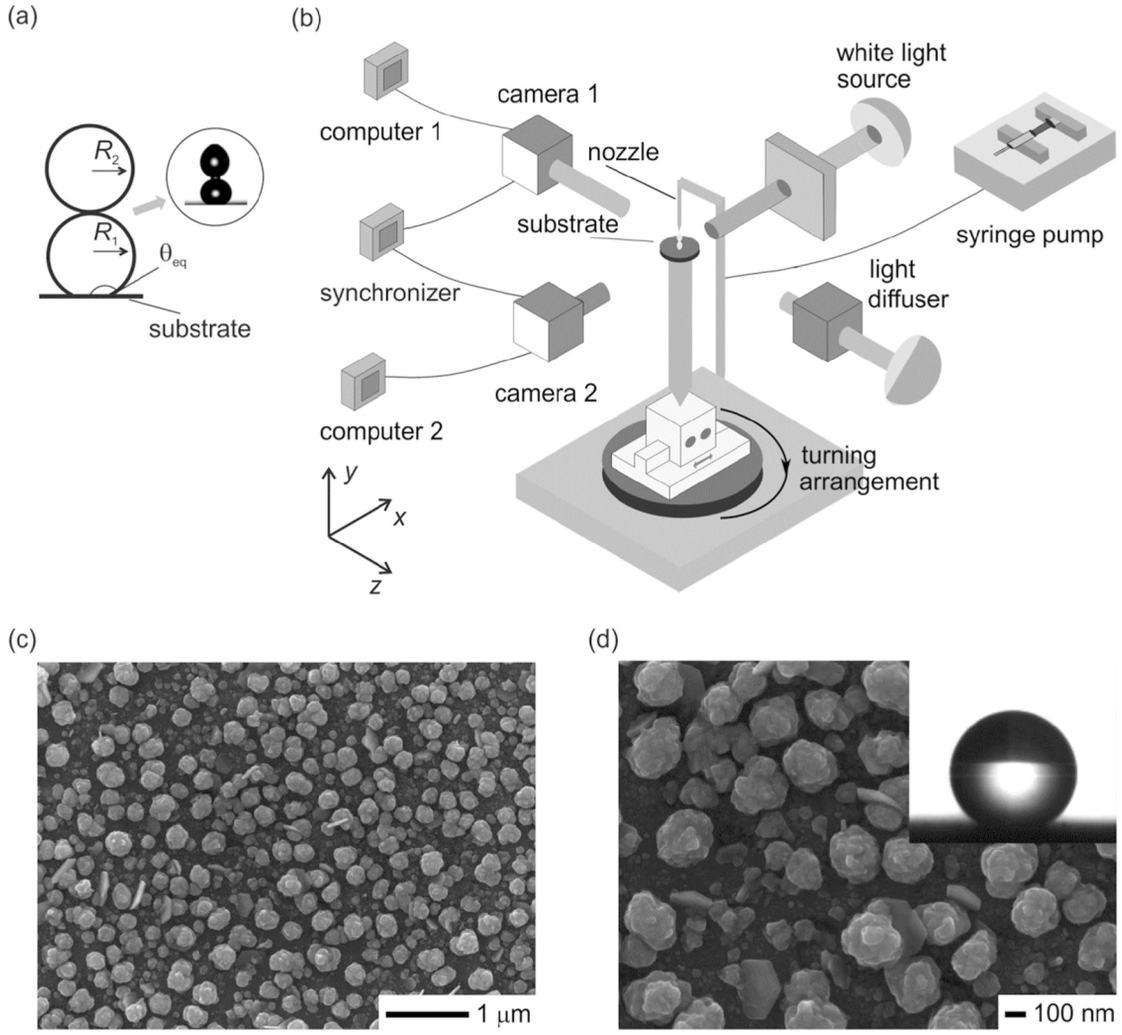

Fig. 1 **a** Configuration of a liquid drop placed vertically above the other over a hydrophobic surface; **b** Schematic of the experimental apparatus setup to study coalescence; **c-d** Field emission scanning electron microscopy images of the as-prepared copper substrate at low (×30 000) and high (×50 000) magnifications showing flowers of copper oxide responsible for surface hydrophobicity

2 Experimental arrangement and numerical simulation

The orientation of the two coalescing sessile drops is shown in Fig. 1a. The schematic of the experimental setup including the substrate and the two-view imaging arrangement is shown in Fig. 1b. First, a liquid drop of desired volume is introduced over the substrate using a syringe pump and allowed to come to equilibrium. Subsequently, the second drop of a given volume is slowly allowed to grow over the first till it naturally detaches from the nozzle. The nozzles of the syringe pump have an inner diameter of ~ 0.32 mm. A micro-liter syringe pump with a total capacity of 2.5 ml and a 0.02 μl least count is used to deposit the two water drops, each of volume 12.4 μl, above the substrate. The traversing arrangement that mounts the substrate assists in orienting the two views relative to the cameras.

The superhydrophobic substrate is made of copper, and the surface preparation procedure, discussed earlier by Somwanshi et al. (2018, 2020a), is based on chemical texturing. The process gives rise to flower-like structures and the liquid drop sits over them in a Cassie–Baxter configuration (Cassie and Baxter 1944). Substrates have to be carefully stored and vacuum dried ahead of each experiment to attain repeatability in the equilibrium drop shapes and the recorded image sequence. The repeated occurrence of coalescence events eventually wears out the surface, periodically requiring replacement.

Figure 1c and d shows images of the substrate recorded using a field emission SEM (JSM-7100F, JEOL®) at low and high resolutions, respectively. The oxidation of the

surface causes protrusions in the form of micro-flowers measured to be of size 10–200 nm in diameter. Adjacent micro-flowers are separated by air gaps which promotes the Cassie–Baxter wetting regime.

The equilibrium contact angles were measured at 5–10 locations on a larger surface of size 10 mm × 10 mm using a commercial goniometer (Kruss® DSA-100). An image of a liquid drop of 4 µl volume sitting on the textured copper substrate is shown in the inset of Fig. 1d. The equilibrium contact angle was measured to be $150 \pm 4°$ with a contact angle hysteresis of $10 \pm 2°$. These angles were practically independent of drop volume for Bond numbers in the range $0.1 < \mathrm{Bo} < 0.2$. The repeatability in achieving surface morphology followed by the coalescence process was confirmed from a set of nominally identical experiments.

Two independent diffuse white light sources have been used for illumination during the coalescence process. Two synchronized high-speed monochrome CCD cameras with a recording rate of 20,000 fps (FASTCAM® SA-1.1 and FASTCAM® SA-5 at a resolution of 512 × 512 pixels for a shutter opening of 50 ns) with 8-bit digitization record the image sequences. For the experiments of the present work, an area of 7.382 mm × 7.382 mm and 9.079 mm × 9.079 mm for Cameras FASTCAM® SA-1.1 and FASTCAM® SA-5, respectively, was resolved by 512 × 512 pixels. Locally developed electronic circuits synchronize the camera operations, followed by data transfer to a commercial PC. The substrate is horizontal, the two viewing planes are vertical passing through the initial mid-plane of the two drops, and in turn, are orthogonal to each other. Each imaging axis connecting the vertical plane to the camera is horizontal. Image sequences of drop merging have been analyzed for centroidal velocity, footprint radius and the dynamic contact angle using methods described in an earlier work (Somwanshi et al. 2018). The point of difference with the present work is the availability of two orthogonally placed cameras with a high frame rate of 20,000 fps (at 512 × 512 pixel resolution). In the previous study, the camera speed was 4000 fps at this resolution and only one camera was used. Hence, in the present work, the degree of axisymmetry of the coalescence process is examined in greater detail. In addition, the study resolves additional details of the coalescence phenomenon such as the growth and formation of a liquid bridge joining the two drops. Shear rates generated prior and after the instant of recoil are also available with additional temporal resolution.

Numerical simulation of the interfacial shapes has been carried out as follows. The Navier–Stokes equations solve for the distribution of velocity and pressure within and around the merging drops along with the phase-field method for tracking the moving liquid–air interface. The shape evolution of the drop is predicted by the Cahn–Hilliard model that is solved along with the Navier–Stokes equations in conservative form (Yurkiv et al. 2018). Density and dynamic viscosity in the computational domain are defined using the rule-of-mixtures with reference to the phase-field variable. The fluid media are taken to be incompressible. The three-phase contact line motion is represented using contact line models as discussed in Sect. 3.5. Numerical simulations have been performed using COMSOL®, a commercial solver for multi-phase flow. Issues such as mesh independence, validation and mass balance have been discussed by the authors in a previous study (Somwanshi et al. 2020a). The specification of the mobility tuning parameter is important since it affects interface sharpness and phase-level mass balance. In the present study, mass balance errors were controlled first by using a significantly refined mesh, making the simulation less sensitive to the tuning parameter. The extent of refinement is decided by the resolution of the interface thickness based on Cahn number, defined in the nomenclature. A value of the Cahn number of the order of 10^{-2} yields a good balance between mass loss and computational effort (Yue et al. 2010) and has been adopted in the present work. With the finest grid selected, the maximum mass loss was less than 0.3% for a mobility tuning parameter in the range of 100–130 leading to a good match with the experiments. Smallest value of mobility tuning parameter is selected for maintaining the sharpness of the interface. Hence, the mobility tuning parameter is selected as 100 in the present simulations. The simulation is axisymmetric while the time step is jointly selected with the mesh size to ensure a high degree of mass balance. Experimentally recorded images have subsequently been compared against numerical simulation.

3 Results and discussion

The data obtained from experiments are discussed below in eight sections. These are velocity and timescales (Sect. 3.1); axisymmetry of the coalescence process (Sect. 3.2); recoil (Sect. 3.3); bridge dynamics (Sect. 3.4); contact angle modeling (Sect. 3.5); wall shear rate (Sect. 3.6); coalescence of unequal volume drops (Sect. 3.7) and energy budget (Sect. 3.8). In these experiments, the total droplet volume, radius ratio, surface characteristics, and ambient conditions are maintained constant, while the evolution of the merging droplets is investigated. Numerically determined drop shapes and the internal pressure distribution are included in Sect. 3.3 for comparison.

3.1 Velocity and timescales

To present the instantaneous images of coalescence recorded by the two cameras, the time evolution of the drop shapes is split into appropriate regimes. Distinct timescales can be identified with appropriate force pairs, namely surface

tension-viscous (S-V), inertia-surface tension (I-S), and inertia-viscous (I-V), respectively. Scale analysis related to these regimes is discussed by the authors (Somwanshi et al. 2020a) earlier and is not repeated.

Table 1 compares the expected velocity and timescales in the experiments as a function of the total droplet volume. The corresponding dimensionless parameters are also listed. The dimensionless numbers are estimated for ultrapure water at 25 °C ($\rho = 998$ kg/m^3; $\mu = 1.003 \times 10^{-3}$ Pa-s; $\sigma = 72.8 \times 10^{-3}$ N/m.). The capillary length is seen to be 0.91 mm ($Bo = 0.11$) for a combined droplet volume of 24.7 µl and is the characteristic length scale of the experiment.

The velocity scale for the initially motionless drops cannot be explicitly described. The velocity scales associated with pairs of forces, namely, S-V, I-S, and I-V, respectively, are derived as:

$$U = \frac{\sigma}{\mu}, U = \sqrt{\frac{\sigma}{\rho R}}, U = \sqrt{gR} \tag{1}$$

The Bond number for the combined drop volume being 0.11, flow is strongly influenced by surface tension while gravity plays a secondary role. The magnitude of velocity based on the scaling σ/μ is 72.6 m/s. Such large velocities are not seen in experiments. Using a velocity scale $(\sigma/\rho R)^{1/2}$, the characteristic value is found to be ~ 0.3 m/s. Velocities of this order are realized in the early stages of the experiments. Hence, the velocity scale $(\sigma/\rho R)^{1/2}$ based on inertia and surface tension is adopted as a velocity scale for forming all dimensionless parameters. This velocity scale makes Weber number unity and $Oh = 1/Re$. In an experiment, initial velocities generated are of the order of $(\sigma/\rho R)^{1/2}$ and diminish owing to viscous dissipation over a longer time period.

Timescales associated with the respective force pairs, namely, inertia-surface tension, viscous-surface tension and inertia-viscous can now be calculated as:

$$t_{IS} = \sqrt{\frac{\rho R^3}{\sigma}}, t_{VS} = \frac{\mu R}{\sigma}, t_{IV} = \frac{R^2}{\nu} \tag{2}$$

Table 1 shows that the V-S timescale is in microseconds; I-S timescale is of the order of milliseconds, and I-V is in seconds. With a camera speed of 20,000 frames per second, coalescence over the V-S timescale has not been resolved. However, longer timescales and lower velocities associated with the I-S and I-V timescales are clearly observed in the present set of experiments. The I-V timescale is particularly long (~ 800 ms). The dissipation referred here occurs within the bulk of the liquid drop by viscosity and also the resistance to movement of the three-phase contact line relative to the substrate.

An image sequence of the coalescence event as seen in the front and the side views within the I-S timescale is presented in Fig. 2. Companion figures for the inertia-viscous regime are given in Fig. 3 (see multimedia view for Figs. 2 and 3). The I-S timescale gauged from recorded images is found to be 15 ms each for the front and the side views during the early stages when the changes in the drop shape are substantial. The I-V timescale in the image sequence is of the order of 300 ms in later stages. These differences in timescales are consistent with the definitions given in Eq. 2 and are clearly observed from scale analysis as well as the experimental data.

Comparing with coalescence of drops placed side-by-side, the first point of contact in vertically oriented drops is above the first sessile drop. In this respect, the initial evolution of the combined drop qualitatively resembles coalescence of drops merging in free space. The drops merge with the formation of a neck-shaped bridge between them. The liquid–air interface then grows outward and is followed by large oscillations in the drop shape. In the long run, the kinetic energy acquired by the liquid mass is dissipated by viscosity and the drop approaches the equilibrium configuration.

It is evident from the front view, Fig. 2a, c and the side view, Fig. 2b, d that the neck joining the drops is formed during 0–2 ms. The neck evolves in shape and curvature in the second stage and induces large fluid velocities and drop oscillations. The drop with convex curvature is a region of positive pressure, while the neck has negative curvature and is a region of negative pressure relative to the ambient. The

Table 1 Orders of magnitude of dimensionless numbers $We = \frac{\rho U^2 R}{\sigma}$, $Fr = \frac{U^2}{gR}$, $Re = \frac{\rho UR}{\mu}$, $Bo = \frac{\rho g R^2}{\sigma}$ *and* $Oh = \frac{\mu}{\sqrt{\rho R \sigma}}$ that appear during the coalescence of water drops; velocity scale U is taken as $(\sigma/\rho R)^{1/2}$ where R is the base radius of the merged drop at equilibrium. Inertia-surface tension (I-S), viscous-surface tension (V-S), and inertia-viscous (I-V) timescales for coalescence of water drops under ambient conditions is presented

Combined volume, µl (U, m/s)	Base radius, (mm)	Dimensionless numbers					Timescales		
		We	*Fr*	*Re*	*Bo*	*Oh*	t_{IS}, ms	t_{VS}, µs	t_{IV}, ms
20 (0.29)	0.845	1	10.39	247	0.096	4.05×10^{-3}	2.879	11.65	0.711×10^3
25 (0.28)	0.911	1	8.96	256	0.112	3.89×10^{-3}	3.219	12.55	0.826×10^3
30 (0.27)	0.968	1	7.94	264	0.126	3.78×10^{-3}	3.526	13.34	0.932×10^3

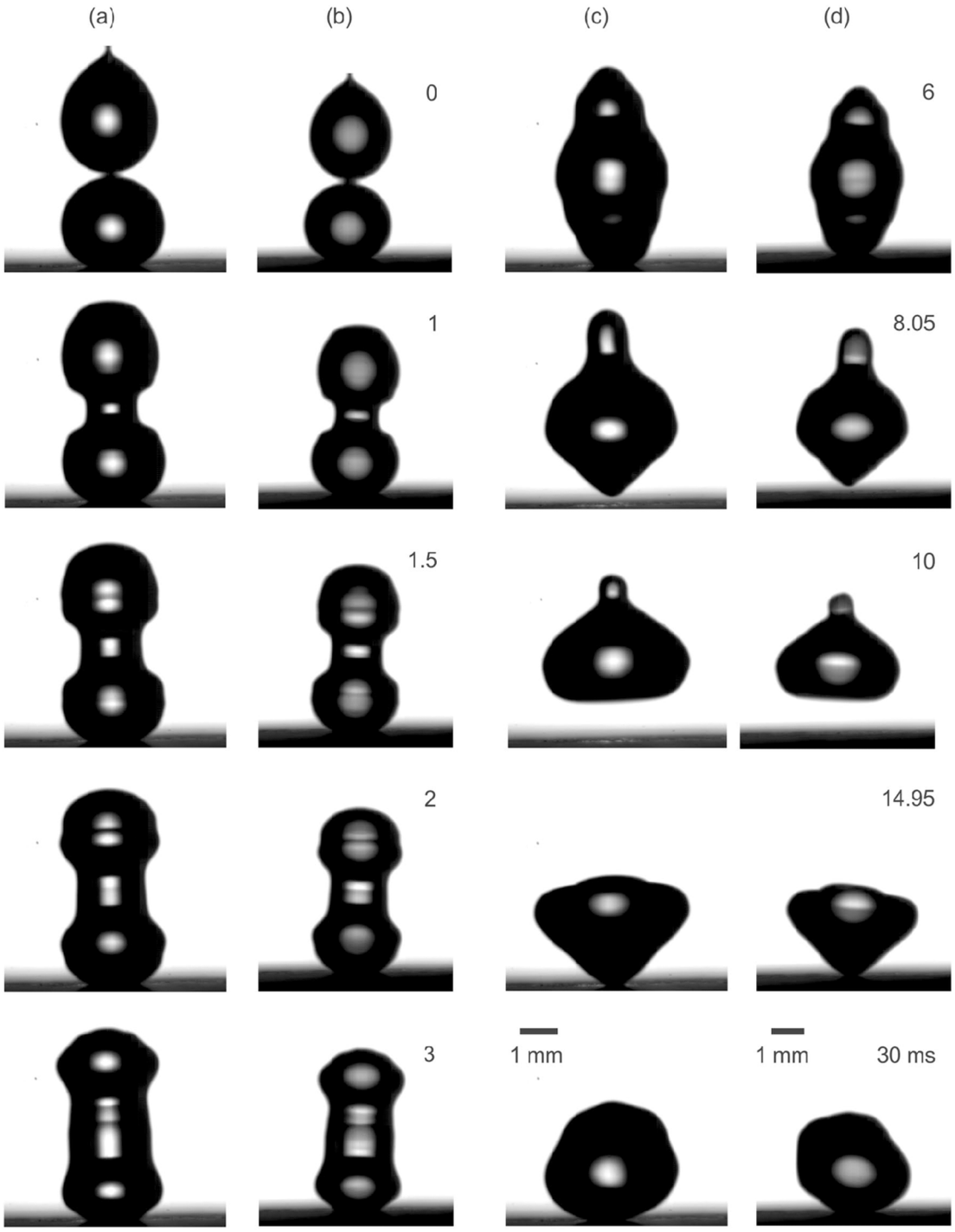

Fig. 2 Image sequence of the coalescence process for drops of equal volumes ($R^*=1$) with a combined Bond number (Bo) = 0.11 in the short-term inertia-surface tension regime; **a**, **c** are front views and **b**, **d** are side views at various instants of time. Also see multimedia view

flow of the liquid toward the neck is the origin of mixing between the drops and the formation of a composite whole. Following the first process of neck formation, the second consequence of coalescence is drop recoil away from the wall where the drop is lifted off. Recoil is seen in the present set of experiments to last over the 8–15 ms time interval. The instant, height and duration of recoil is related to the drop volumes and the equilibrium contact angle of the liquid relative to the surface. For the choice of parameters in the present set of experiments ($Bo=0.11$, $\theta_e=150°$), the following

observations are recorded. The formation of the neck and the bulge occurs over ~ 0–8 ms and ~ 8–300 ms, respectively. The instant of recoil occurs at 8.05 (± 0.5) ms with a recoil height of 1.05 (± 0.01) mm lasting over a duration of ~ 6.9 (± 0.5) ms. Here, the uncertainty estimates have been determined via a set of repeatability experiments. The above trends are seen in both orthogonal views (Figs. 2a, c compared with Figs. 2b, d) while drop shapes look quite similar as well. The slight difference in the frame sizes is related to those in the pixel specifications of the cameras. Hence, coalescence in the inertia-surface tension (I-S) regime is seen to be axisymmetric, being driven by the initial departure of the interface shape from equilibrium, difference in the respective surface energies, and transformation of excess surface energy to kinetic energy followed by viscous dissipation. The axisymmetric character of coalescence is discussed further in the following section.

3.2 Axisymmetry of the coalescence process

Image sequence of the coalescence event as seen in the front view and the side view is shown in Figs. 2 and 3. The inertia-surface tension regime is covered in Fig. 2, while the inertia-viscous regime is presented in Fig. 3. The image pairs show a great degree of similarity at early stages as well as the late stages, suggesting axisymmetry for the entire duration of the coalescence process. At intermediate time instants, large oscillations of the bridge induced within the inertia-surface tension timescale (< 30 ms) diminish in time due to viscous dissipation, attaining equilibrium over a period of around 300 ms. Following recoil, the drop spreads over the surface, its footprint increases with time and there are instants when symmetry in the two views is occasionally broken. Overall, the two views of drop coalescence (Figs. 2 and 3a, c compared to Figs. 2 and 3b, d) show considerable similarity over the entire time elapsed. Similarity in the two views is pronounced at time instants beyond 80 ms. Hence, for the purpose of numerical modeling, axisymmetry in flow distribution may be taken to be applicable in the inertia-surface tension and inertia-viscous regimes of the coalescence process.

The centroid position has been estimated using image analysis of the recorded video in two views—the front and the side. The centroid-position data with time are fitted using a seventh-order polynomial in the early stages and the sine function in later stages with an exponentially decaying amplitude function in time. These functions are differentiated with respect to time to yield the centroid velocity. Since the image contains information on two components of displacement, two components of the centroid velocity are recovered. The vertical velocity component is shared by the two views, while two other components define velocity over a horizontal plane parallel to the substrate. Thus, with two orthogonal views, all three Cartesian velocity components of the centroid can be estimated.

The vertical component of the centroid velocity of the coalesced drop, estimated from the front and the side views, is shown in Fig. 4. The two regimes, namely inertia-surface tension and inertia-viscous, are separately shown in Fig. 4a and b. The first regime occurs over 0–30 ms, and the second is spread over 30 to 300 ms and beyond. The initial centroidal velocities are quite large and change with time, corresponding to the large interface deformation. The long-time trend is oscillatory whose amplitude decays with time. The vertical velocity components recorded from the two views are practically identical and confirm axisymmetry of the merger process. Quantitatively, the maximum difference between the vertical velocity components in the two views was found to be ± 2% in the inertia-surface tension regime. In subsequent figures, data related to the front view alone are presented. Since the present configuration remains close to axisymmetric, the horizontal component of centroidal velocity is significantly smaller and is not discussed further.

3.3 Recoil of the coalesced drop

The extent to which velocities are generated and the height of recoil attained can be gauged from surface energy analysis of the initial (1 and 2) and final (3) interface configurations. The respective surface energy levels at equilibrium are of the order of:

$$E_1 = \sigma A_1,\ E_2 = \sigma A_2,\ E_3 = \sigma A_3 \tag{3}$$

The surface energies of the drop placed below, the one placed above and the coalesced drop are denoted by symbols E_1, E_2 and E_3, respectively, and the corresponding gas–liquid interfacial areas by symbols A_1, A_2 and A_3, respectively. The equilibrium contact angle of the liquid relative to the surface in an ambient environment is denoted as θ_e. The surface areas of the drop placed below and the coalesced drop are given by:

$$A_1 = 2\pi R_1^2\left(1-\cos\theta_e\right) A_3 = 2\pi R_3^2\left(1-\cos\theta_e\right) \tag{4}$$

The area A_2 for the full spherical drop placed above is simply calculated as $A_2 = 4\pi R_2^2$. Hence, the relative excess surface energy is defined as

$$E^* = \frac{\left(E_1+E_2-E_3\right)}{E_3} = \frac{\left((R^*)^2+\frac{2}{C_1}\right)}{\left((R^*)^3+\frac{4}{C_2}\right)^{2/3}} - 1 \tag{5}$$

Here, $C_1 = 1-\cos\theta_e$, $C_2 = 2-3\cos\theta_e+\cos^3\theta_e$ and $R^* = R_1/R_2$. Equation (5) includes the result that the volume of drop 3 is equal to the sum of the volumes of drops 1 and 2. The equilibrium contact angle and the radius ratio strongly

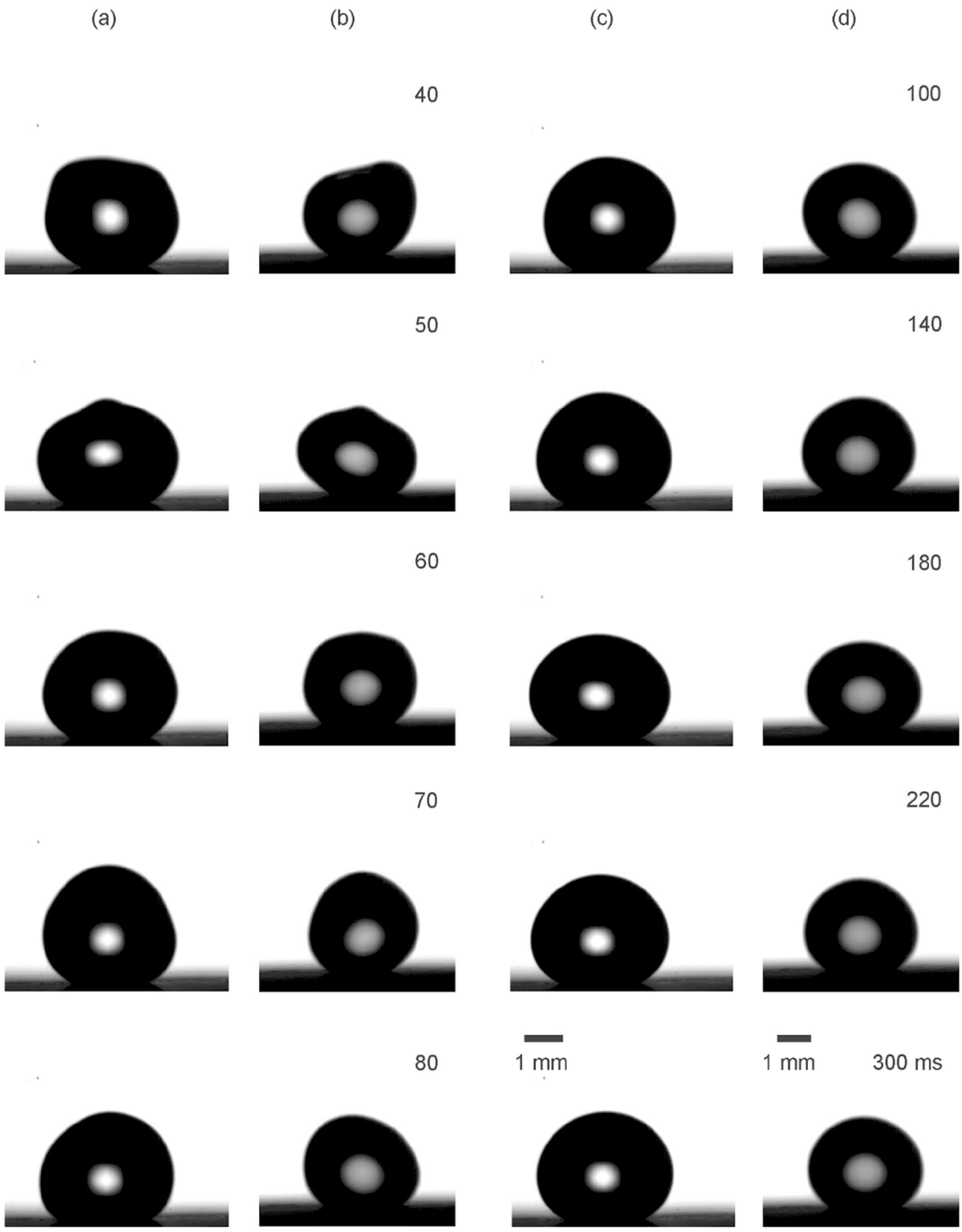

Fig. 3 Image sequence of the coalescence process for drops of equal volumes ($R^*=1$) with a combined Bond number (Bo) = 0.11 in the long-term inertia-viscous regime; **a**, **c** are front views and **b**, **d** are side views at various instants of time. Also see multimedia view

influence the relative excess energy. In the limit of $\theta_e \rightarrow \pi$, the excess energy function E^* approaches a minimum, showing that coalescence dynamics is dominated by surface energy exchanges while volumetric viscous dissipation itself plays the role of a limiter for the velocity magnitude. The instant of recoil is decided by the availability of the excess surface energy; hence, the pressure difference needed to overcome gravity, at a given instant of time.

Gravity and internal capillary pressure are other important forces that control the movement of the coalesced drop.

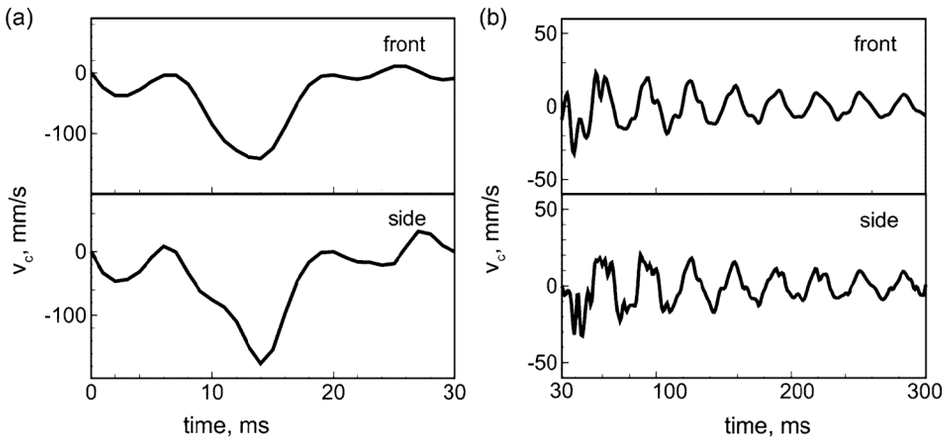

Fig. 4 Vertical velocity of the centroid of the combined drop as a function of time estimated using two-view imaging of the coalescence process in the **a** inertia-surface tension and **b** inertia-viscous regime

The instant of recoil on the surface is influenced by gravity though the Bond number is less than unity. The role of the initial capillary pressure difference can be studied along the following lines. Neglecting the presence of the substrate, the initial pressure difference between the two drops is given by

$$\Delta p = p_1 - p_2 = 2\sigma \frac{R_2 - R_1}{R_1 R_2} \tag{6}$$

In the framework of the simplified analysis presented here, it is zero for equal volume drops. Relative to the neck where pressure may be approximated as the datum value, the pressure difference driving fluid motion is

$$p_1 - p_{atm} = \frac{2\sigma}{R_1} \tag{7}$$

The excess pressure and the surface energy function are large when both drops are small and determine the velocities created in the drop. Hence, they govern the rate of formation and growth of neck curvature leading to the moment of recoil. For equal volume drops, the initial capillary pressure difference relative to the neck depends on the radius of the lower drop and determines the height and duration of recoil. On the other hand, for a given R_2, it is to be expected for unequal volume drops that the height of recoil will approach $2R_1$ for $R_1 \to 0$ on superhydrophobic surfaces.

Numerically determined interface shapes of the merging drops are shown in Fig. 5, both within the I-S and the I-V regimes. The distinctive features of coalescence including neck and bulge formation, recoil instant of ~ 8 ms with a recoil height of ~ 1 mm, the recoil duration and long-term viscous dissipation are reproduced fully in simulations. The interface shapes in Fig. 5 show a good degree of similarity with experimental images shown in Figs. 2 and 3. This favorable comparison confirms the axisymmetry during coalescence of drops in a vertical configuration.

The origin of recoil within the inertia-surface tension regime can be traced to pressure variation within the drop. Pressure distribution within the merging drops has been determined from numerical simulation (Somwanshi et al. 2020a) and shown in Fig. 6. Pressure distribution in the vertical direction during the initial time instants shown does not appear to be influenced by gravity. Hence, pressure changes in the I-S regime, Fig. 6, are simultaneous with changes in the drop shape and its curvature. The region around the neck has a lower pressure as shown by a lighter shade while pressures are higher toward the extremes where the drop curvature is large and positive; equivalently, drop radius at the top is small and convex. These extreme positions move vertically inward, leading to a possibility of recoil. Strictly speaking, the two drops are not identical since the lower one is placed on the solid substrate. The resulting curvature is smaller than for a spherical drop, internal pressure is higher, and the pressure difference relative to the neck is higher for the lower drop compared to the one above. Accordingly, Fig. 6 shows that the vertical movement of the lower drop is greater than the one above, resulting in visible recoil.

Recoil from coalescence has also been reported in dropwise condensation over hydrophobic surfaces (Cha et al. 2016; Fil et al. 2020), drop dynamics in microgravity, in the form of levitation of drops over a liquid–vapor interface (Fedorets et al. 2020) and in coalescence of drops placed side-by-side (Wasserfall et al. 2017; Wang and Ming 2019; Liu et al. 2021). The effect of the texturing pattern on the droplet jumping velocity was examined by Wang et al. (2021). Recoil was also observed for a vertically impacting drop over Teflon and parafilm substrates (Sankaran et al. 2021). The present work reveals recoil of the merged drop for the first time in vertical coalescence from experiments as well as simulation.

3.4 Bridge dynamics

The bridge formed by molecular adhesion around the first point of contact of the two drops initiates the formation of a single liquid entity. Bridge evolution is seen clearly within

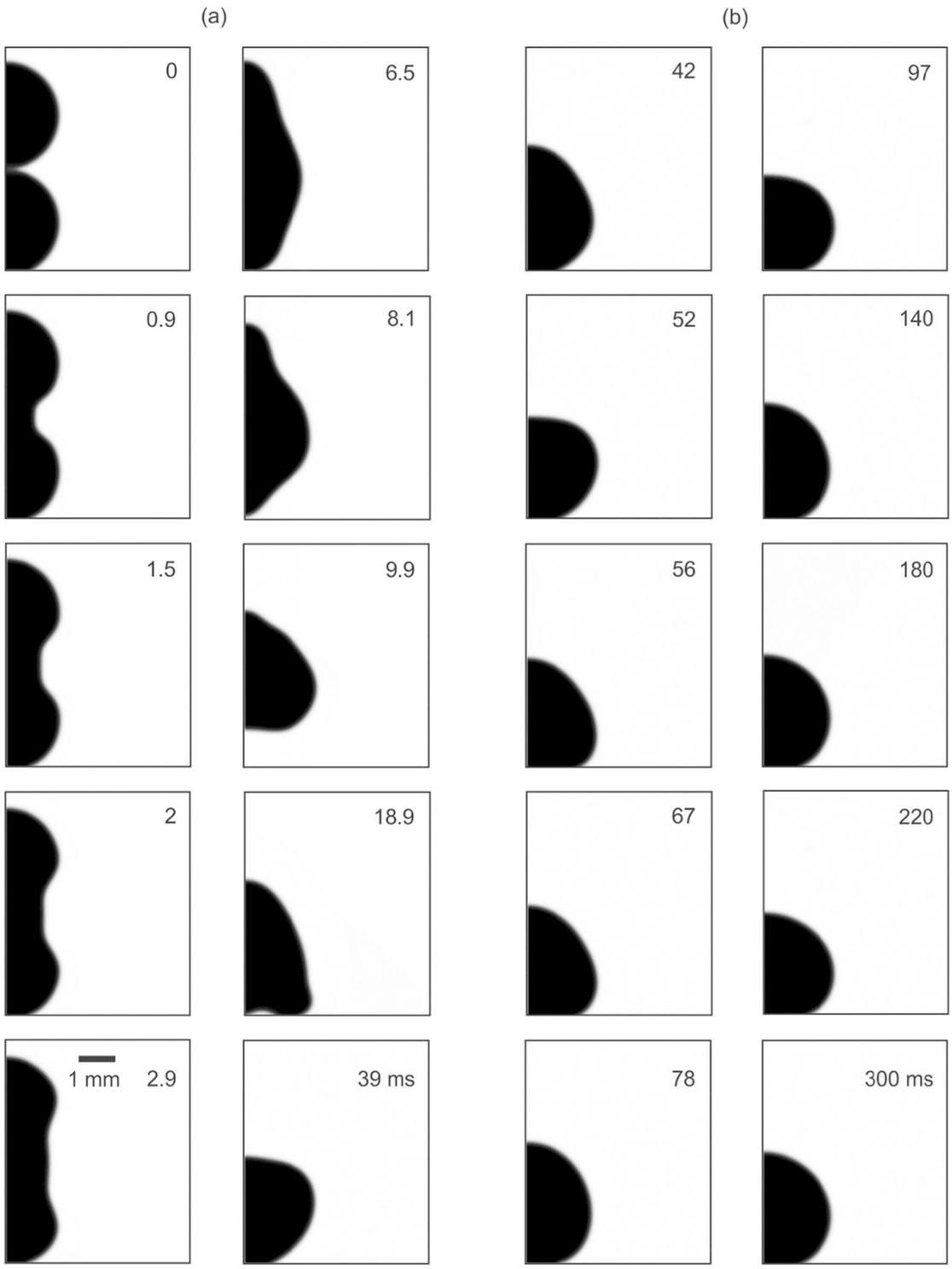

Fig. 5 Image sequence of the coalescence process for drops of equal volumes ($R^*=1$) with a combined Bond number (Bo) = 0.11 determined using numerical simulation for the **a** inertia-surface tension and **b** inertia-viscous regime

the inertia-surface tension regime. Later, in the inertia-viscous regime, a single large liquid drop shows curvature oscillations and bulk movement over the substrate. Within the inertia-surface tension regime, the bridge is characterized by a bulge as well as a neck. These are, respectively, characterized by positive and negative curvatures. The

growth of the bulge radius continues into the inertia-viscous regime, representing the curvature of the combined drop. In contrast, the neck fades away in the initial stages and is not formed at later times. Positive curvature of the bulge is indicative of positive pressure within the drop relative to the atmosphere. In contrast, the neck is a region of negative pressure. This pressure difference generates large velocity magnitudes within the drop leading to interface deformation, possible recoil, and long-time oscillations. Table 1 shows the estimated velocity magnitude in the I-S regime to be ~ 280 mm/s, while Fig. 4 shows the experimentally recorded peak velocity of the centroid to be ~ 150 mm/s, negative, attained soon after recoil.

For curvature calculations, the instantaneous images are first converted into a binary form. Following edge detection of the interface, a quadratic function $y = c_1x^2 + c_1x + c_3$ is fitted through the coordinates of the three points falling on the boundary. Adjacent segments are overlapped to maintain functional continuity. With a numerical evaluation of the derivatives, the local curvature R_l is then given in terms of the local x and y coordinates as

$$R_l = \frac{d^2y}{dx^2}\left[1 + \left(\frac{dy}{dx}\right)^2\right]^{-3/2} \tag{8}$$

Figure 7a shows the temporal variation of the instantaneous bulge radius from the front side, determined from Eq. 8, in the inertia-surface tension regime. Figure 7b is a companion plot for the neck radius during the early time instants corresponding to this regime. Figure 7c is the temporal variation of the bulge radius over a longer time frame that includes the inertia-viscous regime. The bulge and neck radii vary with position over the interface. In addition, Figs. 7a–c shows the largest value realized at a given instant. A comparable plot in the side view found to be similar to the front view and is not repeated. The bulge and neck radii are largely constant except for a damped oscillatory trend; the neck vanishes ahead of recoil though the oscillations in the bulge radius persist over a longer time period. In Fig. 7, a continuous line is drawn from experimental data in the front view, the shaded circles are an average of the front and side view, while open circles are from numerical simulation. The match between experiments and simulation in terms of the bulge radius is good though some discrepancy is seen between the two, in terms of the neck radius. A possible reason could be related to the small negative neck radius, small internal pressure, and large velocities that drive the recoil process, resulting in a loss of axisymmetry. The match between experiments and full three-dimensional simulation was seen to be comparatively better but is not discussed here.

Figure 7d shows the variation of footprint radius with time where experimental data (continuous line and shaded circles) are compared with numerical simulation (open circles). Time instants post-recoil are considered. The comparison is seen to be favorable. The changes in the footprint radius are quite large in the inertia-surface tension regime in contrast to the inertia-viscous regime, highlighting once again the two distinct timescales. In addition, the persistent long-term oscillations in the footprint are consistent with those in the bulge radius (Fig. 7c).

Referring to Fig. 7b, the magnitude of the neck radius scales as $t^{0.5}$ with a constant of proportionality of 1.27 (regression coefficient = 0.994) over a time duration of 0—8 ms. For experimental data, the dimensionless expression for the initial evolution of the neck radius (R_n) is written as

$$\frac{R_n}{R} = 1.271\left(\frac{t}{t_{IS}}\right)^{1/2} \tag{9}$$

Here, R is the footprint radius (= 0.91 mm) used as a length scale in Table 1. The magnitude of the neck radius decreases later while the neck itself vanishes beyond the I-S regime and is not relevant for the longer time period of viscous dissipation. The largest positive bulge radius and the largest negative neck radius define the limits of pressure extremes that appear in the combined drop in the I-S regime

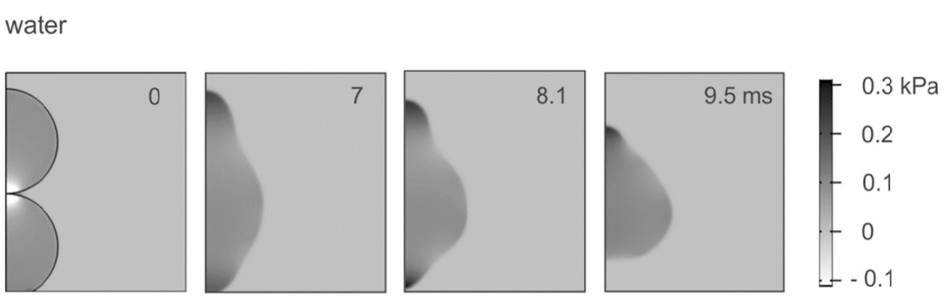

Fig. 6 Numerically determined pressure variation in the coalescing drops around the instant of recoil relative to the datum. Outside the liquid drops, pressure is atmospheric (= 0). The initial drop shapes as well as the shapes of the combined drop is shown. Regions of high pressure are darker than regions of low pressure. Drops are of equal volumes and the recoil instant is ~ 8 ms in water

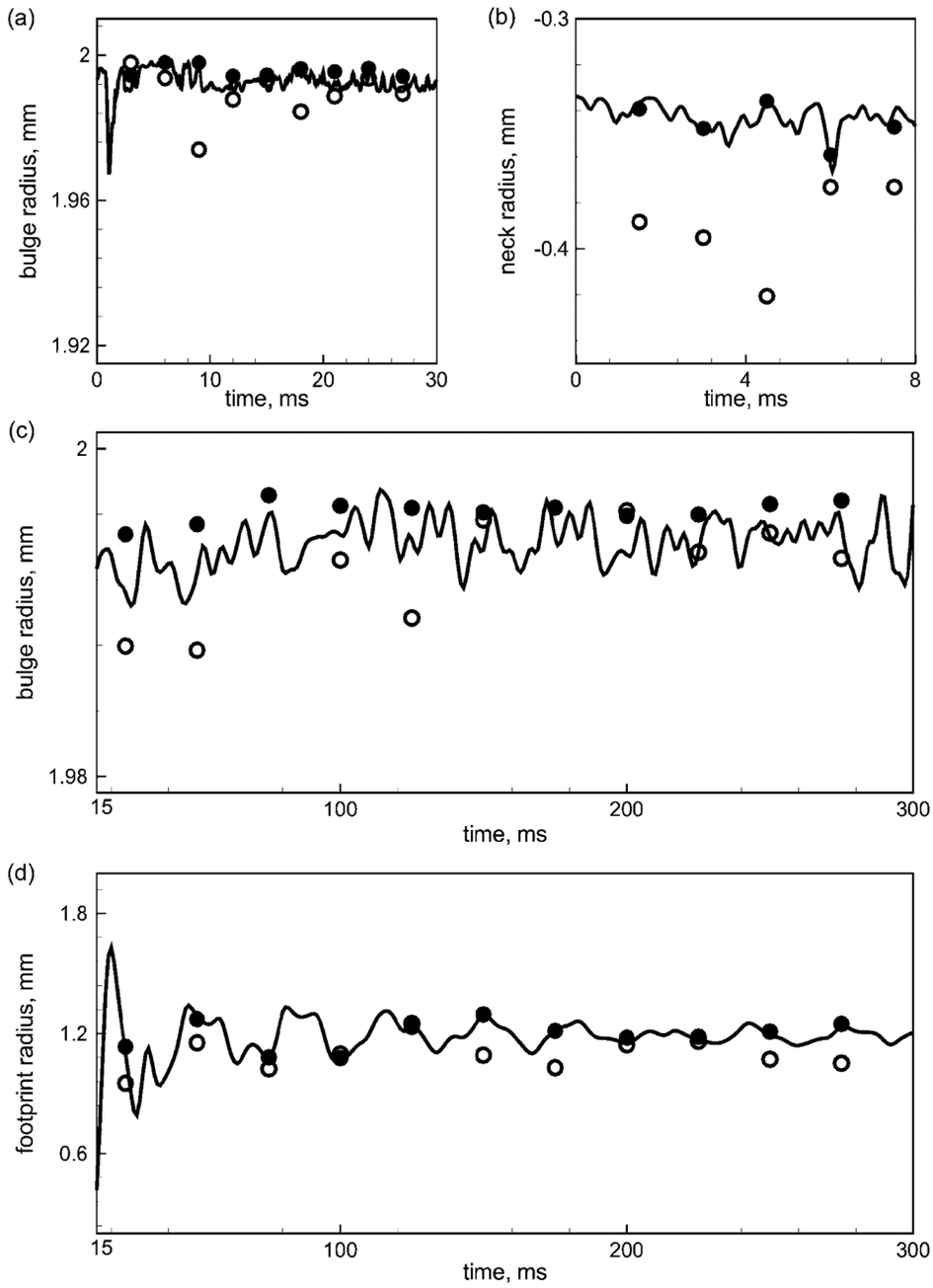

Fig. 7 Variation of curvature in terms of the peak neck and bulge radii with time in the inertia-surface tension **a**, **b** and **c** inertia-viscous regimes; **d** temporal variation of footprint radius during coalescence of equal volume drops; continuous line is drawn from the front view; shaded circles show experimental data averaged over front and side views while open circles show data obtained from numerical simulations. The equilibrium footprint in **d** is 0.91 mm

during the merging process. In the I-V regime, the bulge radius alone is relevant and the internal pressure in the drop is everywhere positive.

The changes in the interface curvature with time during coalescence of drops in the vertical configuration have been sparsely discussed in the literature. In a coalescence study over a partially wetting surface, Lee et al. (2012) showed the initial scaling of the bridge width and bridge height be $t^{0.29}$ and $t^{0.5}$, respectively. In configurations similar to the present work but without a substrate, namely, free space coalescence, the growth of the bulge radius has been reported from high-speed imaging experiments to increase as $t^{0.5}$ for coalescence of equal volume drops (Duchemin et al. 2003; Wu et al. 2004; Aarts et al. 2005; Thoroddsen et al. 2005; Ristenpart et al. 2006). In a recent work, Perumanath et al. (2019) used MD simulation to show that the bridge formed during coalescence of nanometer drops is initiated by thermal fluctuations present over the gas–liquid interface. The bridge formed after contact evolves over a thermal length scale away from the collision axis. Over a timescale of picoseconds, the growth of the bridge radius is linear in time and was labeled the thermal regime. Subsequently, the $t^{0.5}$ scaling for the viscous-capillary regime of bridge growth was restored. The present study shows the scaling to be

applicable, also, for coalescence of vertically aligned drops over a superhydrophobic surface in the inertia-surface tension regime.

3.5 Contact angle modeling

Centroid displacements relative to the joint initial centroid position of the merging drops and are estimated from images recorded using the two cameras. The coordinate data are numerically differentiated with time to obtain centroidal velocity components. Footprint radius is estimated using wall pixel data of the image. A fourth-order polynomial is fitted through the liquid interface near the wall, and the dynamic (also called, apparent) contact angle is determined from the slope of the fitted curve at the wall. The contact line velocity is obtained by numerically evaluating the derivative of footprint radius with time.

Figures 8a–b shows the experimentally determined variation of vertical component of centroidal velocity and the contact line velocity along the substrate as a function of time in the I-S and I-V regimes, respectively. The dashed segment is the duration of recoil. The initial motion of the drop is in the vertical direction, the coalescence process is nearly axisymmetric, and the horizontal component of velocity is correspondingly small. At later times, the drop spreads over the substrate and the horizontal component of velocity becomes larger. The vertical component of the centroid velocity is smaller than the contact line speed in both regimes, indicating unpinned motion of the contact line over the superhydrophobic surface. Large oscillations setup in the contact line motion are dissipated over the I-V regime, approaching zero in the long run.

Figures 8c–d shows the variation of the apparent contact angle as a function of time in the I-S and I-V regimes, respectively. Large variations of the dynamic contact angle are seen in the I-S regime, though an approach to the equilibrium value (of 150°) via oscillations is seen in the I-V regime.

In numerical simulations, surface characteristics are included when the equilibrium contact angle is prescribed. During motion of the three-phase contact line, the quantity of interest is the dynamic contact angle. The outcome of numerical simulations is greatly influenced by the prescription of the dynamic contact angle since it acts as a boundary condition to resolve the singularity at the three-phase contact line. The experiments of the present study show that the dynamic contact angle can substantially depart from the equilibrium value as seen in Fig. 8c in the I-S regime. Long-term oscillations (Fig. 8d) are, however, bounded by the contact angle hysteresis, about 10°, in the present set of experiments.

In simulations, one approach to the specification of the dynamic contact angle is via contact angle models that relate the instantaneous contact angle with the contact line velocity. Various dynamic contact line models have been reported in the literature. Two such models have been chosen for comparison and are given below. Here, the capillary number is defined in terms of the contact line velocity as:

$$Ca = \frac{\mu U_{cl}}{\sigma} \tag{10}$$

In the Cox model (Cox 1986), the macroscopic region is connected theoretically to the microscopic region using a slip length that permits drop sliding over the surface. The dynamic contact angle is then shown to relate to contact line velocity as:

$$\theta_d^3 = \theta_e^3 + 144Ca \tag{11}$$

Hoffman (1975) studied experimentally the temporal variation of the shape of the advancing liquid–air interface inside a glass capillary. The experimental data cover a wide capillary number range, namely, $4 \times 10^{-5} < \mathrm{Ca} < 36$. Using this data, an empirical correlation for the dynamic contact angle was proposed by Kistler (1993) as:

$$\begin{aligned} &\theta_d = f_H\left[Ca + f_{HI}(\theta_e)\right] \\ &f_H(z) = \arccos\left\{1 - 2\tanh\left[5.16\left[\frac{z}{1+1.31z^{0.99}}\right]^{0.706}\right]\right\} \\ &where\ (f_{HI})^{0.706} = \frac{1}{5.16}\left[1 + 1.31(f_{HI})^{0.99}\right]^{0.706} \arctan h\left(\frac{1-\cos\theta_e}{2}\right) \end{aligned} \tag{12}$$

Here, $f_H(z)$ is the Hoffmann function and $f_{HI}(z)$ is the inverse Hoffmann function. Each contact line model given above allows unpinned contact line motion with a dynamic contact angle prescribed at the three-phase contact line as a kinematic constraint. The drop shape that evolves with time is determined jointly with the flow field during numerical simulation.

Figures 8e–f shows the variation of the dynamic contact angle as a function of the contact line velocity in the I-S and I-V regimes, respectively. Both, the Cox and the Kistler models, are shown. Experimental data, particularly post-recoil, are included for comparison as open squares. In the I-S regime, deviations between the model and the experiment are large. After viscous effects become important, the difference becomes smaller in the I-V regime, and the drop spreads continuously over the surface. In this respect, the dynamic contact angle models can be seen to be applicable for drops spreading continuously over a surface, becoming inappropriate when interface deformations are relatively large. Between the two models of Cox and Kistler, the latter shows a better match with the present set of experiments.

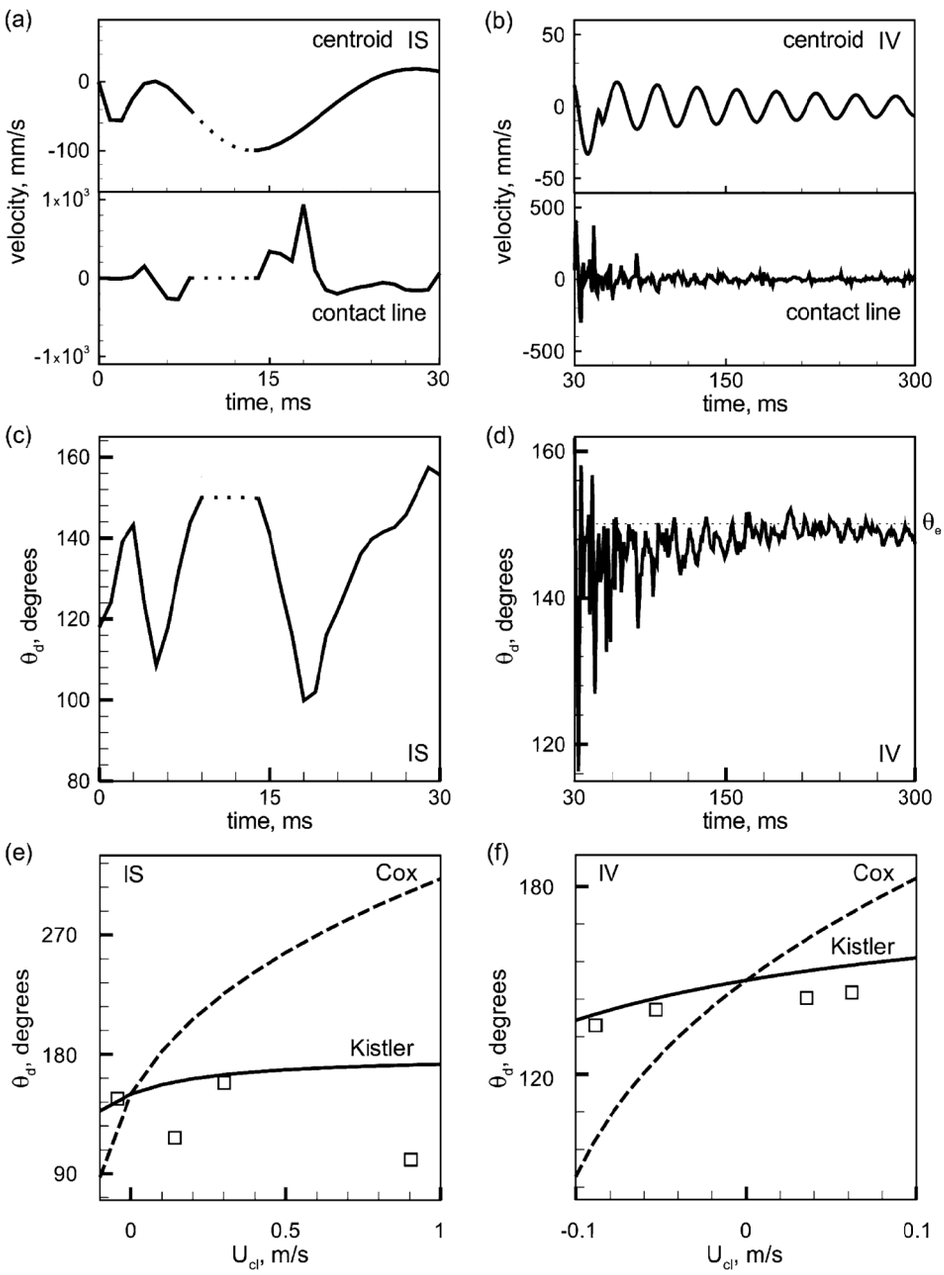

Fig. 8 Coalescence characteristics of drops of equal volumes ($R^*=1$) in terms of the time-variation of the centroidal and contact line velocities **a**, **b** in I-S and I-V regimes; **c**, **d** dynamic contact angle variation with time in the I-S and I-V regimes; **e**, **f** dynamic contact angle variation as a function of contact line velocity from experiments and comparison with contact line models in I-S and I-V regimes, respectively. Open symbols in **e** and **f** show experimental data. Dotted sections in **a** and **c** refer to the recoil interval. The equilibrium contact angle shown in **d** is 150°

3.6 Wall shear rate

Temporal variation of shear rate estimated using the experimentally recorded image sequence in the front view is shown in Fig. 9a. For shear rate calculations, the near wall x-velocity distribution between the centroid and the wall is taken to be linear from the centroid velocity to zero and the wall derivative is explicitly evaluated. Once again, the side view data were quite similar to the front and are not repeated. Vertical velocities are large, but the merger is close to axisymmetric and the horizontal component of velocity is much smaller. Accordingly, the initial shear rates in the vertical configuration are small. The shear rates in the vertical arrangement increase, particularly after recoil. Shear rates are zero during recoil (over the time interval of ~ 8–15 ms). Recoil is further indicated in Fig. 9. Shear rate oscillations are damped in the long run. In comparison with the sessile configuration, shear rates for vertical coalescence are substantially smaller by two orders of magnitude (Somwanshi et al. (2018)). Figure 9b shows internal pressure fluctuations determined in the present set of experiments. Here, pressure $p(t)$ has been determined relative to atmospheric as

$$p = \frac{2\sigma}{R_{avg}}; \frac{1}{R_{avg}} = \frac{1}{N}\sum_{i=1}^{N} R_l(i) \tag{13}$$

Here, σ is the surface tension coefficient for an air–water interface and R_{avg} is the average radius of curvature of the liquid drop. The latter is determined as the reciprocal of the average of the local curvature in each of the images using Eq. 8. The kinematic equivalent of pressure (in units of ms^{-1}) is obtained by dividing pressure by the dynamic viscosity of water. Figure 9b shows that pressure amplitudes are substantially larger than the shear rate and approach a finite value in the long run. The initial large-amplitude oscillations correspond to large interface deformations associated with the I-S regime. The long-term value of pressure corresponds to the internal pressure in the merged drop under equilibrium conditions. These observations are of significance from the viewpoint of mechanical loading of the substrate and long-term sustainability of hydrophobicity (Somwanshi et al. 2018).

3.7 Drops of unequal volumes

Figure 10 shows two orthogonal views of drop coalescence when the smaller drop is kept below at a combined Bond number of 0.11 and a radius ratio of 0.6. In experiments, the cameras simultaneously acquired the image sequences. The processes of neck and bulge formation, footprint oscillations and mild recoil at around 5 ms are visible in both views. The shapes seen in the two views are quite similar, confirming axisymmetry of the coalescence process for unequal volume drops.

3.8 Energy budget

The following notation is adopted in the present discussion. With m and V as the mass and volume of the combined drop, u_{res} is the instantaneous resultant velocity of the centroid, g is the acceleration due to gravity, y_{c} is the instantaneous position of the centroid in the vertical direction, R_{b} is the footprint radius, and U_{cl} is the contact line velocity. The definitions of the energy rate components of the merging drop are provided in Eqs. 14–18 below:

$$\text{Surface energy release}: E_s = \frac{\mathrm{d}}{\mathrm{d}t}\left(4\pi R_{avg}^2\sigma\right) = 8\pi\sigma R_{avg}\left(\frac{dR_{avg}}{dt}\right) \tag{14}$$

$$\text{Kinetic energy}: E_k = \frac{\mathrm{d}}{\mathrm{d}t}\left(\frac{1}{2}mu_{res}^2\right) = \left(mu_{res}\frac{\mathrm{d}u_{res}}{\mathrm{d}t}\right); u_{res} = \sqrt{u_c^2 + v_c^2 + w_c^2} \tag{15}$$

$$\text{Gravitational energy}: E_g = mg\frac{\mathrm{d}y_c}{\mathrm{d}t} = mgv_c \tag{16}$$

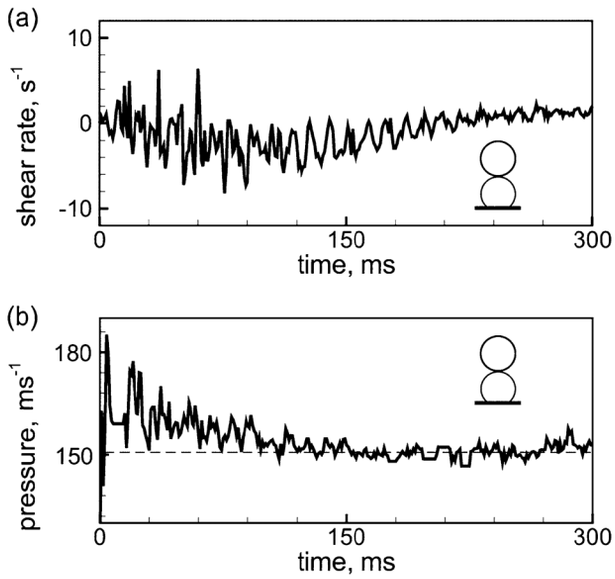

Fig. 9 **a** Temporal variation of the experimentally determined wall shear rate induced during coalescence of drops of equal volumes (Bo = 0.11). **b** Temporal variation of the experimentally determined excess pressure scaled by dynamic viscosity for the vertically aligned drops of equal volumes (Bo = 0.11)

$$\text{Viscous dissipation}: E_{vis} = \mu\left(\frac{u_c}{y_c}\right)^2 V \tag{17}$$

$$\text{Contact line dissipation}: E_{CL} = \sigma\left(\cos\theta_d - \cos\theta_e\right)2\pi R_b u_c \tag{18}$$

The kinetic and gravitational energy rates, namely, changes with respect to time are estimated using the data of the centroid position. The local curvature at all the pixels on the interface is calculated by using Eq. (7) with the curve-fitted interface position data. The reciprocal of arithmetic mean of curvatures ($R_l(i)$) is considered as an average radius for the calculation of surface energy (Eq. 14). Contact line dissipation is estimated using dynamic contact angle obtained for each frame of the image sequence along with the contact line velocity. Of interest to the present discussion is the rate at which energy transformations occur in the I-S and the I-V regimes shown, respectively, in Fig. 11a and b. Temporal variations of the instantaneous energy rates (μW) based on changes in surface energy, gravitational, kinetic energy, viscous dissipation at the contact line as well as the total are shown in this figure.

The process of coalescence changes the relative magnitudes of the energy components that, in turn, change sharply with time, Fig. 11. The energy rates of all components diminish to zero at equilibrium. As discussed in Sect. 3.3, coalescence of drops over a superhydrophobic surface is

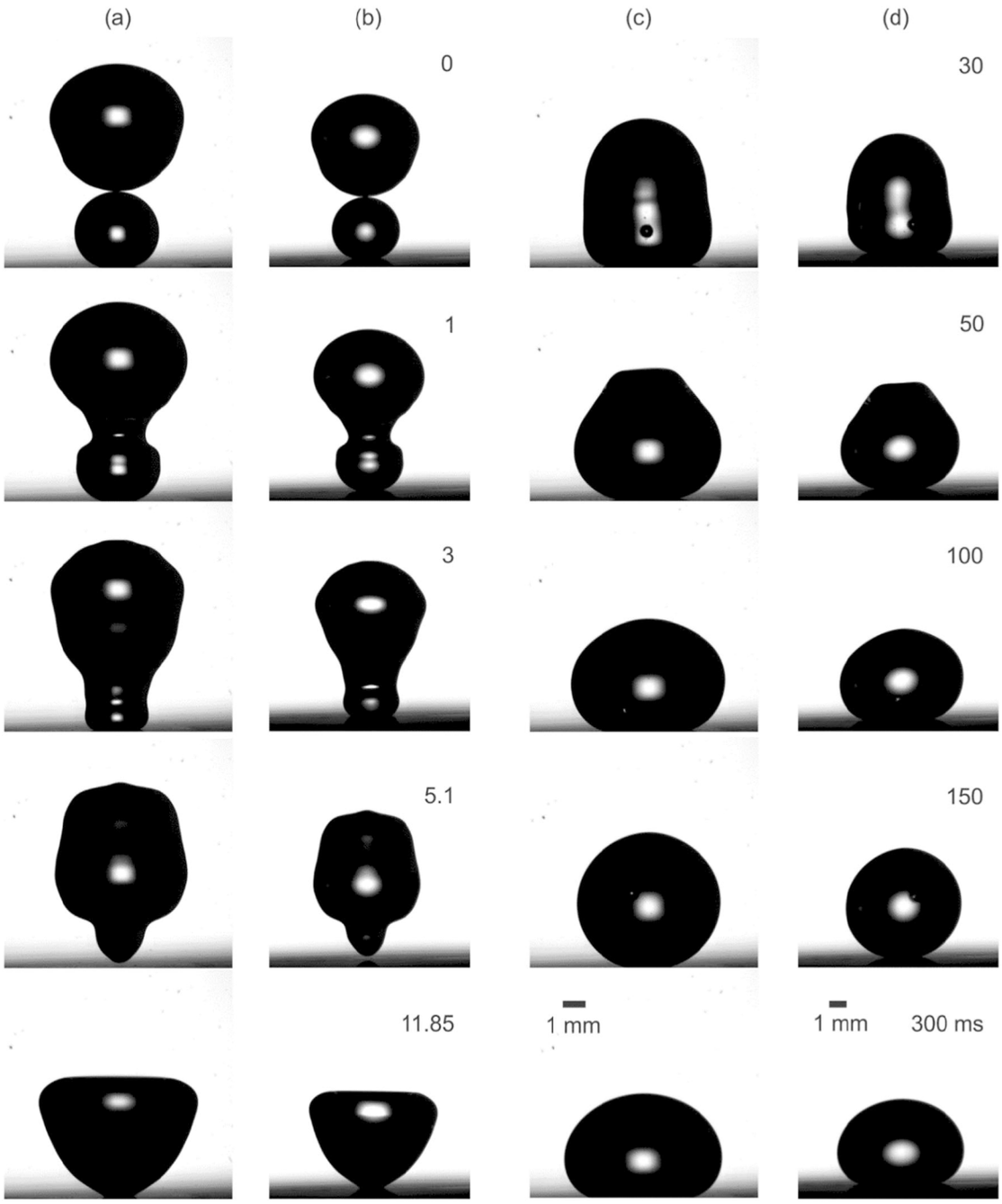

Fig. 10 Image sequence of the coalescence process recorded in two views for drops of unequal volumes ($R^*=0.6$) with a combined Bond number Bo = 0.11; **a**, **c** are the front views and **b**, **d** are side views at various instants of time

dominated by surface energy exchanges as opposed to viscous dissipation in the bulk of the liquid. Using the terminology of Eq. 5, the difference between the initial and the final energy levels is 0.32 μJ which is dissipated over ~ 300 ms, giving rise to an average dissipation rate of around 10^{-3} μW. This number is consistent with the expression given by Eq. 17. Figure 11 shows that viscous dissipation in the bulk is quite small over the entire duration of the experiment, when compared to changes in surface energy.

Changes in the average drop curvature generate corresponding changes in surface energy of the drop as a whole. At small time, the sudden reduction in interface curvature is shown in Fig. 11a owing to an increase in the kinetic energy of the liquid mass. The main source of drop oscillations over

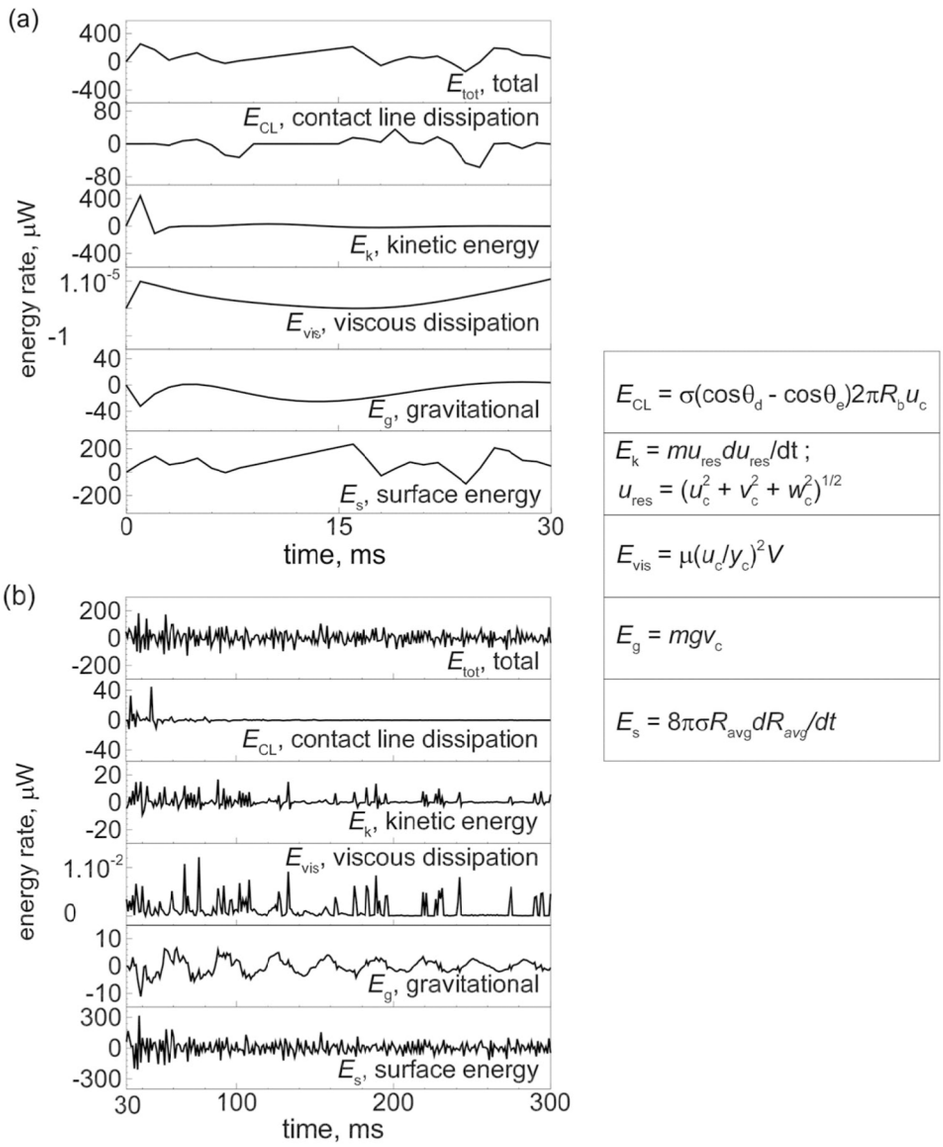

Fig. 11 Temporal variation of the changes in the energy components during coalescence of drops of equal volumes in **a** inertia-surface tension and **b** inertia-viscous regimes

a longer time interval is also the change in surface energy related to small-scale drop deformation (Fig. 11b). Changes in kinetic and gravitational energy arise from gradual changes in the drop shape in the I-S regime (Fig. 11a that includes recoil) and interface oscillations in the I-V regime (Fig. 11b). Contact line dissipation is significant in the latter part of the I-S regime and the early part of the I-V regime when the contact line velocity over the substrate is relatively high. As the drop attains equilibrium, contact line velocity approaches zero and contact line dissipation also reduces to zero. As a consequence, long-term oscillations of the drop are balanced by those in kinetic energy and gravitation. Thus, in the I-V regime, viscous dissipation is related to that at the contact line and is active during its early stages, while the long-term oscillations are inertial in origin. Viscous dissipation in the bulk continues to be present, though with a small amplitude and suggests that drop oscillations may be expected to continue for a much longer duration beyond the experimentally recorded time. Accordingly, the rate of change of total energy shows fluctuations over the time frame studied.

These trends for coalescence in the vertical direction can be compared to horizontally placed side-by-side coalescence discussed by Somwanshi et al. (2018) Specifically, the horizontal velocity component is much smaller in the present study, leading to smaller viscous stresses and hence dissipation in the bulk. Comparing the two configurations, the vertical velocity component is significantly larger in the present work, leading to measurable changes in the gravitational energy. In terms of the two sources of dissipation, the one at the contact line is seen to be significant and in excess of the bulk dissipation.

4 Conclusions

Coalescence process of two water drops of equal volume in a vertical alignment and placed over a chemically textured superhydrophobic surface (equilibrium contact angle, $150 \pm 4°$) was imaged at 20,000 fps using two synchronized cameras. Experimentally recorded drop shapes matched those from numerical simulation. The image sequence was analyzed to locate the centroid of the coalesced drop in every frame as well as the interface curvature, footprint radius and the dynamic contact angle. Though the very early interactions in the viscous-surface tension (VS) regime could not be resolved, drop movement in the I-S and I-V regimes could be delineated in the present set of experiments. The early time scale (0–30 ms) was related to a balance of inertia and surface tension (I-S), with bridge formation between the drops as the dominant event. It was followed by large oscillatory velocities over 30–300 ms, being characteristic of a balance of inertia and viscous forces (I-V). Specific observations derived from the experiments are given below.

1. Using two high-speed cameras placed orthogonally, the coalescence process was seen to be practically axisymmetric over the time duration of interest. Accordingly, the experimental data matched simulations based on an axisymmetric coordinate system.
2. For the coalescence configuration studied, recoil of the merged drop away from the surface was observed. The first instant of recoil was 8.05 ms, lasting for around 6.9 ms with a recoil height of 1.05 mm, in agreement with numerical simulation. Internal pressure variations in the drop were seen to correlate with interface curvature and explained the origin of recoil.
3. The instantaneous changes in bulge and footprint radii matched numerical simulations. Neck formation was momentary till recoil and showed some departure from simulation data, suggesting possible three dimensionality in the early stages of coalescence.
4. The dynamic contact angle variation lost correlation with the contact line velocity in the inertia-surface tension (I-S) regime. The correlation was restored in the inertia-viscous (I-V) regime when the drop response was oscillatory in time.
5. Energy analysis showed changes in surface curvature as the primary factor contributing to changes in kinetic and gravitational energy. Energy was largely dissipated due to motion of the contact line and to a smaller extent in the form of viscous dissipation in the bulk.

List of symbols

A	Gas–liquid interface area (m^2)
Bo	Bond number $\left(= \Delta\rho g R^2/\sigma\right)$
Ca	Capillary number $\left(= \mu U_{cl}/\sigma\right)$
Cn	Cahn number $\left(= \varepsilon_{pf}/d\right)$
d	Diameter (m)
E^*	Excess surface energy
E	Energy rate (W)
$f_H(z)$	Hoffman's function
$f_{HI}(z)$	Inverse Hoffman's function
Fr	Froude number $\left(= U^2/gR\right)$
g	Acceleration due to gravity (m^2/s)
L	Capillary length scale $\left(= r\sin\theta_e\right)$ (m)
m	Mass (kg)
Oh	Ohnesorge number $\left(= \mu/\sqrt{\rho R\sigma}\right)$
p	Pressure (N/m^2)
p_{atm}	Atmospheric pressure (N/m^2)
Δp	Pressure difference $\left(= p_1 - p_2\right)$ (N/m^2)
r	Radius (m)
R, R_b	Footprint radius $\left(= r\sin\theta_e\right)$ (m)
R^*	Radius ratio $(= R_1/R_2)$
R_{avg}	Average radius (m)
Re	Reynolds number $(= \rho UR/\mu)$
R_1	Local curvature (m^{-1})
R_n	Neck radius (m)
t	Characteristic timescale (s)
U	Velocity scale $\left(= \sqrt{\sigma/\rho R}\right)$ (m/s)
U_{cl}	Contact line velocity (m/s)
V	Drop volume $\left[= \pi r^3(2 - 3\cos\theta_e + \cos^3\theta_e)/3\right]$ (m^3)
We	Weber number $\left(= \rho RU^2/\sigma\right)$
x, y	Instantaneous position of the points located on the liquid–air interface (m)
y_c	Instantaneous vertical position of the centroid (m)
z	Parameter

Greek letters

χ	Mobility tuning parameter (m-s/kg)
ε_{pf}	Parameter controlling interface thickness (m)
γ	Mobility $\left(= \chi\varepsilon_{pf}^2\right)$ (m^3-s/kg)
θ_{adv}	Advancing contact angle (Radians)
θ_d	Dynamic contact angle (Radians)
θ_e	Equilibrium contact angle (Radians)
θ_{rcd}	Receding contact angle (Radians)
μ	Dynamic viscosity (Pa-s)
ρ	Density (kg/m^3)
σ	Surface tension (N/m

Subscript

1, 2	Drop placed on the substrate and the one above it
3	Combined drop
CL	Contact line dissipation
g	Gravitational energy rate

Supplementary Information The online version contains supplementary material available at https://doi.org/10.1007/s00348-022-03394-w.

Acknowledgements Financial support for colleagues from India was provided by the Department of Science & Technology, India from an Indo-Russian Project (DST/ME/2018193) and is gratefully acknowledged. Financial support for colleagues from Russia was received from the Russian Science Foundation (Project No. 21-79-10373). Measurement of the wetting angle of the substrate is performed under state contract with IT SB RAS.

Declarations

Conflict of interest The authors declare that they have no conflict of interest.

References

Aarts DGAL, Lekkerkerker HNW, Guo H, Wegdam GH, Bonn D (2005) Hydrodynamics of droplet coalescence. Phys Rev Lett 95:164503

Abouelsoud M, Li X, Peng L, Bai B (2018) Crown behavior during a concentric collision of a falling droplet onto a sessile droplet. Exp Fluids 59:162

Ajaev VS, Kabov OA (2017) Heat and mass transfer near contact lines on heated surfaces. Int J Heat Mass Transf 108(Part A):918–932

Ajaev VS, Kabov OA (2021) Levitation and self-organization of droplets". Annu Rev Fluid Mech 53:203–225

Andrieu C, Beysens DA, Nikolayev VS, Pomeau Y (2002) Coalescence of sessile drops. J Fluid Mech 453:427–438

Cassie ABD, Baxter S (1944) Wettability of porous surfaces. Trans Faraday Soc 40:546–551

Castrejón-Pita JR, Betton ES, Kubiak KJ, Wilson MCT, Hutchings IM (2011) The dynamics of the impact and coalescence of droplets on a solid surface. Biomicrofluidics 5:014112

Cha H, Xu C, Sotelo J, Chun JM, Yokoyama Y, Enright R, Miljkovic N (2016) Coalescence-induced nanodroplet jumping. Phys Rev Fluids 1:064102

Chu F, Li S, Ni Z, Wen D (2020) Departure velocity of rolling droplet jumping. Langmuir 36(14):3713–3719

Cox R (1986) The dynamics of the spreading of liquids on a solid surface Part 1. Viscous flow. J Fluid Mech 168:169–194

Duchemin L, Eggers J, Josserand C (2003) Inviscid coalescence of drops. J Fluid Mech 487:167–178

Estes KA, Mudawar I (1995) Correlation of Sauter mean diameter and critical heat flux for spray cooling of small surfaces". Int J Heat Mass Transf 38(16):2985–2996

Fedorets AA, Gabyshev DN, Marchuk IV, Kabov OA (2020) Droplets jump at the cluster coalescence with the locally heated liquid layer. Interfacial Phenomena and Heat Transfer 8(4):337–343

Fil BEI, Kini G, Garimella S (2020) A review of dropwise condensation: Theory, modeling, experiments, and applications. Int J Heat Mass Transf 160:120172

Hoffman RL (1975) A study of the advancing interface. I. Interface shape in liquid-gas systems. J Colloid Interf Sci 50(2):228–241

Jaiswal A, Khandekar S (2021) Dynamics of a droplet impacting a sessile droplet on a superhydrophobic surface: role of boundary conditions during droplet placement. J Flow Visualiz Image Process 28(4):69–89

Kabov OA, Zaitsev DV, Kirichenko DP, Ajaev VS (2017) Interaction of levitating microdroplets with moist air flow in the contact line region. Nanoscale Microscale Thermophys Eng 21(2):60–69

Khandekar S, Muralidhar K (2014) Dropwise condensation on inclined textured surfaces. Springer Briefs in Thermal Engineering and Applied Science. Springer, New York

Kim YH, Yoo B, Anthony JE, Park SK (2012) Controlled deposition of a high-performance small-molecule organic single-crystal transistor array by direct ink-jet printing. Adv Mater 24(4):497–502

Kistler SF (1993) Hydrodynamics of wetting. In: Berg JC (ed) Wettability. Marcel Dekker, New York

Kumar M, Bhardwaj R, Sahu K (2020) Coalescence dynamics of a droplet on a sessile droplet. Phys Fluids 32:012104

Lee MW, Kang DK, Yoon SS, Yarin AL (2012) Coalescence of two drops on partially wettable substrates. Langmuir 28(8):3791–3798

Li R, Ashgriz N, Chandra S, Andrews JR, Drappel S (2010) Coalescence of two droplets impacting a solid surface. Exp Fluids 48:1025–1035

Liu C, Zhao M, Zheng Y, Cheng L, Zhang J, Tee CATH (2021) Coalescence-induced droplet jumping. Langmuir 37(3):983–1000

Narhe R, Beysens D, Nikolayev VS (2004) Contact line dynamics in drop coalescence and spreading. Langmuir 20(4):1213–1221

Perumanath S, Borg MK, Chubynsky MV, Sprittles JE, Reese JM (2019) Droplet coalescence is initiated by thermal motion. Phys Rev Lett 122:104501

Plog J, Jiang Y, Pan Y, Yarin AL (2021) Coalescence of sessile droplets driven by electric field in the jetting-based 3D printing framework. Exp Fluids 62:56

Ristenpart WD, McCalla PM, Roy RV, Stone HA (2006) Coalescence of spreading droplets on a wettable substrate. Phys Rev Lett 97:064501

Sankaran A, Wu J, Granda R, Yurkiv V, Mashayek F, Yarin AL (2021) Drop impact onto polarized dielectric surface for controlled coating. Phys Fluids 33:062101

Schweikert K, Sielaff A, Stephan P (2019) On the transition between contact line evaporation and microlayer evaporation during the dewetting of a superheated wall. Int J Thermal Sci 145:106025

Schweikert K, Sielaff A, Stephan P (2019b) Heat flux during dip-coating of a superheated substrate. Interf Phenom Heat Transf 7(3):269–281

Somwanshi PM, Muralidhar K, Khandekar S (2018) Coalescence dynamics of sessile and pendant liquid drops placed on a hydrophobic surface. Phys Fluids 30:092103

Somwanshi PM, Muralidhar K, Khandekar S (2020) Coalescence of vertically aligned drops over a superhydrophobic surface. Phys Fluids 32:052106

Somwanshi PM, Muralidhar K, Khandekar S, Vyacheslav C (2020b) Mixing and wall heat transfer during vertical coalescence of drops placed over a superhydrophobic surface. Interf Phenom Heat Transf 8(3):207–224

Thoroddsen ST, Takehara K, Etoh TG (2005) The coalescence speed of a pendent and a sessile drop. J Fluid Mech 527:85–114

Wang K, Ma X, Chen F, Lan Z (2021) Effect of a superhydrophobic surface structure on droplet jumping velocity. Langmuir 37(5):1779–1787

Wang Y, Ming P (2019) Dynamic and energy analysis of coalescence-induced self-propelled jumping of binary unequal-sized droplets. Phys Fluids 31:122108

Wasserfall J, Figueiredo P, Kneer R, Rohlfs W, Pischke P (2017) Coalescence-induced droplet jumping on superhydrophobic surfaces: Effects of droplet mismatch. Phys Rev Fluids 2:123601

Wu M, Cubaud T, Ho C-M (2004) Scaling law in liquid drop coalescence driven by surface tension. Phys Fluids 16:L51–L54

Yin C, Wang T, Che Z, Jia M, Sun K (2019) Critical and optimal wall conditions for coalescence-induced droplet jumping on textured superhydrophobic surfaces. Langmuir 35(49):16201–16209

Yue P, Zhou C, Feng JJ (2010) Sharp-interface limit of the Cahn-Hilliard model for moving contact lines. J Fluid Mech 645:279–294

Yurkiv V, Yarin AL, Mashayek F (2018) Modeling of droplet impact onto polarized and nonpolarized dielectric surfaces. Langmuir 34:10169–10180

Zhang FH, Li EQ, Thoroddsen ST (2009) Satellite formation during coalescence of unequal size drops. Phys Rev Lett 102:104502

Publisher's Note Springer Nature remains neutral with regard to jurisdictional claims in published maps and institutional affiliations.

Applied Thermal Engineering 205 (2022) 117932

Contents lists available at ScienceDirect

Applied Thermal Engineering

journal homepage: www.elsevier.com/locate/ate

Research paper

The multiscale boiling investigation on-board the International Space Station: An overview

A. Sielaff [a,*], D. Mangini [b,1], O. Kabov [c], M.Q. Raza [d], A.I. Garivalis [e], M. Zupančič [f], S. Dehaeck [g], S. Evgenidis [h], C. Jacobs [i], D. Van Hoof [i], O. Oikonomidou [h], X. Zabulis [j], P. Karamaounas [j], A. Bender [a], F. Ronshin [c,k], M. Schinnerl [a], J. Sebilleau [d], C. Colin [d], P. Di Marco [e], T. Karapantsios [h], I. Golobič [f], A. Rednikov [g], P. Colinet [g], P. Stephan [a], L. Tadrist [k]

[a] Institute for Technical Thermodynamics, Technische Universität Darmstadt, Alarich-Weiss-Str. 10, 64287 Darmstadt, Germany
[b] cosine measurement systems B.V., Oosteinde 36, 2361 HE Warmond, The Netherlands
[c] Kutateladze Institute of Thermophysics, Lavrentyev Prospekt, 1, Novosibirsk, 630090, Russia
[d] Université de Toulouse, Institut de Mécanique des Fluides de Toulouse (IMFT), 2 Allée du Professeur Camille Soula, 31400 Toulouse, France
[e] University of Pisa, DESTEC, Largo Lucio Lazzarino 1, 56122 PISA, Italy
[f] University of Ljubljana, Faculty of Mechanical Engineering, Askerceva 6, SI-1000, Ljubljana, Slovenia
[g] Université libre de Bruxelles, TIPs Laboratory, CP 165/67, Av. F.D. Roosevelt 50, 1050 Brussels, Belgium
[h] Department of Chemical Technology and Industrial Chemistry, Faculty of Chemistry, Aristotle University, University Box 116, 541 24 Thessaloniki, Greece
[i] Belgian User Support and Operations Centre (B.USOC), Ringlaan 3, 1180 Brussels, Belgium
[j] Institute of Computer Science, Foundation for Research and Technology, Hellas, N. Plastira 100 Vassilika Vouton, 700 13, Heraklion, Crete, Greece
[k] Aix Marseille Université, CNRS, Laboratoire IUSTI, UMR 7343, 13453 Marseille, France

ARTICLE INFO

Keywords:
Multiscale boiling
Shear flow
Electric field
Pool boiling
International space station
Microgravity

ABSTRACT

This publication lays the foundation for the description of the Multiscale Boiling Experiment, which was conducted within two measurement campaigns on the International Space Station between 2019 and 2021. The experiment addresses fundamental questions about two-phase heat transfer during boiling processes. For this purpose, single or few subsequential bubbles are selectively ignited on a heated substrate using a short laser pulse. A detailed investigation of the phenomena is possible, as the boiling process is temporally slowed down and spatially enlarged in microgravity. Within the Multiscale Boiling Project, the undisturbed growth of the bubbles, the influence of a shear flow, and the influence of an electric field are investigated within the same test facility using FC-72 as working fluid. Within the project, thirteen research groups from eight countries are collaborating. Over 3000 data sets have been generated over an 11-month measurement period. In the context of this publication, besides the motivation and necessity of such investigations, the basic structure of the experiment, the objectives of the investigations, and the organization are described. Finally, first results of the investigations are presented. Therefore, this publication has the primary aim to serve as a basis for many further planned publications and present the project as a whole.

1. Introduction and motivation

Boiling is a process used in many engineering fields such as energy conversion, environmental applications, food and chemical process industries, and the space sector. It is also encountered in the natural environment, such as geothermal water, geysers, and volcanoes. As a result, there is a great diversity of situations in which boiling processes are present and must be well understood and better controlled. Pioneering work in the field of boiling goes back to Nukiyama's work in 1934 [1]. Nukiyama initially proposed the boiling curve. This curve characterizes the heat transmitted from the heated wall to the boiling liquid as a function of the wall superheat and allows the link between the heat transfer and the boiling regimes. Since then, a huge number of publications were proposed in literature. The majority of the studies are experimental, having an empirical character because of the complexity of the mechanisms. These are, next to others, the heat transfer coupling, nucleation, bubble dynamics, natural convection, evaporation, quenching, condensation, contact line dynamics, wettability, thermocapillary,

* Corresponding author.
E-mail address: sielaff@ttd.tu-darmstadt.de (A. Sielaff).
[1] Former: HE Space Operations BV, Huygensstraat 44, 2201 DK, Noordwijk, The Netherlands.

https://doi.org/10.1016/j.applthermaleng.2021.117932
Received 31 August 2021; Received in revised form 23 November 2021; Accepted 8 December 2021
Available online 1 January 2022
1359-4311/© 2022 The Authors. Published by Elsevier Ltd. This is an open access article under the CC BY-NC-ND license (http://creativecommons.org/licenses/by-nc-nd/4.0/).

Nomenclature

Symbols

a	thermal diffusivity ($m^2\ s^{-1}$)
C	curve
cg	center of gravity
c	constant
d	diameter (m)
E	electric field intensity ($V\ m^{-1}$)
Q	flow rate ($mL\ min^{-1}$)
F	force (N)
g	gravity ($m\ s^{-2}$)
Δh_v	heat of evaporation ($J\ kg^{-1}\ K^{-1}$)
h	height (m)
I	image
k	thermal conductivity ($W\ m^{-1}\ K^{-1}$)
Nu	Nusselt number
p	pressure (bar)
Pr	Prandtl number
$\dot{q}$	heat flux ($W\ m^{-2}$)
r	radius (m)
R_a	roughness average (μm)
R_z	mean roughness depth (μm)
T	temperature (K)
t	time (s)
U	voltage (V)
V	volume (m^3)

Greek Symbols

α	heat transfer coefficient ($W\ m^{-2}\ K^{-1}$)
β	contact angle (°)
ρ	density ($kg\ m^{-3}$)
σ	surface tension ($N\ m^{-1}$)

Subscripts

ap	apex
b	bubble
bf	bubble foot
dep	departure
elec	electrode
eq	equivalent
gr	growth rate
l	liquid
L	left
lp	laser pulse
mtcr	micro thermocouple rack
on	switching on
off	switching off
R	right
sat	saturation
sub	subcooling
set	set point
v	vapor
w	wall
wait	waiting time
x	x-direction
y	y-direction

and nonequilibrium effects. In most cases, the authors provide characteristic curves of the heat transfer and correlations for applications such as the design of evaporators, steam generators, thermosiphons, and heat pumps. Among these studies, several authors have proposed correlations for evaluating the heat flux density based on the thermo-physical properties of the fluid and the wall (see, for example, Forster and Zuber [2], Forster and Greif [3], Kutateladze [4], Rohsenow [5], Han and Griffith [6], Cooper [7], Stephan and Abdelsalam [8], Gorenflo [9]). The correlations for the evaluation of the heat transfer coefficient, as a function of fluid properties, heat flux, and wall properties, are mostly valid only in the same range of parameters. Dhir [10] emphasized that the correlations' usefulness diminishes very rapidly as parameters of interest start to fall outside the range of physical parameters, for which the correlations are developed. An extrapolation of these relations is not possible or is subjected to significant uncertainties. The massive number of physical phenomena governing the heat and mass transfer process restricts these equations' usability. Two of the most well-known equations for predicting heat transfer can be considered as examples. While the Stephan–Preußer [11] equation (see Eq. (1)) calculates the heat transfer directly from material and process parameters, the Gorenflo equation [9] uses a comparison value estimating the corresponding influences of changing properties (such as for heat flux or pressure). It is also noticeable that the Gorenflo equation does not include the influence of gravity. The Stephan–Preußer equation does not consider the heater material and its shape, which is of great importance for Gorenflo. Despite the effects not considered in the corresponding equations, the already large number of influencing factors underlines the complexity in the prediction and description of boiling processes. Therefore, any study permitting to isolate each factor as much as possible and to look at it from a fundamental point of view would be of great value.

$$Nu = 0.0871 \left(\frac{\dot{q}\, d_b}{k_l\, T_{sat}}\right)^{0.674} \left(\frac{\rho_v}{\rho_l}\right)^{0.156} \left(\frac{\Delta h_v {d_b}^2}{{a_l}^2}\right)^{0.371} \times \left(\frac{{a_l}^2 \rho_l}{\sigma d_b}\right)^{0.350} Pr_l^{-0.162} \tag{1}$$

$$Nu = \frac{\alpha d_b}{k_l} \tag{2}$$

$$\alpha = \frac{\dot{q}}{(T_w - T_{sat})} \tag{3}$$

$$d_b = 0.0149\, \beta \left(\frac{2\sigma}{g\,(\rho_l - \rho_v)}\right)^{0.5} \tag{4}$$

In Eq. (1), Nu is the Nusselt number defined in Eq. (2), α the heat transfer coefficient defined in Eq. (3), $\dot{q}$ the heat flux density, d_b the bubble departure diameter defined in Eq. (4), k_l the liquid thermal conductivity, T_{sat} the saturation temperature, T_w the wall temperature, ρ_v and ρ_l the vapor and liquid densities, respectively, σ the surface tension, g gravitational acceleration, Δh_v the heat of evaporation, a_l the liquid thermal diffusivity, Pr_l the liquid Prandtl number, and β the contact angle in degree.

1.1. Boiling in microgravity

As stated in the previous section, the physics of the boiling process is still poorly understood because of the complexity of the phenomena involved. At first glance, one might therefore assume that the primary purpose of boiling studies in microgravity would be building correlations for future space applications like cryogenic fuel storage, propulsion, life support systems, and cooling systems, comparable to

the correlations experimentally investigated under earth gravity. A simple comparison shows that these existing equations are not suitable for reduced gravity (beyond their previously described limitations). If one changes the gravity in the two equations mentioned above with respect to any reference value, the Gorenflo equation shows no influence of gravity at all. The Stephan–Preußer equation shows a $\alpha \propto g^{-0.101}$ relationship, while the correlation of Raj et al. [12], developed especially for variable gravity, shows a $\alpha \propto g^{0.196}$ relationship (for a nondimensional wall temperature of 0.5), having a completely different trend.

The creation of such correlations is a pronounced goal, especially regarding later technical applications. However, on more detailed consideration, the experimental investigation of boiling processes under microgravity offers far greater potential. A microgravity environment can allow a better comprehension of the underlying phenomena in the boiling process. Gravity tends indeed to make the understanding of the boiling process extremely complex for several reasons. First of all, the thermally-driven buoyancy flows overshadow other important physical phenomena such as thermo-capillary flows, bubble-induced convection, and transient thermal diffusion, to cite a few. Such phenomena are not only surpassed by the thermally driven buoyancy flows, but they are also intrinsically coupled with them. Such a coupling effect is highly non-linear. As such, the unique possibility of a better comprehension of all the physical phenomena that are masked by gravity is only possible if the overall physical process is studied and analyzed in microgravity. Moreover, considering that the gas and liquid densities differ by several orders of magnitude, hydrostatic stresses cause vertically-orientated forces. The vapor/liquid interface can also be distorted if the hydrostatic pressure gradients are comparable or exceed surface tension stresses. Microgravity thus can clarify the evaluation and the understanding of natural stresses (e.g., static pressure, capillarity), and/or imposed stresses (e.g., shear, electrostatic) on the boiling process. Moreover, microgravity tends to slow down and enlarge phenomenological events. When gravity dominates, the bubble departure and interface instabilities tend to occur at time and length scales that strain the capabilities of scientific measurement equipment. A microgravity environment exposes boiling phenomena in such a way that facilitates higher temporal and spatial resolution, offering more in-depth insight into underlying physics.

Next to the design of two-phase heat transfer systems for space applications, the scientific potential of investigating boiling processes in microgravity led to the start of such investigations as soon as the technical conditions were met. Most of the low gravity experiments were initiated using ground-based facilities like drop towers (e.g., [13]). Since the end of the 1980s, next to drop tower experiments, experiments were carried out using short-duration microgravity facilities like parabolic flights (e.g., [14–18]), and sounding rockets (e.g., [19–21]). In the 90's, the shuttle was used to perform experiments [22,23]. Further research had been performed within a SJ-8 [24] or Foton [25] satellite. In addition, two pool boiling and one flow boiling experiment could already be carried out on-board the International Space Station (ISS) [26–28]. All previous space experiments have already demonstrated a significant influence of gravity on the boiling process. In spite of the great potential, the study of boiling processes in microgravity also brings particular technical challenges. In order to be able to investigate the phenomena mentioned above in the best possible way, a single bubble or several bubbles should be able to grow as undisturbed as possible in a defined far field. In addition, a measurement technique with a high spatial and temporal resolution is necessary. For the performance of several successive experiments, it is necessary to remove the bubbles from the experimental area or to recondense them. Furthermore, especially in microgravity, disturbances can also occur due to uncontrolled nucleation and subsequent coalescence of several bubbles. Hence, this has to be controlled by the chosen experimental setup. For more extended test periods, it is also necessary to remove the bubbles from the heating surface during the test, since otherwise the complete test area will be covered with vapor after a particular time, which will lead to a significant influence of the heater size, geometry, and experimentation time on the heat transfer [27]. The implementation and the realization of the described conditions are primarily influenced and limited by the chosen test platform. Therefore, the available platforms will be briefly discussed in the following.

1.2. Microgravity platforms: The International Space Station as a research tool for pool boiling experiments

Several platforms are currently available to carry out experiments in weightlessness, or reduced gravity [29]. Common to all platforms is that an experimental container is exposed to a free fall for a given time. Next to others, this free fall can be achieved in a drop tower, a parabolic flight, a rocket, various satellites, or installing the experiment onboard the International Space Station. However, the platforms differ significantly in the experiment's permissible size, the accessibility during the investigation, possible data transfer, the duration of microgravity, and its quality. In Fig. 2 the different platforms are compared in terms of microgravity quality and duration. One of the most common platforms is a drop tower. For example, the ZARM at the University of Bremen (Germany) has a drop tower with a height of about 120 m, from which a capsule with an experimental setup is dropped. To increase the duration of the experiments, a catapult that shoots the capsule upwards can be used. In this case, the duration of microgravity is up to 9.2 s. Another ground-based platform used for performing tests at different gravity levels is a parabolic flight. As in the drop tower, the experimental setup is in free fall. One parabolic maneuver lasts about one minute. During the parabolic maneuver, the acceleration value changes from normal to increased (1.8 g to 2 g) for about 20 s, then microgravity (1×10^{-2} g) sets in for approximately 20 s, after that, within 20 s, the flight takes place at an increased acceleration value (1.8 g to 2 g) to recover to normal flight. A unique feature of this platform is that the scientists are in the aircraft at the same time and can directly interact with the experiment. In addition, all gravity levels between 0 g to 1 g can be set, extending the reduced gravity duration. Sounding rockets represent another possible platform for performing tests in microgravity, allowing up to 13 consecutive minutes of microgravity (MAXUS type Sounding Rocket). Commands are sent to the equipment located inside the rocket directly during the experiment. The residual acceleration in microgravity is less than 1×10^{-4} g. Satellites and shuttles were also used to conduct experiments in microgravity. The experiment duration is generally much longer than for sounding rockets. Other circumstances, such as data transfer, depend highly on the respective mission. Space Stations are high-end platforms for many different experiments. Experiments are carried out on the International Space Station (since 1998) and Mir station (1986–2001). Another space station is planned to be launched in 2021 — the China Large Modular Space Station. The European Space Agency has integrated the research module Columbus within the International Space Station in February 2008 including ready-to-experiment workbenches, like the hydrodynamic research stand (Fluid Science Laboratory — FSL). The residual acceleration measures about 1×10^{-4} g and could even be less depending on the vibrational frequencies [30]. A constant data transfer is possible in both directions, so that even during a campaign the test execution can be influenced based on the prior measurement results. (See Fig. 1).

1.3. Research and publication objectives

The boiling processes to be investigated take place under microgravity for several seconds. Times for setting the process parameters are in the range of several minutes. To cover a sufficient parameter range, microgravity of a long duration is therefore necessary. The required high-resolution measurement techniques will generate a vast amount of data. In order to influence the further course of the measurement based on initial results during the experimental campaign, these data

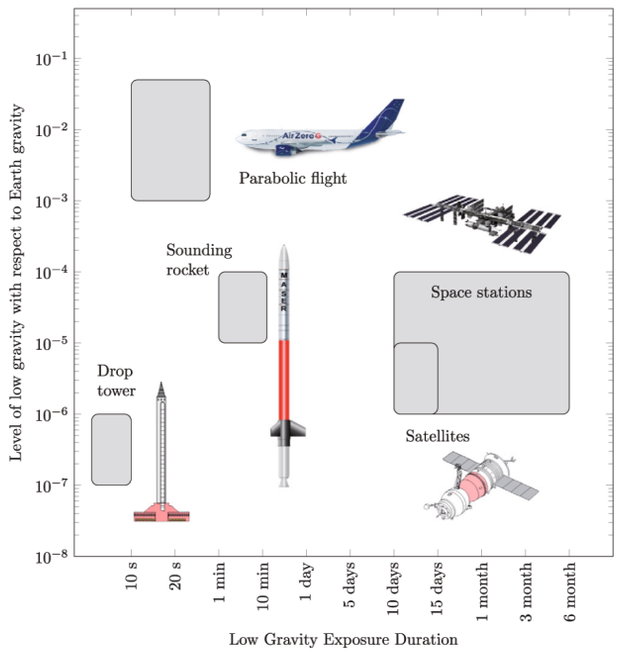

Fig. 1. Comparison of gravity levels (relative to Earth gravity) and their durations for different microgravity platforms.

must be transferred to Earth throughout the campaign, which requires an appropriate communication platform. Finally, the quality of microgravitation must be good enough to exclude any significant interference from the experimental platform. Hence, the International Space Station was chosen as the ideal experimental platform for this project because it fulfills all major requirements mentioned above.

The Multiscale Boiling Experiment investigates a single or a low number of several bubbles under microgravity conditions. A complex diagnostic system, with synchronized infrared (IR) and high-speed black and white (BW) imaging, should lead to a better comprehension of the overall process and is intended to contribute to an authoritative database for the validation of numerical models. The removal of vapor above the heated surface, which is essential for more extended technical use, can be done in microgravity through shear flow or electric field. These techniques will not only be used in this project but will be investigated for the first time under such conditions. Furthermore, a direct comparison to boiling with and without these external forces is possible.

As described in the previous section, many questions remain unanswered despite much previous work on boiling, in normal and microgravity conditions. To contribute to the clarification, the Multiscale Boiling Project (also known as RUBI) has been started in 2005. Supported by several preliminary works in the laboratories of the participating institutions as well as on parabolic flights (e.g. Nejati et al. [31]), Airbus DS could complete the development and setup of the experiment in 2019. Afterward, the experiment was launched towards the ISS on July, 25th 2019, where it became operational on September, 6th 2019.

In this publication, the project will be presented as a whole for the first time. In the following, the detailed objectives of the project, as well as the organization (Section 2), will be presented. The experimental setup, the execution of the experiment, and the evaluation will be described in detail. More detailed descriptions, for example, of the individual evaluations, will be described in dedicated publications in the future, as this would go beyond the scope of a single publication. Section 4 gives a first insight into the scientific results of the project.

2. The multiscale boiling experiment

2.1. Objectives

The objectives of the Multiscale Boiling Project can be divided into six groups. While the first four objectives had been investigated within the described experimental setup, this was unfortunately not possible for objectives five and six due to technical limitations. Therefore, they will not be further discussed. These objectives will be investigated in the future as part of the project.

Objective 1: *Observation of the contact line behavior on single bubbles*

From many previous investigations, it is known that the contact area between the heated surface, vapor, and liquid contributes significantly to the heat transfer during boiling and thus has a significant influence on the process. Due to the slowed growth in weightlessness, micro-scale effects in this area can be investigated in detail. In particular, the wall temperature and its distribution, the contact angle of the bubble, and the heat flux density that is transferred are to be mentioned.

Objective 2: *Observation of individual bubble growth*

During bubble boiling, the applied heat causes the liquid in the superheated area near the wall to evaporate and accumulate in bubbles due to surface tension. Thus, a single bubble represents an elementary cell of boiling. The life cycle of a bubble consists of nucleation, growth rates, and departure. The aim is to investigate the heat and mass transport concerning the individual life phases in more detail. Also, the influences of Marangoni convection and non-condensable gases are to be examined more closely. Nucleation, growth, and departure of a bubble are subject to a wide variety of force influences. The dominant factor of gravity in ground experiments can be eliminated in this investigation. For the observation of single bubbles' growth, the external forces of a shear flow and an electric field are, therefore, in the foreground in this aspect.

Objective 3: *Influence of an electric field*

An electrode placed above the nucleation site is supplied with a high voltage source. A sufficiently strong electric field can affect bubble growth rates, shapes and heat flux densities. Besides, an electric field can also cause a movement or a departure of the entire bubble, making the technology a possible substitute for gravity. In this sub-area, the influences of the electric field must be comprehensively investigated.

Objective 4: *Influence of a Shear flow*

Like with an electric field, an external force can also be applied to a bubble by shear flow. Furthermore, a shear flow has a significant influence on the thermal boundary layer in which a bubble grows. Both effects are also superimposed by the force of gravity in ground experiments. This section aims to investigate significant phenomena between shear flow, thermal boundary layer, and bubble growth.

Objective 5: *Single bubbles in binary mixtures*

The influence of a second or even more components is significant in the boiling process. In the area of the highest heat and mass transfer, a concentration of less volatile components occurs, and thus the material properties at the microscale level show significant differences. This subarea aims to investigate the influence on heat flow and bubble growth. Since a fluid change is not possible on the International Space Station due to technical limitations, this goal will be achieved by the already mentioned additional parabolic flights and further ground experiments.

Objective 6: *Influence of bubble interaction*

As clarified in Objective 1, a single bubble represents the boiling process' elementary cell. In technical applications, the growth of several bubbles nearby leads to interaction and coalescence, which significantly influence the boiling process and the heat flux density. Thus, this sub-section represents the largest scale range in the presented investigation and the interface to global studies and correlations. A systematic study of bubble coalescence, similarly to the situation in Objective 5, is not explicitly foreseen in the experimental setup due to the technical limitations. However, spontaneous bubble interactions are used, and further studies will be accomplished in the framework of additional laboratory and parabolic flight experiments.

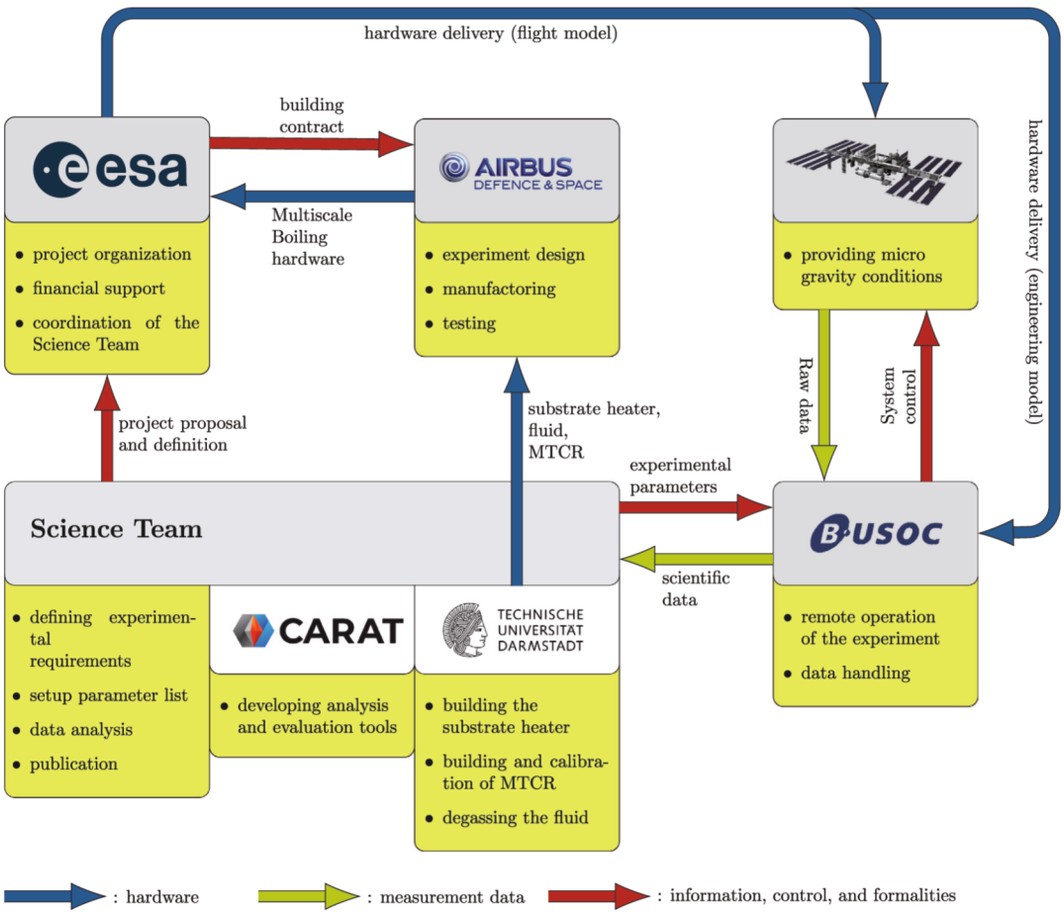

Fig. 2. Organizational structure in the Multiscale Boiling Project.

2.2. Organization

To successfully implement such an ambitious project, good cooperation between different partners is essential. Fig. 2 shows the organizational structure within this project in a simplified form. After the team of scientists developed the idea for this project, a corresponding application for implementation is submitted to the European Space Agency (ESA). After examination and approval, ESA takes over the project organization and provides the necessary financial means. Within the framework of a tender, Airbus Defence and Space was subsequently selected as the industrial partner to build and test the experiment hardware according to the Experimental Scientific Requirements (ESR) defined by the scientists. The heater developed by the TU Darmstadt, which had already been tested in the laboratory and on several parabolic flights, was intended for use onboard the ISS and was therefore provided by the Science Team.

The hardware was designed so as to fit in a so-called experiment container (EC) for the Fluid Science Laboratory (FSL), which is one of the experiment hosting racks in the European Columbus model on the International Space Station. After completing the hardware, the functionality was verified in the Misson Test 1 and the Science Validation Test (SVT) at Airbus. The hardware was handed over to ESA upon the successful completion of these tests. The hardware consisted out of two similar Experiment Containers: one Flight Model (FM) used to conduct the actual experiment in microgravity, and one Engineering Model (EM) used on ground for additional testing, operator training, or in support of anomaly resolution. During the SVT almost 100 experiments were performed on ground with the FM, to compare results achieved with the same hardware at different g-levels. The on-orbit operation, preparation, and execution were performed by the Belgian User Support and Operations Centre (B.USOC) on behalf of ESA. The Multiscale Boiling hardware FM was sent to the International Space Station on a SpaceX Dragon Capsule (SpaceX CRS-18 mission) and installed by the ESA astronaut Luca Parmitano on August, 9th 2019 in the FSL in the Columbus module of the ISS (see Fig. 3). Once the hardware is installed, the entire experiment can be controlled from ground without the intervention of an astronaut. The B.USOC executed the Multiscale Boiling experiment runs based on the parameters defined by the Science Team after commissioning and further testing. The data collected was then converted into readable formats and made available to the scientists for further analysis. The CARAT group was founded to unify the algorithms for evaluation and analysis and to evaluate the massive amounts of data efficiently. Within this group, the corresponding tools are collaboratively created, extended, and validated. They are available to the whole team.

3. Experimental setup, on-orbit calibration, and test execution

3.1. Experimental setup

To achieve the objectives presented in Section 2.1, the experimental setup sketched in Fig. 4 was designed and built. The working fluid is

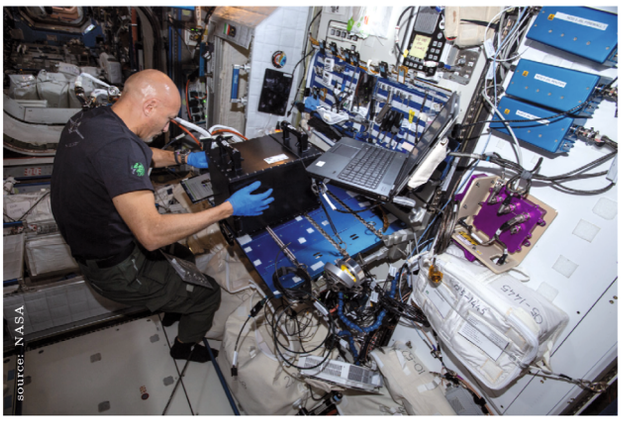

Fig. 3. Luca Parmitano prepares the Multiscale Boiling EC for installation within the FSL.

degassed FC-72 (C_6F_{14}). The test cell consists of an aluminum block thermalized by Peltier elements. In the bottom area of the cell, the infrared transparent heater is installed so that it is leveled with the surrounding cell. The heater consists of a coated barium-fluoride crystal (see Section 3.2). To be able to thermalize the fluid, a preheater and a condenser are used. Both are — like the cell itself — flowed through by a pump. This pump is also used to achieve the objectives shown in Section 2.1, i.e., to apply external forces to a bubble through a shear flow. The flow rate is adjustable and can be controlled by a separate flowmeter. There is a honeycomb in the inlet area of the cell and a flow guide at the inlet and outlet to even out the flow. The use of preheaters and condensers is necessary to adjust the system parameters and protect the pump against cavitation, as the working fluid is used near its saturation point. The size of the cell is designed to measure bubble up to a diameter of 10 mm. The influence of an electric field (see Objective 3) can be examined using the electrode placed centrally above the heater. The electrode has a shape similar to a washer and is continuously adjustable in height between 6 mm to 10 mm (distance from the heater surface). Further, it can be brought to a so-called homing position, fully retracted far away from the heated surface. An additional bellow is included for adjusting the system pressure by increasing or decreasing the system volume accordingly. This makes it easy to investigate different subcoolings at a given fluid temperature. Besides, the bellow is used to condense remaining vapor bubbles after a test by increasing the pressure far above saturation (generally 1.3 bar).

In addition to several pressure and temperature sensors distributed in the setup, and the volume flow sensor mentioned above, the setup contains three primary measuring techniques. A micro thermocouple rack probe (MTCR) consists of four ≤100 µm thick measuring points, to measure the profile of the thermal boundary layer. The MTCR is applied at an angle of 43° (to the boiling surface). The individual measurement points have a distance of 3 mm to each other. Like the electrode, the probe is freely movable in height along its axis with a smallest distance to the heated surface of 0.36 mm (with respect to the lowest of the four measurement tips). For safety reasons, the motion of one actuator is possible solely if the other one is in its homing position. In this way, a possible interference between the MTCR and the electrode is avoided by hardware. The shape of the bubbles is recorded from the side by a black and white high-speed camera. A high-speed infrared camera records the temperature field of the heater at the bottom of the coated layer. From these images, the temporally and spatially resolved heat flux profiles can be calculated (see Section 3.4.2).

Table 1
Operating range and parameters of the experiment.

Test cell		
Pressure (experiments)	500 to 1000	mbar
Pressure (recondensation and thermalization)	500 to 1500	mbar
Temperature	30 to 70	°C
Flow rate	100 to 700	mL min^{-1}
Leakage rate (He)	1.63×10^{-5}	mbar L s^{-1}
Leakage rate (SF6) calculated	2.74×10^{-6}	ppmv/s
Measuring frequency	1	Hz
Heater		
Heat flux	0 to 2	W cm^{-2}
Range with no parasitic nucleation	0 to 1.2	W cm^{-2}
Laser		
Power	177	mW
Pulse duration	0 to 1000	ms
Electrode		
Distance from surface at usage	6 to 10	mm
Voltage	0 to 15	kV
Microthermocouple rack		
Distance from surface at usage	≥ 0.36	mm
Measuring frequency	≤ 10	kHz
High-speed black and white camera		
Used field of view	22.27 × 15.18	mm
Used no. of pixels	1100 × 750	pixel
measuring frequency	≤ 500	Hz
High-speed infrared camera		
Field of view	4.98 × 26.56	mm
No. of pixels	120 × 640	pixel
Measuring wavelength	8 to 14	µm
Measuring frequency	≤ 240	Hz

To create a bubble at a desired time and place, the heater contains a defined cavity in the substrate's middle (see Section 3.2). Secondly, a laser beam is used to overheat the cavity to ignite the first bubble.

A picture of the open experimental container is shown in Fig. 5. In the middle of the picture one can see the boiling cell ① with the electrode above the substrate heater. Above the boiling cell one can see the actuator of the electrode ② and the one of the MTCR ③. Below the boiling cell the infrared camera ④ is mounted, right to the preheater ⑤. On the lower right part the electronics and measurement technique ⑥ can be seen. The black and white camera is located behind the boiling cell and cannot be seen from this perspective.

The operating range of the experiment and relevant operating parameters are shown in Table 1. A very detailed description of the experimental setup and an error estimation is omitted at this point and will be presented in a dedicated future publication.

3.2. Substrate heater

The heater consists of a 5 mm thick barium-fluoride crystal. There is a 2.5 mm chamfer on the upper side, so the surface onto the fluid has a diameter of 20 mm. The crystal is optically transparent in the range of 150 nm to 15 µm wavelength. In the middle of the surface, the crystal contains an L-shaped cavity created by ultrashort pulse laser ablation. The cavity has a diameter of 30 µm and a depth of 200 µm. The lateral length below the surface is 100 µm. The L-shape is chosen to hold a small amount of vapor inside the cavity. Especially for measurements with shear flow and an electric field, when bubble departure is expected, this should enable continuous nucleation on the smooth surface without renewed overheating by the laser. The crystal is first coated with chromium nitride and then with chromium using physical vapor deposition. Both layer thicknesses are about 400 nm. The lower layer (chromium nitride) is used to increase the emissivity to ensure a more accurate temperature measurement with the infrared camera. The upper layer serves primarily as a Joule heater. Besides,

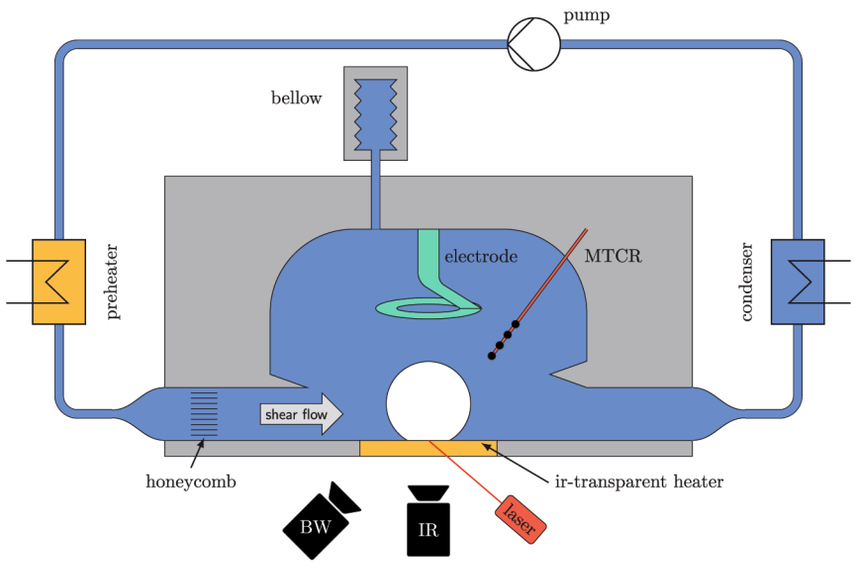

Fig. 4. Schematic of the experimental setup. The black and white camera captures the bubble from the side (image plane of the sketch) with back illumination.

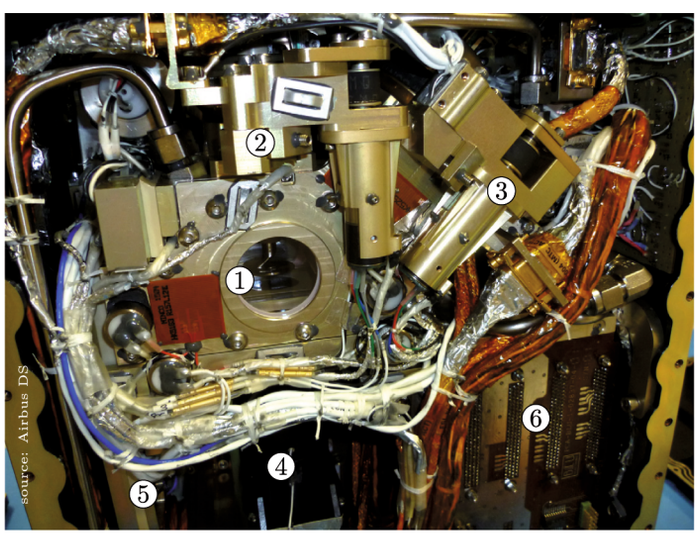

Fig. 5. Picture of the open experimental container. 1: boiling cell with the high voltage electrode above the substrate heater; 2: actuator of the high voltage electrode; 3: actuator of the micro thermocouple rack; 4: infrared camera; 5: preheater; 6: electronics and measurement.

this upper layer increases the overall emissivity of the structure to > 0.9. The surface roughness of the coated heater (with the exception of the cavity) is $R_a < 0.02\,\mu m$ and $R_z < 0.11\,\mu m$ [31]. At the chamfer of the substrate heater, a copper layer is used on each side to reduce the contact resistance and hence avoid parasitic boiling at these positions.

Besides, this layer increases the overall emissivity of the structure to > 0.9. At the chamfer of the substrate heater a copper layer is used on each side to reduce the contact resistance and hence avoid parasitic boiling at these positions.

The coating of the crystal is designed in a tailored form to minimize the probability of parasitic boiling at the edges of the crystal while keeping the heating power in the scientifically interesting area as homogeneous as possible.

To ensure a flat connection to the cell, the crystal is enclosed by a polyetheretherketone (PEEK) cover, which at the same time, transfers the force required to seal the assembly to the crystal. Since the E-modulus of PEEK is too low to provide a flat surface and to apply the necessary force for a sufficient seal, the cover is reinforced with stainless steel rails at the sides. The heater assembly is shown in Fig. 6. As the same setup has already been used in a parabolic flight campaign more details can be found in Nejati et al. [31].

3.3. Test execution

The operations of the first Multiscale Boiling campaign started on September, 6th 2019 and lasted until March 5th 2020. Afterward, a second campaign was performed between October, 15th 2020 and

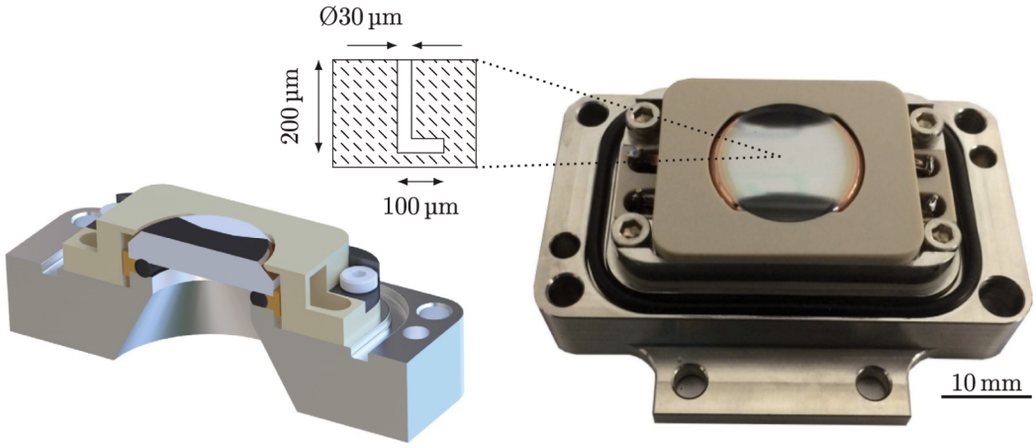

Fig. 6. Assembly of the substrate heater: On the left side without connecting cables. On the right side as picture with an enlargement of the artificial cavity as cut view.

January, 13th 2021. After the initial installation of the hardware and the successful activation, a series of commissioning activities was performed. These included both a functional checkout of the hardware as well as a science commissioning. Part of the functional checkout consisted in collecting a series of reference infrared images at various liquid temperatures, required for the calibration of the high-speed infrared camera. The science commissioning was mainly a repetition of the experiment runs performed during the Science Validation Test campaign on ground. The commissioning activities were successfully completed on September, 23th 2019 and were followed by a science campaign starting on October, 1st 2020. The science runs were monitored and commanded from ground by B.USOC, taking into account the input and requests of the science team. A high level schematic of the end-to-end data flow is presented in Fig. 7. From the experimental container the data are transferred through the Fluid Science Laboratory (FSL) and the Columbus module to the communication system of the ISS. Due to the low altitude of the ISS (approx. 400 km), a permanent direct connection to Earth would only be possible by means of multiple ground stations spread all over the world. Therefore, the signal is transmitted to the ground stations via the Tracking and Data Relay Satellite System (TDRSS) with a geostationary orbit (approx. 40 000 km). NASA sorts the signals and forwards the Columbus Module data to the Columbus Control Center (ColCC) in Oberpfaffenhofen. The ColCC sorts the data according to their affiliation. All data concerning the Multiscale Boiling Experiment is transferred to the B.USOC in Brussels. The B.USOC operators can receive data from the EC as well as send commands to the EC. All participating scientific groups have read-only access via a user home base and can follow the EC data in real time. The duration of the communication is generally less than 1 s for sending a command and receiving the corresponding response by a B.USOC operator.

The execution of the experiment is driven by the Experiment Procedure (EP), a collection of Tool Command Language (TCL) scripts. A custom TCL interpreter residing on the FSL main computer executes the EP. The EP can send commands to the FSL main computer via interface functions and can read telemetry values via a mechanism that links telemetry elements to TCL variables through a monitoring table. The EP can also receive on event telemetry from the EC and FSL subsystems, but also messages from ground. The EP functions can be called directly by dedicated telecommands, or through a text file referred to as parameter table, which allows for the semi-automatic execution of the experiment. The parameter tables are prepared by B.USOC and uplinked to the ISS on regular basis. An experiment is defined by the following parameters: The liquid pressure p_l, the saturation temperature T_{sat}, the subcooling T_{sub}, the heat flux of the substrate heater $\dot{q}$, the electrical voltage applied on the electrode U_{elec}, the flow rate Q, the height of the electrode above the substrate heater h_{elec}, the height of the MTCR above the substrate heater h_{mtcr}, the time between the activation of the substrate heater and the onset of the laser pulse t_{wait}, the duration of the laser pulse t_{lp}.

Concerning the scientific objectives (see Section 2.1) four main categories of experiments are defined within this 10 dimensional parameter space:

- **Pool Boiling:** No flow or electric field is applied. The electrode is at its highest position and the micro-thermocouple rack as close as possible to the substrate heater, i.e. at 0.36 mm above the heater.
- **Shear Flow:** Similar to pool boiling but shear flow is applied.
- **Electric Field:** No flow is applied and the MTCR is at its highest position. The electrode is lowered to a position between 10 mm and 6 mm above the substrate heater.
- **Shear Flow and Electric Field:** Similar to electric field experiments but with active flow.

Fine-tuning. A first phase in the experiment execution was the so-called fine-tuning, where the system characteristics in microgravity are investigated. The liquid cell contains several temperature sensors and auxiliary heaters, which provide a mean to control the temperature of the liquid. Due to the absence of gravity, the setting for these heaters will deviate from the configuration used during ground tests. The needed temperature setpoint and homogeneity to perform a measurement had been set to:

$$|T_l - T_w| \leq 0.5\,\mathrm{K} \tag{5}$$

$$\max(|T_l - T_i|) \leq 0.5\,\mathrm{K} \tag{6}$$

$$|T_l - T_{set}| \leq 0.1\,\mathrm{K} \tag{7}$$

where T_l is the liquid temperature, T_w is the wall temperature, T_i are the temperatures measured by the various temperature sensors inside the liquid, and T_{set} is the desired temperature. In this case the wall temperature T_w describes the temperature of the sensors inside the aluminum housing, and not the temperature of the substrate heater measured by the infrared camera. The liquid temperature, T_l, is calculated as the average value of at least 4 temperature sensors inside the liquid of which one near the inlet, one near the outlet, and two in the stagnant zone. Similarly, the wall temperature, T_w, is calculated as the average of temperature sensors inside the cell housing. Once the

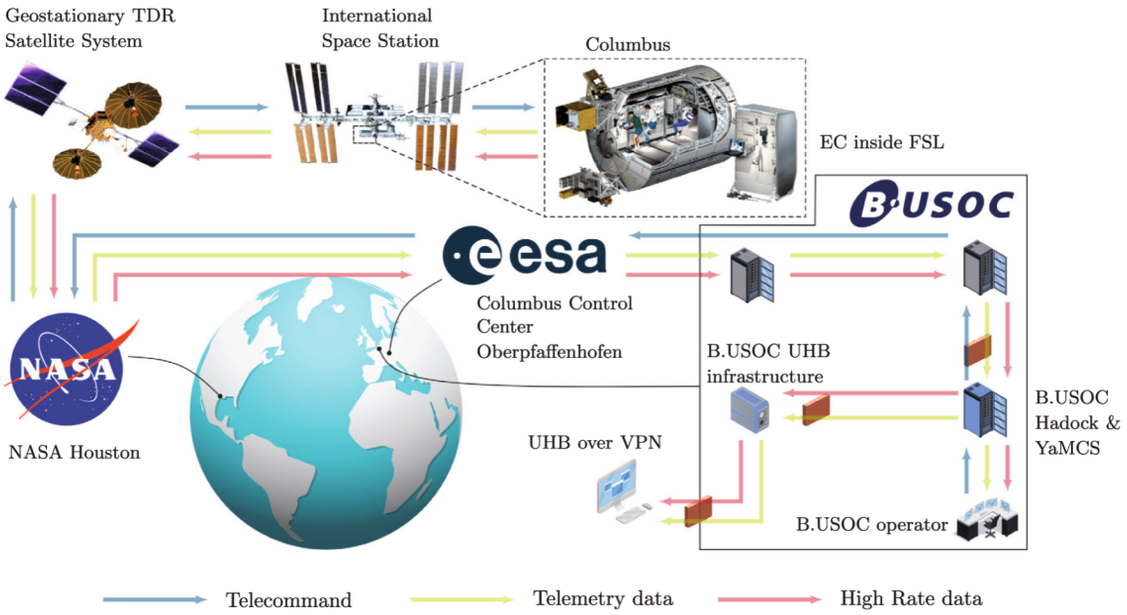

Fig. 7. High level overview of the end-to-end data flow, showing the Telemetry and Telecommand flow and High Rate Data path.

liquid has the desired temperature within the allowed levels of accuracy and homogeneity, the pressure is lowered to the experiment pressure and the substrate heater activated at the desired heat flux level. The laser pulse was activated at 1 s, 2 s, 3 s, 5 s, 10 s, 15 s, 20 s, and 25 s, after the activation of the substrate heater. This was repeated for 3 different values of laser pulse duration, namely 5 ms, 10 ms, and 20 ms. From the results of these tests the science team could narrow down the parameter space of interest and define the final parameters for the science runs.

Science runs. For the first phase of the mission a total number of 674 experiments have been defined, of which 268 pool boiling, 103 shear flow, 255 electric field, and 48 shear flow and electric field. Each experiment has been repeated at least three times. This resulted in a total of more than 2000 runs. During one science run, 5000 black and white images are recorded at 500 frames per second. The recording starts 1s before the laser pulse. In parallel 2400 infrared images are recorded at 240 fps. Temperature data from the MTCR sensors are available at 2000 Hz from the activation of the substrate heater until the end of the experiment, which is typically 9 s after the laser pulse. In total, one science run generates around 6.5 GB of data. This data is stored on the Video Monitoring Unit of the FSL rack and downlinked to ground using the High Rate Data Link at a maximum bandwidth of 32 Mbps. On the black and white images a PNG lossless level 3 compression is applied, reducing the data to 2.5 GB per run. The science data as well as the real-time telemetry (1 Hz housekeeping and health, and status data) are stored on the servers at B.USOC and are available to the science team. During the on-orbit execution some technical problems arised. For most of them a work around could be found not jeopardizing the mission objectives. However, two failures had significant impact on the scientific scope of the experiment: the failure of the high-speed IR camera and the blocking of the MTCR movement. The issue with the MTCR occurred right after the completion of the commissioning, and it was no longer possible to lower the MTCR to the desired position above the substrate heater. The MTCR was then left in the homing position for the rest of the campaign. The infrared camera was lost when 59% of the first mission was completed, with science data already available for all the 4 types of experiments. Within the second mission more than 1000 runs were performed similarly to the first mission with slightly adapted parameters, following the evaluation of the data from the first mission by the science teams. For appr. 50 experiments, the frame rate of the camera was halved in order to double the recording duration. For investigations using an electric field, an additional option was created to switch the electric field on or off during the experiment.

The 10-dimensional parameter space mentioned above can be reduced to 7 parameters for scientific analysis. Pressure and saturation temperature are separated from each other for operational reasons but can be converted into each other for scientific analysis. The height of the MTCR is omitted due to the defect mentioned in Section 3.3 in the early phase of the first campaign. The laser's pulse duration was set to 20 ms after completion of the fine-tuning, with a few exceptions, and is therefore not a variable in the scientific evaluation. The parameters used in both phases in the four main areas of investigation (pool boiling, shear flow, electric field, shear flow + electric field) are summarized in Fig. 8. The different parameters can be seen on the x-axis. The numbers in the individual boxes indicate the corresponding value of the parameter. On the y-axis, the number of runs performed with this value is plotted in stacked form. The coloring of a box shows the percentage distribution of this number among the 4 main areas of investigation.

3.4. Data evaluation

Most of the measured data is provided to the scientists in calibrated form and readable format. Otherwise, the conversion tools required for this purpose are given, or a detailed description is presented to convert the raw data. These include thermocouple and Pt100 temperature measurements, pressure sensor data, gravity data, synchronization data, facility and process parameters, just to name a few. All these data can be obtained by the data streams shown in Fig. 7. For further scientific evaluation, especially the data of the black and white camera as well as the available data of the infrared camera must be subjected to additional post-processing and analysis. These are summarized in the following two sections. Regarding the black and white data, the size and shape of the bubble are in the foreground; regarding the infrared data, the subsequential calculation of the heat flow is of interest.

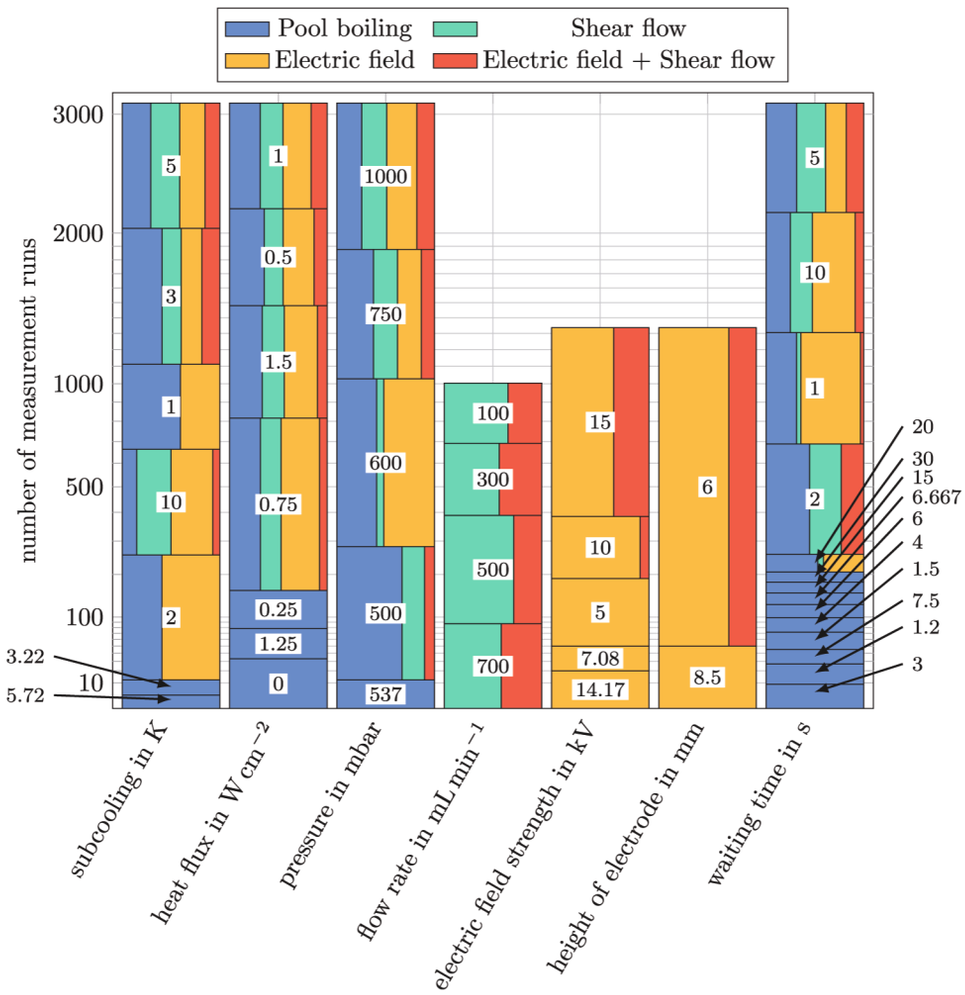

Fig. 8. Distribution of scientific parameters with respect to the four main areas of investigation (pool boiling, shear flow, electric field, shear flow + electric field). Each column is sorted by the amount of measurement taken at the specific parameter (number inside the box).

3.4.1. Black and white images

Images obtained from multiscale boiling experiment include several properties that make the accurate detection of bubbles' contour a challenging image analysis problem. These are:

- Light from the light source can reflect on the bubbles' interface causing specular highlights at the bubbles contour. This can cause a very low contrast at the actual location of bubbles' contour, while reinforcing high gradient at spurious locations.
- Self-reflections of the bubbles and the substrate on the bubbles' surface.
- The superheated fluid layer (especially close to the heated substrate) causes a gradient in the optical refraction index of the fluid. Hence the bubbles' shape can be distorted due to this non-uniform temperature profile of the surrounding liquid.

The steps of applied image processing algorithm are briefly described hereafter. The input to the computation is named image I (Fig. 10(a)). A coarse silhouette (blob) approximation of the bubble is obtained through background subtraction of the current image with the initial frame of the scene (Fig. 10(b)). A curve, C, is fitted to the points of its silhouette contour using least-squares method (Fig. 10(c)). Curve C is either a circle or an ellipse depending on user input and is not related to the real shape of the bubble but rather to its appearance in the image. Due to optical distortion, a spherical bubble that would appear ideally as a circle, may be better approximated in the image by an ellipse. As further clarified below, this choice regards solely the image approximation of the bubble and not the 3D interpretation of this measurement. A coarse-to-fine approach follows to detect the baseline of the bubble, using its reflection. The image row where the baseline occurs is initially localized at the bottom of the silhouette contour. A local optimization refines this localization, measuring vertically the symmetry in image intensities above and below the candidate image row b_c. The sum of absolute differences across the corresponding pixels as defined from the reflection of each candidate row, is used as the cost function. Contact points estimates, p and q, are initially guided by the intersections of C with row b_c. The Harris operator [32] is computed in their neighborhoods and the strongest local maximum in each of them is found. The final baseline row, b, is the average of the y-coordinates of these maxima (Fig. 10(d)).

The contour of the bubble is then detected. The region surrounding curve C is warped in a rectangular polar image V, where columns correspond to the circumference of C. According to the chosen C shape, circle or ellipse, this region is respectively an annulus or an elliptical ring.

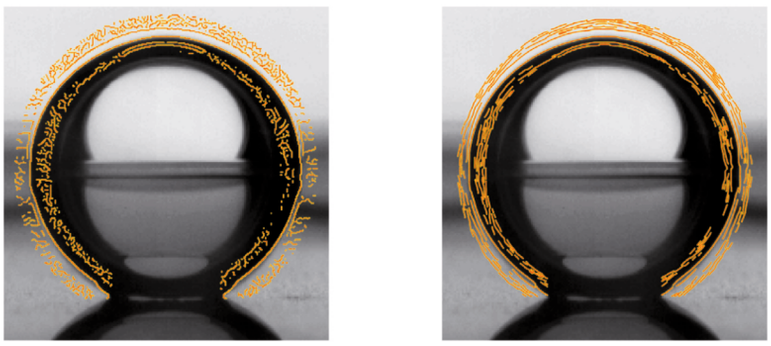

Fig. 9. Comparison of the detected edges (orange lines) for the conventional Canny method (left) with the proposed advanced method for bubble shapes (right). The edge detection is just performed close to the bubble's interface (see Fig. 10(c)).

Edge detection in image V is simplified as follows. The magnitude of V vertical gradient is computed and its local extrema are detected across the columns with sub-pixel accuracy. The resultant locations are treated as image edges. In order to detect even the faintest edges that may be part of the contour, the detection of local extrema is set to be sensitive even to minute amplitude. However, this effect is reduced since only the vertical direction in V corresponds to the radial direction, with respect to C, in I. The result of the proposed edge detection method is compared against the widest-used generic edge detection method [33], using the same extremum detection sensitivity, as shown in Fig. 9. In that figure, the detected edges using the conventional and the proposed method are superimposed as colored dots. Connected edges are then linked into segments based on 8-neighbor connectivity and disallowing connectivity in cases of junctions (edges with more than one neighbor) (Fig. 10(e)). The obtained segments are evaluated as to their compatibility to the shape of the bubble. This compatibility is determined by their curvature profile, as segments with bents do not comply to the smooth bubble contour and convexity. In addition, outlier segments with large distances from the size-dominant segments are also removed. Finally, the outmost of the segment points, if any, per each polar direction is the boundary point detection for that bearing. The result is a clockwise-ordered set of points forming a contour (Fig. 10(f)). Given the points of the boundary detection, several choices for approximating bubble contour with a curve are available (Fig. 10(g)). This curve is independent of C used to detect contour points and its selection is driven by the operator. The following approximations are currently employed: (a) One circle, based on the full contour, (b) One circle, based on the top-half contour, (c) Two circles, based on the left-half and right-half of the contour, and (d) One ellipse, based on the full contour. The different approaches can be chosen accordingly for the pool boiling, shear flow, and electric field cases due to the different bubble shapes to achieve an optimized result. An overview of the aforementioned computational steps is shown in Fig. 10. The figure shows the original image (a) on the top. The six images below illustrate the algorithmic steps, zooming in the image region where the bubble appears. The first image (b) shows the coarse silhouette obtained through background subtraction. In the second (c), curve C is superimposed in green color and the boundaries of the surrounding in blue and red. In the third step (d), the baseline row b and contact points p and q are plotted superimposed. Further, the third image shows the detected edges, and the fourth image (e) the segments of linked edges. The fifth image (f) shows the outermost of the segment points, and the sixth image (g) the fitted curve. In the last stage, a circle approximation is employed.

3.4.2. Infrared images

The significant benefit of the IR data is not only the pure measurement of the heater surface temperature, but even more the subsequent calculation of the heat flux from the heater to the fluid. Since the heat flux from the heater to the fluid depends on several factors, a more complex evaluation is required. The general procedure of this evaluation will be described in the following. A more detailed description of all individual points and an error analysis will be presented in future publications. There are so-called reference images for all measurements, which are taken before the heater is switched on. In most cases, the recording of the IR camera starts shortly before the nucleation is generated by the laser to distribute the available recording time as best as possible to the bubble growth. The heating phase, which can last several seconds, is therefore not measured. In some cases, especially in shear flow, the entire period from the heater on would be recorded by the IR camera. For these cases, the steps four and five of the following list can be neglected. The general approach for the calculation is as follows:

1. The raw infrared data are calibrated and filtered.
2. The temperature of the heater outside the field of view of the infrared camera during the runtime of the camera is calculated by averaging the measured temperature values over each streamwise position for every time.
3. The electrical power dissipation over the heater surface is calculated by using a finite element analysis to accurately capture the heat flux transferred to the liquid from the heater at every position.
4. The flow velocity profile in the liquid is calculated by numerical simulation based on the given parameter set.
5. The initial temperature of the heater is calculated. This is done by using the known preheat time (the time the heater was running, before the infrared data is collected), the volume flow rate in the liquid phase through the test cell, the flow profile, the (locally resolved) electrical heater output power, and the initial subcooling of the liquid in a finite element calculation. With these information, the heat transport in the heater and the heat transfer to the surrounding liquid phase is assessed and the resolved temperature of the heater for every preheat time is obtained. This step is decisive because the three-dimensional temperature distribution in the heater has a significant influence on the heat flow calculation. However, this cannot be measured and must therefore be calculated.
6. The heat flux is calculated with a finite element analysis of the entire heater. The previously obtained initial heater temperature is used as the initial condition, and the infrared data is used as

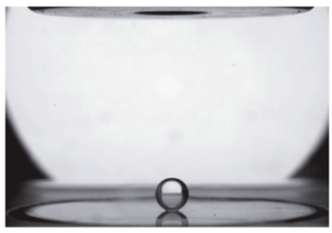

(a) Original image

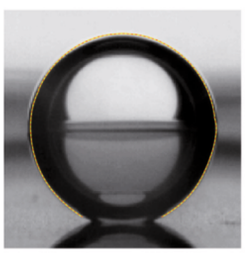

(b) Silhouette of the bubble by background subtraction

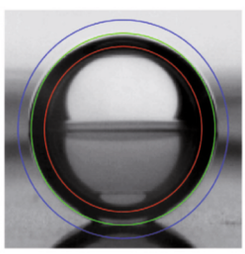

(c) Curve C (green) and boundaries of the bubble (red and blue)

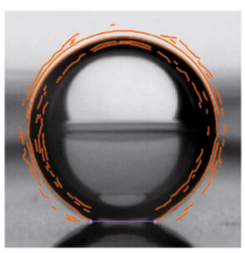

(d) Previous picture with superimposed baseline row (b), contact point (p and q), and dectected edges

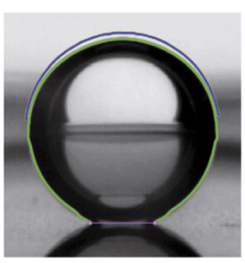

(e) Segment of the linked edges

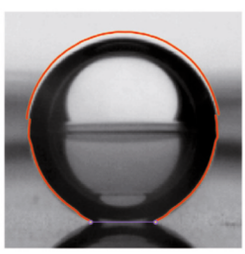

(f) Outermost of the segment points

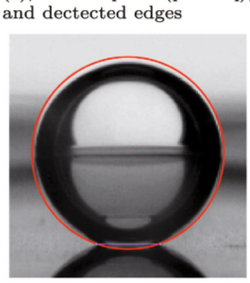

(g) Fitted curve by circle approximation in this case

Fig. 10. Computational steps of black and white image processing pipeline.

a time dependent temperature boundary condition. By solving the transient heat conduction in the heater, the heat flux from the heater to the liquid is found. This heat flux is then corrected for the electrical heater input (see step number 3) and the heat input from the laser (from a dedicated measurement). To reduce the time required for computing, both parts are not included in the finite element analysis of this step.

Fig. 11 shows a picture of the black and white camera (top) with the corresponding calibrated temperature field (middle) and the calculated distribution of the heat flux density. The example is taken from a shear flow test series.

4. Initial results

The following section provides an insight into the results of the four study groups and presents a basic comparison of the individual forces on the boiling process. In Fig. 12 the influence of the different applied forces are shown for the same set of parameters (if applicable). For pool boiling (top left), the round, undisturbed shape of the bubble is clearly visible. The bubble does not move away from the substrate heater under the given conditions. Its growth is only affected by reaching an outer wall or by stopping the experiment. For the electric field (top right), the deformation of the bubble is clearly visible. It shows an elongated geometry. In addition, the electric field causes the bubble to depart from the substrate heater. Under the given conditions, the bubble departs after about 4.8 s. The influence of the shear flow is shown at the bottom left. It can be seen that the bubbles are carried along by the shear flow and leave the heater surface. Under the given conditions, about 3 bubbles per second depart from the nucleation site. The additional switching on of an electric field (bottom right) shows a secondary influence on the bubble formation under the given conditions. Similarly to the shear flow case, about 3 bubbles per second depart from the nucleation site. The size of the bubble is also similar. Later on, the bubbles are clearly accelerated by the electric field, which can be seen by the larger distances between the bubbles and also by the peculiar shape of the bubble at the highest distance from the nucleation site. The video for the corresponding illustration is available at https://doi.org/10.48328/tudatalib-618. In the following, the influences of the individual main branches will be discussed in more detail.

4.1. Pool boiling

For pool boiling without external forces such as shear flow or electric field, the bubbles can theoretically grow indefinitely in weightlessness. In the current experiment, they are primarily limited by the experimental execution duration and the cell's spatial limitation. Additionally, the minimal residual gravity or other instabilities may

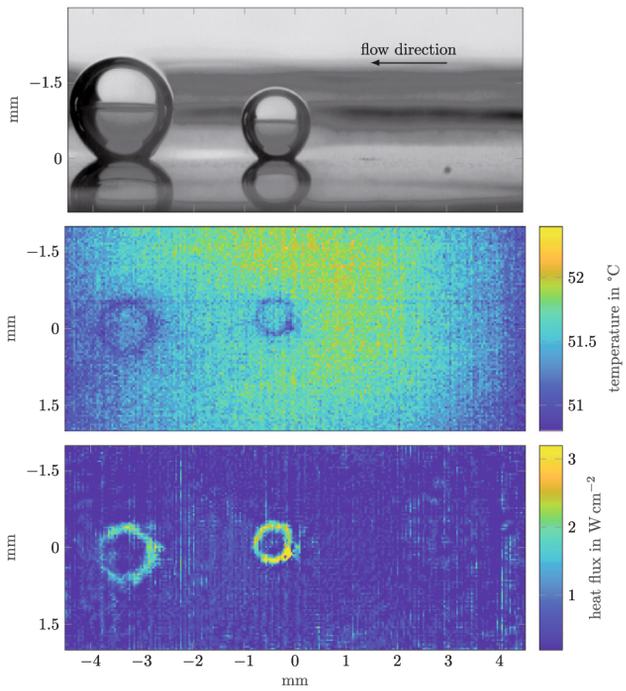

Fig. 11. Example calculation of the heat flux density distribution (bottom) based on the calibrated temperature field (middle) for a shear flow run. The top picture shows the corresponding BW image.

Table 2
Experimental parameters used in the reference runs.

p_l =	600 mbar
T_{sat} =	42.4 °C
T_{sub} =	3 °C
T_l =	39.4 °C
$qdot$ =	0.75 W cm^{-2}
t_{wait} =	5 s

cause the bubble to move slightly on the heater. Should the bubble leave the artificial nucleation site by this movement, new bubbles will form at this site, and bubble coalescence will occur. This can lead to further motion as well as oscillations of the bubble contour.

To check the experiments' reproducibility over the long period, the so-called reference case was performed regularly during both campaigns. Overall 25 reference case runs had been performed on 9 different days. The parameters of the reference case are shown in Table 2. The reference case is carried out independently of the MTCR and the electrode's position not to frequently move the actuators. To the extent that this can affect the space available for bubble growth, only the early bubble growth times will be compared. Fig. 13 shows the bubble diameter versus time for 8 different reference case runs covering the whole period of the mentioned two campaigns. It can be seen that the bubble growth behaves very comparably for all the experiments performed. The reference case runs performed at the end of the second campaign show a slightly larger bubble volume. For all evaluated references case runs so far the deviation between all (including not shown) runs is 3.3%. It is calculated by averaging the quotient of standard deviation and mean bubble size at each time step.

Based on the described reference case, the influences of the main parameters (pressure, heat flux, waiting time, and subcooling) are shown in Fig. 14. The dashed green line represents the reference case. It can be seen that the heating power and the subcooling have the most significant influence on the bubble growth. Concerning the waiting time, it can be seen that a qualitatively different curve results for a very short waiting time. This can be explained as follows. The bubble is generated by the additional laser energy during ignition (177 mW for 20 ms). Subsequently, however, due to the short preheating time (1 s with 0.75 W cm^{-2}) and the existing subcooling (3 K), there is not yet enough energy available for the bubble to grow in a qualitatively comparable way to the other experiments. A smaller influence of the waiting time on the bubble growth can be seen for longer waiting times. The pressure has a less significant influence on the growth of the bubble in the used parameter range. This is because the energy provided for evaporation is comparable between the different cases. Different bubble sizes can be primarily attributed to a change in vapor density.

In summary, it can be said that the effects of the individual parameters correspond to expectations. The bubble size increases with increasing heating power, increasing waiting time, decreasing subcooling and decreasing pressure.

4.2. Shear flow

Unlike pool boiling, multiple consecutive bubbles were formed on the substrate heater during boiling in shear flow. The bubbles depart from the nucleation site by sliding along the heated wall. For high values of the heat flux, the frequency of bubble formation increases and the bubbles may coalesce. A summary of the shear flow runs with the coalescence events is presented in Fig. 18 and will be discussed below.

The temporal evolution of the bubble equivalent diameter at p_l = 750 mbar, T_{sub} = 5 K, $\dot{q}$= 1 W cm^{-2}, Q = 300 mL min^{-1}, and t_{wait} = 5 s is shown in Fig. 15. The corresponding image of the bubbles, for t = 4.4 s, is shown in Fig. 12. Once the laser pulse activated the nucleation site, this leads to the nucleation of a first bubble. When the bubble grows to a particular size, it detaches from its position and continues to slide on the substrate heater due to the shear flow. Sliding of the bubble away from its position allows the formation of a new bubble at the nucleation site, and the cycle continues. The vertical dashed lines in Fig. 15 correspond to the departure of the bubble from the nucleation site, by sliding along the wall. The detachment diameter of the bubbles increases with time, because the thickness of the thermal boundary layer is also increasing with time.

The variation of different geometrical parameters of the bubble (corresponding to the second nucleating bubble shown in Fig. 15) with time during the life-time of growth and sliding at p_l = 750 mbar, T_{sub} = 5 K, $\dot{q}$ = 1 W cm^{-2}, Q = 300 mL min^{-1} is shown in Fig. 16(a). Similar to the bubble equivalent diameter d_b, bubble foot diameter d_{bf} is also observed to increase with time, which is in contrast to the quasistatic growth of an injected air bubble with a contact line pinned at the injection hole as reported in the literature [34]. This can be attributed to the evaporation at the bubble foot during boiling. cg_x and cg_y are the coordinates of the center of gravity with respect to the nucleation site (O, inset image, Fig. 16(a)). cg_y follows a trend similar to the bubble diameter d_b, however, cg_x initially remains quasi-static followed by a gradual increase with time, indicating the detachment/sliding of the bubble away from the nucleation site with a constant velocity. It should be noted that the bubble continues to grow during the sliding motion as the substrate heater was maintained at the superheated condition due to continuous heating. The corresponding variations of the contact angles at the advancing and receding fronts are presented in Fig. 16(b).

The temporal evolution of the bubble growth shown in Fig. 15 follows the relation $d_b = c_{gr}t^{0.5}$, which is the characteristic of the heat-diffusion controlled bubble growth [35]. The constant c_{gr} captures the rate of bubble growth and depends on the temperature of the liquid and substrate heater, liquid properties and flow conditions [7,36,37]. Larger value of c_{gr} suggests relatively larger bubble growth rate. The plot of constant c_{gr} versus liquid flow rate Q at heat fluxes of $\dot{q}$= 0.5 W cm^{-2} and 1 W cm^{-2}, and at p_l = 750 mbar, T_{sub} = 5 K is shown in Fig. 17(a). Each data point corresponds to the average value of

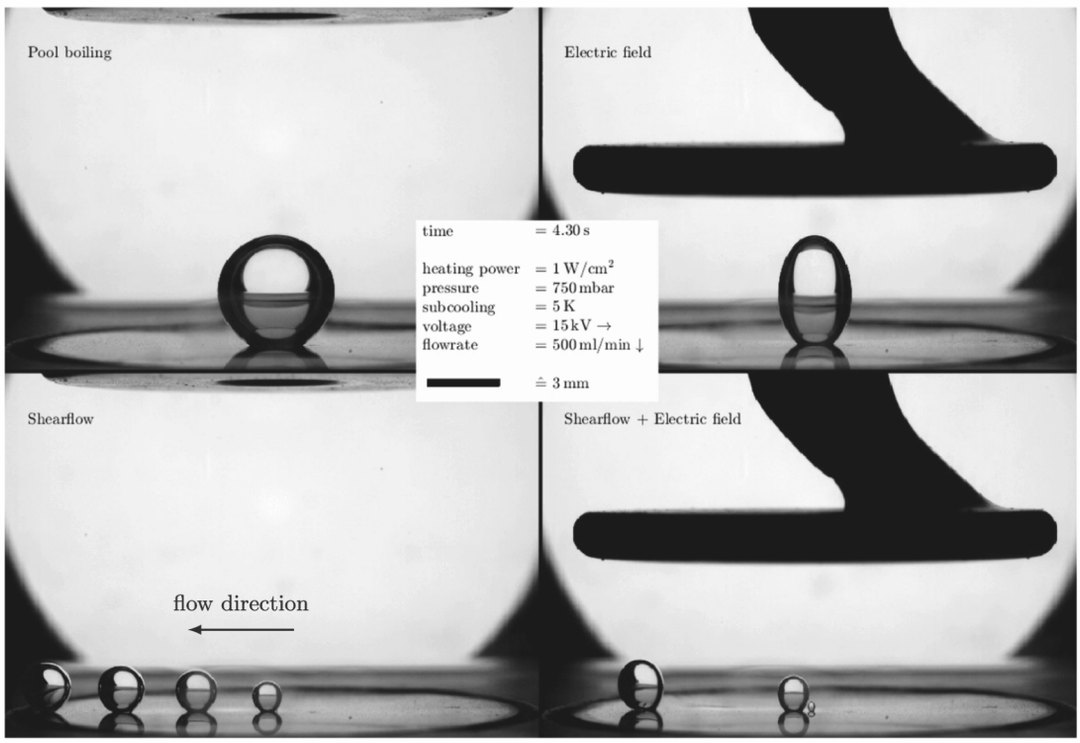

Fig. 12. Comparison of the different external forcing factors.

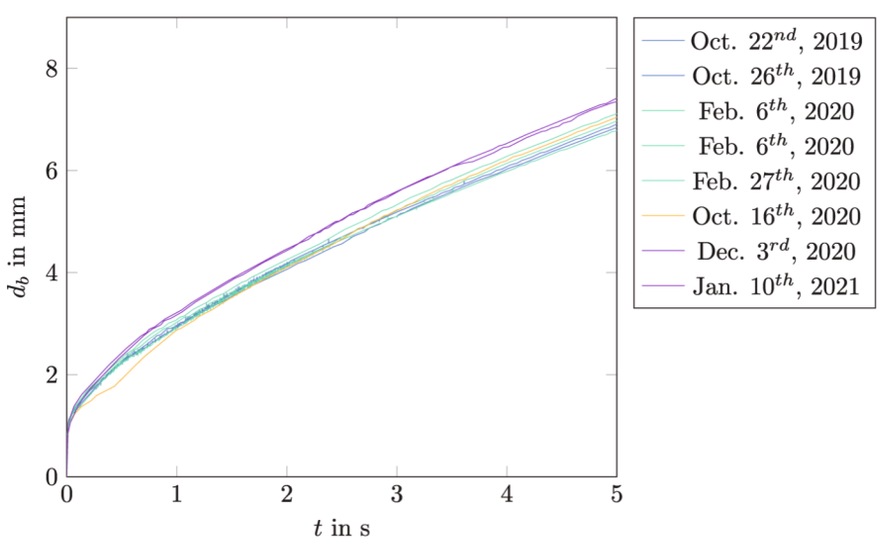

Fig. 13. Comparison of bubble diameter (resulting from circle fit approximation) for the pool boiling reference runs on different days during the mission.

c_{gr} for all the bubbles for a given experimental run (for instance, see Fig. 15) and error bar indicates the corresponding standard deviation. Heat transfer during subcooled boiling in microgravity condition is primarily governed by the evaporation in the contact line region and condensation at the bubble top [16]. Increase in the liquid flow rate results in the formation of a thinner superheated layer above the wall, which essentially reduces the evaporation at the contact line and in the near wall region. Moreover, the condensation of the bubble also increases due to increase in liquid flow rate and the exposure to relatively larger portion of the bubble to the subcooled liquid. The cumulative effect is to reduce the bubble growth rate. As a result, the value of c_{gr} gradually decreases with the increase in the liquid flow rate (Fig. 17(a),

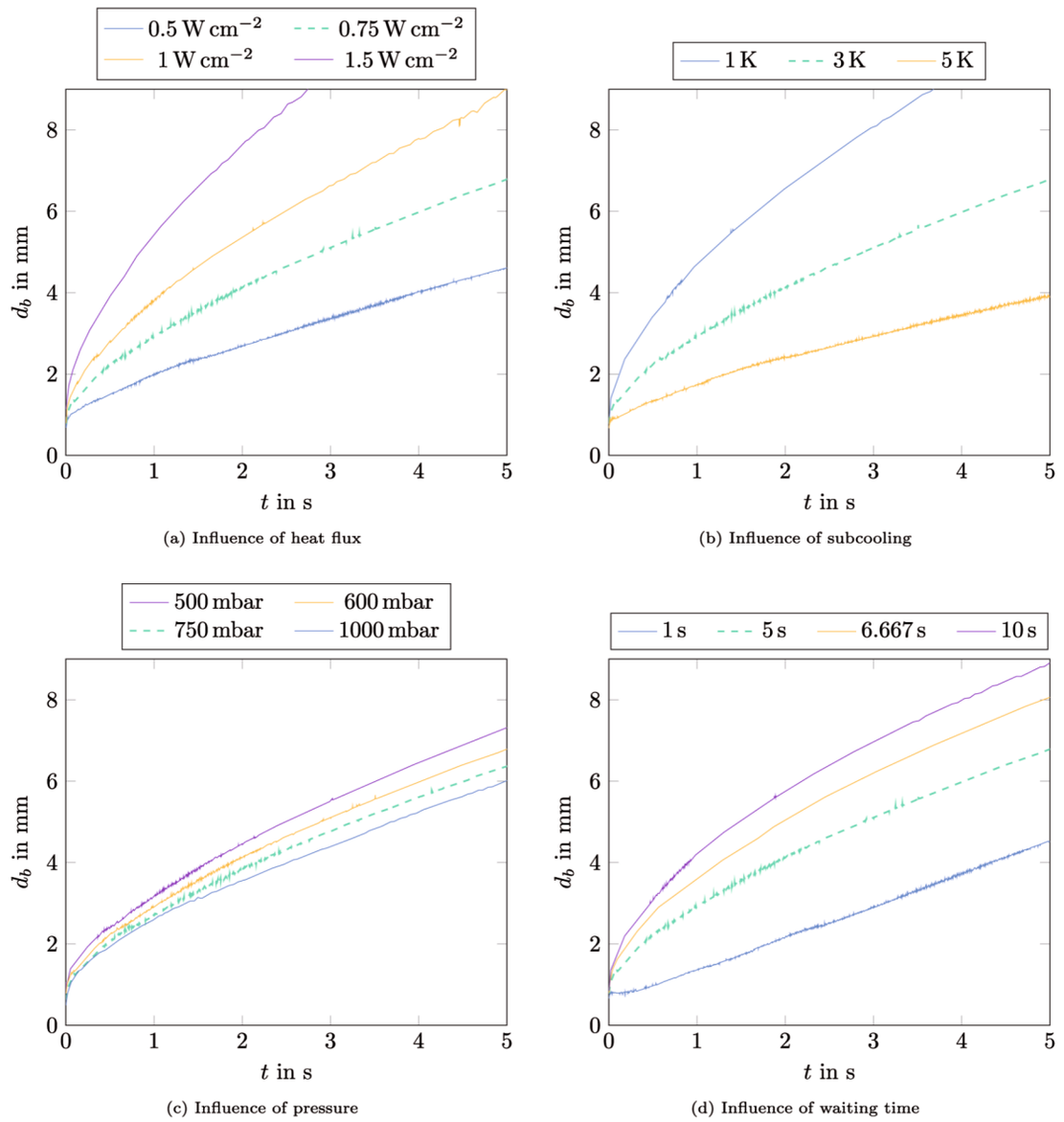

Fig. 14. Comparison of the major influencing parameters on bubble growth based on the reference case conditions (dashed green line). In each diagram, the other parameters are as the reference case ones (cf. Table 2).

1 W cm^{-2}). Similarly, thickness of the superheated layer above the wall also reduces at lower heat flux values, leading to the decrease in the contact line evaporation. Consequently, relatively smaller value of c_{gr} at low heat flux (Fig. 17(a), 0.5 W cm^{-2}) can be attributed to the decrease in bubble growth rate due to the reduced superheated layer thickness. Moreover, the value of c_{gr} is not significantly changed by the liquid flow rate at low heat flux of 0.5 W cm^{-2}. This can be attributed to the relatively small thickness of the superheated layer above the wall.

The plot of the equivalent bubble departure diameter $d_{dep,eq}$ measured at the initiation of sliding motion versus liquid flow rates at heat fluxes of $\dot{q}$= 0.5 W cm^{-2} and 1 W cm^{-2} is shown in Fig. 17(b). As the bubble does not have a circular shape under the effect of external forces, the equivalent bubble diameter $d_{b,eq}$ is used in the following. Increased drag force on the bubble at larger flow rate causes early departure. Consequently, departure diameter decreases with the increase in flow rate.

Boiling experiments with a shear flow also opened an opportunity to study bubble coalescence and the effects associated with this phenomenon. Microgravity eliminates the buoyancy-induced differences in rise velocity between bubbles of different sizes [38], making the coalescence process less complex. Colin et al. [39] already proposed a model to predict bubble size distribution in a tube during bubbly flow in microgravity and found that coalescence significantly affects the bubble size. Apart from that, coalescence may also promote bubble lift-off due to an additional upward force that appears during the merger, which influences boiling heat transfer [40]. In normal gravity conditions, there are many experimental evidences proving that horizontal bubble coalescence may result in enhanced heat transfer and

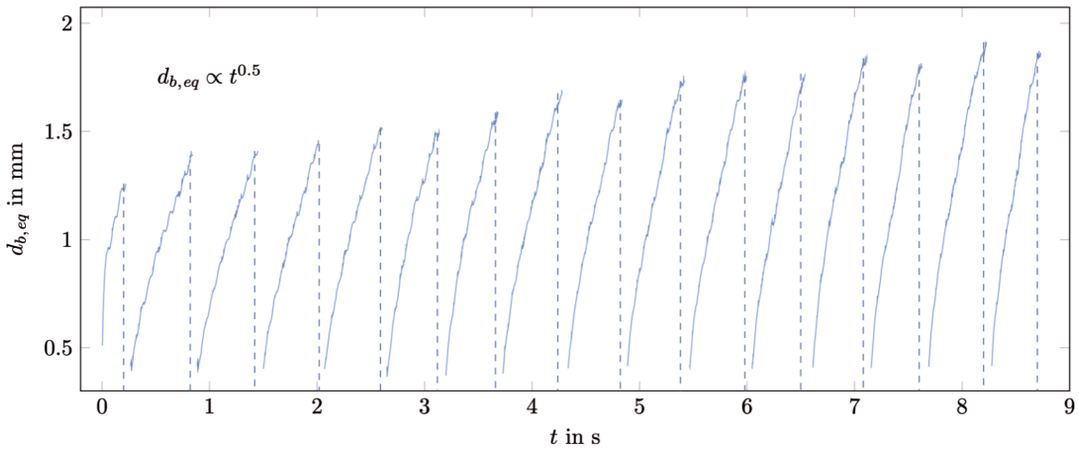

Fig. 15. The variation of bubble equivalent diameter with time. Vertical dashed line indicates sliding of bubble due to shear flow.

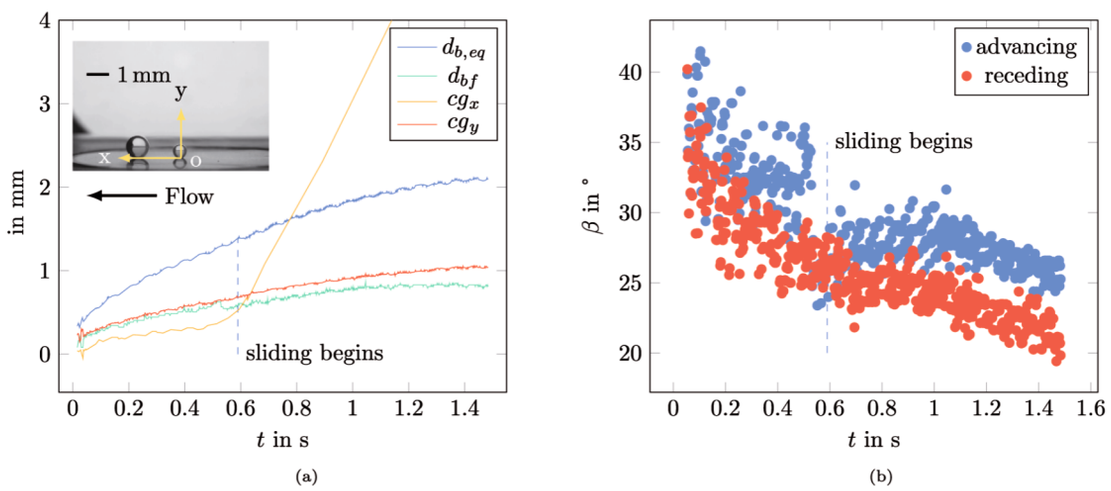

Fig. 16. The variation of bubble equivalent diameter, foot diameter, x and y-coordinate of center of gravity with time (a) and the corresponding contact angles (b).

faster liquid replenishment of active nucleation sites [41–44]. However, only few publications are available for microgravity conditions [45,46], none of them specifically focusing on coalescence in shear flow boiling. In-depth analysis of experimental result from both missions will provide new insights into the bubble coalescence phenomenon. Even though the designed boiling cell is not specifically targeting the bubble coalescence, the shear flow boiling provided a satisfactory number of bubble interactions. The Science team already identified experimental conditions under which the coalescence events are likely to occur. Out of the 84 analyzed experimental runs, 47 (i.e. 55.9%) of them exhibited one or more (up to 10) horizontal coalescence events, ranging from small two-bubble mergers to horizontal chain coalescence of several bubbles. The sunburst diagram in Fig. 18 shows from the center outward the effects of subcooling, heat flux, shear flow rate, waiting time and saturation temperature on detected bubble coalescence, respectively. First observations indicate that subcooling temperature together with heat flux are the dominating factors on the appearance of coalescence under shear flow conditions, followed by shear flow rate and waiting time. Initial results also show that saturation temperature (i.e. the system pressure) plays a minor role in the occurrence of coalescence event.

4.3. Electric field

During the first campaign the electric field was active during all phases of the experiment (heating of the surface for the duration of t_{wait}, laser pulse, bubble nucleation, growing and detachment). Within the second campaign the electric field was switched off during waiting time, laser pulse and bubble nucleation; then, at a defined time t_{on} it was switched on to be switched off after another amount of time t_{off}. Both experiment sequences are shown in Fig. 19. In the following it is referred to the first campaign, namely the electric field is kept always on. Fig. 20 shows the clear effect of different electric field levels on bubble shape, due to an additional electric stress applied at the liquid–vapor interface.

For some experiments (e.g. low subcoolings and high heat fluxes) at the lower values of electric field intensity the bubble grew too large and interacted with the electrode before detachment. It was decided to repeat those experiments moving the electrode at larger distance from the surface and keeping the same average intensity of electric field; furthermore, those runs give the opportunity to study the influence of the electrode geometrical configuration on the process.

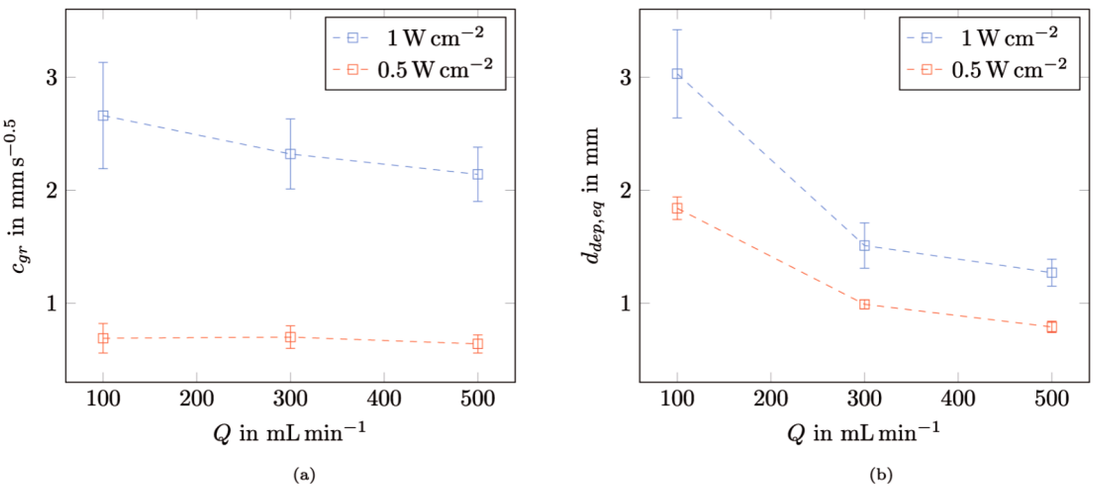

Fig. 17. (a) Constant c_{gr} and (b) bubble departure diameter versus liquid flow rate at heat fluxes of $\dot{q}$= 0.5 W cm^{-2} and 1 W cm^{-2}, and at p_l = 750 mbar, T_{sub} = 5 K.

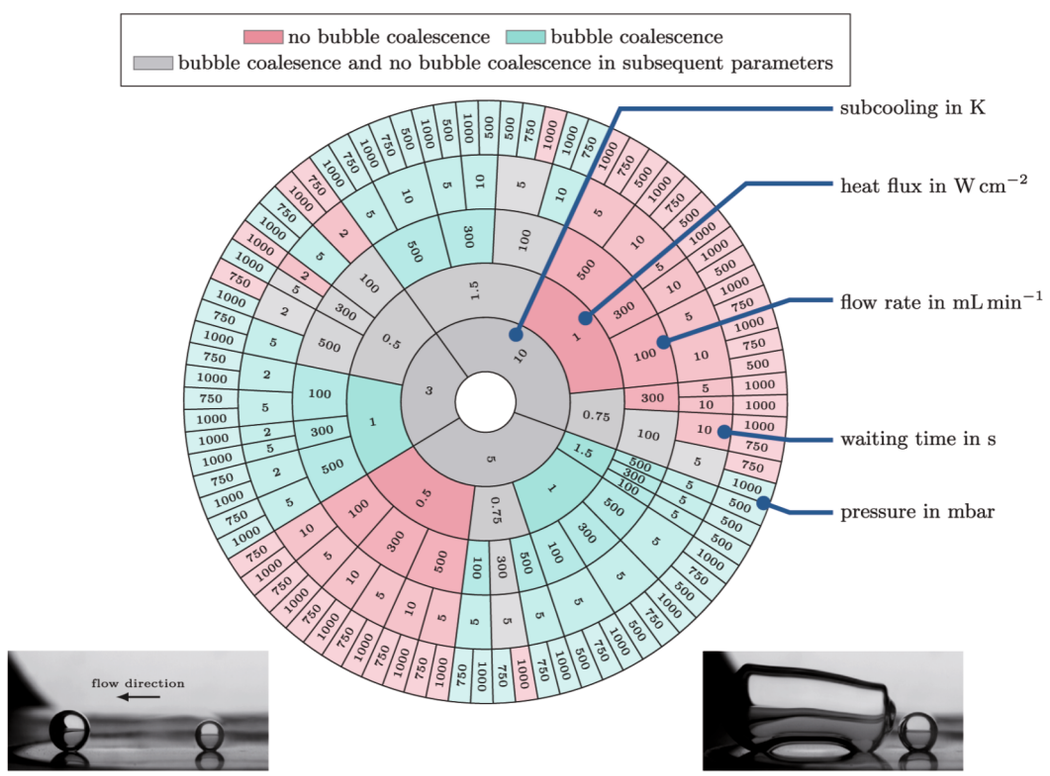

Fig. 18. The occurrence of shear flow bubble coalescence under various experimental conditions in microgravity. Experimental parameters of both pictures: left T_{sub} = 10 K, $\dot{q}$ = 1 W cm^{-2}, Q = 100 mL min^{-1}, t_{wait} = 10 s, p_l = 500 mbar - right T_{sub} = 5 K, $\dot{q}$ = 1 W cm^{-2}, Q = 100 mL min^{-1}, t_{wait} = 5 s, p_l = 500 mbar.

Fifty experiments were repeated with the electrode at 8.5 mm (instead of 6 mm) with applied voltages of 7.08 kV and 14.17 kV corresponding to a mean electric field intensity of 0.83 MV m^{-1} and 1.67 MV m^{-1}.

The images of the bubbles obtained through shadowgraphy using a BW camera were processed via a Matlab code. The bubble contour was detected and the most interesting geometrical parameters were recorded: bubble volume, bubble equivalent diameter, bubble foot diameter, bubble height, bubble curvature at the apex and bubble contact angle (example in Fig. 21). The bubble shape was influenced by the electric field at every time of the test: increasing the voltage, the bubble shape was increasingly elongated in vertical direction and compressed in radial direction (as already noted in [47,48]). With an applied voltage of 5 kV (corresponding to a field intensity of 0.83 MV m^{-1} for

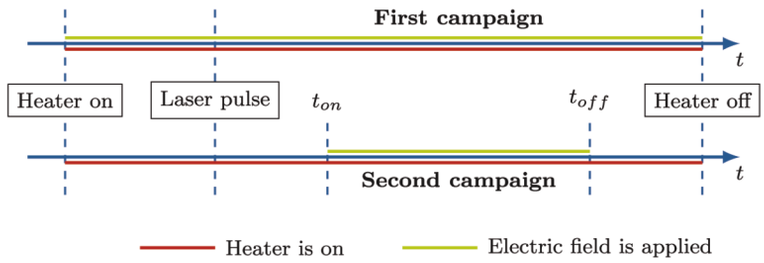

Fig. 19. Comparison of the electric field operation between the first and second campaign.

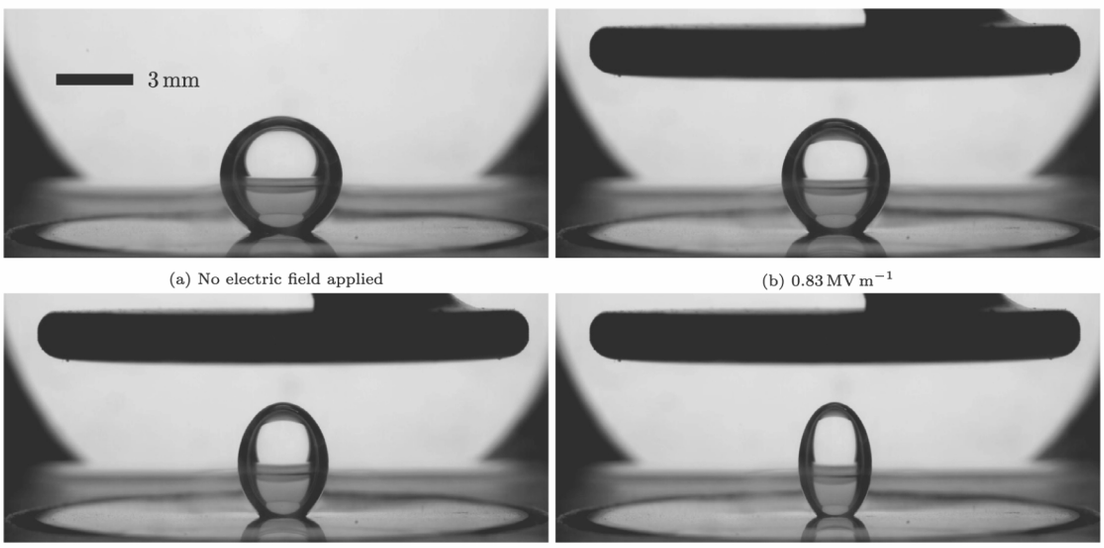

Fig. 20. Effect of the electric field on the bubble shape for different values of electric field intensity $E = U_{elec}/h_{elec}$.

a distance of 6 mm) the bubble shape was still nearly spherical. The most remarkable effect of the electric field is the bubble detachment (see Figs. 21 and 22), which always occurred when the bubble received enough energy to grow sufficiently in the amount of time available for the experiment (that was 9 s in total). Detachment occurred even for the lowest value of the electric field; detachment volume and detachment foot diameter decreased as the electric field increased and, consequently, the detachment frequency increased (see Fig. 22). The values of the detachment volume as a function of the electric field (for the same other input parameters) appeared to be constant and well reproducible, demonstrating the capability of electric field to promote regular bubble detachment in microgravity. After a small transitional period, also the detachment frequency became stationary. After detachment, the bubble was lifted off towards the electrode.

Using the geometrical parameters reported in Fig. 21, it is possible to calculate the forces acting on the bubble [47–49], namely force due to internal overpressure, force due to surface tension and inertial force, if not negligible. The unbalance of these known forces yields the experimental value of resulting force, to be compared later with numerical models of the electric force. An example of the experimental calculated forces is shown in Fig. 23.

4.4. Electric field + shear flow

The combined effect of shear flow and electric field was also investigated as an alternate strategy to remove bubble from the heater surface in the absence of buoyancy. Presence of electric field considerably influenced dynamics of bubble growth even in the presence of shear flow. The effect of electric field was to create a surface force, which elongates the bubble. Note that this elongation exposed the bubble to a higher velocity and may ease its detachment. Consequently, in contrast to the shear flow without electric field, bubbles were deformed in the presence of electric field to a nearly ellipsoidal shape with the major axis normal to the wall. The temporal evolution of the bubble height at p_l = 750 mbar, T_{sub} = 5 K, $\dot{q}$= 1 W cm^{-2} and intermediate flow rate of Q = 300 mL min^{-1} with and without electric field (voltage 15 kV) is shown in Fig. 24(a). When the size of the bubble was small, the effect of electric field was relatively less discernible whereas at larger size bubble deformation was more visible. This is evident from the relatively larger height (h) and larger h/d ratio in the presence of electric field, see Fig. 24(a) and 24(b), respectively.

Moreover, even in the presence of electric field bubbles continued to move along the direction of shear flow. No departure in the normal direction away from the wall was observed. However, at the low flow rate of Q = 100 mL min^{-1} relatively larger bubbles formed

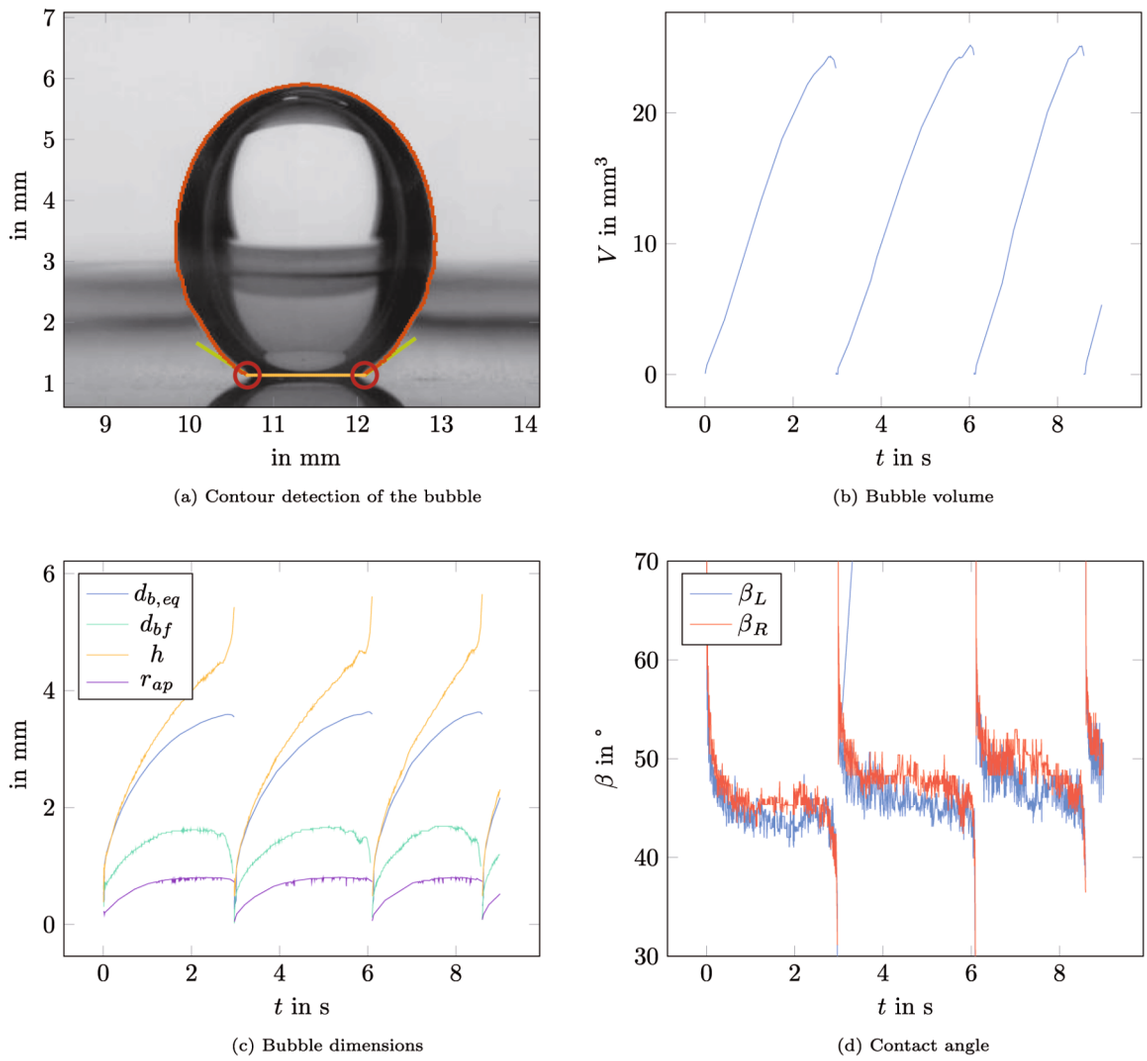

Fig. 21. An example of Matlab code edge detection process (a), bubbles volume (b), bubbles equivalent diameter, foot diameter, height and apex radius (c), left and right contact angles (d). Experimental parameters: $p_l = 600\,\text{mbar}, T_{sub} = 5\,\text{K}, \dot{q} = 0.75\,\text{W cm}^{-2}, t_{wait} = 10\,\text{s}, E = 2.5\,\text{MV m}^{-1}$.

in comparison with higher flow rate conditions, as the electric field force dominated over the drag force acting on the bubble due to the shear flow. This forced the bubble to depart in the normal direction away from the substrate without any sliding motion (see, Fig. 25), which was similar to the case of pool boiling with electric field. The video for the corresponding illustration is available at https://doi.org/10.48328/tudatalib-618. A more detailed analysis of these complex interrelationships will follow in future publications.

5. Conclusion

The Multiscale Boiling Project is the first experiment in the history of boiling research that combines both undisturbed bubble growth and the influence of external forces (namely shear flow and electric fields) within one facility. The project was conducted within two measurement campaigns on-board the International Space Station from 2019 to 2021. After completing the measurements, the experimental setup will be handed over to the Science Team for further investigations on ground in summer 2021. Despite the intermittent failures of the infrared camera and the blocked adjustment of the MTCR height, a majority of the objectives presented in Section 2.1 could be achieved. Objectives 1–4 were achieved within the conducted investigation. Bubble interactions (objective 6) were also observed and investigated. These were not initiated in a controlled way as such a feature was not included in the setup design for reasons of space. Rather they occurred in a more sporadic way in the studies related to objectives 1–4 and were captured by observations. The situation is similar with objective 5. The exchange or explicit addition of a second fluid were not possible under the imposed space restrictions. This objective is to be investigated with further ground tests and investigations, for example, in parabolic flights. In addition, the return of the EC enables the investigation of different gravity conditions with the otherwise same parameters as used on the ISS as well as a comparison to the experiments performed on ground during the SVT before the mission. Further experiments in long-term microgravity could give valuable insights into boiling mechanisms. Other liquid mixtures could be tested, coupled with IR camera measurement, allowing the validation of numerical models.

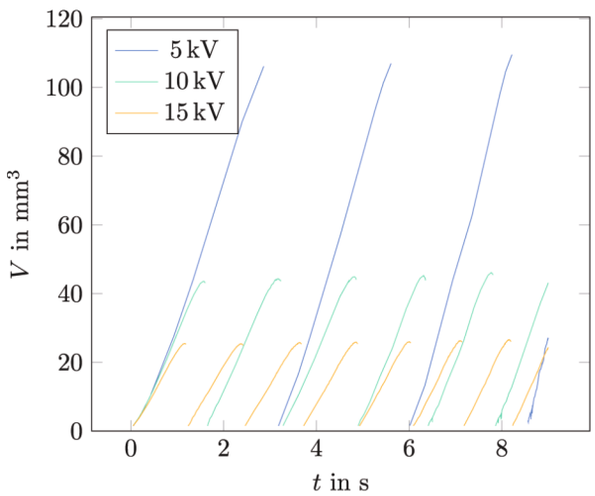

Fig. 22. Bubble volume and frequency for different strength of the electric field.

Within this publication, a first overview of the project as a whole was given. It explains the complex setup, the experiment execution on the ISS, and the significant aspects of the evaluation. In the context of initial analyzes, the high reproducibility of the experiments could be demonstrated in pool boiling by repeated execution of the reference case. Furthermore, the general trends observed regarding the variation of heat flux, waiting time, pressure, and subcooling correspond to the preliminary expectations. Among these parameters, the pressure level showed the weakest influence on bubble growth under otherwise comparable conditions. For experiments performed with a shear flow, a bubble grows at the cavity and departs by sliding along the heated surface. This process continues cyclically. The bubbles' size and frequency of formation depend on the heat flux, the liquid flow rate, and subcooling. When the frequency of detachment of the bubble is high enough, coalescence events between sliding bubbles are observed. The primary outcome of electric field runs is demonstrating its capability to promote stable bubble detachment even in microgravity. The detachment volume depends on electric field intensity, while detachment frequency is a function of other parameters, such as pressure, subcooling, and mainly heat flux and thermal boundary layer extension (waiting time). The effectiveness in continuously removing vapor from the heated surface was demonstrated successfully. The next steps will focus on a detailed analysis of bubble dynamics, force and stress balances, detachment mechanisms, and heat transfer rates to highlight and quantify the differences with bubble dynamics in terrestrial conditions. The combined effect of shear flow and the electric field was also investigated as an alternate strategy to remove bubbles from the heater surface in the absence of buoyancy. Under the electric field effect, the bubble is elongated perpendicularly to the substrate and thus exposed to a higher velocity of the shear flow, promoting its detachment. For the lowest flow rate, the bubble is detached perpendicularly to the substrate due to the dominant effect of the electric field. For moderate and high flow rates, the bubble is elongated but does not detach from the substrate. Instead, the bubble departs from the nucleation site by sliding along the substrate. In the following analyzes, the forces on the bubble are to be investigated in more detail, and, if possible, a boundary map is to be created under which conditions breakage from or slipping along the substrate occur.

In the future, it is planned to publish further detailed descriptions of the individual aspects like the design details, the heat transfer calculation, and the image processing of the black and white data, in addition to the scientific results themselves. Therefore, several groups of the Science Team are dealing with data processing and analysis and have already launched a benchmark study for image data post-processing of bubble growth characteristics in four directions. Namely: pool boiling, shear flow, electric field, and the combined effect of shear flow and electric field. In order to be able to evaluate the horrendous amount of data, further work is being done on sharing and optimizing evaluation algorithms and procedures. With the large amount of data available, each group of the Science Team will investigate the physics of bubble behavior in several operating conditions. Several joint papers will be published in the near future, focusing on specific aspects of the bubble behavior in various situations. Finally, all these results will be used for better understanding and modeling of the boiling processes.

Declaration of competing interest

Peter Stephan reports financial support was provided by German Aerospace Center. Catherine Colin reports financial support

Acknowledgment

The present work has been carried out in the framework of the European Space Agency Research Projects AO-2004-111: BOILING, AO-1999-110: EVAPORATION, AO-2004-096: CONDENSATION. We thank all the Multiscale Boiling Science Team Members of the different institutions involved:

Technical University of Darmstadt, Institute for Technical Thermodynamics
Aix-Marseille University, IUSTI
University of Pisa
Institute of Thermal-Fluid Dynamics, ENEA
Institut de Mécanique des Fluides de Toulouse, University of Toulouse
Aristotle University of Thessaloniki
Institute of Computer Science, FORTH
Transfers, Interfaces and Processes, Université libre de Bruxelles
University of Ljubljana
LAboratoire PLAsma et Conversion d'Energie
University of Padova
Kutateladze Institute of Thermophysics, Novosibirsk
University of Hyogo
Kyushu University
Kobe University

for their contribution in making possible the implementation of the experiment on-board the International Space Station, the authors would also like to gratefully thank ESA, and in particular Olivier Minster, Anne Pacros, Balázs Tóth, and Marco Braibanti for their interest and support to the activities linked to Multiscale Boiling, and for the fruitful discussions. The authors would also like to thank AIRBUS (with particular gratitude to the project manager, Olaf Schoele-Schulz), as well as B.USOC for the kind cooperation during all the pre-flight, in-flight and post-flight operations.

Co-authors from the Technical University of Darmstadt would like to thank the German Aerospace Center (DLR) for the financial support in the framework of the Vapor II project, grant no. 50WM1959. Co-authors from the Institut de Mécanique des Fluides de Toulouse would like to thank the French Space Agency CNES for its support through a post-doc grant, funding, and organization of parabolic flight campaigns. Co-authors from the University of Ljubljana would like to acknowledge funding by the Slovenian Research Agency (P2-0223 and J2-2486). Co-authors from the Kutateladze Institute of Thermophysics would like to acknowledge funding by the Russian Science Foundation (Project No. 19-19-00695). Co-authors from IUSTI would like to thank the French Space Agency CNES for its funding and support of boiling experiments. Co-authors from the Université libre de Bruxelles would like to acknowledge the financial support from BELSPO (PRODEX Heat Transfer).

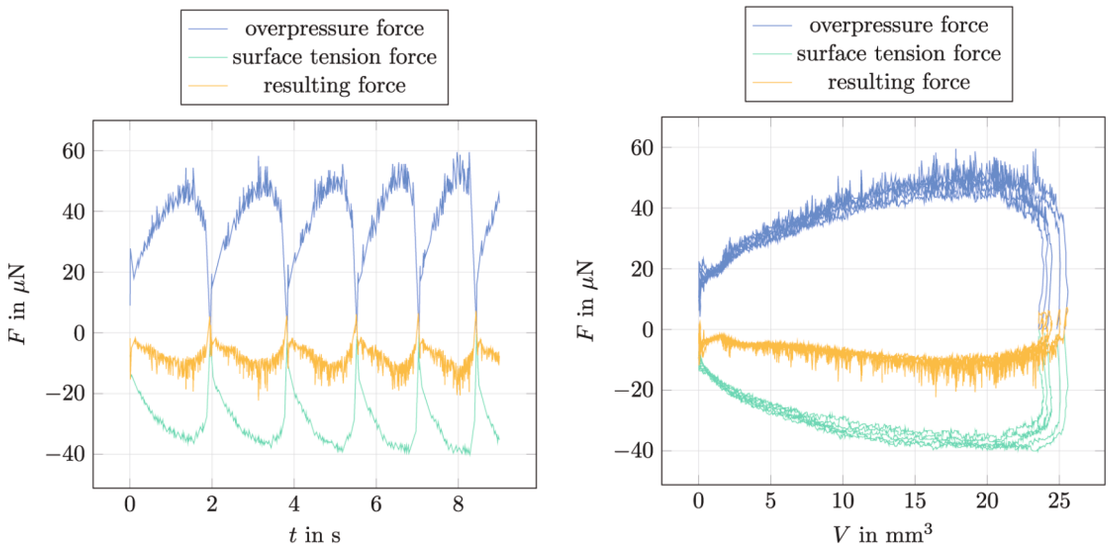

(a) Force on the bubble over time

(b) Force on the bubble versus bubble volume

Fig. 23. Vertical force balance on bubbles. Experimental parameters : p_l = 1000 mbar, T_{sub} = 5 K, $\dot{q}$= 1 W cm^{-2}, t_{wait} of 10 s, E = = 2.5 MV m^{-1}.

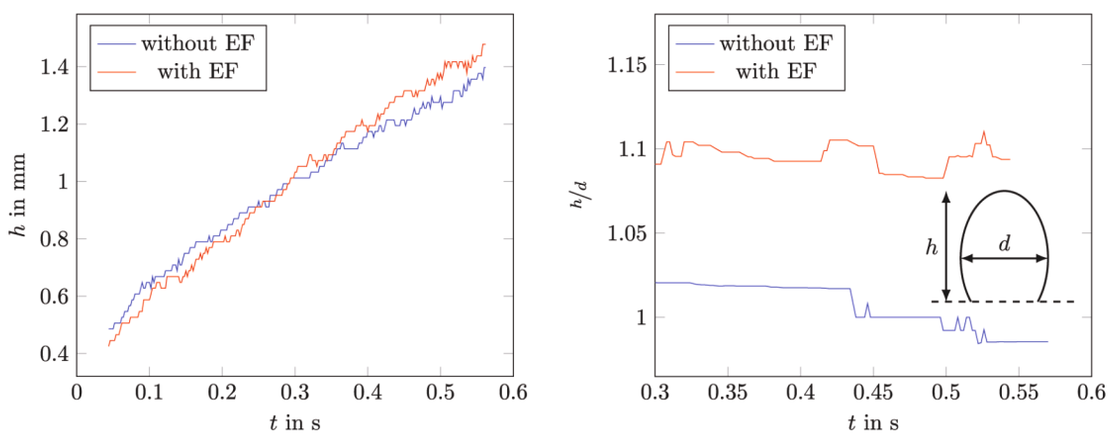

(a)

(b)

Fig. 24. The plot of (a) bubble height and (b) h/d ratio versus time, where d is diameter measured parallel to the substrate (shown in (b)) during boiling with and without electric field.

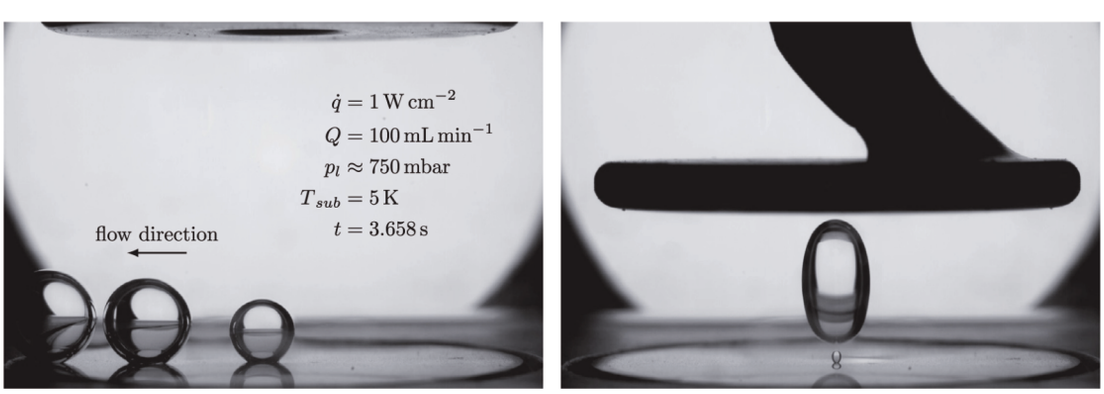

(a) Shear flow

(b) Shear flow and electric field

Fig. 25. Comparison of bubble behavior during boiling with (a) shear flow and (b) shear flow with electric field at low flow rate of Q = 100 mL min^{-1}.

References

[1] S. Nukiyama, The maximum and minimum values of the heat q transmitted from metal to boiling water under atmospheric pressure, J. Soc. Mech. Eng. (206) (1934) 367–374.

[2] H.K. Forster, N. Zuber, Growth of a vapor bubble in a superheated liquid, J. Appl. Phys. 25 (4) (1954) 474–478, http://dx.doi.org/10.1063/1.1721664.

[3] K. Engelberg-Forster, R. Greif, Heat transfer to a boiling liquid—mechanism and correlations, J. Heat Transfer 81 (1) (1959) 43–52, http://dx.doi.org/10.1115/1.4008129.

[4] S.S. Kutateladze, Boiling heat transfer, Int. J. Heat Mass Transfer 4 (1961) 31–45, http://dx.doi.org/10.1016/0017-9310(61)90059-X.

[5] W.M. Rohsenow, A Method of Correlating Heat Transfer Data for Surface Boiling of Liquids, Technical Report, No. 5, Massachusetts Institute of Technology, Heat Transfer Laboratory, 1951, URL http://hdl.handle.net/1721.1/61431.

[6] C.-Y. Han, P. Griffith, The mechanism of heat transfer in nucleate pool boiling - Part I, Int. J. Heat Mass Transfer 8 (6) (1965) 887–904, http://dx.doi.org/10.1016/0017-9310(65)90073-6.

[7] M.G. Cooper, The microlayer and bubble growth in nucleate pool boiling, Int. J. Heat Mass Transfer 12 (8) (1969) 915–933, http://dx.doi.org/10.1016/0017-9310(69)90155-0.

[8] K. Stephan, M. Abdelsalam, Heat-transfer correlations for natural convection boiling, Int. J. Heat Mass Transfer 23 (1) (1980) 73–87, http://dx.doi.org/10.1016/0017-9310(80)90140-4.

[9] D. Gorenflo, D. Kenning, H2 pool boiling, in: VDI Heat Atlas, Springer Berlin Heidelberg, Berlin, Heidelberg, 2010, pp. 757–792, http://dx.doi.org/10.1007/978-3-540-77877-6_45.

[10] V.K. Dhir, Nucleate and transition boiling heat transfer under pool and external flow conditions, Int. J. Heat Fluid Flow 12 (4) (1991) 290–314, http://dx.doi.org/10.1016/0142-727X(91)90018-Q.

[11] P. Stephan, B1 fundamentals of heat transfer, in: VDI Heat Atlas, Springer Berlin Heidelberg, Berlin, Heidelberg, 2010, pp. 15–30, http://dx.doi.org/10.1007/978-3-540-77877-6_115.

[12] R. Raj, J. Kim, J. McQuillen, Gravity scaling parameter for pool boiling heat transfer, J. Heat Transfer 132 (9) (2010) 091502, http://dx.doi.org/10.1115/1.4001632.

[13] R. Siegel, Effects of reduced gravity on heat transfer, in: J.P. Hartnett, T.F. Irvine (Eds.), in: Advances in Heat Transfer, vol. 4, Elsevier, 1967, pp. 143–228, http://dx.doi.org/10.1016/S0065-2717(08)70274-0.

[14] T. Oka, Y. Abe, K. Tanaka, Y.H. Mori, A. Nagashima, Observational study of pool boiling under microgravity, JSME Int. J. II 35 (2) (1992) 280–286, http://dx.doi.org/10.1299/jsmeb1988.35.2_280.

[15] J. Straub, M. Zell, B. Vogel, Pool boiling in a reduced gravity field, in: Proceeding of International Heat Transfer Conference 9, Begellhouse, Connecticut, 1990, pp. 91–112, http://dx.doi.org/10.1615/IHTC9.1860.

[16] O. Kannengieser, C. Colin, W. Bergez, Influence of gravity on pool boiling on a flat plate: Results of parabolic flights and ground experiments, Exp. Therm Fluid Sci. 35 (5) (2011) 788–796, http://dx.doi.org/10.1016/j.expthermflusci.2010.04.010.

[17] N. Schweizer, P. Di Marco, P. Stephan, Investigation of wall temperature and heat flux distribution during nucleate boiling in the presence of an electric field and in variable gravity, Exp. Therm Fluid Sci. 44 (2013) 419–430, http://dx.doi.org/10.1016/j.expthermflusci.2012.08.002.

[18] S. Fischer, S. Herbert, A. Sielaff, E.M. Slomski, P. Stephan, M. Oechsner, Experimental investigation of nucleate boiling on a thermal capacitive heater under variable gravity conditions, Microgravity Sci. Technol. 24 (3) (2012) 139–146, http://dx.doi.org/10.1007/s12217-011-9273-6.

[19] H. Ohta, M. Kawaji, H. Azuma, K. Inoue, K. Kawasaki, S. Okada, S. Yoda, T. Nakamura, Heat transfer in nucleate pool boiling under microgravity condition, in: Heat Transfer Conference, vol. 2, 1998, pp. 401–406, URL http://www.dbpia.co.kr/journal/articleDetail?nodeId=NODE00337809.

[20] O. Kannengieser, C. Colin, W. Bergez, Pool boiling with non-condensable gas in microgravity: Results of a sounding rocket experiment, Microgravity Sci. Technol. 22 (3) (2010) 447–454, http://dx.doi.org/10.1007/s12217-010-9211-z.

[21] C. Colin, O. Kannengieser, W. Bergez, M. Lebon, J. Sebilleau, M. Sagan, S. Tanguy, Nucleate pool boiling in microgravity: Recent progress and future prospects, C. R. Mec. 345 (1) (2017) 21–34, http://dx.doi.org/10.1016/j.crme.2016.10.004.

[22] H. Lee, Herman Merte Jr., F. Chiaramonte, The pool boiling curve in microgravity, in: 34th Aerospace Sciences Meeting and Exhibit, American Institute of Aeronautics and Astronautics, Reston, Virigina, 2012, p. 01151996, http://dx.doi.org/10.2514/6.1996-499.

[23] S.M.M. Steinbichler, J. Straub, Nucleate boiling heat transfer on a small hemispherical heater and a wire under microgravity, in: Heat Transfer Conference, vol. 2, 1998, pp. 539–544, URL http://www.dbpia.co.kr/journal/articleDetail?nodeId=NODE00337832.

[24] J.-F. Zhao, J. Li, N. Yan, S.-F. Wang, Bubble behavior and heat transfer in quasi-steady pool boiling in microgravity, Microgravity Sci. Technol. 21 (S1) (2009) 175–183, http://dx.doi.org/10.1007/s12217-009-9151-7.

[48] P. Di Marco, R. Kurimoto, G. Saccone, K. Hayashi, A. Tomiyama, Bubble shape under the action of electric forces, Exp. Therm Fluid Sci. 49 (2013) 160–168, http://dx.doi.org/10.1016/j.expthermflusci.2013.04.015.

[25] V. Shevtsova, D.E. Melnikov, C.J. Legros, The post flight study of micro accelerations on-board of Russian spacecraft FOTON-12, 2002, URL https://www.researchgate.net/publication/236024379_The_Post_Flight_Study_of_Microacceleration_The_Post_Flight_Study_of_Micro_Accelerations_On-Board_of_Russian_Spacecraft_FOTON-12.

[26] R. Raj, J. Kim, J. McQuillen, Pool boiling heat transfer on the international space station: Experimental results and model verification, J. Heat Transfer 134 (10) (2012) http://dx.doi.org/10.1115/1.4006846.

[27] G.R. Warrier, V.K. Dhir, D.F. Chao, Nucleate pool boiling eXperiment (NPBX) in microgravity: International Space Station, Int. J. Heat Mass Transfer 83 (2015) 781–798, http://dx.doi.org/10.1016/j.ijheatmasstransfer.2014.12.054.

[28] K. Inoue, H. Ohta, Y. Toyoshima, H. Asano, O. Kawanami, R. Imai, K. Suzuki, Y. Shinmoto, S. Matsumoto, Heat loss analysis of flow boiling experiments onboard International Space Station with unclear thermal environmental conditions (1st report: Subcooled liquid flow conditions at test section inlet), Microgravity Sci. Technol. 33 (2) (2021) http://dx.doi.org/10.1007/s12217-021-09869-5.

[29] V.A. Thomas, N.S. Prasad, C.A.M. Reddy, Microgravity research platforms - A study, Current Sciences 79 (3) (2000) 336–340.

[30] N. Sentse, ESA user guide to low gravity platforms, 2014, URL https://www.esa.int/Science_Exploration/Human_and_Robotic_Exploration/Research/European_user_guide_to_low_gravity_platforms.

[31] I. Nejati, A. Sielaff, B. Franz, M. Zimmermann, P. Hänichen, K. Schweikert, J. Krempel, P. Stephan, A. Martin, H. Scheerer, T. Engler, M. Oechsner, Experimental investigation of single bubble nucleate boiling in microgravity, Microgravity Sci. Technol. (2020) http://dx.doi.org/10.1007/s12217-020-09813-z, 1875–0494.

[32] C. Harris, M. Stephens, A combined corner and edge detector, in: C.J. Taylor (Ed.), Procedings of the Alvey Vision Conference 1988, Alvey Vision Club, 1988, pp. 23.1–23.6, http://dx.doi.org/10.5244/C.2.23.

[33] J. Canny, A computational approach to edge detection, IEEE Trans. Pattern Anal. Mach. Intell. PAMI-8 (6) (1986) 679–698, http://dx.doi.org/10.1109/TPAMI.1986.4767851.

[34] M. Lebon, J. Sebilleau, C. Colin, Dynamics of growth and detachment of an isolated bubble on an inclined surface, Phys. Rev. Fluids 3 (7) (2018) http://dx.doi.org/10.1103/PhysRevFluids.3.073602.

[35] M.S. Plesset, S.A. Zwick, The growth of vapor bubbles in superheated liquids, J. Appl. Phys. 25 (4) (1954) 493–500, http://dx.doi.org/10.1063/1.1721668.

[36] B.B. Mikic, W.M. Rohsenow, P. Griffith, On bubble growth rates, Int. J. Heat Mass Transfer 13 (4) (1970) 657–666, http://dx.doi.org/10.1016/0017-9310(70)90040-2.

[37] G. Duhar, G. Riboux, C. Colin, Vapour bubble growth and detachment at the wall of shear flow, Heat Mass Transf. 45 (7) (2009) 847–855, http://dx.doi.org/10.1007/s00231-007-0287-y.

[38] M.J. Prince, H.W. Blanch, Bubble coalescence and break-up in air-sparged bubble columns, AIChE J. 36 (10) (1990) 1485–1499, http://dx.doi.org/10.1002/aic.690361004.

[39] C. Colin, X. Riou, J. Fabre, Bubble coalescence in gas–liquid flow at microgravity conditions, Microgravity Sci. Technol. 20 (3–4) (2008) 243–246, http://dx.doi.org/10.1007/s12217-008-9031-6.

[40] H.S. Abarajith, V.K. Dhir, G. Warrier, G. Son, Numerical simulation and experimental validation of the dynamics of multiple bubble merger during pool boiling under microgravity conditions, Ann. New York Acad. Sci. 1027 (1) (2004) 235–258, http://dx.doi.org/10.1196/annals.1324.020.

[41] I. Golobic, J. Petkovsek, D.B.R. Kenning, Bubble growth and horizontal coalescence in saturated pool boiling on a titanium foil, investigated by high-speed IR thermography, Int. J. Heat Mass Transfer 55 (4) (2012) 1385–1402, http://dx.doi.org/10.1016/j.ijheatmasstransfer.2011.08.021.

[42] T. Chen, J.N. Chung, Coalescence of bubbles in nucleate boiling on microheaters, Int. J. Heat Mass Transfer 45 (11) (2002) 2329–2341, http://dx.doi.org/10.1016/S0017-9310(01)00334-9.

[43] T. Chen, J.N. Chung, Heat-transfer effects of coalescence of bubbles from various site distributions, Proc. R. Soc. Lond. Ser. A Math. Phys. Eng. Sci. 459 (2038) (2003) 2497–2527, http://dx.doi.org/10.1098/rspa.2003.1133.

[44] A. Coulibaly, J. Bi, D.M. Christopher, Experimental investigation of bubble coalescence heat transfer during nucleate pool boiling, Exp. Therm Fluid Sci. 104 (2019) 67–75, http://dx.doi.org/10.1016/j.expthermflusci.2019.01.024.

[45] Q. Kang, H.L. Cui, L. Hu, L. Duan, W.R. Hu, Experimental investigation on bubble coalescence under nonuniform temperature distribution in reduced gravity, J. Colloid Interface Sci. 310 (2) (2007) 546–549, http://dx.doi.org/10.1016/j.jcis.2007.02.020.

[46] J. Kim, Review of nucleate pool boiling bubble heat transfer mechanisms, Int. J. Multiph. Flow. 35 (12) (2009) 1067–1076, http://dx.doi.org/10.1016/j.ijmultiphaseflow.2009.07.008.

[47] G. Saccone, A.I. Garivalis, P. Di Marco, Electrohydrodynamics and boiling: Experiments, numerical calculation and modeling of Maxwell stress tensor and electric force acting on bubbles, J. Electrost. 103 (2020) 103413, http://dx.doi.org/10.1016/j.elstat.2019.103413.

[49] P. Di Marco, The use of electric force as a replacement of buoyancy in two-phase flow, Microgravity Sci. Technol. 24 (3) (2012) 215–228, http://dx.doi.org/10.1007/s12217-012-9312-y.

ResearchGate

See discussions, stats, and author profiles for this publication at: https://www.researchgate.net/publication/348287911

Levitation and Self-Organization of Droplets

Article *in* Annual Review of Fluid Mechanics · January 2021

DOI: 10.1146/annurev-fluid-030620-094158

CITATIONS
17

READS
582

2 authors:



Vladimir S Ajaev
Southern Methodist University
86 PUBLICATIONS **1,393** CITATIONS

SEE PROFILE



Oleg Alexandrovitch Kabov
Kutateladze Institute of Thermophysics of SB RAS
306 PUBLICATIONS **3,957** CITATIONS

SEE PROFILE

Some of the authors of this publication are also working on these related projects:

Investigation of Anomalous Transport Phenomena During Evaporation from Nano-Engineered Surfaces View project

Investigation of the nanocoatings effect on heat transfer enhancement in microsystems View project

All content following this page was uploaded by Vladimir S Ajaev on 12 January 2021.

The user has requested enhancement of the downloaded file.

ANNUAL REVIEWS

Annual Review of Fluid Mechanics

Levitation and Self-Organization of Droplets

Vladimir S. Ajaev[1] and Oleg A. Kabov[2,3]

[1]Department of Mathematics, Southern Methodist University, Dallas, Texas 75275, USA; email: ajaev@smu.edu

[2]Kutateladze Institute of Thermophysics, Siberian Branch of the Russian Academy of Sciences, Novosibirsk, 630090, Russia

[3]Novosibirsk State University, Novosibirsk, 630090, Russia

Annu. Rev. Fluid Mech. 2021.53:203-225. Downloaded from www.annualreviews.org
Access provided by 2603:8081:1407:a861:f5e6:c438:d4ff:bfb on 01/08/21. For personal use only.

ANNUAL REVIEWS CONNECT
www.annualreviews.org
• Download figures
• Navigate cited references
• Keyword search
• Explore related articles
• Share via email or social media

Annu. Rev. Fluid Mech. 2021. 53:203–25

The *Annual Review of Fluid Mechanics* is online at fluid.annualreviews.org

https://doi.org/10.1146/annurev-fluid-030620-094158

Copyright © 2021 by Annual Reviews.
All rights reserved

Keywords

evaporation, Stefan flow, Leidenfrost effect, flotation, Marangoni flow

Abstract

We review studies of levitating droplets over liquid–gas interfaces and dry solid surfaces with a focus on the physical mechanisms of levitation under different conditions. A fascinating physical phenomenon of self-organization of levitating droplets into large arrays is described and explanations for this unusual behavior are reviewed. Closely related topics of nonisothermal flotation and levitation of evaporating droplets over a pool of nonvolatile liquid, as well as recent advances in the study of the Leidenfrost effect, are also discussed.

1. INTRODUCTION

In 1971, Vincent Schaefer, a longtime collaborator of Irving Langmuir at General Electric Research Laboratory and an expert in atmospheric science, wrote a short paper that provided remarkable insights into the mechanism by which a layer of white mist forms above a hot cup of tea or coffee (Schaefer 1971). When vapor is transported away from the hot free surface and cools down by contact with colder air, tiny droplets of condensate can form. The droplets drift downward as their weight is increased by condensation. However, instead of falling back into the liquid, they slow down on approach to the liquid surface and then levitate for extended periods of time. A photograph from a recent observation of this phenomenon is reproduced in **Figure 1*a***, together with a magnified image showing individual droplets. Remarkably, all droplets levitate at the same height and are approximately uniform in size, with radii on the order of 10 μm.

While providing an everyday example of droplet levitation, a tea cup is clearly not a proper tool for reproducible experimental studies of this fascinating phenomenon. More recently studies were conducted using setups in which droplets levitated over evaporating thin liquid layers of uniform thickness. A hot spot of a typical diameter of several millimeters on the substrate is created using, e.g., a localized light beam or small heating element (Fedorets 2004, 2005; Fedorets et al. 2011). These setups led to well-controlled studies of levitation and to the discovery of another remarkable phenomenon: The droplets not only levitate at the same height but also organize themselves into compact regular arrays, termed droplet clusters, such as the one shown in the top-down snapshot in **Figure 1*b***. The size of the cluster increases gradually as more condensate droplets are formed and join the array. The droplets tend to be larger in the middle where the temperature is higher. The ordering of microdroplets over evaporating liquid surfaces was also observed in configurations where the heating was not localized. For example, inspired by a 1922

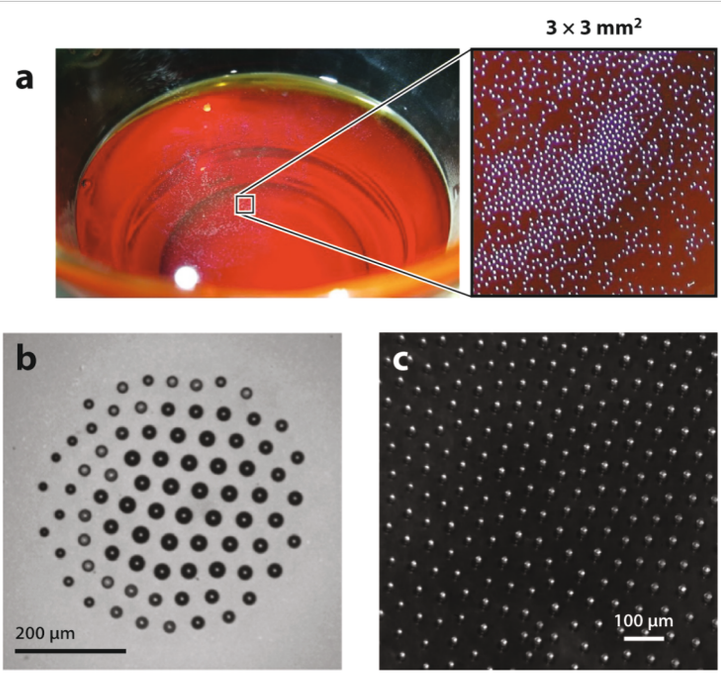

Figure 1

(*a*) White mist formed over a cup of tea, with the magnified section showing individual droplets levitating at the same height. (*b*) Top view of a droplet cluster. (*c*) Top view of levitating water droplets over a uniformly heated liquid layer with a metal substrate temperature of $T_H = 83$ °C in the setup of Zaitsev et al. (2017). Panels adapted with permission from (*a*) Zaitsev et al. (2018), copyright 2018 Begell House; (*b*) Fedorets et al. (2017), CC-BY 4.0; and (*c*) Zaitsev et al. (2017), copyright 2017 American Physical Society.

Annu. Rev. Fluid Mech. 2021.53:203-225. Downloaded from www.annualreviews.org
Access provided by 2603:8081:1407:a861:f5e6:c438:d4ff:bfb on 01/08/21. For personal use only.

essay by Japanese physicist Torahiko Terada, Umeki et al. (2015) used a rectangular container with hot water in a configuration where the temperature of the liquid surface in the container is close to uniform; in this setup, the levitating droplets still formed ordered arrays. Zaitsev et al. (2017) observed self-organization of droplets over a uniformly heated water layer of thickness ~0.4 mm on a metal substrate. This allowed them to obtain large well-ordered arrays with droplets maintaining the order even as the arrays moved in the horizontal direction. **Figure 1*c*** shows a photograph of part of a large array of self-organized droplets, clearly illustrating a high degree of ordering and droplet size uniformity in the pattern.

The self-organization seen in **Figure 1** takes place when the droplets are never in contact with the free surface of the liquid below them, in contrast to several configurations in which ordering is due to direct interaction of droplets with the surface, e.g., for the case of a vertically vibrating bath (Protière et al. 2006, Eddi et al. 2009). Waves generated by impacts of bouncing droplets result in a complex shape of the liquid surface. For a droplet bouncing off a trough of the surface, successive collisions will not produce any significant shift in the horizontal direction, making the formation of stable self-organized arrays possible. The phenomenon can also be interpreted as a result of the interaction of droplets mediated by the deformation of the liquid surface below them. Such interactions also occur without bouncing, e.g., between floating solid objects, as illustrated by the mutual attraction of Cheerios in a bowl of milk (Vella & Mahadevan 2005). The interaction is mediated by the interfacial deformation and is the result of an interplay between the effects of surface tension and buoyancy. The relative importance of the latter is decreased for microscale colloidal particles. However, by placing such particles at oil–water interfaces with nonzero anisotropic curvature, Ershov et al. (2013) discovered a new mode of interface-mediated interaction between them and used it to demonstrate self-organization of colloidal spheres into a square lattice. Remarkably, deformation of soft solid surfaces can lead to interaction between liquid droplets deposited on them through a mechanism somewhat analogous to the case of floating particles except that the roles of solid and liquid phases are now reversed. This so-called inverted Cheerios effect (Karpitschka et al. 2016) provides insights into possible mechanisms of self-organization on solid substrates and into the mechanics of locomotion of biological cells. The studies of self-organization discussed in the present review are also relevant for better understanding the self-organization of condensed droplets in breath figures used in the fabrication of structured materials (Srinivasarao et al. 2001, Bormashenko et al. 2020) and the formation of two-dimensional (2D) arrays of particles in dusty plasmas (Petrov et al. 2015).

Levitation and the ordering of microscale liquid droplets can be observed over a dry substrate as well. To demonstrate this, Zaitsev et al. (2017) conducted experiments using a liquid layer with a round dry patch on a heated metal substrate. The droplets of condensate form over the evaporating liquid layer via the mechanism described above. Due to uniform heating, the droplet array is mobile. When it approaches the dry patch, the droplets move along the downslope of the free surface under the action of gravity, ending up in the region above the dry patch, as illustrated in **Figure 2*a***. Note that the droplets are deflected upward as they fly over the contact line, i.e., the boundary of the dry patch. Eventually, these droplets approach the dry solid surface but their impact on the surface is almost never observed. Instead, the droplets end up levitating and organize themselves into a regular array, as seen in the top view (**Figure 2*b***). The observed inter-droplet distance in the array is close to the case of self-organization over a liquid surface. Since these droplets are evaporating, the arrays are short-lived compared to the ones shown in **Figure 1** and typically disappear completely within a few seconds.

Levitation of evaporating droplets near solid surfaces is well studied in situations when the surface is heated to a temperature far above the boiling point of the liquid. A droplet near such a hot

Annu. Rev. Fluid Mech. 2021.53:203-225. Downloaded from www.annualreviews.org
Access provided by 2603:8081:1407:a861:f5e6:c438:d4ff:bfb on 01/08/21. For personal use only.

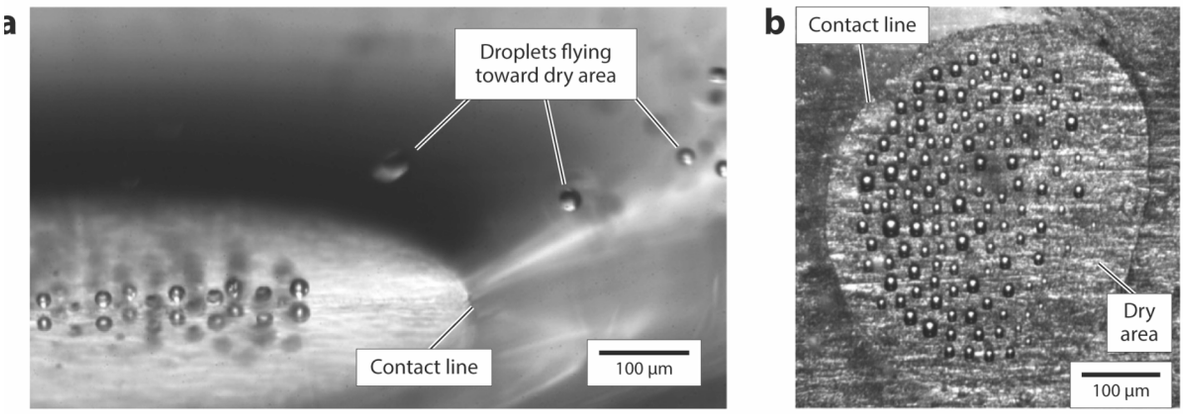

Figure 2

(*a*) Droplets flying over a contact line and ending up over a dry patch on a heated substrate. (*b*) Top view of levitating liquid droplets forming an ordered array over the solid substrate. Figure adapted with permission from Zaitsev et al. (2017), copyright 2017 American Physical Society.

surface quickly forms an insulating vapor layer, allowing it to levitate, a phenomenon known as the Leidenfrost effect (Leidenfrost 1756, Quéré 2013) and schematically illustrated in **Figure 3*a***. The lifetime of the droplet increases dramatically compared to the sessile droplet under the same conditions, as the heat transfer from the hot surface is impeded by the vapor cushion and nucleation of bubbles is prevented due to the lack of contact with the solid. Leidenfrost droplets tend to be highly mobile and nearly spherical when their sizes are below the capillary length, l_c, but they are flattened by gravity at larger sizes. For a liquid of density ρ_l and surface tension σ at its free surface, we define $l_c = (\sigma/\rho_l g)^{1/2}$, with g being the acceleration due to gravity. A photo from a typical experiment is shown in **Figure 3*b***; the vapor layer in this configuration has a thickness on the order of 100 µm, which is much smaller than the droplet size. The distance between the substrate and the droplets in **Figure 2**, on the other hand, is on the same order as their size or larger. Additionally, the substrate temperature in **Figure 2** (85 °C, as measured by thermocouples) is below the boiling temperature of water and far below the temperatures at which the Leidenfrost effect is typically observed. Thus, the classical models of levitation over hot solids, discussed by, e.g., Quéré (2013), are not directly applicable to the situation illustrated in **Figure 2**. Furthermore, self-organization has not been observed in any studies of the Leidenfrost effect.

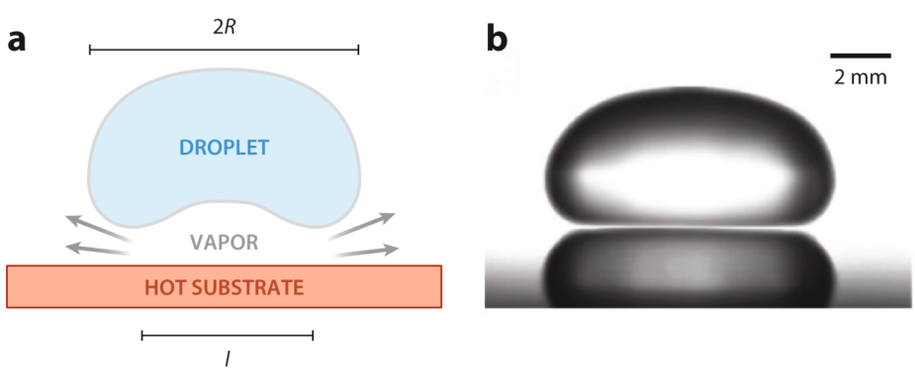

Figure 3

The classical Leidenfrost phenomenon. (*a*) The rapid evaporation of a droplet creates a cushion of vapor that prevents contact with the hot solid. (*b*) Experimental photograph showing a water droplet flattened by gravity levitating above a polished metal plate heated to 300 °C. Panel adapted with permission from Quéré 2013, copyright 2013 Annual Reviews.

Annu. Rev. Fluid Mech. 2021.53:203-225. Downloaded from www.annualreviews.org
Access provided by 2603:8081:1407:a861:f5e6:c438:d4ff:bfb on 01/08/21. For personal use only.

In addition to describing the mechanisms of levitation and self-organization in the configurations illustrated in **Figures 1** and **2**, this review discusses a number of closely related topics, including studies of nonisothermal flotation, i.e., the delay in coalescence between a droplet and liquid bath (Savino et al. 2003), as well as levitation of evaporating liquid droplets over a heated pool of a nonvolatile liquid (Maquet et al. 2016). Also discussed are recent developments in understanding of the Leidenfrost effect since the well-known review by Quéré (2013).

2. APPLICATIONS

While early studies of levitating droplets were primarily motivated by scientific curiosity and fascination with the self-organization phenomena, it has become clear in recent years that these fundamental studies can lead to important practical applications. The work of Fedorets et al. (2015a) overcame an important obstacle to applications of droplet clusters: the continuing growth of droplets by condensation. In a typical experiment, after a few minutes droplets become large enough so that they fall back into the liquid, as described in more detail in Section 3.3 below. In addition to heating the substrate by a laser beam focused to an area of a typical size of ~1 mm in order to maintain evaporation from the water layer, Fedorets et al. (2015a) used four sources of infrared radiation (IR) to provide nearly uniform additional heating of the entire cluster of droplets from the top. This resulted in stabilization of the growth of the droplets and a dramatic increase in the lifetime of the cluster, allowing for the potential use of levitating droplets as containerless chemical microreactors. Of particular interest here are chemical and biochemical reactions whose rates are increased significantly in aqueous droplets compared to bulk water (Nam et al. 2017), a finding that has profound implications for biochemical processes in droplets in Earth's prebiotic atmosphere.

Miniaturization of spray cooling is another potential area of application. The spray cooling technique involves droplets repeatedly striking a hot surface and spreading on it, thus providing a continuous evaporative cooling effect (Kim 2007). For liquids with relatively large latent heat of phase change, the method proves to be efficient on a large scale, but it has not been implemented for microscale systems. One of the obstacles in using spray cooling efficiently on a small scale is the fact that evaporating droplets approaching the hot surface experience the same repulsion force as levitating droplets. This leads to the possibility of significant slowdown of the droplets and mass loss via evaporation before they strike the surface. Understanding the significance of this effect and its role in reduction of heat transfer rates in spray cooling is essential for designing future thermal management systems. In other heat transfer applications, droplet cluster formation can be an unexpected effect that is difficult to avoid. For example, Lyulin et al. (2017) recently observed that a spontaneously formed droplet cluster can affect the dynamics of rupture of evaporating liquid films and shift the location of the rupture point. If such a film is used for cooling a hot surface, formation of a dry patch can lead to a dramatic reduction of cooling efficiency, as the local heat transfer coefficient is much lower in the absence of the liquid film. Thus, the conditions for film rupture resulting in the formation of dry patches are important for these applications.

Kabov et al. (2017) proposed a new method to study gas flow over a dry patch using liquid droplets as tracers. It is well known from studies of evaporating sessile droplets (Deegan et al. 2000, Carle et al. 2016) that the local evaporation rate increases as a contact line is approached and that moist air flow can be generated there as the result of strong evaporation. In the configuration shown in **Figure 2**, the contact line is the boundary of the dry patch, but the same qualitative arguments can be applied. In particular, the moist air flow originating near the contact line explains the upward shift in the droplet trajectories seen in **Figure 2*a***. It is by analyzing these trajectories that Kabov et al. (2017) were able to obtain data on local moist air flow near the contact line. The

Annu. Rev. Fluid Mech. 2021.53:203-225. Downloaded from www.annualreviews.org
Access provided by 2603:8081:1407:a861:f5e6:c438:d4ff:bfb on 01/08/21. For personal use only.

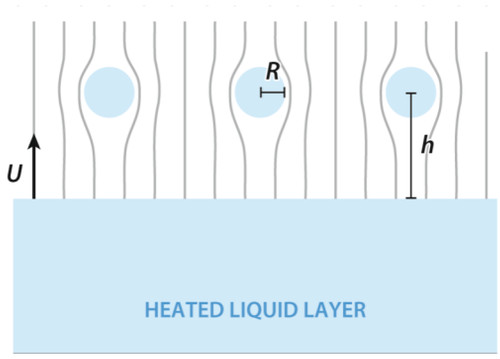

Figure 4

Geometric configuration of an array of droplets of radius R levitating at height h above a heated liquid layer and of the gas flow that provides the Stokes force for levitation. The thin lines represent the upward flow streamlines with characteristic speed U, which are nearly parallel near the liquid surface but deform as the flow goes around the droplets.

position, $\mathbf{r}$, of the center of the droplet, assumed to be spherical of radius R, recorded as a function of time, t, in Cartesian coordinates, satisfies the equation

$$m\mathbf{r}'' = m\mathbf{g} + \mathbf{F}_b + 6\pi\mu R(\mathbf{v} - \mathbf{r}'), \quad 1.$$

where m is the droplet mass; $\mathbf{g}$ is the acceleration of gravity; $\mathbf{F}_b$ is the buoyancy force, which is typically negligible due to a large liquid-to-air density ratio; and μ and $\mathbf{v}$ are the dynamic viscosity and local velocity of the gas phase, respectively. Accurate recording of multiple droplet trajectories thus allows one to find the gas phase velocity, $\mathbf{v}$. Using condensate droplets that are initially very close to the liquid–gas interface as they slide into the dry patch thus provides a unique tool for exploring the region of strong outward flow near the contact line, which is difficult to access via traditional methods such as micro-PIV (particle image velocimetry).

Studies of levitating droplets over dry substrates contribute to our understanding of the Leidenfrost effect over a range of temperatures and of the general conditions when a vapor layer separates a solid surface and liquid, with potential applications being drag reduction and droplet transport in microfluidics. Additionally, Leidenfrost droplets can be used for environment-friendly and low-cost production of nanoparticles and nanoporous metals, as demonstrated by Abdelaziz et al. (2013).

3. DROPLETS OVER LIQUIDS

3.1. Observations and Models of Levitation

Let us now review in more detail work on localized ordered droplet clusters, such as the one shown in **Figure 1*b***. Fedorets's (2004) early experimental studies used layers of water and organic liquids on horizontal substrates with heating produced by a localized light beam or, in later studies (Fedorets 2005), by a Nichrome wire on a copper rod embedded in the substrate. Most recently, Fedorets et al. (2015a) used laser irradiation of a localized area on the substrate. Clusters of levitating droplets were observed for a range of heating conditions. Droplets in the clusters continued to grow by condensation and the distance between the droplets and liquid surface was found to decrease as droplet size increased. Fedorets et al. (2011) provided an important clarification of the levitation mechanism. They identified the gas phase flow of characteristic speed U, originating at the evaporating surface, which is schematically shown in **Figure 4**, as the key factor in levitation. Due to small droplet sizes and moderate evaporation rates, the Reynolds numbers for this flow, $\mathrm{Re} = \rho UR/\mu$, are typically on the order of unity or smaller, meaning that the viscous effects from

Annu. Rev. Fluid Mech. 2021.53:203-225. Downloaded from www.annualreviews.org
Access provided by 2603:8081:1407:a861:f5e6:c438:d4ff:bfb on 01/08/21. For personal use only.

the gas flow around the droplets can provide sufficient upward force to balance gravity and thus lead to levitation. Here and below, ρ denotes the density of the gas phase.

To test their hypothesis about the levitation mechanism, Fedorets et al. (2011) developed an experimental setup that featured two novel ideas: (*a*) the careful measurement of the liquid mass loss by placing the apparatus on a balance and (*b*) the use of an IR camera to study levitating droplet temperatures. For small Reynolds numbers, the upward force on a spherical droplet can be estimated from the classical Stokes drag law, as in Equation 1. The maximum radius of the droplet that can be supported by that force against the downward action of gravity then turns out to be

$$R = \left(\frac{9\mu U}{2\rho_l g}\right)^{1/2}, \qquad 2.$$

where ρ_l is the liquid density. By using the value of U found from the measured evaporative mass loss, Fedorets et al. (2011) determined that the experimental and predicted maximum droplet sizes compare well for higher temperatures but not for lower temperatures. The reason why droplets exhibit a specific height of levitation is not explained by this model.

IR recordings of the droplet cluster were taken from the top, so they provide accurate information about the temperature of the liquid surface and the tops of the droplets (Fedorets et al. 2011, 2013). The images suggest the possibility of significant temperature gradients across the droplet in the vertical direction, although direct measurement of these gradients was not possible due to the positioning of the IR camera. The temperature gradient on the droplet surface can affect gas flow around it (Fedorets 2005) and thus the conditions of levitation through the thermocapillary mechanism, which is discussed in detail below in Section 3.4. However, the relative significance of this mechanism for droplet clusters has not been fully understood.

Zaitsev et al. (2017) further elucidated the nature of the levitation of droplets over liquid surfaces. They argued that the estimates of the gas flow speed, U, in Fedorets et al. (2011) did not account for diffusion mass transport, leading to discrepancies between theory and experiments, especially at lower temperatures. The gas phase surrounding the droplets is a mixture of air and vapor, with vapor concentration being at an equilibrium saturation value, c_e, near the flat liquid surface and at a lower value, c_∞, far above the surface. Continuous evaporation leads to a vapor concentration gradient and thus diffusion of vapor away from the interface. The vapor concentration gradient also implies that there is a gradient of partial density of other components of air in the opposite direction, assuming that the total density of the gas phase is approximately uniform. These components diffuse toward the interface but cannot penetrate it. Therefore, the mass conservation condition requires that there is upward flow, often termed Stefan flow, from the evaporating interface to compensate for the difference in the diffusion fluxes (Sazhin 2014). Once the value of U in Equation 2 is identified as the Stefan flow velocity, comparison between theory and experiment at low temperatures improves significantly. For example, at the lowest heater temperature investigated, Fedorets et al. (2011) predict (after an error in tick labeling in their figure 3 is corrected) that $R \sim 40\ \mu$m, while the Stefan flow model suggests $R = 16.8\ \mu$m, which is much closer to the experimentally observed value of $\sim 10\ \mu$m. Note that as the temperature increases, the partial density of the vapor increases, so the situation becomes qualitatively similar to evaporation into pure vapor. In the latter case, there are no diffusion effects and the gas phase flow of velocity U balances the evaporative mass loss, an implicit assumption made by Fedorets et al. (2011). This argument explains why the agreement between experiments and theory is reasonable at high temperatures in their study.

Coupling between the Stefan flow and diffusion also explains the preferred levitation height chosen by the droplets. Suppose that the droplets are small compared to the levitation height, h,

Annu. Rev. Fluid Mech. 2021.53:203-225. Downloaded from www.annualreviews.org
Access provided by 2603:8081:1407:a861:f5e6:c438:d4ff:bfb on 01/08/21. For personal use only.

and that the convective vapor transport is negligible so that the vapor concentration is described by the steady diffusion equation $\nabla^2 c = 0$. Each condensing droplet acts as a sink for the solution of this diffusion equation. Corresponding corrections for c can be found from the classical method of images. Note that the concentration near the liquid still has to match the equilibrium value of c_e, meaning that the Stefan flow velocity, proportional to $|\nabla c|$, is corrected by a value $\sim R/h^2$. The levitation condition based on this approach is of the form

$$6\pi\mu R\left(U + \delta\frac{R}{h^2}\right) = \frac{4}{3}\pi R^3 \rho_l g, \qquad 3.$$

with δ being a small fitting parameter. This levitation condition suggests that if R_∞ is the droplet radius corresponding to very large levitation height, h, then we have $h \sim (R - R_\infty)^{-1/2}$. Results from different experimental studies turn out to fit this power law (Zaitsev et al. 2017).

As droplet radii increase by condensation, models that represent droplets as point sinks are expected to fail and effects such as the motion of liquid and heat transfer inside the droplet can be expected to affect levitation conditions. These types of phenomena were explored by Fisher & Golovin (2007) using bispherical coordinates to solve equations for Stokes flow and temperature field both inside and outside the droplet, as well as for vapor concentration in air. While droplets were not growing by condensation in their study, this general framework could be used to describe the levitation conditions for the condensate droplet arrays discussed here.

3.2. Mechanisms of Self-Organization

The mechanisms of self-organization of levitating droplets have been discussed by Fedorets et al. (2017) and Zaitsev et al. (2017). There is general consensus that electrostatic interaction is not likely to play a significant role, as the droplet electrical charges are too small. The repulsion force between the droplets can be explained by viscous effects associated with the flow: As two neighboring droplets come closer together, the cross-section of the viscous flow between them, originating at the flat liquid surface, is reduced, thus leading to repulsion—a conclusion opposite to that for inviscid flow models. The repulsion was seen in numerical simulations of spherical particles or droplets in parallel flow for a range of Reynolds numbers (Kim et al. 1993).

The attraction mechanism between the droplets is more controversial. Fedorets et al. (2017) explained the attraction by the radial temperature gradients in the droplet cluster arrangement, a suggestion supported by tracing the motion of individual droplets toward the center of the heated area. However, the droplet arrays observed by Umeki et al. (2015) and Zaitsev et al. (2017) tend to move around, often without a clear preferred direction, yet always retain their structure. One possible explanation can be suggested by recalling that the droplets are continuously condensing, leading to vapor depletion and thus pressure reduction between them. However, there is no quantitative theory describing this effect.

While there is a tremendous amount of literature on microscale droplets and particles, the phenomenon of self-organization of levitating droplets or particles into a single monolayer is very unusual. We are aware of only one other system where such self-organization takes place: a 2D array of hexagonally ordered polystyrene solid particles, as described by Petrov et al. (2015) in experimental studies of dusty plasma in a low-pressure argon environment. The particles are $\sim$10 μm in size and the interparticle distance in the structure is on the order of hundreds of microns, with 2,500–3,000 particles in the layer. Plasma is generated by the radio frequency discharge method, i.e., by applying high AC voltage to two electrodes at radio frequency. The dust particles are electrically charged and ordered structures form in the region of high electric field in the plasma sheath, i.e., the region of excess positive charge formed when electrons are transported

Annu. Rev. Fluid Mech. 2021.53:203-225. Downloaded from www.annualreviews.org
Access provided by 2603:8081:1407:a861:f5e6:c438:d4ff:bfb on 01/08/21. For personal use only.

out of plasma to the bounding surfaces (Fortov et al. 2004). While the significance of electrical charges is in sharp contrast to the situation in the droplet cluster, mathematical analogies can be developed, i.e., by considering hydrodynamic interaction of droplets instead of the electrostatic one. Of particular interest is the fact that studies of dusty plasmas identified specific conditions when self-organization into 2D monolayers is possible, but no analogous conditions for droplet clusters have been discussed, despite the fact that some observations, e.g., by Umeki et al. (2015), have shown much less regular structures than seen in **Figure 1*c***. The degree of regularity can be measured using Voronoi entropy, as proposed by Fedorets et al. (2017), but the connection of this quantity to the physical parameters of interaction between droplets is not yet entirely clear.

Annu. Rev. Fluid Mech. 2021.53:203-225. Downloaded from www.annualreviews.org
Access provided by 2603:8081:1407:a861:f5e6:c438:d4ff:bfb on 01/08/21. For personal use only.

3.3. Cluster Disappearance and Capillary Waves

The levitating droplets forming the cluster continue to slowly increase their size by condensation. Since there is always some size dispersion among the droplets, it seems natural that larger and heavier droplets may occasionally coalesce with the liquid surface when the levitation height becomes comparable to the droplet radius. It may seem that such occasional coalescence events should not have a dramatic effect on the overall global structure of the cluster. However, experimental observations show a different picture. The entire cluster of droplets is destroyed on a very fast timescale, typically in 2–3 ms (Fedorets et al. 2013), after the sinking of the first droplet. Even more puzzling, it was shown that the gap thickness between most droplets and the liquid layer surface is not close to zero just before the cluster disappearance. These observations led to a series of studies using a combination of high-speed video recordings, Schlieren, and IR imaging techniques (Fedorets et al. 2013, 2014, 2015b; Umeki et al. 2015). **Figure 5** shows typical snapshots from an IR camera showing the sequence of events leading to cluster disappearance. The droplet near the edge disappears first. Then a front propagates through the structure very quickly and all droplets end up merging with the liquid layer after about 3 ms. Based on these observations, the following mechanism was suggested. The impact of the initial droplet onto the free surface generates a capillary wave that propagates through the system at a high speed. Simple estimates show that the speed of propagation of the front shown in **Figure 5** matches the speed of capillary waves on the surface of the liquid. The crest of this capillary wave then touches the droplets in the cluster as it propagates through it, resulting in rapid coalescence. However, this explanation remains controversial. It has been argued that the amplitude of the capillary waves is not large enough for the proposed collapse mechanism to be operational. Fedorets et al. (2015b) used the Schlieren method to determine that the amplitude of the capillary wave generated by the collapse of an isolated levitating droplet is in the range of 1–6 microns, which is significantly less than the

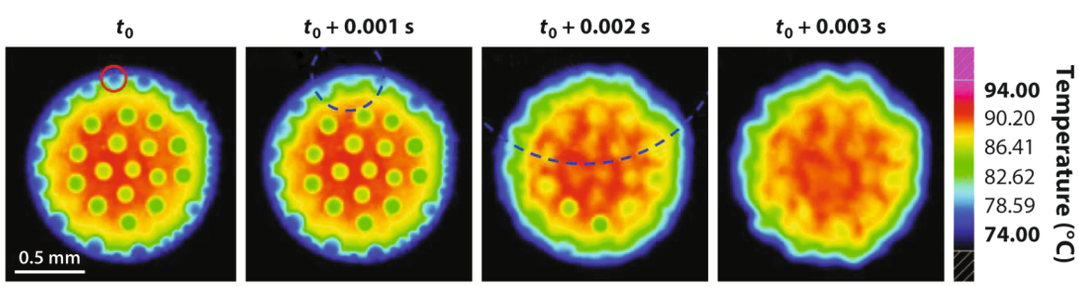

Figure 5

Snapshots showing the collapse of the cluster recorded by an infrared camera after the disappearance of one droplet. The droplet near the edge (*red circle*) disappears first. Then a front (*dashed line*) propagates through the structure very quickly and all droplets end up merging with the liquid layer after about 3 ms. Figure adapted with permission from Fedorets et al. (2013); copyright 2013 Begell House.

droplet–surface gap thickness. Thus, the physics of the collapse process may be more complicated than originally thought.

3.4. Flotation

Osborne Reynolds made early observations of rain striking the surface of small ponds and noted that "drops of water may be seen floating on the surface for some seconds before they disappear" (Reynolds 1881, p. 1). This originated the study of flotation phenomena. While not normally termed "levitation" due to the much shorter timescales during which the droplet remains on the surface before merging with the bulk of the liquid, the physical mechanisms uncovered in studies of flotation have turned out to be relevant to levitation problems, so we feel it is appropriate to discuss them here. The studies of flotation and coalescence can be broadly divided into two categories: isothermal and nonisothermal. The former were reviewed recently by Kavehpour (2015) so we focus on the latter case, specifically a situation when the droplet interacts with a surface with a higher temperature. Thermal effects for this configuration can lead to a significant delay in coalescence compared to the isothermal case (Monti et al. 1998).

Dell'Aversana et al. (1996) and Savino et al. (2003) conducted well-known early detailed studies of nonisothermal flotation. These authors identified the thermal Marangoni effect, i.e., the shear stresses at fluid interfaces due to temperature dependence of the surface tension, as the key physical mechanism in the delay in coalescence of the droplet on top of the large liquid bath of higher temperature T_b. Following the widely used linear approximation (Oron et al. 1997), the surface tension at the liquid–gas interface as a function of local temperature is represented by

$$\sigma(T) = \sigma(T_b) + \sigma_T(T - T_b), \qquad 4.$$

with $\sigma_T < 0$. A droplet of initial temperature $T_d < T_b$ close to the bath surface causes a local decrease in the surface temperature. Corresponding shear stress, shown in **Figure 6*a***, pushes air into the gap between the droplet and the bath so that flotation is possible. This physical mechanism suggests that the gas flow rate into the gap and thus the noncoalescence conditions strongly

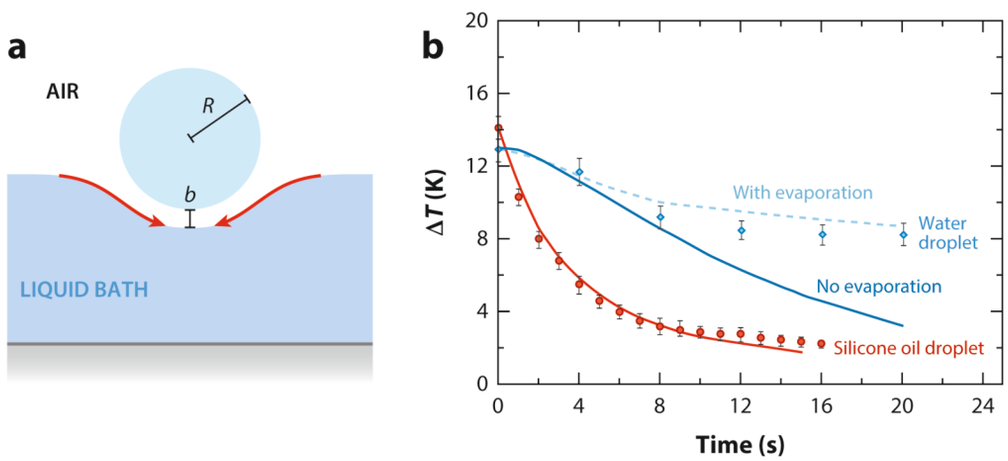

Figure 6

(*a*) Geometric configuration used in studies of flotation. The liquid bath surface deforms due to the presence of the droplet above it; red lines show the direction of thermocapillary stresses at the interface. (*b*) Comparison between experimental (*circles*) and computational (*lines*) results for the time evolution of the temperature difference, ΔT, between floating droplets [water and 100 cSt (centistoke) silicone oil] and the surface of a bath of 3 cSt silicone oil. The dashed line corresponds to a modified numerical model incorporating the effect of evaporation. Panel adapted with permission from Savino et al. (2003), copyright 2003 Cambridge University Press.

Annu. Rev. Fluid Mech. 2021.53:203-225. Downloaded from www.annualreviews.org
Access provided by 2603:8081:1407:a861:f5e6:c438:d4ff:bfb on 01/08/21. For personal use only.

depend on the temperature difference between the droplet and the bath (also termed a pool), motivating Savino et al. (2003) to conduct both experimental and numerical studies of this quantity. IR camera recordings allowed them to determine how the temperature difference ΔT between the top of the droplet and the bath surface away from the droplet decays as a function of time. The results for water and silicone oil droplets over a bath of less viscous silicone oil are shown in **Figure 6*b***, which also presents results from computational studies based on the solution of the continuity, Navier–Stokes, and energy equations in both liquid phases and air. The droplet domain is assumed spherical, while the bath surface shape is calculated from the equation of capillary statics. When evaporation is neglected, computational results agree with experimental data for silicone oil droplets but not water droplets. Savino et al. (2003) showed that modifying the model to include an evaporation effect by adding constant uniform heat flux at the water droplet surface improves the agreement significantly.

In addition to detailed numerical studies, Savino et al. (2003) obtained analytical estimates of the thickness b of the gas layer separating the droplet from the bath using a lubrication-type approach (Oron et al. 1997), assuming b is much smaller than the radial scale for the air gap. The shear stress jump estimate at the surface of the bath is given by $\sigma_T(\overline{T}_d - T_b)/R$, where $\overline{T}_d$ is the average drop temperature. In a steady-state configuration, the flow rate for the gas in the gap is zero, so the contribution of the shear stress to the average air velocity has to be balanced by a part driven by the pressure gradient; the latter can be expressed in terms of the estimated pressure increase, Δp, under the droplet. This pressure increase balances the weight of the droplet in the following levitation condition:

$$\Delta p \frac{1}{4}\pi R^2 = \rho_l g \frac{4}{3}\pi R^3. \qquad 5.$$

For this condition, Savino et al. (2003) used an estimate of the area of the part of the droplet in contact with the bath, $\pi R^2/4$, consistent with the experimentally recorded images. Once Δp is related to the shear stress from the condition of zero total flow rate in the gap, the levitation condition leads to the formula for film thickness,

$$b = \sqrt{\frac{3}{16}\frac{\mu}{\mu_b}\frac{\sigma_T}{\rho g}(\overline{T}_d - T_b)}, \qquad 6.$$

giving typical values of about 10 μm, with μ_b being the viscosity of the liquid in the bath. The estimate of b here does not account for the effects of evaporation and thus may be inaccurate for floating water droplets. The role of evaporation has been further elucidated in subsequent studies described in the next subsection. We note that the topic of coalescence was also discussed in the context of the interaction of two droplets, as reviewed, e.g., by Neitzel & Dell'Aversana (2002). The thermocapillary mechanism of repulsion between the interfaces discussed here is relevant for this configuration as well.

Renewed interest in flotation-type problems is due to recent studies by Geri et al. (2017). They conducted experiments and developed mathematical models of droplet flotation over a bath of the same liquid, of viscosity μ_l, based on the assumption that bath surface deformation is weak, as illustrated in **Figure 7*a*,*b***. In contrast to previous studies, thermocapillary stresses were considered not only at the bath surface but also at the surface of the droplet. The delay in coalescence due to the Marangoni effect is characterized by the delay time, $\tau_d = t_r - t_r^0$, measured by high-speed camera recordings. Here, t_r and t_r^0 are the measured residence times of the droplet for the nonisothermal and isothermal cases, respectively. The moment of coalescence is defined by the appearance of capillary waves on the droplet surface. Based on experimental measurements for several silicone oils spanning a wide range of viscosities, illustrated in **Figure 7*c***, the delay time was found to

Annu. Rev. Fluid Mech. 2021.53:203-225. Downloaded from www.annualreviews.org
Access provided by 2603:8081:1407:a861:f5e6:c438:d4ff:bfb on 01/08/21. For personal use only.

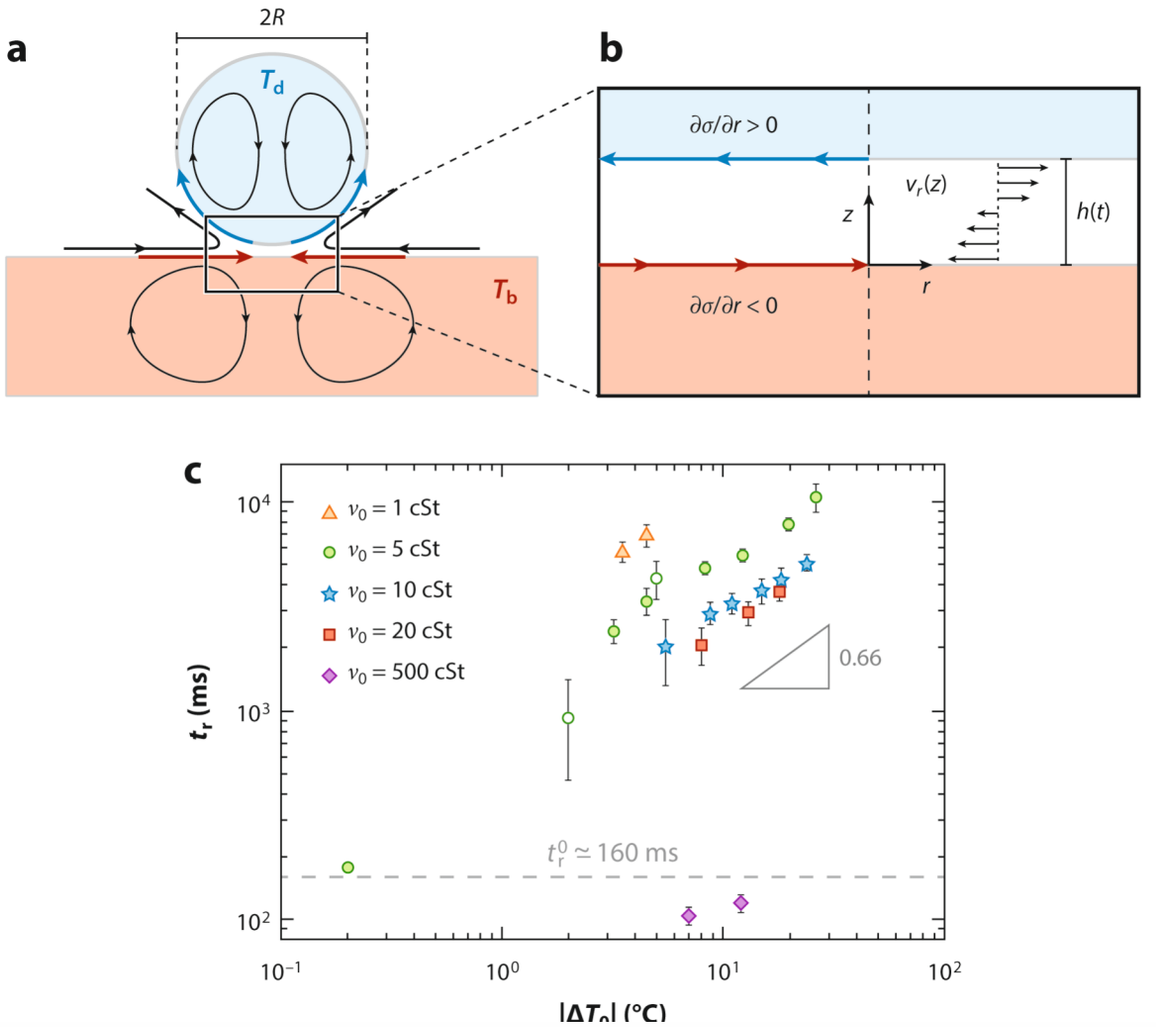

Figure 7

(*a*,*b*) The geometric configuration considered in the study of flotation by Geri et al. (2017) involving a droplet of temperature T_d and radius R floating over a bath of temperature T_b. Red lines show the direction of thermocapillary flow pushing gas into the gap, while blue lines illustrate the opposite effect due to temperature variation along the droplet surface. (*c*) The nonisothermal flotation time, t_r, plotted as a function of the temperature difference, ΔT_0, between the liquid bath and the droplet. Here ν_0 are liquid kinematic viscosities, measured in centistokes (cSt). Figure adapted with permission from Geri et al. (2017), copyright 2017 Cambridge University Press.

depend on the initial temperature difference between the bath and the droplet according to the power law $\tau_d \sim (\Delta T_0)^{2/3}$ as long as the temperature difference is above a certain critical value. Below that value, no difference between the residence time and its isothermal value was detected beyond the usual experimental errors, as was also observed in several earlier experimental studies (Neitzel & Dell'Aversana 2002). In nondimensional terms, the critical temperature difference can be expressed as the critical value of the Marangoni number, $\mathrm{Ma} = |\sigma_T \Delta T_0| R/\mu_l \alpha_l$, where α_l is the thermal diffusivity of the liquid.

In order to describe the experimental observations, Geri et al. (2017) developed an unsteady model of the gas flow in the gap separating the droplet and the liquid bath. To avoid complications due to interface deformations, they considered a simplified geometry in which both bounding surfaces are assumed to be flat, as shown in **Figure 7*b***. The assumptions of the classical lubrication theory (Oron et al. 1997) in this context lead to the radial parabolic velocity profile in terms of $\partial p/\partial r$, the yet-unknown pressure gradient, and the interfacial radial velocities at the top and bottom boundaries of the gas layer, v_d and v_b, respectively; this velocity profile is illustrated schematically in **Figure 7*b***. If the distance between the interfaces, $h(t)$, is decreasing, the rate at which the

Annu. Rev. Fluid Mech. 2021.53:203-225. Downloaded from www.annualreviews.org
Access provided by 2603:8081:1407:a861:f5e6:c438:d4ff:bfb on 01/08/21. For personal use only.

gas is being squeezed from the gap has to match the flow rate obtained by integrating the radial velocity profile, assuming the gas to be an incompressible Newtonian fluid. The balance of the flow rates then leads to

$$\frac{h^3}{6\mu}\frac{\partial p}{\partial r} = r\frac{\partial h}{\partial t} + h(v_\mathrm{d} + v_\mathrm{b}). \qquad 7.$$

The lubrication-type approximation is expected to break down outside the air gap region, so the formulas for velocity and pressure gradient can only be applied when the radial coordinate is below a certain value, R_d, which Geri et al. (2017) assumed to be the characteristic radius of contact of a deformable droplet and a flat surface, R^2/l_c, where l_c is the capillary length of the liquid. Equation 7 can now be integrated with the condition that pressure be at the atmospheric value at $r = R_\mathrm{d}$, leading to a pressure distribution in the gap. Integration of the pressure gives the force acting on the droplet, which can then be balanced by the weight of the droplet, assuming a quasi-static configuration, as was done in Equation 5 except that the left-hand side of that condition is now evaluated more accurately by integrating the radial pressure profile in the gap. The result leads to a single differential equation for the gap thickness, which can be conveniently written in nondimensional form as

$$\frac{\mathrm{d}h^*}{\mathrm{d}t^*} = -h^*\left(\frac{h^{*2}}{2} - \frac{4}{3}\frac{\tau_\mathrm{s}}{\tau_\mathrm{th}}\frac{R}{R_\mathrm{d}}\mathrm{Ma}\right). \qquad 8.$$

Here, the thickness is scaled by its initial value, h_0, and the two characteristic times involved are the isothermal settling time, $\tau_\mathrm{s} = 9\mu R_\mathrm{d}^4/(16\rho_\mathrm{l} g R^3 h_0^2)$, and the thermal diffusion time, $\tau_\mathrm{th} = R^2/\alpha_l$. The nondimensional time is defined as $t^* = t/\tau_\mathrm{s}$. For $\mathrm{Ma} = 0$, the classical squeeze flow under constant force is recovered from Equation 8, with h^* monotonically decreasing with time. There is a critical value of the Marangoni number above which the sign of the right-hand side of Equation 8 changes, suggesting that the gap thickness will not decrease. This critical value was estimated to be near $\approx$100, in good agreement with the experimental results.

While predicting the critical Marangoni number, the argument above does not explain the experimental dependence of t_r on the temperature difference shown in **Figure 7*c*** and in fact seems to contradict the data since the droplet is expected to be floating indefinitely based on the solution of Equation 8. The resolution of this contradiction was provided by a description of the flow in the droplet induced by the Marangoni stresses. This flow defines the timescale of the gradual decrease of the temperature difference between the droplet and the bath. Geri et al. (2017) described this process using the framework developed for scalar mixing in axisymmetric vortex flow and obtained its characteristic timescale, leading to the 2/3 law seen in **Figure 7*c***.

3.5. Leidenfrost over Liquid Surfaces

Maquet et al. (2016) conducted careful experimental and theoretical studies of levitation of evaporating ethanol droplets over the free surface of a large heated pool of silicone oil. In contrast to the previously discussed works of, e.g., Fedorets et al. (2011), the liquid pool evaporation is negligible due to the low volatility of silicone oil. However, the effect of evaporation of the droplet itself is significant and can result in levitation, leading the authors to describe the observed phenomenon as "Leidenfrost over liquid." The overall configuration is similar to the one from Savino et al. (2003), as shown in **Figure 6*a***, except that now not only the pool surface but also the droplet is deformed. These axisymmetric deformations, illustrated in **Figure 8*a***, are described by the functions $e(r)$ and $h(r)$, respectively. A lubrication-type framework (Oron et al. 1997) was used to describe the gas flow in the gap separating the droplet from the pool. The approximation is assumed to be valid for the values of the radial coordinate below a patching point $r = R_*$ shown in **Figure 8*a***, where

Annu. Rev. Fluid Mech. 2021.53:203-225. Downloaded from www.annualreviews.org
Access provided by 2603:8081:1407:a861:f5e6:c438:d4ff:bfb on 01/08/21. For personal use only.

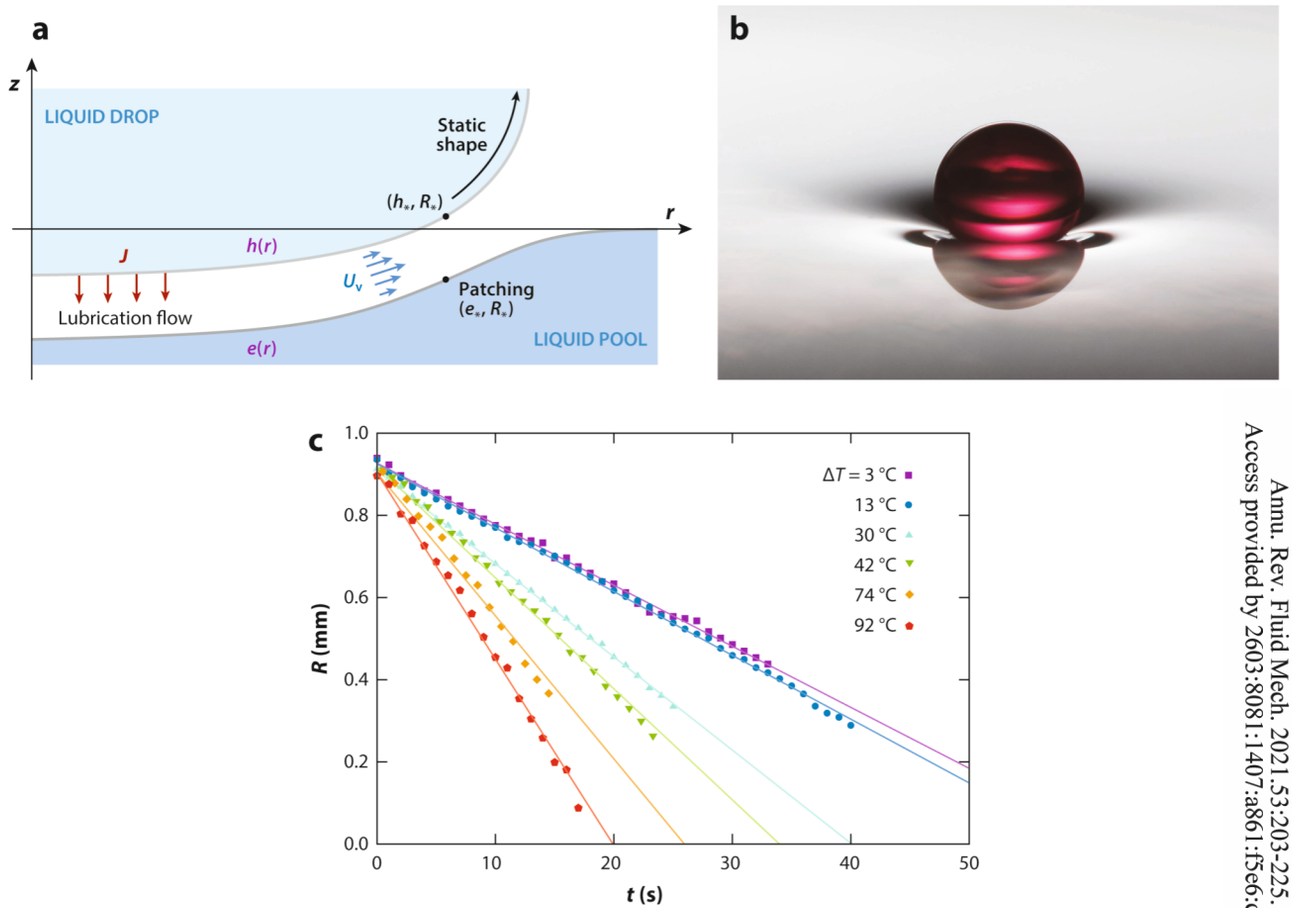

Figure 8

(*a*) Geometric configuration used in Maquet et al.'s (2016) study of gas flow in the gap between the droplet and the pool. Axisymmetric deformations of the pool and the drop are described by the functions $e(r)$ and $h(r)$, respectively. (*b*) Photograph of droplet levitation over a deformed pool. (*c*) Radius R as a function of time t as measured by Maquet et al. (2016). Figure adapted with permission from Maquet et al. (2016), copyright 2016 American Physical Society.

the lubrication-type solution is patched to the capillary static shapes of the droplet and pool surface. The gap velocity profile is driven by the pressure gradient and the Marangoni stresses at the interfaces are neglected, but the interfacial evaporation flux,

$$J = \mathcal{L}^{-1}\lambda\Delta T/(h-e), \qquad 9.$$

is added into the mass balance. Here, $\mathcal{L}$ is the latent heat of phase change, λ is the vapor thermal conductivity, and ΔT is the superheat, i.e., the difference between the pool temperature and the boiling temperature of the liquid of the drop. Maquet et al. (2016) measured the pool deformation, seen in **Figure 8*b***, and showed it to be in excellent agreement with the predictions of their model except for droplets of radii above ~2 mm. The vapor film thickness, $h_f = h - e$, while not measured directly, was obtained from the model for a range of conditions. As in the previously discussed studies, the capillary length of the drop liquid, l_c, turns out to be an important quantity (equal to about 1.56 mm for ethanol). For $R \leq l_c$, the vapor film profile and its dependencies on the droplet size and superheat are similar to the classical results on droplets levitating in the Leidenfrost state over hot solid surfaces. This is generally not surprising since the pool surface deformations in this regime are relatively weak. However, some of the predictions

Annu. Rev. Fluid Mech. 2021.53:203-225. Downloaded from www.annualreviews.org
Access provided by 2603:8081:1407:a861:f5e6:c438:d4ff:bfb on 01/08/21. For personal use only.

differ drastically for the large droplets of radii well above l_c. In particular, the film thickness at the center is expected to increase as $(R/l_c)^{1/2}$. The values of h_f are typically on the order of 10 μm, so experimental measurements to compare with the model predictions seem to be feasible and would certainly be of interest.

Maquet et al. (2016) also recorded the droplet radius as a function of time. For a wide range of droplet sizes and evaporation conditions, the change in the radius can be represented by

$$R = R_0 \left(1 - \frac{t}{\tau}\right)^{\alpha}. \qquad 10.$$

The exponent α depends on the configuration, and τ is the drop lifetime. For the ideally spherical evaporating drop, the value is 1/2, which is the classical *D*-squared law going back to the works of Maxwell. However, it was already established that for strongly deformed Leidenfrost droplets the radius is better described by $\alpha = 2$ (Biance et al. 2003). In contrast, Maquet et al. (2016) found a linear dependence, i.e., $\alpha = 1$, as seen in **Figure 8*c***, and discussed theoretical arguments to justify this dependence. We emphasize that this result is rather unusual since the *D*-squared law is routinely assumed to provide a reasonable approximation of the evaporating droplet radius even near other interfaces.

While the work of Maquet et al. (2016) is based on numerical studies, a follow-up study by Van Limbeek et al. (2019) provided detailed asymptotic analysis, valid for sufficiently small superheat, which gave important insights into the physics of the problem. In particular, the vapor gap thickness profiles for the case of a droplet on a liquid bath were compared with the case of the solid: In the former case there is nearly constant thickness, while for the latter there is a dimple shape, as sketched above in **Figure 3*a***. The pressure gradient for this classical Leidenfrost configuration is fully determined by the gap thickness, while for droplets over a liquid substrate the leading-order pressure gradient is dictated by the substrate curvature. This explains the difference in vapor layer morphologies.

Since the vapor layer between a droplet and a strongly deformed liquid pool is key for the Leidenfrost effect over liquid, it is natural to expect levitation when such a layer is created by evaporation of the liquid pool rather than the droplet. This so-called inverse Leidenfrost phenomenon was indeed observed by Adda-Bedia et al. (2016) for aqueous droplets over a liquid nitrogen bath. Levitation was only possible for sufficiently small droplets, and the total levitation time increased approximately linearly with droplet size but was not very sensitive to changes in droplet density. Starting from the initial condition of room temperature, droplets gradually cooled down and eventually froze due to the low temperature of liquid nitrogen. Adda-Bedia et al. (2016) provided a detailed discussion of mathematical models of the observed phenomenon and historical perspective going back to the classical study of levitation of hot metal particles over a cold liquid bath (Hall et al. 1969). The remarkable self-propulsion of droplets of ethanol and silicone oil over a nitrogen bath in the inverse Leidenfrost configuration was studied recently by Gauthier et al. (2019). Levitating droplets tend to move in straight lines, gradually decelerating as a result of an increase in friction as the vapor layer becomes thinner due to cooling. Reflections off the walls of the container result in a change in the direction of motion. The origin of the symmetry breaking that leads to self-propulsion, also observed in 2D finite-element computations with symmetric initial shapes of the interfaces, is not fully understood and may have to do with interfacial instabilities. Interestingly, even though both the inverse Leidenfrost effect and the droplet clusters discussed in Sections 3.1 and 3.2 involve levitation over evaporating liquid surfaces, the connection between the two phenomena has not been made in the literature. Despite differences between the experimental conditions, most notably strong deformation and the low temperature of the pool used for inverse Leidenfrost studies, we feel that making such a connection could benefit understanding both of the self-propulsion effect and of the ordering of levitating droplets.

Annu. Rev. Fluid Mech. 2021.53:203-225. Downloaded from www.annualreviews.org
Access provided by 2603:8081:1407:a861:f5e6:c438:d4ff:bfb on 01/08/21. For personal use only.

4. DROPLETS OVER DRY SOLIDS

4.1. Leidenfrost Effect: Recent Developments

The classical example of levitation over solid surfaces is, of course, the celebrated Leidenfrost effect described in Section 1 and illustrated in **Figure 3**. A comprehensive review of these types of phenomena has been provided by Quéré (2013), who also gives a fascinating historical perspective going back to Leidenfrost (1756) and to even earlier observations of the same phenomenon by Herman Boerhaave. However, in recent years there have been a few new developments and the objective of the present section is to review some of the recent studies on the topic.

Sobac et al. (2014) carried out detailed studies of the shape of the vapor film separating the Leidenfrost drop and the hot surface. Their lubrication-type approach is very similar to the work on Leidenfrost over liquid discussed in detail in Section 3.5, except that the bottom boundary of the film is flat (corresponding to $e = 0$). The key conclusions included new scaling laws generalizing the well-known results of Biance et al. (2003). The general shape of the droplet is qualitatively consistent with the sketch in **Figure 3*a***. The vapor film thickness scales with the superheat as $(\Delta T)^{1/6}$ in the center and $(\Delta T)^{1/3}$ at the neck, i.e., the minimum of thickness, for a range of parameter values based on numerical solutions. Analysis based on the method of matched asymptotic expansions, valid for sufficiently small values of the superheat, supports the key results obtained from the numerical studies. Vapor film thickness is consistent with interferometric measurements reviewed, e.g., by Quéré (2013).

The shape of the vapor film can be affected by cooling of the substrate due to the presence of a droplet above it, an effect that has been well recognized in studies of flotation but often neglected in the context of the Leidenfrost phenomena. Van Limbeek et al. (2017) incorporated heat conduction in the solid substrate below the levitating droplet into a mathematical framework developed in previous studies and developed an experimental apparatus to detect small variations in the refractive index with temperature using Mach–Zehnder interferometry, to investigate cooling of a quartz plate below the levitating droplet. The temperature decrease was as high as 80 K, in satisfactory agreement with numerical predictions. The model did not account for evaporation from the top of the droplet, which may explain its tendency to slightly underestimate the temperature drop. Substrate cooling leads to a reduction of the vapor film thickness as compared to predictions from Sobac et al. (2014). Increasing the thermal conductivity in the model from the relatively low value corresponding to quartz shows that the isothermal limit is reached near 100 W/(mK), with a further increase having no effect on either temperature profiles or the vapor film thickness for ethanol droplets levitating over a conductive plate several millimeters thick heated from below.

In addition to interferometric measurements, the method of total internal reflection imaging was used to study vapor films for a dynamic configuration involving the impact of an evaporating droplet at a specified speed U onto a hot surface (Shirota et al. 2016). This situation, often called the dynamic Leidenfrost effect, is most relevant for applications such as spray cooling. For ethanol droplets with an impact velocity of 1.3 m/s and substrate temperature below about 180 °C, the area under the base of the spreading droplet wets the substrate, except for locations of nucleating bubbles. At temperatures above ~220 °C, the Leidenfrost configuration is observed, with no contact between the droplet and the substrate. An intermediate regime was also found such that part of the region under the droplet is wetted and the rest of the elongated droplet is nonwetting. Qualitatively similar results were obtained for a range of impact velocities and for another liquid FC-84.

Vakarelski et al. (2012) conducted pioneering experiments on the Leidenfrost effect on textured superhydrophobic surfaces. They found a dependence of the Leidenfrost temperature on the characteristics of the surface and showed that the presence of the texture allows one to avoid

Annu. Rev. Fluid Mech. 2021.53:203-225. Downloaded from www.annualreviews.org
Access provided by 2603:8081:1407:a861:f5e6:c438:d4ff:bfb on 01/08/21. For personal use only.

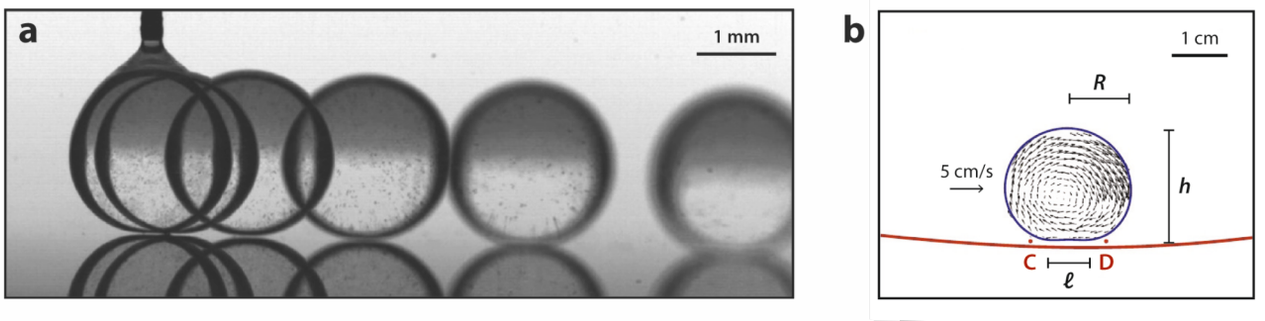

Figure 9

(*a*) Snapshots of a levitating self-propelled droplet, at 94-ms time intervals, gently deposited from a needle on a surface heated to 300 °C. (*b*) Particle image velocimetry measurements showing the velocity inside a quasi-spherical drop immobilized on a slightly curved surface; air entrained by the flow in the layer of horizontal extent ℓ enters from point D and exits at point C. Figure adapted with permission from Bouillant et al. (2018), copyright 2018 Springer Nature.

Annu. Rev. Fluid Mech. 2021.53:203-225. Downloaded from www.annualreviews.org
Access provided by 2603:8081:1407:a861:f5e6:c438:d4ff:bfb on 01/08/21. For personal use only.

the nucleate boiling regime expected when the temperature drops below the Leidenfrost point and the vapor cushion collapses. Motivated by applications to drag reduction, Vakarelski et al. (2012) focused on hot spheres with different surface properties immersed in water, although their conclusions are supported by experiments with heated cylinders immersed in a pool of water.

The exceptional mobility of Leidenfrost droplets presents challenges for experimental observation but also leads to potential applications, e.g., the controlled transport of droplets in microfluidics using asymmetric topographical patterns on a substrate (Linke et al. 2006). The rapid spontaneous motion of droplets on flat heated substrates is often explained by external influences, e.g., air flow or a slight tilt of the surface, coupled with the low friction due to the vapor cushion. This view was challenged in a recent experimental study by Bouillant et al. (2018), who discovered the self-propelled motion of carefully deposited Leidenfrost droplets in the absence of any external source of asymmetry (**Figure 9*a***). Rapid internal flow was observed using the PIV technique (**Figure 9*b***), and the droplet was slightly tilted as it moved. The exact mechanism of symmetry breaking when such a motion is initiated is still not fully understood. Interestingly, the ability of droplets to move spontaneously was also seen in the so-called aerodynamic Leidenfrost configuration, when levitation is the result of rapid motion of the solid substrate, leading to air entrainment and thus the formation of a layer separating the droplet from the substrate (Gauthier et al. 2016). These droplets are found to be moving against the force of gravity when the substrate is tilted.

Another novel direction of Leidenfrost studies is motivated by different choice of materials for the levitating object. Starting with the classical observation of dry ice levitating over a hot metal plate, as described by Quéré (2013), more recently researchers have focused on intermediate situations between the extremes of dry ice and a Newtonian liquid. Waitukaitis et al. (2017) reported studies of droplets of hydrogel over a hot surface that were found to bounce in a sustained fashion rather than levitate. The phase change was shown to provide the mechanical energy needed for bouncing, as the same height was reached after each bounce.

While evaporation of Leidenfrost droplets is relatively slow, they do eventually decrease in size by losing mass. Celestini et al. (2012) conducted observations of Leidenfrost droplets that lost significant mass and observed that sufficiently small droplets started rapidly moving upward, a phenomenon called the takeoff of Leidenfrost droplets, as seen in **Figure 10*a***. To find a criterion for the critical radius, R_l, for the takeoff, one can use the lubrication-type approach discussed in Section 3.5, based on the assumption that the horizontal extent of the vapor film, l, is much smaller than the layer thickness, h. Equation 9 with $e = 0$ as appropriate for the undeformed solid boundary provides an estimate for the evaporation flux, which, together with the mass balance, allows one to express the horizontal velocity as $u \sim l\lambda\Delta T/(h^2\mathcal{L}\rho)$. The pressure increase under the droplet, Δp,

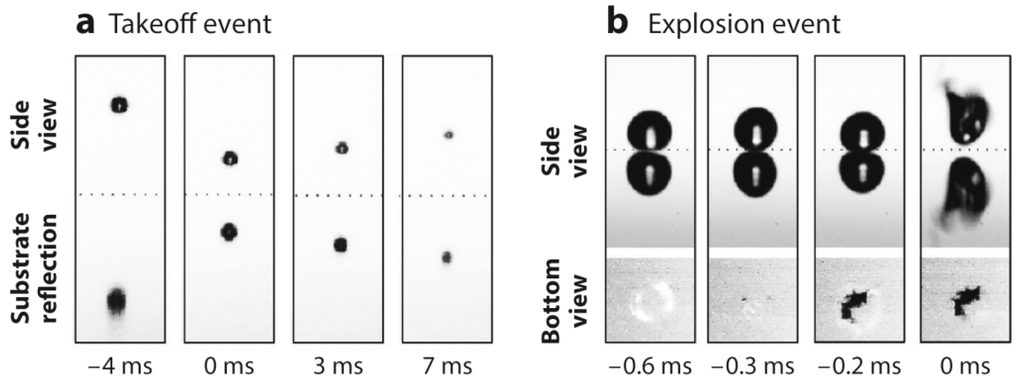

Figure 10

Experimental video frames showing droplet takeoff (*a*) versus explosion (*b*). Figure adapted with permission from Lyu et al. (2019), CC-BY-NC 4.0.

is then estimated from the condition $\Delta p/l \sim \mu u/h^2$ and substituted into the levitation condition, i.e., the condition that the pressure increase in the gap compensates for the weight of the droplet. The lubrication-type argument breaks down at $h \sim l$, providing an estimate for the radius below which the droplet can be expected to take off:

$$R_{\mathrm{l}} = \left(\frac{\mu\lambda\Delta T}{g\mathcal{L}\rho\rho_l}\right)^{1/3}. \tag{11.}$$

The experimental data from studies of water droplets with substrates kept at a temperature of 400 °C show that $R_{\mathrm{l}} \sim 19$ μm, found from the formula above, is indeed a reasonable estimate of the droplet size at which the takeoff starts.

For sizes well below R_{l}, each evaporating droplet can be represented as a point singularity for the solution of the Laplace equation describing heat transfer around it. The Stokes drag force acting on the droplet can then be calculated from the flow generated by the image of the singularity, leading to the formula for the scaled levitation height:

$$\frac{h}{R} = \left(\frac{R_{\mathrm{l}}}{R}\right)^{3/2}, \tag{12.}$$

which is also in agreement with the experimental data on the water droplet takeoff.

Leidenfrost (1756) provided his take on the final stage of the evaporating droplet evolution, observing that "with an audible crack, which with the ears one easily hears, it [the droplet] finishes its existence" [as quoted in Celestini et al. (2012) from the English translation of Leidenfrost (1756)]. This seems to contradict the takeoff scenario, as tiny droplets flying away from the substrate are not likely to generate acoustic effects. Remarkably, this contradiction was fully resolved only very recently by Lyu et al. (2019), who showed that takeoff is not the only scenario possible for the final fate of the Leidenfrost droplet. In fact, the droplet can explode with audible sound, as shown in the video from which **Figure 10*b*** is taken. A map showing transition between the takeoff and explosion regimes was produced by Lyu et al. (2019). Their hypothesis was that liquid contamination is the cause of the explosion. To test this hypothesis, they added microparticles of controlled volume fraction ϕ_{i} and found that the critical radius for explosion, scaled by the initial radius R_{i}, follows the power law

$$\frac{R_{\mathrm{e}}}{R_{\mathrm{i}}} \sim \phi_{\mathrm{i}}^{1/3}. \tag{13.}$$

This power law can be extrapolated to the case of liquids without particles added, giving values consistent with the typical degree of contamination of liquids. The mechanism of explosion is due

Annu. Rev. Fluid Mech. 2021.53:203-225. Downloaded from www.annualreviews.org
Access provided by 2603:8081:1407:a861:f5e6:c438:d4ff:bfb on 01/08/21. For personal use only.

to contact with the hot substrate rather than pressure buildup inside the droplet. We note that for heat transfer applications, the Leidenfrost effect is typically undesirable, so the addition of microparticles offers an approach to enhance heat transfer.

The explosive behavior due to contamination suggests that other types of impurities, such as surfactants, may lead to similar behavior. This was indeed found in the work of Moreau et al. (2019) on the Leidenfrost effect in evaporating surfactant droplets. As the droplet size decreases by evaporation, surfactant micelles accumulate at its surface, forming a gel-like shell. Since the surfactant is nonvolatile, this leads to a sharp increase of droplet temperature, initiating the boiling process in the core and thus leading to droplet explosion.

Annu. Rev. Fluid Mech. 2021.53:203-225. Downloaded from www.annualreviews.org
Access provided by 2603:8081:1407:a861:f5e6:c438:d4ff:bfb on 01/08/21. For personal use only.

4.2. Low-Temperature Leidenfrost and Self-Organization

The experimental work of Zaitsev et al. (2017) showed levitation and self-organization of droplets over a dry patch on the substrate, as discussed above and illustrated in **Figure 2**. To provide a quantitative explanation of levitation, Zaitsev et al. (2017) developed a model for small evaporating droplets, treating each as a source for the hydrodynamic flow in the gas phase. Note that droplets near the hot metal surface immediately start evaporating, in contrast to condensing droplets over the liquid surface, discussed in Section 3.1. The experimental measurements of the radius of the droplet show that for sufficiently small droplets it is described by $R^2 = R_0^2 - \alpha t$. The height of levitation is found from the model to be of the form

$$h = \frac{3}{4}\left(\frac{3\alpha\mu}{\rho g R}\right)^{1/2}. \qquad 14.$$

This formula is based on the assumption that the droplet is a point source generating Stefan flow, which, when reflected off of the solid surface, provides the mechanism for levitation. In other words, the droplets are supported by the gas phase flow, but this flow can be interpreted as generated by the image of the original source (**Figure 11*a***). The method of images for viscous flow can then be used to estimate the velocity of the flow around the droplet and thus the Stokes force associated with the flow. Balancing this force with droplet weight leads to the condition of

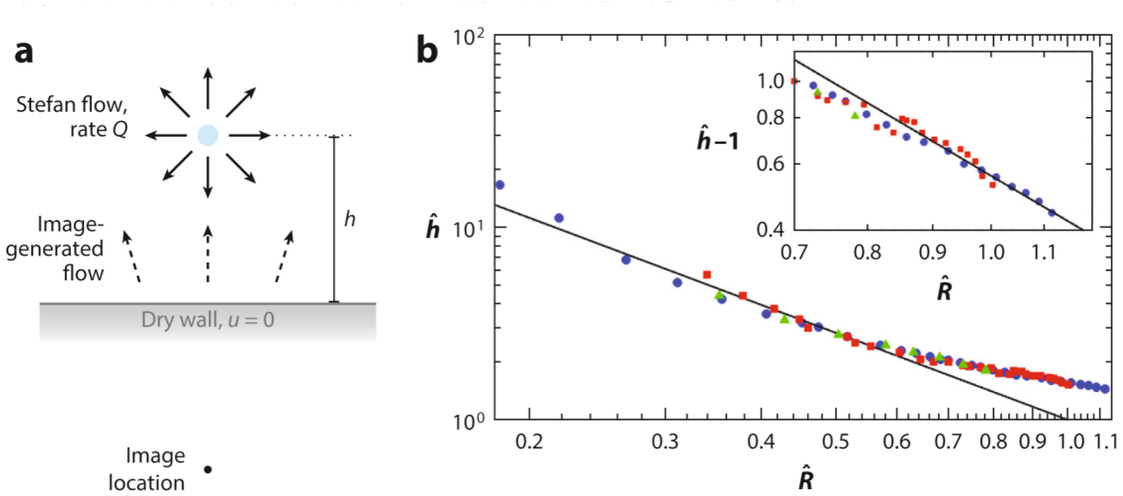

Figure 11

(*a*) The point source model of an evaporating droplet near a hot surface; the location of the image is also shown. (*b*) Comparison of Zaitsev et al.'s (2017) experimental (*symbols*) and theoretical (*solid lines*) results on droplet levitation height, $\hat{h}$, over a dry patch versus its radius, $\hat{R}$, in nondimensional variables. The inset shows details for larger droplets, when a different power law is observed. Figure adapted with permission from Zaitsev et al. (2017), copyright 2017 American Physical Society.

Equation 14. Since levitation is sustained by evaporation of the droplet itself, the situation is somewhat similar to the Leidenfrost effect, but in the range of much lower solid surface temperatures. The comparison between experiment and theory is very good for sufficiently small droplets, illustrated in **Figure 11*b***. The inset shows data for the case of larger droplets and is not described by the model. This can be explained by the fact that the assumption that the droplet is much smaller than the levitation height no longer holds. In this regime, a crossover to a different power law, shown by the solid line in the inset, is observed. Self-organization is described in qualitative terms by a competition between the repulsion of evaporating droplets and the flow toward the center of the dry patch pushing the droplets together. The flow is most likely generated as a result of strong evaporation near the contact line, which is the boundary of the dry patch.

4.3. Thermocapillary Levitation over Solids

The careful studies of flotation over liquid surfaces discussed in Section 3.4 motivated efforts to use the thermocapillary effect to achieve levitation over solid surfaces. Nagy & Neitzel (2008) provided a successful demonstration of such phenomena and their use in microfluidic settings. They heated silicone oil droplets of typical diameters of 1 mm from above by means of laser irradiation and observed them to levitate over a glass surface cooled from below. The temperature gradient caused thermocapillary flow in the droplet, and the interfacial shear stress dragged the gas into the air gap between the droplet and the substrate, a mechanism supported by direct visualization of air flow around the droplet using smoke and sheet illumination. Strong liquid circulation caused by thermocapillary stresses was confirmed by tracking the motion of smoke particles that became attached to the liquid surface. By moving the laser beam that provided heating, they could move the droplet in a controlled fashion. Most importantly, the air gap between the droplet and the substrate persisted during this motion, leading to a dramatic reduction of friction. Another advantage of the technique for microfluidic applications is that sample contamination is avoided due to lack of contact with the solid.

5. SUMMARY AND FUTURE DIRECTIONS

The fascinating phenomena of droplet levitation and self-organization over evaporating liquid surfaces, illustrated above in **Figure 1**, have generated a tremendous amount of experimental data that have resulted in a qualitative understanding of the underlying physical mechanisms. However, quantitative descriptions, especially for larger droplets of radius comparable to the levitation height or horizontal spacing in the array, are still incomplete and could benefit from the approaches described in the present review. In particular, conditions of levitation of large droplets could be determined using the general framework developed in the studies of flotation, the Leidenfrost effect over liquid, and the inverse Leidenfrost effect, as described in Sections 3.4 and 3.5. For large but weakly deformed droplets, the expansion in bispherical coordinates could provide a valuable tool for theoretical studies (Fisher & Golovin 2007). Future directions for experimental research on the topic could include more detailed IR studies to determine temperature gradients along droplet surfaces and systematic investigations of flow inside the droplets. Both of these could elucidate the significance of the Marangoni stresses for these types of problems.

First described in the literature more than 250 years ago, the classical Leidenfrost effect continues to be an active area of research. Remarkable recent advances include the discovery of droplets rapidly flying away from the hot wall and the physical explanation of the explosion of droplets at late stages of evaporation due to the accumulation of impurities. While the Leidenfrost effect provides a way to repel droplets, repulsion is also seen in isothermal systems for superhydrophobic

Annu. Rev. Fluid Mech. 2021.53:203-225. Downloaded from www.annualreviews.org
Access provided by 2603:8081:1407:a861:f5e6:c438:d4ff:bfb on 01/08/21. For personal use only.

surfaces produced by, e.g., nanostructuring. The important question here is what happens when these two mechanisms are combined. Some initial progress in understanding this was made by Bourrianne et al. (2019), but more work is needed to study this so-called cold Leidenfrost regime. Another important issue is understanding the mechanisms of symmetry breaking that lead to spontaneous motion in both the classical Leidenfrost configuration and the inverse Leidenfrost effect.

Examples of low-temperature Leidenfrost phenomena discussed in Section 4.2 naturally invite questions about the forces of interaction between droplets and interfaces. After all, if such forces turn out to be sufficient to support the weight of the levitating droplet, they are not likely to be negligible in several other contexts. There are many contexts in which such interactions are not accounted for but may affect the outcomes of physical phenomena. One such example is spray cooling on small scales. Biological applications also stem from this, most notably the interaction of microdrops with the walls of pulmonary airways (Kleinstreuer & Zhang 2010). Using aerosols for pulmonary drug delivery is common, but the effectiveness of this method depends on how far the droplets can travel through the airways before colliding with the walls. Elaborate numerical simulations of air flows in pulmonary airways have been conducted, allowing one to identify the areas where droplets are likely to collide with the wall, e.g., regions of sharp turns in the direction of the flow. However, similar to the effect leading to droplet levitation described above, the repulsion of droplets from the walls due to local evaporation, which is not negligible at physiological temperatures, has not been incorporated into current models. Such routinely neglected contributions can lead to the changes in the location of droplet deposition.

Annu. Rev. Fluid Mech. 2021.53:203-225. Downloaded from www.annualreviews.org
Access provided by 2603:8081:1407:a861:f5e6:c438:d4ff:bfb on 01/08/21. For personal use only.

DISCLOSURE STATEMENT

The authors are not aware of any biases that might be perceived as affecting the objectivity of this review.

ACKNOWLEDGMENTS

We are grateful to Prof. D. Quéré, Prof. D. Lohse, Prof. O.F. Petrov, and Dr. D. Zaitsev for numerous discussions on the topics of the present review.

LITERATURE CITED

Abdelaziz R, Disci-Zayed D, Hedayati MK, Pöhls JH, Zillohu AU, et al. 2013. Green chemistry and nanofabrication in a levitated Leidenfrost drop. *Nat. Commun.* 4:2400

Adda-Bedia M, Kumar S, Lechenault F, Moulinet S, Schillaci M, Vella D. 2016. Inverse Leidenfrost effect: levitating drops on liquid nitrogen. *Langmuir* 32:4179–88

Biance A-L, Clanet C, Quéré D. 2003. Leidenfrost drops. *Phys. Fluids* 15:1632–37

Bormashenko E, Fedorets AA, Frenkel M, Dombrovsky LA, Nosonovsky M. 2020. Clustering and self-organization in small-scale natural and artificial systems. *Philos. Trans. R. Soc. A* 378:20190443

Bouillant A, Mouterde T, Bourrianne P, Lagarde A, Clanet C, Quéré D. 2018. Leidenfrost wheels. *Nature Phys.* 14:1188–92

Bourrianne P, Lv C, Quéré D. 2019. The cold Leidenfrost regime. *Sci. Adv.* 5:eeaw0304

Carle F, Semenov S, Medale M, Brutin D. 2016. Contribution of convective transport to evaporation of sessile droplets: empirical model. *Int. J. Therm. Sci.* 101:35–47

Celestini F, Frisch T, Pomeau Y. 2012. Take off of small Leidenfrost droplets. *Phys. Rev. Lett.* 109:034501

Deegan RD, Bakajin O, Dupont TF, Huber G, Nagel SR, Witten T. 2000. Contact line deposits in an evaporating drop. *Phys. Rev. E* 62:756–65

Dell'Aversana P, Banavar JR, Koplik J. 1996. Suppression of coalescence by shear and temperature gradients. *Phys. Fluids* 8:15–28

Eddi A, Decelle A, Fort E, Couder Y. 2009. Archimedean lattices in the bound states of wave interacting particles. *Europhys. Lett.* 87:56002

Ershov D, Sprakel J, Appel J, Cohen Stuart MA, van der Gucht J. 2013. Capillarity-induced ordering of spherical colloids on an interface with anisotropic curvature. *PNAS* 110:9220–24

Fedorets AA. 2004. Droplet cluster. *JETP Lett.* 79:372–74

Fedorets AA. 2005. On the mechanism of noncoalescence in a droplet cluster. *JETP Lett.* 81:437–41

Fedorets AA, Dombrovsky LA, Medvedev DN. 2015a. Effect of infrared irradiation on the suppression of the condensation growth of water droplets in a levitating droplet cluster. *JETP Lett.* 102:452–54

Fedorets AA, Frenkel M, Shulzinger E, Dombrovsky LA, Bormashenko E, Nosonovsky M. 2017. Self-assembled levitating clusters of water droplets: pattern-formation and stability. *Sci. Rep.* 7:1888

Fedorets AA, Marchuk IV, Kabov OA. 2011. Role of vapor flow in the mechanism of levitation of a droplet cluster dissipative structure. *Tech. Phys. Lett.* 37:116–18

Fedorets AA, Marchuk IV, Kabov OA. 2013. Coalescence of a droplet cluster suspended over a locally heated liquid layer. *Interfacial Phenom. Heat Transf.* 1:51–62

Fedorets AA, Marchuk IV, Kabov OA. 2014. On the role of capillary waves in the mechanism of coalescence of a droplet cluster. *JETP Lett.* 99:266–69

Fedorets AA, Marchuk IV, Stryzhak PA, Kabov OA. 2015b. Capillary waves at microdroplet coalescence with a liquid layer. *Thermophys. Aeromech.* 22:515–18

Fisher LS, Golovin AA. 2007. Motion of a droplet near an evaporating liquid-gas interface. *Phys. Fluids* 19:032101

Fortov VE, Khrapak AG, Khrapak SA, Molotkov VI, Petrov OF. 2004. Dusty plasmas. *Phys.-Uspekhi* 47:447–92

Gauthier A, Bird JC, Clanet C, Quéré D. 2016. Aerodynamic Leidenfrost effect. *Phys. Rev. Fluids* 1:084002

Gauthier A, Diddens C, Proville R, Lohse D, van der Meer D. 2019. Self-propulsion of inverse Leidenfrost drops on a cryogenic bath. *PNAS* 116:1174–79

Geri M, Keshavarz B, McKinley GH, Bush JWM. 2017. Thermal delay of drop coalescence. *J. Fluid Mech.* 833:R3

Hall RS, Board SJ, Clare AJ, Duffey RB, Playle TS, Poole DH. 1969. Inverse Leidenfrost phenomenon. *Nature* 224:266–67

Kabov OA, Zaitsev DV, Kirichenko DP, Ajaev VS. 2017. Interaction of levitating microdroplets with moist air flow in the contact line region. *Nanoscale Microscale Thermophys. Eng.* 21:60–69

Karpitschka S, Pandey A, Lubbers LA, Weijs JH, Botto L, et al. 2016. Liquid drops attract or repel by the inverted Cheerios effect. *PNAS* 113:7403–7

Kavehpour HP. 2015. Coalescence of drops. *Annu. Rev. Fluid Mech.* 47:245–68

Kim I, Elghobashi S, Sirignano W. 1993. Three-dimensional flow over two spheres placed side by side. *J. Fluid Mech.* 246:465–88

Kim J. 2007. Spray cooling heat transfer: the state of the art. *Int. J. Heat Fluid Flow* 28:753–67

Kleinstreuer C, Zhang Z. 2010. Air flow and particle transport in the human respiratory system. *Annu. Rev. Fluid Mech.* 42:301–34

Leidenfrost JG. 1756. *De Aquae Communis Nonnullis Qualitatibus Tractatus*. Duisburg, Ger.: Ovenius

Linke H, Alemán BJ, Melling LD, Taormina MJ, Francis MJ, et al. 2006. Self-propelled Leidenfrost droplets. *Phys. Rev. Lett.* 96:154502

Lyu S, Mathai V, Wang Y, Sobac B, Colinet P, et al. 2019. Final fate of a Leidenfrost droplet: explosion or takeoff. *Sci. Adv.* 5:eeav8081

Lyulin YV, Spesivtsev SE, Marchuk IV, Kabov OA. 2017. Study of dynamics of thin liquid layer breakdown under conditions of spot heating and formation of a droplet cluster. *Thermophys. Aeromech.* 24:949–52

Maquet L, Sobac B, Darbois-Texier B, Duchesne A, Brandenbourger M, et al. 2016. Leidenfrost drops on a heated liquid pool. *Phys. Rev. Fluids* 1:053902

Monti R, Savino R, Lappa M, Tempesta S. 1998. Behavior of drops in contact with pool surfaces of different liquids. *Phys. Fluids* 10:2786–96

Moreau F, Colinet P, Dorbolo S. 2019. Explosive Leidenfrost droplets. *Phys. Rev. Fluids* 4:013602

Annu. Rev. Fluid Mech. 2021.53:203-225. Downloaded from www.annualreviews.org
Access provided by 2603:8081:1407:a861:f5e6:c438:d4ff:bfb on 01/08/21. For personal use only.

Nagy PT, Neitzel GP. 2008. Optical levitation and transport of microdroplets: proof of concept. *Phys. Fluids* 20:101703
Nam I, Lee JK, Nam HG, Zare RN. 2017. Abiotic production of sugar phosphates and uridine ribonucleoside in aqueous microdroplets. *PNAS* 114:12396–400
Neitzel GP, Dell'Aversana P. 2002. Noncoalescence and nonwetting behavior of liquids. *Annu. Rev. Fluid Mech.* 34:267–89
Oron A, Davis SH, Bankoff SG. 1997. Long-scale evolution of thin liquid films. *Rev. Mod. Phys.* 69:931–80
Petrov OF, Vasiliev MM, Vaulina OS, Stacenko KB, Vasilieva EV, et al. 2015. Solid-hexatic-liquid transition in a two-dimensional system of charged dust particles. *Europhys. Lett.* 111:45002
Protière S, Boudaoud A, Couder Y. 2006. Particle–wave association on a fluid interface. *J. Fluid Mech.* 554:85–108
Quéré D. 2013. Leidenfrost dynamics. *Annu. Rev. Fluid Mech.* 45:197–215
Reynolds O. 1881. On the floating of drops on the surface of water depending only on the purity of the surface. *Proc. Manch. Lit. Philos. Soc.* 21:1–2
Savino R, Paterna D, Lappa M. 2003. Marangoni flotation of liquid droplets. *J. Fluid Mech.* 479:307–26
Sazhin S. 2014. *Droplets and Sprays*. New York: Springer
Schaefer VJ. 1971. Observations of an early morning cup of coffee. *Am. Sci.* 59:534–35
Shirota M, van Limbeek MAJ, Sun C, Prosperetti A, Lohse D. 2016. Dynamic Leidenfrost effect: relevant time and length scales. *Phys. Rev. Lett.* 116:064501
Sobac B, Rednikov A, Dorbolo S, Colinet P. 2014. Leidenfrost effect: accurate drop shape modeling and refined scaling laws. *Phys. Rev. E* 90:053011
Srinivasarao M, Collings D, Philips A, Patel S. 2001. Three-dimensionally ordered array of air bubbles in a polymer film. *Science* 292:79–83
Umeki T, Ohata M, Nakanishi H, Ichikawa M. 2015. Dynamics of microdroplets over the surface of hot water. *Sci. Rep.* 5:8046
Vakarelski IU, Patankar NA, Marston JO, Chan DYC, Thoroddsen ST. 2012. Stabilization of Leidenfrost vapour layer by textured superhydrophobic surfaces. *Nature* 489:274–77
Van Limbeek MAJ, Klein Schaarsberg MH, Sobac B, Rednikov A, Sun C, et al. 2017. Leidenfrost drops cooling surfaces: theory and interferometric measurement. *J. Fluid Mech.* 827:614–39
Van Limbeek MAJ, Sobac B, Rednikov A, Colinet P, Snoeijer J. 2019. Asymptotic theory for a Leidenfrost drop on a liquid pool. *J. Fluid Mech.* 863:1157–89
Vella D, Mahadevan L. 2005. The "Cheerios effect." *Am. J. Phys.* 73:817–25
Waitukaitis S, Zuiderwijk A, Souslov A, Coulais C, van Hecke M. 2017. Coupling the Leidenfrost effect and elastic deformations to power sustained bouncing. *Nat. Phys.* 13:1095–99
Zaitsev DV, Kirichenko DP, Ajaev VS, Kabov OA. 2017. Levitation and self-organization of liquid microdroplets over dry heated substrates. *Phys. Rev. Lett.* 119:094503
Zaitsev DV, Kirichenko DP, Ajaev VS, Kabov OA. 2018. Levitation of ordered arrays of liquid microdroplets over solid-gas and liquid-gas interfaces. In *Proceedings of the 16th International Heat Transfer Conference*, pp. 1471–78. Danbury, CT: Begell House

Annu. Rev. Fluid Mech. 2021.53:203-225. Downloaded from www.annualreviews.org
Access provided by 2603:8081:1407:a861:f5e6:c438:d4ff:bfb on 01/08/21. For personal use only.

Annual Review of
Fluid Mechanics

Volume 53, 2021

Contents

Leonardo da Vinci and Fluid Mechanics
Ivan Marusic and Susan Broomhall 1

Elastic Turbulence: An Experimental View on Inertialess Random Flow
Victor Steinberg 27

Turbulence Processes Within Turbidity Currents
Mathew G. Wells and Robert M. Dorrell 59

Statistics of Extreme Events in Fluid Flows and Waves
Themistoklis P. Sapsis 85

Layering, Instabilities, and Mixing in Turbulent Stratified Flows
C.P. Caulfield 113

The Fluid Mechanics of Cleaning and Decontamination of Surfaces
Julien R. Landel and D. Ian Wilson 147

Mixing by Oceanic Lee Waves
Sonya Legg 173

Levitation and Self-Organization of Droplets
Vladimir S. Ajaev and Oleg A. Kabov 203

Exact Coherent States and the Nonlinear Dynamics of Wall-Bounded Turbulent Flows
Michael D. Graham and Daniel Floryan 227

Statistical Properties of Subgrid-Scale Turbulence Models
Robert D. Moser, Sigfried W. Haering, and Gopal R. Yalla 255

The Fluid Mechanics of Tidal Stream Energy Conversion
Thomas A.A. Adcock, Scott Draper, Richard H.J. Willden, and Christopher R. Vogel ... 287

From Bypass Transition to Flow Control and Data-Driven Turbulence Modeling: An Input–Output Viewpoint
Mihailo R. Jovanović 311

Bluff Bodies and Wake–Wall Interactions
Mark C. Thompson, Thomas Leweke, and Kerry Hourigan 347

Fluids at the Nanoscale: From Continuum to Subcontinuum Transport
Nikita Kavokine, Roland R. Netz, and Lydéric Bocquet 377

Annu. Rev. Fluid Mech. 2021.53:203-225. Downloaded from www.annualreviews.org
Access provided by 2603:8081:1407:a861:f5e6:c438:d4ff:bfb on 01/08/21. For personal use only.

In Pursuit of Designing Multicellular Engineered Living Systems: A Fluid Mechanical Perspective
Jean Carlos Serrano, Satish Kumar Gupta, Roger D. Kamm, and Ming Guo 411

Predicting the Drag of Rough Surfaces
Daniel Chung, Nicholas Hutchins, Michael P. Schultz, and Karen A. Flack 439

The Fluid Dynamics of Disease Transmission
Lydia Bourouiba 473

Numerical Methods for Viscoelastic Fluid Flows
M.A. Alves, P.J. Oliveira, and F.T. Pinho 509

X-Ray Flow Visualization in Multiphase Flows
Alberto Aliseda and Theodore J. Heindel 543

Indexes

Cumulative Index of Contributing Authors, Volumes 1–53 569

Cumulative Index of Article Titles, Volumes 1–53 580

Errata

An online log of corrections to *Annual Review of Fluid Mechanics* articles may be found at http://www.annualreviews.org/errata/fluid

Annu. Rev. Fluid Mech. 2021.53:203-225. Downloaded from www.annualreviews.org
Access provided by 2603:8081:1407:a861:f5e6:c438:d4ff:bfb on 01/08/21. For personal use only.

Applied Thermal Engineering 184 (2021) 115640

Contents lists available at ScienceDirect

Applied Thermal Engineering

journal homepage: www.elsevier.com/locate/apthermeng

Cooling of high-power LEDs by liquid sprays: Challenges and prospects

Sameer Khandekar[a,*], Gopinath Sahu[a], K. Muralidhar[a], Elizaveta Ya Gatapova[b], Oleg A. Kabov[b], Run Hu[c], Xiaobing Luo[c], Liang Zhao[d]

[a] Indian Institute of Technology Kanpur, Kanpur, India
[b] Kutateladze Institute of Thermophysics, SB RAS; Novosibirsk State University, Novosibirsk, Russian Federation
[c] School of Energy and Power Engineering, Huazhong University of Science and Technology, Wuhan 430074, Peoples Republic of China
[d] State Key Laboratory of Multiphase Flow in Power Engineering, Xi'an Jiaotong University, Xi'an, Peoples Republic of China

HIGHLIGHTS

- Next generation high power LEDs require specialized thermal management.
- Spray cooling is potentially an excellent solution for LED packages.
- A comprehensive review of spray cooling in the context of LEDs is presented.
- Thermal and hydrodynamic design strategies of liquid sprays are delineated.
- Intrinsic connection between local droplet level physics and global spray is outlined.

ARTICLE INFO

Keywords:
LEDs
Thermal management
Spray cooling
Droplet impingement

ABSTRACT

Light Emitting Diodes (LEDs) are getting popular due to their wide applicability in various domestic and industrial applications. However, the advent of high-power LEDs is accompanied with the critical issue of higher heat power management, coupled with enhanced flux levels. Natural and forced convection techniques with air as the working fluid are unable to provide thermal management at required operating safe temperatures in several upcoming compact LED array designs. Hence, there is substantial advancement in the development of thermal management solutions for the packaging of high-power LEDs.

Liquid jets and sprays are potential candidates which need further exploration, especially from a point of view of packaging with LED modules. Both configurations can operate in single-phase and two-phase boiling regimes. While considerable literature is available on single-phase liquid jets, liquid sprays pose several challenges in terms of flow parameter management and associated transport physics. In this paper, we review nuances of the latter technology, i.e., spray cooling technique, crucial for thermal management of LEDs. A comprehensive overview of flow distribution and heat transfer during impingement of liquid sprays on heated surfaces is presented from the viewpoint of temperature control of high power LED sources. Additionally, the data presented will help in developing a configuration design of a liquid spray-based thermal management system integrated with high heat flux devices.

1. Introduction

Development in almost every field of critical technology such as defense, avionics, lightings, automobile industry, etc. is characterized by the integration of electronic components, wherein there is an absolute necessity of miniaturization of components. In view of this aggressive trend, there is continuous need for improved thermal management techniques, capable of dissipating high heat fluxes so as to bring the temperature of components within an acceptable range, prevent early component failure and increase reliability.

Over the past two decades, initial efforts for thermal management of high-power electronics focused on single-phase cooling techniques, relying on the sensible heating of the coolant. The development has moved from passive cooling techniques based on natural convection to improved active management with forced convection. However, with increasing demand, the cooling system developers shifted their focus towards two-phase active as well as passive technologies. Two-phase cooling exploits the latent heat as well as the sensible heat of the

* Corresponding author.
E-mail address: samkhan@iitk.ac.in (S. Khandekar).

https://doi.org/10.1016/j.applthermaleng.2020.115640
Received 5 February 2020; Received in revised form 15 June 2020; Accepted 19 June 2020
Available online 23 June 2020
1359-4311/ © 2020 Elsevier Ltd. All rights reserved.

Nomenclature

A	Area of impinging surface (m^2)
A_0	Cross-sectional area of orifice (m)
C	Constant (-)
C_d	Coefficient of discharge (-)
c_p	Specific heat ($J{\cdot}kg^{-1}{\cdot}K^{-1}$)
d	Droplet diameter (m)
d_0	Orifice diameter (m)
$d_{0.5}$	Median diameter (m)
d_{32}	Sauter mean diameter (m)
D	Diameter/hydraulic diameter of test surface (m)
D_{drop}	Initial drop diameter (m)
f	Impact frequency (Hz)
g	Acceleration due to gravity ($m{\cdot}s^{-2}$)
G	Mass flux ($kg{\cdot}m^{-2}\,s^{-1}$)
h_{fg}	Heat of vaporization ($J{\cdot}kg^{-1}$)
h	Heat transfer coefficient ($W{\cdot}m^{-2}{\cdot}K^{-1}$)
H	Nozzle to test surface distance (mm)
k	Thermal conductivity ($W{\cdot}m^{-1}{\cdot}K^{-1}$)
L	Characteristics length (m)
$\dot{m}$	Mass flow rate ($kg{\cdot}s^{-1}$)
N^+	Droplet number Density (-)
n_i	Number of droplets with d_i as diameter
Nu	Nusselt number (-)
ΔP	Pressure difference (bar)
Pr	Prandtl number (-)
q''	Heat flux ($W{\cdot}m^{-2}$)
Q	Liquid flow rate ($l{\cdot}min^{-1}$)
T	Temperature (°C)
r_d	Bubble radius (m)
R	Thermal resistance ($°C\cdot W^{-1}$)
Re	Reynolds number (-)
u	Mean droplet velocity ($m{\cdot}s^{-1}$)
u_m	Mean liquid velocity ($m{\cdot}s^{-1}$)
We	Weber number (-)

Subscripts

A	Case 1
B	Case 2
CHF	Critical heat flux
D	At test surface
Drop	Droplet diameter
f	Fluid
g	Gas
i	Number
l	Liquid
lm	Luminous
in	Inlet
m	Mean/Average
max	Maximum
o	Orifice
sat	Saturation
sub	Subcooling
v	Vapour
w	Wall

Greek letters

α	Thermal diffusivity ($m^2\,s^{-1}$)
Δ	Difference (-)
μ	Dynamic viscosity (Pa·s)
η	Efficiency (-)
ν	Kinematic viscosity ($m^2{\cdot}s^{-1}$)
ρ	Density ($kg{\cdot}m^{-3}$)
σ	Surface tension (N·m)
θ	Angle (degree)

coolant. It removes a much higher wall heat flux than what is possible with single-phase cooling at lower temperature differences [44]. For example, in the laser diodes, there is a requirement to dissipate heat up to ~1 kW/cm^2 at ~300 K; such a demand simply cannot be matched with a single-phase system [9].

Light emitting diodes (LEDs) based on solid-state lighting (SSL) technology are the most promising global lighting source due to their high efficiency and long life. While LEDs are replacing modern luminaires, it has additional applications in human health and well-being, connected lighting with internet of things and artificial intelligence, horticulture lighting for photosynthesis and designs for ecologically conscious lighting that limit lighting-related pollution. The colour of light emitted by LED is determined by the energy band gap (E_g) of the semiconductor used for the LED chip. In an LED, electrons from the *n*-region and holes from the *p*-region recombine at the junction due to the applied voltage. A part of the energy is released in the form of photons during their recombination, as shown in Fig. 1(a). The remaining portion of the released energy is in the form of heat, which needs to be effectively removed so that the device temperature remains below an acceptable operational limit [64].

LEDs offer several advantages over conventional lighting sources: (i) Energy saving: they require comparatively much less input energy for producing an equivalent light intensity. (ii) Warm-up time: the device does not require any heating or turn-on time and lights up quickly. (iii) Size: LEDs are small and compact. (iv) Long lifetime: LEDs have a long operational life of about 50,000 h or more, as compared to incandescent lamps, which have a lifetime of about 10,000 h. (v) Wide color temperature: LEDs offer a wide range of color temperatures (4500–12,000 K). (vi) High reliability: LEDs fail at a lower rate by dimming over a longer time, as compared to incandescent lamps, which have an abrupt failure [61]. Use of LEDs is expected to reduce the net world energy consumption by ~1000 $TW{\cdot}h{\cdot}yr^{-1}$ [74].

Although LEDs possess the advantage of a higher percentage of visible light as compared to earlier light source technologies, Table 1, shows that the non-radiant heat energy component, which constitutes about 70–80%, can raise the junction temperature to ~120 °C, critically damaging the LED. The non-radiative recombination of holes and electrons occurs in the active region of chips and is of two types, namely, Shockley-Read-Hall (SRH) recombination and Augur recombination (AR) [61]. SRH recombination arises due to impurities present in the crystal structure of the semiconductor, creating a new energy level in the forbidden band gap. The probability of SRH recombination increases with increase in temperature. On the other hand, AR occurs when energy released by the electron in the conduction band is absorbed by another electron in the conduction band, or a hole in valence band, instead of releasing it in the form of a photon. The excess energy thus available is released during collision with the crystal lattice [124] and need to be eventually managed/dissipated to the ambient so as to safely maintain the junction temperature.

LEDs in the power range of 20–70 W are widely used in automotive headlights [92], advertising display, streetlamps, traffic lights, and stadium lighting (e.g. ~4 kW net capacity, Bee® LED company). Depending upon the electrical power input, the LEDs can be broadly classified into low power (generally 0.05 W to 1 W, micro/milli amps) and high-power (3 W or even tens of watts, several amperes) [45]. The low power LEDs does not require sophisticated thermal management solutions. The heat flux at chip level can be as high as 250–500 W/cm^2 for the high-power LEDs; e.g., 300 W nominal power LEDs module by

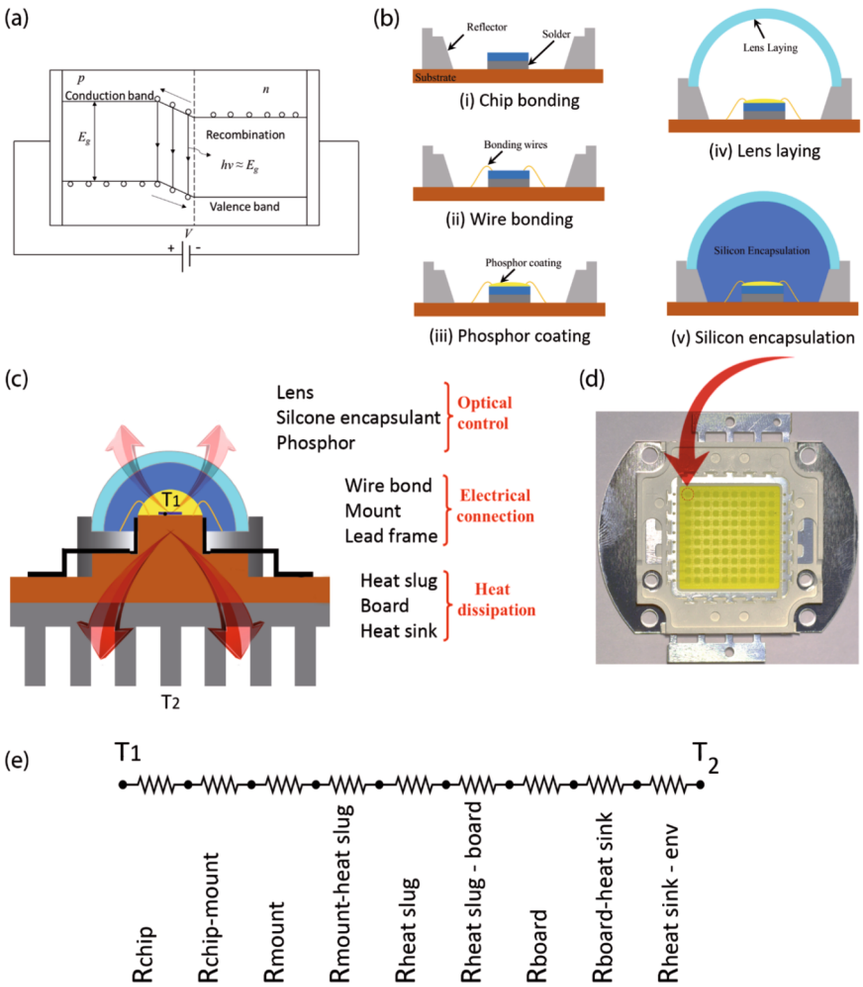

Fig. 1. (a) Working principle of a LED (b) Common steps in LED chip fabrication (c) Features of a LED module, with pathways shown for heat transport (d) Photograph of a high power LED array (e) Thermal resistance network of a LED module.

Huazhong University of Science and Technology, China, operating at 25–36 V and 0.1-7 A [19,92,123]. Hence, an effective cooling technology must be utilized to dissipate the heat power which will improve reliability, lifetime, and overall opto-electro-mechanical performance of high-power LEDs.

In this article, a comprehensive review of spray cooling design methodology and technological aspects, in the context of thermal management of high-power LEDs is presented. Several design equations and correlations of spray cooling are included, at global as well as droplet level interaction with the hot surface, which will be highly beneficial while designing of thermal management techniques for high-power electronic systems. This paper aims to reach to the audience of the engineering and industry community who are involved in applied thermal management of luminaire systems and their applications. In addition, thermo-physical properties of sprays and related physics of heat transfer, is explained with the help of elaborate figures, which meticulously and systematically represent features such as LEDs architecture, spray morphology, experimental setup and results of spray cooling through parametric studies, various phenomenological and qualitative mechanisms of heat transfer occurring during spray impingement phenomena at droplet levels, etc. Some emerging results from the respective laboratories of the present group of authors is also included to supplement the discussion and to provide support to the ongoing arguments.

2. LED packaging and thermal management

Electronic packaging entails the housing, enclosure and

Table 1
Power consumption matrix of common white light sources [25].

	Incandescent Lamps	Fluorescent Lamps	Metal Halide Lamps	LED
Visible Light	8%	21%	27%	20–30%
IR	73%	37%	17%	Negligible
UV	0%	0%	19%	Negligible
Total Radiant Energy	81%	58%	63%	20–30%
Non-Radiant Heat Energy	19%	42%	37%	70–80%
Total Energy	100%	100%	100%	100%

interconnection of integrated circuits to form electronic systems. Along with semiconductor manufacturing, packaging forms the core of the final product. Packaging provides several critical functions including, for example, circuit support and protection, heat dissipation, signal distribution, manufacturability, serviceability and power distribution. The effectiveness, reliability and cost, is strongly determined by the packaging strategy.

Careful scrutiny of the literature on electronic packaging and thermal management suggests that design rules are indeed generic and broadly stated. In addition, most thermal management packaging strategies are, to a large extent, case specific. For example, choosing water vs. a refrigerant as the coolant will drastically change several parameters and operating variables such as material compatibility, operating pressure, temperature, type of gaskets and sealing, filling and maintenance procedure, geometrical shapes of components, coefficient of thermal expansion, pump types in case of active cooling, heat exchanger sizes due to Prandtl number of the chosen liquid, etc. In addition, packaging also depends on the final application and the boundary condition in which the unit/system is expected to perform. Differences will arise in the following contexts: mobile vs. stationary, vertical/horizontal vs. inclined orientation, consumer electronics vs. industrial electronics, available space, quality of place of installation, and ambient temperature.

Before proceeding to discuss thermal design and management strategies for LEDs, it is instructive to understand the basics of LED package design and construction. In lighting applications, LED sources emitting white light are used. However, LED chips emit only monochromatic light, which is changed to white light by three alternate methods, viz., (i) dichromatic technique: mixing of yellow phosphor with blue semiconductor LED, or mixing of yellow and red phosphor with blue LED, (ii) trichromatic technique: mixing of UV LED with three phosphors or mixing of blue and red LEDs with green phosphor, and, (iii) tetrachromatic approach: mixing of UV LED with green, cyan, blue and red phosphor or mixing of blue and red LEDs with cyan and green phosphor [87]. In terms of LED architecture, packages can be classified as (a) phosphor-converted (PC) architecture, which dominates the world market (Method (i)), and (b) Colour-mixed (CM) architecture, which requires further improvement for market acceptability. The efficiency of the luminous source decreases with increasing source multichromaticity. Accordingly, dichromatic sources have the highest luminous efficacy of radiation and the highest potential luminous source efficiency. In contrast, the colour-rendering capability is lowest for dichromatic sources and it increases with the multi-chromaticity of the source. The colour-rendering index can reach values very close to CRI ~ 100 for tetra-chromatic sources [86]. Most white light LEDs use phosphor coating on blue chip. The colour temperature of white light emitted by the LED depends on the proportion of phosphor coating, e.g., cool white light (5000–10000 K) and natural or neutral white light (4000–5000 K) or warm white light (3000–4000 K). Accordingly, the chip, phosphor and lens are the main components determining the optical performance of the LED package. The initial optical power and light luminous efficiency are determined by the chip, luminous flux by the phosphor, and finally the luminous intensity by the lens. The use of an encapsulant of higher refractive index material increases the light extraction efficiency of the chip [89].

The luminous efficacy of the LED is defined as the ratio of the lumens (lm) associated with a given optical power, i.e., the integral of the optical power spectrum $P_o(\lambda)$, weighted by the human eye response $V(\lambda)$, over the wavelength range and the electrical source power P_e. It is given as [113]

$$\eta_{lm} = \frac{\int P_0(\lambda) V(\lambda) d\lambda}{P_e} \quad (1)$$

The maximum luminous efficiency (lm/W) for a white light source which has no loss on conversion from electrical to optical power is 414 lm/W [68]. This value represents the theoretical maximum which any LED may achieve. LED sources fall below this limit but are more efficacious than other conventional or traditional lighting technologies. Contemporary data suggests that the efficacy of cool white light packages have improved from around 25 lm/W to over 160 lm/W in the last 15 years, depending on the colour quality and operational conditions. As compared to the common incandescent lamp (~15 lm/W), halogen lamps (~20 lm/W), and CFL (~70 lm/W), commercial LEDs luminaire (PC-architecture) that deliver high performance have a luminous efficacy of over ~120 lm/W, with the top performance crossing 130 lm/W. Note that these values depends on the current density in the system, values for testing conditions in a laboratory being 35 A/cm^2 [46]. The usable life of LEDs (~50,000–60,000 h) is also an order of magnitude larger than conventional sources that have smaller lifetimes ranging from 1000 h to 25,000 h [72]. Contemporary research is targeting luminous efficacies exceeding 200 lm/W. Owing to quantum mechanical limitations and Stokes losses, practical values for the PC based architecture are expected to saturate at about 225 lm/W. While the present efficacy values for CM-architecture, ~90 lm/W, cannot compete with the PC-architecture, their projected scope of improvement is much higher. Other than luminous efficacy of the LED package, other internal and external phenomena deteriorate LED performance. These include thermal droop effects due to operating current density, LED driver efficiency and fixture efficiency. With these factors, the net light output of contemporary high end LEDs that provide PC-architecture based warm white light is of the order of 65–75% [112].

Fig. 1(b) shows the packaging process of a high-power white LED source with PC-architecture. It is a complex micro-engineering process. During packaging, the LED chip is bonded on the substrate with the help of silver paste for fastening and heat dissipation. The solder is then allowed to flow by melting or heat treatment during the reflow process. While bonding the chip on solder, slight pressure is applied, and special attention and care ensures that there is no resulting geometrical misalignment. The two sides of the chip are bonded onto the lead frame with the help of wires made of copper, gold, or aluminium. A layer of phosphor coating is dispersed on the top surface of the blue chip. As discussed earlier, the function of phosphor is to absorb a portion of blue light and convert it into yellow light, so that the combination becomes white light. To protect the LED chip and wire bonding from a harsh environment, an optical lens is mounted on the chip. The space between LED chip and optical lens is filled by an encapsulant of high refractive index. Silicone is used as an encapsulant due to its stability over a wide temperature range (-115 °C to 260 °C), low moisture absorption, optically clarity (> 95%) and comparatively low resistance. Encapsulant also helps in protecting the chip and bonding wires [61,89].

The packaging of LED affects it's performance parameters such as luminous intensity, luminous efficacy, heat dissipation and reliability. Focusing on one design process of LED packaging can have negative effect on the other. For example, improvement in performance may lead to increase in the cost of LED. Warm light with low correlated colour temperature (CCT) requires higher concentration of phosphor layer, which increases light conversion losses, and eventually decreases the luminous flux [31]. Hence, during designing the packaging, a balance between the contradictory parameters should be ensured. The major components of LEDs and their respective functions are highlighted in Fig. 1(b). In a typical LED packaging, there exists two heat sources: one is the blue LED chip, and the other is the photo-luminescent layer, i.e., the phosphor layer in PC architecture. The first heat source is well known due to the non-unity quantum efficiency in the electroluminescent process of blue chips, while the second one has been neglected for a long time. Luo et al. first observed the silicone carbonization phenomenon due to the phosphor self-heating effect, and developed models to calculate the heat generation in phosphors [59,60]. Due to the self-heating in phosphors, Hu et al. observed that the hot spot in LED packaging may shift from the blue chips to phosphor layer [36–38].

There are three main reasons for operating LEDs at lower temperatures. First, the operating junction temperature strongly affects its output radiant power. Junction temperature also depends on the ambient temperature. When the junction temperature of LEDs increases, both, the forward voltage, and the lumen power output of these devices will decrease. Secondly, thermally induced internal stresses are created that adversely affect the operational life of the system. Lastly, higher the junction temperature, lower is the colour rendering index (CRI), a measure of how close the frequency of the emitted light is, with respect to the specified standard. Other benefits of effective thermal management, include, for example, reduction of overall operational cost due to reduced failures and increased reliability [18,116].

As shown in Fig. 1(c), heat generated at the chip of the LED is dissipated along two paths. One is through the phosphor layer and the encapsulation (upper path), and the second is through the substrate (lower path). The thermal conductivity of silicone and phosphor layer are comparatively quite small and hence, their thermal resistance is quite large. On the other hand, the thermal conductivity of the substrate is large and most of the heat generated at the chip level will pass through the substrate. With the advent of high-power LEDs, the increase in the chip temperature at higher driven current has become a serious issue. Taking the case of 1 W LED, having an area of 1 mm × 1 mm and an efficiency of 30%, heat flux generated is ~70 W/cm^2 at the chip level. The large amount of heat generated by non-radiative recombination raises the junction temperature of the chip T_1 quite sharply. The higher junction temperature will decrease luminous flux, shift wavelength, lower quantum efficiency of phosphor, reduce lifetime and may even cause catastrophic damage of the chip [89]. The maximum limit of the junction temperature T_1, for most of the commercial LEDs is ~120 °C. Hence, thermal management solutions are required for maintaining lower junction temperature for higher luminous flux, longer lifetime and high reliability [45]. Without effective thermal management, a high power LED will burn-out almost instantaneously [13]. A photograph of a 300 W LED module is shown in Fig. 1(d), where 100 chips are bonded on the board.

An effective thermal conductivity network is shown in Fig. 1(e). Such a model representation is used in thermal analyses. The total system resistance is a series sum of all the component resistances shown in the figure. Thus, a representative equation for the total resistance can be written as

$$R_{total} = R_{chip} + R_{chip-mount} + R_{mount} + \cdots + R_{heat-sink-environment} \quad (2)$$

All thermal resistances but one is conduction dominant. Only the last component, wherein the externally fitted heat sink technology comes into action, is governed by laws of convective and radiative heat transfer. It is this last thermal resistance that will be altered by the choice of the relevant thermal management technology for ultimate dissipation to the environment at temperature T_2. The first eight diffusion resistances are primarily attributed to the choice of material, chip design and interconnect architecture, and package design parameters, including interface materials used for assembly. Over the years, package level thermal resistances have gone down considerably, with values ranging from 75 to 120 K/W in pre 1990s, to 10–20 K/W in the year 2000 to less than 3 K/W in 2010 [3,99]. With the advent of high power LED arrays, thermal management must aim at overall thermal resistance values better than 0.5 K/W [62]. Many researchers have studied the optimization of thermal resistance network through commercially available simulation software for estimating effective distribution of temperature and/or heat flux within the chip/module architecture [1,63,80,119]. Such tools are also proving to be very effective in analyzing the system architecture and identify vulnerable junctions.

3. Cooling technology: Classification

Cooling technologies employed for thermal management of high-power LEDs are broadly classified into two categories, namely, passive cooling and active cooling systems, as shown in Fig. 2. In passive cooling, no external power input is required for heat removal; power input is required for removing heat in active cooling systems. In this section, a brief description of different cooling methodologies applied by researchers for real time high-power LEDs is presented.

Passive cooling techniques make use of natural convection with air as the most adopted medium of heat dissipation. A passive natural convection based experimental method for thermal management of LED chips using an optimally designed heat sink was reported by [39], which could maintain the chip temperature below 80 °C, at power level of 16 W. For augmenting heat transfer by reducing the overall thermal resistance in the path of heat flow, passive cooling also employs, for example, mounting a fin type heat sink (with or without an embedded conventional heat pipe), or use two-phase closed thermosyphons [50], vapour chambers [96], embedded flat-plate heat pipes, or phase-change material modules [65], and liquid cooling [5], below the substrate. Management of larger power levels with passive techniques necessitates the usage of phase-change systems such as heat pipes or thermosyphons, as noted. Forced convective active air flow is frequently needed in the last stage of cooling to the ambient, in conjunction with passive heat transfer. For example, conventional wicked heat pipe embedded in heat sink for LED headlamp (power ranges up to 70 W) was experimentally explored by Singh et al. [92]. Such designs are usually lighter per unit power level and have much better thermal performance than conventional finned heat sinks. Similarly, Chen et al. [12] has reported thermal performance of vapour chamber based heat sinks for LED modules. A 27% reduction of substrate surface temperature was

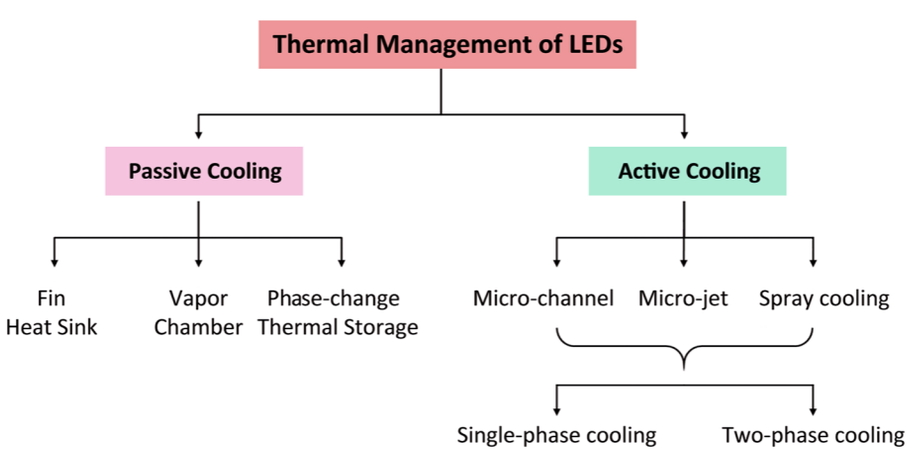

Fig. 2. Various thermal management techniques which can be applied for dissipating heat from high-power LED modules.

recorded as compared to a solid copper plate type sink owing to a reduction in thermal resistance by about 50%. Kang et al. [45] studied the phase-change immersion cooling using ethanol-based coolants for heat management of high-power LED. For an electrical power supply of ~50 W, the junction temperature was kept below 70 °C. Li et al. [50] experimentally investigated thermosyphon heat pipe for cooling of high-power density LED having nominal power of 100 W. This design could remove over ~150 W of heat power while maintaining substrate temperature well below 85 °C. Deng et al. [22] studied the active and passive cooling based thermal management of LED having maximum power of 30 W using dual synthetic jet actuator along with a heat sink combination. This methodology is useful where space constrained is a major issue. Hseih et al. [35] proposed a micro-spray-based cooling system to cool 5 W LED module using DI water as working fluid. A highest heat transfer coefficient of ~9400 W/m^{2}K obtained using single spray cooling which has a nozzle orifice diameter of 35 μm. All such systems described above are usually located on the opposite side of the LED chip, from where a large amount of heat is transferred (see Fig. 1(c)). Passive solutions can cater up to a maximum of about 75–150 W of LED power, beyond which, either they tend to become unwieldy, or costly, or outright ineffective, depending on the design constraints [22,96,104].

The development of high-density LED chip-on-board modules, dissipating beyond 100 W requires designers to opt for active cooling techniques. These essentially involve forced convective heat transfer (see Fig. 3) via a gaseous or a liquid medium. Air is a versatile medium for single-phase forced convection, involving the use of air flow by fans over high performance heat sinks. However, such systems have limitations and overall heat transfer coefficient is rather limited. Microchannel forced flow of pumped liquid is another attractive option. With active cooling strategy, the size of the cooling module can be reduced to about one third, as compared to equivalent thermal capacity passive systems, giving clear advantages on many fronts. While internal convective microchannel flows are attractive (heat transfer coefficient being inversely proportional to channel diameter), a major disadvantage is the high pressure drop requirement and tendency of the flow to be laminar due to small characteristic length of the flow passages. Shear-driven film in microchannel is one of the possible cooling techniques that provide smaller pressure drop and substantial heat transfer enhancement [28,41,43,121]. Another active method is spray and jet cooling. In this paper, we explore spray cooling as an attractive active cooling option for higher heat flux demands, as envisaged in new LEDs designs.

Active cooling involving liquids (microchannels, jets, and sprays) can operate in the single-phase domain i.e., involving only sensible heating of the coolant, when the operating temperature is below the thermodynamic saturation condition. Alternatively, it can operate with accompanying evaporation or boiling heat transfer [93]. In such cases, sensible as well as latent heat of the coolant plays a role, with dominance of the latter in the overall heat transfer process. In the next section, we discuss the nuances of spray technology as a potential option for high power LED modules.

4. Spray impingement cooling

Spray impingement cooling relies on the technique that when a liquid is forced through a small orifice, it breaks into small drops, which can be made to imping on the heated surface to remove heat effectively. Due to the high momentum impact of the drops on the heated surface, a thin liquid layer gets developed on the surface, which enhances the heated transfer. Rendering the liquid volume in the form of small drops creates a very high surface area to volume ratio. In the single-phase

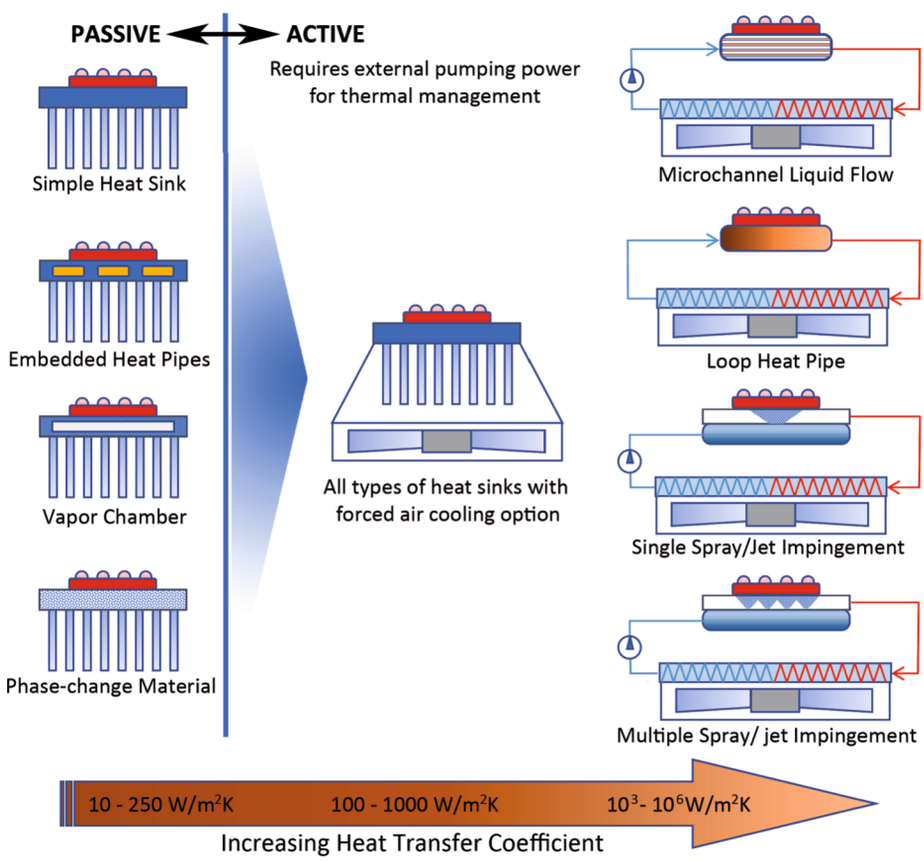

Fig. 3. Schematic arrangement of various passives and active techniques, which may be employed for excess heat removal from LED modules. The range of corresponding heat transfer coefficients possible from these techniques is also shown.

spray cooling mode, heat transfer is enhanced by agitation of the thin liquid film formed on the test surface due to impingement of drops coming from the spray. In the case when liquid film temperature is below the boiling temperature, phase-change heat transfer takes place partly due to thin film evaporation too. The main reason of spray cooling being pursued by many researchers is that it has potential to remove very high heat flux at low wall superheats, precise temperature control, spatial-uniformity of temperature, high CHF (in case of two-phase sprays), near-independent operation with respect to spray orientation and long-term stability [20,118].

Spray cooling can be direct or indirect. In the former, a dielectric coolant impinges directly on the heat source, because of which, unlike indirect cooling, the thermal resistance due to conduction is eliminated. When the sealing of the component is unavoidable, indirect spray cooling can be employed, wherein there exists an isolating substrate between the heating source and the heated zone. Non-dielectric fluids can also be used in this type of spray cooling. Among these, water has superior heat removal capability owing to its large latent heat. However, water may not be compatible with system level integration due to its higher boiling point and electrical conductivity. In addition, for maintaining substrate temperature below 80 °C, low-pressure closed circuit is required. Hence, due to dielectric nature and relatively low boiling point, some refrigerant fluids are being considered in spray cooling, which includes fluorinates (FC-72, FC-84, FC-87, HFE-200, HFE-7100, etc), hydro fluorocarbons HFCs (R134a, R410a, etc.) and the so called 'performance fluids' (PF-5050, PF-5052, PF-5060, PF-5070, etc.) [109,69,76,47,90,29]. For example, it was demonstrated that a closed loop spray-cooling using R410a as the working fluid can handle heat flux as high as ~250 W/cm^2 while maintaining surface temperature well below 30 °C [57]. Along with thermal considerations of the potential coolant, on should also consider its compatibility, safety, and environmental impact of its usage. The other important coolant properties include its dielectric strength, ozone depletion potential, flammability, auto-ignition temperature, global warming potential, etc. To minimize the environmental impact, a refrigerant with good environmental rating should be considered [69]. Table 2 presents a comparison of various phase-change cooling techniques. The CHF for spray cooling as well as jet boiling cooling is very high as compared to other cooling techniques. In addition, while water shows superior performance, in some of these listed systems, the average temperature of the heated surface was above 120 °C, and hence they may not be suitable for LED applications. In addition, it is noted that due diligence in estimating the heat losses and uncertainties may also not be rigourous enough in some cases.

Unlike quenching of high temperature metals and alloys [52], sprays designed for high power LEDs will encounter relatively lower fluxes as well as substrate temperatures, well below CHF conditions. During quenching, sprays can operate in the post-CHF mode as well, encountering temperatures well above the Leidenfrost limits [55]. In that sense, the present discussion applies only to low-temperature sprays.

An interplay of a multitude of flow and geometrical factors simultaneously affect spray cooling performance. Accordingly, conducting controlled experiments as well as mathematical modelling is complex, as compared to other cooling strategies. High operating pressure-drops and un-clean coolant fluids with foreign particles may erode or corrode the nozzle. The performance is diminished, creating a high degree of performance sensitivity on manufacturing tolerances. These are some serious shortcomings of spray cooling systems.

4.1. Experimental design

In the present study, we highlight the complexities involved in developing spray cooling systems and delineate a thermal design process which can be implemented by designers. To highlight the issues involved, the experimental data presented in this section is recorded in a dedicated experimental facility specially designed for studying spray cooling for high power electronic equipment, with special focus on LED applications. The size and overall design of the closed loop spray system largely depends on several parameters like, (i) the flow rate of coolant and working pressure, (ii) type of coolant, (iii) heat flux from LEDs, (iv) characteristics of the condenser unit to cool the mass of evaporated liquid, (v) heat exchanger design to cool back the working fluid to its initial condition, (vi) orientation and functional characteristics of the LED module, etc. The final design of package level management must include optimization of the thermal material research, package design and optimization, thereby overcoming the thermal challenges [26]. A laboratory scale experimental setup for studying thermal-hydrodynamic characteristics of a jet/spray cooling system in a closed-loop, single-component working fluid system, is shown in Fig. 4(a). A pressurized jet (or spray) can be created either by (a) a high pressure positive displacement pumping system, or (b) a stand-alone pressurized liquid coolant tank, or in combination with a pressurized pneumatic tank, connected to an air compressor (Fig. 4(a). A compact gear pump generating high pressure is preferable, as it will reduce the size of the total assembly. The balance of the setup consists of a liquid supply line with inline filter and mass flow meter. The nozzle holder is equipped with the orifice of the required diameter to create the spray. It optionally also has a swirling chamber, where a radial velocity component may be imparted to the coolant to enhance spray characteristics. Depending on the flow conditions and the fluid properties, a monolith jet or a spray will emanate from the orifice. The jet impinges on the heater surface, more generally the LED module, whose thermal management requirement is being developed. The substrate may not be perpendicular to the orifice axis. The substrate can be a simulated electronic device, created by cartridge heaters under a flat surface, or the actual LED module. Depending on the wall heat flux at the substrate, the impinging liquid may undergo phase-change due to evaporation or boiling also. The evaporated mass of vapour, if not removed properly, alters the system pressure. Therefore, special care must be taken to maintain the pressure inside the working test chamber using a local condenser supplied by an independent coolant flow circuit. The circuit is designed in such a way that the condensate can be separately collected for energy auditing.

The excess coolant flows back to the supply pump. In case the supply of liquid is via a pressurized tank system, then a fluid collector is needed. The supply liquid temperature is maintained by a second heat exchanger coupled to a constant temperature bath. If this is not done, then the temperature of liquid supplied to the nozzle inlet increases, which in turn increases the heater substrate temperature. The LED can be mounted on the wall or at any angular position. However, the orientation of spray cooling system has marginal effect on heat transfer performance, for single-phase as well as the boiling regime [33,77,82]. Hence, spray cooling results obtained for the downward facing orientation can be accurately used for estimating performance in other orientations also. The test chamber is equipped with optical windows for high speed videography or laser-based measurements to record important spray diagnostic indicators. Important parameters such as pressure, temperature and flow parameters are monitored online by a PC-based data acquisition system. In the following sections we describe the methodology, parameters of interest and data obtained on such an experimental platform.

Table 2
Comparison of high heat flux removal technologies.

Fluid	Cooling method	h, W m^{-2} K^{-1}	q'' Wcm^{-2}	Authors
Water	Spray cooling	8.38 × 10^4	945	[14]
R-717	Spray cooling	20 × 10^4	910	[8]
Water	Micro-channel	13.2 × 10^4	1016	[51]
Water	Jet impingement	28 × 10^4	1820	[73]
Water	Shear driven liquid film	30 × 10^4	1200	[42]

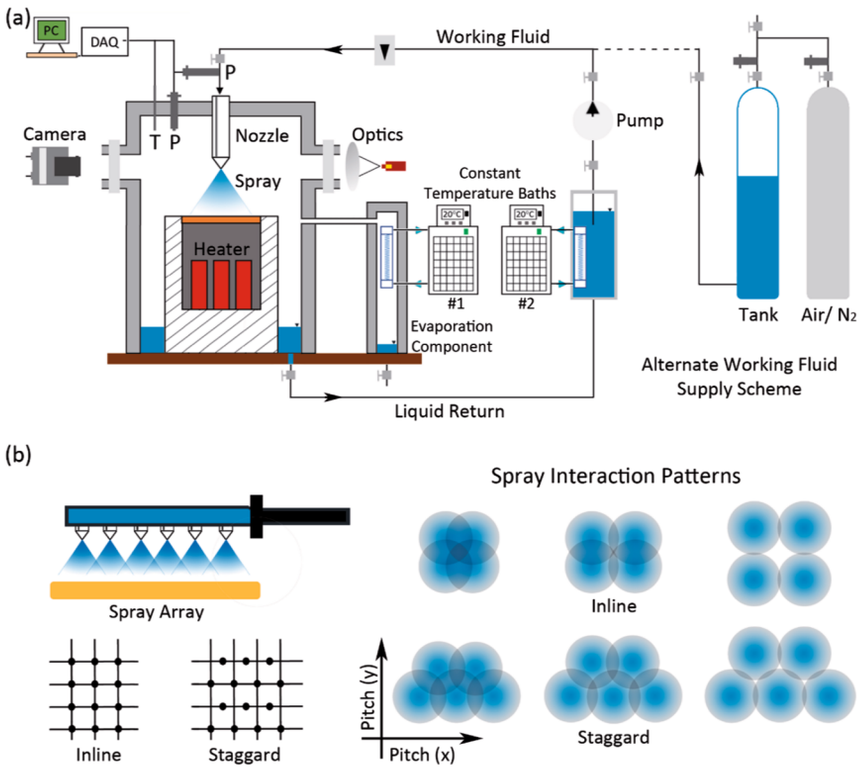

Fig. 4. (a) Details of the experimental setup for analyzing spray cooling technique for high power electronics cooling/ LED thermal management (b) An array of spray nozzles with possible geometrical arrangement – inline and staggered. Depending on the array arrangement, spatial distribution of the ensuing heat transfer coefficient gets augmented.

Specifically, some of the experimental results presented in the subsequent sections while reviewing the literature and its implications are obtained by the authors from a pressure swirl nozzle (orifice diameter 0.594 ± 0.005 mm), which has two tangential inlet ports for imparting tangential motion to the fluid, as shown in Fig. 4(a and b). The test surface of the heater assembly has a diameter of 30 mm. The

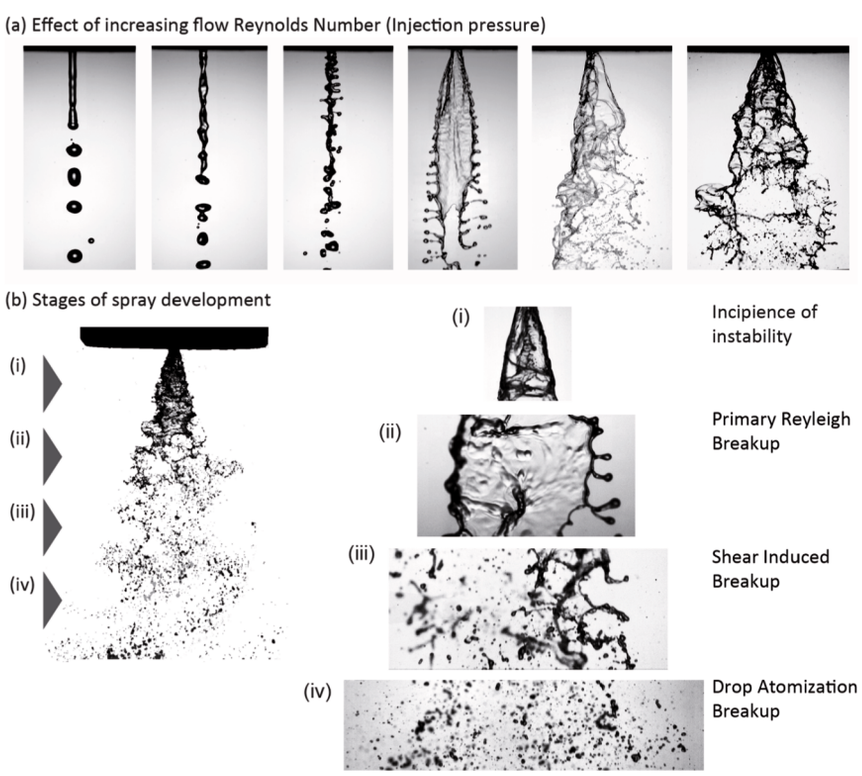

Fig. 5. Photographic details of a liquid spray emanating from an orifice, showing hydrodynamic flow regimes which appear as the spray develops (a) Effect of increasing Reynolds number on spray morphology (b) various stages of spray development (c) details of the hydrodynamic structures in an effusing spray (Experimentally obtained from high speed visualization by the present authors).

spray at room temperature impinges over the surface to remove the imposed thermal load. In view of LED context, a maximum of 40 W/cm^2 is supplied to the heater assembly (Corresponding heat power ~283 W, equivalent to a 400 W LED). The heat transfer rates are largely dominated by single-phase convection conditions. Coolant water flow rates are varied up to 390 ml/min (nozzle outlet Re = 16000, maximum pressure drop = 8 bar). Spray visualization and hydrodynamic characterization are carried out using a high-speed camera (Photron Fastcam®SA3). The recorded image sequence is analyzed using the MATLAB® image processing toolbox. Images are captured at 2000 fps and 1024 × 1024 pixel resolution with 1/300,000th second shutter speed. This high frame rate and shutter speed require high-intensity illumination; hence, an LED is employed as a backlight source. This setup resulted in a digital image pixel size of 16.1 μm in high speed imaging, which facilitated accurate capture of small droplets. Temperature measurements of the heater assembly are carried out by embedded micro-thermocouples (bead diameter = 70 μm; Omega®), till steady-state is achieved for a given electrical power input.

4.2. Hydrodynamic considerations

Spray cooling is a rather unique example wherein the interconnection between hydrodynamics and heat transfer is deeply coupled. Hydrodynamic flow parameters and characteristics such as spray pattern, droplet size distribution, instabilities, flow rate and local velocity distribution, droplet mergers and coalescence and a plethora of other micro/meso and macro-scale flow features strongly affect the resulting heat transfer. It is nearly impossible to imagine thermal design of a spray cooling system, without appreciating the related hydrodynamics. In fact, getting the right hydrodynamic characteristics becomes the primary objective function towards achieving an optimum heat transfer paradigm from sprays.

Fig. 5(a) shows a photograph of a pressurized liquid spray emanating from a single-hole orifice, recorded on the experimental setup described earlier. Sprays display complex fluid structures generated by the disintegration of a liquid sheet or a vortex ring into finer droplets which flow into the surrounding gaseous environment. The pressure energy of the liquid is converted to kinetic energy at the orifice and as the liquid mass flows out, it experiences breakdown from a large to smaller sizes primarily due to Rayleigh instability. High inlet operating injection pressure leads to high liquid efflux velocity, increases the possibility of instabilities at the nozzle exit and in turn, the atomization efficiency [83]. Apart from the geometrical structure and design of the nozzle spray assembly, the atomization process is governed by the thermophysical properties of the fluids involved. Specifically, properties of the dispersed liquid phase and the surrounding gas/vapor continuous phase, such as density, viscosity and surface tension are important. The inertia of the liquid phase augments shear interaction between the liquid and gaseous phases, leading to atomization and turbulence. Liquids with higher viscosity, lead to reduced flow rates and delay in the appearance of instability. The deferment of the disintegration process affects the spray angle as well as the droplet size distribution [75].

Depending on the combination of the operating parameters, several flow structures and hydrodynamic regimes have been identified in the literature [4,66]. Examples are, the Rayleigh breakup regime - also

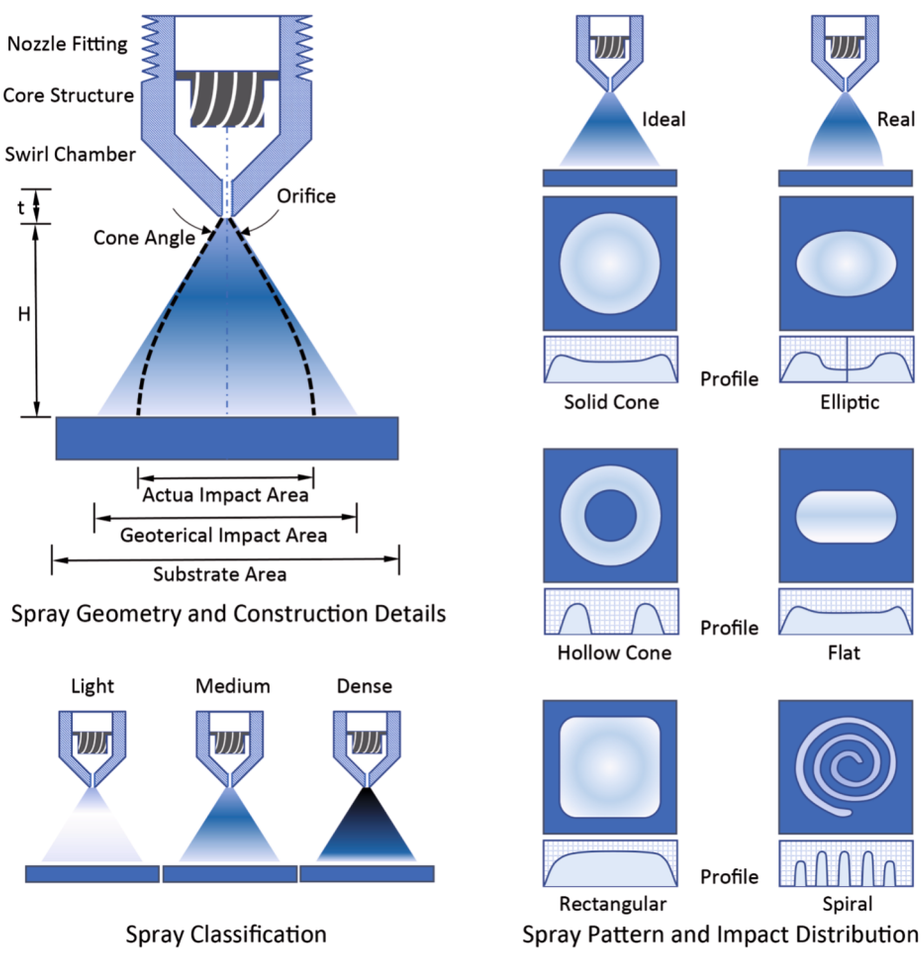

Fig. 6. (a) Detail of the spray nozzle construction, including important geometrical features (b) Classification of a spray based on flow rate of the liquid medium (c) Various types of spray patterns and their impact distribution on the impinging substrate.

called as the drip flow regime [103], the first and second 'wind-induced' regime where shear-induced secondary break-up takes place, and finally the fully developed atomization regime, that is of interest for the present discussion. There are four main regions in the spray zone located directly downstream of the nozzle, as shown in Fig. 5(b). These regions can be characterized as follows:

(i) The presence of a liquid core or sheet – which corresponds to the stretching of the injected mass of liquid.
(ii) The zone of primary break-up where liquid produced after exit from the nozzle orifice. Disintegration is governed by the interfacial instabilities between the dispersed and the continuous phase, wherein fluid disturbances grow during penetration of the liquid fragments into the ambient gas phase.
(iii) The primary break-up is followed by secondary break-up mechanisms wherein the irregular liquid bodies created earlier, further breakdown into sheets, lamellae and large droplets. This step may involve vibrational breakup, bag breakup, sheet stripping, or catastrophic breakup of liquid masses.
(iv) Finally, the process leads to the formation of tiny individual spherical droplets via the atomization break-down process. This is the spray region of interest, which is in the in the far-field region. Flow here is fully dispersed and contains a cloud of round and small droplets, as seen in stage (iv) of Fig. 5(b). Further discussion on the spray evolution is presented in Section 4.3.

In the spray region, engineering parameters of interest are droplet size, its distribution and number density, its formation pattern, and the average velocity. Depending on local pressure and temperature conditions, very small droplets may also evaporate before they hit the substrate. Since individual droplets of different sizes have their own velocities, inter-droplet collisions, coalescence, as well as ternary breakup is possible during the passage of the ensemble of droplets, before, during and after impact over the substrate [30].

Designing or choosing a liquid flow nozzle for a specific application requires fundamental knowledge of nozzle construction and its flow characteristics. Unfortunately, there are no common internationally standards for nozzle classification and performance analysis. Individual nozzle manufacturers, while giving basic common performance data and constructional or functional information, use their own standards and testing protocols for creating specifications [49]. The basic geometrical construction of a nozzle assembly is simple. It consists of the nozzle body, the core (including filters, swirl plates, and turbulators), liquid entry connection and the orifice from which the spray pattern emerges out (Fig. 6(a)).

System level hydrodynamic performance testing and selection of nozzles requires seven fundamental specifications. These are: (i) operating nozzle pressure (ii) flow rate of the liquid (iii) spray angle and width (iv) efflux pattern of the spray, (v) flow distribution (vi) droplet size distribution, and (vii) force impact distribution over the substrate. Not all specifications or parameters are required every time; it depends on the objectives of the specific application. Two other specifications include the material used for construction and the connection used for liquid delivery. Nozzle construction materials are stainless steel (various grades for corrosion and erosion resistance), brass (easy to handle but less resistant to wear), or less common materials such as polymers that offer better chemical compatibility with corrosive liquids. Superior corrosion-abrasion-wear resistance is also offered by special grade ceramics or hard steel alloys containing tungsten, molybdenum, nitrides of boron and carbon, for example. Nozzle fittings can be threaded or flanged, the choice of which depends on the operating pressure and availability of space.

The operating parameters of a nozzle are briefly described here.

(i) Operating pressure: This is the fluid inlet pressure, measured at a point close to the nozzle inlet. It provides the energy required to create the spray and determines, for a given liquid flow rate and orifice diameter, other important quantities such as droplet size distribution, cone angle, its width and force field created on the target substrate.

(ii) Liquid flow rate: It is the amount of liquid sprayed from the orifice of the nozzle per unit time. The orifice diameter, cross-sectional area and operating pressure will determine the flow rate, as follows:

$$Q = A_0 u_m \tag{3}$$

Here, u_m is the mean efflux velocity of the spray, given by

$$u_m = C_d \sqrt{\frac{2\Delta p}{\rho_l}} = C_d \sqrt{2gH} \tag{4}$$

The coefficient of discharge C_d, whose value depends on the geometrical features of the nozzle, represents the conversion efficiency of available pressure energy to kinetic energy of the liquid and lies between 0 and 1. For $C_d = 1$, u_m represents the characteristic velocity scale of the system. Hence,

$$C_d = \frac{0.5\rho_l u_m^2}{\Delta p} \tag{5}$$

The operating pressure is substantially larger than the atmospheric pressure and $\Delta p \sim p$. From the above equation, it follows that

$$\frac{Q_A}{Q_B} = \frac{\sqrt{p_A}}{\sqrt{p_B}} \tag{6}$$

The flow rate of a spray nozzle is thus proportional to the square root of the operating inlet pressure. Coefficient of discharge is a fundamental characteristic of a spray nozzle [6] and hence, the flow rate and pressure drop across the current pressure swirl nozzle is measured to characterize it in terms of the coefficient of discharge. The flow rate clearly increases with an increase in pressure drop across the nozzle; however, the coefficient of discharge is approximately constant, as shown in Fig. 7. The coefficient of discharge has a direct relationship with geometrical features of the spray nozzle. Hence, it needs to be determined individually for each nozzle configuration.

Flow rate and operating pressure are affected by clogging of foreign particles that may be present in the working fluid. Pre-inlet filters and choosing wear-resistant materials are some of the ways to avoid degradation of nozzles by foreign particle clogging.

Liquid flow rate is one of the most important parameters affecting spray performance in terms of heat transfer. When specified as volumetric flux, i.e. $m^3/(m^2s)$, the applicable area in the denominator can be (a) the area of cross section of the orifice, where the volumetric flux refers to the nozzle, (b) local/infinitesimal area on the impacted substrate, where the reference is the target on which the spray impinges, or

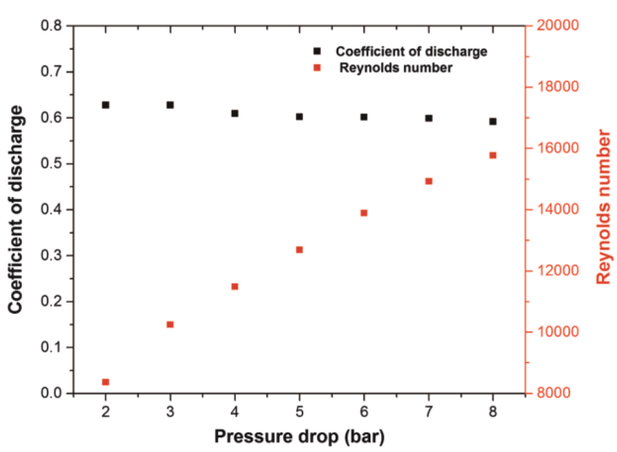

Fig. 7. Variation of coefficient of discharge with pressure drop across the spray nozzle used in the experimental set-up described in Section 4.1 – corresponding Reynolds number at the nozzle exit is also given on the secondary axis.

(c) the total area of the spray cover on the substrate. In some special cases, the entire area of the target substrate may also be chosen as the basis for specifying the volumetric flux, as in Fig. 6(a).

(iii) Spray angle and its width: As shown in Fig. 6(a), the angle at which the liquid spray comes out from the nozzle orifice is the spray angle or, the cone angle. At a specified distance from the nozzle, the liquid fans out a width on the target substrate and is referred to as the spray width. Since viscous interaction with the surrounding gas may be significant, the value realized in the experiment may differ from the theoretical geometrical value (Fig. 6 (b)). Both, spray angle and width are functions of the operating pressure. (Fig. 7). High speed imaging followed by digital image processing is a common method of measuring the spray cone angle. A flow chart representing an algorithm for image analysis is presented in Fig. 8.

Sprays are inherently unsteady, and the instantaneous cone angle may vary considerably from the average. The cone angle increases with pressure drop (which is also a function of flow Re) due to an increase in the tangential velocity of the stream coming out of the swirl plate [117]. Average and maximum cone angles increase with an increase in flow inlet Reynolds number across the nozzle, as in Fig. 9, as observed in the present study. Increase in cone angle further increases the area covered by the spray over the heated surface for a given nozzle height. This is a favourable outcome for removing the heat load from a large area. In case of spray arrays, cone angle and nozzle pitch must be adjusted to cover the required area, as shown earlier in Fig. 4(b).

(iv) Spray pattern: The geometrical cross-sectional pattern of the spray emerging from the orifice can change drastically, depending on several factors. Accordingly, several patterns can be obtained, as presented in Fig. 6(c). For example, the dispersing patterns can be focused circular dot(s), solid conical, hollow conical, rectangular shaped, and multi-nozzle overlapping cones. The final application may determine the required spray pattern. It should be noted that a certain minimum distance is needed after the liquid leaves the nozzle orifice for the flow to be considered as fully developed. During this traverse, the bulk liquid volume emanating from the orifice eventually breaks down into finer droplets by the action of hydrodynamic instabilities, turbulent mixing, and primary and secondary vortex break-up. Efflux from an array of nozzles can interact with each other, producing more complex flow pattern distribution (Fig. 4(b)). Heat transfer characteristics can accordingly be quite diverse.

(v) Flow distribution: Across the section of the nozzle spray, the flow rate will not be uniform but will attain a universal distribution. For example, the flow can be distributed in a convex, concave, or trapezoidal shape, depending on the nozzle type, orifice geometry, and array configuration, as depicted in Fig. 6(c).

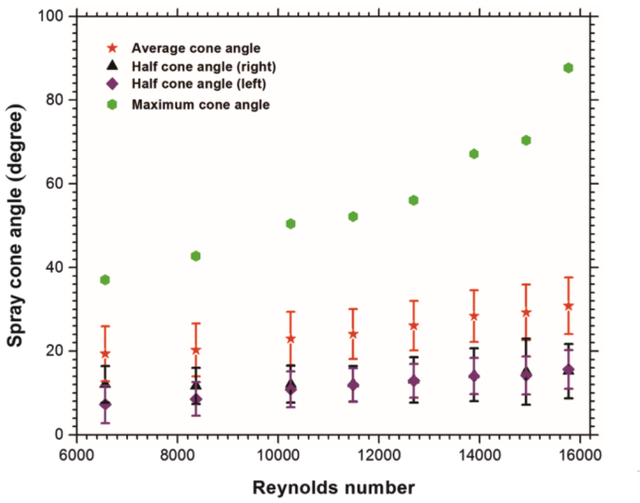

from experiments performed by the authors, as described in Section 4.1 for different flow rates of liquid emanating from a pressure swirl nozzle.

(vi) Droplet size and distribution: This is one of the most important parameters that influences thermal transport at the substrate. It depends on the type of nozzle, orifice geometry, operating pressure, thermodynamic condition of the ambient, liquid flow rate, and fluid properties [15]. While we do not include mist flows in the present discussion, it is known that finer droplet size distribution is generally obtained [78]. There are several methods to determine droplet size distribution. The primary ones include: (a) Non-invasive laser-based methods (b) Stroboscopic methods coupled with high speed visualization (c) Spray visualization or deposition on a flat substrate using a microscope. There are several ways by which droplet size can be specified, the most popular being the Sauter Mean Diameter (SMD). It is defined as the diameter of drop that has same volume-to-surface area ratio as that of entire spray [94]. Numerically is written as follows,

$$d_{32} = \frac{\sum n_i d_i^3}{\sum n_i d_i^2} \tag{7}$$

This is commonly abbreviated as d_{32} or SMD. Other ways of

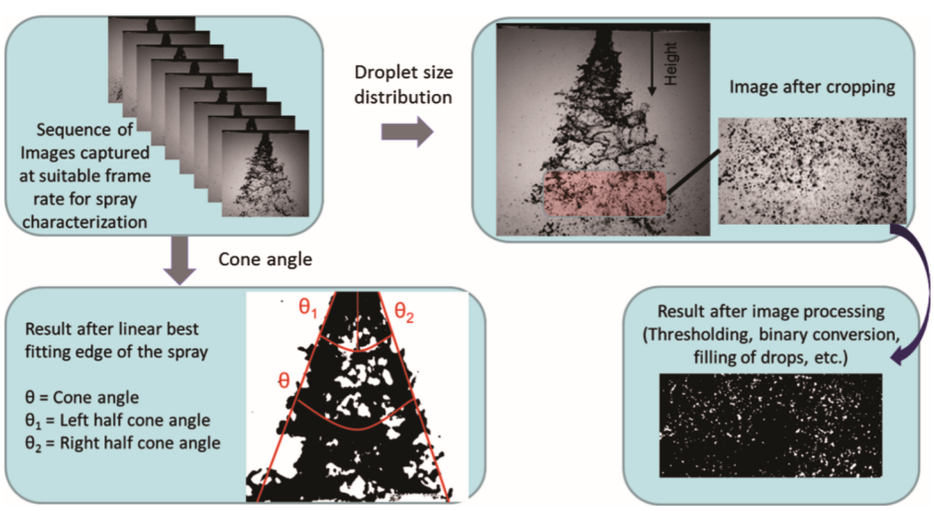

Fig. 8. Flow chart showing the sequence of image analysis algorithm developed and followed by the present authors for spray characterization (cone angle and droplet size distribution).

expressing droplet size include arithmetic (d_{10}) or number mean and the mean diameter over volumetric, i.e., the De Brouckere mean (d_{43}). Most sprays will have a droplet size distribution across their efflux cross-section, i.e., a range of droplet sizes represented by a distribution histogram. Special techniques are needed to produce a specified distribution with small standard deviation or mono-dispersed characteristics.

There are several correlations for SMD available in the literature, depending on the nozzle type and operating parameters. Confining our discussion to simple solid cone pressure nozzle, a popular correlation, valid for liquids with vastly different surface tension (such as FC-72 and water) is given by Estes and Mudawar [24] as

$$\frac{d_{32}}{d_0} = 3.67\left(We_0^{\frac{1}{2}} Re_0\right)^{-0.259} \tag{8}$$

where d_o is the nozzle orifice diameter, in the range of 0.762–1.7 mm, and We_o and Re_o are, respectively, the Weber and Reynolds numbers based on orifice conditions. These dimensionless quantities are defined as

$$We_0 = \frac{\rho_g\left(2\Delta p/\rho_l\right)d_0}{\sigma} \tag{9}$$

$$Re_0 = \frac{\rho_l\left(\sqrt{2\Delta p/\rho_l}\right)d_0}{\mu_l} \tag{10}$$

Researchers have proposed several correlations to determine the SMD of sprays. Many of these correlations are based on scaling of the relevant forces leading to power law type relationships among relevant non-dimensional numbers. The correlations mentioned in Eqs. (11)–(13) below are used for comparison of droplet size distribution (SMD for present experimental conditions) at various pressure drops.

$$\frac{d_{32}}{d_0} = 13.62We_0^{-0.12}Re_0^{-0.26} \text{ [16]}, \tag{11}$$

$$d_{32} = 7.3\sigma^{0.6}\mu_l^{0.2}\rho_l^{-0.2}m_l^{0.25}\Delta p_l^{-0.4} \text{ [79]}, \tag{12}$$

$$d_{32} = 4.4\sigma^{0.6}\mu_l^{0.16}\rho_l^{-0.16}m_l^{0.22}\Delta p_l^{-0.43} \text{ [40]}, \tag{13}$$

While the best estimates of SMD can only be determined from experiments, the procedure is rather complex. Alternatively, the above equations can provide a reasonable and sufficiently accurate first approximation. As shown in Fig. 10, SMD decreases with an increase of inlet Reynolds number across the nozzle. Nozzle geometrical parameters and liquid properties largely influence spray properties such as cone angle, droplet count, and probability distribution of the droplet sizes. The performance of a pressure swirl nozzle adopted in the present study is examined in terms of the fraction of drops falling in a size range, as shown in Fig. 11. The droplet counts, as well as mass efflux of coolant, increases with the pressure drop across the nozzle. Also, the fraction of relatively large drops (> 300 μm) decreases with increasing pressure, being attributed to the increased probability of secondary atomization, clearly seen in the video record.

If the cone angle of the spray, θ, is known, the correlation by [7] can be utilized, to calculate the median diameter of the spray, $d_{0.5}$, and is given by

$$\frac{d_{0.5}}{d_0} = \frac{9.5}{\left[\Delta p^{0.37}\sin\left(\theta/2\right)\right]} \tag{14}$$

The median droplet diameter of sprays changes as a function of the axial distance z, downstream of the nozzle orifice. This is due to the interplay of inter-particle collision, entrainment, and shear interaction with the surrounding gaseous medium. A reasonable estimate of the mean diameter with the downstream distance (valid for d_o = 0.762 – 1.7 mm, and volumetric flow rate = 0.53 to 5.89 l/min) is given by [16] as follows:

$$\frac{d_{0.5}}{d_0} = 0.523We_0^{-0.659}Re_0^{0.203}(H/d_0)^{-0.361} \tag{15}$$

(vii) Spray impact distribution: When a spray hits a target substrate, momentum transfer generates a local force distribution due to the impacting droplets. On most occasions, the droplets impinge a thin film of liquid which gets formed on the substrate. The resulting pressure distribution over the substrate is required for design applications. The resultant force can be estimated as

$$F = C\rho_l Q\sqrt{2gH} \tag{16}$$

For a given flow rate, impact due to an impinging spray is proportional to the square root of nozzle pressure, i.e. the flow velocity. For a given nozzle, spray impact follows the spray distribution, which depends on the type of spray [114]. Usually, a correction factor is employed depending on the nozzle type, to correct the force field given by Eq. (16). Accurate estimation of local momentum transfer is better provided by dedicated experimental data, rather than theoretical considerations that tend to be simplified and hence prone to errors.

(viii) Inclined sprays: Sprays need not always impinge perpendicular to the substrate. They can also be at an angle to the substrate. Inclining the spray can offer certain advantages in packaging. However, radial isotropy of the spray is lost by inclination.

Two possible constraints under which spray nozzles can be inclined are depicted in Fig. 12(a) and (b), respectively. In the first, the cone angle N_1 remains unchanged even after inclination. It can be moved by keeping the height H_1 constant, to a new position N_2, as shown. In doing so, the spray impact area increases from A_1 to A_2, so also the radius at which the nozzle is placed increases from R_1 to R_2. Such a move changes the droplet size distribution, as well as the spray pattern over the area of interest. Alternatively, we may incline the nozzle to keep its original radius identical, i.e. $R_1 = R_3$. In this case, at position N_3, the height of the nozzle as well as its pattern and droplet size distribution are altered. Yet another way to incline the nozzle is to move to a new position N_4, where the impact area remains identical to $A_1 = A_4$. However, it changes both, the nozzle radius (R_4), as well as the height of the nozzle (H_4), severely affecting the resultant droplet size and pattern at the substrate over the zone of interest.

In the second case, as seen in Fig. 12(b), the impact area is always maintained identical by changing either (i) the radius R_2, maintaining its height $H_2 = H_1$, or, (ii) changing the height (H_3), bit maintaining its

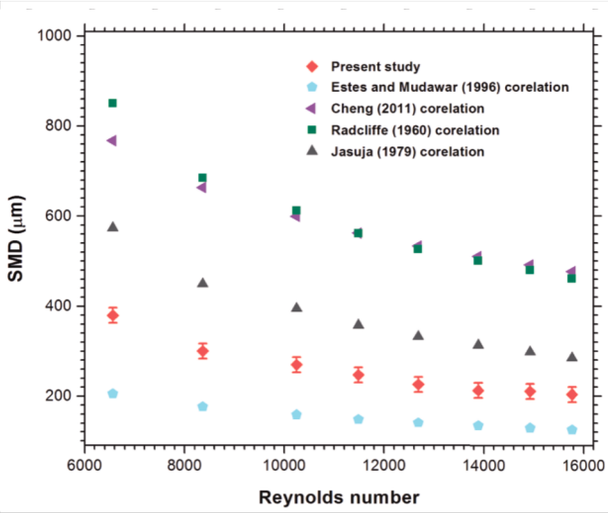

Fig. 10. Average drop size distribution (SMD) of the spray, obtained from the experimental set-up of Section 4.1, at a height of 20 mm from nozzle exit, plotted against inlet Reynolds number, and its comparison with published correlations.

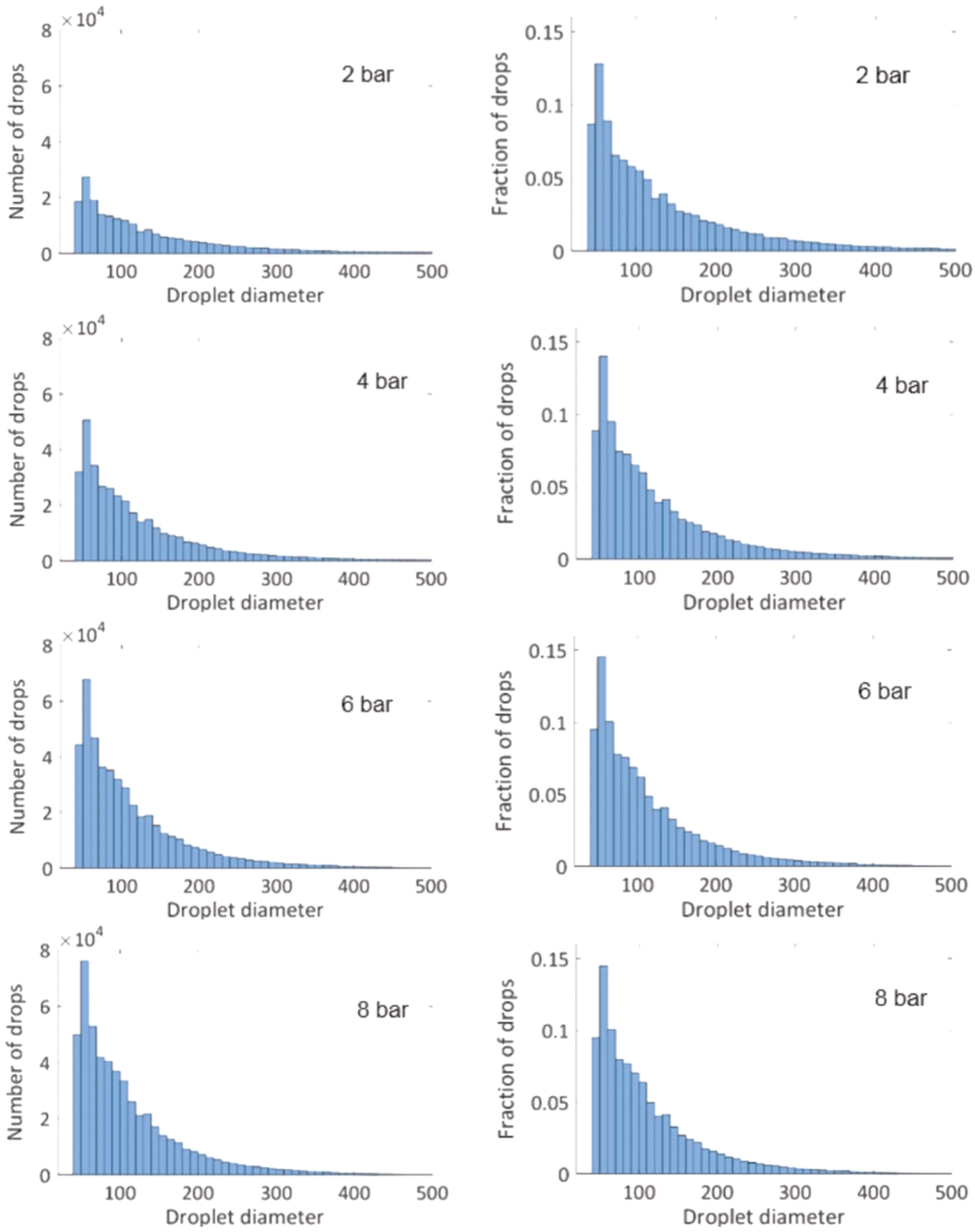

Fig. 11. Number of drops and their size distribution in the spray, at different pressure drops, measured at a height of 20 mm from the nozzle exit, obtained from the experimental set-up of Section 4.1.

radius ($R_1 = R_3$). However, in both these configurations, the nozzle cone angle needs to be altered, to maintain the area of spray impact be de identical ($A_1 = A_2 = A_3$). A change in cone angle alters the droplet size, number density as well as its impact pattern.

As heat transfer is a strong function of droplet size distribution, number density, and impact pattern, it is evident that inclining the spray opens up a plethora of possibilities [82]. It is for these reasons that experimental data from inclined sprays described in the literature are difficult to compare and evaluate. Nevertheless, inclined nozzles do offer an extended variety in configurations for thermal management, as is seen in Fig. 13.

4.3. Thermal considerations

Although the pressure-drop penalties are rather high, spray cooling techniques can provide one of the highest heat transfer coefficients. This is possible because several heat transfer mechanisms operate simultaneously during spray cooling. These include (i) single-phase convective heat transfer in thin liquid films; (ii) enhanced single-phase turbulent heat transfer in thin liquid films due to droplet impact and mixing; (iii) interfacial evaporative heat transfer; (iv) primary heterogeneous nucleate boiling heat transfer; (v) secondary nucleation mechanism; (vi) bubble interaction with thin liquid films; and, (vii) transient conduction effects due to rapid bubble nucleation and removal [110]. Hence, spray cooling easily exceeds the performance provided for example, microchannel flow boiling or liquid jet cooling. Moreover, the impact area of sprays is larger than jets, and hence resulting spatial distribution of heat transfer coefficient is also more uniform. Under the influence of many impacting droplets providing additional pressure on the substrate, the CHF crisis is also considerably delayed.

In the following paragraphs, we discuss local heat transfer mechanisms that are responsible for the excellent global performance of the spray impingement cooling technique. Attention is drawn towards Fig. 13, where several of the underlying mechanisms of heat transfer

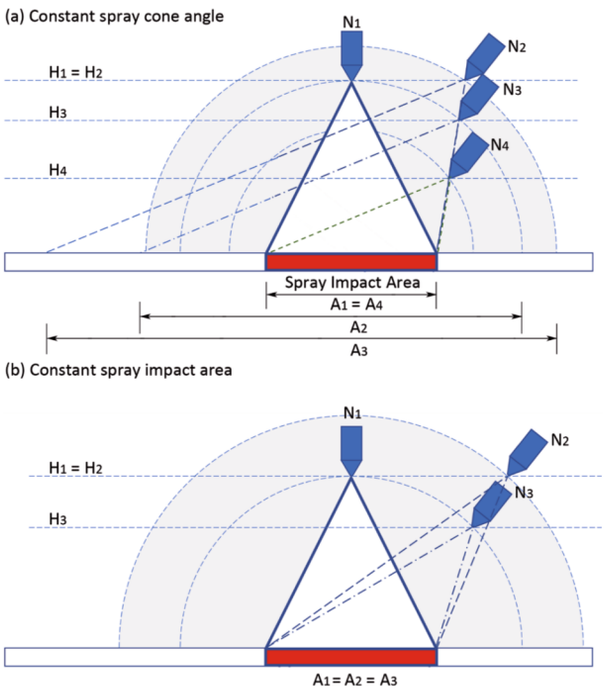

Fig. 12. Different configurations in which a spray can be inclined with respect to the heated substrate; (a) Keeping the cone angle constant and (b) Keeping the spray impact area to be constant.

are qualitatively depicted. While several studies have been conducted in the past for hydrodynamic characterization of sprays, the underlying mechanisms of thermal transport during spray impingement are still not very clear. This continues to remain a topic of contemporary research.

When the fully developed atomized spray hits a heated solid substrate (such as the heat sink/ thermal base plate of an electronic/LED module), momentum transfer takes place between the droplets and the substrate (Fig. 13(a)). Several intertwined heat transfer mechanisms come into play, depending on the temperature of the substrate. In applications such as electronics thermal management and LED cooling, it is a specified heat flux which needs to be removed to keep the operating temperature of the substrate in an acceptable working range. As the wall heat flux increases, the temperature of the substrate will attain a steady-state, depending on the effective heat transfer coefficient achieved by the operating conditions such as quality of atomization of the spray [106]. Referring to Fig. 13(b), a thin liquid film of size ranging from a ten of microns to several hundred microns is generally observed over the hot substrate, where single-phase convective heat transfer mechanism sets in. The atomized drops emanating from the spray hit this radially flowing liquid thin film, generating turbulence in the upper portions of the film, Fig. 13 (c). Close to the substrate, a laminar sub-layer will exist. High momentum flux is transferred from the spray to the thin liquid layer. This leads to transverse and longitudinal mixing of fluid layers, as well as localized thinning of the liquid film at select locations, greatly enhancing the heat transfer. Diffusive heat transfer in the thin film region also leads to evaporation at the liquid interface, further reducing the thermal resistance to heat transfer from the substrate to the fluid phase.

As the heat flux to the substrate is increased, Fig. 13(d), thermodynamic conditions for heterogeneous nucleation will eventually become favorable. This leads to bubble generation inside the liquid thin film on the hot substrate, leading to the dominance of two-phase heat transfer, with latent heat paying a decisive role in energy management. Surface roughness, wettability and nucleation site density become parameters of interest. Boiling curves, qualitatively like pool boiling, can be obtained for spray boiling as well. These broadly indicate regions of single-phase, nucleate boiling, transition boiling and film boiling, passing through the zone of critical heat flux (CHF) [105]. Unlike simple pool boiling however, nucleating bubbles cannot grow to sizes large enough for buoyancy to initiate their release from the substrate. In case of sprays, bubbles nucleate within a radially moving thin liquid film, with considerable momentum transfer imparted by the impinging droplets. The shear stress in the flow and the turbulence created by the impinging droplets dislodges the growing vapor droplets. This intense interaction of impinging droplets and nucleating bubbles creates additional turbulence and contributes towards further

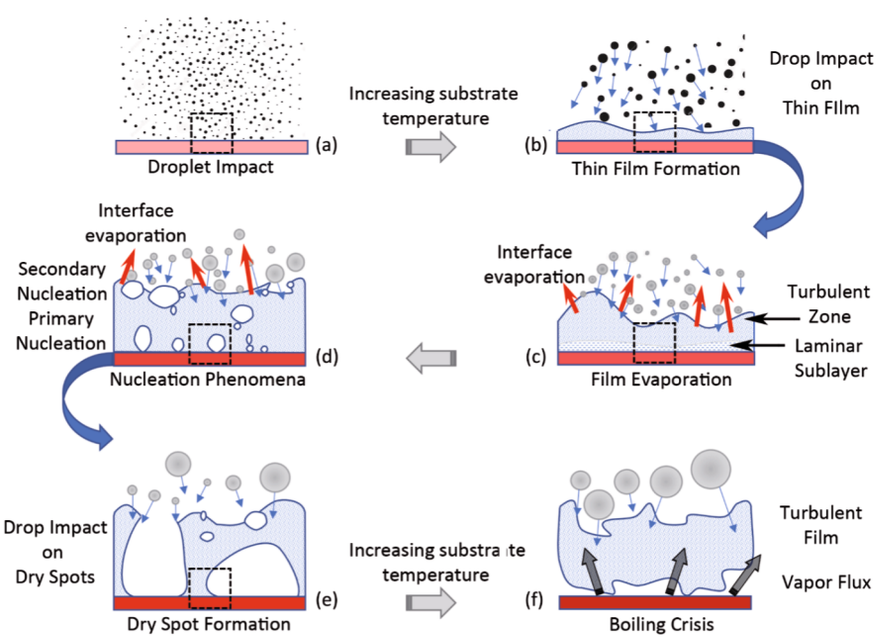

Fig. 13. Various phenomenological and qualitative mechanisms of heat transfer occurring during spray impingement phenomena, as the applied heat flux to the substrate increases.

enhancement of heat transfer by an order of magnitude relative to pool boiling. It is also known that impinging droplets entrain the surrounding gas within the liquid film that serve as secondary nucleation sites, leading to further increase in heat fluxes, Fig. 13(d). Secondary nucleation sites are also produced by the bursting of the rising bubbles from the substrate. The bursting of the bubbles creates liquid splashing and small secondary droplets on the liquid film interface. When they fall on the liquid film, entrainment of the surrounding vapor creates an opportunity for additional nucleation sites formed on the interface. Research indicates that the number of such secondary nucleation depends on droplet flux and the surface temperature. Its contribution can be substantial (50% to 80%) in the overall heat transfer budget [88,17]. The existence of secondary nucleation is undoubtedly established by scrutinizing the bubble frequency and surface superheat data, vis-à-vis the wall heat flux [67,111].

Further increase in heat flux will lead to a situation where dry spots start appearing on the substrate, Fig. 13(e). Such a situation is a precursor to the boiling crisis, contact line dynamics and enhanced heat transfer in the contact line region. In addition, some droplets impinge directly on dry spots and rapidly evaporate after spreading, or disintegration, depending on local wettability and impact velocity. The enhanced vapour flux moving away from the substrate starts interacting with the thin film as well as droplet flux coming in the opposite direction. Practically all seven mechanisms of heat transfer, as started earlier, simultaneously manifest themselves under most operating conditions. Ultimately, increasing the heat flux further will trigger a boiling crisis and dry out, leading to rapid increase in substrate temperature, arising from a swift reduction in the heat transfer coefficient, Fig. 13(f). This eventual transition with respect to the increasing heat flux is delayed in case of a spray because of the uniform and continued droplet flux on the liquid thin film and the enhanced levels of transverse and longitudinal mixing, sustained continuously by the impinging drops. Post CHF mechanisms are similar to what happens in the case of pool boiling. Radiation plays a role, and a significant reduction in heat transfer coefficient is obtained due to vapour blanketing effects. From a LED cooling perspective, post-CHF regime is certainly undesirable and is not discussed further.

From a practical design point-of-view, there are two important heat flux levels which need to be ascertained. These are: (a) Conservative operating maximum heat flux for a given spray impingement cooling system in terms of the steady-state temperature, T_{safe}, which cannot be exceeded due to the safety, performance, and material limitations of the electronic or the LED system mounted on it. (b) Critical heat flux CHF, which is the ultimate heat flux the system can remove before the boiling crisis sets in, under a given set of operating conditions, Fig. 14. In (b) the temperature of the substrate T_{sub} can be much larger than what is permitted for safety, namely, T_{safe}. For a given operating condition, the safe maximum heat flux will usually be smaller than the CHF. A designer must be aware of both these limits, as they define the nominal and ultimate upper bounds, respectively, for wall temperature.

4.3.1. Single-phase heat transfer

Spray cooling heat transfer is mainly dominated by single-phase regime at high subcooling and at low superheat of the impinging coolant. The single-phase regime of heat transfer offers high operational stability and good uniformity of the surface temperature distribution, both features being favourable for thermal management of high power LEDs [17]. After the spray hits the substrate, a thin liquid film is formed close to the substrate, along with the formation of a hydraulic jump along the outer periphery. This process is like a liquid jet impinging normally over a surface. Comparatively speaking, single-phase heat transfer has lower heat dissipation capability as compared to the boiling/phase-change regime, Fig. 14. The dominant heat transfer mechanism includes local liquid film convection, enhanced heat transfer in thin liquid films due to droplet impact on its top interface, and impact induced mixing, and to some extent, interfacial evaporative heat transfer. Spray cooling parameters to be optimized can be classified as (i) nozzle geometry and position relative to the substrate (ii) droplet size distribution, mean droplet velocity, and volumetric flux of the coolant, (iii) surface texturing, and (iv) thermal boundary conditions of the test surface.

Various Nusselt number ($Nu_D = \frac{hD}{k_f}$) correlations are available in the literature for single-phase heat transfer with sprays related to flow rate, droplet diameter, heated surface size, and nozzle orifice diameter. Heat transfer rate significantly improves by increasing the liquid flow rate and by decreasing the coolant inlet temperature [97]. One such example of a correlation is given in Eq. (17), which is valid for the Prandtl number range between 2.09 and 7.74 and Reynolds number ($Re_D = \frac{u_m D}{\nu}$) range from 520 to 2600. Here, the Nu and Re are based on diameter of the heated surface. The thermophysical properties of the liquid coolant are evaluated at the average of surface and fluid inlet temperature.

$$Nu_D = 0.675 Re_D^{0.77} Pr_f^{0.84} \tag{17}$$

Heat transfer correlation based on Sauter Mean Diameter (d_{32}) of the droplet has been proposed for various orientations of the spray nozzle by Rybicki and Mudawar [82] (Eq. (18)). Nusselt number and Reynolds number are evaluated based on the droplet distribution of the spray. Experimental data was generated with three nozzles, having a nominal orifice diameter of 0.77 mm, 1.19 mm and 1.70 mm, respectively, with flow rates of the coolant (PF-5052) varying between 3.08×10^{-6} to 20.93×10^{-6} m^3/s. The correlation is given as

$$Nu_{d_{32}} = 4.7 Re_{d_{32}}^{0.61} Pr_f^{0.32} \tag{18}$$

where

$$Nu_{d32} = \frac{q''}{T_w - T_{in}} \frac{d_{32}}{k_f} \text{ and} Re_{d_{32}} = \frac{u_m d_{32}}{\nu} \tag{19}$$

The effect of subcooling of the incoming fluid for a full cone spray nozzle was studied by Cheng et al. [16]. Here, Nusselt number is correlated with Reynolds number, Weber number, Prandtl number and the non-dimensional degree of subcooling, Eq. (20). For generating this correlation, experiments were carried out with a spray impinging at an angle of ~30° and nozzle diameter of 0.2 mm. The flow rate of the coolant was varied from 100×10^{-6} m^3/s to 144×10^{-6} m^3/s, with inlet temperature variation from 19 °C to 35 °C. The height of the spray from the substrate was changed from 3 mm to 10 mm. The correlation reads

$$Nu_D = 0.036 Re_{d_{32}}^{1.04} We_{d_{32}}^{0.28} Pr_f^{0.51} \left[3.02 + \left(\frac{T_w - T_f}{T_{sat}} \right)^{1.53} \right] \tag{20}$$

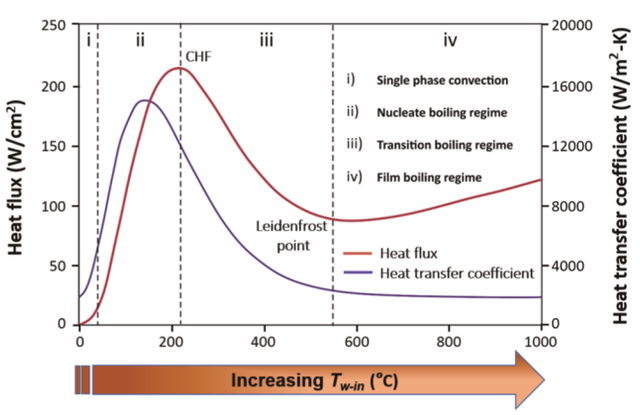

Fig. 14. Schematic diagram of regimes of heat transfer in spray cooling depending upon operating surface temperature (data corresponds to coolant water, 10 kg/m^{2}s, T_{inlet} = 18 °C, full cone nozzle, as reported by [105]).

A similar study was carried out using pressure swirl nozzle to understand the effect of nozzle height and subcooling on single-phase heat transfer by Xie et al. [108]. The proposed correlation is applicable over $12{,}600 \le Re \le 20{,}250$, $4.2 \le \frac{T_w}{T_{sat}-T_f} \le 5.2$ and $0.2 \le H/D \le 1$ and is given as

$$Nu_D = 8.705 Re_0^{0.323} \left(\frac{T_w}{T_{sat}-T_f}\right) e^{-0.4268(H/D)} \quad (21)$$

Researchers have proposed empirical correlations for heat transfer coefficient based on the mass flow rate of coolant and pressure drop across the nozzle, along with thermo-physical properties of the liquid [21]. Under given operating conditions of spray cooling, flow rate is the major influencing factor and a higher mass flow rate can remove a higher heat flux from the test surface [120]. This is also highlighted by experiments with spray impingement cooling under the single-phase cooling regime investigated by the present authors, as described earlier in Section 4.1. Water was used as the working fluid due to superior thermal properties and ease of availability. As shown in Fig. 15, surface temperatures decrease with an increase in water flow rate for a given heating level. The maximum heat transfer coefficient of ~15.7 kW/m^{2}K is achieved at the highest water flow rate of 350 ml/min (Re = 13990) while surface temperature is well below the safe reliability limit of LEDs). In this experimental study, coolant water inlet temperature is maintained at 20 °C, height between the orifice and the heater surface is 15 mm, and the spray impinges at the centre point of the heated surface. It is observed that, at a low flow rate of 50 ml/min, the heated surface temperature exceeded (80 °C) at a heat flux of 40 W/cm^2. Hence, for a given LED module, the flow rate of coolant must be such that it must remove the thermal load form the heated area, while maintaining the temperature to a safe level. The effect of nozzle tip to plate distance, on the heat transfer rate was also explored by the present authors, in view of the packaging requirements of spray cooling. As seen in Fig. 16, nozzle height has a marginal effect on the heat transfer rate for the range of 5–25 mm. However, when the nozzle height was very less (below 1.5 mm, smaller than capillary length scale of water) and at a low flow rate, thermal performance of the spray decreases due to formation of a liquid bridge between nozzle and heated surface. Large height of nozzle is undesirable as it will increase the system space, lead to inefficient packaging solution, and will decrease the thermal effectiveness. The maximum heat flux considered is 40 W/cm^2 and inlet fluid temperature was varied between 20 °C and 60 °C.

In the closed loop operation of spray cooling of a packaged unit, inlet temperature of the coolant may vary due to insufficient cooling of the spent fluid to the ambient. Fig. 17 shows that a higher inlet temperature of the impinging water spray increases the temperature of the heating surface for obvious reasons; simultaneously, it also increases the probability of exceeding the safe temperature limit. Hence, closed loop packaging strategies for spray cooling technology should include spray parameters like optimum flow rate, nozzle height and issue related to increase in inlet coolant temperature, during their design cycle. More systematic experiments, with coolants other than water are also needed to supplement the present available database.

4.3.2. Nucleate boiling regime

This regime of heat transfer has received considerable attention for its characteristic features to remove very high heat flux from a heated surface. The slope between heat flux and surface temperature obtained during single-phase heat transfer can be substantially enhanced with a marginal increase in surface temperature, with the onset of phase-change phenomena. The zone (ii) indicated in Fig. 14 represents nucleate boiling, where frequency of bubble formation increases exponentially with a rise in the surface temperature, leading to complex interaction among the incoming droplets from the spray, liquid film, and vapour bubbles. The thin liquid film can transport a higher heat load, which is further supported by secondary nucleation where the impinging droplets rupture the growing bubbles to create an enhanced bubble nucleation frequency. It is understood that spray cooling has three distinct modes of operation depending on applied heat flux or the substrate temperature. These are evaporative spray cooling or 'dry' state, film cooling or 'flood' state and Leidenfrost state, in which spray droplets accumulate over the heated surface due to vapour inertial interaction. Spray evaporative cooling has the highest coolant utilization capability; however, it is difficult to control constancy of the wall surface superheat. From a thermal management perspective, film cooling is desirable as it manifests in higher stability of surface temperature, along with a higher heat transfer coefficient. As discussed in the previous section, a nonlinear relationship between heat load and surface temperature can be attributed to primary heterogeneous nucleate boiling, secondary nucleation, bubble interaction with thin liquid films, transient conduction, and interfacial evaporation in thin films. Nucleate boiling heat transfer is significantly affected by a complex interaction of surface temperature of the heated surface, thermophysical properties of the coolant, thermal-hydraulic characteristics of the spray, surface finish, and ambient pressure conditions [101]. Therefore, significant effort of researchers has been on empirical correlations to quantify heat transfer behaviour, rather than undertaking a detailed numerical or physical modelling of spray cooling.

Ghodbane et al. [29] developed a general heat transfer correlation, Eq. (22), for subcooled Freon-113, while investigating the effect of mass flux, droplet size, and velocity distribution for various nozzle distances. This correlation reads

$$\frac{q''H}{\mu_f h_{fg}} = 10.55 We_{d32}^{0.6} \left[\frac{C_f (T_w - T_f)}{T_{sat}}\right]^{1.46} \quad (22)$$

The correlation is valid for $2557 \le Re \le 61878$, $2200 \le We \le 13750$, $7.5 \le Pr \le 10.5$, $18 \le H \le 35$ and $0.12 \le q'' \le 50$ W/cm^2. For a wider range of droplet size and velocities, Holman et al. [32] presented the following expression:

$$\frac{q''H}{\mu_f h_{fg}} = 9.5 We_{d32}^{0.6} \left[\frac{C_f (T_w - T_f)}{T_{sat}}\right]^{1.5} \quad (23)$$

Hsieh et al. [34] experimentally studied the effect of high latent coolant fluids such as water and ammonia, with changing spray mass fluxes and degree of subcooling on spray cooling performance. The authors concluded that low degree of subcooling delays the onset of nucleate boiling. The authors reported water to have superior cooling

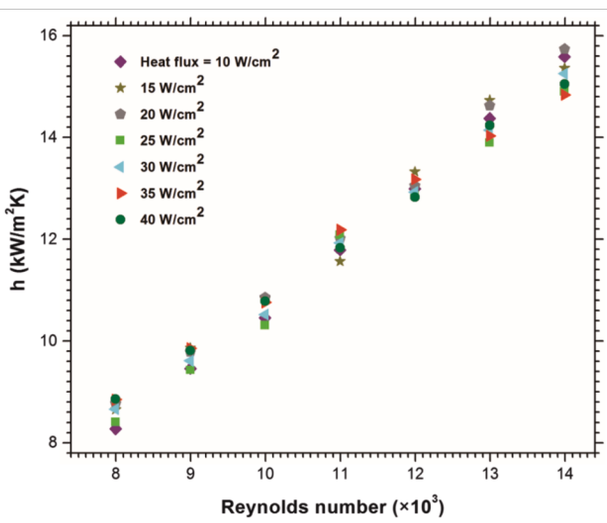

Fig. 15. Heat transfer coefficient (measured at the test surface, as described in Section 4.1) for various Reynolds numbers; experiments are conducted for different wall heat flux conditions.

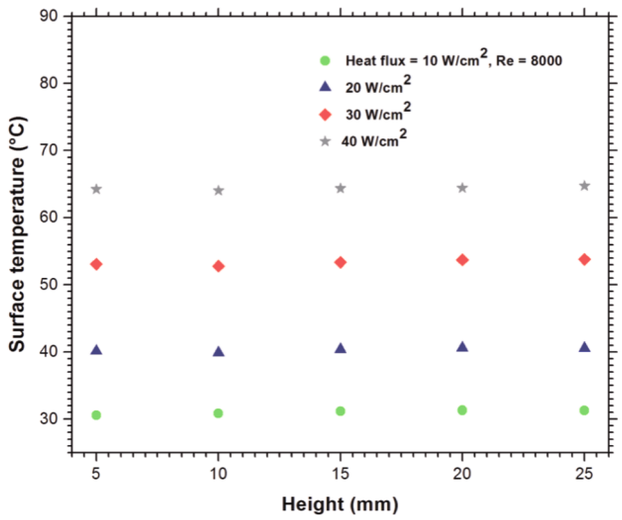

Fig. 16. Effect of nozzle to test surface height on surface temperature for single-phase spray impingement cooling at $Re = 8000$ and different wall heat flux conditions, obtained from the experimental set-up of Section 4.1.

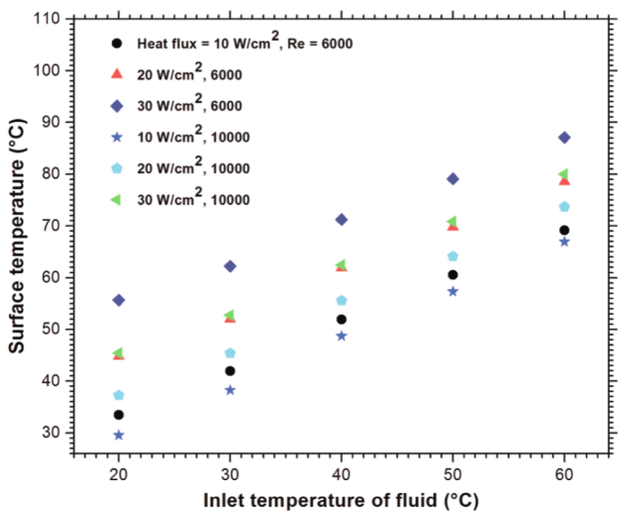

Fig. 17. Effect of coolant water inlet temperature (degree of subcooling) on the substrate maximum temperature for different heat flux and flow rates ($Re = 6000$ and 10000, respectively), obtained from the experimental set-up of Section 4.1.

performance compared to ammonia. The correlations presented by this group for water and ammonia, respectively are

$$\frac{q''H}{\mu_f h_{fg}} = 15.6\left(\frac{\rho_f u^2 d_{32}}{\sigma}\right)^{0.59}\left[\frac{C_f(T_w - T_f)}{h_{fg}}\right]^{1.68} \quad (water) \tag{24}$$

$$\frac{q''H}{\mu_f h_{fg}} = 2.1\left(\frac{\rho_f u^2 d_{32}}{\sigma}\right)^{0.66}\left[\frac{C_f(T_w - T_f)}{h_{fg}}\right]^{1.51} \quad (ammonia) \tag{25}$$

The ranges of parameters for the above correlations are as follows. For water, $220 \le Re \le 370$, $80 \le We \le 231$, 7.5 ≤ degree of subcooling ≤ 10.5, whereas for ammonia, it is $165 \le Re \le 277$, $50 \le We \le 152$ and 2 °C ≤ degree of subcooling ≤ −4 °C. The diameter of the heated test section was 80 mm, the height of the nozzle, with orifice diameter 0.38 mm, was equal to 60 mm for all the experiments.

The experimental data of Liu et al. [58] was analyzed to obtain the nucleate boiling correlation for spray cooling performance of R-134a for pressures from 0.2 to 0.4 MPa. The authors concluded that spray efficiency and CHF increase with system pressure. The following correlation was proposed for $0.311 \le Ja \le 0.067$, $0.017 \le We \le 0.022$ and $3.67 \times 10^9 \le \frac{\rho_f \sigma \dot{m}}{\mu_f^3} \le 1.01 \times 10^{10}$.

$$\frac{q''}{\rho_f Q h_{fg}} = 0.086\left(\frac{\rho_f Q^2 d_{32}}{\sigma}\right)^{-1.594}\left[\frac{C_f(T_w - T_f)}{h_{fg}}\right]^{1.503}\left(\frac{\rho_f \sigma \dot{m}}{\mu_f^3}\right)^{0.517} \times \left(\frac{\rho_f}{\rho_g}\right)^{0.916}\left[\frac{1}{r_d}\sqrt{\frac{\sigma}{g(\rho_f - \rho_g)}}\right]^{0.418} \tag{26}$$

Yoshida et al. [115] studied spray cooling at reduced gravity, where the nucleate boiling heat transfer correlation only depends on the surface temperature of the heated surface. Under reduced gravity, heat transfer rate has marginal dependency on spray hydrodynamics. Water and FC-72 were sprayed over an ITO heater using a full cone nozzle, resulting in droplet size distribution ranging from 54 to 386 μm. The other spray parameters were 1 bar ≤ Δp ≤ 4 bar, $30 \le We \le 622$, 0.000142 $m^3/(m^2s)$ ≤ Volume flux ≤ 0.000370 $m^3/(m^2s)$. The heat flux data was correlated as, $q'' \propto (T_w - T_f)^m$where the value of m was in the range of 1.7–2 for water and 0.5 for FC-72. Dou et al. [23] and Qiao and Chandra [77] studied quenching of hot metals using spray impingement cooling, where they observed similar results, with the heat transfer rate from a spray only marginally dependent on hydrodynamics.

Xie et al. [107] numerically simulated spray cooling performance using Monte-Carlo algorithm, where the droplet impingement model of heat transfer was based on the concept proposed earlier by Kreitzer and Kuhlman [48]. However, the model focuses only on few aspects of the full-scale problem and does not discuss secondary droplet formation, droplet impingement of liquid film, and secondary nucleation, in detail. Other researchers have explored spray cooling using numerical simulation of nucleate boiling, for single droplet impingement over a heated surface, by varying the thermophysical and hydrodynamics conditions of the droplet. The growth of bubbles in a liquid film during nucleation boiling regime along with droplet impact over the growing bubble has been simulated by Sarkar and Selvam [84]. Although various nucleate boiling correlations for spray cooling conditions have been proposed by researchers, the inherent complexity of the mechanism precludes development of a complete analytical model.

4.3.3. Critical heat flux

Critical heat flux (CHF) is the maximal heat flux during boiling heat transfer that any phase-change cooling technology can achieve, including spray cooling, Fig. 14. With further increase in heat flux, inefficient heat transfer through the blanketed vapour film results in physical burnout of the heated material. The CHF limit lies in-between the nucleate boiling regime and transient boiling regime. In a spray cooling system, CHF depends upon thermophysical properties, hydrodynamic characteristics such as droplet size and velocity, and degree of subcooling, along with the surface texture of the heated surface. The highest reported value of CHF for water spray cooling varies with experimental conditions; for example, a value of 500 W/cm^2 has been reported by Lin and Ponnappan [56], 638 W/cm^2 by Mudawar and Valentine [71] and 945.7 W/cm^2 by Chen et al. [14]. For thermal management of high-power electronics, dielectric refrigerants such as PF-5060, PF-5052, FC-72, FC-77 and FC-87 have also been explored. However, they have considerably lower CHF values. In this context, the maximum spray cooling efficiency can be defined as the ratio of CHF to the maximum heat transfer removing potential of the coolant fluid, namely

$$\eta = \frac{q''_{CHF}}{\rho_f Q[h_{fg} + c_{p,f}(T_w - T_{in})]} \tag{27}$$

Mudawar and Valentine [71] experimentally studied water spray cooling for a surface temperature maintained below 400 °C, where the authors primarily studied the effect of spray hydrodynamics and subcooling on the quenching curve. The authors proposed a correlation for predicting CHF and the maximum surface temperature. The experimental test conditions include, $0.6 \times 10^{-3} \leq$ spray volumetric flux $\leq 9.96 \times 10^{-3}$ m^3/(m^{2}s), mean droplet diameter ranging from 0.434 mm to 2.005 mm and the exit spray velocity ranging from 10.6 m/s to 26.5 m/s. For these conditions, CHF and maximum surface temperature were correlated with the relevant spray impingement parameters as

$$\frac{q''_{CHF}}{\rho_f h_{fg} Q} = 134.3\left\{1 + 0.0118\left(\frac{\rho_g}{\rho_f}\right)^{1/4}\left[\frac{\rho_f c_{p,f}(T_w - T_{in})}{\rho_g h_{fg}}\right]\right\}\left(\frac{\rho_f Q d_{32}}{\sigma}\right)^{-0.192} \tag{28}$$

$$T_{\max} = 18\left[(\rho_g h_{fg} Q)\left(\frac{\sigma}{\rho_f Q d_{32}}\right)^{0.198}\right]^{1/5.55} + T_{in} \tag{29}$$

It has been suggested that an optimum nozzle height exists in spray cooling to obtain the highest CHF [70]. Correspondingly, the heater size and spray angle can be carefully selected to take advantage of the highest spray cooling efficiency. The correlation mentioned in Eq. (30) below includes experimental data of spray angle, nozzle height, volumetric flux, and other flow characteristics, for a given heater length. However, it has been developed for full cone sprays nozzles over a wide range of flow rates and subcooling of the coolant at the inlet plane. The range of validity of the correlation has not been specified by the authors.

$$\frac{q''_{CHF}}{\rho_f h_{fg} Q} = 1.467\left\{\cos\left(\frac{\theta}{2}\right)\left[1 + \cos\left(\frac{\theta}{2}\right)\right]\right\}^{0.3}\left(\frac{\rho_f}{\rho_g}\right)^{0.3}\left(\frac{\rho_f Q d_{32}}{\sigma}\right)^{-0.35}\left\{1 + 0.0019\left[\frac{\rho_f c_{p,f}(T_w - T_{in})}{\rho_g h_{fg}}\right]\right\} \tag{30}$$

It is reported that micro-porous surface coatings can enhance CHF by 50–80% compared to a plane surface in spray impingement boiling experiments [98]. The experimental conditions here are: volumetric flow rate ranging from 1.1 cm^3/s to 15.8 cm^3/s, subcooling from 0 °C to 30 °C for HFE-7100 liquid, orifice diameter was fixed at 0.762 mm and the spray cone angle was 56°. The correlation below matches well with those of other researchers, with a maximum error of ± 30%.

$$\frac{q''_{CHF}}{\rho_f h_{fg} Q} = 2.14\left(\frac{\rho_f}{\rho_g}\right)^{0.3}\left(\frac{\rho_f Q d_{32}}{\sigma}\right)^{-0.363}\left\{1 + 0.0058\left[\frac{\rho_f c_{p,f}(T_w - T_{in})}{\rho_g h_{fg}}\right]\right\} \tag{31}$$

Another CHF correlation presented by Silk et al. [91] using functional dependence of various non-dimensional numbers is presented below in Eq. (32). This correlation has been evaluated in 85 test cases to check its applicability. The functionality was found to be quite good.

$$q''_{CHF} = 5.3 Re_D^{0.55} Pr_f^{0.33}\left\{\frac{0.8[c_{p,f}(T_w - T_{in})/h_{fg}] + 1}{(\rho_f/\rho_g)^{0.4}}\right\}\left(\frac{\pi N^+ d_{32}^3}{6}\right)^{0.09} \times \left(\frac{k_f}{L}\right)\left(\frac{h_{fg}}{c_{p,f}}\right) \tag{32}$$

Ciofalo et al. [21] studied the dependency of CHF on high mass flux water sprays (8–80 kg/m^{2}s) for a fixed nozzle height. The authors concluded that CHF is insensitive to droplet diameter distribution, but significantly affected by mass flux and average droplet velocity. For a lower coolant mass flux (0.33–32.7 kg/m^{2}s), marginal dependency of the hydrodynamics of spray on CHF was seen, as summarized in Eqs. (33) and (34) below:

$$q''_{CHF} = 0.869 \times 10^6 (G u_m^2)^{0.245} \tag{33}$$

$$q''_{CHF} = 1.759 \times 10^6 G^{0.567} \tag{34}$$

Sawyere et al. [85] developed a generalized correlation for the effect of droplet diameter, impact frequency and droplet impact velocity on CHF, for Weber and Strouhal number ranges of 175–730 and 7×10^{-3} to 30×10^{-3}respectively. The correlation given in Eq. (35) is valid for f = 12–42 Hz, diameter = 1.5–2.7 mm, and subcooling temperature of 75 °C.

$$\frac{q''_{CHF}}{\rho_f h_{fg} u_0} = 1.623\left(\frac{\rho_f u^2 d_0}{\sigma}\right)^{-0.315}\left(\frac{f d_0}{u_0}\right)^{0.0465} \tag{35}$$

4.4. Local droplet level considerations

The primary focus of this article is to delineate system level design considerations of a spray-based LED cooling system. However, it is well known that the global thermal-hydrodynamic performance of sprays is affected by the local behaviour of how an ensemble of individual droplets interacts with the substrate level features. While spray cooling mechanisms entail more complexity than just substrate level momentum and thermal interactions of one or more droplets, it is instructive to understand local mechanisms to appreciate the nuances of spray impingement cooling.

The most important local transport phenomenon that needs attention and understanding includes (i) droplet spreading on dry and wet surfaces with low and high Weber numbers; (ii) droplet chain impacting a substrate; (iii) coalescence mechanisms in various orientations; (iv) evaporation from fluid-vapor interface of films and droplets; (v) secondary nucleation mechanisms; and (vi) onset of CHF.

In the following paragraph, we provide a brief overview of drop level effects. The interested reader is directed towards the large body of literature available on subjects such as drop impact, coalescence, and evaporation controlled by capillarity. It suffices to mention here that understanding and subsequent estimation of the global performance of sprays can be greatly enhanced by increasingly incorporating local effects towards development of an inclusive mathematical model.

A spray cooling system comprises an ensemble of droplets hitting a hot substrate. Hence, for a given liquid spray system, parameters such as the relation between the individual drop sizes, their impact velocity, the wettability of the substrate and its temperature should be considered for design. One of the important criteria of system design is to prevent droplet rebound and hence, provide good contact of the liquid with the heated surface and enhance heat transfer. Maximum spreading diameter achieved by the droplet after its impact on the substrate is one of the identifying parameters, which will depend on Weber and Reynolds numbers and the equilibrium contact angle [81]. Although there are many correlations proposed for estimating the maximum droplet spreading diameter [122] two expressions proposed by Roisman and co-workers [81,10] are quoted here as representative estimates which agree well with experimental data [102]:

$$\frac{D_{drop_{\max}}}{D_{drop}} = 0.87 Re_{drop}^{0.2} - 0.4 Re_0^{0.4} We_{drop}^{-0.5} \tag{36}$$

$$\frac{D_{drop_{\max}}}{D_{drop}} = 0.87 Re_{drop}^{0.2} - 0.48 Re_{drop}^{0.4} We_{drop}^{-0.5}\ (\theta \to \pi) \tag{37}$$

Investigations of drop impact on a surface heated below the Leidenfrost point is in demand for potential applications in several high-heat flux cooling technologies involving phase-change heat transfer. In turn, Leidenfrost temperature depends on the drop size and surface wettability; the latter is also important for drop rebound. It has

been demonstrated that the Leidenfrost temperature is higher on heated surfaces with better wettability [95]. Regime maps in the form of T_W – *We* (surface temperature – Weber number) and T_W – *U* (surface temperature – impact velocity) for drops impacting a heated surface have also been generated by different authors with wettability as a parameter, as shown in Fig. 18 [10,100,122] . The main regimes considered are contact boiling, Leidenfrost boiling, transition boiling with identification of the critical parameters for film boiling, rebound and breakup with secondary droplet atomization [10,54,100,122]. Systematic experiments are needed to investigate the range of all possible influences on vapor layer development beneath the drop. For impact velocity in the range 0.5–3 m/s and surface temperatures below 150 °C, contact boiling is expected over a hydrophilic surface [54,53,100,10]; and [27]. This regime can be considered as a reference point for designing spray cooling systems, where chip surface and junction temperatures should not exceed 100 °C. For the temperature range of 20–150 °C spreading behavior and maximum spreading diameter are sensitive to Weber number and practically independent of surface temperature. However, rollback behavior depends strongly on the surface temperature [27]. The contact line velocity at the rollback stage will also depend on temperature. A rise in temperature leads to a considerable reduction in the contact diameter of the liquid column and also, an increase of the height of the liquid column at the splashing stage, as seen in Fig. 19; for more details of the experiments please refer to [27]. Micro-drop detachment from the liquid column is observed for a substrate temperature of 60–100 °C. These effects can be associated with an increase in the rollback velocity due to the reduction in viscosity as well as a reduction in surface tension with increasing temperature. Hence, the surface temperature influences liquid properties, the resulting droplet dynamics and in turn, the wall heat transfer enhancement. The drop breaks up into several sessile micro-drops after spreading when the surface temperature is much higher than the boiling point of the liquid (i.e. 130 °C). As a consequence, rollback and rebound are suppressed (Fig. 20). This results in contact boiling, enhancing the local heat transfer rate.

Several thermometry techniques have been introduced for understanding temperature evolution and heat transfer enhancement during events involving droplet contact. Chatzikyriakou et al. [11] used a high-resolution, high-speed infrared camera to measure the temperature on the surface in contact with the droplet. Combining

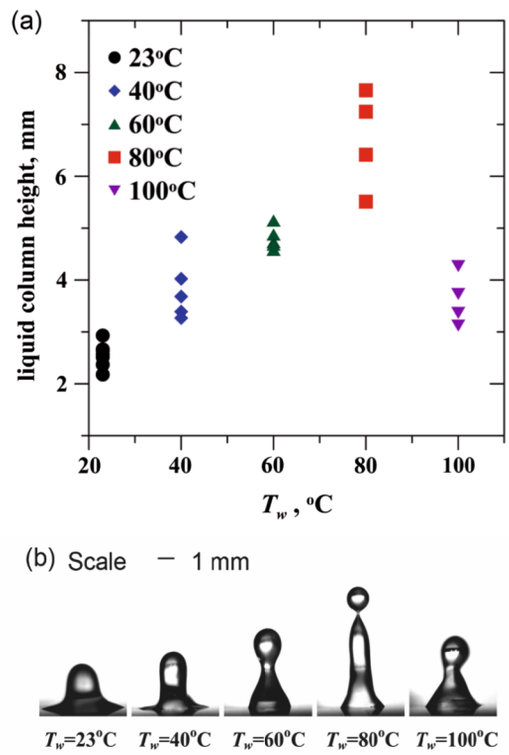

Fig. 19. (a) Variation of liquid (water) column height as a function of substrate temperature when the droplet makes an impact. The corresponding photographs are shown below in (b) [27].

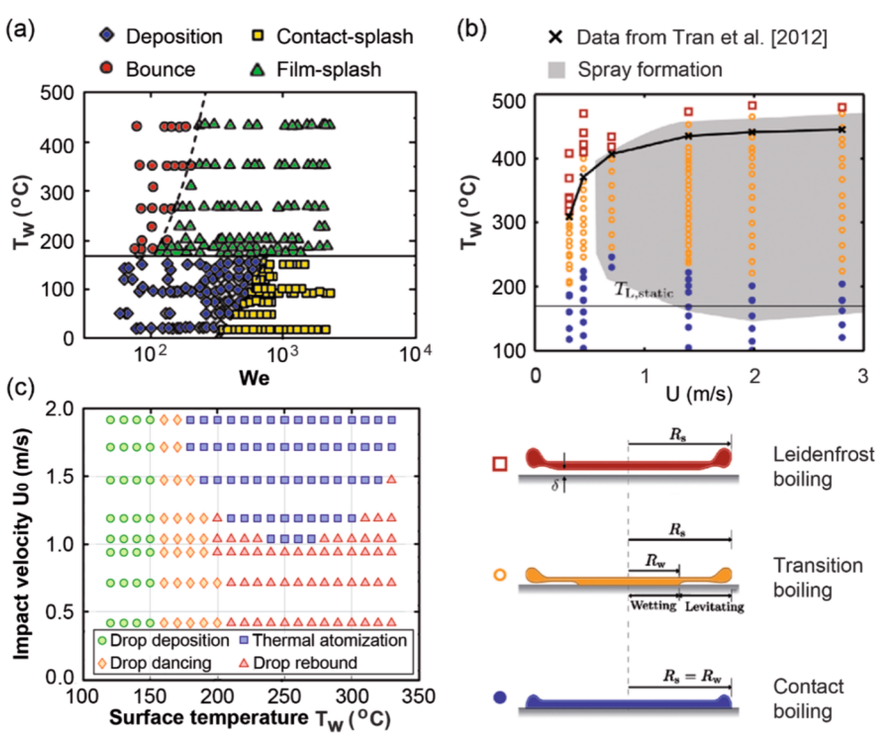

Fig. 18. Single droplet impact on hot surfaces (adapted from [10,100,122]) (a) Substrate temperature versus droplet Weber number, ethanol [122] (b) Flow pattern map showing three prominent regimes after the drop impact, based on substrate temperature and droplet impact velocity, water [100] (c) Similar regime map showing the four regimes [10].

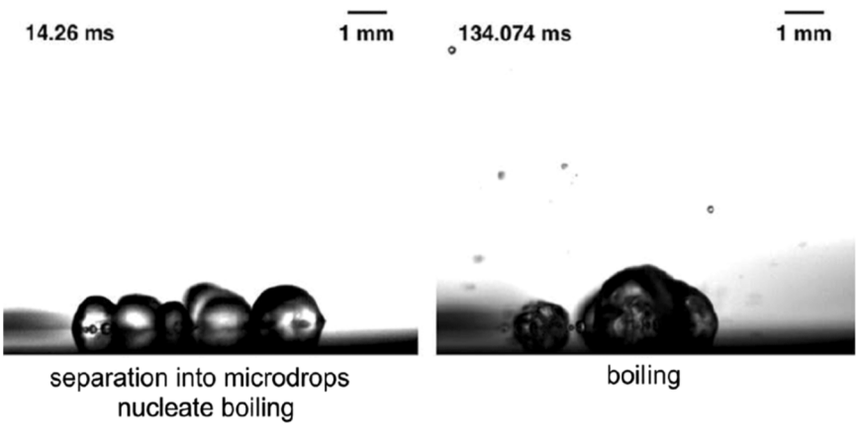

Fig. 20. Contact boiling with post-impact separation of droplet into micro-drops [27].

temperature distribution with an inverse heat conduction model, the local transient heat flux of droplet impact was calculated. It was shown that the heat flux during direct contact with the droplet can reach the order of a few MW/m^2. Temperature sensitive paints can be considered as a prospective technique for heat transfer measurements with high speed and high spatial resolution as demonstrated for pool and flow boiling experiments [2].

In summary, the rich physical phenomena of single drop impact on hot surfaces exemplify their high potential and yield a comprehensive perspective of droplet-based cooling technique for thermal management. More experiments are needed to grasp the full physics of the process.

5. Conclusions and outlook

Solid-state lighting and ancillary systems affect the performance and output of several core sectors, which together constitute a major portion of the world economic activity. An attractive feature of the LED technology is the combination of compact size, high power efficiency, and possibility of fast glow control. One of the most important consequences of large-scale adoption of the LED technology is a dramatic reduction of electricity costs. Hence, LEDs are used in diverse applications and are fast replacing conventional luminaire.

Traditional methods of addressing the heat dissipation problem includes passive fin cooling coupled with natural convection. The heat generated by the LEDs is conducted to the cooling fins via the base, and then dissipated into ambient air. However, this method is only suitable for low power consumption LED lamps. Heat dissipation from many contemporary LED modules have come to a stage that established cooling technologies cannot meet the industry requirement, and disruptive technologies are the need of the hour.

Most performance parameters of LEDs are closely related to the temperature of the p-n junction, making the cooling solution an important step in creating the LED system. A considerable part of electric power supplied to LED (70–80%) is released as heat. The power of 5 W dissipated from 1 mm^2 crystal surface corresponds to the average heat release density of 500 W/cm^2. Distribution of the heat flux in the crystal is also not uniform and may locally exceed 1500 W/cm^2. If heat generated is not removed quickly, these LEDs may overheat, and their efficiency and service life can be significantly reduced. This is particularly true when LEDs are arranged side-by-side in a large density array.

With the advent of high-power LEDs, it is necessary to incorporate efficient thermal management solutions in the packaging of LEDs. Higher power LEDs are required to be actively cooled due to higher heat generation. Spray cooling is one such cooling technology that has been addressed in the present study. Fundamental work has been reported on liquid jets, spray hydrodynamics, evaporation and boiling, and translational research is now required to package the available solutions for commercial LED applications. To this effect, an experimental study on heat transfer during spray cooling with flow rate and subcooling temperature as parameters has been carried out. The quantities of interest are heat transfer coefficient and temperature of the heater surface. The average droplet size across the nozzle decreases with increase in the flow rate. Hence, flow rate is a quantity of importance. Water is an acceptable medium to create a spray and cool high-power LEDs. However, it requires proper packaging techniques to be employed. Even with single-phase spray cooling, considerably high LED heat fluxes can be handled with surface temperatures not exceeding the upper safe limit. Lower surface temperature is obtained at higher degree of subcooling and with sprays, necessary for improved performance of the LED and reliability. While, spray hydrodynamics has been extensively studied, the associated wall heat transfer needs to be explored. In this context, understanding the physics of local impact and transport is the key to the development of the next generation high heat flux cooling technologies.

As showed by several authors, jet and spray cooling systems are promising candidates for a high-power LED and can be embedded on it. However, an important packaging requirement of jet/spray cooling systems is size optimization and fluid volume inventory which should be minimized. A large number of engineering and fundamental problems arise in this direction. Fluid properties, latent heat of vaporization, wettability and relatively low Weber number can play important role on heat transfer enhancement.

Declaration of Competing Interest

The authors declare that they have no known competing financial interests or personal relationships that could have appeared to influence the work reported in this paper.

Acknowledgements

The authors are thankful for research funding jointly provided by the Ministry of Education and Science of the Russian Federation (Agreement 14.613.21.0067, Project Identifier RFMEFI61317X0067); Department of Science and Technology, Government of India, under the International Multilateral Regional Cooperation Program [Project #DST/IMRDC/BRICS/ Pilot Call/HPCSLED/2017 (G)]; and the Ministry of Science and Technology of the People's Republic of China (Project No. 2017YFE0100600). Author GS is supported by Visvesvaraya PhD funding scheme by MEITY, Government of India (Project Identifier MEITY-PHD-1926).

References

[1] B. Abdelmlek, Z.A. Khaoula, R. Ghnay, K. Abderrazak, K. Charrada, G. Zissis, Effect of thermal conduction path deficiency on thermal properties of LEDs package, Appl. Therm. Eng. 102 (2016) 251–260.

[2] H. Al Hashimi, C.F. Hammer, M.T. Lebon, D. Zhang, J. Kim, Phase-change heat transfer measurements using temperature-sensitive paints, J. Heat Transfer 140 (2018) 031601.

[3] M. Arik, C.A. Becker, S.E. Weaver, J. Petroski, Thermal management of LEDs: Package to system, in: Third Int. Conf. Solid State Light, 2004, 5187, 64.

[4] W.D. Bachalo, Spray diagnostics for the twenty-first century, Atom. Sprays 10 (2000) 439–474.

[5] H. Baumgartner, A. Vaskuri, P. Kärhä, E. Ikonen, A temperature controller for high power light emitting diodes based on resistive heating and liquid cooling, Appl. Therm. Eng. 71 (1) (2014) 317–323.

[6] L.P. Bayvel, Liquid Atomization, CRC Press Routledge, 2019 ISBN 0-89116-959-8.

[7] C. Bonacina, S. Del Giudice, G. Comini, Dropwise evaporation, J. Heat Trans. 101 (1979) 441–446.

[8] H. Bostanci, D.P. Rini, J.P. Kizito, V. Singh, S. Seal, L.C. Chow, High heat flux spray cooling with ammonia: investigation of enhanced surfaces for CHF, Int. J. Heat Mass Transf. 55 (2012) 3849–3856.

[9] L. Branko, K. Roy, A very high flux in microchannel heat exchanger for cooling of semi-conductor laser diode arrays, Proc. IEEE Trans. Components - Part B 19 (1996) 444–451.

[10] J. Breitenbach, V. Roisman, C. Tropea, From drop impact physics to spray cooling models: a critical review, Exp. Fluids 59(3) (2018) 55 (21 pages).

[11] D. Chatzikyriakou, S.P. Walker, C.P. Hale, G.F. Hewitt, The measurement of heat transfer from hot surfaces to non-wetting droplets, Int. J. Heat Mass Transf. 54 (2011) 1432–1440.

[12] L. Chen, D. Deng, Q. Huang, X. Xu, Y. Xie, Development and thermal performance of a vapor chamber with multi-artery re-entrant micro-channels for high-power LED, Appl. Therm. Eng. 166 (2020) 114686(10 pages).

[13] Q. Chen, Q. Chen, R. Hu, X. Luo, Is thermal management outside the package enough for higher LED reliability?, in: Proc. Electron. Packag. Technol. Conf. (EPTC-14), 2014, pp. 1068–1070.

[14] R.H. Chen, L.C. Chow, J.E. Navedo, Effects of spray characteristics on critical heat flux in subcooled water spray cooling, Int. J. Heat Mass Transf. 45 (2002) 4033–4043.

[15] R.H. Chen, L.C. Chow, J.E. Navedo, Optimal spray characteristics in water spray cooling, Int. J. Heat Mass Transf. 47 (2004) 5095–5099.

[16] W.L. Cheng, F.Y. Han, Q.N. Liu, H.L. Fan, Spray characteristics and spray cooling heat transfer in the non-boiling regime, Energy 36 (2011) 3399–3405.

[17] W.L. Cheng, W.W. Zhang, H. Chen, L. Hu, Spray cooling and flash evaporation cooling: The current development and application, Renew. Sustain. Energy Rev. 55 (2016) 614–628.

[18] S. Chhajed, Y. Xi, Y.L. Li, T. Gessmann, E.F. Schubert, Influence of junction temperature on chromaticity and color-rendering properties of trichromatic white-light sources based on light-emitting diodes, J. Appl. Phys. 97 (2005) 1–8.

[19] A. Christensen, S. Graham, Thermal effects in packaging high power light emitting diode arrays, Appl. Therm. Eng. 29 (2009) 364–371.

[20] X. Chunlin, Spray/jet cooling for heat flux high to 1 kW/cm^2, in: Annu. IEEE Semicond. Therm. Meas. Manag. Symp., 2003, pp. 159–163.

[21] M. Ciofalo, I.D. Piazza, V. Brucato, Investigation of the cooling of hot walls by liquid water sprays, Int. J. Heat Mass Transf. 42 (1999) 1157–1175.

[22] X. Deng, Z. Luo, Z. Xia, W. Gong, L. Wang, Active-passive combined and closed-loop control for the thermal management of high-power LED based on a dual synthetic jet actuator, Energy Convers. Manag. 132 (2017) 207–212.

[23] R. Dou, Z. Wen, G. Zhou, Heat transfer characteristics of water spray impinging on high temperature stainless steel plate with finite thickness, Int. J. Heat Mass Transf. 90 (2015) 376–387.

[24] K.A. Estes, I. Mudawar, Correlation of sauter mean diameter and critical heat flux for spray cooling of small surfaces, Int. J. Heat Mass Transf. 38 (1995) 2985–2996.

[25] A. Fan, R. Bonner, S. Sharratt, Y.S. Ju, An innovative passive cooling method for high performance light-emitting diodes, in: Annu. IEEE Semicond. Therm. Meas. Manag. Symp., 2012, pp. 319–324.

[26] R. Faranda, S. Guzzetti, G.C. Lazaroiu, S. Leva, Refrigerating liquid prototype for LED's thermal management, Appl. Therm. Eng. 48 (2012) 155–163.

[27] E.Y. Gatapova, E.O. Kirichenko, B. Bai, O.A. Kabov, Interaction of impacting water drop with a heated surface and breakup into microdrops, Interfac. Phenom.; Heat Transf. 6 (1) (2018) 75–88.

[28] E.Y. Gatapova, O.A. Kabov, Shear-driven flows of locally heated liquid films, Int. J. Heat Mass Transf. 51 (2008) 4797–4810.

[29] M. Ghodbane, J.P. Holman, Experimental study of spray cooling with Freon-113, Int. J. Heat Mass Transf. 34 (4–5) (1991) 1163–1174.

[30] D.R. Guildenbecher, C. López-Rivera, P.E. Sojka, Secondary atomization, Exp. Fluids 46 (2009) 371–402.

[31] B. Hahn, A. Weimar, M. Peter, J. Baur, High-power InGaN LEDs: Present status and future prospects, Light. Diodes Res. Manuf. Appl. (2008) 691004.

[32] J.P. Holman, C.M. Kendall, Extended studies of spray cooling with Freon-113, Int. J. Heat Mass Transf. 36 (8) (1993) 2239–2241.

[33] C.C. Hsieh, S.C. Yao, Evaporative heat transfer characteristics of a water spray on micro-structured silicon surfaces, Int. J. Heat Mass Transf. 49 (5–6) (2006) 962–974.

[34] S.S. Hsieh, T.C. Fan, H.H. Tsai, Spray cooling characteristics of water and R-134a. Part I: Nucleate boiling, Int. J. Heat Mass Transf. 47 (2004) 5703–5712.

[35] S.S. Hsieh, Y.F. Hsu, M.L. Wang, A microspray-based cooling system for high powered LEDs, Energy Convers. Manag. 78 (2014) 338–346.

[36] R. Hu, B. Cao, Y. Zou, Y. Zhu, S. Liu, X. Luo, Modeling the light extraction efficiency of bi-layer phosphor in white LEDs, IEEE Photon. Technol. Lett. 25 (12) (2013) 1141–1144.

[37] R. Hu, X. Luo, H. Zheng, Hotspot location shift in the high power phosphor converted white light-emitting diode package, Japanese J. Appl. Phys. 51 (2012) 09MK05.

[38] R. Hu, S. Yu, Y. Zou, H. Zheng, F. Wang, S. Liu, X. Luo, Near-/mid-field effect of color mixing for single phosphor-converted light-emitting diode package, IEEE Photon. Technol. Lett. 25 (3) (2013) 246–249.

[39] H. Jang, J.H. Lee, C. Byon, B.J. Lee, Innovative analytic and experimental methods for thermal management of SMD-type LED chips, Int. J. Heat Mass Transf. 124 (2018) 36–45.

[40] A.K. Jasuja, Atomisation of crude oil and residual fuel oils, Trans. ASME 101 (1979) 250–258.

[41] O.A. Kabov, Y.V. Lyulin, I.V. Marchuk, D.V. Zaitsev, Locally heated shear-driven liquid films in microchannels and minichannels, Int. J. Heat Fluid Flow 28 (2007) 103–112.

[42] O.A. Kabov, D.V. Zaitsev, E. Tkachenko, Interfacial thermal fluid phenomena in shear-driven thin liquid films, in: Proc. Int. Heat Transf. Conf. 2018 (Begell House Digital Library), 2018, pp. 1061–1067.

[43] O.A. Kabov, D.V. Zaitsev, V.V. Cheverda, A. Bar-Cohen, Evaporation and flow dynamics of thin, shear-driven liquid films in microgap channels, Exp. Therm. Fluid Sci. 35 (2011) 825–831.

[44] S.G. Kandlikar, A.V. Bapat, Evaluation of jet impingement, spray and micro-channel chip cooling options for high heat flux removal, Heat Transf. Eng. 28 (2007) 911–923.

[45] X. Kang, Y. Wang, Q. Huang, Y. Cui, C. Wang, C. Wen, J. Fan, Phase-change immersion cooling high power light emitting diodes and heat transfer improvement, Microelectron. Reliab. 79 (2017) 257–264.

[46] N. Khan, N. Abas, Comparative study of energy saving light sources, Renew. Sustain. Energy Rev. 15 (2011) 296–309.

[47] J.S. Kim, W.H. Cha, K.N. Rainey, S. Lee, S.M. You, Parametric investigation of liquid cooling module using FC-72, in: Thermomechanical Phenomena in Electronic Systems -Proc. Intersociety Conf., # 1645402, 2006, pp. 612–619.

[48] P.J. Kreitzer, J.M. Kuhlman, Spray cooling droplet impingement model, in: Proc. 10th AIAA/ASME Joint Thermophys. Heat Transf. Conf., Chicago, USA, 2010, pp. 1–15.

[49] A. Lefebvre, V. Mcdonell, Atomization and Sprays, 2nd Ed., ISSN: 1044-5110, CRC Press, 2017.

[50] J. Li, W. Tian, L. Lv, A thermosyphon heat pipe cooler for high power LEDs cooling, Heat Mass Transf. 52 (2016) 1541–1548.

[51] W. Li, X. Qu, T. Alam, F. Yang, W. Chang, J. Khan, C. Li, Enhanced flow boiling in microchannels through integrating multiple micro-nozzles and re-entry micro-cavities, Appl. Phy. Lett. 110 (1) (2017) 014104.

[52] G. Liang, I. Mudawar, Review of spray cooling – Part 1: Single - phase and nucleate boiling regimes and critical heat flux, Int. J. Heat Mass Transf. 115 (2017) 1174–1205.

[53] G. Liang, I. Mudawar, Review of spray cooling – Part 2: High temperature boiling regimes and quenching applications, Int. J. Heat Mass Transf. 115 (2017) 1206–1222.

[54] G. Liang, S. Shen, Y. Guo, J. Zhang, Boiling from liquid drops impact on a heated wall, Int. J. Heat Mass Transf. 100 (2016) 48–57.

[55] Y. Liao, D. Eggenschwiler, P. Furrer, R. Wang, K. Boulouchos, Heat transfer characteristics of urea-water spray impingement on hot surfaces, Int. J. Heat Mass Transf. 117 (2018) 447–457.

[56] L. Lin, R. Ponnappan, Heat transfer characteristics of spray cooling in a closed loop, Int. J. Heat Mass Transf. 46 (2003) 3737–3746.

[57] Y.K. Lin, Z.F. Zhou, Y. Fang, H.L. Tang, B. Chen, Heat transfer performance and optimization of a close-loop R410a flash evaporation spray cooling, Appl. Therm. Eng. 159 (2019) 113966.

[58] J. Liu, R. Xue, L. Chen, X. Liu, Y. Hou, Influence of chamber pressure on heat transfer characteristics of a closed loop R134-a spray cooling, Exp. Therm. Fluid Sci. 75 (2016) 89–95.

[59] X. Luo, X. Fu, F. Chen, H. Zheng, Phosphor self-heating in phosphor converted light emitting diode packaging, Int. J. Heat Mass Transfer 58 (2013) 276–281.

[60] X. Luo, R. Hu, Calculation of the phosphor heat generation in phosphor-converted light-emitting diodes, Int. J. Heat Mass Transfer 75 (2014) 213–217.

[61] X. Luo, R. Hu, S. Liu, K. Wang, Heat and fluid flow in high-power LED packaging and applications, Prog. Energy Combust. Sci. 56 (2016) 1–32.

[62] X. Luo, S. Liu, A microjet array cooling system for thermal management of high-brightness LEDs, IEEE Trans. Adv. Packag. 30 (2007) 475–484.

[63] Y. Ma, R. Hu, X. Yu, W. Shu, X. Luo, A modified bidirectional thermal resistance model for junction and phosphor temperature estimation in phosphor-converted light-emitting diodes, Int. J. Heat Mass Transfer 106 (2017) 1–6.

[64] S.R. Maeng, S.C. Ko, Thermal characteristics for chip on metal package of LED lighting module, Mater. Sci. Semicond. Process 38 (2015) 357–361.

[65] S. Mahmoud, A. Tang, C. Toh, R. Al-Dadah, S.L. Soo, Experimental investigation of inserts configurations and PCM type on the thermal performance of PCM based heat sinks, Appl. Energy 112 (2013) 1349–1356.

[66] P. Marmottant, E. Villermaux, On spray formation, J. Fluid Mech. 498 (2004) 73–111.

[67] R. Mesler, A mechanism supported by extensive experimental evidence to explain high heat fluxes observed during nucleate boiling, AIChE J. 22 (1976) 246–252.

[68] P. Morgan Pattison, M. Hansen, J.Y. Tsao, LED lighting efficacy: status and

directions, Compt. Rend. Phys. 19 (2018) 134–145.
[69] I. Mudawar, D. Bharathan, K. Kelly, S. Narumanchi, Two-phase spray cooling of hybrid vehicle electronics. components and packaging technologies, Trans. IEEE Compon. Packaging Technol. 32 (2) (2009) 501–512.
[70] I. Mudawar, K.A. Estes, Optimizing and predicting CHF in spray cooling of a square surface, J. Heat Transfer 118 (1996) 672–679.
[71] I. Mudawar, W.S. Valentine, Determination of the local quench curve for spray-cooled metallic surfaces, J. Heat Treat. 7 (1989) 107–121.
[72] N. Narendran, Y. Gu, Life of LED-based white light sources, IEEE/OSA, J. Disp. Technol. 1 (2005) 167–170.
[73] M.R. Overholt, A. Mccandless, K.W. Kelly, C.J. Becnel, S. Motakef, Micro-jet arrays for cooling of electronic equipment, in: ASME Int. Conf. Microchannels Minichannels, ICMM 2005, 2005, Paper number 75250.
[74] S. Pimputkar, J.S. Speck, S.P. DenBaars, S. Nakamura, Prospects for LED lighting, Nat. Photon. 3 (2009) 180–182.
[75] H. Pitsch, O. Desjardins, Detailed numerical investigation of turbulent atomization of liquid jets, Atom. Sprays 20 (2010) 311–336.
[76] R.L. Puterbaugha, K.L. Yerkes, S.K. Thomas, Partially confined FC-72 spray-cooling performance: effect of dissolved air, J. Thermophys. Heat Transfer 23 (3) (2009) 582–591.
[77] Y.M. Qiao, S. Chandra, Spray cooling enhancement by addition of a surfactant, J. Heat Transfer 120 (1998) 92–98.
[78] C. Quinn, D.B. Murray, T. Persoons, Heat transfer behaviour of a dilute impinging air-water mist jet at low wall temperatures, Int. J. Heat Mass Transf. 111 (2017) 1234–1249.
[79] A. Radcliffe, Fuel injection, high speed aerodynamics and jet propulsion, in: W.R. Hawthorne, W.T. Olson, (Eds.), Princeton Univ. Press, Princeton, NJ, 1960.
[80] E. Raypah, M.K. Dheepan, M. Devarajan, F. Sulaiman, Investigation on thermal characterization of low power SMD LED mounted on different substrate packages, Appl. Therm. Eng. 101 (2016) 19–29.
[81] I.V. Roisman, Inertia dominated drop collisions –II: An analytical solution of the Navier-Stokes equations for a spreading viscous film, Phys. Fluids 21 (5) (2009) 052104.
[82] J.R. Rybicki, I. Mudawar, Single-phase and two-phase cooling characteristics of upward-facing and downward-facing sprays, Int. J. Heat Mass Transf. 49 (2006) 5–16.
[83] A. Saha, J.D. Lee, S. Basu, R. Kumar, Breakup and coalescence characteristics of a hollow cone swirling spray, Phys. Fluids 24 (2012) 124103.
[84] S. Sarkar, R.P. Selvam, Direct numerical simulation of heat transfer in spray cooling through 3D multiphase flow modelling using parallel computing, J. Heat Transf. 131 (2009) 1–8.
[85] M.L. Sawyer, S.M. Jeter, S.I. Abdel-Khalik, A critical heat flux correlation for droplet impact cooling, Int. J. Heat Mass Transf. 40 (1997) 2123–2131.
[86] F.E. Schubert, Light-Emitting Diodes, Cambridge University Press, 2012 ISBN: 9780511790546.
[87] F.E. Schubert, J.K. Kim, Solid-state light sources getting smart, Science 308 (2005) 1274–1278.
[88] T.A. Shedd, A.G. Pautsch, Spray impingement cooling with single- and multiple-nozzle arrays. Part II: Visualization and empirical models, Int. J. Heat Mass Transf. 48 (2005) 3176–3184.
[89] L. Sheng, X. Luo, LED Packaging for Lighting Applications-Design, Manufacturing and Testing, Wiley Online Books, 2011.
[90] H. Shou-Shing, F. Tsung-Cheng, T. Huang-Hsui, Spray cooling characteristics of water and R-134a. Part I: Nucleate boiling, Int. J. Heat Mass Transf. 47 (26) (2004) 5703–5712.
[91] E.A. Silk, J. Kim, K. Kiger, Energy conservation based spray cooling CHF correlation for flat surface small area heaters, in: Proc. ASME/JSME Therm. Engg. Heat Transf. Summer Conf. and ASME InterPACK 2007 Conference, 2007, pp. 805–813.
[92] R. Singh, M. Mochizuki, T. Yamada, T. Nguyen, Cooling of LED headlamp in automotive by heat pipes, Appl. Therm. Eng. 166 (2020) 114733 (7 pages).
[93] P. Smakulski, S. Pietrowicz, A review of the capabilities of high heat flux removal by porous materials, micro channels and spray cooling techniques, Appl. Therm. Eng. 104 (2016) 636–646.
[94] W.A. Sowa, Interpreting mean drop diameters using distribution moments, Atomization Sprays 2 (1992) 1–15.
[95] Y. Takata, S. Hidaka, J.M. Cao, T. Nakamura, H. Yamamoto, M. Masuda, T. Ito, Effect of surface wettability on boiling and evaporation, Energy 30 (2005) 209–220.
[96] Y. Tang, L. Lin, S. Zhang, J. Zeng, K. Tang, G. Chen, W. Yuan, Thermal management of high-power LEDs based on integrated heat sink with vapour chamber, Energy Convers. Manag. 151 (2017) 1–10.
[97] Y. Tao, X. Huai, L. Wang, Z. Guo, Experimental characterization of heat transfer in non-boiling spray cooling with two nozzles, Appl. Therm. Eng. 31 (2011) 1790–1797.
[98] S.J. Thiagarajan, S. Narumanchi, R. Yang, Effect of flow rate and subcooling on spray heat transfer on microporous copper surfaces, Int. J. Heat Mass Transf. 69 (2014) 493–505.
[99] D.B. Tuckerman, R.F.W. Pease, High-performance heat sinking for VLSI, IEEE Electron. Device Lett. EDL-2 (1981) 126–129.
[100] M.A.J. Van Limbeek, P.B.J. Hoefnagels, C. Sun, D. Lohse, Origin of spray formation during impact on heated surfaces, Soft Matter 13 (2017) 7514–7520.
[101] M. Visaria, I. Mudawar, Effects of high subcooling on two-phase spray cooling and critical heat flux, Int. J. Heat Mass Transf. 51 (2008) 5269–5278.
[102] C.W. Visser, P.E. Frommhold, S. Wildeman, R. Mettin, D. Lohse, C. Sun, Dynamics of high-speed micro-drop impact: Numerical simulations and experiments at frame-to-frame times below 100 ns, Soft Matter 11 (2015) 1708–1722.
[103] F. Wang, O. Tschukin, G.C. Marques, M. Selzer, J. Aghassi-Hagmann, B. Nestler, Breakup of liquid jets and the formation of satellite and sub satellite droplets, arXiv:1805.06818 [physics.flu-dyn], 2018, pp. 1–5.
[104] H. Wang, F. Wang, Z. Li, Y. Tang, B. Yu, W. Yuan, Experimental investigation on the thermal performance of a heat sink filled with porous metal fibre sintered felt/paraffin composite phase change material, Appl. Energy 176 (2016) 221–232.
[105] J. Wendelstorf, K.H. Spitzer, R. Wendelstorf, Spray water cooling heat transfer at high temperatures and liquid mass fluxes, Int. J. Heat Mass Transf. 51 (2008) 4902–4910.
[106] C. Xiao, Q. Tian, C. Zhou, J. Li, W. Zhu, A novel cooling system based on heat pipe with fan for thermal management of high-power LEDs, J. Opt. 46 (2017) 269–276.
[107] J. Xie, T.N. Wong, F. Duan, Modelling on the dynamics of droplet impingement and bubble boiling in spray cooling, Int. J. Therm. Sci. 104 (2016) 469–479.
[108] J.L. Xie, Z.W. Gan, F. Duan, T.N. Wong, S.C.M. Yu, R. Zhao, Characterization of spray atomization and heat transfer of pressure swirl nozzles, Int. J. Therm. Sci. 68 (2013) 94–102.
[109] Z.B. Yan, K.C. Toh, F. Duan, T.N. Wong, K.F. Choo, P.K. Chan, Y.S. Chua, Experimental study of impingement spray cooling for high power devices, Appl. Therm. Eng. 30 (10) (2010) 1225–1230.
[110] Z. Yan, R. Zhao, F. Duan, T. Neng, K. Chuan, K. Fah, P. Keong, Y. Sheng, Spray Cooling, Chapter in - Two Phase Flow, Phase Change and Numerical Modeling, IntechOpen, 2011, ISBN: 978-953-307-584-6.
[111] J. Yang, L.C. Chow, M.R. Pals, Nucleate boiling heat transfer in spray cooling, J. Heat Transfer 118 (1996) 668–671.
[112] H. Ye, M. Mihailovic, C.K.Y. Wong, H.W. Van Zeijl, A.W.J. Gielen, G.Q. Zhang, P.M. Sarro, Two-phase cooling of light emitting diode for higher light output and increased efficiency, Appl. Therm. Eng. 52 (2013) 353–359.
[113] S. Ye, F. Xiao, Y.X. Pan, Y.Y. Ma, Q.Y. Zhang, Phosphors in phosphor-converted white light-emitting diodes: Recent advances in materials, techniques and properties, Sci. Eng. Reports 71 (2010) 1–34.
[114] Y. Yonemoto, T. Kunugi, Analytical consideration of liquid droplet impingement on solid surfaces, Sci. Rep. 7 (2017) 1–11.
[115] K.I. Yoshida, Y. Abe, T. Oka, Y.H. Mori, A. Nagashima, Spray cooling under reduced gravity condition, J. Heat Transf. 123 (2001) 309–318.
[116] G.Q. Zhang, Solid state lighting reliability: components to systems, in: W.D. van Driel, X.J. Fan (Eds.), Solid State Lighting Technology and Application Series, Springer, 2013, ISSN: 978-1-4614-3066-7.
[117] T. Zhang, B. Dong, X. Chen, Z. Qiu, R. Jiang, W. Li, Spray characteristics of pressure-swirl nozzles at different nozzle diameters, Appl. Therm. Eng. 121 (2017) 984–991.
[118] Z. Zhang, J. Li, P.X. Jiang, Experimental investigation of spray cooling on flat and enhanced surfaces, Appl. Therm. Eng. 51 (2013) 102–111.
[119] J. Zhou, J. Huang, Y. Wang, Z. Zhou, Thermal distribution of multiple LED module, Appl. Therm. Eng. 93 (2016) 122–130.
[120] N. Zhou, F. Chen, Y. Cao, M. Chen, Y. Wang, Experimental investigation on the performance of a water spray cooling system, Appl. Therm. Eng. 112 (2017) 1117–1128.
[121] E.Ya. Gatapova, O.A. Kabov, I.V. Marchuk, Thermocapillary deformation of a locally heated liquid film moving under the action of a gas flow, Tech. Phys. Lett. 30 (5) (2004) 418–421.
[122] G. Liang, I. Mudawar, Review of drop impact on heated walls, Int. J. Heat Mass Transf. 106 (2017) 103–126.
[123] E.Ya. Gatapova, G. Sahu, S. Khandekar, R. Hu, Thermal management of high-power LED module with single-phase liquid jet array, Appl. Therm. Eng. (2020) (submitted for publication).
[124] Clemens J.M. Lasance, András Poppe (Eds.), Thermal management for LED applications, Solid State Lighting Technology and Application Series, Springer Nature, 978-1-4614-5090-0, 2014.

Levitation of evaporating microscale droplets over solid surfaces

Vladimir S. Ajaev
Department of Mathematics, Southern Methodist University, Dallas, Texas 75275, USA

Dmitry V. Zaitsev and Oleg A. Kabov
Institute of Thermophysics, SB RAS, Novosibirsk 630090, Russia
and Novosibirsk State University, Novosibirsk 630090, Russia

(Received 23 August 2020; accepted 19 April 2021; published 20 May 2021)

We develop an analytical model to describe recent experimental observations of levitation of evaporating microscale droplets over heated solid surfaces at temperatures far below the Leidenfrost point. Viscous flow patterns around the droplet are determined from the solution of the equation for the Stokes stream function in bipolar coordinates. The results are compared to the predictions of models representing microscale droplets as point sources in the Stokes flow equations. Formulas for the force acting on the droplet as a result of moist air flow around it are derived and used to obtain predictions of levitation height as a function of droplet size which are in very good agreement with the experimental data. In addition to gravity, three physical mechanisms are identified which contribute to the force acting on the droplet: repulsive interaction of the droplet with the solid, spatially nonuniform evaporation along the liquid surface, and thermocapillary effect. The first two act against gravity and allow droplets to levitate despite competing thermocapillary stresses which push the moist air out of the region between the droplet and the solid. Relative importance of the three mechanisms is evaluated based on an analytical model of heat transfer both inside and outside of the droplet.

DOI: 10.1103/PhysRevFluids.6.053602

I. INTRODUCTION

Models of evaporating droplets are important for a wide range of applications such as spray cooling, internal combustion engines, and aerosol drug delivery [1–3]. Droplet sizes in many of these applications are well below the capillary length of the liquid (about 2.7 mm for water), so the free surface shapes, dominated by the capillary forces, are nearly spherical. This offers advantages for mathematical modeling, as Maxwell [4] first demonstrated by using a steady diffusion equation to describe spherically symmetric distribution of vapor around the droplet. The balance between evaporative mass loss and the diffusion flux away from the droplet in this framework leads to the classical D^2 law, i.e., the conclusion that the square of the droplet diameter will decrease as a linear function of time, a trend indeed observed in many experimental studies [5].

Predictions of diffusion-based evaporation models can strongly deviate from the experimental data due to convective flow in the gas around the droplet. The flow can be caused by factors not related to the presence of the droplet, e.g., natural convection, or generated by the droplet itself. The latter has to do with the fact that, even in spherically symmetric geometry, mass transfer around the droplet is not purely diffusive, as was first pointed out in the classical works of Stefan [6] and Fuchs [7]. The following simple argument [5] illustrates the origin of convective mass transfer known as Stefan flow. Suppose gradient of partial density of vapor in the moist air is established as a result of evaporation from the droplet surface. Assuming the total density of the gas phase to

 ©2021 American Physical Society

be constant, there also has to be gradient, in the opposite direction, of the partial density of the remaining components of air, i.e., nitrogen, oxygen, etc. Thus these components are transported towards the free surface. However, since these gas molecules do not penetrate the free surface, flow has to develop to ensure the global mass conservation condition. The effect becomes stronger as the evaporation intensity increases. Over the past several decades, a number of modeling studies and numerical simulations of evaporating droplets and Stefan flow were conducted, reviewed by, e.g., Sirignano [2] and Sazhin [5].

When an evaporating droplet ends up in the vicinity of a solid surface, the evaporation can lead to a repulsive force. The most dramatic demonstration of this effect is the well-known Leidenfrost phenomenon [8,9]. While originally observed for macroscale droplets, more recently the Leidenfrost effect was studied extensively for microscale droplets as well, typically the ones formed from larger droplets as a result of gradual mass loss by evaporation. A number of novel phenomena such as sudden droplet takeoff and explosive breakup at sufficiently small size were observed and explained [10,11]. However, it is important to emphasize that all studies of the Leidenfrost effect consider relatively high temperatures, far above the boiling point of liquid.

Recent experiments conducted in our group illustrated that the mechanism of repulsion of evaporating droplets from solid surfaces is operational and can lead to levitation at temperatures far below the Leidenfrost point and even below the boiling temperature of the liquid [12–14]. It was established in previous studies that small droplets of condensate can form and levitate over the surfaces of evaporating liquid layers [15,16]. This phenomenon is similar to formation of a layer of fine mist over a cup of tea or coffee [17]. While in all these previous studies droplets were levitating near the free surface of liquid, Zaitsev *et al.* [13] created a dry patch in the evaporating layer and focused on the behavior of the condensate droplets which ended up over the dry patch rather than near the surface of the liquid layer. Remarkably, these droplets were levitating as well until they completely evaporated. To explain the phenomenon, a mathematical model was developed which treats levitating droplets as point sources. The model is shown to agree with experiments for droplets of small sizes, but failed to describe experimental trends for larger droplets. The present study will address the effect of finite droplet size on the levitation conditions. The flow around the droplet will be described, in the Stokes flow approximation, using an analytical approach based on bipolar coordinates.

An important outcome of our study is a formula for the force acting on the droplet, a useful result for applications, some of which are not directly related to levitation. In fact, a levitating droplet is a unique tool for studies of repulsive interaction between droplets and flat interfaces. Since the droplet is at rest, its weight, easily estimated from the image analysis, is equal to the force that repels it from the interface. Such force is important to know in a number of applications. For example, in spray cooling [1], repulsion of droplets from a heated surface can result in dramatic decrease of heat transfer efficiency. In the commonly used drug delivery method by aerosol inhalation, the microscale aqueous droplets are carried by the air flow into pulmonary airways [3]. The location of droplet deposition at the walls of the airways is a key parameter determining the success of the therapy and that location can change due to repulsive droplet-wall interaction typically not accounted for in the numerical models.

Stokes flow around a spherical droplet in the presence of another droplet or near a flat interface has been described analytically using bipolar coordinates in a number of well-known studies [18–20]. The governing equations are reformulated in terms of the Stokes stream function, leading to a single equation which is then solved using the method of separation of variables. The technique has been adopted to situations when evaporation is taking place at the liquid-gas interfaces [21,22]. In particular, interaction of two evaporating spherical droplets was investigated by Oguz *et al.* [22]. They imposed uniform evaporation velocities at liquid-gas interfaces and thus did not have to model heat transfer in order to describe droplet interaction. More elaborate models of the two-droplet configuration with evaporation [23], based on earlier pioneering studies from combustion literature [24,25], account for heat transfer both inside and outside of the droplets.

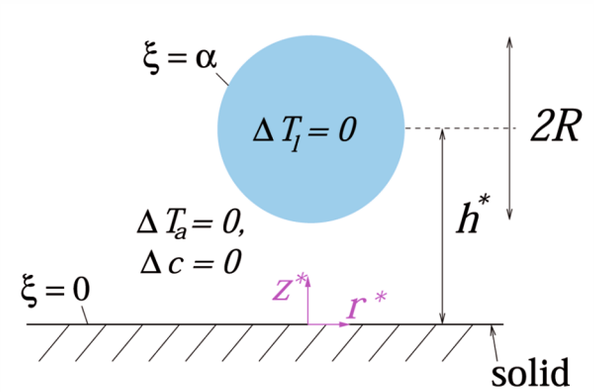

FIG. 1. Sketch of the geometric configuration—an evaporating spherical droplet of radius R near a heated solid surface. Dimensional cylindrical coordinates (r^*, z^*) are shown in the sketch and governing equations for heat transfer in liquid and air are specified. Vapor diffusion in air is coupled to the thermal problem via conditions at the droplet surface.

Zhang and Gogos [26] used bipolar coordinates to investigate evaporation of droplets near hot surfaces under conditions motivated by experimental studies of the Leidenfrost phenomenon so that evaporation rate is high and the temperatures are typically above 500 K. In the present study, we apply this general framework to droplet evaporation at moderate temperatures [13]. Our study is different from Zhang and Gogos [26] in the following four aspects. First, the moderate temperature values allow us to identify the limit of small vapor concentration leading to dramatic simplification of the model. Second, we investigate the effect of Marangoni stresses on the flow around the droplet. Third, we consider a droplet in an imposed external temperature gradient rather than using the condition of constant temperature away from the droplet. Finally, while the work of Zhang and Gogos [26] was purely theoretical, we provide direct comparison of our results to experimental data.

The paper is organized as follows. In Sec. II, we discuss the geometric configuration and the heat transfer model for both inside and outside of the droplet, coupled to the steady diffusion equation for vapor concentration in air. Due to small values of the Péclet number, the governing equations for heat transfer are decoupled from the fluid flow description. Once temperature and evaporative mass flux are found on the droplet surface, the fluid flow problem can be solved using the Stokes flow approximation, the subject of Sec. III. Flow patterns found from the solution of the flow equations are described in Sec. IV, followed by the calculation of the force acting on the droplet in Sec. V. Thermocapillary effects are discussed in Sec. VI. Predictions of the model are compared to the experimental data in Sec. VII. Finally, conclusions are presented in Sec. VIII.

II. PROBLEM GEOMETRY AND HEAT TRANSFER MODEL

Consider a spherical droplet of radius R evaporating near a heated solid surface, as sketched in Fig. 1. The dimensional cylindrical coordinates (r^*, z^*) are also shown in the sketch, with the z^* axis coinciding with the axis of symmetry of the configuration. Levitation height, i.e., the distance between the center of the droplet and the solid, is denoted by h^*. In experiments, typical values of the droplet levitation height are below 30 μm, i.e., the droplets are very close to the heater [13]. The droplet radii are initially near 15 μm but gradually decay as a result of evaporation at a rate $\dot{R} \sim 5$ μm/s. Conservation of mass then suggests the value of moist air velocity near droplet surface $V^* = \dot{R}\hat{\rho}$, with $\hat{\rho}$ denoting the liquid-to-air density ratio. The significance of convective heat transfer is measured by the Péclet number, $\mathrm{Pe} = RV^*/\kappa$, where κ is the thermal diffusivity of moist air. Using $\hat{\rho} = 1.24 \times 10^3$ and $\kappa = 2.30 \times 10^{-5}$ m^2/s, based on moist air properties at 85 °C [27], we estimate the maximum Péclet number to be 4×10^{-3}. The droplet radii would have to be about 3.7 mm for the Péclet number to reach unity under the conditions of experiment of Zaitsev *et al.* [13]. Thus, in our modeling, we will neglect all contributions from convective heat transfer and

write the governing equations for the temperatures in the liquid (T_l) and air (T_a), both scaled by the heated solid surface temperature T_H, as

$$\Delta T_l = 0, \quad \Delta T_a = 0. \tag{1}$$

The length variables r and z in the present section are nondimensionalized by R. Vapor concentration c, scaled by the equilibrium saturation concentration at the temperature T_H, is also described by the Laplace's equation,

$$\Delta c = 0, \tag{2}$$

since the diffusion coefficient of vapor is of the same order of magnitude as thermal diffusivity of moist air and thus the corresponding Péclet numbers for mass transport are small as well.

We follow numerous previous studies [18,20,22,26] and define bipolar coordinates (ξ, η) related to the cylindrical ones via

$$r^* = \frac{R \sinh\alpha \sin\eta}{\cosh\xi - \cos\eta}, \quad z^* = \frac{R \sinh\alpha \sinh\xi}{\cosh\xi - \cos\eta}, \tag{3}$$

where $\alpha = \cosh^{-1}(h^*/R)$. With these choices, the surface of the sphere in Fig. 1 corresponds to $\xi = \alpha$, while the solid is at $\xi = 0$. The boundary conditions at the heated solid surface are formulated as

$$T_a|_{\xi=0} = 1, \tag{4}$$

$$\left.\frac{\partial c}{\partial \xi}\right|_{\xi=0} = 0. \tag{5}$$

At the droplet surface, the temperature is continuous and equilibrium vapor concentration is assumed to be a linear function of the scaled interfacial temperature T_i, leading to the nondimensional boundary conditions

$$T_a|_{\xi=\alpha} = T_l|_{\xi=\alpha} = T_i, \tag{6}$$

$$c|_{\xi=\alpha} = 1 + \gamma(T_i - 1), \tag{7}$$

with $\gamma = \gamma^* T_H/\rho_{\text{sat}}$, γ^* being the rate of change of the dimensional equilibrium vapor saturation density in air with temperature, and ρ_{sat} the value of this density at the temperature T_H. We assume the linear relationship given by (7) to be valid for a sufficiently wide range of temperatures so that γ^* and ρ_{sat} can be evaluated at the reference temperature T_H instead of the actual interfacial temperature. Concentration and temperature gradients are related through the energy balance at the interface, expressed as

$$E\left(1 - \frac{\rho_{\text{sat}}}{\rho}c\right)\left(k\frac{\partial T_a}{\partial \xi} - \frac{\partial T_l}{\partial \xi}\right) = -\frac{\partial c}{\partial \xi}, \tag{8}$$

where the evaporation parameter E is related to the latent heat of phase change $\mathcal{L}$ and vapor diffusion coefficient in air D via

$$E = \frac{k_l T_H}{\mathcal{L} D \rho_{\text{sat}}}, \tag{9}$$

$k = k_a/k_l$, k_i denotes thermal conductivity of air ($i = a$) and liquid ($i = l$), respectively, and ρ is the moist air density. Apart from differences in notation, Eq. (8) is equivalent to the condition used by Zhang and Gogos [26] in their model of Leidenfrost droplets. However, at moderate temperatures well below the Leidenfrost point, vapor saturation density is a small fraction of the total moist air density and Eq. (8) simplifies to

$$E\left(k\frac{\partial T_a}{\partial \xi} - \frac{\partial T_l}{\partial \xi}\right) = -\frac{\partial c}{\partial \xi}. \tag{10}$$

Finally, we assume that far above the droplet, the concentration is a constant value denoted by c_∞ and air temperature approaches a linear profile with specified gradient,

$$T_a = 1 - Gz. \tag{11}$$

Thus an imposed constant temperature gradient is assumed throughout the zone of the experiment. This may appear to contradict the expectation that an unsteady heat conduction model would be more appropriate to describe heat exchange between the metal heater, switched on at the start of the experiment ($t^* = 0$) and generating heat at a constant rate thereafter, and stationary air which is initially at room temperature [13]. Indeed, there is a classical solution of the 1D heat equation for this configuration [28], which predicts the dimensional heat flux q in the air to be

$$q(z^*) = q(0)\left(1 - \mathrm{erf}\frac{z^*}{2\sqrt{\kappa t^*}}\right). \tag{12}$$

In experiments, the heater is turned on for a few minutes before the measurements. Using $t^* \sim 10^2$ s and $z^* \sim 10^{-4}$ m, a value of about an order of magnitude larger than the levitation height, leads to the conclusion that the error function term in the equation is $\sim 10^{-3}$ and thus the imposed temperature gradient can be assumed constant in the region considered in the model. The simplified argument presented here is only valid since the droplets are close to the solid surface and is not meant to rule out unsteady and convective effects in heat transfer in air far above the dry patch over which the droplets are levitating. Based on measured dimensional values of $|dT^*/dz^*|$ on the order of 10 K/mm in experiments with a configuration similar to the one of interest for the present study [29], the values of the parameter $G = R|dT^*/dz^*|/T_H$ in Eq. (11) are $\sim 10^{-4}$. This small value could be set to zero, leading to the standard constant far-field temperature condition used in several previous studies of both droplets and bubbles near heated solid walls [26,30]. However, we feel that it is appropriate to use the nonzero gradient since in experiment heat is continuously generated in the metal substrate and at least part of it is removed through air, suggesting a vertical temperature gradient there.

Following the general approach of the pioneering studies of Zhang and Gogos [26] and Fisher and Golovin [20], we write

$$T_a = 1 - \frac{G\,\sinh\alpha\,\sinh\xi}{\cosh\xi - \cos\eta} + \sqrt{\cosh\xi - \cos\eta}\sum_{n=0}^{\infty} A_n \sinh\left[\left(n + \frac{1}{2}\right)\xi\right] P_n(\cos\eta), \tag{13}$$

$$T_l = \sqrt{\cosh\xi - \cos\eta}\sum_{n=0}^{\infty} B_n e^{-(n+\frac{1}{2})\xi} P_n(\cos\eta), \tag{14}$$

where P_n denotes the Legendre polynomial of degree n. The terms proportional to $\cosh(n + \frac{1}{2})\xi$ in the expansion for T_a are not included since they contradict the condition from Eq. (4). Also, since T_l is assumed bounded inside the droplet (including the point corresponding to $\xi \to \infty$), only decaying exponentials are included in the expansion for T_l.

The solution for vapor concentration c is expressed in the same coordinate system as

$$c = c_\infty + \sqrt{\cosh\xi - \cos\eta}\sum_{n=0}^{\infty}\left\{C_n \sinh\left[\left(n + \frac{1}{2}\right)(\xi - \alpha)\right]\right.$$
$$\left. + D_n \cosh\left[\left(n + \frac{1}{2}\right)(\xi - \alpha)\right]\right\} P_n(\cos\eta). \tag{15}$$

Application of the boundary conditions (5) and (7) allows us to express the concentration in terms of the expansion coefficients B_n from Eq. (14) as follows:

$$c = c_\infty + \sqrt{\cosh\xi - \cos\eta}\sum_{n=0}^{\infty}\left\{\tanh\left[\left(n+\frac{1}{2}\right)\alpha\right]\sinh\left[\left(n+\frac{1}{2}\right)(\xi-\alpha)\right]\right.$$
$$\left.+\cosh\left[\left(n+\frac{1}{2}\right)(\xi-\alpha)\right]\right\}(\sqrt{2}\tilde{c}+\gamma B_n)e^{-(n+\frac{1}{2})\alpha}P_n(\cos\eta), \tag{16}$$

where $\tilde{c} = 1 - c_\infty - \gamma$. In deriving this expression we used an identity that follows directly from the expansion of the generating function for Legendre polynomials [31],

$$(\cosh\alpha - \cos\eta)^{-1/2} = \sqrt{2}\sum_{n=0}^{\infty} e^{-(n+\frac{1}{2})\alpha}P_n(\cos\eta). \tag{17}$$

The coefficients B_n are in turn expressed in terms of A_n using Eq. (6) as

$$B_n = \sqrt{2} - \sqrt{2}(2n+1)G\,\sinh\alpha + A_n e^{(n+\frac{1}{2})\alpha}\sinh\left(n+\frac{1}{2}\right)\alpha. \tag{18}$$

Assuming the temperature to be sufficiently low so that $\rho_{\text{sat}} \ll \rho$, Eq. (10) can now be used to derive a linear system of equations for the coefficients A_n. The result is shown in the Appendix. Solving this system in MATLAB, we obtained the temperature distributions for T_a and T_l in terms of nondimensional coordinates $(r, z) = (r^*/R, z^*/R)$. Figure 2 (top) illustrates a typical solution for parameter values (listed in the caption) based on the physical properties of moist air at 50 °C found from Tsilingiris [27]. We plot the distribution of rescaled temperature $\hat{T}$ defined by

$$\hat{T} = \frac{T - T_0}{1 - T_0}, \tag{19}$$

where T_0 is the temperature (scaled by T_H) at the coldest point of the free surface, which according to our solutions is at the top of the droplet. The value of G is found based on the temperature gradient of ~10 K/mm, while $c_\infty = 0.95$ reflects the fact that the observed evaporation rate of droplets is relatively slow [13], most likely due to the fact that vapor concentration in the region where droplets are observed in experiments is much higher than in the ambient air. This is consistent with the observations of vapor filling the region above the dry patch as a result of intense evaporation from the surrounding liquid layer [12]. Specifically, we estimated the value of the far-field concentration, which was not measured experimentally, by first finding the solution in terms of c_∞ and then adjusting its value iteratively until the rate of mass loss matches the experimentally measured value.

Let us now discuss the physical interpretation of the result shown in Fig. 2 (top). Away from the droplet (near $r = 6$ in the plot) the temperature slowly decays away from the solid surface (located at $z = 0$) as dictated by the imposed temperature gradient G. It is immediately obvious that the presence of the droplet leads to significant perturbation of the temperature field near the heater creating a region of reduced temperature as compared to the profile without the droplet. Note that the results are quasisteady, so the lower temperature of the droplet compared to its surroundings is not a result of the droplet not having enough time to heat through. We believe the result can be explained by a combination of two physical effects. The first one is evaporative cooling: as the liquid evaporates, energy has to be supplied from the outside to maintain evaporation and thus a temperature gradient is established. The second effect, also seen in models of nonevaporating droplets [20], has to do with the droplet thermal conductivity being much larger than that of the surrounding air leading to drastic reduction of temperature gradient through the droplet compared to the imposed gradient.

The plot in Fig. 2 (top) may suggest that the droplet is at uniform temperature, but in reality the bottom of the droplet facing the hot solid surface is still at a higher temperature than the top, as illustrated in Fig. 2 (bottom). Temperature variation across the droplet is higher when the droplet

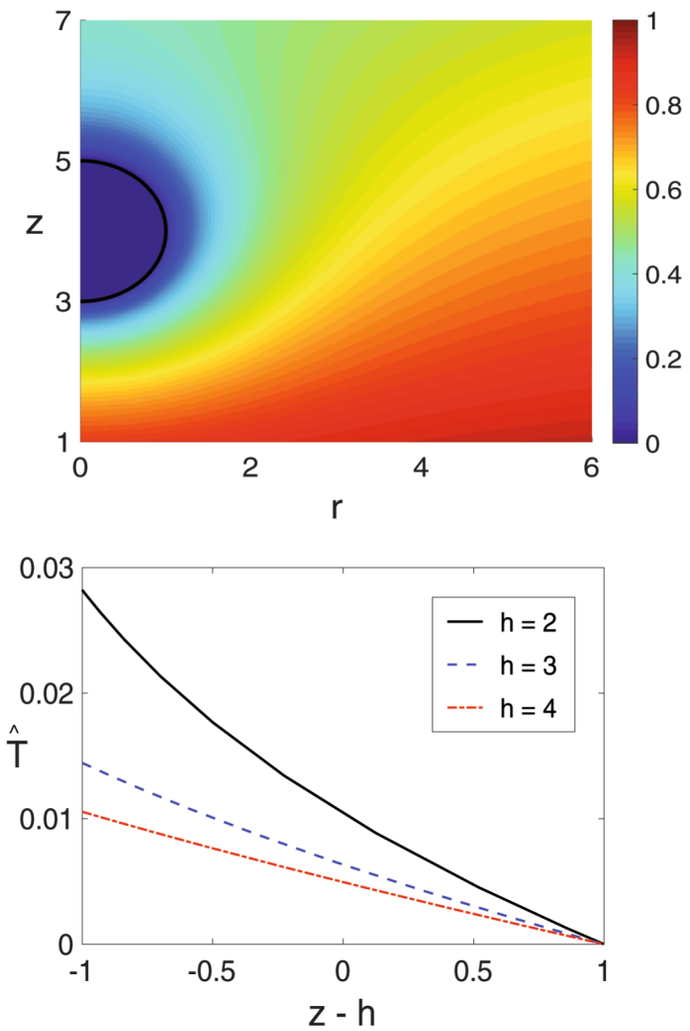

FIG. 2. (Top) Nondimensional temperature distribution both inside and outside of the droplet for $k = 0.042$, $E = 36.1$, and $\gamma = 15.6$. The liquid-gas interface location is shown by the thick black line, the temperature distributions are axially symmetric, and half of the cross section is shown. (Bottom) Droplet surface temperature as a function of the vertical coordinate measured from the position of the center of the droplet, presented in nondimensional variables.

is closer to the hot solid (smaller h), but for all cases the temperature gradient in the liquid is at least an order of magnitude lower than the imposed gradient. That has important implications for shear stresses at the droplet surface due to temperature variation along the interface, i.e., Marangoni stresses, which can be drastically overestimated if the imposed temperature gradient is used to find the temperature variation.

Once the coefficients B_n are found, Eq. (16) can be used to determine vapor concentration distribution and thus calculate the nondimensional evaporative mass flux at the droplet surface, $J \equiv -\partial c/\partial n$. In order to illustrate the degree of nonuniformity of the profile across the droplet, we subtract the value J_0 corresponding to the center of the droplet and plot the result in Fig. 3 for three different droplet locations. Note that the negative values of J do not correspond to condensation but rather indicate values smaller than J_0. The result for $h = 2$ (solid line) may appear counterintuitive since it shows a decrease in the evaporation rate near the bottom of the droplet, despite the fact that this part of the free surface faces the hot surface. We believe the observation can be explained by geometric confinement: as the droplet gets closer to the solid surface, diffusion of vapor away from the free surface is impeded by the presence of the solid, resulting in slower evaporation. This explanation is supported by the fact that J at the bottom of the droplet increases relative to J_0 as

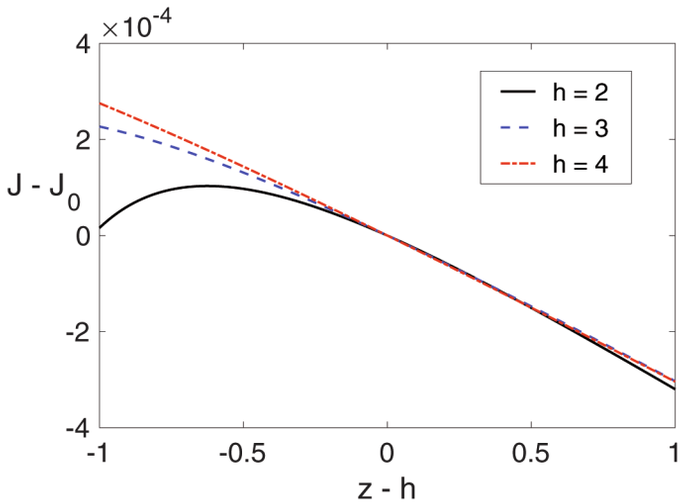

FIG. 3. Scaled evaporation rates along the surface of the droplet plotted in terms of scaled vertical coordinate for different locations of the droplet, measured from $z = h$. The parameter values are the same as in Fig. 2.

the droplet moves away from the solid (dashed and dot-dashed lines in Fig. 3). In fact, the profile is basically linear at $h = 4$ and higher values of h (not shown), i.e., when the droplet is sufficiently far away from the solid. A higher evaporation rate at the bottom and lower rate at the top are dictated there by the imposed temperature gradient.

The results presented so far are valid for relatively low heater temperature since the saturation vapor density has to be a fraction of the moist air density to justify the use of Eq. (10). For the solid surface temperatures in the range between 80 °C and 100 °C, in which many experiments were conducted, Eq. (8) should be used instead. This makes the problem nonlinear, but only at the final step of the solution when the series expansions for temperature and concentration are substituted into Eq. (8). We have carried out this final step of the solution using `fsolve` from MATLAB Optimization Toolbox with a typical result illustrated in Fig. 4. The parameter values are calculated based on $T_H = 85$ °C and the value of c_∞ is adjusted to match the measured evaporation

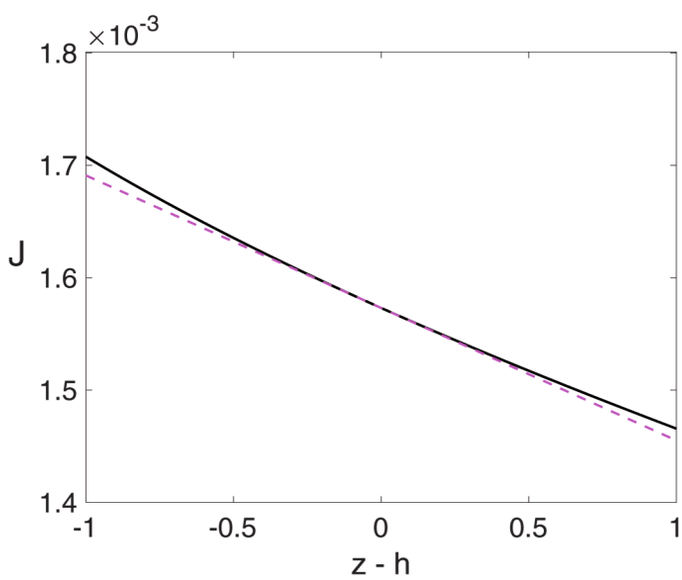

FIG. 4. Scaled evaporation rate plot for $k = 0.04$, $E = 8.53$, $\gamma = 13.3$, and $c_\infty = 0.90$ found based on Eq. (8), solid line. A linear approximation to the profile is shown by the dashed line.

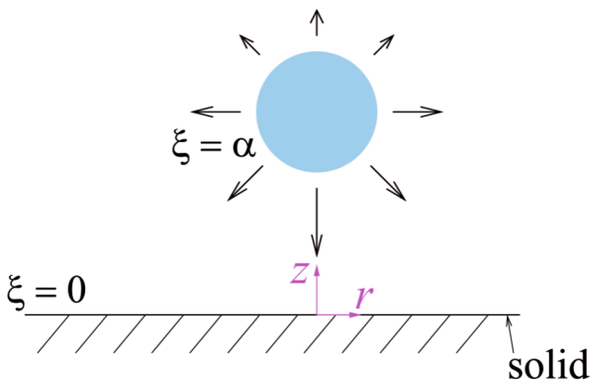

FIG. 5. Sketch illustrating nondimensional coordinates and geometry for the fluid flow model, with arrows schematically showing the direction of the flow away from the droplet surface, with stronger evaporation near the bottom. Stokes flow model is used to describe flow in the gas phase, while internal circulation is neglected due to very low values of the air-to-liquid viscosity ratio.

rate in [13]. Remarkably, the solution is still well approximated by a linear function, which is shown by magenta dashed line in Fig. 4. The slope of this line, defined by the derivative of J at $z = h$, is used in the next section to find the evaporation velocity profile.

III. FLUID FLOW MODEL

Let us now turn to the mathematical description of the flow around a spherical droplet evaporating in the presence of a solid (Fig. 5). Evaporation is nonuniform due to the temperature gradient established along the droplet surface as predicted by the heat transfer and diffusion model from the previous section. The flow in moist air around the droplet generated by the evaporation will be described using the Stokes flow approximation. Even though air viscosity is relatively low, typical values of air flow Reynolds numbers for microscale droplets of interest here are well below unity. For example, in the experimental configuration of Zaitsev *et al.* [13] the Reynolds numbers for the gas phase flow are estimated to be below 0.1.

The discussion of the vapor diffusion model in the previous section suggests a natural choice of the Stefan flow velocity scale

$$V^* = \frac{D\rho_{\mathrm{sat}}}{\rho R}. \tag{20}$$

The Stokes stream function ψ, scaled by R^2V^*, is introduced so that the scaled velocity components are expressed by

$$(u_\xi, u_\eta) = \frac{(\cosh\xi - \cos\eta)^2}{\sinh^2\alpha\,\sin\eta}\left(\frac{\partial\psi}{\partial\eta}, -\frac{\partial\psi}{\partial\xi}\right). \tag{21}$$

The equation of continuity is then satisfied automatically. The momentum equations can be reformulated in terms of the stream function, leading to

$$E^4\psi = 0, \tag{22}$$

where the operator E^2 for axisymmetric flow is defined by

$$E^2 = \frac{\sin\eta(\cosh\xi - \cos\eta)}{\sinh^2\alpha}\left[\frac{\partial}{\partial\xi}\left(\frac{\cosh\xi - \cos\eta}{\sin\eta}\frac{\partial}{\partial\xi}\right) + \frac{\partial}{\partial\eta}\left(\frac{\cosh\xi - \cos\eta}{\sin\eta}\frac{\partial}{\partial\eta}\right)\right]. \tag{23}$$

The standard no-penetration condition ($u_\xi = 0$) implies that the Stokes stream function is equal to a constant value, which can be denoted by ψ_0, along the solid boundary. Since ψ is defined up to an arbitrary constant, we choose $\psi_0 = 0$. Then, the no-penetration and no-slip ($u_\eta = 0$) conditions

are expressed as

$$\psi|_{\xi=0} = 0, \qquad \left.\frac{\partial \psi}{\partial \xi}\right|_{\xi=0} = 0. \tag{24}$$

At the droplet surface, we specify instantaneous evaporation velocity, assumed to be varying linearly in the direction of the imposed temperature gradient, leading to

$$\left.\frac{(\cosh\alpha - \cos\eta)^2}{\sinh^2\alpha\,\sin\eta}\,\frac{\partial \psi}{\partial \eta}\right|_{\xi=\alpha} = -V_0 + V_1(z-h). \tag{25}$$

Here we use a linear approximation for the evaporation velocity as a function of vertical coordinate since evaporative flux variation can be accurately approximated by a linear function, as illustrated by, e.g., the dashed line in Fig. 4. For each fluid flow solution reported, we first solved the corresponding thermal and diffusion problems as formulated in Sec. II to determine V_0 (equal to $-\partial c/\partial n$ at $z = h$) and V_1. Integrating Eq. (25) in η gives

$$\psi|_{\xi=\alpha} = \frac{V\,\sinh^2\alpha}{\cosh\alpha - \cos\eta} - \frac{\frac{1}{2}V_1\sinh^4\alpha}{(\cosh\alpha - \cos\eta)^2} + A'\sinh^2\alpha. \tag{26}$$

Here $V \equiv V_0 + V_1 h$ and the integration constant, A', is determined from the condition that ψ is constant on the symmetry line (where $u_\eta = 0$), leading to

$$A' = -\frac{V + \frac{1}{2}V_1(1-\cosh\alpha)}{1+\cosh\alpha}. \tag{27}$$

Finally, motivated by the much larger viscosity of the liquid compared to air, we impose the no-slip condition at the free surface,

$$\left.\frac{\partial \psi}{\partial \xi}\right|_{\xi=\alpha} = 0, \tag{28}$$

but more detailed discussion of alternative conditions can be found below in Sec. VI. Substantial reduction in mobility of air-water interfaces in small-scale systems is a well-documented effect, e.g., in studies of film drainage [32].

Evaporation at the liquid surface implies that the droplet radius and thus the value of α are changing, making the flow unsteady. We assume the evaporation to be sufficiently slow so that a quasisteady approximation can be used, i.e., that the flow patterns at any moment in time are well described by the solution of the steady-state Stokes flow problem corresponding to the droplet radius at that time.

IV. FLOW PATTERNS

The general solution of Eq. (22) can be written as an expansion of the Stokes stream function in Gegenbauer polynomials of index $-1/2$ [18,21,22],

$$\psi = (\cosh\xi - \cos\eta)^{-3/2}\sum_{n=-1}^{\infty} W_n(\xi)\,C_{n+1}^{-1/2}(\cos\eta). \tag{29}$$

Following Stimson and Jeffery [18], the coefficients of the expansion are often expressed as

$$W_n(\xi) = A_{0n}\cosh n_-\xi + B_{0n}\sinh n_-\xi + C_{0n}\cosh n_+\xi + D_{0n}\sinh n_+\xi, \tag{30}$$

with $n_- = n - 1/2$, $n_+ = n + 3/2$. However, in the present study we use equivalent expressions suggested by Oguz *et al.* [22],

$$W_n(\xi) = \bar{A}_n \frac{\sinh n_-(\alpha - \xi)}{\sinh n_-\alpha} + \bar{B}_n \frac{\sinh n_-\xi}{\sinh n_-\alpha} + \bar{C}_n \left(\frac{\sinh n_-(\alpha - \xi)}{\sinh n_-\alpha} - \frac{\sinh n_+(\alpha - \xi)}{\sinh n_+\alpha} \right) + \bar{D}_n \left(\frac{\sinh n_-\xi}{\sinh n_-\alpha} - \frac{\sinh n_+\xi}{\sinh n_+\alpha} \right), \quad n \geqslant 1, \tag{31}$$

with the coefficients $\bar{A}_n$, $\bar{B}_n$, $\bar{C}_n$, and $\bar{D}_n$ to be determined from the boundary conditions. Furthermore, the conditions of axial symmetry allow one to express W_0 and W_{-1} in terms of only two constants [21], denoted by A and B, so that

$$W_{-1}(\xi) = A\left(\cosh \frac{3\xi}{2} + 3 \cosh \frac{\xi}{2} \right) + B\left(\sinh \frac{3\xi}{2} - 3 \sinh \frac{\xi}{2} \right), \tag{32}$$

$$W_0(\xi) = A\left(\cosh \frac{3\xi}{2} + 3 \cosh \frac{\xi}{2} \right) - B\left(\sinh \frac{3\xi}{2} - 3 \sinh \frac{\xi}{2} \right). \tag{33}$$

The boundary conditions at the solid given by Eq. (24) can now be expressed as conditions for W_n and their derivatives,

$$W_n(0) = 0, \tag{34}$$

$$W_n'(0) = 0. \tag{35}$$

At the droplet surface, Eqs. (26) and (28) lead to the conditions

$$W_n(\alpha) = \frac{\sinh^2 \alpha}{\sqrt{2}} \left[\frac{3A'}{4} \left(\frac{e^{-\alpha n_+}}{n_+} - \frac{e^{-\alpha n_-}}{n_-} \right) + \left[V + V_1 \left(n + \frac{1}{2} \right) \sinh \alpha \right] e^{-\alpha(n+1/2)} \right], \tag{36}$$

$$W_n'(\alpha) = \frac{3 \sinh^3 \alpha}{2\sqrt{2}} e^{-\alpha(n+1/2)} \left\{ A' - \frac{(2n+1)V}{\sinh \alpha} - V_1 \left[\left(n + \frac{1}{2} \right) \cosh \alpha + \left(n + \frac{1}{2} \right)^2 \sinh \alpha \right] \right\}. \tag{37}$$

The advantage of using the form of the solution given by (31) instead of (30) is that the conditions (34) and (36) immediately give formulas for two sets of coefficients,

$$\bar{A}_n = 0, \quad \bar{B}_n = W_n(\alpha). \tag{38}$$

The two remaining boundary conditions can then be used to find $\bar{C}_n$ and $\bar{D}_n$, as shown in the Appendix which also outlines the calculation of the coefficients A and B in Eqs. (32) and (33). The description of the viscous flow around the evaporating droplet is now complete. To summarize, the Stokes stream function is represented analytically by Eq. (29). The functions $W_n(\xi)$ are defined by Eqs. (31)–(33) with the coefficients from (38), (A4), (A5), and (A7).

To illustrate the moist air flow patterns around evaporating droplets in situations relevant for experimental study of Zaitsev *et al.* [13], the following solution procedure was adopted. We start by evaluating the key parameters of the thermal problem from Sec. II at the experimentally measured value of the heater temperature. For example, at $T_H = 85\,^\circ\mathrm{C}$ we get parameter values listed in the caption of Fig. 4; note that c_∞ is estimated from the droplet evaporation rate found based on the experimentally measured radius as a function of time, $R(t)$. The full thermal problem with the nonlinear version of the interfacial energy balance, Eq. (8), is then solved as outlined in Sec. II, leading to the scaled evaporative flux profiles such as the one illustrated by the solid line in Fig. 4. The linearized version of the profile (dashed line in the same figure) is then used to determine the input parameters V_0 and V_1 for the flow problem.

The contour plots of the Stokes stream function found from (29), truncated at $n = 10$, are shown in Fig. 6. The plots represent two different values of nondimensional height $h = h^*/R$ corresponding

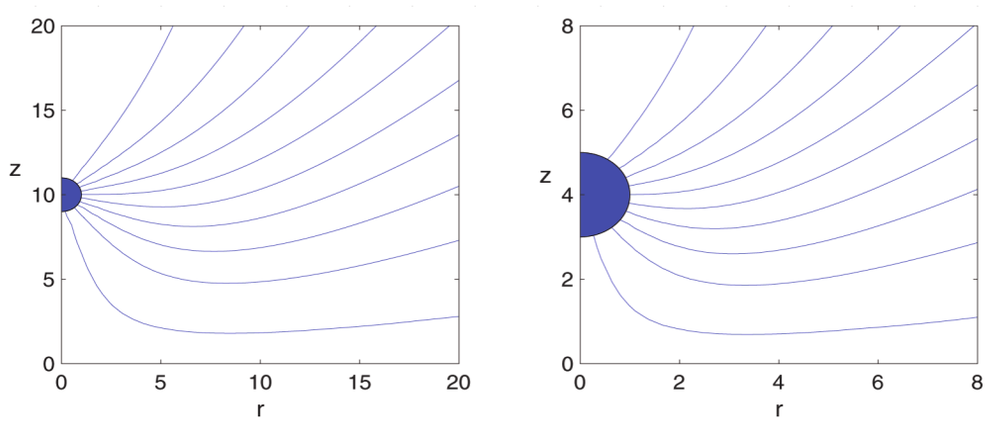

FIG. 6. Flow patterns for evaporating droplet of radius $R = 5$ μm at different heights based on the analytical solution for the Stokes stream function in bipolar coordinates. Scaled levitation heights are $h = 10$ (left) and $h = 4$ (right). Cylindrical coordinates are scaled by the droplet radius.

to two distinct configurations, both encountered in experiments: a small droplet far away from the solid surface and a larger droplet evaporating closer to the solid, i.e., at a distance comparable to its radius. For both cases, the lines under the droplet are bent significantly due to the presence of the solid which cannot be penetrated by the fluid. For the larger h, the lines remain straight near the droplet surface—an indication that flow is nearly spherically symmetric there and only weakly disturbed by the presence of the solid surface far below. For the smaller scaled height, bending starts close to the droplet surface, which is consistent with flow away from the symmetry line in the gas confined between the droplet and the solid. Such flow can be expected to compensate for mass transfer from the evaporating droplets, a situation qualitatively similar to the one seen in the classical studies of the Leidenfrost phenomenon [8].

While our analytical solution for the Stokes stream function is an infinite series, the functions $W_n(\xi)$ in Eq. (29) decay rapidly as n is increased for all values of ξ, so in practice only a few terms in the series are needed to obtain very accurate solutions. In order to illustrate this point, we studied the error in representation of the boundary conditions characterized by the norm of the difference between the truncated series with N terms and the specified boundary values of ψ. Since the boundary conditions at the solid boundary are satisfied exactly due to the way our solution is constructed, we focus on the boundary conditions at the droplet surface. Specifically, we define the norm

$$E_N = \left[\int_0^{\pi} (\psi_N - \psi_B)^2 d\eta\right]^{1/2}, \tag{39}$$

where ψ_N is the solution at $\xi = \alpha$ given by Eq. (29) but with summation only up to $n = N$ instead of $n = \infty$ and ψ_B is the value of the Stokes stream function at the droplet surface according to Eq. (26). As a measure of relative accuracy of the approximation, we use the scaled quantity $\tilde{E}_N = E_N/\psi_{B\max}$, where $\psi_{B\max}$ is the maximum value of ψ at the droplet surface. Figure 7 shows that $\tilde{E}_N$ decays rapidly as N is increased, indicating that keeping only the first few terms in the expansion is sufficient for obtaining very accurate results. Remarkably, even at $N = 2$, the relative error is already on the order of 10^{-3}. Small values of $\tilde{E}_N$ seen in Fig. 7 together with similar results for ψ_ξ on the boundary (not shown) provide a verification that our analytical solution is indeed correct. Note that the solution given by Eq. (29) satisfies Eq. (22) exactly by construction.

As the droplet size decreases in the configuration of Fig. 5, it is natural to expect the flow pattern to resemble that for a point source near a wall. The inviscid counterpart of this problem is a classical example of the method of images: a source of strength Q at $z^* = h^*$ and an image source of the same strength placed at $z^* = -h^*$ generate the same flow pattern in the physical domain as the source and a solid wall, with the no-penetration condition satisfied everywhere along $z^* = 0$. Remarkably,

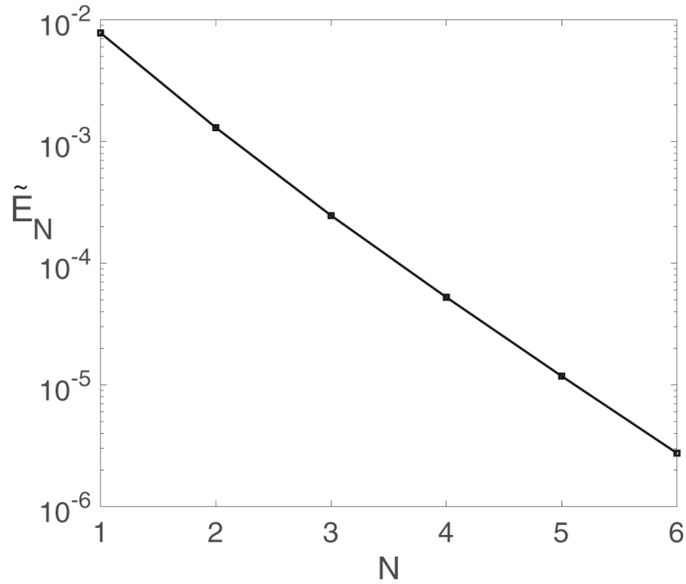

FIG. 7. Scaled error norm of the representation of the stream function with the first N terms in the series expansion shown as a function of the number of terms for $h = 2$.

similar ideas can be applied to the Stokes flow except that three singularities have to be placed simultaneously at the location $z^* = -h^*$ to ensure that not only the no-penetration but also the no-slip condition is satisfied at $z^* = 0$. As shown by Blake and Chwang [33], these singularities are a source, a Stokeslet doublet, and a potential dipole, leading to the velocity field

$$u_i = \frac{Q}{4\pi}\left[\frac{x_i - x_{0i}}{|\mathbf{x}-\mathbf{x}_0|^3} - \frac{x_i}{|\mathbf{x}|^3} + \frac{6x_i x_3^2}{|\mathbf{x}|^5} + 2h^*\left(\frac{\delta_{i3}}{|\mathbf{x}|^3} - \frac{3x_i x_3}{|\mathbf{x}|^5}\right)\right], \quad i = 1, 2, 3. \tag{40}$$

Here we use Cartesian coordinates with the origin at the location of the image, with $\mathbf{x}$ being the position vector and $\mathbf{x}_0$ the value of the position vector corresponding to the location of the actual physical source. The x_3 axis is in the vertical direction and δ denotes the Kronecker delta. The flow pattern defined by (40) can now be compared to the predictions of our model, i.e., the velocity components found from the Stokes stream function based on Eq. (21). Figure 8 illustrates a typical comparison for scaled radial and vertical velocity components plotted as functions of radial coordinate in the plane corresponding to $z = (h-1)/2$, i.e., halfway between the bottom of the droplet and the solid surface for two different levitation heights. Even though strictly speaking the method of images is valid in the limit of infinitely small droplet radius, i.e., $h \to \infty$, it clearly provides rather accurate velocity predictions even at the moderately large values of h, e.g., $h = 10$ shown in the top plots in Fig. 8. However, for smaller nondimensional levitation heights, the differences in the predictions of the model become significant, as seen in the bottom two images in Fig. 8. In particular, the method of images tends to underestimate the velocity under the droplet.

The method of images provides a simple physical interpretation of the experimentally observed ability of evaporating microscale droplets to levitate at temperatures well below the Leidenfrost point [13]. According to Eq. (40), the flow generated by the image has the upward velocity at the location of the droplet given by

$$U = \frac{3Q}{16\pi h^{*2}}. \tag{41}$$

Thus the droplet ends up being suspended in this upward flow and, for sufficiently small weight and strong evaporation, it will be able to levitate. More detailed discussion of the levitation conditions is provided below.

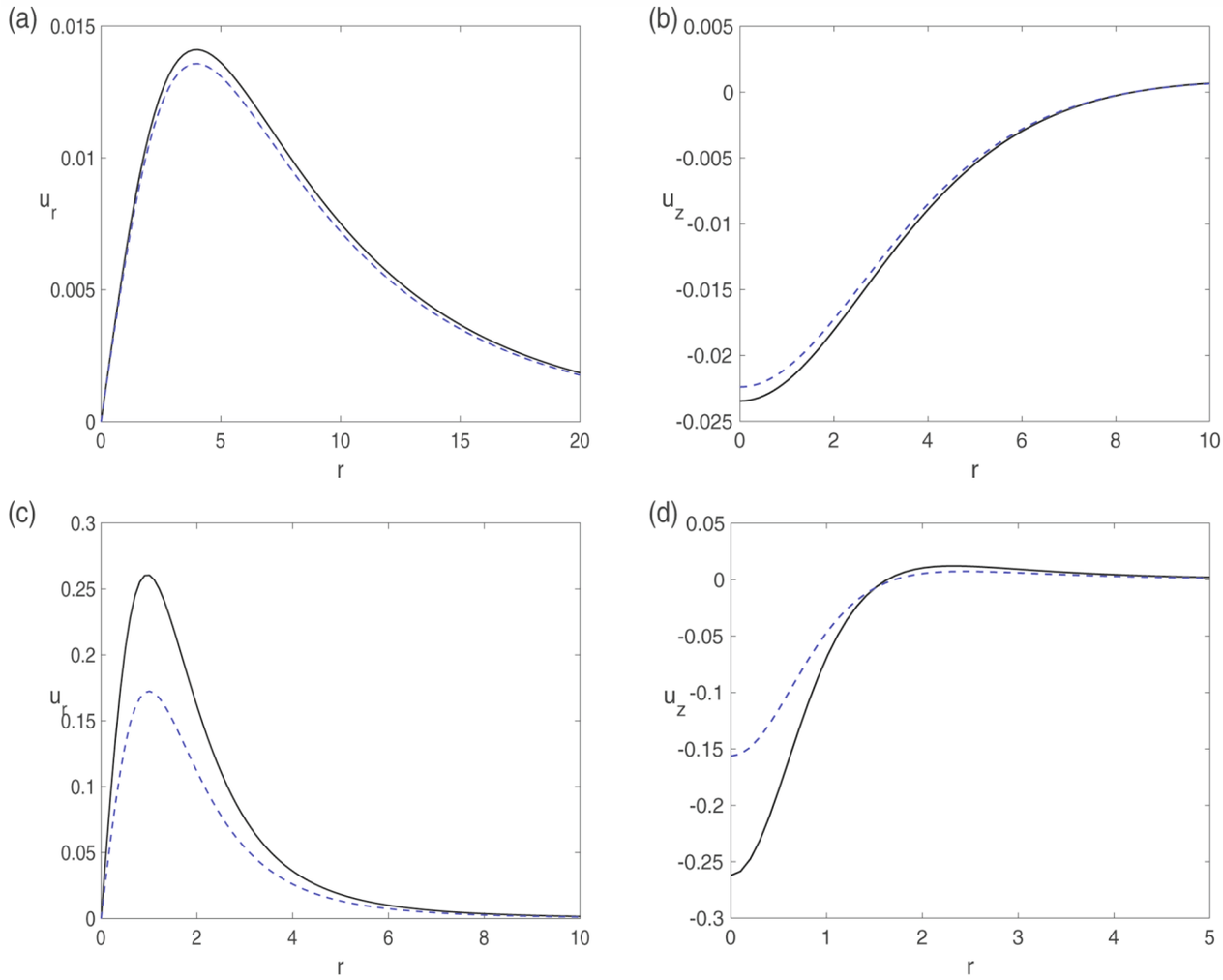

FIG. 8. Profiles of nondimensional radial (a), (c) and vertical (b), (d) velocities at $z = (h-1)/2$ corresponding to $h = 10$ (top plots) and $h = 2$ (bottom plots). Solid lines represent the model predictions based on (29), while dashed lines are obtained from the method of images, Eq. (40).

V. STOKES FORCE

Let us now turn to the calculation of the force acting on the droplet from the flow around it. This force is the key quantity needed for determination of levitation conditions as well as describing motion of evaporating droplets near interfaces in other applications such as spray cooling. For the Stokes stream function represented by Eq. (30), the general formula for the dimensional force has been first derived by Stimson and Jeffery [18]. While their geometric configuration is different, the result for the force was presented in terms of the coefficients of the general solution given by Eqs. (29) and (30) and is therefore applicable to our configuration as well. With the alternative form of the solution given by (31)–(33), their formula can be expressed as

$$F = 2\sqrt{2}\pi \frac{\mu R V^*}{\sinh\alpha}\left[4B - \sum_{n=1}^{\infty}\left(\frac{\bar{B}_n + \bar{D}_n - (\bar{A}_n + \bar{C}_n)\cosh n_-\alpha}{\sinh n_-\alpha} + \frac{\bar{C}_n \cosh n_+\alpha - \bar{D}_n}{\sinh n_+\alpha}\right)\right], \quad (42)$$

where μ is the moist air viscosity. For small droplets levitating far above the heater (large h), the expression for the force is expected to be equivalent to the classical Stokes law,

$$F_0 = 6\pi\mu R U, \quad (43)$$

with U found from Eq. (41). In order to illustrate departures from this formula, it is convenient to define the nondimensional force $\hat{F} = F/F_0$. This quantity is plotted in Fig. 9 as a function of the

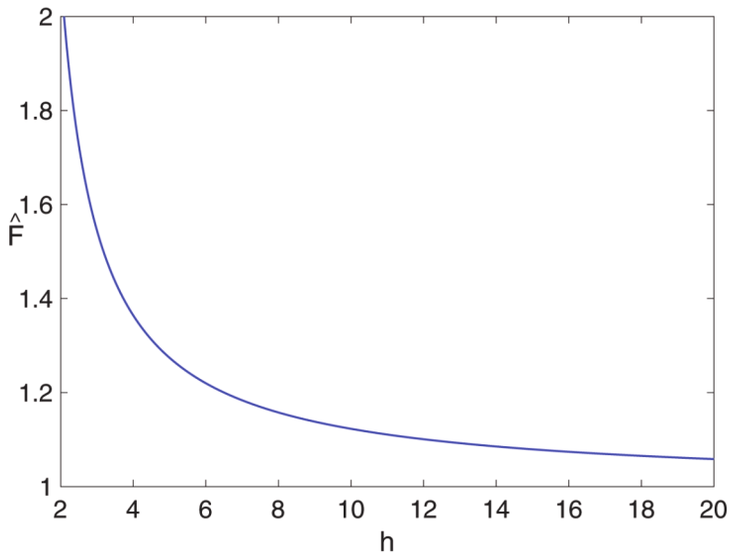

FIG. 9. Vertical force, scaled by F_0 from (43), acting on an isolated evaporating droplet near a solid surface, as a function of the scaled distance between droplet's center and the solid surface, for uniform evaporation velocity at the interface, $V^* = 0.01$ m/s.

scaled levitation height. As expected, $\hat{F}$ approaches unity at large h, i.e., where the method of images is valid. However, as h is decreased, due to either increase in the radius or decrease in distance to the solid, the force becomes significantly larger than expected from (41) and (43). For example, a droplet of radius 2 μm at a distance of 10 μm experiences repulsion force almost 30% greater than predicted if the droplet is treated as a point source. The discrepancy between the predictions of the two models increases dramatically as $h \to 1$, i.e., when the gap between the droplet and the solid becomes vanishingly small. This is not surprising since maintaining viscous flow in the narrow gap requires substantial increase in the pressure under the droplet, leading to sharp increase in the force acting on it, an effect qualitatively similar to strong repulsion of Leidenfrost droplets [8,34] from hot surfaces. There are, however, important quantitative differences since our model focuses on evaporation at much lower temperatures, motivated by experiments conducted for solid surface temperatures in the range of 50–100 °C [13,35], and does not account for interface deformation at the bottom of the droplet.

Let us now vary V_1 to investigate the effect of nonuniform evaporation (due to local temperature gradient near the heater) on the force F. Typical force vs distance curves for two realistic nonzero values of V_1 together with the case of uniform evaporation (dashed line) are shown in Fig. 10 (top). The predictions for all three cases are similar at h below $\sim$2, but deviate strongly for large values of h at which evaporation nonuniformity leads to higher values of the repulsion force. The fact that the force does not decay to zero when the droplet is far away from the solid may appear puzzling, but can be explained by observing that the net momentum lost by the droplet during evaporation with nonzero V_1 is in fact not zero even when no solid is present. This net momentum can assist in droplet levitation and contribute to the takeoff phenomenon seen in several experimental studies of evaporating microscale droplets ([10,11]; see also Supplemental Material from [13]). We note that Fig. 10 (top) shows relative value of the force (scaled by F_0), but the actual force magnitude approaches constant at large h^*. To verify this, we plotted the dimensional force as a function of dimensional height in Fig. 10 (bottom). The asymptotic behavior for the nonzero value of V_1 clearly shows that far away from the solid the force does not decay to zero, in contrast to the case of $V_1 = 0$ when the force is solely due to droplet-solid interaction.

VI. THERMOCAPILLARY STRESSES

The temperature gradient in the gas phase near the heater implies that thermocapillary stresses at the droplet surface may need to be accounted for. Accurate and complete description of the

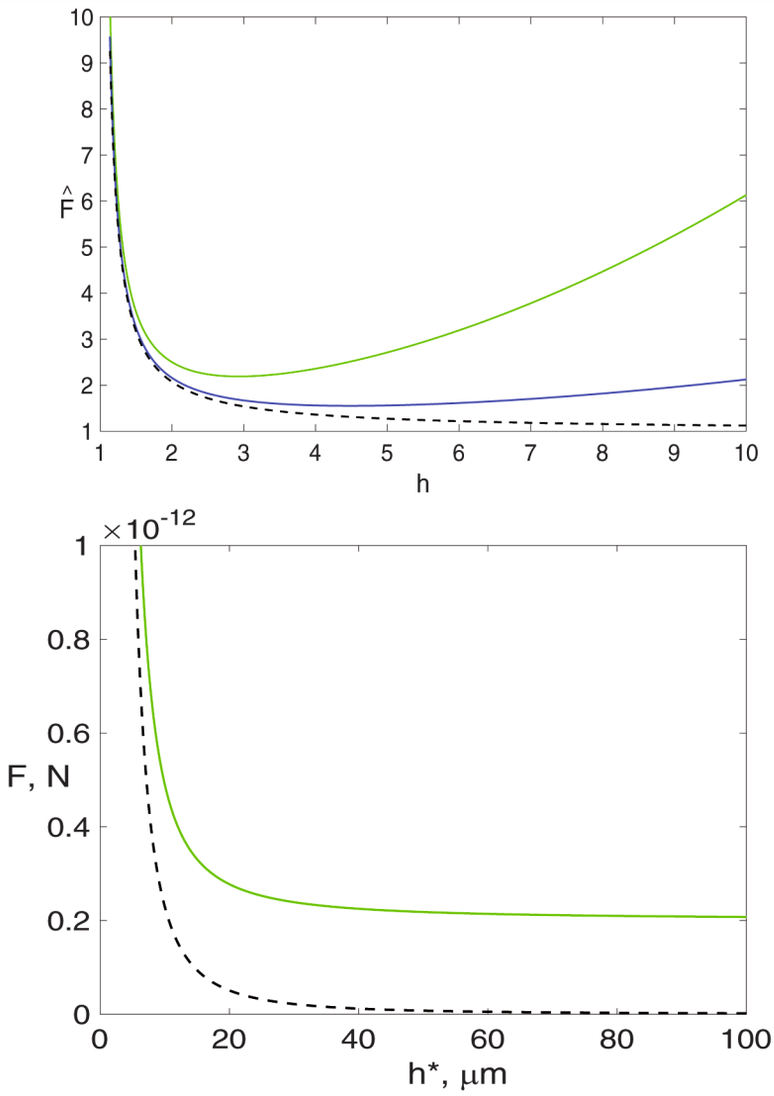

FIG. 10. (Top) Scaled force acting on the droplet ($R = 2\ \mu$m; $V^* = 0.01$ m/s) as predicted by models with different temperature gradients, characterized by different values of V_1: $V_1 = 0.01V_0$ (blue line); $V_1 = 0.05V_0$ (green line). The dashed line corresponds to $V_1 = 0$. (Bottom) For $V_1 = 0.05V_0$, the same result is plotted in dimensional variables, with dashed line showing dimensional force for $V_1 = 0$.

Marangoni effect would require solving coupled equations for viscous flow both inside and outside of the droplet with the shear stress condition incorporating thermocapillary stresses. This type of solution is beyond the scope of the present study. Instead, our objective here is to evaluate the significance of the Marangoni effect using a simple modification of the flow model developed in Sec. III. Specifically, instead of the no-slip condition at the droplet surface we impose the value of the tangential velocity that matches the classical Hadamard-Rybczynski–type solution as applied to a spherical droplet in uniform vertical temperature gradient [36]. In our formulation, this strategy implies replacing the boundary condition (28) with

$$\left.\frac{\partial \psi}{\partial \xi}\right|_{\xi=\alpha} = \frac{v_T \sinh^3\alpha \, \sin^2\eta}{(\cosh\alpha - \cos\eta)^3}, \tag{44}$$

where v_T is the scaled maximum value of the Marangoni-induced velocity at the droplet surface, typically well below unity. Using the series expression from (29), the condition (44) can be

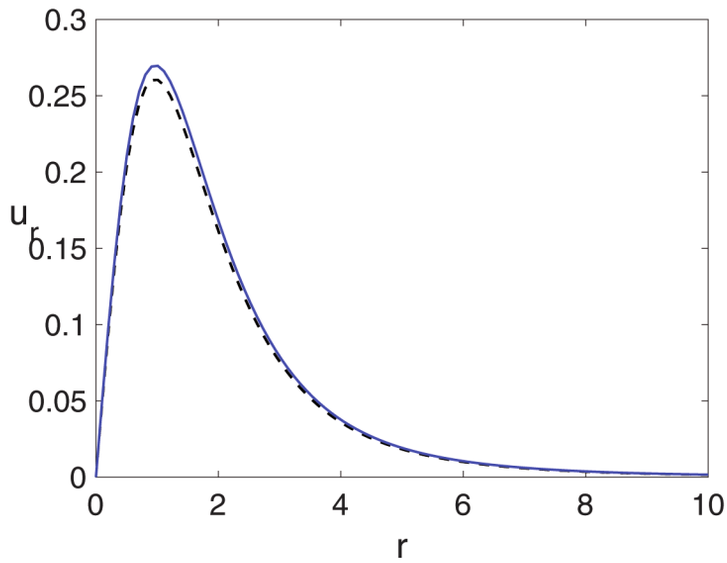

FIG. 11. Comparison of predictions of models with and without thermocapillary effect, with solid line corresponding to $v_T = 0.01$ and dashed line to $v_T = 0$. All results are obtained at $R = 2$ μm, $V_1 = 0$; the plot represents the radial velocity at $z = 1/2$ for $h = 2$.

reformulated in terms of expansion in Gegenbauer polynomials as follows:

$$\frac{2}{3\,\sinh^3\alpha}\sum_{n=-1}^{\infty} W_n'(\alpha)\,C_{n+1}^{-1/2}(\cos\eta) = (\cosh\alpha-\cos\eta)^{1/2}A' + \frac{V}{(\cosh\alpha-\cos\eta)^{1/2}} - \frac{V_1\sinh^2\alpha}{2(\cosh\alpha-\cos\eta)^{3/2}} + \frac{2v_T}{3}\frac{\sin^2\eta}{(\cosh\alpha-\cos\eta)^{3/2}}. \quad (45)$$

One could now proceed to formulating the condition for $W_n'(\alpha)$ analogous to Eq. (37) and then solving the problem for the stream function. However, there is a simple observation which allows one to drastically simplify the calculation. The right-hand side of Eq. (45) can be made identical to the previously discussed case of $v_T = 0$ by the following transformation of the key parameters:

$$A' \to A' - \tfrac{2}{3}v_T, \quad V \to V + \tfrac{4}{3}v_T\cosh\alpha, \quad V_1 \to V_1 + \tfrac{4}{3}v_T. \quad (46)$$

Both flow patterns and force acting on the droplet can then be determined from the previously derived results. Figure 11 shows typical radial velocity profiles halfway between the bottom of the droplet and the solid with and without the thermocapillary effect taken into account. Slight increase in the radial velocity is seen for nonzero v_T (solid line), consistent with the linearity of Stokes flow suggesting superposition of the additional thermocapillary contribution and the flow caused by evaporation at the liquid surface.

The action of thermocapillary stresses pushing moist air away from the axis of symmetry, where the drop surface temperature is the highest, suggests that the force acting on the droplet should be reduced for nonzero v_T due to reduction of pressure under the droplet. We checked that this is indeed the case, but the effect is rather small under realistic conditions, mostly due to the fact that droplet surface is close to isothermal even under the imposed temperature gradient, as was demonstrated in our solution of the heat transfer problem above. We also note that in experiments water is typically used and so potential surface contamination may affect the surface tension variation.

VII. COMPARISON WITH EXPERIMENTS

Experimental measurements of the droplet levitation height have been carried out for arrays of evaporating droplets formed over a dry patch in a thin layer of water on a metal surface, as shown in

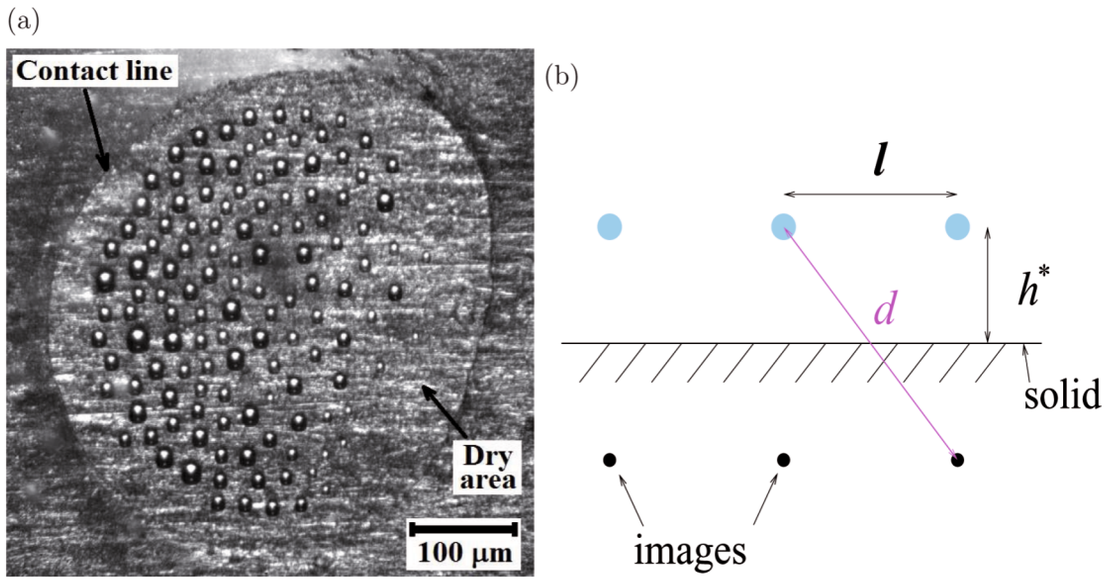

FIG. 12. (a) Photo of an array of droplets levitating over a dry patch at 85 °C, from [13]. (b) Sketch illustrating the calculation of correction factor due to interaction of droplet with images.

the top-view picture in Fig. 12(a). The droplets were formed by condensation of vapor over the liquid layer and ended up levitating in the dry-patch region after flying over the contact line, as described in detail in several recent studies [12,13,35,37]. Levitation height was recorded and compared to the predictions of the model representing droplets as point sources by Zaitsev *et al.* [13]. They suggested that a correction factor should be introduced in the expression for the upward force to account for the effect of flow generated by neighboring droplets and their images. The sketch in Fig. 12(b) illustrates the correction factor estimate using a two-dimensional version of the problem in which all droplets are on a straight line, separated by the distance l from each other. The droplet in the middle is at a distance $d = \sqrt{l^2 + 4h^{*2}}$ from the image of its neighbor on the right, and the flow generated by that image has a vertical component calculated from Eq. (40) to be $6Qh^3/(\pi d^5)$. A similar argument can be made for the three-dimensional case except that the velocity correction has to be multiplied by 6—the typical number of nearest neighbors in the two-dimensional array. Based on images such as the one shown in Fig. 12(a), we find that $l \sim 2h^*$ gives a reasonable estimate of interdroplet distance, leading to the final result for the correction factor to the Stokes drag force:

$$\beta_F = 1 + \frac{3}{2\sqrt{2}}. \tag{47}$$

Zaitsev *et al.* [13] used similar arguments although they ended up with a larger value of β_F (corresponding to β^2 in their notation), as appropriate for larger levitation heights. Estimating the upward force from (43) with that correction factor, they predicted levitation height as a function of droplet radius and compared it with the experimental data. The agreement was good for large levitation heights ($h \sim 10$), thus providing important early support for the hypothesis of the levitation mechanism through the flow generated by the evaporation of the droplet itself rather than other convective flows in the moist air. However, the model did not agree with the experimental data when levitation height was comparable to the radius. The disagreement was not only quantitative but qualitative, as theory predicted the dimensional levitation height to decrease with the radius, while experimental data showed gradual increase in this quantity.

Let us now discuss how the model formulated in Sec. III compares with the experimental data. We assume that the quasisteady approximation formulated there is acceptable for evaluating the upward force acting on the droplet and use the balance between Stokes force and droplet weight

written in the form

$$\tfrac{4}{3}\pi R^3 \rho_l g = \beta_F F. \tag{48}$$

Here ρ_l is liquid density, g is acceleration of gravity, F is determined from (42), the value of evaporation velocity is found from the rate of change of the radius based on experimental measurements, and the correction factor is given by Eq. (47). Strictly speaking, the argument used in deriving Eq. (47) is valid only for point sources, but we use the same value of the correction factor for finite-size droplets, assuming that inaccuracies in β_F introduce errors comparable to other effects we are neglecting in this section by setting V_1 and v_T to zero, e.g., neglecting spatial nonuniformity of evaporative flux and thermocapillary stresses. Since local temperature gradients were not measured in experiments, an attempt to include these effect would introduce additional fitting parameters which would have to be adjusted during comparison between experiment and theory. Instead, we focus on the main physical effect here, the repulsive interaction between droplets and the solid surface, and neglect smaller secondary effects.

The right-hand side of Eq. (48) is a function of h, so it gives an implicit equation for levitation height, solved using `fzero` subroutine in MATLAB. The comparison between the predictions of our model and the experiments is illustrated in Fig. 13. Levitation height (scaled by R) is shown as a function of the nondimensional droplet radius defined by

$$\hat{R} = R\left(\frac{\mu V^*}{\rho_l g}\right)^{-1/2} \tag{49}$$

for four different droplets, represented by different marker types, at the same experimental conditions corresponding to the metal substrate temperature of 85 °C, as measured by thermocouples. First, we note that the vast majority of experimental data seen in Fig. 13 (top) lies either on or very close to the theoretical curve (solid line). There is some disagreement at small $\hat{R}$, which we believe to be due to a combination of three factors. First, the estimate of the coefficient β_F from Eq. (47) becomes increasingly inaccurate since the interdroplet distance is not changing significantly for smaller droplets while levitation height increases (note that a larger value of $\beta_F = 3.4$ was used in Zaitsev *et al.* [13] for small droplets, which, however, is no longer accurate for larger droplets of interest here). Second, the accuracy of experimental measurement is reduced for droplets of small size since the optical resolution is limited, which also explains the significant experimental scatter seen in the plot. Third, as the droplet height increases, convective flow in the gas not related to the presence of droplets is likely to contribute more to the balance of forces acting on the droplet. Experiment and theory also diverge slightly at larger $\hat{R}$. To better illustrate this region, we plot the data and the solid line corresponding to the theory in log-log coordinates over a subset of the values of $\hat{R}$ in Fig. 13 (bottom). The theory tends to slightly overpredict the levitation height at larger $\hat{R}$, although it is clearly much more accurate than the approximate model based on the method of images, shown by the dashed line for comparison. It is also important to note that neglecting the nonuniformity of evaporation rate and thermocapillary stresses can contribute to the discrepancies at smaller levitation heights. In particular, thermocapillary stresses tend to reduce the upward force acting on the droplet, and thus can lead to lower levitation height than predicted by the models without thermocapillarity. However, without direct measurements of the temperature gradient near the heater it remains unclear if the only reason for discrepancy is the flow induced by thermocapillary stresses.

VIII. CONCLUSIONS

We developed an analytical model of flow around an evaporating spherical droplet near a heated solid surface based on solving the equation for the Stokes stream function in bipolar coordinates. The model allows us to calculate the force acting on the droplet and determine levitation height as a function of evaporation conditions. Previous modeling efforts treated droplets as point sources and did not match the experimental data except for very small values of the radius. We show that

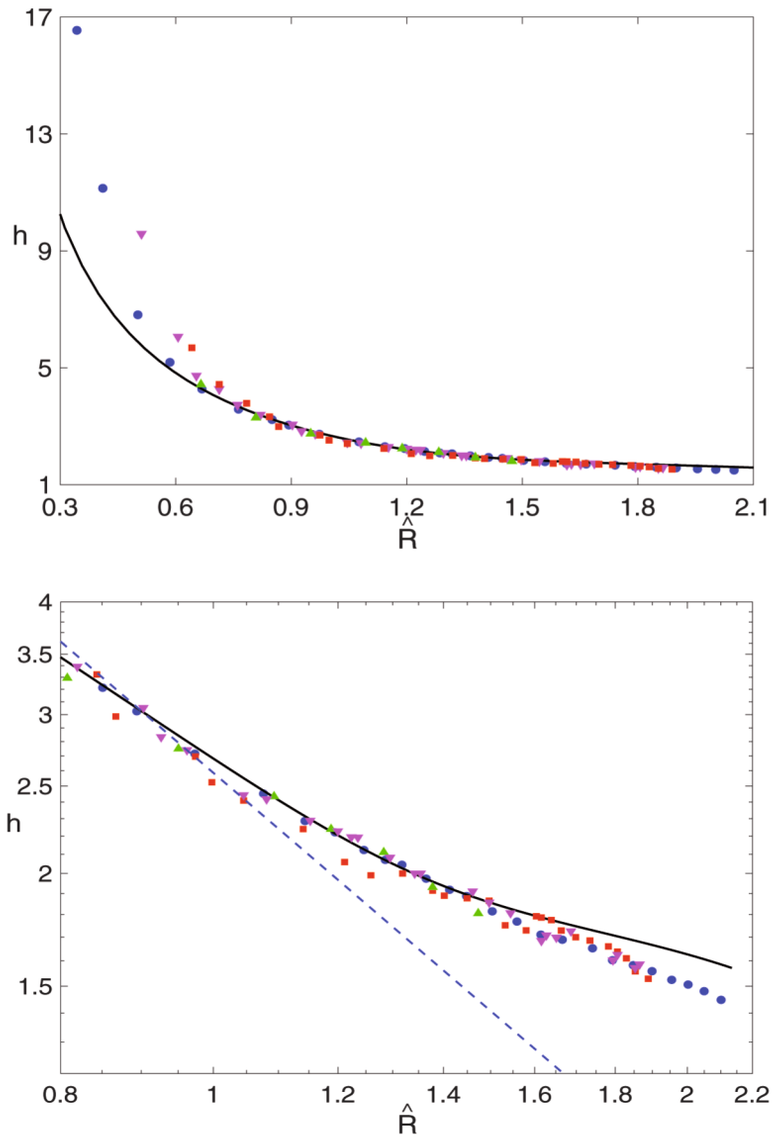

FIG. 13. (Top) Comparison between the experimental (markers, representing four different droplets under the same experimental conditions) and theoretical results (solid line, $V_1 = v_T = 0$) for scaled levitation height. (Bottom) The subset of the same results (for $\hat{R} \geqslant 0.8$) plotted in log-log coordinates, with the dashed line corresponding to the model representing droplets as point sources.

our model provides a much better agreement with the experimental results from studies of arrays of droplets levitating over heated dry solid surfaces at temperatures below 100 °C. Possible reasons for remaining discrepancies between experiment and theory are identified, including convective air flow not related to the presence of the droplet and thermocapillary stresses pushing the moist air out of the gap between the droplet and the heater.

Our approach provides a natural framework for incorporating thermocapillary stresses into the models of evaporating droplets. In the present study, we only took an initial step in that direction by considering prescribed tangential velocity at the droplet surface based on classical solutions for viscous flow inside and outside of a droplet placed in a temperature gradient, as derived by Young *et al.* [36]. While generally not a very strong effect, it can still affect levitation conditions, especially if the repulsive hydrodynamic interaction with the solid is weak. The Marangoni effect is also competing with the force due to nonuniform evaporation, leading to net momentum loss pushing the droplet in the upward vertical direction. To evaluate the relative importance of these

effects, we developed an analytical model of heat transfer both inside and outside of the droplet coupled with vapor diffusion through air. The model shows that the vertical temperature gradient along the droplet surface is much smaller than the temperature gradient in air away from the droplet. Evaporation is stronger at the bottom of the droplet than at the top but is found to unexpectedly weaken as the droplet gets closer to the wall, an effect explained by the geometric confinement that impedes vapor diffusion away from the free surface.

We used the measured values of the rate of decrease of the radius in our comparison between theory and experiment. It is interesting to note that estimates based on the classical Maxwell-type models of diffusive evaporation predict significantly faster evaporation rate if the humidity far away from the droplet is assumed to be at the value corresponding to ambient air. Observed evaporation rates suggest that air around the droplet has high vapor concentration, most likely due to intensive evaporation from the liquid layer surrounding the dry patch [12]. Nonuniformity of vapor concentration around the droplets can also explain the deviations from the classical D^2 law predicted by Maxwell-type models of evaporating droplets in the experimental data [35].

It is seen in the experimental photos such as Fig. 12(a) that levitating droplets tend to form ordered arrays. The quantitative description of this self-organization is beyond the scope of the present paper, but we believe that the method based on bispherical coordinates discussed in the present work will be applicable to studies of self-organization as well since it allows one to determine forces of pairwise interaction between droplets.

ACKNOWLEDGMENTS

The work was supported by the Russian Science Foundation (Grant No.18-19-00538). We thank D. P. Kirichenko for valuable discussions and for sharing experimental data with us.

APPENDIX

For the heat transfer model of Sec. II, the coefficients A_n satisfy

$$\begin{aligned}
&-n(k\,\cosh n_-\alpha+\sinh n_-\alpha+E^{-1}\gamma\,\tanh n_-\alpha\,\sinh n_-\alpha)A_{n-1}\\
&+[(k-1)\sinh\alpha\,\sinh\bar n\alpha+2\bar n\,\cosh\alpha(k\,\cosh\bar n\alpha+\sinh\bar n\alpha)\\
&+E^{-1}\gamma(\sinh\alpha+2\bar n\,\cosh\alpha\,\tanh\bar n\alpha)\sinh\bar n\alpha\big]A_n\\
&-(n+1)(k\,\cosh n_+\alpha+\sinh n_+\alpha+E^{-1}\gamma\,\tanh n_+\alpha\,\sinh n_+\alpha)A_{n+1}\\
&=\sqrt{2}\,e^{-\alpha\bar n}[\sinh\alpha-2\bar n\,\cosh\alpha+G\,\sinh\alpha\{2k\,\cosh\alpha-2\bar n[(2k+1)\sinh\alpha-2\bar n\,\cosh\alpha]\}\\
&-E^{-1}(\sinh\alpha+2\bar n\,\cosh\alpha\,\tanh\bar n\alpha)(1-c_\infty-2\gamma G\,\sinh\alpha)]\\
&+\sqrt{2}n\,e^{-n_-\alpha}[1-2n_-G\,\sinh\alpha+E^{-1}\tanh n_-\alpha(1-c_\infty-2\gamma n_-G\,\sinh\alpha)]\\
&+\sqrt{2}(n+1)e^{-n_+\alpha}[1-2n_+G\,\sinh\alpha+E^{-1}\tanh n_+\alpha(1-c_\infty-2\gamma n_+G\,\sinh\alpha)]. \qquad \text{(A1)}
\end{aligned}$$

Here $\bar n=n+1/2$, $n_+=n+3/2$, and $n_-=n-1/2$.

For the flow model of Sec. III, the conditions given by Eqs. (24) and (28) lead to

$$(n_+\coth n_+\alpha-n_-\coth n_-\alpha)\bar C_n+(n_-\mathrm{csch}\,n_-\alpha-n_+\mathrm{csch}\,n_+\alpha)\bar D_n=-n_-W_n(\alpha)\mathrm{csch}\,n_-\alpha, \qquad \text{(A2)}$$

$$\begin{aligned}
&(n_+\mathrm{csch}\,n_+\alpha-n_-\mathrm{csch}\,n_-\alpha)\bar C_n-(n_+\coth n_+\alpha-n_-\coth n_-\alpha)\bar D_n\\
&\quad=-n_-W_n(\alpha)\coth n_-\alpha+W_n'(\alpha). \qquad \text{(A3)}
\end{aligned}$$

The solution of this linear system is

$$\bar{C}_n = \Delta_n^{-1}[n_- n_+ W_n(\alpha)(\cosh n_+\alpha - \cosh n_-\alpha) + W_n'(\alpha)(n_+ \sinh n_-\alpha - n_- \sinh n_+\alpha)], \tag{A4}$$

$$\begin{aligned}\bar{D}_n = \Delta_n^{-1}\{&n_- W_n(\alpha)[n_- \sinh n_-\alpha \sinh n_+\alpha + n_+(1 - \cosh n_+\alpha \cosh n_-\alpha)] \\ &+ W_n'(\alpha)(n_+ \cosh n_+\alpha \sinh n_-\alpha - n_- \cosh n_-\alpha \sinh n_+\alpha)\},\end{aligned} \tag{A5}$$

$$\Delta_n = 2n_- n_+(\cosh n_+\alpha \cosh n_-\alpha - 1) - (n_-^2 + n_+^2)\sinh n_+\alpha \sinh n_-\alpha. \tag{A6}$$

Let us now discuss the procedure for finding the coefficients A and B appearing in Eqs. (32) and (33). Since the stream function is zero at $\xi = 0$ and $\eta = \pi$, the value of A is immediately found to be zero. Application of the condition (26) at $\eta = 0$ leads to the determination of the value of B. To summarize the results, we write

$$A = 0, \quad B = \frac{2\sqrt{2}\,\sinh^3(\alpha/2)(V - V_1\cosh\alpha)}{\sinh\frac{3\alpha}{2} - 3\,\sinh\frac{\alpha}{2}}. \tag{A7}$$

[1] J. Kim, Spray cooling heat transfer: The state of the art, Int. J. Heat Fluid Flow **28**, 753 (2007).

[2] W. Sirignano, *Fluid Dynamics and Transport of Droplets and Sprays*, 2nd ed. (Cambridge University Press, Cambridge, UK, 2014).

[3] C. Kleinstreuer and Z. Zhang, Airflow and particle transport in the human respiratory system, Annu. Rev. Fluid Mech. **42**, 301 (2010).

[4] J. C. Maxwell, Diffusion, collected scientific papers, *Encyclopedia Britannica* (Cambridge University Press, Cambridge, 1890), Vol. II, pp. 625–646.

[5] S. Sazhin, *Droplets and Sprays* (Springer-Verlag, London, 2014).

[6] J. Stefan, Versuche uber die verdampfung, Sitz. k. Akad. Wiss. Wien II **65**, 385 (1873).

[7] N. Fuchs, *Evaporation and Droplet Growth in Gaseous Media* (Pergamon, London, 1959).

[8] D. Quéré, Leidenfrost dynamics, Annu. Rev. Fluid Mech. **45**, 197 (2013).

[9] T. Tran, H. J. J. Staat, A. Prosperetti, C. Sun, and D. Lohse, Drop Impact on Superheated Surfaces, Phys. Rev. Lett. **108**, 036101 (2012).

[10] F. Celestini, T. Frisch, and Y. Pomeau, Take Off of Small Leidenfrost Droplets, Phys. Rev. Lett. **109**, 034501 (2012).

[11] S. Lyu, V. Mathai, Y. Wang, B. Sobac, P. Colinet, D. Lohse, and C. Sun, Final fate of a Leidenfrost droplet: Explosion or takeoff, Sci. Adv. **5**, eeav8081 (2019).

[12] O. A. Kabov, D. V. Zaitsev, D. P. Kirichenko, and V. S. Ajaev, Interaction of levitating microdroplets with moist air flow in the contact line region, Nanoscale Microscale Thermophys. Eng. **21**, 60 (2017).

[13] D. V. Zaitsev, D. P. Kirichenko, V. S. Ajaev, and O. A. Kabov, Levitation and Self-Organization of Liquid Microdroplets Over Dry Heated Substrates, Phys. Rev. Lett. **119**, 094503 (2017).

[14] V. S. Ajaev and O. A. Kabov, Levitation and self-organization of droplets, Annu. Rev. Fluid Mech. **53**, 203 (2021).

[15] A. A. Fedorets, Droplet cluster, JETP Lett. **79**, 372 (2004).

[16] A. A. Fedorets, I. Marchuk, and O. Kabov, Role of vapor flow in the mechanism of levitation of a droplet-cluster dissipative structure, Tech. Phys. Lett. **37**, 116 (2011).

[17] V. J. Schaefer, Observations of an early morning cup of coffee, Am. Sci. **59**, 534 (1971).

[18] M. Stimson and G. B. Jeffery, The motion of two spheres in a viscous fluid, Proc. R. Soc. A **111**, 110 (1926).

[19] H. Brenner, The slow motion of a sphere through a viscous fluid towards a plane surface, Chem. Eng. Sci. **16**, 242 (1961).

[20] L. S. Fisher and A. A. Golovin, Motion of a droplet near an evaporating liquid-gas interface, Phys. Fluids **19**, 032101 (2007).

[21] H. N. Oguz and S. S. Sadhal, Growth and collapse of translating compound multiphase drops: Analysis of fluid mechanics and heat transfer, J. Fluid Mech. **179**, 105 (1987).
[22] H. N. Oguz, A. Prosperetti, and D. Antonelli, The hydrodynamic interaction of two slowly evaporating spheres, Phys. Fluids A **1**, 1656 (1989).
[23] G. E. Cossali and S. Tonini, Variable gas density effects on transport from interacting evaporating spherical drops, Int. J. Heat Mass Transf. **127**, 485 (2018).
[24] T. Brzustowski, E. Twardus, S. Wojcicki, and A. Sobiesiak, Interaction of two burning fuel droplets of arbitrary size, AIAA J. **17**, 1234 (1979).
[25] A. Umemura, S. Ogawa, and N. Oshima, Analysis of the interaction between two burning droplets, Combust. Flame **41**, 45 (1981).
[26] S. Zhang and G. Gogos, Film evaporation of a spherical droplet over a hot surface: Fluid mechanics and heat/mass transfer analysis, J. Fluid Mech. **222**, 543 (1991).
[27] P. T. Tsilingiris, Thermophysical and transport properties of humid air at temperature range between 0 and 100 °C, Energy Convers. Manage. **49**, 1098 (2008).
[28] L. R. Glicksman and J. H. Lienhard V, *Modeling and Approximation in Heat Transfer* (Cambridge University Press, Cambridge, UK, 2016).
[29] E. Arinshtein and A. A. Fedorets, Mechanism of energy dissipation in a droplet cluster, JETP Lett. **92**, 658 (2010).
[30] S. S. Sadhal, Heat transport to a slowly growing bubble on a solid surface, Q. J. Mech. Appl. Math. **42**, 477 (1989).
[31] N. N. Lebedev, *Special Functions and their Applications* (Dover, New York, 1972).
[32] R. Manica and D. Y. C. Chan, Drainage of the air-water-quartz film: experiments and theory, Phys. Chem. Chem. Phys. **13**, 1434 (2011).
[33] J. R. Blake and A. T. Chwang, Fundamental singularities of viscous flow, Part I, J. Eng. Math. **8**, 23 (1974).
[34] B. Sobac, A. Rednikov, S. Dorbolo, and P. Colinet, Leidenfrost effect: Accurate drop shape modeling and refined scaling laws, Phys. Rev. E **90**, 053011 (2014).
[35] D. V. Zaitsev, D. P. Kirichenko, A. I. Shatekova, V. S. Ajaev, and O. A. Kabov, Experimental and theoretical studies of ordered arrays of microdroplets levitating over liquid and solid surfaces, Interfac. Phenom. Heat Transfer **6**, 219 (2018).
[36] N. O. Young, J. S. Goldstein, and M. J. Block, The motion of bubbles in a vertical temperature gradient, J. Fluid Mech. **6**, 350 (1959).
[37] O. A. Kabov, D. V. Zaitsev, D. P. Kirichenko, and V. S. Ajaev, Investigation of moist air flow near contact line using microdroplets as tracers, Interfac. Phenom. Heat Transfer **4**, 207 (2016).

Microgravity Science and Technology (2021) 33: 53
https://doi.org/10.1007/s12217-021-09892-6

ORIGINAL ARTICLE

Heat Flux Density Evaluation in the Region of Contact Line of Drop on a Sapphire Surface Using Infrared Thermography Measurements

A. L. Karchevsky[1] · V. V. Cheverda[1,2] · I. V. Marchuk[1,2] · T. G. Gigola[2,3] · V. S. Sulyaeva[4] · O. A. Kabov[2,3]

Received: 15 December 2020 / Accepted: 18 May 2021 / Published online: 14 August 2021
© The Author(s), under exclusive licence to Springer Nature B.V. 2021

Abstract
The paper presents a new tool "the method of IR transparent thick plate" that can be used to study the heat and mass transfer processes in the air-liquid-solid contact line area. Its distinctive feature as compared to the previously known methods is the solution of the initial-boundary problem for the heat conductivity equation, which in terms of mathematics is a correct problem. Currently, the heat and mass transfer processes in the area of the contact line are not completely understood because of its small size and a limited set of applied research methods. The challenges in modeling of contact line phenomena have to do with the fact that several physical effects such as evaporation, viscous flow, surface tension, thermocapillary stresses, London-van der Waals forces, disjoining pressure, nonequilibrium effects are coupled together and all significant in this highly localized region. This leads to difficulties in both mathematical modeling and design of experiments. The experimental part of the study includes the evaporation of a liquid drop on a sapphire substrate. The upper part of the sapphire glass is coated with a high heat-resistant black graphite paint (Graphit 33), which is a non-transparent for visual and IR-rays. Measurements of various physical, chemical and geometrical properties of this coating have been done by electron microscopy and other techniques. Trial experiments on the drop evaporation were carried out. The sapphire surface temperature fields after single drop deposition were obtained using the IR-scanner. The experimental local heat flux distribution at drop evaporation on the sapphire surface with two small local highs close to the contact line regions has been measured.

Keywords Liquid drop · Contact wetting line · Sapphire · Mathematical modelling · Heat flux density · The method of IR-transparent thick plate

PACS 44.90.+c · 02.30.Jr

Mathematics Subject Classification 80A20 · 80M25

Introduction

The literature review shows that a tremendous research work was carried out on many aspects of sessile drop evaporation because of its applications in agriculture, medicine, microelectronics, microfluidics, thin film coating, spray cooling and many others (Erbil 2012; Cazabat and Guèna 2010; Mollaret et al. 2004). In the very general case the evaporation rate of the sessile drop is limited by the following mechanisms: 1) heat transfer through the liquid-solid interphase (Morozova and Novopashin 2019); 2) convective and diffusive heat transfer inside the liquid to the interface (Hu and Larson 2006; Bouchenna et al. 2015); 3) the transfer of molecules across the liquid-gas interface (through the Knudsen layer, Gatapova et al. 2017); 4) the convective and diffusive transport of heat and vapor in the surrounding gas (Carle et al. 2013); 5) diffusive heat transfer in the substrate (Dunn et al. 2009; Sobac and Brutin 2012; Saada et al. 2013; Bouchenna et al. 2017). It should be noted that the flow pattern inside the drop is resulting from the competition of the following three effects: 1) the radial flow caused by

✉ A. L. Karchevsky
karchevs@math.nsc.ru

[1] Novosibirsk State University, Novosibirsk 630090, Russia

[2] Kutateladze Institute of Thermophysics SB RAS, Novosibirsk 630090, Russia

[3] Novosibirsk State Technical University, Novosibirsk 630073, Russia

[4] Nikolaev Institution of Inorganic Chemistry SB RAS, Novosibirsk 630090, Russia

the liquid loss at the gas-liquid solid contact line (CL); 2) the thermo-capillary flow resulting from the surface tension gradient due to temperature variation at the gas-liquid interphase; 3) the flow induced by the thermal buoyancy due to variation of liquid density with temperature. The flow inside the drop may lose stability and even more complicated patterns may appear (Brutin et al. 2011a, b).

The published literature shows that the processes on the sides of the drop near the contact line gas-liquid solid play an important role for sessile drop evaporation, internal fluid flow and external gas-vapor mixture flow and drop spreading (Sobac and Brutin 2011; Kabov et al. 2018). The ring-shaped stains that remain after the complete evaporation of the drop with some micro-particles can be one of example. Deegan et al. (2000) explained the particle deposition by the effect of an outward radial flow due to the high evaporation near the contact line. Dhavaleswarapu et al. (2010) have found using microparticle image velocimetry that the velocity increases as the contact line is approaching. Fig. 1 shows a schematic of heat transfer at sessile drop evaporation. We may conclude that the problem of heat transfer at sessile drop evaporation is quite complicated for the numerical and mathematical modelling. It is especially true if evaporation takes place on a textured surface or surface with micro or nanocoating, where in a very general case the thermal conductivity of the attached layer to the solid interphase in the same way as for nanoparticles (Dmitriev 2015). In some cases, a remarkable contribution to thermal resistance of the liquid-solid interface can be made by Kapitza thermal resistance (Ge et al. 2006). It is important to mention that the thermal resistance of the liquid-solid interphase and thermal resistance in the Knudsen layer became significant at low pressure and for the very last stage of the drop evaporation when the geometrical parameters of the drops became microns or even hundreds of nanometers (Gatapova et al. 2018).

A several theoretical models are existing, which take into account: surface tension, evaporation, thermocapillarity, gravity, disjoining pressure and heat conduction in the solid substrate (Sodtke et al. 2008). This paper proposes a new tool to study heat and mass transfer processes in the area of the air-liquid-solid contact line and a meniscus. Currently, the heat and mass transfer processes in the area of the contact line are not completely understood because of its small size and a limited set of applied research methods (Ajaev and Kabov 2017). In the number of physical models, it is expected that the entire solid surface can be covered by a submicron adsorbed film with a thickness on the order of 10 nm (Potash and Wayner 1972; Panchamgam et al. 2008). In this case the air-liquid-solid contact line is a transition region from a macroscale shape of the liquid (meniscus) to the adsorbed film. The contact line area is often called 'microregion', especially in the context of boiling, or 'apparent contact line region'. The challenges in modeling of contact line phenomena have to do with the fact that several physical effects such as evaporation, viscous flow, surface tension, thermocapillary stresses, London-van der Waals forces, disjoining pressure, non-equilibrium effects in the Knudsen layer near the gas-liquid interphase (Polikarpov et al., 2019) are coupled together and all signifficant in this highly localized region. This leads to difficulties in both mathematical modeling and design of experiments. A configuration of the local view of the transition region between an adsorbed film and the macroscale meniscus sketched in Fig. 2. The contact line is characterized by an enhanced heat transfer coefficient that was confirmed by Stephan and Brandt (2004). The use of this effect can be a promising solution to design new cooling systems (Stephan and Busse 1992; Kabov et al. 2017).

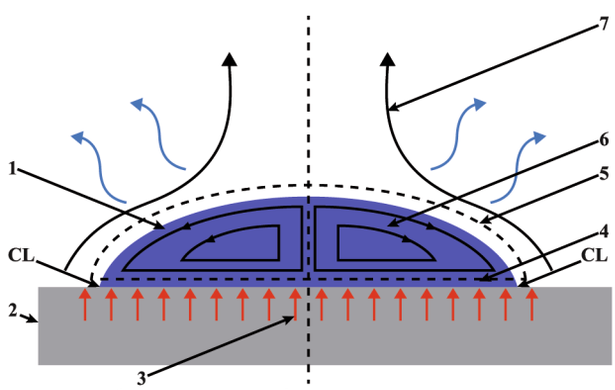

Fig. 1 A schematic of heat transfer at sessile drop evaporation: (1) – evaporated sessile liquid drop, (2) – sapphire substrate, (3) – diffusive heat transfer in the substrate, (4) – the Kapitza thermal resistance, (5) – the Knudsen layer, (6) – convective and diffusive heat transfer, (7) – the convective and diffusive transport of heat and vapor in the surrounding gas, (CL) – the gas-liquid solid contact line

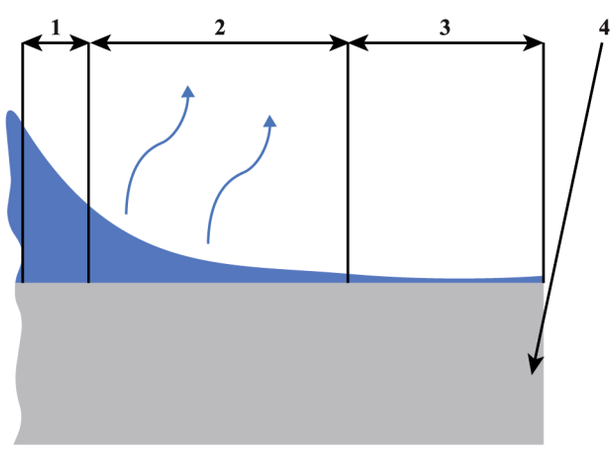

Fig. 2 A sketch of the local view of the transition region between an adsorbed film (3) and the macroscale meniscus (1) with microregion (2), i.e. the gas-liquid solid contact line, (4) – substrate

There are several techniques to determine the heat flux in the contact line area of evaporating drops, rivulets and meniscus: one of these techniques is the method based on the use of special paint, sensitive to temperature (temperature-sensitive paints (TSP)). In the work of Schweizer and Stephan (2009), the distribution of heat flux in the region of the vapor bubble at pool boiling is investigated during parabolic flights. Using this method, Jo et al. (2019) investigated the distribution of temperature and heat flux in a pulsating heat pipe. The advantages of this method are non-contact measurements (i.e. thermocouples and heat flow sensors are not used), the ability to observe the temperature distribution for a large area and with good resolution, the low time delay (i.e. the method can be used for fast processes). The disadvantage of using this method is the degradation of paint over time and certain temperature restrictions (80^oC).

Another method to determine the heat flux in the contact line area of a liquid drop on the heated surface is the heated-thin-foil technique. This method, used to determine the heat flux density based on wall surface temperature measurements using infrared thermography, is described in detail in Carlomagno and De Luca (1989), Astarita et al. (2000), Carlomagno and Cardone (2010). In the work of Gibbons et al. (2018) the temperature distribution on the foil side opposite to the drop is filmed using an IR camera. The heat flux is determined for each element of the image using the energy balance. The authors showed the local increase in the heat flux in the contact line area.

The thin metallic foil method is used to determine length and thickness of the liquid microlayer during dewetting of FC-72 liquid in meniscus (Schweikert et al. 2019a). Several instabilities have been observed in contact line: droplets formation, dry area formation, thinning and breakup. A heat flux in a liquid meniscus is determined by IR measurements of temperature distribution in CaF_2 glass heated by 500 nanometers chromium coating (Schweikert et al. 2019b). It was demonstrated that in microlayer evaporation regime, the local heat flux in the contact line region is highest for short microlayers and slowly decreases as the microlayer length grows. The heated-thin-foil technique was improved in the works of Karchevsky (2013) and Karchevsky et al. (2016) for the study of stationary transfer processes. This technique has been successfully applied in several works (Marchuk et al. 2015; Cheverda et al. 2016; Cheverda and Karchevsky 2016; Cheverda et al. 2017) to study the heat flux in the contact line area of a liquid drop situated on a horizontally heated foil, as well as to study the heat flux in the contact line area of a flowing rivulet on a vertical heated thin foil. In both cases, the authors revealed a local increase in the heat flux in the contact line area. In the work of Karchevsky (2018), it was shown how heated-thin-foil technique can be applied for measurements in non-stationary transfer processes.

In the above works, when studying stationary transport processes, the problem of determining the heat flux was reduced mathematically to solving the Cauchy problem for the Laplace equation, while in the case of non-stationary processes - to solving the problem of thermal conductivity with data on the timelike boundary. In both cases, the problems are incorrect and require special methods of solving. Incorrectness manifests itself in the fact that the presence of even small errors in the measured data can lead to great errors in the solution. A small sickness of the heated foil helps to minimalize these errors.

The axisymmetric method is used to determine the heat flux and temperature distributions in sapphire plate for high substrate temperature (high speed of drop evaporation-non-stationary problem) (Chaze et al. 2019). This method is approved for water drop impact to the sapphire plate. The heat flux is reconstructed for all steps of drop impact and it can be noted that the heat flux is higher close to the edges of the drop, due to the fact that the cooling has started earlier in the central region of the impact. The authors do not take into account differences in heat conductive coefficient for different directions (23.1 W/m K along the *C*-axis and 25.2 W/m K along the *C*-axis).

In this paper, a new method is proposed for determining the heat flux density in the air-liquid-solid contact line area. The essence of this method is that instead of a thin foil, sapphire glass is used. The transparency of the glass allows measuring the temperature exactly on the surface where the liquid drop is located, rather than on the opposite side, as in the thin foil method. In this case, to solve the thermal conductivity problem, we get the correct problem. The next chapters provide the description of the experimental setup as well as the formulas derived to solve the mathematical problem.

An understanding of the physical processes occurring in an evaporating drop of liquid will be used in further analysis of the experimental data on the dynamics and heat transfer of a liquid drop under weightlessness (ARLES experiment of the European Space Agency). The Maser rocket with several experiments on board (including a drop of liquid) launched to a height of 245 km and fell down (Lappa 2004). The time of zero gravity was about 6 minutes. In the ARLES experiment (June 2019) during zero gravity, hydrodynamics and heat transfer in an evaporating drop were studied. The proposed method and obtained results may be useful in the future, for another experiment of the European Space Agency on-board the International Space Station. The “Drop Evaporation” experiment intends to study evaporating sessile drops of pure fluids as well as binary mixtures with or without an electrical field including instabilities occurring in the drop. Before, it was investigated liquid drop (deionized water, FC-72, HFE-7100) formation and dynamics during parabolic flights (Kabov and Zaitsev 2013). It is

demonstrated that it is possible to create sessile liquid drop with low surface tension during low gravity experiment and gravity force is one of the major factor for contact angle (Brutin et al. 2009).

Experiment

The experimental part of this study includes the evaporation of a liquid drop on a substrate. A schematic diagram illustrating the experimental setup is presented in Fig. 3.

Sapphire glass of a rectangular shape ($40 \times 40\,\mathrm{mm}^2$) with the thickness of 6.4 mm is fixed in the water heat exchanger made of aluminum (see Fig. 3). The upper part of the sapphire glass is coated with a high heat-resistant black graphite paint (Graphit 33), which is a non-transparent for visual and IR-rays.

The procedure for paint coating is tested several times to obtain a quite uniform coating with the thickness about 5-10 μm. To study this coating by electron microscopy (JEOL 6700F) silicon wafer has been used (Fig. 4). The surface of the coating is represented by layered grains up to several micrometers in size. The average thickness of paint is also measured (Fig. 4b) and it is about 8.5 μm. An elemental composition of this paint on the silicon substrate is determined by X-ray energy dispersive spectroscopy (Fig. 4c) and it consists of carbon with a small amount of oxygen. The signal of Si is due to the silicon wafer and it is not taken into account.

The heat exchanger, which is used for thermal stabilization of the substrate, is connected to the thermostat LOIP. The thermostat sets the correct temperature. Thus, the boundary condition of temperature constancy on the lateral surfaces is realized for the sapphire substrate. A drop of liquid is placed on the top of this coating after the sapphire heating process has stabilized, i.e. the sapphire crystal temperature becomes equilibrium. To generate the desired drop on the substrate a programmable syringe pump Cole-Parmer EW-74905-54 is used.

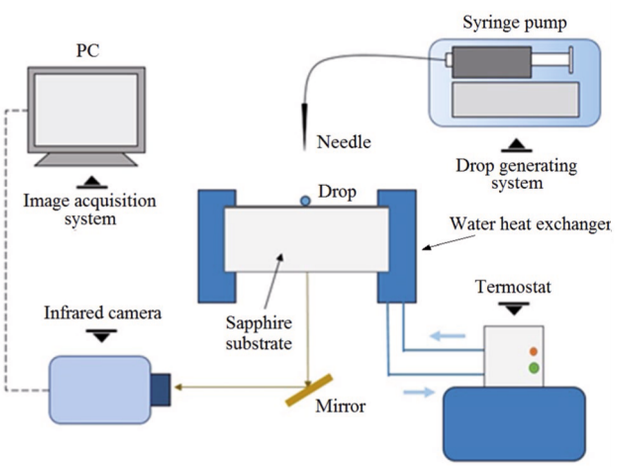

Fig. 3 Schematic diagram illustrating the experimental setup

The coating temperature is measured using a Titanium 570M infrared scanner and a gold-plated mirror. Sapphire is transparent in the working optical range of the used IR-camera (3.7-4.8 μm). Therefore, using the IR-scanner, the temperature distribution on the surface of the sapphire glass where the liquid drop is located can be measured. The resolution of IR-scanner in experiments is 640×512 pixels, scanning frequency is 50 Hz, and temperature resolution is 0.1 K. A small mirror is mounted below the heat exchanger with the sapphire glass. The infrared camera picks the infrared rays from the bottom surface of the substrate reflected from the mirror. The temperature and humidity of the ambient air are measured using the Testo 646 multimeter.

An ultra-purified water, obtained with the help of the Milli-Q system is used as a working liquid. By the contact angle measurements system DSA-100 the advancing (Fig. 5a) and receding (Fig. 5b) contact angles for water on the sapphire substrate without the paint have been measured. The results are 95.8^o and 25.4^o, respectively. The same measurements have been done for sapphire with paint coating. As a result, the advancing angle is equal to 149.3^o (Fig. 5c) and receding angle is equal to 19.1^o (Fig. 5d).

Trial experiments on the drop evaporation were carried out. The sapphire surface temperature fields after single drop deposition were obtained using the IR-scanner. Fig. 6 presents the spread behavior of the tiny drops of $6.2\mu l$ volume over the coated sapphire substrate surface. The heat exchanger was heated with water to the temperature of 60^oC and 80^oC, respectively. At the first moment the temperature under the drop goes down but then the drop is heated to the substrate temperature and completely evaporated.

The heat transfer coefficient between the sapphire plate and the air is determined by the experimental method. To do this, the heat exchanger is heated with water to a certain temperature, and then the temperature of the glass surface is measured using an IR scanner. The heat transfer coefficient α is determined based on the measurements obtained by solving the thermal conductivity equation in the plate and heat exchange with the surrounding air. In the work of Marchuk et al. (2015), the average heat transfer coefficient 17.3 $\mathrm{W/m^2K}$ for heated thin foil was measured at relatively low heating intensities.

Mathematical Solution of the Problem

Mathematical Statement of the Problem

Consider a sapphire glass with linear dimensions: $x \in [0, A]$, $y \in [0, B]$, and $z \in [0, h]$. Denote $V = \{(0, A) \times (0, B) \times (0, h)\}$ and let W be the side surface: $W = \partial V \setminus \{z = 0\} \setminus \{z = h\}$ (see Fig. 7).

The process of heat propagation in sapphire glass is described by the thermal conductivity equation:

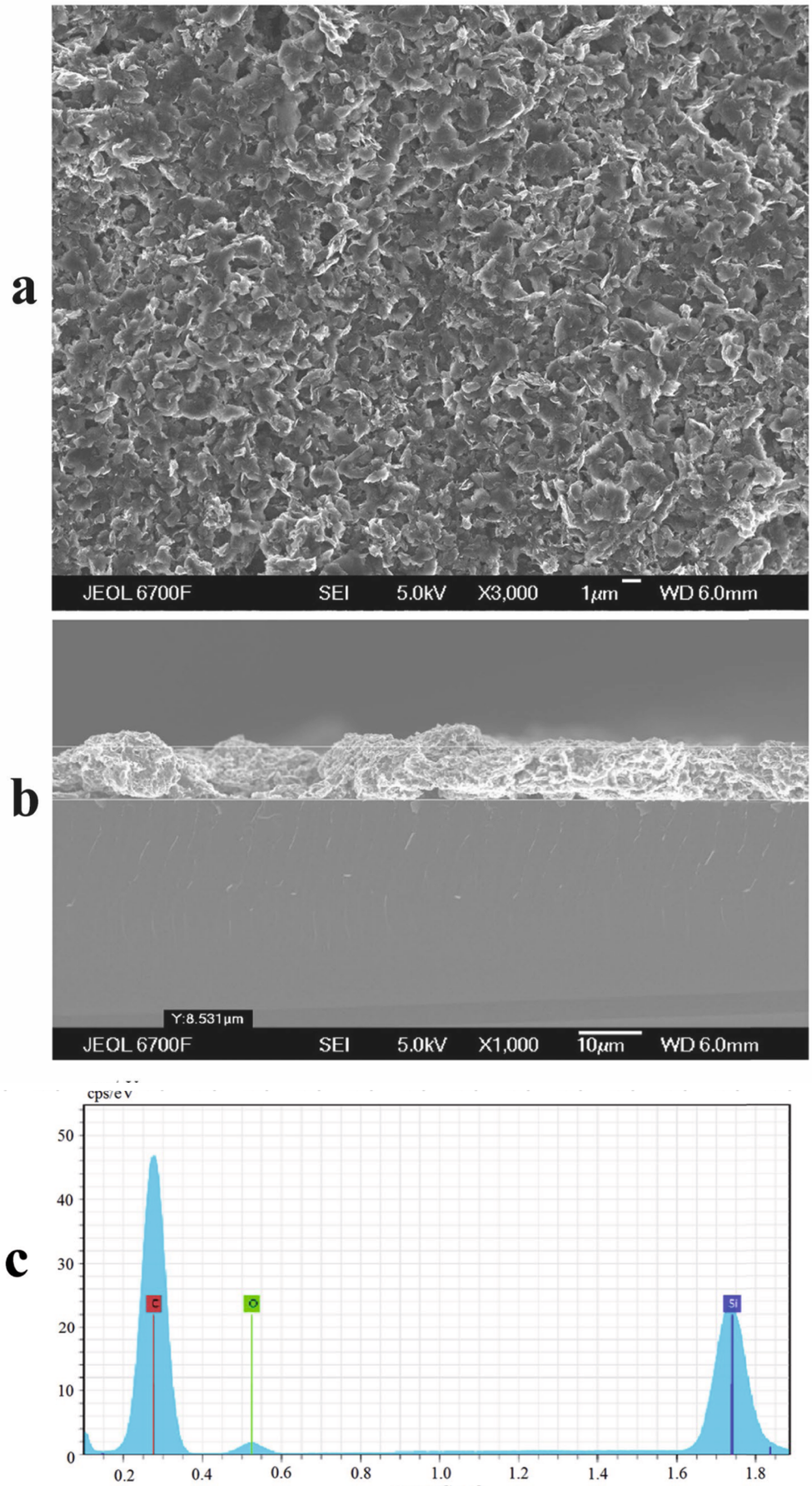

Fig. 4 The SEM-image of paint coating on silicon substrate **a**, the thickness measurement **b**, and the elemental composition of this paint **c**

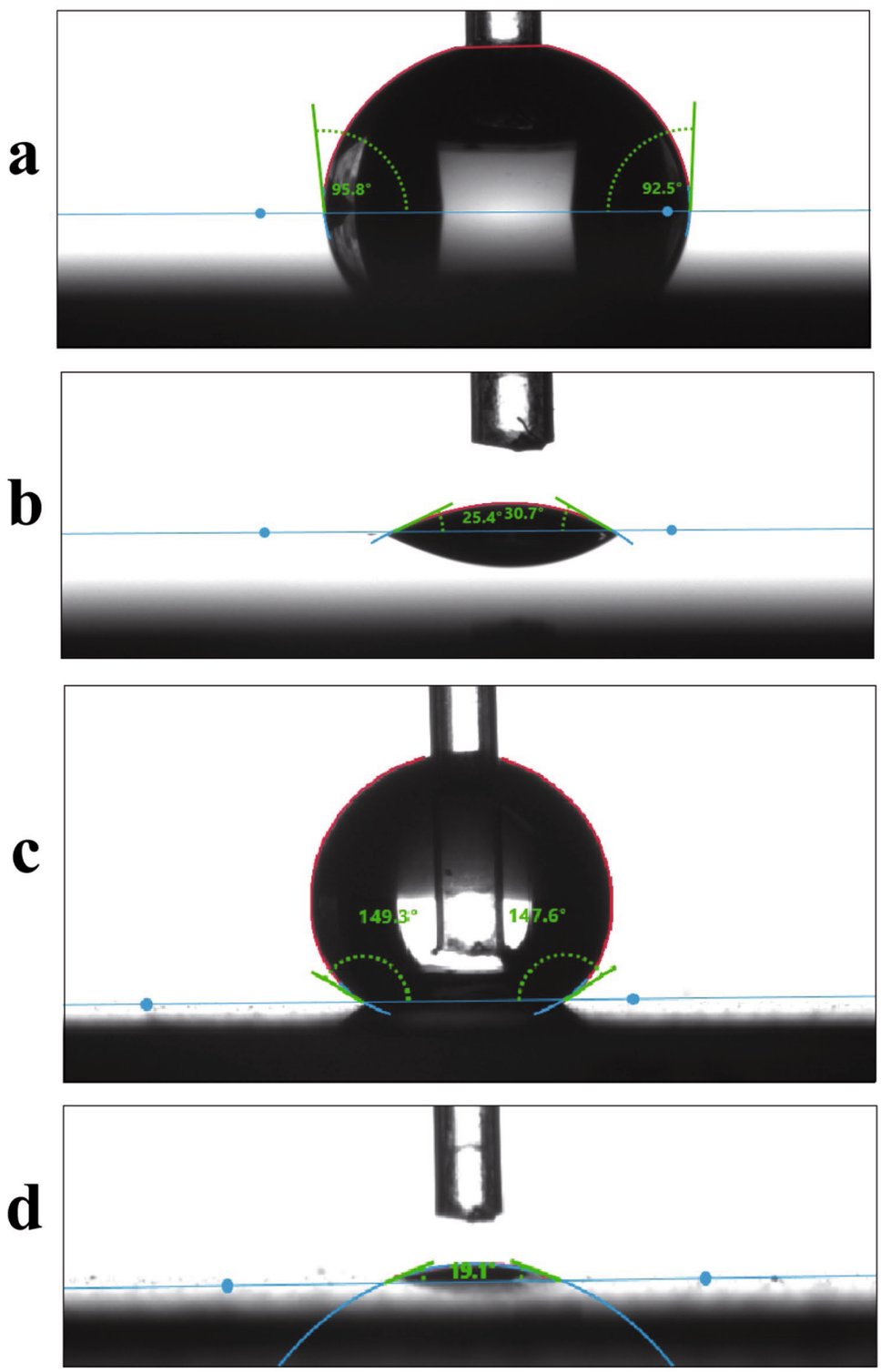

Fig. 5 The hysteresis of wettability measurements for sapphire (advancing **a** and receding **b** contact angles) and sapphire with paint (advancing **c** and receding **d** contact angles) by Kruss DSA-100 system)

$$\rho C\frac{\partial T}{\partial t} = \lambda\frac{\partial^2 T}{\partial z^2} + \lambda_0\left(\frac{\partial^2 T}{\partial x^2} + \frac{\partial^2 T}{\partial y^2}\right), \quad (x, y, z) \in V. \qquad (1)$$

Here λ is the thermal conductivity coefficient of sapphire in the direction of the C-axis, λ_0 is the thermal conductivity coefficient of sapphire perpendicular to the C-axis (we assume that the C-axis of sapphire coincides with the axis Oz), ρ is the density of sapphire, C is the heat capacity of sapphire, $k = \lambda/(\rho C)$ and $k_0 = \lambda_0/(\rho C)$ are corresponding thermal diffusivity coefficients.

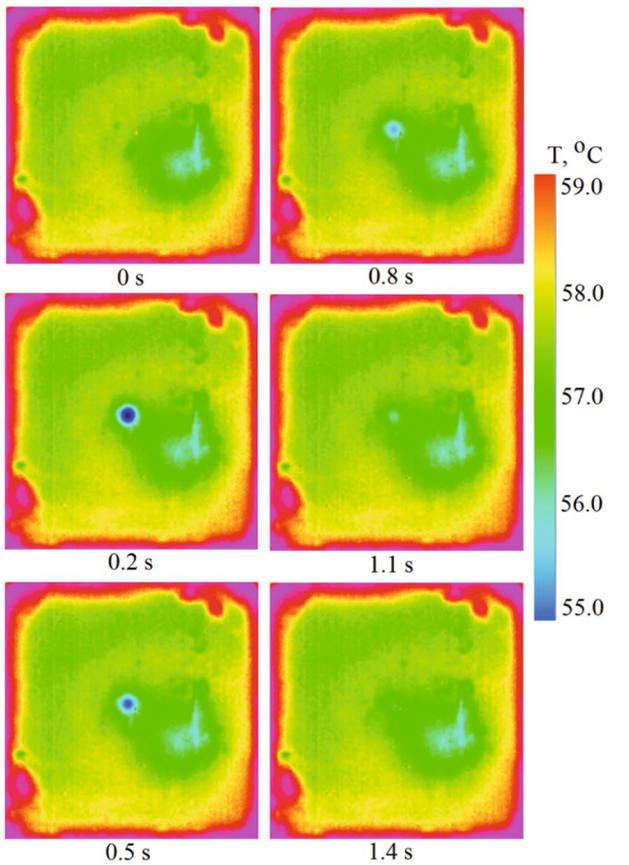

Fig. 6 Single drop evaporation over the sapphire substrate surface: sapphire substrate surface temperature before deposition of the 6.2μl volume drop is equal to 60°C, ambient temperature is equal to 27°C

The temperature is measured at the upper part of V region's boundary,

$$T|_{z=h} = T_h(x, y, t). \tag{2}$$

We consider that the convective heat flux on the lower part of V region's boundary is determined by the Newton-Richman law (Newton's law of cooling)

$$\lambda \frac{\partial T}{\partial z}\bigg|_{z=0} = \alpha\big(T|_{z=0} - T_\epsilon(x, y)\big). \tag{3}$$

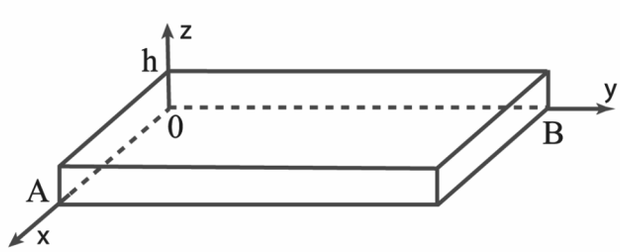

Fig. 7 Linear dimensions of sapphire glass

A constant temperature is maintained on the lateral walls of the sapphire glass

$$T|_W = T_W. \tag{4}$$

We believe that at the initial time the temperature distribution of the glass is known:

$$T|_{t=0} = \tau(x, y, z). \tag{5}$$

Here λ, λ_0, ρ, and C are considered to be known constants. The function $\tau(x, y, z)$ is the solution to the following stationary problem:

$$0 = \lambda \frac{\partial^2 \tau}{\partial z^2} + \lambda_0 \left(\frac{\partial^2 \tau}{\partial x^2} + \frac{\partial^2 \tau}{\partial y^2} \right), \tag{6}$$

$$\lambda \frac{\partial \tau}{\partial z}\bigg|_{z=0} = \alpha\big(\tau|_{z=0} - T_\epsilon(x, y)\big), \quad \tau|_{z=h} = \tau_h(x, y), \tag{7}$$

$$\tau|_W = T_W. \tag{8}$$

The function $T_\epsilon(x, y)$ has the form

$$T_\epsilon(x, y) = T_W - (T_W - T_{atm})\eta(x;A, \epsilon)\eta(y;B, \epsilon), \tag{9}$$

where

$$\eta(x;A, \epsilon) = \begin{cases} \big[1 - \cos(\pi x/\epsilon)\big]/2, & 0 \le x < \epsilon, \\ 1, & \epsilon \le x \le A - \epsilon, \\ \big[1 - \cos(\pi(A - x)/\epsilon)\big]/2, & A - \epsilon < x \le A, \end{cases}$$

here T_{atm} is the ambient temperature, the parameter ϵ is considered to be known and is set from the experiment depending on design of the aluminum heat exchanger.

It is necessary to define the flux

$$Q(x, y, t) = \lambda \frac{\partial T}{\partial z}\bigg|_{z=h}. \tag{10}$$

The convective heat transfer coefficient for a horizontal plate was experimentally measured in Marchuk et al. (2015) and averaged $\alpha = 17.3$ W/m^{2}K. In the numerical calculations of equations (1)-(5) using experimental data, it is assumed to use this value of the convective heat transfer coefficient. Additionally, numerical calculations will be performed for the heat transfer coefficients $\alpha \pm 10\%$ in order to evaluate the effect of the heat transfer intensity on the lower side of the sapphire plate on the accuracy of determining the heat flux density. It should be noted that this effect is assumed to be insignificant due to the rather large thickness of the sapphire plate and the significantly higher thermal conductivity of sapphire as compared to air.

We should explain why we chose T_ϵ in the form (9). It is easy to see that on the lower and upper edges of the

rectangular area (see Fig. 7) $\partial T/\partial z = 0$. This means that the value of $T|_{z=0} - T_\epsilon(x, y)$ and $\tau|_{z=0} - T_\epsilon(x, y)$ at these points are equal to zero. Therefore, to match the values on the edges, the function T_ϵ was chosen, where the function $\eta(x;A, \epsilon)$ is shown in Fig. 8.

Perhaps such a choice of the boundary condition does not exactly reflect the behavior of functions on the boundary. On the other hand, it is well known that for elliptic and parabolic equations, the differences in the behavior of functions on the boundary quickly disappear with distance from the boundary (Tikhonov and Samarskii 1977, Pinchover and Rubinstein 2005). An important convenience for the numerical algorithm is that we have simple expansions in Fourier series. To determine the α and ϵ parameters, a procedure is proposed in the next paragraph.

Experimental Determination of the α and ϵ Parameters

Consider a stationary process that is described by the following differential equation:

$$0 = \lambda \frac{\partial^2 \tilde{\tau}}{\partial z^2} + \lambda_0 \left(\frac{\partial^2 \tilde{\tau}}{\partial x^2} + \frac{\partial^2 \tilde{\tau}}{\partial y^2} \right). \tag{11}$$

On the upper surface of the glass, the temperature can be measured

$$\tilde{\tau}|_{z=h} = \tau_h(x, y). \tag{12}$$

Let's assume that the temperature on the lower side of the glass is the same

$$\tilde{\tau}|_{z=0} = \tau_h(x, y). \tag{13}$$

On the side surface

$$\tilde{\tau}|_W = T_W. \tag{14}$$

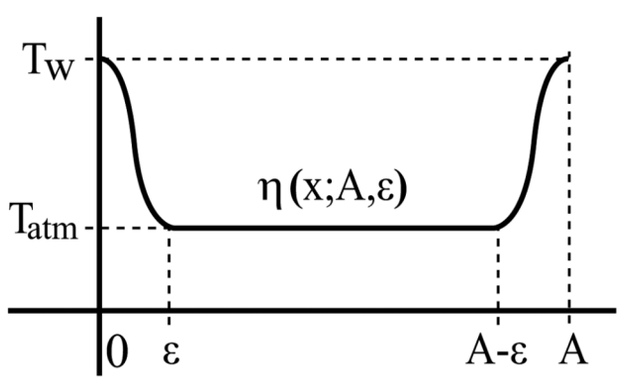

Fig. 8 Function $\eta(x;A, \epsilon)$

The solution of the stationary problem (11)-(14) is represented as the sum $\tilde{\tau}(x, y, z) = T_W + w(x, y, z)$.

The function $w(x, y, z)$ can be represented as a series

$$w(x, y, z) = \sum_{k,n=1}^{\infty} w_{kn}(z) \sin(\nu_{xk} x) \sin(\nu_{yn} y),$$

$$[-2mm] \nu_{xk} = k\pi/A, \quad \nu_{yn} = n\pi/B.$$

Here function $w_{kn}(z)$ is a solution to the problem:

$$\frac{\partial^2 w_{kn}}{\partial z^2} = (l\nu_{kn})^2 w_{kn}, \quad w_{kn}(0) = \phi_{kn}, \quad w_{kn}(h) = \phi_{kn}, \tag{15}$$

where $l = \sqrt{\lambda_0/\lambda}$, $\nu_{kn} = \sqrt{\nu_{xk}^2 + \nu_{yn}^2}$, and ϕ_{kn} is the Fourier series expansion coefficient of the function $\phi(x, y) = \tau_h(x, y) - T_W$.

Easy to obtain

$$w_{kn}(z) = \frac{\phi_{kn}}{1 + e^{-l\nu_{kn} h}} \left(e^{l\nu_{kn}(z-h)} + e^{-l\nu_{kn} z} \right),$$

whence it follows that

$$W_{kn} \equiv \lambda \left. \frac{\partial w_{kh}}{\partial z} \right|_{z=0} = -\sqrt{\lambda_0 \lambda}\, \phi_{kn} \nu_{kn} \frac{1 - e^{-l\nu_{kn} h}}{1 + e^{-l\nu_{kn} h}}$$

and

$$q(x, y) \equiv \lambda \left. \frac{\partial \tilde{\tau}}{\partial z} \right|_{z=0} = \sum_{k,n=1}^{\infty} W_{kn} \sin(\nu_{xk} x) \sin(\nu_{yn} y). \tag{16}$$

Constants α and ϵ can be determined from solving the minimization problem:

$$J[\alpha, \epsilon] \equiv \int_0^A \int_0^B \left[q(x, y) - \alpha \left(\tau_h(x, y) - T_\epsilon(x, y) \right) \right]^2 \mathrm{d}y\mathrm{d}x \tag{17}$$

$$\rightarrow \min.$$

If $min\, J[\alpha, \epsilon] = 0$, then the problems (6)-(8) and (11)-(14) are equivalent, if not, then the value of $min\, J[\alpha, \epsilon]$ will be an indicator of their nonequivalence.

The Solution of the Stationary Poblem (6)-(8)

The solution of the stationary problem (6)-(8) is represented as the sum $\tau(x, y, z) = T_W + u(x, y, z)$.

The function $u(x, y, z)$ can be represented as a series

$$u(x, y, z) = \sum_{k,n=1}^{\infty} u_{kn}(z) \sin(\nu_{xk} x) \sin(\nu_{yn} y),$$

Here function $u_{kn}(z)$ is a solution to the problem:

$$\frac{\partial^2 u_{kn}}{\partial z^2} = (l\nu_{kn})^2 u_{kn}, \tag{18}$$

$$[-2mm] u'_{kn}(0) = -\gamma(u_{kn}(0) + \vartheta_{kn}), \quad u_{kn}(h) = \phi_{kn},$$

where $\gamma = \alpha/\lambda$, ϑ_{kn} is the Fourier series expansion coefficient of the function $\vartheta(x, y) = T_W - T_e(x, y)$.

The solution to the problem (18) can be obtained in the following form:

$$\begin{aligned} u_{kn}(z) =& \frac{(l\nu_{kn}-\gamma)\phi_{kn} - \vartheta_{kn}\mathrm{e}^{-l\nu_{kn}h}}{(l\nu_{kn}-\gamma) + (l\nu_{kn}+\gamma)\mathrm{e}^{-l\nu_{kn}h}}\mathrm{e}^{l\nu_{kn}(z-h)} \\ &+ \frac{(l\nu_{kn}+\gamma)\phi_{kn}\mathrm{e}^{-l\nu_{kn}h} + \vartheta_{kn}}{(l\nu_{kn}-\gamma) + (l\nu_{kn}+\gamma)\mathrm{e}^{-l\nu_{kn}h}}\mathrm{e}^{-l\nu_{kn}z}. \end{aligned} \tag{19}$$

The Solution of the Nonstationary Problem (1)-(4)

The solution to the stationary problem (1)-(4) is represented as the sum $T(x, y, z, t) = T_W + u(x, y, z) + v(x, y, z, t)$.

The function $v(x, y, z, t)$ satisfies the following setting of a problem

$$\rho C\frac{\partial v}{\partial t} = \lambda\frac{\partial^2 v}{\partial z^2} + \lambda_0\left(\frac{\partial^2 v}{\partial x^2} + \frac{\partial^2 v}{\partial y^2}\right), \tag{20}$$

$$\lambda\frac{\partial v}{\partial z}\bigg|_{z=0} = \alpha v|_{z=0}, \quad v|_{z=h} = \psi(x, y, t), \tag{21}$$

$$v|_W = 0, \tag{22}$$

$$v|_{t=0} = 0, \tag{23}$$

where $\psi(x, y, t) = T_h(x, y, t) - T_W - \phi(x, y)$, and the matching conditions $\psi|_{t=0} = 0$ are true. The function $v(x, y, z, t)$ can be represented as a series

$$v(x, y, z, t) = \sum_{k,n=1}^{\infty} v_{kn}(z, t)\sin(\nu_{xk}x)\sin(\nu_{yn}y).$$

Here function $v_{kn}(z, t)$ is a solution to the problem:

$$\rho C\frac{\partial v_{kn}}{\partial t} = \lambda\frac{\partial^2 v_{kn}}{\partial z^2} - \lambda_0\nu_{kn}^2 v_{kn}, \tag{24}$$

$$\lambda\frac{\partial v_{kn}}{\partial z}\bigg|_{z=0} = \alpha v_{kn}|_{z=0}, \quad v_{kn}|_{z=h} = \psi_{kn}(t), \tag{25}$$

$$v_{kn}|_{t=0} = 0. \tag{26}$$

Let $\hat{v}_{kn}(z, p)$ be the Laplace image of the function $v_{kn}(z, t)$. It is easy to see that it satisfies the problem

$$\frac{\partial^2 \hat{v}_{kn}}{\partial z^2} = \zeta_{kn}^2\hat{v}_{kn}, \ \lambda\frac{\partial \hat{v}_{kn}}{\partial z}\bigg|_{z=0} = \alpha\hat{v}_{kn}|_{z=0}, \ \hat{v}_{kn}|_{z=h} = \hat{\psi}_{kn}(p), \tag{27}$$

where $\zeta_{kn} = (1/\sqrt{k})\sqrt{p + k_0\nu_{kn}^2}$ and $\hat{\psi}_{kn}(p)$ is Laplace image of function $\psi_{kn}(t)$. The solution to the problem (26) can be obtained in the following form

$$\hat{v}(z, p) = \frac{(\zeta_{kn}-\gamma)\mathrm{e}^{\zeta_{kn}z} + (\zeta_{kn}+\gamma)\mathrm{e}^{-\zeta_{kn}z}}{(\zeta_{kn}-\gamma)\mathrm{e}^{\zeta_{kn}h} + (\zeta_{kn}+\gamma)\mathrm{e}^{-\zeta_{kn}h}}\hat{\psi}_{kn}(p). \tag{28}$$

The Expression for the Flux at the Surface $\{z = h\}$

To calculate the flux on the surface $\{z = h\}$, we use the obtained equations (19) and (28).

Denote $Q_{kn}^0 = \lambda\dfrac{\partial u_{kn}}{\partial z}\bigg|_{z=h}$. From (19) it follows

$$\begin{aligned} Q_{kn}^0 =& \sqrt{\lambda\lambda_0}\nu_{kn}\left[\frac{(l\nu_{kn}-\gamma) - (l\nu_{kn}+\gamma)\mathrm{e}^{-2hl\nu_{kn}}}{(l\nu_{kn}-\gamma) + (l\nu_{kn}+\gamma)\mathrm{e}^{-2hl\nu_{kn}}}\phi_{kn}\right. \\ &\left. - \frac{2\mathrm{e}^{-2hl\nu_{kn}}}{(l\nu_{kn}-\gamma) + (l\nu_{kn}+\gamma)\mathrm{e}^{-2hl\nu_{kn}}}\vartheta_{kn}\right]. \end{aligned} \tag{29}$$

Denote $Q_{kn}^1(p) = \lambda\dfrac{\partial \hat{v}_{kn}}{\partial z}\bigg|_{z=h}$, which is the Laplace image for the function $Q_{kn}^1(t) = \lambda\dfrac{\partial v_{kn}}{\partial z}\bigg|_{z=h}$.

From (28) it follows

$$\begin{aligned} &\left[\frac{2}{\zeta_{kn}+\gamma} - \frac{1}{\zeta_{kn}} + \frac{1}{\zeta_{kn}}\mathrm{e}^{-2h\zeta_{kn}}\right]\hat{Q}_{kn}^1 \\ =&\left[1 - \frac{2\gamma}{\zeta_{kn}+\gamma} - \mathrm{e}^{-2h\zeta_{kn}}\right]\hat{\psi}_{kn}. \end{aligned} \tag{30}$$

The following relations are known for the inverse Laplace transform (Bateman and Erdelyi, 1954)

$$\frac{1}{\sqrt{p}} \to \frac{1}{\sqrt{\pi t}}, \quad \frac{1}{\sqrt{p}+\gamma} \to \frac{1}{\sqrt{\pi t}} - \gamma\mathrm{e}^{\gamma^2 t}\mathrm{erfc}(\gamma\sqrt{t}),$$

$$\frac{1}{\sqrt{p}}\mathrm{e}^{-\alpha\sqrt{p}} \to \frac{1}{\sqrt{\pi t}}\mathrm{e}^{-\alpha^2/4t}, \quad \mathrm{e}^{-\alpha\sqrt{p}} \to \frac{\alpha}{2\sqrt{\pi t^3}}\mathrm{e}^{-\alpha^2/4t}.$$

Given these relations, we apply the inverse Laplace transform to the equality (30), and obtain

$$\begin{aligned} &\int_0^t \mathrm{e}^{-k_0\nu_{kn}^2 s}K(s)Q_{kn}^1(t-s)\mathrm{d}s \\ =&\lambda\psi_{kn}(t) - \lambda\int_0^t \mathrm{e}^{-k_0\nu_{kn}^2 s}R(s)\psi_{kn}(t-s)\mathrm{d}s, \end{aligned} \tag{31}$$

where

$$K(t)=\frac{1}{\sqrt{\pi t}}+\frac{e^{-h^2/kt}}{\sqrt{\pi t}}-\frac{2\alpha e^{\alpha^2 t/\lambda\rho C}}{\sqrt{\lambda\rho C}}\operatorname{erfc}\left(\alpha\sqrt{t}/\sqrt{\lambda\rho C}\right),$$

$$R(t)=\frac{2\alpha}{\sqrt{\lambda\rho C}}\left[\frac{1}{\sqrt{\pi t}}-\frac{\alpha e^{\alpha^2 t/\lambda\rho C}}{\sqrt{\lambda\rho C}}\operatorname{erfc}\left(\alpha\sqrt{t}/\sqrt{\lambda\rho C}\right)\right]+\frac{h}{\sqrt{k\pi t^3}}e^{-h^2/kt}.$$

The relation (31) can be considered as a Volterra integral equation of the 1st kind of convolution type to determine the functions $Q^1_{kn}(t)$ $(k,n=1,2,...)$. Due to the properties of the kernel, this integral equation cannot be reduced to the Volterra integral equation of the 2nd kind, nevertheless, there are methods to solve it (see, for example, Verlan' and Sizikov 1986; Manzhirov and Polyanin 2000; Polyanin and Manzhirov 2003; Karchevsky 2017; Karchevsky 2020). It follows from the relations (29) and (31) that the flux on the surface $(z=h)$ can be computed using the equation

$$Q(x,y,t)=\sum_{k,n=1}^{\infty}\left[Q^0_{kn}+Q^1_{kn}(t)\right]\sin(\nu_{xk}x)\sin(\nu_{yn}y). \tag{32}$$

Experimental Result (Stationary Case)

In this section, we present the result of calculating the flux (10) in the stationary case.

In the course of laboratory experiments, the following data were obtained: 1) the temperature distribution on the surface $(x,y,z=h)$, i.e. function $\tau_h(x,y)$; 2) the temperature distribution on the surface $(x,y,z=h)$ with a drop settling on it, i.e. function $T_h(x,y)$. Fig. 9a and 9b shows these functions after preprocessing: the results of measurements with "dead pixels" was removed, the functions was smoothed with a moving average over 49 points.

Temperature of heat exchanger $T_W=69^oC$, ambient temperature $T_{atm}=27^oC$, $\lambda=23.1$ W/m K, $\lambda_0=25.2$ W/m K, the diameter of the drop is around 3 mm and volume 6.1 microliters.

The problem (11)-(14) was solved (the steady state of heating of the sapphire glass was controlled by an IR-scanner and was reached approximately 1-2 minutes after heating the heat exchanger), the value $q(x,y)$ (16) was calculated and the minimization problem (17) was solved. For minimization the conjugate gradient method can be used (Polak 1971; Vasil'ev 1988), the gradient was calculated with the help of author's approach (Karchevsky 2000, 2009; Romanov and Karchevsky 2018; Dedok et al. 2019). The obtained values are $\alpha=14$ W/m^{2}K and $\epsilon=0.82$ mm.

The problem (6)-(8) has been solved (the stationary temperature distribution is achieved around 1 minute after drop placement on the sapphire surface), Fig. 9c shows the flux $Q(x,y)$ on the surface $(x,y,z=h)$, Fig. 9d presents the values of the flux on the interval $(0\le x\le A, y=B/2, z=h)$.

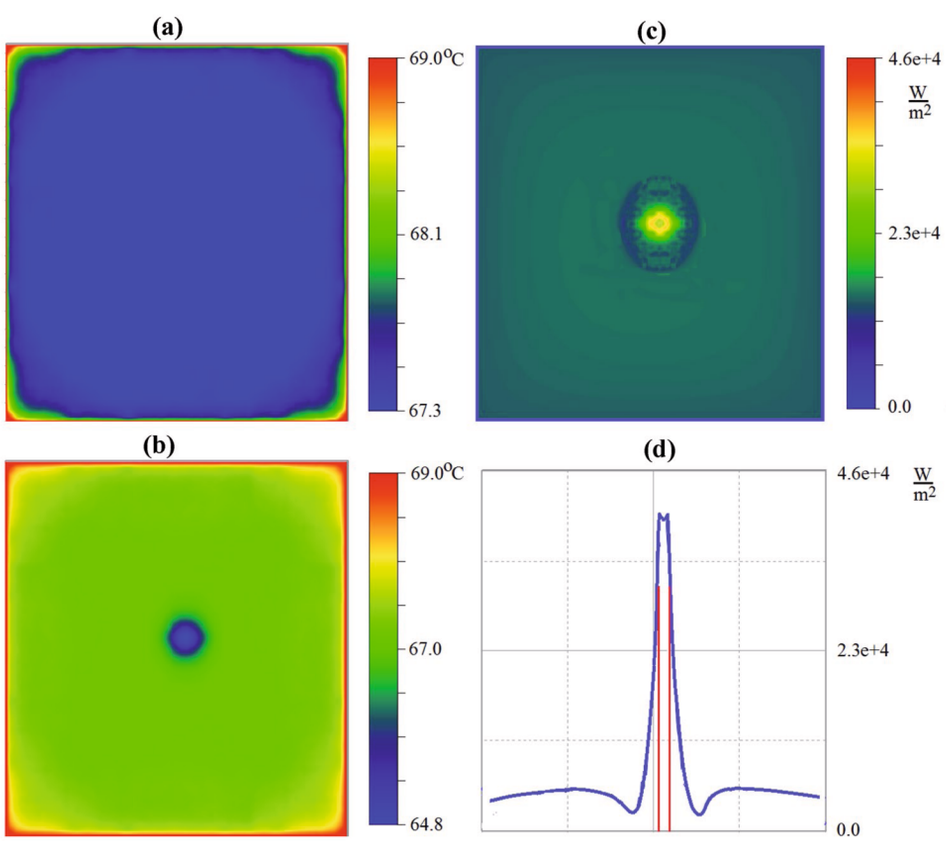

Fig. 9 **(a)** function $\tau_h(x,y)$ after preprocessing, **(b)** functions $T_h(x,y)$ after preprocessing, **(c)** calculated flux $Q(x,y)$, **(d)** value of the flux $Q(x,B/2)$, red vertical lines indicate droplet boundaries

Close to the contact line region of drop one can see the maximum of heat fluxes, this behavior of the flux corresponds to the results of the work by Karchevsky 2013, Karchevsky et al. 2016, Marchuk 2015, Cheverda et al. 2016, Cheverda and Karchevsky 2016, Cheverda et al. 2017, Cheverda et al. 2018. The Fig. 9c and 9d show that a decrease in the heat flux density is observed near the droplet. This is explained by the cooling of the sapphire surface near the drop and, consequently, by a decrease in heat transfer to the surrounding space.

Conclusions

The paper presents a new tool "the method of IR transparent thick plate" that can be used to study the heat and mass transfer processes in the air-liquid-solid contact line area and some preliminary experimental results. Its distinctive feature as compared to the previously known methods is the solution of the initial-boundary problem for the heat conductivity equation, which in terms of mathematics is a correct problem. For example, the method to determine heat transfer in contact line for thin metallic foil is based on solving the Cauchy problem for the Laplace equation in this case the problem is incorrect. The experimental part of the study includes the evaporation of a liquid drop on a sapphire substrate. The upper part of the sapphire glass is coated with a high heat-resistant black graphite paint (Graphit 33), which is a non-transparent for visual and IR-rays. Measurements of various physical, chemical and geometrical properties of this coating have been done by electron microscopy and other techniques. Trial experiments on the drop evaporation were carried out. The sapphire surface temperature fields after single drop deposition were obtained using the IR-scanner. The solution of the nonstationary heat transfer problem in the sapphire glass has been performed and the mathematical expressions for the heat flux determination at the surface where the drop evaporation take place have been provided. The experimental local heat flux distribution at drop evaporation on the sapphire surface with two small local highs close to the contact line regions has been measured. This behavior of the heat flux distribution well corresponds to the results previously published in the literature. This new method with sapphire glass plate will help to understand heat transfer mechanism in contact line of liquid-solid-gas interface. It can be used to postprocess experimental data for future space experiments with heat transfer in contact line.

Acknowledgements The work is supported by the Russian Science Foundation (No. 18-19-00538). Measurement of the limiting wetting angle of the substrate is performed in the framework of the state assignment of the Kutateladze Institute of Thermophysivs SB RAS. Measurement by electron microscopy JEOL 6700F is performed in the framework of the state assignment of the Nikolaev Institute of Inorganic Chemistry SB RAS.

Declarations

Conflicts of Interest The authors declare that they have no conflict of interest.

References

Ajaev, V.S., Kabov, O.A.: Heat and mass transfer near contact lines on heated surfaces. Int. J. Heat Mass. Tran. **108**, 918–932 (2017)

Astarita, T., Cardone, G., Carlomagno, G.M., Meola, C.: A survey on infrared thermography for convective heat transfer measurements. Opt. Laser Technol. **32**, 593–610 (2000)

Bateman, H., Erdelyi, A.: Tables of Integral Transforms, vol. 1. McGraw-Hill Book Co., New York (1954)

Bouchenna, C.H., Saada, M.A., Chikh, S., Tadrist, L.: Investigation of Thermo-Capillary Flow Inside an Evaporating Pinned Water Droplet. Interfacial Phenom. Heat Transf. **3**, 185–201 (2015)

Bouchenna, C.H., Saada, M.A., Chikh, S., Tadrist, L.: Generalized formulation for evaporation rate and flow pattern prediction inside an evaporating pinned sessile drop. Int. J. Heat Mass. Tran. **109**, 482–500 (2017)

Brutin, D., Zhu, Z., Rahli, O., Xie, J., Liu, Q., Tadrist, L.: Sessile Drop in Microgravity: Creation, Contact Angle and Interface. Microgravity Sci. Technol. **21**, 67–76 (2009)

Brutin, D., Sobac, B., Rigollet, F., Le Niliot, C.: Infrared visualization of thermal motion inside a sessile drop deposited onto a heated surface. Exp. Thermal Fluid Sci. **35**, 521-530 (2011a)

Brutin, D., Sobac, B., Loquet, B., Sampol, J.: Pattern Formation in Drying Drops of Blood. J. Fluid Mech. **667**, 85-95 (2011b)

Carle, F., Sobac, B., Brutin, D.: Experimental Evidence of the Atmospheric Convective Transport Contribution to Sessile Droplet Evaporation. Appl. Phys. Lett. **102**, 061603 (2013)

Carlomagno, G.M., Cardone, G.: Infrared thermography for convective heat transfer measurements. Exp. Fluids **49**, 1187–1218 (2010)

Carlomagno, G.M., De Luca, L.: Infrared thermography in heat transfer. Handbook of Flow Visualization, Ed. Hemisphere, London, Chapter **32**, 531–553 (1989)

Cazabat, A.M., Guéna, G.: Evaporation of macroscopic sessile droplets. Soft Matter **6**, 2591–2612 (2010)

Chaze, W., Caballina, O., Castanet, G., Pierson, J.F., Lemoine, F., Maillet, D.: Heat flux reconstruction by inversion of experimental infrared temperature measurements - Application to the impact of a droplet in the film boiling regime, Int. J. Heat Mass. Tran. **128**, 469–478 (2019)

Cheverda, V.V., Marchuk, I.V., Karchevsky, A.L., Orlik, E.V., Kabov, O.A.: Experimental investigation of heat transfer in a rivulet on the inclined foil. Thermophys. Aeromechanics **23**, 415–420 (2016)

Cheverda, V., Karchevsky, A.: The heat flux near the contact line of the droplets on the heated foil, MATEC Web of Conf. **84**, 00007 (2016)

Cheverda, V.V., Karchevsky, A.L., Marchuk, I.V., Kabov, O.A.: Heat flux density in the region of droplet contact line on a horizontal surface of a thin heated foil. Thermophys. Aeromechanics **24**, 803–806 (2017)

Cheverda V.V., Ponomarenko T.G., Karchevsky A.L., Kabov O.A.: Heat flux density measurements in the contact line of the heated sessile droplet/falling down liquid rivulet, Int. Heat Transfer Conf. 6633–6640 (2018)

Dedok, V.A., Karchevsky, A.L., Romanov, V.G.: A Numerical Method of Determining Permittivity from the Modulus of the Electric Intensity Vector of an Electromagnetic Field. J. Ind. Appl. Math. **13**, 436–446 (2019)

Deegan, R.D., Bakajin, O., Dupont, T.F., Huber, G., Nagel, R.S.: Contact line deposits in an evaporating drop. Phys. Rev. E **62**, 756–765 (2000)

Dhavaleswarapu, H.K., Migliaccio, Ch.P., Garimalla, S.V., Murthy, J.Y.: Experimental investigation of evaporation from low contact angle sessile drops. Langmuir **26**, 880–888 (2010)

Dmitriev, A.S.: Introduction to nano-thermal physics. Moskow, BINOM, Laboratory of Knowledge (2015)

Dunn, G., Wilson, S., Duffy, B., David, S., Sefiane, K.: The strong influence of substrate conductivity on droplet evaporation. J. Fluid Mech. **623**, 329–351 (2009)

Erbil, H.Y.: Evaporation of pure liquid sessile and spherical suspended drops: a review. Adv. Colloid Interface Sci. **170**, 67–86 (2012)

Gatapova, E.Y., Graur, I.A., Kabov, O.A., Aniskin, V.M., Filipenko, M.A., Sharipov, F., Tadrist, L.: The temperature jump at water - air interface during evaporation. Int. J. Heat Mass. Tran. **104**, 800–812 (2017)

Gatapova, E.Y., Shonina, A.M., Safonov, A.I., Sulyaeva, V.S., Kabov, O.A.: Evaporation dynamics of a sessile droplet on glass surfaces with fluoropolymer coatings: focusing on the final stage of thin droplet evaporation. Soft Matter **14**, 1811–1821 (2018). https://doi.org/10.1039/c7sm02192e

Ge Z.B., Cahill D.G., Braun P.V.: Thermal Conductance of Hydrophilicand HydrophobicInterfaces. Phys. Rev. Lett. **96**, 186101 (2006)

Gibbons, M., Di Marco, P., Robinson, A.J.: Local heat transfer to an evaporating superhydrophobic droplet. Int. J. Heat Mass. Tran. **121**, 641–652 (2018)

Hu, H., Larson, R.G.: Marangoni effect reverses coffee-ring depositions. J. Phys. Chem. B **110**, 7090–7094 (2006)

Jo, J., Kim, J., Kim, S.J.: Experimental investigations of heat transfer mechanisms of a pulsating heat pipe. Energy Convers. Manag. **181**, 331–341 (2019)

Kabov, O.A., Zaitsev, D.V., Kirichenko, D.P., Ajaev, V.S.: Interaction of Levitating Microdroplets with Moist Air Flow in the Contact Line Region. Nanoscale Microscale Thermophys. Eng. **21**, 60–69 (2017)

Kabov, O.A., Gatapova, E.Y., Semenov, A.A., Jutley, M., Ajaev, V.V., Kirichenko, E.O., Feoktistov, D.V., Kuznetsov, G.V., Zaitsev, D.V.: Experimental and Numerical Studies of Evaporation of a Sessile Water Drop on a Heated Conductive Substrate. Interfacial Phenom. Heat Transf. **6**, 421–435 (2018)

Kabov, O.A., Zaitsev, D.V.: The effect of wetting hysteresis on drop spreading under gravity. Dokl. Phys. **58**, 292–295 (2013)

Karchevsky, A.L.: Numerical Solution to the One-Dimensional Inverse Problem for an Elastic System. Doklady **375**, 235–238 (2000)

Karchevsky A.L., Simultaneous reconstruction of permittivity and conductivity, J. Inverse Ill-Posed Probl. **17**, 385-402 (2009)

Karchevsky, A.L.: Reformulation of an inverse problem statement that reduces computational costs. Eurasian J. Math. Comput. Appl. **1**, 4–20 (2013)

Karchevsky, A.L., Marchuk, I.V., Kabov, O.A.: Calculation of the heat flux near the liquid-gas-solid contact line. Appl. Math. Model. **40**, 1029–1037 (2016)

Karchevsky, A.L.: Development of the heated thin foil technique for investigating nonstationary transfer processes. Interfacial Phenom. Heat Transf. **6**, 179–185 (2018)

Karchevsky, A.L.: On a solution of the convolution type Volterra equation of the 1st kind. Advanced Math. Models & Applications **2**, 1–5 (2017)

Karchevsky, A.L.: Solution of the Convolution Type Volterra Integral Equations of the First Kind by the Quadrature-Sum Method. J. Appl. Ind. Math. **14**, 503–512 (2020)

Lappa, M.: Fluids, Materials and Microgravity: Numerical Techniques and Insights into the Physics, 1st edn. Elsevier Science, Oxford, England (2004)

Manzhirov, A.V., Polyanin, A.D.: Integral equations. Faktorial Press, Moskva, Methods of Solution. Handbook (2000)

Marchuk I., Karchevsky A., Surtaev A., Kabov O.: Heat flux at the surface of metal foil heater under evaporating sessile droplets. Int. J. Aerosp. Eng. **2015**, 391036 (2015)

Mollaret, R., Sefiane, K., Christy, J.R.E., Veyret, D.: Experimental and numerical investigation of the evaporation into air of a drop on a heated surface. Chem. Eng. Res. Des. **82**, 471–480 (2004)

Morozova, M.A., Novopashin, S.A.: Influence of Interfacial Phenomena on Viscosity and Thermal Conductivity of Nanofluids. Interfacial Phenom. Heat Transf. **7**, 151–165 (2019)

Panchamgam, S.S., Chatterjee, A., Plawsky, J.L., Wayner, P.C., Jr.: Comprehensive experimental and theoretical study of fliuid flow and heat transfer in a microscopic evaporating meniscus in a miniature heat exchanger. Int. J. Heat Mass. Tran. **51**, 53685379 (2008)

Pinchover, Y., Rubinstein, J.: An Introduction to Partial Differential Equations. Cambridge University Press, Cambridge (2005)

Polak, E.: Computational Methods in Optimization: A Unified Approach, Mathematics in Science and Engineering, vol. 77, Academic Press (1971)

Polikarpov, A.P., Graur, I.A., Gatapova, E.Y., Kabov, O.A.: Kinetic simulation of the non-equilibrium effects at the liquid-vapor interface. Int. J. Heat Mass. Tran. **136**, 449–456 (2019)

Polyanin, A.D., Manzhirov, A.V.: Handbook for integral equations. Fizmatlit, Moskva (2003)

Potash, M., Wayner, P.C., Jr.: Evaporation from a two-dimensional extended meniscus. Int. J. Heat Mass. Tran. **15**, 1851–1863 (1972)

Romanov, V.G., Karchevsky, A.L.: Determination of permittivity and conductivity of medium in a vicinity of a well having complex profile. Eurasian Journal of Mathematical and Computer Applications **6**, 64–74 (2018)

Saada, M.A., Chikh, S., Tadrist, L.: Evaporation of a sessile drop with pinned or receding contact line on a substrate with different thermophysical properties. Int. J. Heat Mass. Tran. **58**, 197–208 (2013)

Schweikert, K., Sielaff, A., Stephan, P.: Heat flux during dip-coating of a superheated substrate. Interfacial Phenom. Heat Transf. **7**, 269–281 (2019)

Schweikert K., Sielaff A., Stephan P.: On the transition between contact line evaporation and microlayer evaporation during the dewetting of a superheated wall. Int. J. Therm. Sci. **145**, 106025 (2019)

Schweizer, N., Stephan, P.: Experimental study of bubble behavior and local heat flux in pool boiling under variable gravity conditions. Multiph. Sci. Technol. **21**, 329–350 (2009)

Sobac, B., Brutin, D.: Triple-Line Behavior and Wettability Controlled by Nanocoated Substrates: Influence on Sessile Drop Evaporation. Langmuir **27**, 14999–15007 (2011)

Sobac, B., Brutin, D.: Thermal effects of the substrate on water droplet evaporation. Phys. Rev. E **86**, 021602 (2012)

Sodtke, C., Ajaev, V., Stephan, P.: Dynamics of volatile liquid droplets on heated surfaces: theory versus experiment. J. Fluid Mech. **610**, 343–362 (2008)

Stephan, P.C., Busse, C.A.: Analysis of the heat transfer coefficient of grooved heat pipe evaporator walls. Int. J. Heat Mass. Tran. **35**, 383–391 (1992)

Stephan, P., Brandt, C.: Advanced capillary structures for high performance heat pipes. Heat Transf. Eng. **25**, 78–85 (2004)

Tikhonov, A.N., Samarskii, A.A.: Equations of mathematical physics. Nauka, Moskva (1977)

Vasil'ev, F.P.: Numerical Methods for Solving Extremal Problems. Nauka, Moskva (1988)

Verlan', A.F., Sizikov, V.S.: Integral equations: methods, algorithms, codes. Handbook, Kiev, Naukova dumka (1986)

Publisher's Note Springer Nature remains neutral with regard to jurisdictional claims in published maps and institutional affiliations.

Interaction of advancing contact lines with defects on heated substrates

Vladimir S. Ajaev,[1,*] Elizaveta Ya. Gatapova,[2,3] and Oleg A. Kabov[2,3]
[1]*Department of Mathematics, Southern Methodist University, Dallas, Texas 75275, USA*
[2]*Kutateladze Institute of Thermophysics SB RAS, Lavrentyev Ave., 1, Novosibirsk, 630090, Russia*
[3]*Novosibirsk State University, Novosibirsk, 630090, Russia*

(Received 31 October 2019; accepted 23 January 2020; published 18 February 2020)

We consider an advancing contact line traveling over a region of locally modified wetting or thermal substrate properties. A lubrication-type model is developed to account for coupling of viscous flow, evaporation, surface tension, and disjoining pressure. Stick-slip-type behavior is found for a range of conditions as the contact line passes over the defect and explained by a temporary increase in the local stresses disrupting the liquid supply into the contact line region. A simple estimate of the degree of contact line slowdown is obtained and compared with the numerical simulation results. Tangential stresses arising from the action of the electric field on the interfacial changes are accounted for in our model; neglecting them would lead to an overprediction of the time of interaction between the contact line and the defect. Increasing the substrate temperature uniformly has little effect on contact line motion, but local increase of the temperature enhances the tendency of the contact line to be pulled back by the defect, an effect explained by the Marangoni stresses.

DOI: 10.1103/PhysRevE.101.022801

I. INTRODUCTION

Moving contact lines on heated surfaces appear in many applications such as spray cooling [1,2], boiling [3–5], heat pipes [6,7], and fuel cells [8]. In the context of the present work, we define a contact line as a line along which a liquid-gas interface comes into contact with a flat solid substrate based on macroscale observations. This definition includes the case of the so-called apparent contact line, corresponding to a situation when the solid is covered with an ultrathin wetting film but still appears dry on macroscale. The existence of adsorbed films in confined liquid-vapor systems was verified in several careful experimental studies [9,10]. The experimental results are consistent with the predictions of theoretical models originated in the classical works of Potash and Wayner [11] and Moosman and Homsy [12].

The challenges in mathematical modeling of moving contact lines stem from coupling of the effects of phase change, surface tension, viscous flow, and substrate wetting properties. Numerous studies of moving contact lines on heated substrates are a subject of recent comprehensive review articles [13,14]. Here we focus on a special case of when the solid substrate is spatially heterogeneous due to nonuniformity of either the local wetting properties or local temperature. Our interest stems from both the fundamental issue of how substrate imperfections affect contact line motion and heat transfer applications in which patterned and structured surfaces have been increasingly used for heat transfer enhancement for a variety of configurations [15].

Experimental studies of dynamic contact lines on heterogeneous surfaces reported a phenomenon of the so-called stick-slip motion in which a contact line remains stationary for a period of time and then rapidly advances until suddenly coming to a halt again [16]; the process is then repeated periodically. Quantitative modeling of this phenomena is a difficult problem, since an attempt to impose a contact angle, i.e., specify the angle between the local tangent to the fluid interface and the substrate, leads to a nonintegrable shear-stress singularity [17,18]. The presence of ultrathin precursor films ahead of advancing contact lines on spatially homogeneous nonheated substrates, detected in a number of experimental studies [19,20], has been suggested as a possible physical mechanism for removing the singularity [17]. However, alternative mechanisms for removing the singularity have been proposed in the literature, e.g., hydrodynamic slip at the liquid-solid interface [21,22]. The slip models have been implemented in several elaborate numerical studies [23,24].

A novel approach to overcoming the challenge of describing contact line motion over *heterogeneous* substrates was introduced in the works of Schwartz [25] and Thiele *et al.* [26,27]. Instead of imposing a contact angle condition, these authors describe substrate heterogeneity using spatially varying disjoining pressure. The concept of disjoining pressure, introduced in the pioneering works of Derjaguin *et al.*, is used to account for unbalanced intermolecular interactions and a number of other physical effects which become important when liquids are confined between two interfaces which are very close to each other, typically at a distance of about 100 nm or less [28,29]. While initially developed for perfectly wetting liquids, the disjoining pressure approach was later successfully applied to situations when the macroscopic contact angle is not zero but the solid substrate is still covered by an ultrathin film, a configuration often referred to as pseudopartial wetting [30,31]. For water and aqueous solutions, the disjoining pressure is usually approximated by a two-component expression [28,32], where the first component accounts for London–van der Waals dispersion forces,

*ajaev@smu.edu

 ©2020 American Physical Society

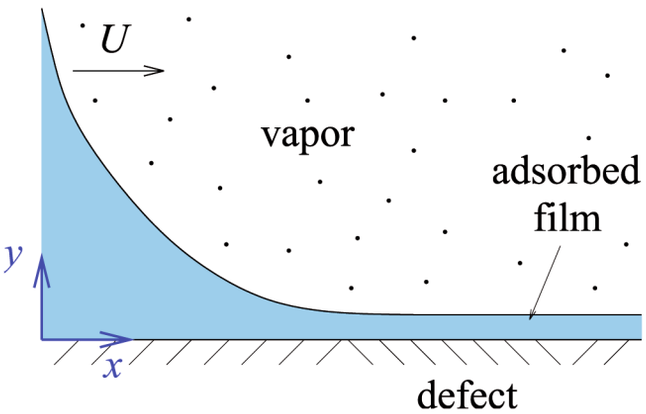

FIG. 1. Sketch of an apparent contact line advancing towards a substrate defect.

while the second one has to do with electrostatic interactions due to electrical charges at the solid-liquid and liquid-gas interfaces and the rearrangement of ions in the liquid. The two-component disjoining pressure approach allowed Thiele and Knobloch [26] to uncover rich bifurcation dynamics associated with pinning and depinning of droplets moving under external forcing, such as gravity. However, no phase change at the interface was considered by these authors.

The approach of Thiele *et al.* [26,27] was first applied to situations with evaporation in our recent study [33]. However, that work was mostly focused on the heat transfer aspects of the problem and only dealt with receding contact lines. Furthermore, it had two important limitations: the assumption of uniformity of the substrate temperature and neglect of the component of the shear stress at the interface due to action of the electric field on the interfacial charges [34]. In the present study we overcome both of these limitations.

II. FORMULATION

We consider a configuration of a liquid meniscus advancing in a capillary at a controlled speed, see Fig. 1. The liquid phase has density ρ and viscosity μ, the gas phase is assumed to be pure vapor of the same liquid, and the surface tension at the interface is σ. This configuration is directly relevant to the situation when a liquid plug is moving in pulsating heat pipes [6] and some flow boiling configurations [35], but can also be thought of as a simple model system for fundamental studies of interaction of advancing contact lines with substrate heterogeneities.

The starting point for our analysis is the general system of Navier-Stokes, continuity, and energy equations coupled to the equation describing the electrostatic effects. A number of simplifications are made to these equations using the ideas from the standard lubrication-type analysis [36–40]. It is convenient to outline these simplifications using nondimensional variables.

Let us discuss the choice for nondimensional velocities and coordinates. There are clearly two characteristic velocities in the problem. The first one is the dimensional velocity of forced motion of the meniscus U^*, controlled experimentally by, e.g., changing the pressure gradient in the capillary tube. The second one, denoted by U_e, is related to the flow which supports the evaporation process at the interface. If the limiting factor for the rate of phase change is the supply of heat to the interface and the superheat is given by ΔT, this velocity can be estimated as $U_e = k\Delta T/\rho\mathcal{L}R_0$, where k is the thermal conductivity of the liquid, $\mathcal{L}$ is the latent heat, and R_0 is the length scale set by the macroscopic geometry away from the contact line, e.g., the radius of curvature of a meniscus moving in a channel. Either U^* or U_e could be used as the velocity scale; we use the latter to facilitate easier comparisons with several recent studies [33,40]. The capillary number based on this velocity, $\mathrm{Ca} = \mu U_e/\sigma$, is typically very small, allowing one to use asymptotic methods to describe the apparent contact line region. Specifically, the lubrication-type model we are using is applicable when $\mathrm{Ca} \ll 1$ and the vertical length scale is much smaller than the horizontal one. Under these conditions, the local balance of viscous and capillary forces leads to the well-known Landau-Levich-Bretherton scaling [38,41]. In the present framework, this implies using $\mathrm{Ca}^{1/6}R_0$ and $\mathrm{Ca}^{1/3}R_0$ as the scales for the Cartesian coordinates x and y, respectively. We note that there is also another length scale in the problem, the Debye length defined by

$$\lambda_D = \sqrt{\frac{\epsilon k_B T^*}{e^2 \sum_{k=1}^{N} n_k^{(0)} z_k^2}}, \tag{1}$$

where ϵ is the electric permittivity of the liquid, k_B is the Boltzmann constant, and T^* is the dimensional temperature; we assume that the liquid contains N different types of ions of valencies z_k and bulk concentrations $n_k^{(0)}$ $(k = 1, 2, \ldots, N)$. Since the electrostatic effects make a substantial contribution to the disjoining pressure only when the electrical double layers formed near the interfaces overlap, we assume the Debye length to be of the same order of magnitude as the film thickness. In our formulation this corresponds to the assumption of the ratio $\kappa = \mathrm{Ca}^{1/3}R_0/\lambda_D$ being an order one quantity in the asymptotic limit of $\mathrm{Ca} \to 0$. This is a reasonable assumption due to small values of the Debye length, which are typically below 1 micron.

The potential of the electric field in the liquid phase is described by the classical Poisson's equation,

$$\nabla^2\psi^* = -\frac{\rho_E}{\epsilon}, \tag{2}$$

where ρ_E is the bulk charge density. Assuming the Boltzmann distribution for the ion concentrations allows one to rewrite Poisson's equation in the form

$$\nabla^2\psi^* = -\sum_{k=1}^{N} \frac{n_k^{(0)} e z_k}{\epsilon} \exp\left(\frac{z_k e\psi^*}{k_B T^*}\right). \tag{3}$$

For electric potentials well below the value of $k_B T/e$ (about 25 mV), the right-hand side of Eq. (3) can be linearized, an approach known as the Debye-Hückel approximation. With the Debye length defined by (1), we write the linearized equation in the form

$$\nabla^2\psi^* = \lambda_D^{-2}\psi^*. \tag{4}$$

With our choice of length scales, this approximation leads to the following leading-order equation for the nondimensional

potential,

$$\psi_{yy} = \kappa^2 \psi. \tag{5}$$

Here the potential is scaled by $q^*\lambda_D/\epsilon$, q^* being the dimensional charge density at the fluid interface, assumed constant and spatially uniform along the interface, with typical value on the order of 0.1mC/m^2, although some experimental studies report much smaller values; see, e.g., Ketelaar and Ajaev [40] for a discussion of experimental results. The substrate charge density $\tilde{q}$, scaled by q^*, is either constant or a prescribed function of the spatial coordinate. These conditions allow us to determine the potential from Eq. (5) and then express its value at the fluid interface, denoted by $\hat{\psi}$, as

$$\hat{\psi} = \frac{\tilde{q} + \cosh(\kappa h)}{\sinh(\kappa h)}, \tag{6}$$

where h is the liquid layer thickness scaled by $\text{Ca}^{1/3}R_0$.

The electrostatic effects in the contact line region are commonly described in terms of the so-called electrostatic component of disjoining pressure, Π_e. Detailed derivations of the general formulas for this quantity can be found, e.g., in the classical book of Derjaguin *et al.* [28] and in Appendix 1 of Kuchin *et al.* [42]. Taking advantage of the small ψ and the fixed charge density condition at the fluid interface, the nondimensional form of Eq. (8) of Ref. [42] reduces to the following simple form,

$$\Pi_e = \frac{Q}{2}(\hat{\psi}^2 - 1). \tag{7}$$

The dimensionless parameter $Q \equiv q^{*2}R_0/(\sigma\epsilon)$, often referred to as the electric Weber number, determines the relative magnitude of the Maxwell stresses at the fluid interface as compared to the surface tension. By substituting Eq. (6) into the formula for Π_e, the latter can be explicitly related to the film thickness via

$$\Pi_e = Q\left[\frac{1 + 2\tilde{q}\cosh(\kappa h) + \tilde{q}^2}{2\sinh^2(\kappa h)}\right]. \tag{8}$$

The structural component of disjoining pressure is neglected in the present study, but the contribution of the London–van der Waals component is retained, leading to the expression for the total disjoining pressure of the form

$$\Pi = \frac{\alpha}{h^3} + \Pi_e, \tag{9}$$

where $\alpha = |A|/(\sigma R_0^2\text{Ca})$, and A is the Hamaker constant, which measures the contribution of unbalanced London–van der Waals interactions to stresses in thin liquid layers [28,29]. Viscous flow which supplies liquid for evaporation is driven by a combination of the gradients of capillary and disjoining pressure, so the lubrication-type velocity profile [36–38] in the reference frame moving with the contact line at speed U is given by

$$u = -\tfrac{1}{2}(h_{xx} + \Pi)_x(y^2 - 2yh) - U + \tau y. \tag{10}$$

Here we introduced scaled tangential stress τ at the interface which is due to a combination of the Marangoni effect, i.e., the dependence of surface tension on temperature, and the action of electric field on the interfacial charges. The latter term is often neglected, but for small Ca it is actually of the same asymptotic order as the electrostatic contribution to the normal stress [34,40,43]. Accounting for both sources of variation of the interfacial shear stress leads to the following expression:

$$\tau = -\kappa^{-1}Q(\hat{\psi}_h h_x + \hat{\psi}_x) - \text{Ma}\, T_x^i, \tag{11}$$

where $\text{Ma} = \gamma\Delta T/(\sigma\text{Ca}^{1/3})$ is the modified Marangoni number expressed in terms of the slope γ of $\sigma(T)$ curve, T^i is the scaled interfacial temperature, defined in terms of its dimensional counterpart and the equilibrium saturation temperature T_s^* as

$$T^i = \frac{T^{i*} - T_s^*}{\Delta T}. \tag{12}$$

In the derivation of Eq. (11) we followed the same steps as described in detail in two recent studies [33,40]. Both capillary and electrostatic effects result in the shift of the equilibrium saturation temperature. In the constant-curvature meniscus region away from the apparent contact line, these effects are small so that the equilibrium saturation temperature there is actually close to the value that corresponds to a flat liquid-vapor interface with negligible effect of electrical charges. However, in the apparent contact line region, the high curvature and relatively large disjoining pressure lead to significant departures from the local equilibrium saturation temperature. In nondimensional terms, the shift is characterized by the nondimensional parameter $\delta = \sigma T_s^*/(\rho R_0 \Delta T \mathcal{L})$. Furthermore, departures from thermodynamic equilibrium due to phase change are measured by the parameter $K = kT_s^*\sqrt{2\pi\bar{R}T_s^*}/(2\rho_v R_0 \mathcal{L}^2\text{Ca}^{1/3})$ that emerges from the nondimensional form of the classical Hertz-Knudsen relation [44]. Detailed asymptotic derivation of this relation from the kinetic gas theory can be found, e.g., in Chap. 6 of Ref. [38]. The pressure and temperature jumps obtained by direct kinetic simulation are discussed in Polikarpov *et al.* [45]. Experimental investigations of this interfacial phenomenon are presented in [46]. In the present study we use the classical approach, which is valid when the mass flux in the energy balance is maximal and the heat flux in vapor phase is negligible [45,46]. Combining the boundary condition for the pressure drop at the liquid-vapor interface with the Hertz-Knudsen equation leads to the following relation between the evaporative mass flux and temperature at the liquid-vapor interface:

$$KJ = T^i - \delta(h_{xx} + \Pi). \tag{13}$$

Suppose the dimensional solid wall temperature is T_w^*, which is either constant or a specified function of the coordinate. Let us define the corresponding nondimensional quantity according to

$$T_w = \frac{T_w^* - T_s^*}{\Delta T}. \tag{14}$$

In the framework of our lubrication-type model, the temperature profile across the liquid layer is linear and therefore the interfacial and the solid wall temperatures are related by

$$T^i = T_w - Jh. \tag{15}$$

Substituting this expression into Eq. (13) leads to

$$J = \frac{T_w - \delta(h_{xx} + \Pi)}{K + h}. \tag{16}$$

The specified value of T_w implies that the model does not account for heat conduction in the solid substrate, an effect which may result in reduction of the heat flux and can in principle be incorporated into our model using the approach discussed, e.g., in Schweikert *et al.* [47]. For a heated wall at temperature T_w evaporation is suppressed when the value of J in Eq. (16) is zero, meaning that $\delta\Pi(h_0) = T_w$. If this equation has a positive solution h_0, then the ultrathin flat film of thickness h_0 is expected to form on the substrate. For disjoining pressure dominated by the London–van der Waals component, h_0 can always be found as long as the Hamaker constant A is negative.

The integral mass balance in nondimensional form in the lubrication-type framework is given by

$$h_t + J + \left(\int_0^h u\,dy\right)_x = 0. \tag{17}$$

Substituting the velocity profile from Eq. (10) together with Eq. (11) into the integral mass balance leads to the evolution equation,

$$h_t - Uh_x + J + \frac{1}{3}\Big[h^3\Big(h_{xx} + \frac{\alpha}{h^3} + \Pi_e\Big)_x\Big]_x - \frac{1}{2}\big[h^2\big(\kappa^{-1}Q(\hat{\psi}_h h_x + \hat{\psi}_x) + \mathrm{Ma}\,T_x^i\big)\big]_x = 0. \tag{18}$$

The boundary conditions for this equation are

$$h(0,t) = h_m, \quad h_{xx}(0,t) = 1, \quad h_x(L,t) = h_{xxx}(L,t) = 0, \tag{19}$$

where h_m is chosen large enough so that the effects of disjoining pressure near the left endpoint of the domain are negligible; in a typical simulation below, $h_m = 20$ and $L = 10$. The specified value of h_{xx} reflects the condition of constant curvature of the meniscus away from the wall, while the two conditions at $x = L$ are formulated to ensure that the interface remains flat in the ultrathin-film region. Equation (18) with these boundary conditions has been solved numerically using the finite-difference method with DVODE software package [48]. Local mesh refinement is implemented near the contact line.

III. MOTION OVER HOMOGENEOUS SUBSTRATE

In order to better understand the role of different factors in the determination of the interface shape and flow structure near an apparent contact line, let us first consider its motion over the substrate with spatially homogeneous properties. In the reference frame moving with the speed U, numerical simulations indicate that, following a short transient, a steady state is reached. The resulting shape of the interface in the apparent contact line region is shown by the solid line in Fig. 2(a). The interface has nearly constant curvature near the left end of the domain but then flattens near $x \sim 4.1$, indicating a transition to the flat ultrathin film. The dashed line in the plot indicates the constant-curvature line which matches the behavior of the interface near the left endpoint of the computational domain. The point of intersection of this line with the horizontal axis is used to define the position of the apparent contact line, x_{CL}, as is common in the literature;

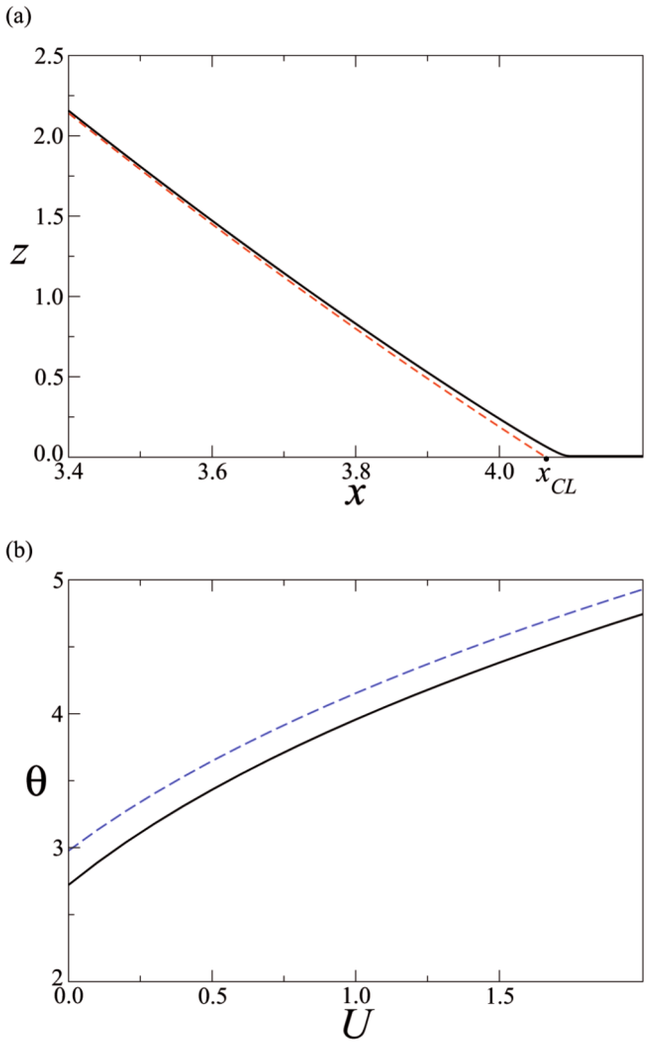

FIG. 2. Numerical results for homogeneous substrates: (a) steady interface shape in the apparent contact line region in the reference frame moving with the speed $U = 0.1$ for $\tilde{q} = 0$, with dashed line showing the constant-curvature fit to the interface; (b) apparent contact angle as a function of nondimensional speed for $\tilde{q} = 0$ (solid line) and $\tilde{q} = -1$ (dashed line). For all simulations, $\mathrm{Ma} = Q = 1$, $\kappa = 5$, $K = 0.01$, $\alpha = 10^{-5}$, $T_w = 0.1$, $\delta = 2 \times 10^{-4}$.

the magnitude of the dashed line slope at the point of intersection defines the apparent contact angle, θ. Alternatively, the contact line position can be defined by the maximum of local curvature; we verified that both definitions lead to similar conclusions about the contact line dynamics.

The rapid change of the interfacial curvature near $x \sim 4.1$ in Fig. 2(a) implies that the scaled capillary pressure, $-h_{xx}$, is significant in that region. However, the disjoining pressure, negligible near the left end of the computational domain, can become large in the contact line region. Indeed, in order to suppress evaporation in the flat thin film, i.e., ensure that the evaporative flux J is zero, the disjoining pressure there has to satisfy $\Pi = T_w/\delta$. Thus, both capillary and disjoining pressure gradients contribute to the flow that supplies liquid into the transition region, as needed to maintain evaporation

and continuous advancement of the contact line. There are also two additional physical effects due to shear stresses, as seen in Eq. (11); let us discuss their relative significance. The Marangoni stresses are expected to make a small contribution for uniformly heated substrates, since the interfacial temperature gradient is proportional to the small parameter δ; we verified this by running the code at different values of Ma and observing the change in the interface shape to be very small. To investigate the contribution of electrostatic effects to the shear stress, we use an estimate $\hat{\psi} \sim (\kappa h)^{-1}$ in place of Eq. (6), as appropriate for small film thickness in the transition region and for $\tilde{q}$ near zero. The component of the flow rate due to electrostatically induced shear stress in Eq. (18) can then be estimated by

$$\frac{Qh^2}{2\kappa}\hat{\psi}_h h_x \approx -\frac{Q}{2\kappa^2}h_x. \tag{20}$$

This flow contribution is comparable to that from the electrostatic disjoining pressure gradient, although it can still be negligible if the London–van der Waals component of disjoining pressure dominates, i.e., if $\Pi_x \sim -3\alpha h_x/h^4$ is large compared to other pressure gradients in the system. This can happen when the electric Weber number Q is small or when the inverse scaled Debye length κ is large.

Let us now discuss how the apparent contact angle θ, defined by the slope of the dashed line in Fig. 2(a) at $x = x_{CL}$, depends on dynamics and the substrate properties. We plot the angle as a function of the contact line speed in Fig. 2(b) for different values of the substrate charge density. The contact angles become larger when $\tilde{q}$ is increased and as the contact line speed increases. It is also clear from the plot that the contact angle is not very sensitive to $\tilde{q}$, as the difference between the two curves in Fig. 2(b) is rather small. The contact-angle correction is approximately the same for all values of the velocity investigated, which is not surprising given that $\tilde{q}$ characterizes a static property of the substrate not likely to be strongly coupled to flow dynamics.

When a contact line advances under the isothermal conditions, the cube of the dynamic contact angle is a linear function of $\mu U^*/\sigma$ for sufficiently small capillary numbers [17]. Our result in Fig. 2(b) shows qualitatively similar dependence since the angle increases with the speed and the curve $\theta(U)$ is concave down. However, we did not observe quantitative agreement with the isothermal results. This is not surprising, since our apparent contact angle value depends on complicated coupling between flows generated by contact line advancement and by the evaporation.

IV. INTERACTION WITH WETTABILITY DEFECT

Let us now consider a situation when an advancing contact line approaches an isolated wettability defect, which is incorporated into our model through the spatially dependent disjoining pressure, based on Eq. (8) with

$$\tilde{q} = q_d \exp\left[-\frac{(x - x_d)^2}{l_d^2}\right]. \tag{21}$$

Thus, the defect is basically a region of substrate where surface charges are presently characterized by three parameters: the maximum charge density q_d, location x_d, and the characteristic width l_d. Highly localized defects correspond to small values of the parameter l_d. While we focus on a specific method for wetting properties modification, i.e., surface charges, the conclusions are expected to be applicable to other situations when the disjoining pressure is spatially dependent.

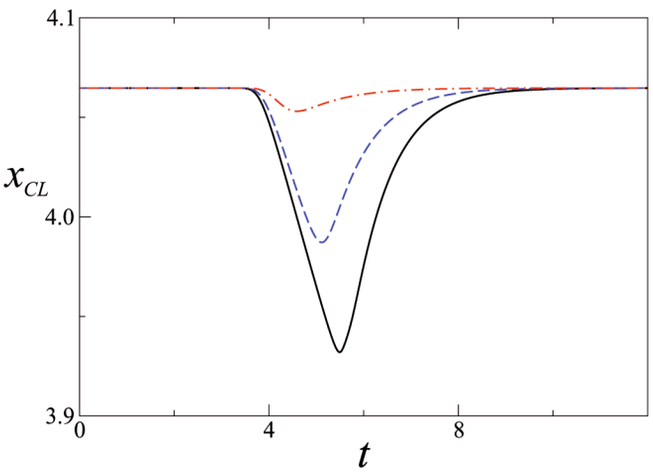

FIG. 3. Position of the advancing contact line as a function of time for $U = 0.1$, $l_d = 0.03$, and different defect amplitudes, $q_d = -1$ (solid line), $q_d = -0.5$ (dashed line), and $q_d = -0.1$ (dot-dashed line). All other parameter values are the same as in Fig. 2.

The substrate temperature for now is assumed uniform, an assumption to be revisited later in the present study. One may argue that this assumption is not realistic since the local change of chemical properties of the substrate should also be accompanied by the change in the thermal properties. However, there are well-known experimental techniques which allow one to modify the wetting properties only, e.g., by using very thin layers of coating [15,49].

A. Contact line dynamics

We solve Eq. (18) numerically with the initial conditions corresponding to the defect being far ahead of the contact line, $x_d = 4.5$. The position of the apparent contact line x_{CL} is then found from the numerical interface shape as illustrated in Fig. 2(a), i.e., as the point of intersection of the constant-curvature fitting meniscus with the substrate and plotted as a function of time in Fig. 3. The position is recorded in moving reference frame, so the negative slope corresponds so the slowdown of the advancing contact line. This slowdown is followed by an acceleration of the contact line after the defect is passed, both features being consistent with the experimentally observed stick-slip behavior. Comparison between the three lines in Fig. 3 illustrates the importance of the defect amplitude: the maximum of the slope magnitude and thus the degree of contact line slowdown decrease with the decrease in the magnitude of q_d. Figure 3 also shows that the total time of interaction of the contact line with the defect, estimated as the time it takes to recover the original contact line speed from the moment when the slowdown started, increases with defect amplitude.

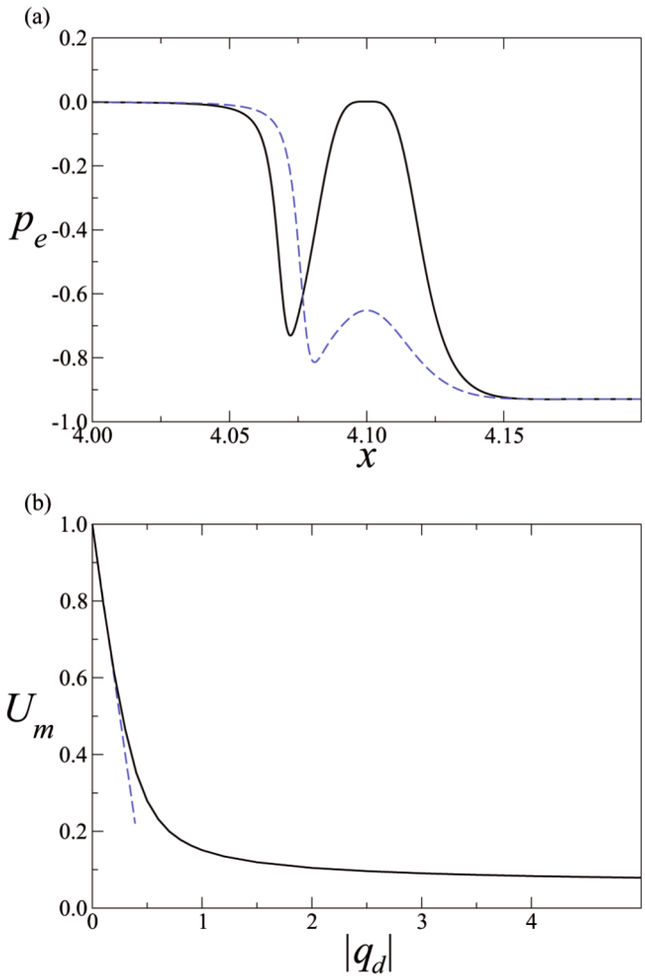

FIG. 4. (a) The electrostatic contribution to the effective pressure in the film $p_e = -\delta\Pi_e/T_w$ as a function of the coordinate for $q_d = -1$ (solid line), $q_d = -0.5$ (dashed line); (b) minimum contact line speed recorded during the interaction of the contact line with the defect is shown as a function of defect amplitude (for negative q_d); dashed line shows the prediction of the approximate model, Eq. (23).

Let us now discuss the physical explanation of the numerical results illustrated in Fig. 3. When the defect is far ahead of the contact line, the situation is similar to the homogeneous substrate case, Sec. III; liquid supply into the transition region is maintained by capillary and disjoining pressure gradients together with the tangential stresses. When the contact line region encounters the defect, the newly introduced charges in the electrical double layer near the solid partially neutralize the charges in the film and the osmotic pressure is decreased, meaning that the local effective pressure (including hydrodynamic and osmotic components) is increased. This pressure acts against the flow of the liquid into the apparent contact line region, as illustrated in Fig. 4(a). Both lines in the figure represent the electrostatic contribution to the effective pressure in the film, scaled by the maximum disjoining pressure, as a function of the coordinate but for different defect amplitudes. The pressure barrier introduced by the defect naturally increases as the amplitude is increased, as seen by comparing the solid and dashed lines in the figure. The contact line slowdown becomes more significant since the liquid flow has to overcome higher stresses, consistent with the result shown in Fig. 3.

To further elucidate the role of the defect amplitude, we plot the minimum contact line speed U_m during the interaction with the defect, scaled by U, as a function of the magnitude of q_d in Fig. 4(b), solid line. For higher defect amplitudes, the contact line slows down dramatically almost to the point of pinning, while weak defects can be passed with only slight decrease in the velocity, so that $U_m \sim 1$. For the latter case, a simple estimate of the degree of the slowdown can be obtained using the following arguments. The local change in the disjoining pressure induced by the presence of the defect is estimated from Eq. (8) as

$$\Delta\Pi_e \sim Qq_d(\kappa h)^{-2} \tag{22}$$

for $\kappa h \ll 1$ and $|q_d| \ll 1$. Assuming the defect width is comparable to the length scale of the interface shape change in the transition region, which is typically the case in our simulations, we can then state that the pressure gradient driving the flow into the contact line region reduces by a factor of $1 - 2|q_d|$ due to the defect. If the corresponding change in the flow rate is compensated by the change in the speed of the contact line, then the contact line speed has to decrease by the same factor, leading to the following simple nondimensional estimate:

$$U_m = 1 - 2|q_d|. \tag{23}$$

The dashed line in Fig. 4(b) represents this equation and agrees with the numerical results surprisingly well, even for $|q_d|$ as large as $\sim$0.3. Note that the argument does not account for complicated nonlinear coupling between contact line motion, evaporation, viscous flow, and tangential stresses, and thus is expected to break down for sufficiently large $|q_d|$, which is indeed seen in Fig. 4(b). Clearly, at large defect amplitudes the contact line slows down, basically to the point of pinning, in qualitative agreement with experimental data showing that only sufficiently strong defects lead to contact line pinning. In our model, complete pinning ($U_m = 0$) is not seen since the Hamaker constant is not affected by the defect and thus the London–van der Waals component of disjoining pressure continues to support slow contact line advancement even near the defect. We verified that U_m can be further reduced below the values seen in Fig. 4(b) by making α smaller.

Based on the estimate of U_m, Eq. (23), the total time of interaction of the contact line with defect is given by $l_d/[U(1 - 2|q_d|)]$. Note that this value, consistent with the result in Fig. 3, can be an order of magnitude larger than expected from the rough estimate, l_d/U, not accounting for the contact line slowdown.

Estimates such as Eq. (23) highlight the crucial role of the defect amplitude for the dynamics and suggest that the significance of the defect width l_d is less important, a conclusion supported by our numerical simulations. For example, the results in Fig. 5 show that the change of the defect width by a factor of 3 results in only a relatively small change in the contact line dynamics. Comparing the two curves in the figure, it is clear that more localized defects result in more contact line slowdown (indicated by the higher slope of the

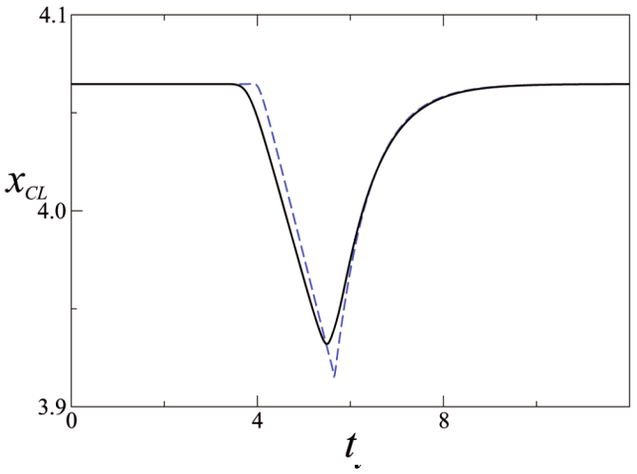

FIG. 5. Position of the advancing contact line as a function of time for $T_w = 0.1$, $q_d = -1$, and different defect widths, $l_d = 0.03$ (solid line) and $l_d = 0.01$ (dashed line).

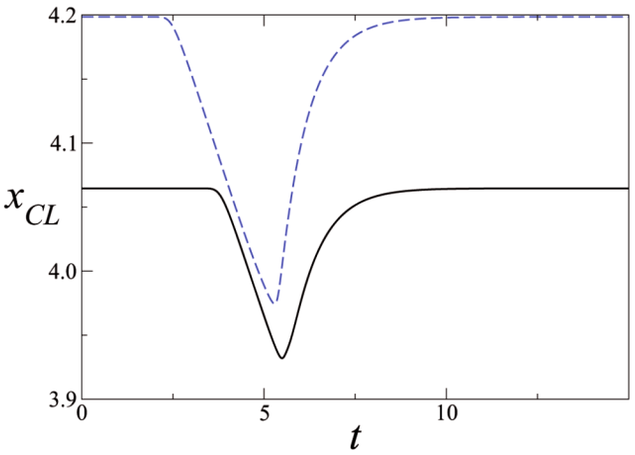

FIG. 6. Position of the advancing contact line as a function of time predicted by the solution of Eq. (18), solid line, and by the simplified version of the same model obtained by setting the shear stress τ to zero, dashed line.

dashed line) for the same defect amplitude at the first stage of interaction with the defect, while the contact line relaxation to the original speed at the second stage of the process is almost unaffected. The latter conclusion is not surprising, since the timescale of relaxation is determined by the timescale of viscous flow in the film after the contact line already passed the defect.

B. Shear stress at the interface

The shear stresses at the liquid-vapor interface, represented by Eq. (11) above, are often neglected in simulations of moving contact lines. However, our estimates of their relative importance in Sec. III suggests that even for the homogeneous substrates the condition of negligible shear stress is often not satisfied; we expect the shear-stress contribution to become even more significant when an additional short length scale is introduced due to the defect. It is therefore instructive to investigate the role of shear stresses in contact line dynamics in the presence of evaporation. Figure 6 illustrates the predictions of the contact line motion by our model and a simplified version of the same model with the interfacial stress τ set to zero. We observe that the simplified model overestimates the degree of the pull-back by the defect and that the discrepancy can be significant. Both the minimum contact line speed and the total time of interaction with the defect are not predicted correctly.

To better understand the role of the shear stress in the overall dynamics of the system, let us start by discussing the case of a homogeneous substrate. The electric potential $\hat{\psi}$ from Eq. (6) increases as the interface approaches the substrate, i.e., in the positive x direction. Based on Eq. (11), the interfacial stress vector is in the opposite direction. This can be explained in physical terms by electrical charges near the interface interacting with their electrostatic images which have the same sign (due to zero derivative condition on the potential at the wall); thus there is repulsive interaction pushing the interfacial charges away from the substrate. An additional smaller contribution due to the Marangoni effect acts in the same direction since the interfacial temperature is increased as the hot wall is approached, see Eq. (10). The flow generated by all these tangential stresses is in the direction opposite to the main flow supplying the liquid into the region of high evaporation. By artificially removing the tangential stress component, we eliminate these extra contributions and the contact line is expected to shift to the right, as indeed is seen in Fig. 6.

When a defect is introduced, with no contribution from shear-induced flow, all adjustments for altered local wetting properties are made in the pressure gradient value, meaning that larger changes in pressure and thus stronger interface deformation can be expected. This results in a larger shift in the apparent contact line position, as seen in Fig. 6.

C. Effects of evaporation

One of the key features of the proposed model is substrate heating and the resulting evaporative mass loss which is coupled to liquid flow. To the best of our knowledge, the interaction of advancing contact lines with defects in the presence of evaporation has not been addressed in the literature previously, despite its importance for numerous heat transfer applications such as boiling and spray cooling. In order to get some insight into how the stick-slip motion can be affected by the evaporation, we carried out numerical simulations at different values of the substrate superheat.

When the defect is far ahead of the contact line, the steady-state solutions will be different depending on the superheat. In addition to changes in the local structure of the solutions, there is also a shift in the contact line location which is purely due to the boundary condition of the specified thickness at the left end of the computational domain, a shift which has no physical significance. Therefore, we present all of our results in terms of the contact line position $\hat{x}_{CL}$ measured relative to its value for the homogeneous substrate. The simulation results for a range of values of T_w between 0.05 and 0.3 show that the increase in the superheat has little effect on the slope of the line, i.e., the value of U_m, at the first stage of the process

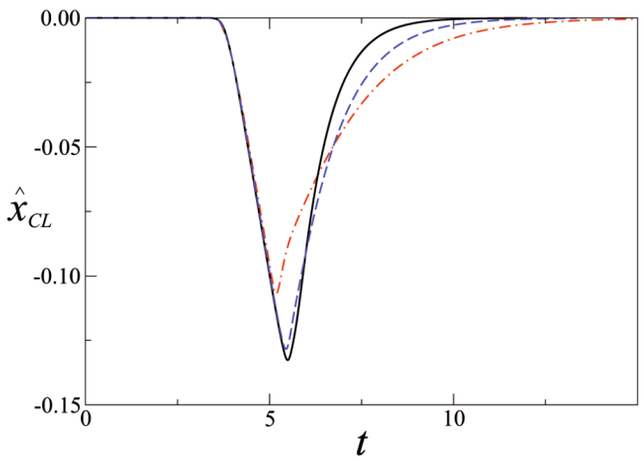

FIG. 7. Shift in the position of the advancing contact line as a function of time for $T_w = 0.02$ (dot-dashed line), $T_w = 0.05$ (dashed line), and $T_w = 0.1$ (solid line).

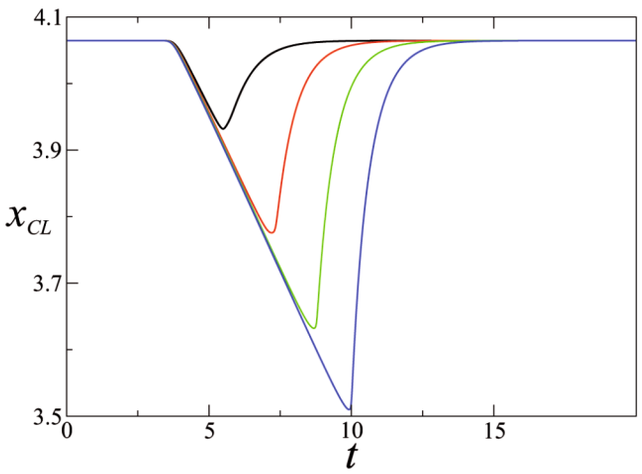

FIG. 8. Position of the advancing contact line as a function of time for the values of T_d equal to (from top curve to bottom) 0.1, 0.15, 0.2, 0.25 with $T_{w0} = 0.1$, $q_d = -1$, $l_d = 0.03$.

of contact line–defect interaction, as seen by comparing the solid and dashed lines in Fig. 7. This is not surprising based on the arguments made in Sec. IV A about the defect amplitude being the key quantity determining the degree of the contact line slowdown. The relaxation of the interface after the defect passed proceeds faster for higher temperature, as the interface can now adjust to the equilibrium shape not only via surface tension effects but also via evaporative mass transport. The evaporative mechanism can be expected to weaken significantly at lower temperatures, which was indeed observed in our simulations for T_w near 0.02 and below, illustrated by the dot-dashed line in Fig. 7. At these low temperatures, the degree of the contact line pullback during the interaction with the defect also starts to decrease slightly.

V. NONUNIFORM SUBSTRATE TEMPERATURE

Nonuniformity of the substrate chemical properties often leads to the nonuniformity of the thermal properties as well, unless special care is taken to avoid the latter. Furthermore, substrate temperature can be highly nonuniform in electronics cooling applications, often characterized by the formation of the so-called hot spots [50]. When such a substrate is cooled by a thin-film flow [51,52], the film can rupture, leading to formation of moving contact line on a substrate with highly nonuniform temperature. The objective of the present section is to analyze how the *local* change in the substrate temperature could lead to changes in the contact line motion and conditions of pinning. We take the Gaussian-type temperature profile

$$T_w = T_{w0} + (T_d - T_{w0}) \exp\left[-\frac{(x - x_d)^2}{l_d^2}\right], \qquad (24)$$

with the maximum temperature T_d in the middle of the defect assumed to be higher than the value away from it, T_{w0}. Local increase in the substrate temperature is shown to increase the degree of contact line pinning significantly, as illustrated in Fig. 8. The overall time of the interaction of the contact line with the defect also increased substantially. We attribute these changes to the Marangoni effect pushing liquid away from the hotter region encountered during the contact line advancement. The Marangoni effect was rather small previously due to the interface temperature gradient being proportional to the small parameter δ. However, for nonuniform substrate temperature the term T_w in Eq. (15) is also a function of the spatial coordinate and thus contributes to the temperature gradient; that term is independent from δ and is not expected to be small.

VI. CONCLUSIONS

We investigated the interaction of advancing contact lines with defects. For most of our study, we focus on the situation when the wetting properties of the substrate are changed locally, e.g., by the presence of electrical surface charges, but the temperature and thermal properties remain uniform. The defect amplitude, a measure of the magnitude of the change in the local wetting properties, is identified as the key parameter in the dynamics of the contact line. For the case of local modification of the substrate properties by surface charges, the amplitude can be interpreted simply as the local scaled charge density. Stick-slip type behavior is found for sufficiently large defect amplitudes; weak defects result only in slight reduction of the contact line speed. For the latter case, a simple analytical model predicts linear decrease of contact line velocity with the defect amplitude; the analytical formula matches the numerical result in the region where both are applicable. The contact line dynamics is much less sensitive to the changes in the defect width and the substrate temperature, as long as the latter remains spatially uniform.

The classical disjoining pressure models involve modifications in the normal stress balance at the interface but not in the shear stress. Our results point to the limitations of this approach, especially for the interaction between a contact line and a highly localized defect. The tangential stress is shown to be comparable to the normal stress contributions of the electrostatic forces. Its relative importance increases as the

Debye length is increased. Models neglecting the shear-stress effects at the interface tend to overestimate the degree of the vapor-liquid interface deformation.

The effect of local change in the substrate temperature is investigated and shown to result in a dramatic increase of the degree of the contact line pull-back by the defect and the overall time of the interaction. This dynamics is explained by the role of the Marangoni stresses, which induce the flow away from a hot region encountered during the advancement of the contact line, a different mechanism of contact line pinning not related to the wetting properties of the substrate.

Our results indicate that contact line motion is very sensitive even to small defects on the substrate. Thus, accurate experimental recording of contact line velocity can provide valuable information about the chemical properties and degree of uniformity of the substrate on micro- or even nanoscale. Such properties, including the presence of defects, can be investigated by a variety of methods such as scanning electron microscopy, but these methods require much more sophisticated equipment than simple experimental study of contact line motion.

ACKNOWLEDGMENT

This study was supported by the Russian Science Foundation (Project No. 19-19-00695).

[1] C. Sodtke and P. Stephan, Int. J. Heat Mass Transfer **50**, 4089 (2007).
[2] J. Kim, Int. J. Heat Fluid Flow **28**, 753 (2007).
[3] P. C. Stephan and C. Brandt, Heat Transfer Eng. **25**, 78 (2004).
[4] V. K. Dhir, G. R. Warrier, and E. Aktinol, J. Heat Transfer **135**, 061502 (2013).
[5] A. Urbano, S. Tanguy, G. Huber, and C. Colin, Int. J. Heat Mass Transf. **123**, 1128 (2018).
[6] V. Srinivasan, V. Marty-Jourjon, S. Khandekar, F. Lefèvre, and J. Bonjour, Int. J. Heat Mass Transf. **89**, 176 (2015).
[7] S. Lips, V. Sartre, F. Lefevre, S. Khandekar, and J. Bonjour, Interfacial Phenom. Heat Transf. **4**, 33 (2016).
[8] E. F. Médici and J. S. Allen, Int. J. Heat Mass Transf. **65**, 779 (2013).
[9] S. S. Panchamgam, J. L. Plawsky, and P. C. Wayner Jr., Exp. Therm. Fluid Sci. **30**, 745 (2006).
[10] S. S. Panchamgam, A. Chatterjee, J. L. Plawsky, and P. C. Wayner Jr., Int. J. Heat Mass Transfer **51**, 5368 (2008).
[11] M. Potash and P. C. Wayner Jr., Int. J. Heat Mass Transfer **15**, 1851 (1972).
[12] S. Moosman and G. M. Homsy, J. Colloid Interface Sci. **73**, 212 (1980).
[13] P. A. Raghupathi and S. G. Kandlikar, Int. J. Heat Mass Transf. **95**, 296 (2016).
[14] V. S. Ajaev and O. A. Kabov, Int. J. Heat Mass Transfer **108**, 918 (2017).
[15] A. R. Betz, J. Xu, H. Qiu, and D. Attinger, Appl. Phys. Lett. **97**, 141909 (2010).
[16] H. Tavana, G. Yang, C. M. Yip, D. Appelhans, S. Zschoche, K. Grundke, M. L. Hair, and A. W. Neumann, Langmuir **22**, 628 (2006), .
[17] P. G. de Gennes, Rev. Mod. Phys. **57**, 827 (1985).
[18] E. B. Dussan, Annu. Rev. Fluid Mech. **11**, 371 (1979).
[19] H. Hervet and P. G. de Gennes, C.R. Acad. Sci. Paris II **299**, 499 (1984).
[20] H. P. Kavehpour, B. Ovryn, and G. H. McKinley, Phys. Rev. Lett. **91**, 196104 (2003).
[21] C. Huh and L. Scriven, J. Colloid Interface Sci. **35**, 85 (1971).
[22] H. P. Greenspan, J. Fluid Mech. **84**, 125 (1978).
[23] P. D. Spelt, J. Comput. Phys. **207**, 389 (2005).
[24] S. Afkhami, S. Zaleski, and M. Bussmann, J. Comput. Phys. **228**, 5370 (2009).
[47] K. Schweikert, A. Sielaff, and P. Stephan, Interfacial Phenom. Heat Transf. **7**, 269 (2019).
[48] A. C. Hindmarsh, P. N. Brown, K. E. Grant, S. L. Lee, R. Serban, D. E. Shumaker, and C. S. Woodward, ACM Trans. Mathematical Software (TOMS) **31**, 363 (2005).
[49] B. Sobac and D. Brutin, Langmuir **27**, 14999 (2011).
[25] L. W. Schwartz, Langmuir **14**, 3440 (1998).
[26] U. Thiele and E. Knobloch, Phys. Rev. Lett. **97**, 204501 (2006).
[27] P. Beltrame, P. Hänggi, and U. Thiele, Europhys. Lett. **86**, 24006 (2009).
[28] B. V. Derjaguin, N. V. Churaev, and V. M. Muller, *Surface Forces* (Plenum Press, NY, 1987).
[29] J. N. Israelachvili, *Intermolecular and Surface Forces*, 3rd ed. (Academic Press, San Diego, 2011).
[30] F. Brochard-Wyart, J. M. Di Meglio, D. Quere, and P. G. De Gennes, Langmuir **7**, 335 (1991).
[31] V. S. Ajaev, T. Gambaryan-Roisman, and P. Stephan, J. Colloid Interface Sci. **342**, 550 (2010).
[32] A. Sharma and A. T. Jameel, J. Colloid Interface Sci. **161**, 190 (1993).
[33] E. Gatapova, O. A. Kabov, and V. S. Ajaev, Int. J. Heat Mass Transfer **142**, 118355 (2019).
[34] C. Ketelaar and V. S. Ajaev, Phys. Rev. E **91**, 052403 (2015).
[35] S. G. Kandlikar, Exp. Therm. Fluid Sci. **26**, 389 (2002).
[36] A. Oron, S. H. Davis, and S. G. Bankoff, Rev. Mod. Phys. **69**, 931 (1997).
[37] R. V. Craster and O. K. Matar, Rev. Mod. Phys. **81**, 1131 (2009).
[38] V. S. Ajaev, *Interfacial Fluid Mechanics: A Mathematical Modeling Approach* (Springer, New York, 2012).
[39] Y. Kabova, V. Kuznetsov, O. Kabov, T. Gambaryan-Roisman, and P. Stephan, Int. J. Heat Mass Transfer **68**, 527 (2014).
[40] C. Ketelaar and V. S. Ajaev, Phys. Fluids **27**, 112110 (2015).
[41] V. S. Ajaev and G. M. Homsy, J. Colloid Interface Sci. **240**, 259 (2001).
[42] I. V. Kuchin, O. K. Matar, R. V. Craster, and V. M. Starov, Soft Matter **10**, 6024 (2014).
[43] S. R. Maduar, A. V. Belyaev, V. Lobaskin, and O. I. Vinogradova, Phys. Rev. Lett. **114**, 118301 (2015).
[44] R. W. Schrage, *A Theoretical Study of Interface Mass Transfer* (Columbia University Press, New York, 1953).
[45] A. Polikarpov, I. Graur, E. Gatapova, and O. Kabov, Int. J. Heat Mass Transfer **136**, 449 (2019).
[46] E. Y. Gatapova, I. A. Graur, O. A. Kabov, V. M. Aniskin, M. A. Filipenko, F. Sharipov, and L. Tadrist, Int. J. Heat Mass Transfer **104**, 800 (2017).
[50] A. Bar-Cohen, J. R. Sheehan, and E. Rahim, Microgravity Sci. Technol. **24**, 1 (2012).
[51] E. Y. Gatapova and O. A. Kabov, Int. J. Heat Mass Transfer **51**, 4797 (2008).
[52] O. A. Kabov, D. V. Zaitsev, V. V. Cheverda, and A. Bar-Cohen, Exp. Therm. Fluid Sci. **35**, 825 (2011).

Патенты полученные в период 2017 – 2022 (14) *

1. * Кабов О.А., Чеверда В. В., Быковская Е.Ф., Сибиряков Н.Е., Способ охлаждения электронного оборудования. Патент РФ № 2755608 от 17.09.2021.
2. * Кабов О.А., Чеверда В. В. Двухфазная, гибридная, однокомпонентная система охлаждения электронного оборудования. Патент РФ № 2760884 от 01.12.2021.
3. * Кабов О.А., Гатапова Е. Я., Быковская Е.Ф. Способ охлаждения электронного оборудования с использованием комбинированных пленочных и газокапельных потоков. Патент РФ № 2732624 от 21.09.2020.
4. * Кабов О.А., Гатапова Е.Я., Быковская Е.Ф. Способ охлаждения электронного оборудования пленочными и капельными потоками жидкости с использованием оребрения. Патент РФ № 2706325 от 15.11.2019.
5. * Чиннов Е.А., Кабов О.А. Испарительная система охлаждения светодиодного модуля. ***Евразийский патент*** №029368 от 30.03.18.
6. Кабов О.А., Зайцев Д.В., Люлин Ю.В., Быковская Е.Ф., Устройство для испарения жидкости. Патент РФ №2649164 от 30.03.18.
7. Кабов О.А., Зайцев Д.В., Быковская Е.Ф. Способ охлаждения электронного оборудования с использованием комбинированных пленочных и капельных потоков жидкости. Патент РФ №2649170 от 30.03.18.
8. Кабов О.А., Марчук И.В., Люлин Ю.В. Интенсивный конденсатор пара с контрастным и градиентным смачиванием. Патент РФ №2640888 от 12.01.2018.
9. Кабов О.А., Марчук И.В., Люлин Ю.В., Быковская Е.Ф. Плоский эффективный конденсатор-сепаратор для микрогравитации и транспортных приложений. Патент РФ № 2640887 от 12.01.2018.
10. Кабов О.А., Гатапова Е.Я. Интенсифицирующая теплообменная поверхность для удлинения динамического мениска. Патент РФ №2637802 от 07.12.2017.
11. Кабов О.А., Люлин Ю.В., Марчук И.В., Быковская Е.Ф. Эффективный конденсатор пара для условий микрогравитации. Патент РФ № 2635720 от 15.11.2017.
12. Кабов О. А., Чеверда В. В., Марчук И. В., Быковская Е.Ф. Устройство для формирования микроручейкового течения жидкости в микро- и миниканалах. Патент РФ № 2629516 от 29.08.2017.
13. Кабов О.А., Гатапова Е.Я., Орлик Е.В., Зайцев Д.В., Чиннов Е.А., Быковская Е.Ф. Устройство формирования пристенных капельных течений жидкости в микро- и мини-каналах. Патент РФ № 2620732 от 29.05.2017.
14. Кабов О.А., Люлин Ю.В., Марчук И.В. Конденсатор-сепаратор для двухкомпонентных двухфазных систем. Патент РФ № 2614897 от 30.03.2017.

* - звездочкой отмечены патенты, включенные в подборку избранных трудов (5)

РОССИЙСКАЯ ФЕДЕРАЦИЯ

ПАТЕНТ

НА ИЗОБРЕТЕНИЕ

№ 2755608

Способ охлаждения электронного оборудования

Патентообладатель: ***федеральное государственное автономное образовательное учреждение высшего образования "Новосибирский национальный исследовательский государственный университет" (Новосибирский государственный университет, НГУ) (RU)***

Авторы: ***Кабов Олег Александрович (RU), Чеверда Вячеслав Владимирович (RU), Быковская Елена Федоровна (RU), Сибиряков Николай Егорович (RU)***

Заявка № **2020142120**
Приоритет изобретения **18 декабря 2020 г.**
Дата государственной регистрации
в Государственном реестре изобретений
Российской Федерации **17 сентября 2021 г.**
Срок действия исключительного права
на изобретение истекает **18 декабря 2040 г.**

Руководитель Федеральной службы
по интеллектуальной собственности

ДОКУМЕНТ ПОДПИСАН ЭЛЕКТРОННОЙ ПОДПИСЬЮ
Сертификат 0x02A5CFBC00B1ACF59A40A2F08092E9A118
Владелец **Ивлиев Григорий Петрович**
Действителен с 15.01.2021 по 15.01.2035

Г.П. Ивлиев

РОССИЙСКАЯ ФЕДЕРАЦИЯ

ПАТЕНТ

НА ИЗОБРЕТЕНИЕ

№ 2760884

ДВУХФАЗНАЯ, ГИБРИДНАЯ, ОДНОКОМПОНЕНТНАЯ СИСТЕМА ОХЛАЖДЕНИЯ ЭЛЕКТРОННОГО ОБОРУДОВАНИЯ

Патентообладатель: ***Федеральное государственное бюджетное учреждение науки Институт теплофизики им. С.С. Кутателадзе Сибирского отделения Российской академии наук (RU)***

Авторы: ***Кабов Олег Александрович (RU), Чеверда Вячеслав Владимирович (RU)***

Заявка № **2020143554**
Приоритет изобретения **29 декабря 2020 г.**
Дата государственной регистрации
в Государственном реестре изобретений
Российской Федерации **01 декабря 2021 г.**
Срок действия исключительного права
на изобретение истекает **29 декабря 2040 г.**

Руководитель Федеральной службы
по интеллектуальной собственности

ДОКУМЕНТ ПОДПИСАН ЭЛЕКТРОННОЙ ПОДПИСЬЮ
Сертификат 0x02A5CFBC00B1ACF59A40A2F08092E9A118
Владелец **Ивлиев Григорий Петрович**
Действителен с 15.01.2021 по 15.01.2035

Г.П. Ивлиев

РОССИЙСКАЯ ФЕДЕРАЦИЯ

ПАТЕНТ

НА ИЗОБРЕТЕНИЕ

№ 2732624

СПОСОБ ОХЛАЖДЕНИЯ ЭЛЕКТРОННОГО ОБОРУДОВАНИЯ С ИСПОЛЬЗОВАНИЕМ КОМБИНИРОВАННЫХ ПЛЕНОЧНЫХ И ГАЗОКАПЕЛЬНЫХ ПОТОКОВ

Патентообладатель: ***Федеральное государственное бюджетное учреждение науки Институт теплофизики им. С.С. Кутателадзе Сибирского отделения Российской академии наук (ИТ СО РАН) (RU)***

Авторы: ***Кабов Олег Александрович (RU), Гатапова Елизавета Яковлевна (RU), Быковская Елена Фёдоровна (RU)***

Заявка № **2019144491**

Приоритет изобретения **27 декабря 2019 г.**

Дата государственной регистрации в Государственном реестре изобретений Российской Федерации **21 сентября 2020 г.**

Срок действия исключительного права на изобретение истекает **27 декабря 2039 г.**

Руководитель Федеральной службы по интеллектуальной собственности

Г.П. Ивлиев

РОССИЙСКАЯ ФЕДЕРАЦИЯ

ПАТЕНТ

НА ИЗОБРЕТЕНИЕ

№ 2706325

СПОСОБ ОХЛАЖДЕНИЯ ЭЛЕКТРОННОГО ОБОРУДОВАНИЯ ПЛЕНОЧНЫМИ И КАПЕЛЬНЫМИ ПОТОКАМИ ЖИДКОСТИ С ИСПОЛЬЗОВАНИЕМ ОРЕБРЕНИЯ

Патентообладатель: ***Федеральное государственное бюджетное учреждение науки Институт теплофизики им. С.С. Кутателадзе Сибирского отделения Российской академии наук (ИТ СО РАН) (RU)***

Авторы: ***Кабов Олег Александрович (RU), Гатапова Елизавета Яковлевна (RU), Быковская Елена Фёдоровна (RU)***

Заявка № **2018146202**

Приоритет изобретения **25 декабря 2018 г.**

Дата государственной регистрации в Государственном реестре изобретений Российской Федерации **15 ноября 2019 г.**

Срок действия исключительного права на изобретение истекает **25 декабря 2038 г.**

Руководитель Федеральной службы по интеллектуальной собственности

Г.П. Ивлиев

ЕВРАЗИЙСКАЯ ПАТЕНТНАЯ ОРГАНИЗАЦИЯ
ЕВРАЗИЙСКОЕ ПАТЕНТНОЕ ВЕДОМСТВО

ЕВРАЗИЙСКИЙ ПАТЕНТ

ЕВРАЗИЙСКИЙ ПАТЕНТ

№ 029368

Название изобретения:

«ИСПАРИТЕЛЬНАЯ СИСТЕМА ОХЛАЖДЕНИЯ СВЕТОДИОДНОГО МОДУЛЯ»

Патентовладелец (льцы):

ФЕДЕРАЛЬНОЕ ГОСУДАРСТВЕННОЕ БЮДЖЕТНОЕ УЧРЕЖДЕНИЕ НАУКИ ИНСТИТУТ ТЕПЛОФИЗИКИ ИМ. С.С. КУТАТЕЛАДЗЕ СИБИРСКОГО ОТДЕЛЕНИЯ РОССИЙСКОЙ АКАДЕМИИ НАУК (ИТ СО РАН) (RU)

Изобретатель (и):

Чиннов Евгений Анатольевич, Кабов Олег Александрович (RU)



Заявка №:	**201600127**
Дата подачи заявки:	**22 августа 2014 г.**
Дата выдачи патента:	**30 марта 2018 г.**

Настоящим удостоверяется, что евразийский патент выдан на изобретение с формулой, опубликованной в Бюллетене Евразийского патентного ведомства «Изобретения (евразийские заявки и патенты)» № 3 / 2018 год.

При уплате установленных годовых пошлин патент действует на территории государств - участников Евразийской патентной конвенции – Азербайджанской Республики, Кыргызской Республики, Республики Армения, Республики Беларусь, Республики Казахстан, Республики Таджикистан, Российской Федерации, Туркменистана.

ТЛЕВЛЕСОВА Сауле Январбековна
Президент Евразийского патентного ведомства